

# **Acta Geodaetica, Geophysica et Montanistica Hungarica**

**VOLUME 20, NUMBER 1, 1985**

**EDITOR-IN-CHIEF**

**A TÁRCZY-HORNOCH**

**EDITOR**

**J VERŐ**

**EDITORIAL BOARD**

**A ÁDÁM, GY BARTA, B BÉLL, P BIRÓ,**

**L KAPOLYI, F KOVÁCS, F MARTOS, A MESKÓ, D RÁCZ,**

**J SOMOGYI, J ZÁMBÓ**



**Akadémiai Kiadó, Budapest**

AGGM 20 (1) 1—197. (1985) HU ISSN 0374-1842

# ACTA GEODAETICA, GEOPHYSICA et MONTANISTICA HUNGARICA

## A Quarterly Journal of the Hungarian Academy of Sciences

---

*Acta Geodaetica, Geophysica et Montanistica (AGGM)* publishes original reports on geodesy, geophysics and minings in English.

AGGM is published in yearly volumes of four numbers by

AKADÉMIAI KIADÓ

Publishing House of the Hungarian Academy of Sciences  
H-1054 Budapest, Alkotmány u. 21.

Manuscripts and editorial correspondence should be addressed to

*AGGM Editorial Office*  
H-9401 Sopron P.O. Box 5

*Subscription information*

Orders should be addressed to

KULTURA Foreign Trading Company  
H-1389 Budapest P.O. Box 149

## INSTRUCTIONS TO AUTHORS

*Manuscripts* should be sent to the editors (MTA Geodéziai és Geofizikai Kutató Intézet, AGGM Editorial Office, H-9401 Sopron, P.O.Box 5, HUNGARY). Only articles not submitted for publication elsewhere are accepted.

Manuscripts should be typewritten in duplicate, double-spaced, 25 lines with 50 letters each. The papers generally include the following components, which should be presented in the order listed.

1. Title, name of author(s), affiliation, dateline, abstract, keywords
2. Text, acknowledgements
3. References
4. Footnotes
5. Legends
6. Tables and illustrations

1. The *affiliation* should be as concise as possible and should include the complete mailing address of the authors. The *date of receipt* of the manuscript will be supplied by the editors. The abstract should not exceed 250 words and should clearly and simply summarize the most important methods and results. 5–10 significant expressions describing the content are used as *keywords*. Authors may recommend these keywords.

2. The *text* should be generally in English and as short and clear as possible. From Hungarian authors papers are also accepted in Hungarian.

The section heading should *not* be underlined or in capitals.

Please note that underlining denotes special types:

- single underlining: italics
- double underlining: bold-face roman

**ACTA GEODAETICA,  
GEOPHYSICA et MONTANISTICA  
HUNGARICA**

A Quarterly Journal of the Hungarian Academy of Sciences

EDITOR-IN-CHIEF

A Tárczy-Hornoch

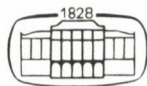
EDITOR

J Verő

EDITORIAL BOARD

A Ádám, Gy Barta, B Béll, P Biró, L Kapolyi,  
F Kovács, F Martos, A Meskó, D Rácz, J Somogyi, J Zábó

VOLUME 20



Akadémiai Kiadó, Budapest  
1985



## CONTENTS

The presumable connection between the internal structure of the Earth and geodynamics — <i>Barta Gy</i> .....	3
Remarks on seismicity estimations in Hungary — <i>Bisztricsány E</i> .....	7
Origin and dynamics of Earth's core — <i>Savić P</i> and <i>Teleki G</i> .....	13
Some properties of the Earth's core looked upon on the basis of investigations of the force fields of the Earth — <i>Barta Gy</i> .....	29
New points of view for determining the parameters of the reference ellipsoid of the Earth — <i>Hajósi A</i> .....	61
Geophysical aspects in the selection of a geodynamic test area in Transdanubia (Western Hungary). Contribution to the International Lithosphere Programme — <i>Ádám A</i> .....	71
Measurement of the plasma parameters in the ionosphere by night with retarding potencial analyzers on board of the geophysical rocket Vertical-10 — <i>Bencze P, Kovács K, Szemerey I, Afonin V, Bezrukih V V</i> .....	81
Elastodynamics expressed in terms of Maxwell's theory of electrodynamics, cylindrical wave propagation and elastic wave propagation in inhomogeneous media — <i>Förtsch O</i> and <i>Koch E</i> .....	85
Connection between the interplanetary medium and pulsations of the geomagnetic field with periods 1–600 s — <i>Holló L</i> .....	127
Telluric and magnetotelluric information about the geological structure of Transdanubia — <i>Nemesi L, Hobot J, Varga G</i> .....	135
Introduction to the series "Conducting crustal anomalies in geothermally active areas" — <i>Ádám A, Fournier H, Verő J</i> .....	151
Magnetotelluric results in North-East Iceland — Electrical conductivity, temperature, crust- and mantle structure — <i>Beblo M, Björnsson A</i> .....	153
The hot dome of Taco Ralo, in the NW of Argentine — <i>Vatin-Perignon N, Composiello C, Mamani M, Maidana A, Keller M, Gasco J C, Fournier H, Febrer J</i> .....	159
Magnetotelluric exploration in the Meager Mountain geothermal area, Canada — <i>Flores C, Kurtz R D, DeLaurier J</i> .....	165
Electric conductivity increases in the Earth's crust in Transdanubia (W-Hungary) — <i>Ádám A</i> ..	173
Deep electrical conductivity in Eastern Siberia — <i>Shilovsky A P</i> .....	183
Professor Antal Tarczy-Hornoch 85 years — <i>Somogyi J</i> .....	187
Professor György Barta 70 years — <i>Meskó A</i> .....	189
<i>Book reviews</i>	
Geochemistry of Sedimentary Ore Deposits, Maynard J B — <i>Kisházi P</i> .....	191
Terrigenous Clastic Depositional Systems, Galloway W E, Hobday D K — <i>Polcz I</i> .....	191
Dissolved loads of rivers and surface water quantity/quality relationships — <i>Fehér J</i> .....	192
Hydrology of humid tropical regions, Keller R ed. — <i>Bálint G</i> .....	194

Principia of system-contemplation of the mining chemistry — <i>Bella L, Tóth J</i> .....	199
A new dressing technology system of domestic iron ores — <i>Balla L sen.</i> .....	209
Explosion risk of coal dust (methane) — inert material mixtures — <i>Bánhegyi M, Egyedi J</i> .....	219
Some aspects to the comprehensive interpretation of filtration process-control and reservoir-chemical interactions — <i>Rác D</i> .....	233
Interfacial and capillary phenomena in the displacement of oil by CO <sub>2</sub> — <i>Bauer K</i> .....	241
Redox method for the investigation of coal quality — <i>Mrs. Milley-Tóth J</i> .....	253
Interfacial energy and pore structure — <i>Balla L, Milley Gy, Wagner O</i> .....	261
Rapid pyrolysis of Hungarian brown coals — <i>Gerej J, György I</i> .....	273
Examination of relations between osmotic properties of shales and drilling problems occurring during drill-out — <i>Berlinger H, Molnár J</i> .....	283
Reservoir damage by phase dispersion during multiple gas-water displacements — <i>Kretzschmar H J, Czolbe P</i> .....	293
Laboratory investigation of residual phase distribution in consolidated sandstones — <i>Weinhardt B, Heinemann Z</i> .....	303
Geochemical components of the effect mechanism of oil displacement with carbon dioxide — <i>Németh E</i> .....	319
Adsorption from binary liquid mixtures on the heterogeneous surfaces of actual solids; excess isotherms and heats of immersion — <i>Rudziński W, Zajac J</i> .....	337
The measurement of capillary pressure at a moving boundary — <i>Rác G, Ludányi B</i> .....	355
Preparation and application of low solid containing and solid-free drilling fluids — <i>Dormán J</i> ..	365
Effect of rock temperature on rock and gas outbursts — <i>Somosvári Zs</i> .....	375
Effect of the protective layer mining method on the reduction of rock and gas outburst danger — <i>Somosvári Zs</i> .....	397
Calculation of air losses and suitable ventilator distances for ventilating pipes — <i>Janositz J</i> ....	409
Study of joint application of anionic and nonionic surfactants in enhanced oil recovery — <i>Lakatos J, Milley Gy, Tóth J, Kristóf M, Capelle A, Wagner O, Lakatos-Szabó J, Felián B</i> .....	425
Integrating effect of hydromechanization of mining technological systems — <i>Patvaros J</i> .....	447
Materials law of isotropic rock continua — <i>Horváth R</i> .....	453
Properties of the Poynting-Thomson standard body during load decrease — <i>Horváth R</i> .....	463

## AUTHOR INDEX

- Ádám A 71, 151, 173  
 Afonin V V 81  
 Bálint G 194  
 Balla L 261  
 Balla L sen. 209  
 Bánhegyi M 219  
 Barta Gy 3, 29  
 Bauer K 241  
 Bebló M 153  
 Balla L 199  
 Bencze P 81  
 Berlinger H 283  
 Bezrukih V V 81  
 Bisztricsány E 7  
 Björnsson A 153  
 Capelle A 425  
 Composiello C 153  
 Czolbe P 293  
 DeLaurier J 165  
 Dormán J 365  
 Egyedi J 219  
 Febrer J 159  
 Fehér J 192  
 Felián B 425  
 Flores C 165  
 Förtsch O 85  
 Fournier H 151, 159  
 Galloway W E 191  
 Gasco J C 159  
 Gerej J 273  
 György I 273  
 Hajósy A 61  
 Heinemann Z 303  
 Hobday D K 191  
 Hobot J 135  
 Holló L 127  
 Horváth R 453, 463  
 Janositz J 409  
 Keller M 159  
 Keller R 194  
 Kisházi P 191  
 Koch E 85  
 Kovács K 81  
 Kretzschmar H J 293  
 Kristóf M 425  
 Kurtz R D 165  
 Lakatos I 425  
 Lakatos-Szabó J 425  
 Ludányi B 355  
 Maidana A 159  
 Mamani M 159  
 Maynard J B 191  
 Meskó A 189  
 Milley Gy 261, 425  
 Milley-Tóth J 253  
 Molnár J 283  
 Nemesi L 135  
 Németh E 319  
 Patvaros J 447  
 Polcz I 191  
 Rácz D 233  
 Rácz G 355  
 Rudziński W 337  
 Savić P 13  
 Shilovsky A P 183  
 Somogyi J 187  
 Somosvári Zs 375, 397  
 Szemerey I 81  
 Teleki G 13  
 Tóth J 199, 425  
 Varga G 135  
 Vatin-Perignon N 159  
 Verő J 151  
 Wagner O 261, 425  
 Weinhardt B 303  
 Zajac J 337



## KEYWORD INDEX

- adsorbed gas 375
- adsorption 337
- air loss 409
- air pipe fans 425
- analytical mining chemistry 199
- anionix surfactants 425
- anomaly 135, 153, 173, 183
- Argentina 159
- average permeability 261
- Baikal rift zone 183
- basaltic melt 153
- breaking 199
- brown-coal pyrolysis 273
- Canada 165
- capillary pressure 355
- capillary rise 355
- carbonate iron ores 209
- carbon-dioxide injection 319
- celestial bodies 13
- change of wettability 241
- chemical effects 233
- clay minerals 241, 283
- clays 283
- CO<sub>2</sub> 241, 319
- coal dust 219
- coal qualification 253
- CO<sub>2</sub>-flooding 241
- collision 159
- conductivity anomaly 135, 153
- continuum 463
- core 13
- core dimensions 303
- core shape 13
- creeping 463
- crust 173
- crustal conductivity anomaly 153, 183
- cyclic gas-water displacements 293
- cylindrical waves 85
- deformation 453, 463
- deformation tensor 453
- density distribution 29, 61
- density inhomogeneity 29
- dispersion effect 293
- displacement 233, 293, 303, 319, 425
- displacement liquids 425
- displacement mechanism 319
- displacement tests 303
- dissolving effect of CO<sub>2</sub> 319
- dressing technology 209
- drift 3
- drilling fluid 365
- drilling hydraulics 365
- drilling rate 365
- dynamic capillary pressure 355
- earthquake 7
- aerthquake magnitude 7
- Earth rotation 3
- Eart's core 13
- Eastern Sibiria 183
- eccentric core 13
- elastic deformation 463
- elastic waves 85
- elastodynamics 85
- ellipsoid 61
- energy inhomogeneity 3
- enhanced oil recovery 303
- evolution 13
- evolution of the Earth 13
- excavation methods 447
- explosion chamber 219
- explosion effects 219
- explosion risk 199, 219
- explosions 219
- explosiveness 219
- extended Laplacian operator 85
- field experiment 319
- fire dump 219
- fire protection 199
- flushing fluid 365
- foam formation 293
- formation damage 365
- free gas 375

gasification 199  
gas mobility reduction 293  
gas outburst danger 375, 397  
gas pressure 375, 397  
gas storage 293  
gas-water displacements 293  
genetic series 283  
geodynamics 3  
geodynamic test area 71  
geoelectric survey 135  
geoid 3, 29, 61  
geomagnetic pulsations 127  
geothermal area 165  
geothermal field 159  
geothermal gradient 375  
graphite 173  
heat flow 375  
heterogeneity 337  
high-level geoid 29  
homogeneous materials 463  
Hungary 7  
hybrid mixture 219  
hydrocarbon recovery 233  
hydromechanization 447  
Iceland 153  
illite 283  
inhibition 261  
IMF direction 127  
IMF intensity 127  
immersion heat 337  
inertization 219  
inhomogeneity 3, 29  
inhomogeneous media 85  
injection 425  
intensity maps 7  
interfacial energy 261  
internal structure of the Earth 61  
ion-exchange 319  
ionosphere 81  
iron ores 209  
isotherms of adsorption 337  
isotropic materials 463  
Laplacian operator 85  
leaching 199  
linear displacement tests 303  
load decrease 463  
load increase 463  
macroseismic data 7  
magnetic separation 209  
magnetotellurics 135, 153, 159, 165  
maps 7  
material inhomogeneity 3  
materials equation 453  
maximum seismic intensity maps 7  
Maxwell's quantities 85  
Maxwell's theory 85  
Meager MTS 165  
mechanical stresses 233  
melt 153  
methane 375  
methane explosion damping traps 219  
mid oceanic rift 153  
mine fire protection 199  
mineral dressing 199  
mining chemistry 199  
mining safety 199  
mining system 447  
mobility 233  
mobility reduction 293  
modification 241  
modulated elastic waves 85  
montmorillonite 283  
moving boundary 355  
Nazca plate 159  
nonionic surfactants 425  
oceanic rift 153  
oil recovery 303, 425  
oil swelling 241, 319  
Onsager's theory 453  
osmotic phenomena 283  
outburst danger 375, 397  
permeability 261, 365  
physico-chemical effects 233  
plasma parameters in the ionosphere 81  
plate 159  
plate collision 159  
pore gas pressure 375  
pore size distribution 261  
pore structure 261  
pore structure modification 241  
potential analyzer 81  
Poynting-Thomson body 453, 463  
preparatory activity 199  
pressure gradient 303  
pulsations 127  
protective layer 397  
pyrolysis 273  
qualification 253  
recovery 233  
redox potential 253  
reference ellipsoid 61  
residual phase distribution 303  
retarding potential analyzer 81  
reversal of genetic series 283  
rheology of rocks 453  
rift zone 183  
rock continuum 453, 463  
rocket measurements 81  
rock outburst danger 397  
rock parameters 397  
rock temperature 375  
role of clay minerals 241  
rotation 3  
rotation of celestial bodies 13

rotation-symmetrical density distribution 29, 61  
safety 199  
seismic hazard 7  
seismic intensity maps 7  
seismicity of Hungary 7  
sequential injection 425  
Siberia 183  
solar wind 127  
solid-free drilling fluid 365  
specific methane output 375  
stress tensor 453, 463  
surface heterogeneity 337  
survey 135  
swelling 241, 283, 319  
swelling of clays 283  
tar formation 273  
tellurics 135  
tensides 293  
terrestrial heat flow 375  
thermal treatment 199  
Transdanubia 71, 135, 173  
transient montmorillonite/illite minerals 283  
Ukk — Türje region 71  
underground gas storage 293  
uniaxial state of stress 463  
ventilation 409  
ventilator distance 409  
water-wet porous medium 303  
waves 85  
waves in inhomogeneous media 85  
well completion drilling hydraulics 365  
westward drift 3



## CONTENTS

The presumable connection between the internal structure of the Earth and geodynamics — <i>Barta Gy</i> .....	3
Remarks on seismicity estimations in Hungary — <i>Bisztricsány E</i> .....	7
Origin and dynamics of Earth's core — <i>Savić P</i> and <i>Teleki G</i> .....	13
Some properties of the Earth's core looked upon on the basis of investigations of the force fields of the Earth — <i>Barta Gy</i> .....	29
New points of view for determining the parameters of the reference ellipsoid of the Earth — <i>Hajósy A</i>	61
Geophysical aspects in the selection of a geodynamic test area in Transdanubia (Western Hungary). Contribution to the International Lithosphere Programme — <i>Ádám A</i> .....	71
Measurement of the plasma parameters in the ionosphere by night with retarding potential analyzers on board of the geophysical rocket Vertical-10 — <i>Bencze P, Kovács K, Szemerey I, Afonin V</i> <i>V, Bezrukih V V</i> .....	81
Elastodynamics expressed in terms of Maxwell's theory of electrostatics, cylindrical wave propagation and elastic wave propagation in inhomogeneous media — <i>Förtsch O</i> and <i>Koch E</i> .....	85
Connection between the interplanetary medium and pulsations of the geomagnetic field with periods 1–600 s — <i>Holló L</i> .....	127
Telluric and magnetotelluric information about the geological structure of Transdanubia — <i>Nemesi</i> <i>L, Hobot J, Varga G</i> .....	135
Introduction to the series "Conducting crustal anomalies in geothermally active areas" — <i>Ádám A,</i> <i>Fournier H, Verő J</i> .....	151
Magnetotelluric results in North-East Iceland — Electrical conductivity, temperature, crust- and mantle structure — <i>Beblo M, Björnsson A</i> .....	153
The hot dome of Taco Ralo, in the NW of Argentina — <i>Vatin-Perignon N, Comosiello C, Mamani M,</i> <i>Maidana A, Keller M, Gasco J C, Fournier H, Febrer J</i> .....	159
Magnetotelluric exploration in the Meager Mountain geothermal area, Canada — <i>Flores C, Kurtz R</i> <i>D, DeLaurier J</i> .....	165
Electric conductivity increases in the Earth's crust in Transdanubia (W-Hungary.) — <i>Ádám A</i>	173
Deep electrical conductivity in Eastern Siberia — <i>Shilovsky A P</i> .....	183
Professor Antal Tárczy-Hornoch 85 years — <i>J Somogyi</i> .....	187
Professor György Barta 70 years — <i>A Meskó</i> .....	189
 <i>Book reviews</i>	
Geochemistry of Sedimentary Ore Deposits, Maynard J B — <i>Kisházi P</i> .....	191
Terrigenous Clastic Depositional Systems, Galloway W E, Hobday D K — <i>Polcz I</i> .....	191
Dissolved loads of rivers and surface water quantity/quality relationships — <i>Fehér J</i> .....	192
Hydrology of humid tropical regions, Keller R ed. — <i>Bálint G</i> .....	194



## THE PRESUMABLE CONNECTION BETWEEN THE INTERNAL STRUCTURE OF THE EARTH AND GEODYNAMICS

GY BARTA<sup>1</sup>

[Manuscript received November 14, 1983]

In geodynamic investigations one has to take into account the material- and energy-inhomogeneity of the entire body of the globe; among the causes of geodynamical phenomena, mechanical energies may play an important role.

**Keywords:** Earth rotation; energy inhomogeneity; geodynamics; geoid; material inhomogeneity; westward drift

Geological movements observed on the surface of the Earth used to be explained in general by means of convective currents. The origin of the currents could be attributed to inhomogeneity of the crust and mantle, respectively to volume changes of the various domains.

Here I should like first of all to attire attention to the fact that geodynamic movements can be influenced besides heat energies also by mechanical ones. On the other hand it is not desirable that in geodynamical investigations affecting the whole Earth, various material domains of the globe should be treated separately one from another, since the core and mantle of the Earth form a unit after all and each of them contributes to the tectonic movements of the Earth according to its special peculiar position and inhomogeneity, its material state and energy content. Neglecting a certain domain within the investigations will surely unfavourably influence overall statements and estimates. It seems to us that the study of the density and energy inhomogeneity of the various material domains of the Earth is of special importance as regards geodynamic investigations. In my inaugural lecture (Barta 1985) I discussed the fact that the geoid figure can be looked upon as a sum of two rotation-symmetrical forms. Determination of these component forms is by no means a simple task as regards both the mathematical as well as the physical side of the problem. Computation of these forms can be undertaken in two ways: either using data systems along main circles (i.e. distributed along lines) or data systems distributed on the whole map of the geoidal surface. These two different approaches of the geoid form furnish the same zonal harmonic coefficients if and only if the symmetry axes of the component forms have been suitably chosen. Thus, the method furnishes means of an exact determination of

<sup>1</sup> Institute of Geophysics, Loránd Eötvös University, 1083 Budapest, Kun Béla tér 2.

the axis directions of the rotation-symmetrical forms — provided that no other disturbing component does occur.

In order to reduce the disturbing effect of the density inhomogeneities as much as possible the geoid figure for the 6000 km level was used. For a better approximation of the physical reality also the habitual value of the flattening of the Earth figure had to be modified, i.e. its components due to the rotation and to internal inhomogeneities were to be separated. The part of the flattening due to the internal inhomogeneities is unequivocally defined. The separation is treated in detail in the present paper especially because it is most interesting for the geodesists.

Considerations and computations have given the result that the main part of the geoid is in fact the sum of two rotation-symmetrical forms, the geoid anomalies can be deduced from two rotation-symmetrical deep seated mass asymmetries and the system of anomalies can only be interpreted in that way. The residual picture remaining after the determination of the deep-seated parts represents the effect caused by the surface inhomogeneities.

Within the crust and upper mantle the inhomogeneity of the density manifests itself in the relief and its effect can be immediately seen. Of course an inhomogeneity producing a global effect does not exist in the relief picture, as it has been treated in detail by Barta (1985).

The place of the supposable inhomogeneities with global effect can be determined by the following considerations. The material of the middle, respectively lower mantle is in a plastic state and in these domains the gravity is nearly the same as at the surface. This force would arrange the materials during geological eras — owing to the “shaking” effect of the tidal wave going around the globe every half day — according to their density, those of lesser density rising and those of higher density sinking to the level corresponding to their density value. Thus, we cannot suppose within these mass domains the existence of very global inhomogeneities, especially in case of a rotation-symmetrical arrangement.

In contrary to the mantle, in the core of the Earth  $g$  is quickly diminishing and in the centre its value vanishes. Therefore, the inner core is floating in the liquid material of the outer core owing to the absence of a force field and it takes its position at the point where the sum of force-effects for it is zero. According to this consideration the most simple inhomogeneity may be the eccentricity of the inner core. The rotation-symmetrical forms representing the main anomalies of the geoid are brought about in all probability by the mass inhomogeneities existing within the core. These being located in a liquid environment are capable of very quick geological changes, i.e. the gravitational anomaly system may be exposed to variations with an order of magnitude of thousand years like the magnetic secular variations. This supposition could be proven if a western drift of a speed similar to that experienced with the magnetic anomalies could be detected also in the anomalies of the gravity field. With the present measuring accuracy such a proof seems to be possible within a few decades.

If it is so, then the inner core moves westwards — probably due to tidal forces. In the course of the movement convectional eddies are formed and inhomogeneity appears through the effect of pressure differences around the direction of the movement as axis. The character of these inhomogeneities corresponds to the requirements of rotational symmetry and globality.

The westward drift outlined above is slowing down the rotation of the Earth and it transforms into heat the mechanical energy being inherent in the rotation of the globe. These energies are rather great (their order of magnitude is  $10^{27}$  erg/year) and cannot be neglected from the point of view of dynamics of Earth. A further significant advantage of energies thus appearing is that they are highly capable of producing horizontal (tangential) accumulation which could be used for explaining geodynamical movements. The changes of heat energies supporting the convection currents of the mantle are very great indeed, they are greater by more than an order of magnitude ( $2.5 \cdot 10^{28}$  erg/year) than the mechanical energies mentioned above. Nevertheless, their distribution is of a central character in general and the isothermic surfaces are roughly parallel to the level surfaces, thus only a small part of them can bring about horizontal movements.

Thus we may conclude that from the point of view of geodynamical investigations a thorough knowledge of the inhomogeneity of the material of the core and of the interrelation of the material domains of the core and mantle as well as their correct interpretation is of utmost importance.

### References

- Barta Gy 1985: Some properties of the Earth's core looked upon on the basis of investigations of the force fields of the Earth. *Acta Geod. Geoph. Mont. Hung.* (present issue)



## REMARKS ON SEISMICITY ESTIMATIONS IN HUNGARY

E BISZTRICSÁNY<sup>1</sup>

[Manuscript received November 30, 1983]

The earthquake intensities assessed in the recent past were overestimated especially for relatively greater events. Therefore a revision was necessary for the earlier determined intensities and the frequency-magnitude equation. The revaluation of the intensities occurred partly on the basis of catalogue data, where the signal duration makes possible the computation of magnitudes, partly after thorough investigation of macroseismic data.

**Keywords:** earthquake magnitude; macroseismic data; maximum seismic intensity maps; seismic hazard; seismicity of Hungary

Since long time the seismological experts are frequently requested to give professional advice about seismic hazard of a lesser or greater area. Therefore in the last six decades several seismic maps were prepared, but their forms have changed from time to time, namely the area of seismic active zones has grown with the progress of time. The reasons of the changes are as follows:

- relatively stronger ( $M \geq 5$ ) earthquakes are very rare in Hungary, and recent events occurred in many cases on places qualified silent,
- in general, the knowledge about the faults is uncertain and therefore the sites of the future sources are unknown, and the above mentioned seismicity maps were sometimes historically experienced maximum intensity maps (Figs 1, 2 and 3).

These maps, of course, are incomplete, because they do not give information about:

- the site of future events
- the frequency of events
- the expected maximum intensity of events
- the attenuation of intensity with increasing epicentral distance.

These requirements are rather satisfied with seismic risk maps where a probabilistic approach is applied. For this method, among others, a correct knowledge of the intensities of the historical earthquakes is necessary. First of all, the reliability of the historical data is to be cleared. A catalogue of detailed historical source was

<sup>1</sup> Geodetic and Geophysical Research Institute of the Hungarian Academy of Sciences, Seismological Observatory, Budapest Meredek u. 18, H-1112

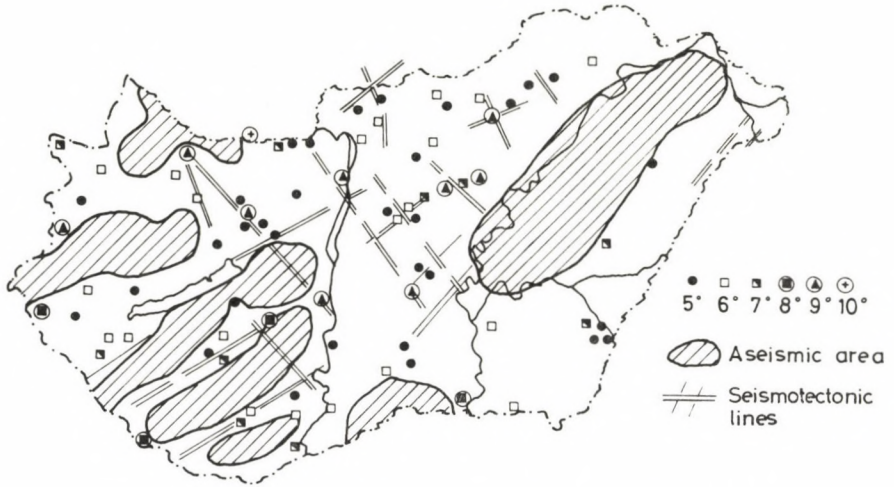


Fig. 1. Seismicity map compiled by Réthly, data used from 455 to 1918

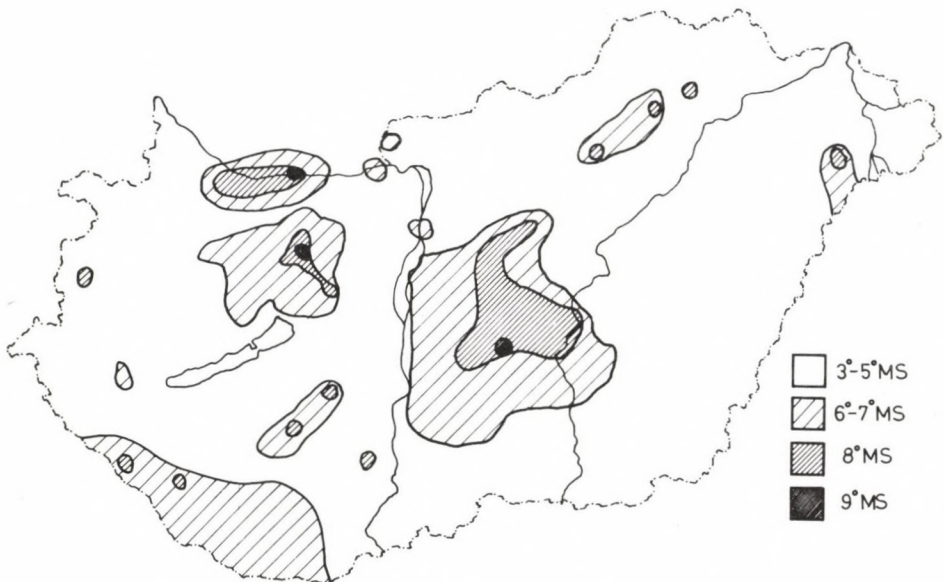


Fig. 2. Maximum intensity map compiled by Simon

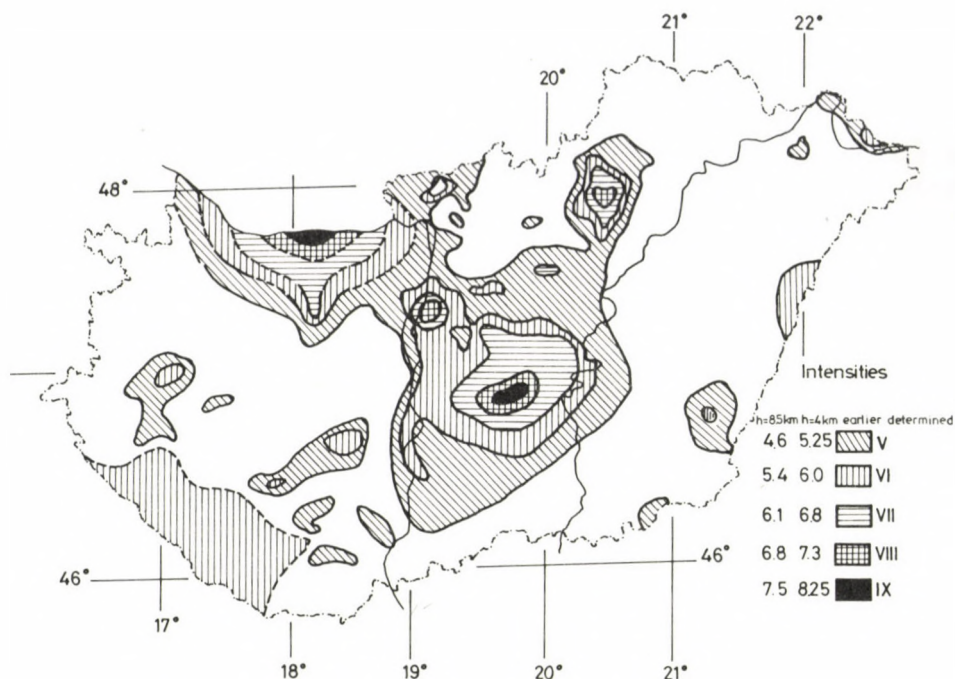


Fig. 3. Maximum intensity map, compiled by Bisztricsány, Csomor and Kiss

compiled by Réthly (1952). His book gives the most important data of the earthquake events from 455 to 1918 and many experts used these data as basis. Réthly estimated the intensities of the earthquakes if it was possible. The uncertainty of the data has started here. It is not clear where the author used Mercalli or Rossi-Forel or Cancani scales.

Another uncertainty originates from the incompleteness of data. The history and so the catalogue contains only three events from 455 to 1000, twenty from 1001 to 1500, and from 1501 to 1918 about seven hundred earthquakes.

It is clear that this catalogue gives information about sites of historical events only, it is unsuitable for estimation of frequency of events. One part of the data is unreliable for determination of intensities even if they originate from the beginning of this century. Generally it was the impression that the greater intensities were overestimated in the catalogue. The reason of the overestimation is that the greater part of dwellings, especially in villages, was built from adobe or bricks with very poor mortar in Hungary, but the recently applied scales were made for better quality houses.

The first seismograph was set up in Hungary in 1905, therefore in favourable cases we could get data from seismograms but the greater part of seismograms was destroyed in the second world war. There is only one possibility to determine the

magnitude, namely from data of bulletins, because the catalogue contains the signal durations and from the equation

$$M_D = a \log t + b$$

(where  $t$  is the signal duration in minutes) the magnitudes of local earthquakes can be determined. From the equation  $M_D = f(I_0)$ , the epicentral intensities can be estimated, too. The differences between intensities estimated earlier and recently can be compared from the following table:

**Table I.** Intensities in degree

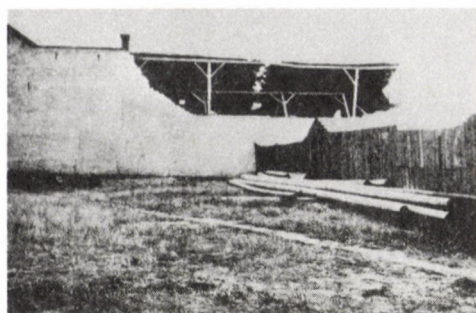
Earlier estimated	Estimated from $M_D$	
	$h = 4$ km	$h = 8$ km
2	3.2	2.3
3	3.75	2.8
4	4.6	3.75
5	5.5	4.6
6	6.3	5.4
7	7.0	6.1
8	7.7	6.8
9	8.35	7.5

Since the most frequent focus depth is 8 km in the Carpathian Basin, the discrepancies between intensities estimated earlier and recently are significant.

With these data, the frequency — magnitude equation computed earlier will also change. In verification of the above mentioned concept the Gomba earthquake of March 15, 1908 recorded by a Wiechert seismograph in Budapest will be quoted. The first onset occurred at 17<sup>h</sup> 38<sup>m</sup> 11<sup>s</sup> and the end of signals was recorded at 17<sup>h</sup> 40<sup>m</sup> 06<sup>s</sup>. On the basis of signal duration  $M_D = 3.25$  and the estimated intensity is  $4 < I_0 < 5$ . The earlier estimated intensity from Réthly's catalogue is  $8 < I_0 < 9$ . The difference is significant.

Another example: the Kecskemét earthquake July 8, 1911. The first onset was recorded at 1<sup>h</sup> 02<sup>m</sup> 06<sup>s</sup> and the end of signals was at 1<sup>h</sup> 16<sup>m</sup>. From the signal duration  $M_D = 5$  and  $I_0 = 7$ , the intensity estimated earlier by Réthly was  $9^\circ < I_0 < 10^\circ$ . The difference is also great. This result was controlled by the data of damages, the number of dwellings was 11 000 at Kecskemét in 1911. 110 families were removed from their flats because of damages (see Figs 4a, 4b, 4c, 4d). It means that the number of stronger damaged flats was 1% of the total number of dwellings. In accordance with the MSK scale, this agrees with 7° instead of the earlier estimated  $9^\circ < I_0 < 10^\circ$ . Therefore the intensities estimated by  $M_D$  values give more reliable data for planning of buildings and settlements in the environment of Kecskemét and help to save an essential sum of money.

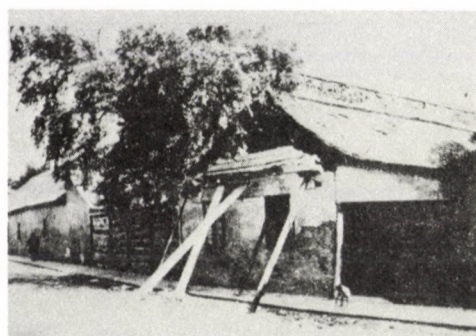
## SEISMICITY IN HUNGARY



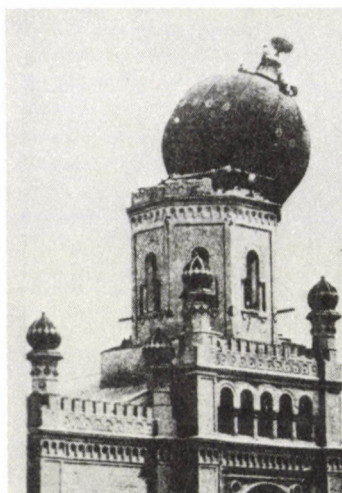
a



b



c



d

Fig. 4.a, b, c, d Dwellings and the synagogue damaged at Kecskemét earthquake, July 8, 1911

## References

- Bisztricsány E 1959: On the new method of determining earthquake magnitudes. *Travaux Scientifiques. Ser. A. Fasc. 20.* (UGGI conference in Toronto, 1957)
- Bisztricsány E 1982: Difficulties of the seismic risk determination in Hungary. ESC conference in Leeds (in press)
- Bisztricsány E, Csomor D, Kiss Z 1961: Earthquake zones in Hungary. *Annales Univ. Sci. Budapest, Sec. Geol.*
- Réthly A 1952: Earthquakes in the Carpathian Basin (in Hungarian). *Akadémiai Kiadó, Budapest*
- Simon B 1941: Die Erdbebenstätigkeit des Ungarischen Beckens. *Veröffentlichungen der Reichsanstalt f. Erdbebenforschung in Jena, No. 40.*
- Szeidovitz G 1983: Seismic risk of Budapest. Manuscript



## ORIGIN AND DYNAMICS OF EARTH'S CORE

P SAVIĆ<sup>1</sup> and G TELEKI<sup>2</sup>

[Manuscript received December 12, 1983]

On the basis of Savić's hypothesis (Savić 1961) of the origin of rotation of celestial bodies, the authors considered the formation and development of the Earth and its layers. In connection with the Earth's core, they conclude that it has been formed as the consequence of an evolution process, that it is not in a wholephase state, and that it has the shape of an ellipsoid with an eccentric position.

**Keywords:** core shape; Earth's core; eccentric core; evolution of the Earth; rotation of celestial bodies

### 1. Introduction

Starting from the facts that the rotation of celestial bodies around their own axes and the revolution around the center of gravity of a multibody system represent a general form of motion, one of the authors of this article posed the question about the origin of rotation of a system of particles and of individual celestial bodies. That was the first time that such a problem was raised in science and an answer given in the form of a hypothesis (Savić 1961). According to this hypothesis, a general property of a macrosystem of particles must correspond to a general form of motion, which is common to all and is independent of the composition of the system. In other words, if all systems of particles of sufficiently large mass have the same form of motion — i.e. rotation around their axis — then the source of this rotation must lie in the structure of the particles. We thus come to the atoms of the chemical elements. By developing this idea in a number of papers published in the last two decades — the partial list of which is given at the end of this article — it was possible to come to the following general conclusions:

1.1 Every large body, such as the large masses of celestial bodies, represents an assembly of an enormous number of atoms of elements of which such a body is composed;

1.2 Every system of particles is subjected to gravitational attraction toward its center of gravity and to loss of heat by radiation in the surrounding space, the result of

<sup>1</sup> Serbian Academy of Sciences and Arts Belgrade, Knez Mihailova ulica 35, Yougoslavia

<sup>2</sup> Astronomical Observatory Belgrade, Volgina 7, YU 11050

these two effects being the contraction of the system and therefore the increase of its density;

1.3 Due to this density increase, the atoms in the interior of the body are subjected to increased pressure;

1.4 Increased pressure deforms the electron shells of atoms and brings about the displacement of electrons to higher energy levels, this causing the layering of the system;

1.5 Under sufficiently high pressure the electrons are ejected from their atom shells and electron-deficient atoms are thus produced;

1.6 These electron-deficient atoms have a free magnetic moment, the coupling of which produces magnetism of the whole system;

1.7 Because of the resulting magnetism, the electron-deficient layer becomes the promoter of rotation; this layer, by friction of the phase (contact) surfaces, brings about the whole system (celestial body) into rotational motion.

Thus, rotation, as a general form of motion of a system of particles, can be explained by the pressure exerted by the weight of a column of material on its base and the resulting deformation of the structure of the electron shells in atoms, irrespective of their chemical nature.

It was found empirically that the mean densities of the individual layers and of the body as a whole satisfy the relationship

$$\sigma = \sigma_0 2^\varphi, \quad (1)$$

where  $\sigma_0 = 4/3 \text{ g cm}^{-3}$  and  $\varphi$  is a complex function related to the interactions of the electron shells, which has integer solutions for transitions from one phase to another. It was shown that such a relationship (1) could be applied both to the members of the solar system and to the layers of the individual celestial bodies, i.e. that it has a more general character.

From this hypothesis (Savić 1961), the Savić–Kašanin theory (Savić and Kašanin 1962–1965, 1976) about the behaviour of material under high pressure was developed, which was specially applied for the first time in more details to the Earth by Savić and Kašanin (1965). This was possible since the magnitude of the Earth's mass satisfies the necessary conditions, and that explains why the Earth has a magnetic field and its proper rotation. For the Moon, for example, this is not the case — it has only two layers, and this is not sufficient to produce a proper magnetic field and to bring about rotation which is different from the period of revolution.

The formation of the Earth's core is considered as one stage in the development of the Earth. It can be said that the formation of the core is the final act of Earth's layering, since a body of such a mass can have only a central layer (core) and three layers around it, i.e. in total four layers — and that is the present constitution of our planet. The question remains whether the formation of the core is completed or not, but

certainly a body of such a mass (as the Earth) and under such physical conditions will not have more layers than four.

After this general introduction, we shall present details of the theory itself and give results of its application to the Earth (Savić and Kašanin 1965) and particularly to its core.

## 2. Phenomena in bodies of large masses

### 2.1 General relationships

Under the influence of processes described in 1.1 to 1.7, in a system of large masses (for the definition of "large masses" see paragraphs 2.2 and 2.3) some macroscopic phenomena occur, about which the following will be mentioned:

2.11 If the pressure increases uniformly, the density ( $\sigma$ ) of the system changes stepwise and, therefore, the system undergoes layering or becomes polyphasic. From one density jump to the other, i.e. in the limits of one phase, the physico-chemical properties do not change markedly. For each phase we have the quantities<sup>1</sup>

$$\sigma_i^* \quad \text{and} \quad \sigma_i^0 < \sigma_i^*$$

so that the density  $\sigma_i$  in phase  $i$  is

$$\sigma_i^0 \leq \sigma_i \leq \sigma_i^*.$$

Starting from (1), the following relationships between the densities are obtained:

$$\left. \begin{aligned} \sigma_i^* &= 2\sigma_{i-1}^* = \sigma_0^* 2^i \\ \sigma_i^0 &= \frac{1}{\alpha_i} \sigma_i^* \end{aligned} \right\} \quad (2)$$

where

$$\sigma_0^* = \frac{1}{3} \frac{A}{\bar{V}} \quad (\text{all quantities are in the C.G.S. system}),$$

$A$  — atomic weight of the element,

$\bar{V}$  — zeropoint volume,

$$\alpha_i \begin{cases} = 6/5 \text{ for odd } i, \\ = 5/3 \text{ for even } i. \end{cases}$$

2.12 Since there are  $N = 6.023 \cdot 10^{23}$  atoms in  $A$  grams of the element, each single atom will be enclosed in a cube of edge  $2a_i$ , so that

$$N \cdot (2a_i)^3 = V_i,$$

<sup>1</sup> The upper index <sup>0</sup> refers to the beginning and the upper index \* to the end of phase  $i$ .

where  $V_i$  is the volume of the homogeneous mass of  $A$  grams at density  $\sigma_i$ . The value  $a_i$  is designated as the radius of action of the atom at density  $\sigma_i$  (this is not the effective radius of the atom). The potential energy of an electron at the distance  $a_i$  from the proton is given by  $E_i = e^2/a_i$ , where

$$e = 4.803 \cdot 10^{-10} \text{ g}^{1/2} \cdot \text{cm}^{3/2} \cdot \text{s}^{-1}.$$

The stepwise changes of density are caused by the discrete atomic structure of the elements; namely, under high pressures the electrons are displaced from their levels and the energy  $E_i$  makes jumps when passing from one phase to another. In certain transitions this leads to ionization, when the isoenergetic electrons leave the atoms.

2.13 The pressure at the end of phase  $i$  is

$$p_i^* = \frac{e^2}{24} \beta_i \frac{1}{(a_i^*)^4} \quad (3)$$

and at the beginning of phase  $i$

$$p_i^0 = p_{i-1}^* = \frac{e^2}{24} \beta_{i-1} \alpha_{i-1}^{-4/3} \frac{1}{(a_i^0)^4}, \quad (4)$$

where

$$\beta_i \begin{cases} = 1.12785 & \text{for odd } i, \\ = 1.39224 & \text{for even } i, \end{cases}$$

and

$$\beta_{i-1} \cdot \alpha_{i-1}^{-4/3} \begin{cases} = 0.70455 & \text{for odd } i, \\ = 0.28446 & \text{for even } i. \end{cases}$$

The pressure in phase  $i$  is

$$p_i = \frac{e^2}{24} f_i(a_i) \frac{1}{(a_i)^4}, \quad (5)$$

where the function  $f_i(a_i)$  depends on  $\beta_i$ ,  $\beta_{i-1}$  and  $\alpha_{i-1}$ , and also on the relative change of the accumulated energy in phase  $i$ .

2.14 If the system is composed of elements of atomic weights  $A'$ ,  $A''$ ,  $\dots$ , and with zeropoint volumes  $\bar{V}'$ ,  $\bar{V}''$ ,  $\dots$ , and in one gram of this mixture there are  $n'$ ,  $n''$ ,  $\dots$  grams of these elements, then the mixture shows the same properties as if it were composed of only one element of atomic weight  $A$ :

$$1/A = n'/A' + n''/A'' + \dots \quad (6)$$

and with zeropoint volume  $\bar{V}$ :

$$V = (n' \bar{V}'/A + n'' \bar{V}''/A'' + \dots) A. \quad (7)$$

## 2.2 Spherical bodies at 0 °K

Since an increase in pressure causes an increase in temperature, and this produces an effect which is opposite to that of pressure increase, we shall first confine our considerations to a system of particles at 0 °K. In that case the following can be concluded:

2.21 If the mass is larger than about  $10^{30} A^{-2}$ , concentric layers must be formed in the body, with density jumps even when the chemical composition does not change with depth, since these jumps are the consequence of the discrete structure of the electron shells in atoms.

2.22 Such a body cannot have a mass larger than  $6.5 \cdot 10^{30} A^{-2}$ , if all the atoms in the core are not completely free of their electrons.

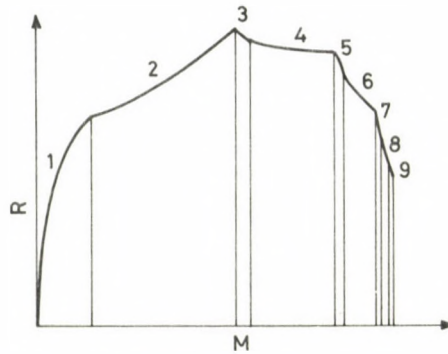


Fig. 1. Radius ( $R$ ) as a function of mass ( $M$ ) in a body in the process of formation, at 0 °K (Savić and Kašanin 1962–1965). The values on the curve refer to particular phases

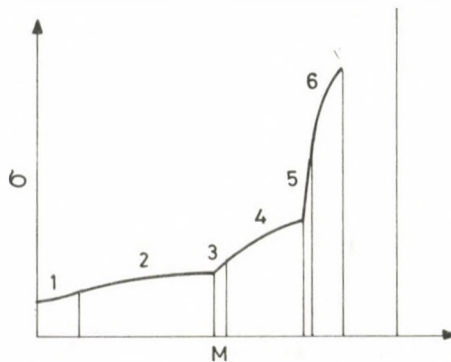


Fig. 2. Mean density ( $\sigma$ ) in function of mass ( $M$ ) in a body in the process of formation, at 0 °K (Savić and Kašanin 1962–1965). The values on the curve refer to particular phases

2.23 When the mass increases, the radius of the body first increases, and then decreases, as shown in Fig. 1. How much does the radius decrease, depends on when the last electron is ejected. Naturally, during this process the mean density of the body will also change — as can be seen in Fig. 2.

2.24 A complete body is a body of order  $i$  with its core in phase  $i$  and its outermost layer in phase 1. A non-layered complete body is of order  $k$ , i.e.  $i=1$ . A layered complete body of order  $i$  has  $k=i-1$  layers surrounding the central layer (core). Table I shows the ratios of density, mean density and pressure in the layers to the respective quantities in the core, and also the ratios of radius and mass of particular layers to the corresponding quantities of the whole body — irrespective of chemical composition. The mass of a complete body can be calculated from

$$M = G_i 10^{30} A^{-2}, \quad (8)$$

where  $G_i$  is a constant for the given phase  $i$ . A complete body will have the smallest mass when it is of order 1 and at  $0^\circ\text{K}$ , and this amounts to  $9 \cdot 10^{29} A^{-2}$

Table I contains data only for the phases  $i=2, 3$  and  $4$ , since these can be expected in the case of the Earth. Evidently, bodies with larger masses than the Earth's mass can have, and actually do have, more phases, and hence more layers.

It is understandable that Table I gives only an approximate illustration of bodies in various phases, since the tabulated data were obtained by using mean and idealized conditions, and under the assumptions that the body is physically and chemically homogeneous and that there are no other factors influencing its development (as, for example, the tidal effect). Nevertheless, some general conclusions can be reached — as will be shown in 3.3. We only wish here to emphasize the stepwise development when

**Table I.** Ratios of density, mean density and pressure in the layers to the respective elements in the core, and ratios of radius and mass in the layers to the corresponding quantities of the whole body. The data refer to  $0^\circ\text{K}$

Phase $i$	Layers $k=i-1$	Density ratio		Pressure ratio		Radius ratio		Mass ratio	Mean density ratio
		beginning of layer	end of layer	beginning of layer	end of layer	beginning of layer	end of layer		
2	0	1	0.600	1	0.321	0	0.809	0.691	0.764
	1	0.500	0.417	0.321	0.157	0.809	1	1	
3	0	1	8.833	1	0.490	0	0.492	0.259	0.458
	1	0.500	0.300	0.490	0.157	0.492	0.841	0.779	
	2	0.250	0.208	0.157	0.079	0.841	1	1	
4	0	1	0.600	1	0.321	0	0.553	0.448	0.378
	1	0.500	0.417	0.321	0.157	0.553	0.684	0.648	
	2	0.250	0.150	0.157	0.051	0.648	0.890	0.903	
	3	0.125	0.104	0.051	0.025	0.890	1	1	

passing from an even to an odd, and from an odd to an even phase — as can be seen by comparing data for several phases. More detailed data relevant to this subject can be found in Savić and Kašanin (1962–1965) (particularly 1963).

2.25 A non-layered incomplete body does not fill the whole phase, but only a part of it. In a layered complete body either the core does not fill the whole phase, or the outermost layer is in a phase higher than 1 or only in a part of phase 1.

### 2.3 Spherical bodies at temperatures above 0 °K

What has been said in the preceding section about bodies at 0 °K, is also valid, with some modifications, for bodies having a temperature higher than absolute zero. The conclusions in 2.21, 2.23 and 2.25 can be applied without changes.

2.31 The upper limit for the mass, mentioned in 2.22, will now be

$$6.5 \cdot 10^{30} A^{-2} \left( 1 + \frac{T_i}{\Theta_i} \right)^{3/2},$$

where  $T_i$  is the constant temperature in each point of the body, and  $\Theta_i$  is the increase in the temperature which makes it possible to pass from the highest to the lowest point of a same phase, under the corresponding pressures.

2.32 The changes which must be made in 2.24 refer to Table I and to the calculation of the mass of a complete body.

In Table I the column with pressure values must be replaced by the corresponding values at a given temperature.

The mass of a complete body with surface temperature  $T_1$  is

$$M' = \left( 1 + \frac{2^{1/6} \cdot T_1^0}{\Theta_1} \right)^{3/2} G_i 10^{30} A^{-2} \quad (9)$$

and the radius

$$R' = \left( 1 + \frac{2^{1/6} \cdot T_1^0}{\Theta_1} \right)^{1/2} D_i 10^{10} (\bar{V})^{-1/3} \cdot A^{-1}, \quad (10)$$

where  $G_i$  and  $D_i$  are constants for the given phases, and  $\Theta_1 = 6.166 \cdot 10^4 (\bar{V})^{1/3}$ .

2.33 There are certain limitations for complete bodies which should be mentioned:

2.331 There is a limit to the order of a complete body which can never be exceeded and is certainly less than 50.

2.332 If the accumulated energy is the source of heat in a complete body, then there is a limit which cannot be exceeded by the temperature of any complete body at any point, and which is certainly below  $7.35 \cdot 10^9$  °K.

2.333 There is a limit which the mass of any complete spherical body without its own rotation, regardless of its temperature and the material it is made of, cannot exceed unless its atoms loose their  $K$ -electrons; this limit is certainly less than  $2.6 \cdot 10^{39}$  grams.

2.334 There exists a limit which the radius of any complete body without its own rotation cannot exceed, regardless of its temperature and the material it is made of; this limit is certainly less than  $1.88 \cdot 10^{13}$  cm.

2.335 A complete body without its own rotation, regardless of its temperature and the material it is made of, must not have a mass less than  $1.6 \cdot 10^{25}$  grams.

### 3. The Earth's body — phases of development

We shall consider the development of the Earth starting from the protoplanet Earth-Moon (Savić and Teleki 1978), which was formed by contraction in the cloud of gas and dust surrounding the Sun. Due to contraction, a third layer was produced in this system, in which, by loss of electrons, energy greater than the necessary kinetic energy was liberated, thus giving rise to rotation. This rotational motion caused deformation of the protoplanet fluid body: the originally spherical body was converted to a Jacobi ellipsoid of definite parameters. After that, further condensation occurred, however, no longer only around the protoplanet's center but also about the gravity line of the peripheric lens' zone, this process resulting in the formation of two separate bodies: the Earth and the Moon.

The history of the Earth can thus be envisaged on the basis of the general considerations concerning the development of large systems of particles, which were discussed schematically in the preceding paragraphs.

According to the present composition, one obtains for the Earth the following fundamental data:

$$A = 26.567 \quad \text{and} \quad \bar{V} = 5.999 .$$

3.1 At absolute zero, according to (8), the mass of the Earth in the particular phases has the following values:

$$M(1) = 1.338$$

$$M(2) = 4.811$$

$$M(3) = 5.192$$

$$M(4) = 7.096$$

all in units of  $10^{27}$  grams. A comparison of these values with the present-time mass of the Earth which is  $5.976 \cdot 10^{27}$  grams, shows that the Earth's mass is situated between  $M(3)$  and  $M(4)$ . It follows that when the Earth underwent contraction and

stratification, it had a larger mass than the mass of the stratified body of the same order of magnitude and composition at  $0^\circ\text{K}$ . This indicates that at the beginning the temperature was higher than absolute zero.

3.2 Starting only from the relationship given in (9), and assuming that the total mass of the Earth did not change ( $= 5.976 \cdot 10^{27}$  grams), it is possible to evaluate the surface temperature  $T_1^0$  of the Earth's body in its particular phases. In the starting phase it was about 50 000, in the next phase 4 500, and in phase 3 about 3 000  $^\circ\text{K}$ .

Since the present temperature of the Earth is about 287  $^\circ\text{K}$  (Allen 1964), it follows that from the time of the third phase to the present state, the Earth cooled by about 2 700  $^\circ\text{K}$ .

3.3 Table I gives data only for the phases  $i=2, 3$  and 4, because, with the exception of phase 1, only such states can be expected in the Earth. Therefore, Table I gives a notion about the development of the Earth in its particular phases (for limitations see 2.24). When applying this Table to the Earth, it is necessary to take into account what has already been stated in 2.32, namely that the data about the pressure must be replaced by the corresponding values for a given temperature.

Concerning the development of the Earth, the following conclusions can be made:

3.31 Every transition from phase to phase represents an important change in the inner structure of the Earth. The development is certainly — so to speak — not linear, but occurs in jumps, although it shows some constant tendencies. This can also be seen in Fig. 1.

3.32 A constant decrease in the ratio of the mean density to the density in the center of the core is observed. This is the direct result of increased pressure due to contraction of the body, and we can therefore say that the density in the center of the core increased from phase to phase.

3.33 By comparing the density ratios we can see that the densities decrease in the outer layers from phase to phase. From (2) and from what has been stated in 3.32, it follows that the densities of the particular layers decrease with time, with respect to the density in the center of the body, but increase in absolute value.

3.34 The clearly observable constant decrease of the thickness and mass of the crust indicates that the Mohorovičić-discontinuity approaches more and more the Earth's surface. The fact that the crust becomes increasingly thinner, is considered by Savić and Pavlović (1971) as important in explaining the expansion of the volcanic regions from the geological past to the present time.

3.35 Although it does not follow from Table I, it is reasonable to assume that, because of the constant increase in pressure, the Earth's body contracts continuously, however not linearly but in a pulsating process. Namely, every phase transition is accompanied by the liberation of an enormous amount of energy which brings about an increase in the temperature of the body, and this, in turn, causes an increase in the size of the body. After that cooling occurs, and this whole process, combined with the

tendency to pressure increase, results in a pulsating but constant decrease of the Earth's radius.

3.4 In order to increase stepwise the density of a body from  $\sigma_0^*$  to  $\sigma_1^0$ , i.e. to bring it into phase 1, the required pressure, according to (5), amounts to

$$p_0^* = p_1^0 = \frac{2.517 \cdot 10^{12}}{(\bar{V})^{4/3}} \text{ dyn cm}^{-2}.$$

Similarly, for the density transitions from  $\sigma_1^*$  to  $\sigma_2^0$ , from  $\sigma_2^*$  to  $\sigma_3^0$ , and from  $\sigma_3^*$  to  $\sigma_4^0$ , the following pressures are necessary:

$$p_1^* = p_2^0 = \frac{5.138 \cdot 10^{12}}{(\bar{V})^{4/3}} \text{ dyn cm}^{-2},$$

$$p_2^* = p_3^0 = \frac{15.98 \cdot 10^{12}}{(\bar{V})^{4/3}} \text{ dyn cm}^{-2},$$

$$p_3^* = p_4^0 = \frac{32.62 \cdot 10^{12}}{(\bar{V})^{4/3}} \text{ dyn cm}^{-2}.$$

In the case of the Earth, for  $\bar{V} = 5.999$ , these values are:

$$0.23; 0.47; 1.47 \quad \text{and} \quad 2.99$$

in units of  $10^{12} \text{ dyn cm}^{-2}$ . Therefore, in order for the Earth to get from the original state with density  $\sigma_0^*$  and pressure  $p_0^*$  to the next phase, it is necessary to increase the pressure at the transitions from phase to phase by the following values, given in units of  $10^{12} \text{ dyn cm}^{-2}$ :

$$p_1^* - p_0^* = 0.24$$

$$p_2^* - p_0^* = 1.24$$

$$p_3^* - p_0^* = 2.76.$$

This increase is due to hydrostatic pressure, i.e. pressure of masses of material on the base. By comparing these values with data calculated from the Newtonian gravitational potential, i.e. 0.01; 1.25 and 3.07 (in the same units), it can be seen that only the first values in the two sets show a marked difference. In our opinion, this is due, on the one hand, to the incompleteness of the Earth (see 4.1) and, on the other hand, to the uncertainty in calculations involving the thin Earth's crust.

#### 4. The Earth in its present state

We shall compare our considerations of the present-time Earth with the results of geophysical measurements, using data from Allen (1964).

4.1 Starting from the initial density of the surface layer and from the mean atomic weight of the Earth's system of particles, a model of the Earth can be deduced —

based on the ideas formulated by Savić (1961). This model was originally presented by Savić and Kašanin (1962), and again later — but in more detail and with new values — by Savić and Trifunović (1975). Our Tables II and III contain data from Savić and Trifunović (1975).

If these data are now compared with those given by Allen (1964), one observes an agreement for the three outer layers, but a considerable difference for the core. For that reason we say that the Earth is a layered incomplete body, with properties given in 2.25.

It should be mentioned that besides this model, designated by I, there is another model, designated by II (Savić and Kašanin 1962–1965), which is also based on the expression (2), but involves more reported values and, therefore, cannot be considered as representative of Savić's theory as model I.

4.2 Since the Earth has a core and three surrounding layers — our considerations are here in agreement with geophysical measurements — one could presume that the Earth is in phase 4. However, that the Earth is an incomplete body and that it is not in phase 4, is indicated not only by what was stated above in 4.1, but also by the data given in Table I which were obtained in a somewhat different way than the Earth's model I. From these data it can be also concluded that the core, in particular, differs from the results of the present-time measurements. Naturally, the previously mentioned remarks concerning Table I must here also be taken into consideration.

4.3 As calculated in 3.4, the hydrostatic pressures between the Earth's layers in phase 4 have the following values (starting from the outer boundary surfaces):

$$0.47; 1.47 \text{ and } 2.99$$

whereas Allen (1964) gives:

$$0.09; 1.36 \text{ and } 3.20$$

all in units of  $10^{12} \text{ dyn cm}^{-2}$ . Except for the Mohorovičić-discontinuity, the agreement is good.

**Table II.** Model of the Earth: general data (Savić and Trifunović 1975)

Data	Values
Number of layers	4
Cohesion pressure ( $\text{dyn cm}^{-2}$ )	$0.079 \cdot 10^{12}$
Moment of inertia ( $\text{g cm}^2$ )	$8.0 \cdot 10^{44}$
Ionized mass (g)	$2.19 \cdot 10^{27}$
Mean density of ionized mass ( $\text{g cm}^{-3}$ )	12.13
Magnetic moment ( $\text{g}^{1/2} \text{ cm}^{5/2} \text{ s}^{-1}$ )	$8.483 \cdot 10^{25}$
Force of magnetic pole ( $\text{g}^{1/2} \text{ cm}^{3/2} \text{ s}^{-1}$ )	$2.3815 \cdot 10^{17}$
Distance between the magnetic poles (cm)	$3.562 \cdot 10^8$
Strength of the magnetic field (gauss)	0.67

**Table III.** Model of the Earth: data about the layers (Savić and Trigonović 1975)

Data	Crust		Mantle		Outer Core (Fluid)		Core	
	$X_1^0$	$X_1^*$	$X_2^0$	$X_2^*$	$X_3^0$	$X_3^*$	$X_4^0$	$X_4^*$
Density ( $\text{g cm}^{-3}$ )	2.657	2.952	3.542	5.904	9.840	11.808	14.17	19.97
Depth (km)	0	39	39	2831	2831	4371	4371	6371
Pressures ( $\text{dyn cm}^{-2}$ )	$0.23 \cdot 10^{12}$	$0.47 \cdot 10^{12}$	$0.47 \cdot 10^{12}$	$1.47 \cdot 10^{12}$	$1.47 \cdot 10^{12}$	$2.99 \cdot 10^{12}$	$2.99 \cdot 10^{12}$	
Hydrostatic pressure ( $\text{dyn cm}^{-2}$ )	$0.0108 \cdot 10^{12}$		$1.0055 \cdot 10^{12}$		$2.5321 \cdot 10^{12}$		$4.67 \cdot 10^{12}$	
Mass (g)	$5.626 \cdot 10^{25}$		$3.73 \cdot 10^{27}$		$1.619 \cdot 10^{27}$		$0.572 \cdot 10^{27}$	
Moment of inertia ( $\text{g cm}^2$ )	$1.548 \cdot 10^{43}$		$6.82 \cdot 10^{44}$		$0.933 \cdot 10^{44}$		$0.092 \cdot 10^{44}$	
Mean density ( $\text{g cm}^{-3}$ )	2.84		4.23		10.63		17.07	
Layer thickness (km)	39		2792		1540		1900	

## 5. The Earth's core

### 5.1 *Development*

The development of the core (which represents the inner central layer) in the various phases is described in Table I. As can be seen, this evolution was "sinuous", because of the passage of the Earth's body through different phases. Therefore, one can say that the radius and mass of the central layer underwent pulsatory changes, with a tendency of density increase in the center of gravity.

As stated in 4.1, the Earth is a layered incomplete body, because its core is not situated in the conditions required by the relationships of state corresponding to whole phases (in this case phase 4). The question arises whether the development of the Earth's core will continue or the core will remain in this non-wholephase state.

### 5.2 *Shape and position*

The present core was formed in the Earth's geometrical center, as the result of the pressure of masses, and had originally a spherical or practically spherical shape. Since the Earth already rotated at that time — rotation actually began in phase 3 — there existed the possibility that the centrifugal force would displace the core from its centric position, this being also allowed by the fact that the layer surrounding the core is in a fluid state. Upon such a displacement of the core from its original position, the existing pressure regime operated so that an eccentric core was formed, the position of which was determined by the centrifugal force and the properties of the fluid in which it floated, and the shape by the pressure regime. If these three factors acted in common — and there are no reasons why they should not — then the core should have the shape of an elongated irregular ellipsoid.

That the Earth's core is in an eccentric position is also supported by the investigation of Barta (for example Barta 1977), based on geomagnetic data.

### 5.3 *Time of formation*

To the question when the present-time Earth's core was formed, it is possible to answer only by the interpretation of data which indicate indirectly the period of formation. Depending upon the assumptions used in analyzing these data, one obtains different results for the time of formation.

Murthy (1976) gives a review of the analyses of the core's age and, using data collected in the crust and upper part of the mantle, draws the conclusions that the core was formed in the first  $100 \cdot 10^6$  years of the Earth's history. The major objection to

such an approach is that, although Murthy considers the core to arise as the consequence of an evolutive process, he infers that all the Earth's layers were formed at the same time, i.e. he does not mention the difference in age of these layers. Only in this way it is possible that when Murthy talks about the original mantle, he transfers his conclusions to the core, although he has no proof that the present-time core already existed at that time.

The data mentioned by Murthy can be also interpreted in another way — and we wish here to present our own reflections on that subject.

Let us consider the residual magnetism in the rocks of the Earth's crust. If the age of the oldest rocks with such properties is  $3.8 \cdot 10^9$  years, then this suggests that the Earth's magnetism is at least as old as that. According to the Savić-Kašanin theory (Savić and Kašanin 1962–1965, 1976), the Earth acquired its magnetic field when it became three-layered, and, therefore, one can assume that the Earth's third layer is at least  $3.8 \cdot 10^9$  years old. However, this does not yet mean that by that time the fourth layer also already existed. Since Savić considers the Earth's rotation to be the result of geomagnetic field, it follows that already at that time Earth rotated around its axis.

In our opinion, the age value of  $100 \cdot 10^6$  years, obtained from the analyses of the mantle (Murthy 1976), suggests only that at that time the Earth was at least a two-layered body.

We can therefore say that, according to our views, we still do not have enough elements in order to evaluate the age of the Earth's core. The core, as all the other Earth's layers, is the result of an evolution process, but for the time being it is not clear how long did the particular evolutive phases last.

## 6. Conclusion

On the basis of the Savić-Kašanin theory (1962–1965) of the behaviour of materials under high pressures which was briefly presented in this article, the following conclusions concerning the present-time Earth's core can be made:

- the core is the consequence of an evolution process in the Earth, as a body of large mass;
- the fact that the core is not in a wholephase state indicates that the Earth is not a complete body;
- the core has the shape of an irregular ellipsoid;
- the core is situated in an eccentric position.

### References

- Allen C W 1964: *Astrophysical Quantities*. Second Edition. The Athlone Press
- Barta G 1977: *Geophysik und Geologie*. Leipzig, 1, 3, 5.
- Murthy V R 1976: In: *The Early History of the Earth*. B F Windley (Ed.). J Wiley and Sons, London–New York–Sydney–Toronto. 21.
- Savić P 1961: Bulletin. Académie Serbe des Sciences et des Arts, 26, Classe des Sciences Mathématiques et Naturelles, Sciences Naturelles, Nouvelle série 8, Belgrade, 107.
- Savić P, Kašanin R 1962; 1963; 1964; 1965: Monographs. Serbian Academy of Sciences and Arts, Section for Natural Sciences and Mathematics, 351, 29; 360, 31; 378, 34; 393, 35.
- Savić P, Kašanin R 1965: *Problemy geokhimii*. Nauka, Moscow
- Savić P, Kašanin R 1972: Simpozij o Mohorovicicevom diskontinuitetu. Jugosl. akademija nauka i umjetnosti, Zagreb
- Savić P, Kašanin R 1976: *Povedenie materialov pri vysokikh davlenijakh*. Naukova Dumka, Kiev
- Savić P, Pavlović S 1971: I. Mezd. geokhimiceskij kongress. Moscow
- Savić P, Teleki G 1978: A study of the origin of the Earth-Moon system (Manuscript).
- Savić P, Trifunović D 1975: *MTA X. Osztályának Közleményei*, Budapest, 8, 159.



# SOME PROPERTIES OF THE EARTH'S CORE LOOKED UPON ON THE BASIS OF INVESTIGATIONS OF THE FORCE FIELDS OF THE EARTH<sup>1</sup>

GY BARTA<sup>2</sup>

[Manuscript received December 29, 1983]

The author has carried out further investigations concerning the global density inhomogeneities of the Earth based on a study of the geoid figure. In order to eliminate the influence of surface inhomogeneities, a geoid form valid for the height of 6000 km was used for the computations and so it could be stated that the high level geoid form can be caused by as few as two rotation-symmetrical density distributions. The influence of deep seated global inhomogeneities (originating probably from the core of the Earth) could be separated from those brought about by near surface formations having a local character and a connection was detected between these latter geoidal configurations and the large scale surface geological formations.

**Keywords:** density inhomogeneity; geoid; high-level geoid; rotation-symmetrical density distribution

## Introduction

This lecture is a continuation of my inaugural lecture as corresponding member of the academy delivered 12 years ago. The new results have been built up on the basis of my earlier researches, therefore I should like to give here a short account of the essentials of my previous lecture.

Regular magnetic survey in the Carpathian basin started in 1871 — at a very early date when looked upon from an international point of view. The data series has been interrupted frequently, partly due to technical reasons, partly owing to frontier changes. Therefore it became desirable to compile a new uniform series from partial series of 20–25 years duration as well as from a few smaller fragments. The matching of the series and the interpolation of breaks made a detailed investigation of the magnetic secular variation necessary. In the course of this investigation it turned out that in nearly all observatories a secondary wave of a period of about 50 years has been superposed on the secular variation of magnetic components (Fig. 1), (Barta 1954).

<sup>1</sup> Inaugural lecture at the Hungarian Academy of Sciences

<sup>2</sup> Institute of Geophysics, University Lorand Eötvös, Budapest, Kun Béla tér 2, H-1083

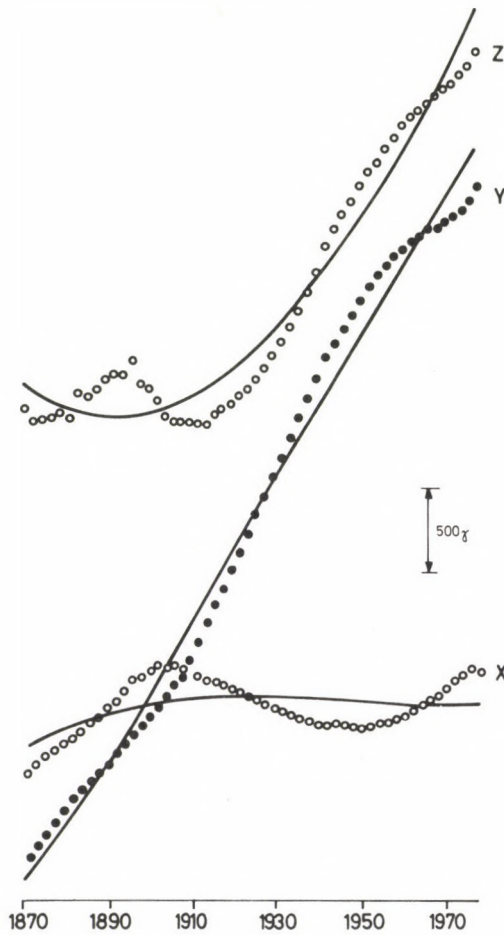


Fig. 1. Secular variation of the terrestrial magnetic field in Hungary

### Development of the ideas of investigations

The secular variation is — as a matter of fact — the movement in space of the endpoint of the magnetic vector. Thus, owing to the superimposed wave this space curve is a helix (Barta 1958a). The position of the individual points of the helix relative to the corresponding points of the curve of the smoothed secular variation is determined by a vector. This vector can be decomposed into tangential and normal components (Fig. 2), the former of which should be called longitudinal, the latter transversal effect. Both effects show some general characteristics. As regards the transversal effect the sense of rotation of the vector when looking at it from the

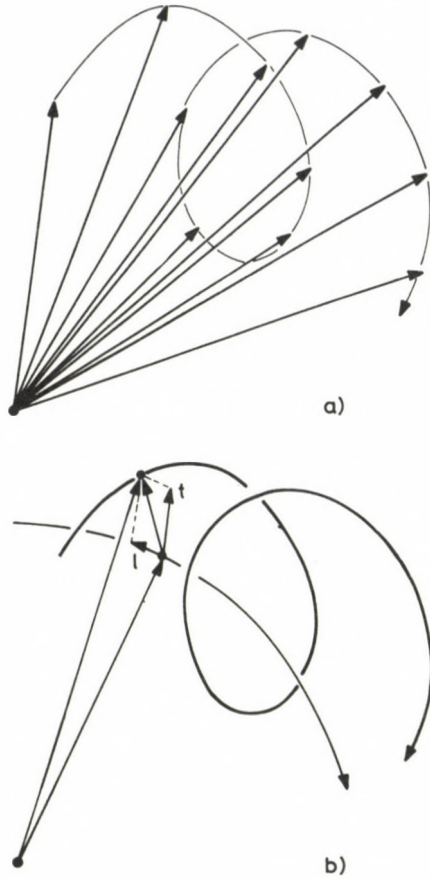


Fig. 2a. Secular change of helicoidal character of the magnetic vector

Fig. 2b. Decomposition of the vector.  $l$  and  $t$  are the tangential, respectively normal-plane components of the vector describing the superimposed wave

direction of the main variation is clockwise (Fig. 3); the extremes of the longitudinal effect appear at the same times in all observatories (Fig. 4). A similar wave can be observed in the variation of the rotational speed of the Earth, in the changes of amplitude of the oscillation of polar altitude, as well as in the sea level oscillation observed at various observatories. All these variations point to significant mass arrangements of a periodicity of about 50 years taking place in the interior of the Earth (Fig. 5). This mass shifting must go on at a very great depth, because movements of such a geologically high velocity can only be supposed there (Barta 1959).

As in the individual features of the magnetic secular variation many general characteristics can be detected it is to be supposed that the entire variation itself

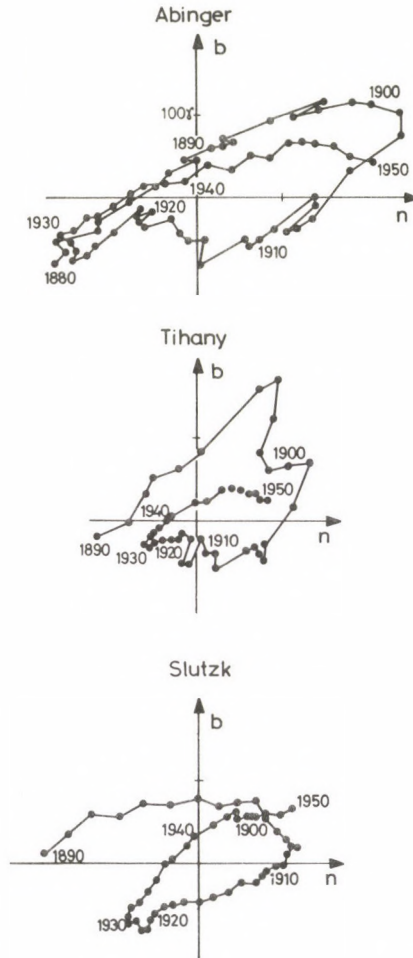


Fig. 3. The transversal wave at some European observatories

contains also similar general features. Having transformed the data of the various observatories into a unified coordinate system we actually detect some global characteristics of the curves of secular variation. Using an orthogonal projection the space curves show a convergence around Pakistan as projection centre, while the curves of the marginal observatories are diverging. The projection figures indicate that the magnetic field has three main directions which are nearly perpendicular to each other, i.e. the direction of the magnetic axis, the eccentricity direction of the best approximating dipole and the direction perpendicular to these two directing just towards Pakistan (Fig. 6), (Barta 1957).

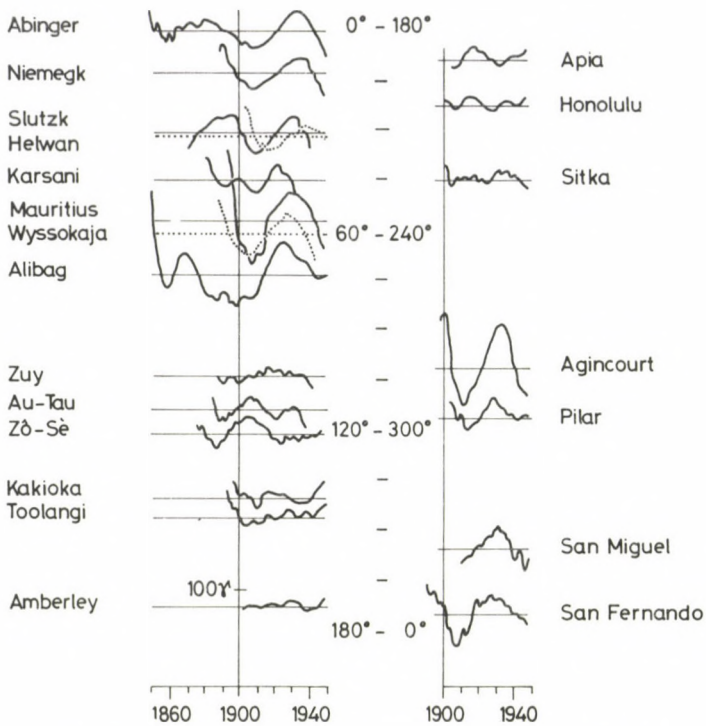


Fig. 4. The longitudinal wave at various observatories of the globe

From the results of magnetic spherical harmonics determined regularly for the past 150 years we know that the eccentric dipole is shifting by about one degree in 5 years towards West. The eccentricity is rather great, amounting to 450 m in our days. If we suppose that this magnetic phenomenon is brought about by an eccentric position of the inner core, then this inhomogeneity must present itself also in the distortion of the figure of the Earth (Fig. 7). This idea could have been taken only as a guess in the early sixties, owing to the lack of correct geoid determinations (Barta 1962c). But the first satellite geoid of 1966 could corroborate this guess. The two greatest anomalies presented themselves around Australia and India; four other characteristic anomalies — though being somewhat less in the intensity — could be found on the northern and southern parts of the Atlantic and Pacific. The interpretation of these latter ones caused some difficulties.

In the course of further investigations I approximated the equatorial cross-section of the geoid by two zonal spherical harmonic series. The pole of the harmonics has been chosen so that the approximation should be the possible most favourable (Fig. 8). Having turned the two curves represented by the spherical harmonics around

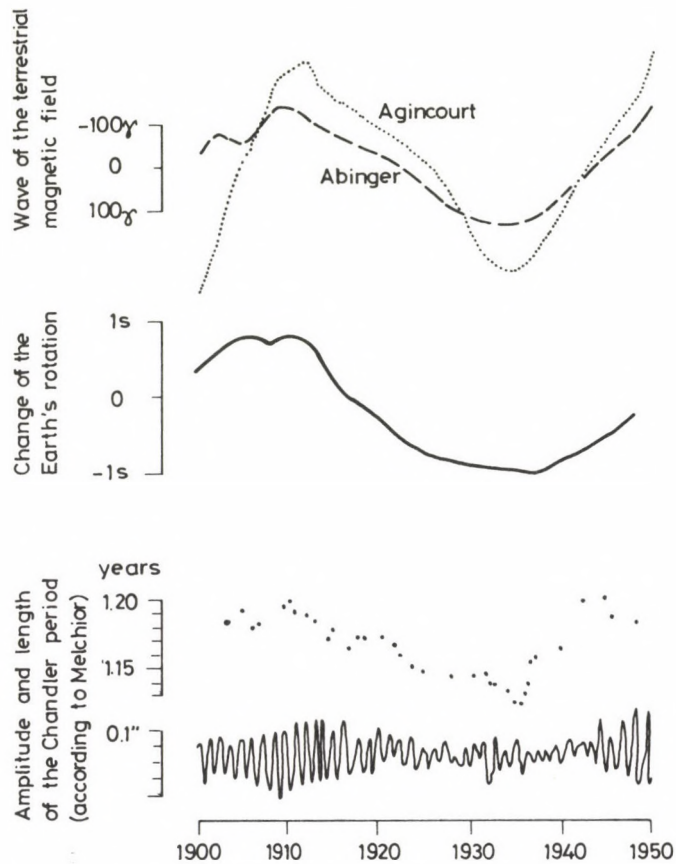


Fig. 5. The longitudinal wave and the 50 years wave observable in the rotation phenomena of the Earth

the symmetry axis we have summarized the anomalies along radial directions. According to the results of the computations, the symmetry axes thus obtained coincide with the magnetic directions mentioned above and directed towards Australia and Pakistan (Fig. 9). On the geoid thus combined also the oceanic anomalies of the temperate latitudes appeared according to sign, dimension and shape i.e. the geoid can be interpreted as sum of two rotation-symmetrical components (Fig. 10), (Barta 1971).

It should be emphasized that in these computations only equatorial data have been used, nevertheless the entire geoidal map has been obtained, i.e. the equatorial data series contains the whole geoid in itself and so the geoid figure is also looked upon as a global phenomenon and the individual geoid undulations cannot be explained separately by local gravity inhomogeneities.



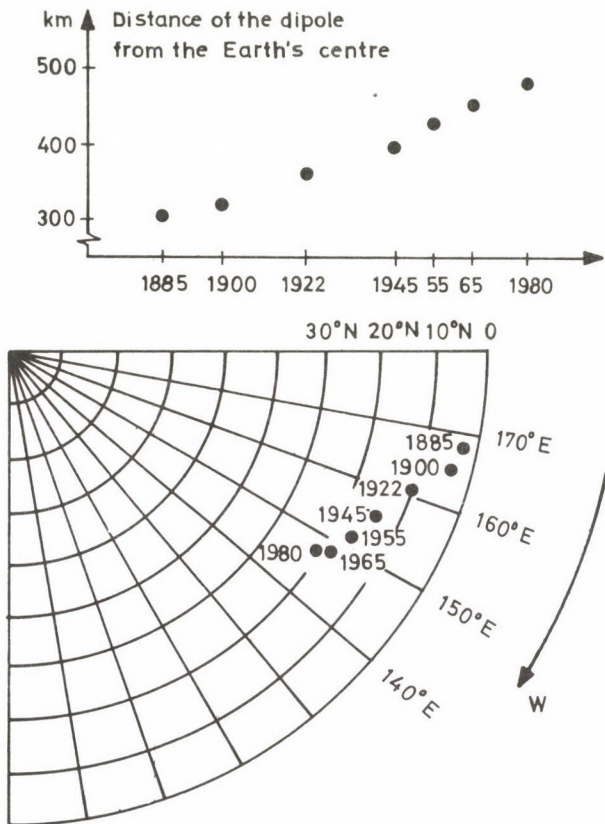


Fig. 7. Wandering of the magnetic dipole during the last 100 years

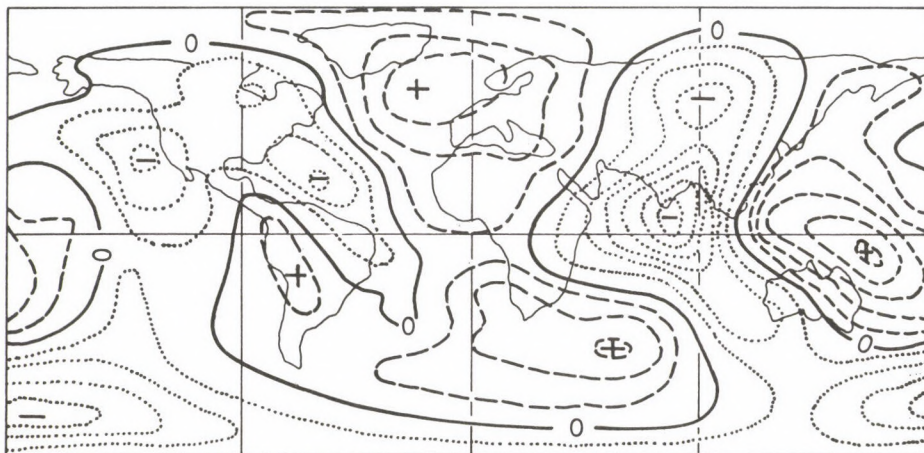


Fig. 8. The SAO I geoid. The distance between contour lines is 15 m

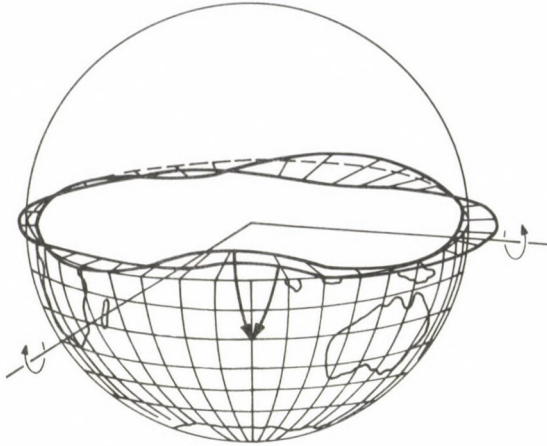


Fig. 9. Computation of the geoid figure from two rotation-symmetrical anomaly systems

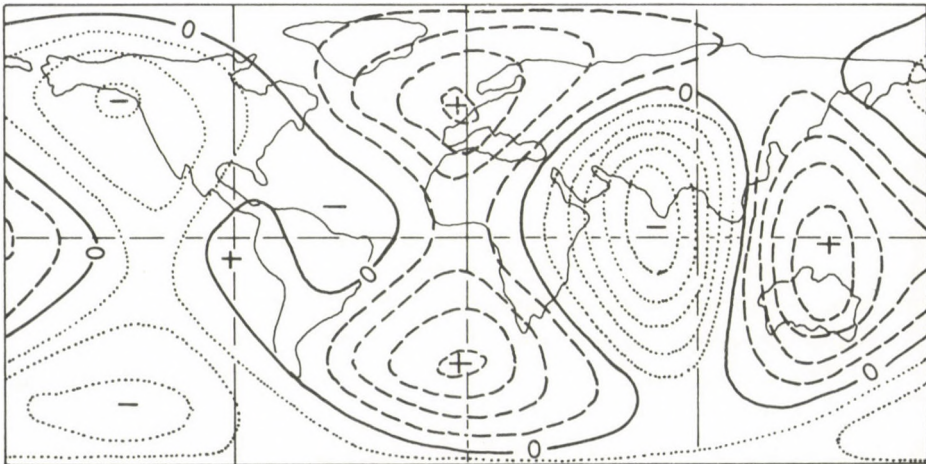


Fig. 10. The geoid figure computed as the sum of two rotation-symmetrical anomaly systems. Distance of the contour lines is 15 m

### Some new considerations and results

This very peculiar geometrical property of the geoid must evidently be due to an important physical cause. In order to accurately recognize this cause I have concentrated further investigations on this geometrical property.

These two regular anomaly systems must be brought about either by the anomaly of a specifically regular mass distribution of the entire globe or — what is more likely — by an asymmetric mass distribution of the Earth's core and by the

movements in connection with it. Thus in what follows these acting media will be called "deep seated sources". If the anomalies brought about by the deep seated sources are subtracted from the whole geoid, then the effect of surface masses is obtained in the residual picture. The knowledge of these, however, may lead to a better recognition of the structure of the crust and upper mantle.

The radial sum of two rotation-symmetrical forms is mirror-symmetric to the plane of the symmetry axes. Concerning the geoid we can easily state that this plane respectively the main circle connected with it is not the equator. Thus in the interest of obtaining a better approximation when computing the geoidal figure we must look for axes directed towards more general positions. The approximation on the other hand is disturbed by the effect of surface masses, the distribution of which cannot be assumed as rotation-symmetrical at all, i.e. we cannot get clearly defined axis intersections representing accurately the effect of deep seated masses.

In order to avoid this difficulty the geoid at a height of 6000 km was used proving that it is the sum of two rotation-symmetrical forms. The choice of such a big height resulted in a filtering effect based on the following reasoning: first of all the inhomogeneous surface masses are small relative to the global mass of the Earth, and in addition they are mainly in isostatic equilibrium. Thus the positive weight corresponding to the lofty mountains is balanced by the less dense mountain roots sinking into the surrounding more dense mantle material. Therefore, this latter mass difference presents itself as a negative mass, as a mass deficit. The intensity of a field of such a structure diminishes with the cube of the distance and it becomes negligible at a relatively small distance from the masses (Fig. 11). And what is more, the unbalanced masses are less by an order of magnitude in relation to the balanced ones and even the effect of such mass differences diminishes only with the square of the distance, their effect is also negligible in great heights owing to their small dimension (Fig. 12).

The disturbing effect of surface masses was significantly decreased, using the filtering effect of the height. This is important as the intricate system of surface sources can not be well described by a simple mathematical formula, while the deep seated sources mentioned above present themselves as the sum of two rotation-symmetrical

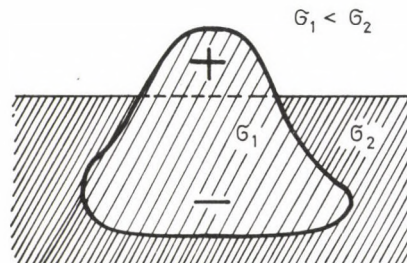


Fig. 11. Dipole character of the mass inhomogeneity due to isostasy

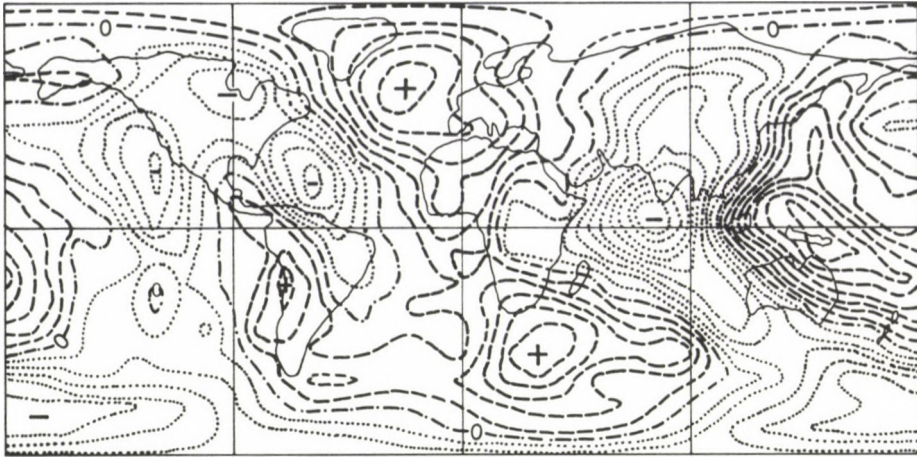


Fig. 12a. The SAO III geoid. Parameters of the reference ellipsoid are:  $a = 6\,378\,140$  m,  $f = 1/298.256$ . The distance between contour lines is 10 m

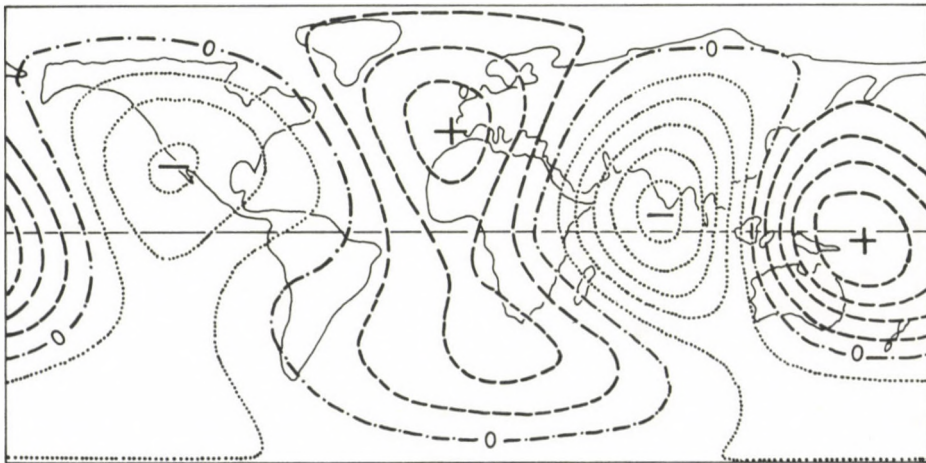


Fig. 12b. The geoid at the height of 6000 km above the surface of the Earth. Parameters of the reference ellipsoid are:  $a = 12\,378\,140$  m,  $f = 1/2327.9$ . The distance between contour lines is 5 m

forms easy to be described. Thus at a height of 6000 km one can clearly determine the axis direction of rotation-symmetrical forms brought about by deep seated sources.

Hajósy at my Institute succeeded to obtain a mathematical criterium of the correct choice of approximating directions. It turned out as a matter of fact that the equation of the surface describing the radial sum of the two rotation-symmetrical forms as a function of special solid angles happens to be the same as the equation of the

intersecting curve lying in the symmetry plane as function of the corresponding plane angles. The reverse of the theorem also holds, i.e. if a surface possesses this analytical property then it is the radial sum of two rotation-symmetrical surfaces. In other words, if one computes the coefficients of the spherical functions from the data of the special main circle only, respectively from the data system of the entire geoid, one must get the same numerical results in both calculations in case of a correct choice of the direction of axes. The computations turned out to be rather lengthy, because the special main circle has been determined just by the directions of the axes (Appendix I).

The problem gets more complicated as the ellipticity due to the internal structure of the Earth had been taken into account in the polar flattening generally used which is not of the same importance in both approximations. If we use e.g. the equator or a main circle near it, the polar flattening is not to be taken into account. But if the global data system is used for the approximation, the polar flattening has an important role. Taking  $1/298.25$  as the value of the flattening the geoid does not contain any polar flattening. But a part of it is caused by the deep seated sources discussed, therefore the computations are to be made on an ellipsoid of a lesser flattening than mentioned above. Recognizing the dimensions of the equatorial ellipse it should be computed on a geoid with a flattening value of  $1/298.75$ , because this does not contain any more the flattening component due to the equatorial ellipticity. This change brings about an increase of 25 m in the polar and a decrease of 13 m in the equatorial radius.

Thus the polar flattening is decomposed into two parts; one of them — the overwhelming one — comes from the rotation, the other — much less — is a consequence of internal mass inhomogeneity. It is known that the flattening of the Earth — with the parameter values accepted today — is by 0.5 percent (i.e. by about 100 m) greater than that allowed by hydrostatic equilibrium. Thus nearly a half of this deviation can be explained by the internal asymmetric inhomogeneity (Fig. 13). The other part may be perhaps the result of an interaction of the two mass domains not taken into account before, but this is still a matter of question.

This change in flattening at the height of 6000 km means that the equatorial major axis is 65 m less than that of the so called best-fitting ellipsoid. The geoid undulation in the geocentric direction ( $\varphi$ ,  $\lambda$ ) directed towards a point  $P$  of the unit sphere is

$$\Delta r(\lambda, \varphi) = a \cdot \sum_{n,m} [C_{nm} \cos m\lambda + S_{nm} \sin m\lambda] \cdot P_{nm}(\cos \varphi),$$

where  $C_{nm}$ , respectively  $S_{nm}$  are the harmonic coefficients of the Earth's gravity potential computed for a height 6000 km;  $a = 12378133.5$  m is the half major equatorial axis.

The value system of the geoid undulations is approximated by the sum of two zonal spherical harmonic series:

$$\Delta r(\lambda_i, \varphi_i) \approx \sum_n A_n P_n(\cos \delta_{1i}) + \sum_n B_n P_n(\cos \delta_{2i}),$$

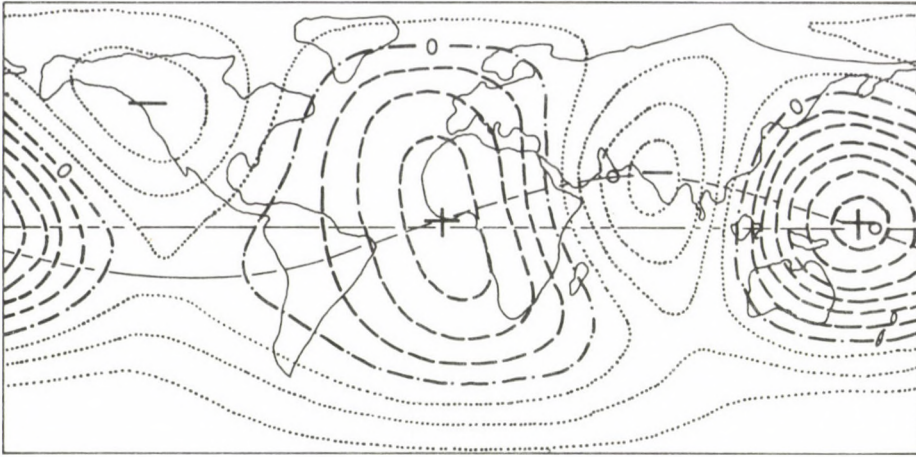


Fig. 13a. The geoid at the height of 6000 km above the surface of the Earth. Parameters of the reference ellipsoid are:  $a = 12\,378\,133$  m,  $f = 1/2337.1$ . The distance between contour lines is 5 m

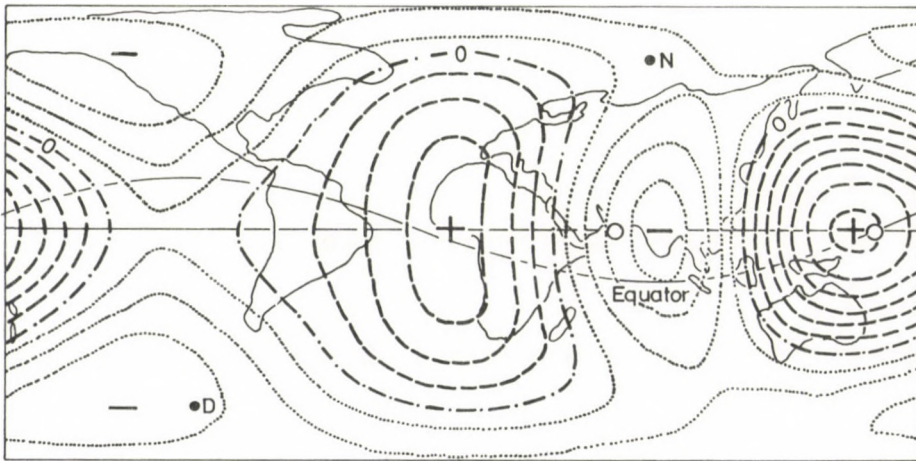


Fig. 13b. The geoid is symmetrical to the plane of the inclined main circle

where  $\cos \delta_{1i}$ , respectively  $\cos \delta_{2i}$  are the spherical distances between fixed points  $P_1$  and  $P_2$  and the point  $P_i$  of the unit sphere (see Fig. 14) and

$$\sum_i \left[ \sum_n A_n P_n (\cos \delta_{1i}) + \sum_n B_n P_n (\cos \delta_{2i}) - \Delta r(\lambda_i, \varphi_i) \right]^2 = \text{minimum.}$$

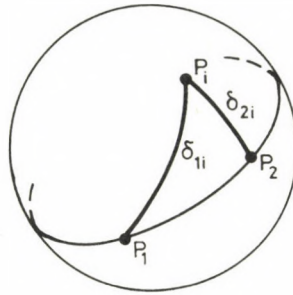


Fig. 14

The coefficients  $A_n$ ,  $B_n$  of the approximating functional series have been computed in two ways. In the so called spatial approximation the entire data system of the geoundulations — along an equidistant degree network — has been involved in the minimum condition, while in case of the so called plane approximation only data of the main circle defined by  $P_1$ ,  $P_2$  have been taken into account.

There is only one pair of points  $P_1$ ,  $P_2$  for which the coefficients  $A_n$ ,  $B_n$  agree with one another (in a good approximation). Their geocentric coordinates are:

$P_1$	$P_2$
74.0°	90.0°
59.5°	163.5°

The numerical coefficients (with a dimension in meters) are:

$n$	$A_n$	$B_n$
2	-0.62	24.36
3	-11.09	12.28
4	-0.56	-0.81
5	0.75	-0.93
6	0.05	0.18
7	-0.07	0.04
8	0.05	0.01

The points  $P_1$ ,  $P_2$  may represent of course centres of small spherical circles, within which an agreement of the two approximations is fulfilled; their radius is about  $0.5^\circ$  around the central points.

The approximation presents very small deviations from the geoid-undulations; the fit of the approximation computed from the ratio of standard deviations is 97

percent. The maximum difference is also very small: about 3 m. Thus at a height of 6000 km the geoid is really the sum of only two rotation-symmetrical forms and the directions of the computed axes are in a close mathematical coordination one with another, therefore their determination should be considered as an accurate one (Fig. 15).

At the same time Hajósy succeeded to prove mathematically that a rotation-symmetrical level surface can be brought about only by masses the density distribution of which is also rotation-symmetrical. This fact together with that applied with the double computation discussed above leads to a statement being mathematically exact which is rather unusual in geophysics. Namely, if the global sources of the geoid figure

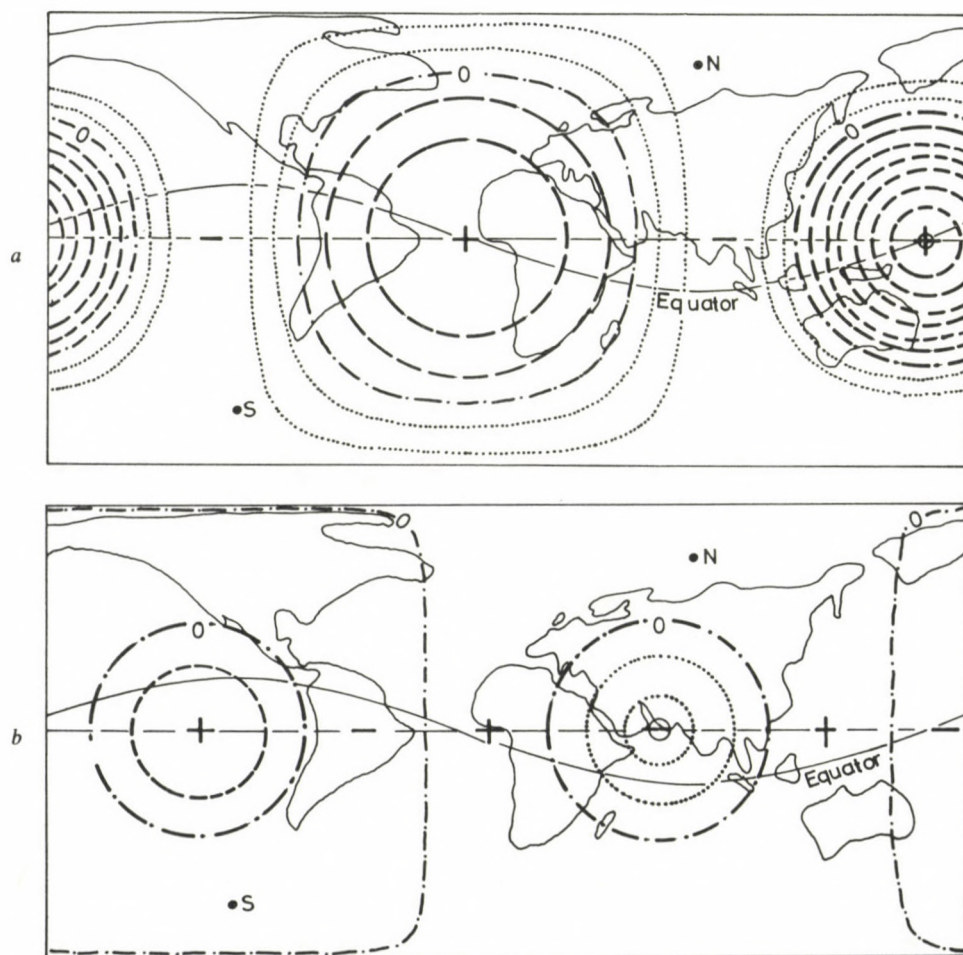


Fig. 15a-b. The rotation-symmetrical surface constructing the geoid. Their radial sum generates the data system of the geoid at the height of 6000 km. The distance between contour lines is 5 m

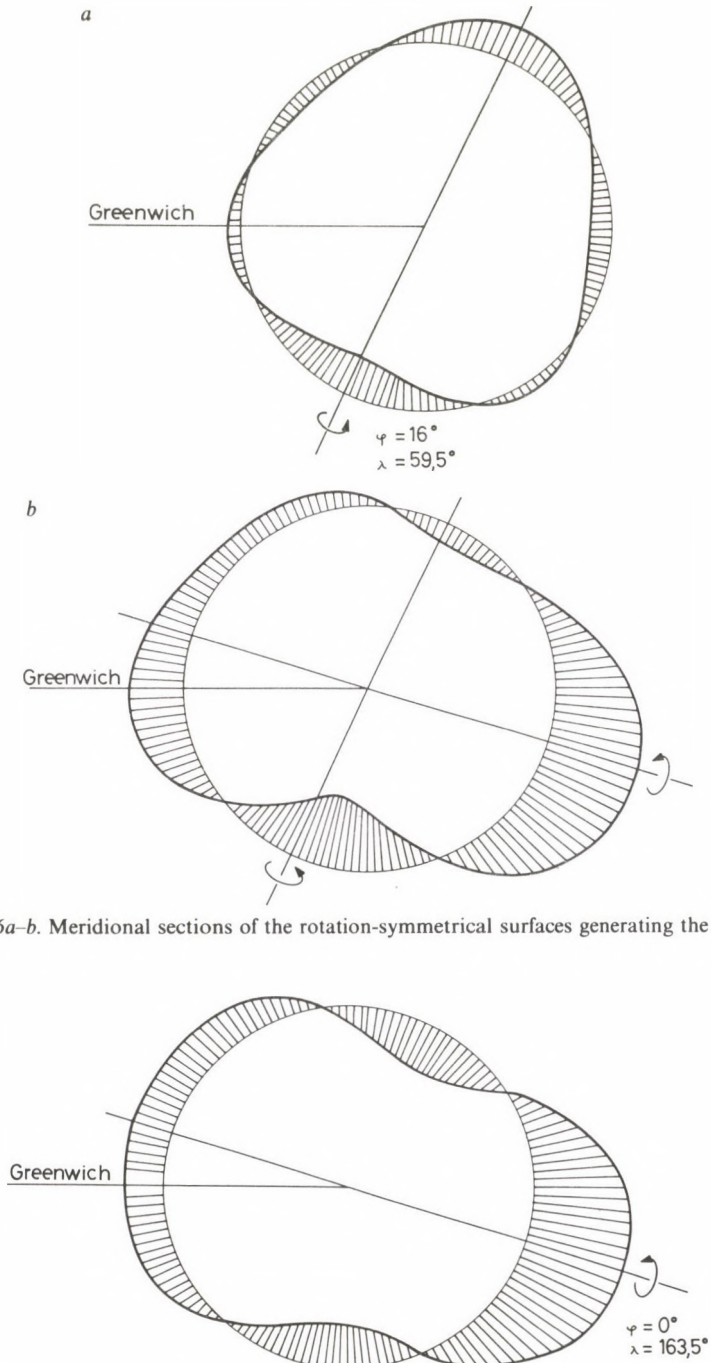


Fig. 16a–b. Meridional sections of the rotation-symmetrical surfaces generating the geoid

Fig. 16c. Radial sum of the curves

have only two rotation-symmetrical components and if these can only be brought about by a rotation-symmetrical mass distribution, then the composition of the geoid figure discussed above is the only possible solution of the problem, the geoid form can be built up so and only so. This excludes, however, the usual explanation that the 6 big geoid anomalies would be brought about by 6 separate mass inhomogeneities at the mantle-core interface. Or if we want to adhere to the supposition of the possible existence of more sources, these can be reduced into two rotation-symmetrical ones (Appendix II).

Naturally, the level anomalies observed at the surface exist also in the depth — in case of sources existing within the core, at the core-mantle interface — but the causal conditions are reversed, i.e. the geoid undulations observed at the surface are not caused by the possible undulations of the core boundary, but both are brought about by the two rotation-symmetrical sources.

A more precise study of the details shows that:

1. The intersecting points of the axes of the rotation-symmetrical forms are near the characteristic points of the magnetic field and in order to assure a better approximation one has to move out from the equator towards north as is the situation in the magnetic case.

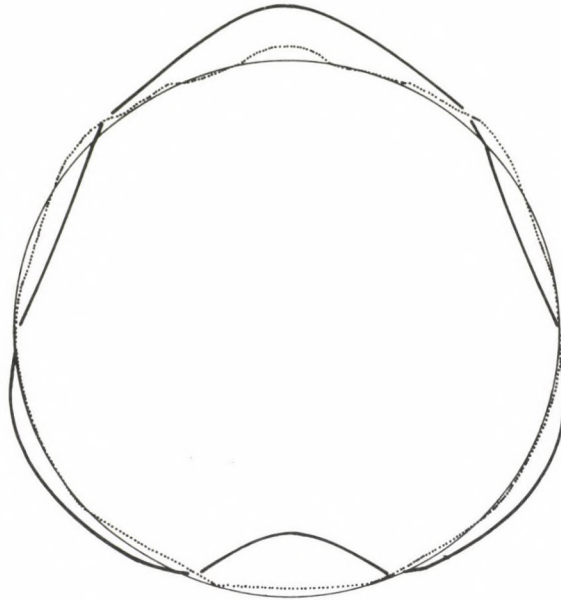
2. The approximating form with an axis pointing towards Australia is elliptic, the difference between the major and minor axes is 72 m; its pointed end is directed towards Australia in all approximations (Fig. 16), showing that the deep seated inner core of a higher density than its surrounding is of an eccentric position towards Australia according to the results of magnetic measurements.

3. The rotation-symmetrical form represented by the axis pointed towards Pakistan has very small coefficients of even order in its spherical function, i.e. this form has no ellipticity. The problem is: what is the mass distribution by which such a niveau-level distortion can be brought about?

4. Having subtracted the deep seated sources — reduced to the surface — the gravity field of the Earth does not possess any north-south asymmetry. The pear-shape of the geoid is only apparent due to the peculiarities of spherical functions (Fig. 17); namely, the axis of rotation is in case of spherical functions a special coordinate direction and the projection into the direction of the axis of any distortion of the geoid form is so to say concentrated into this direction.

These component forms — reduced from the niveau-levels at 6000 km height to the surface — represent by their general features the influences of global mass inhomogeneities on the geoid form. Thus, the deep seated effects — coming from the core — could be separated in the geoid figure from those originating at the surface (Fig. 18, Fig. 19).

A part of these results appeared already in my first inaugural lecture, mainly in form of guesses, but since then they obtained wider interpretation possibilities owing to a more general approximation.



— zonal part the geoid  
 ..... zonal part of the geoid anomalies

Fig. 17. Zonal part of the geoid and of the geoid anomalies

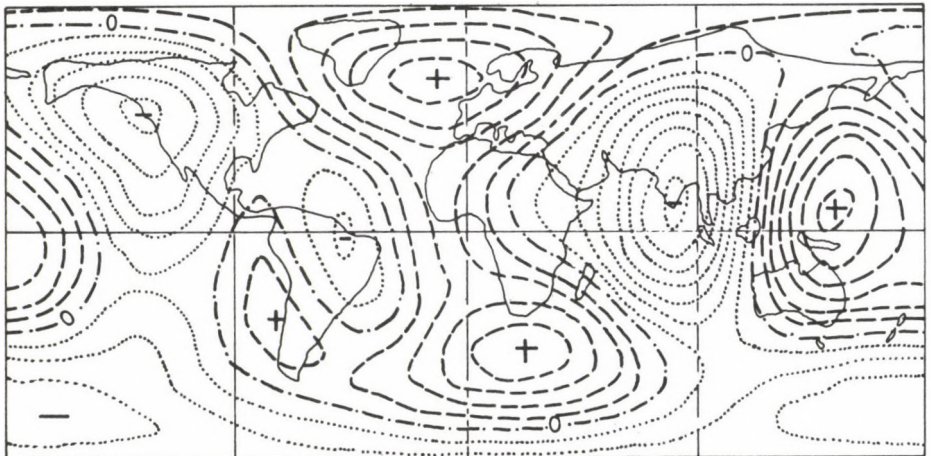


Fig. 18. Geoid undulations of the global sources at the surface of the Earth. The distance between contour lines is 10 m

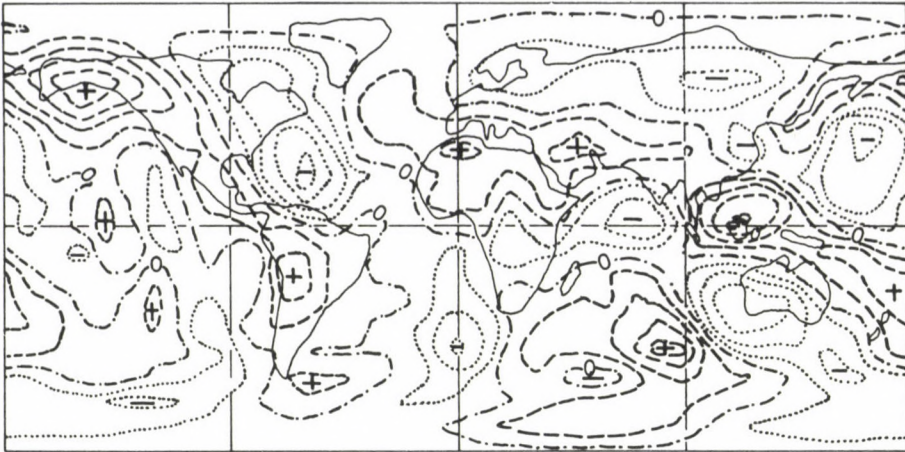
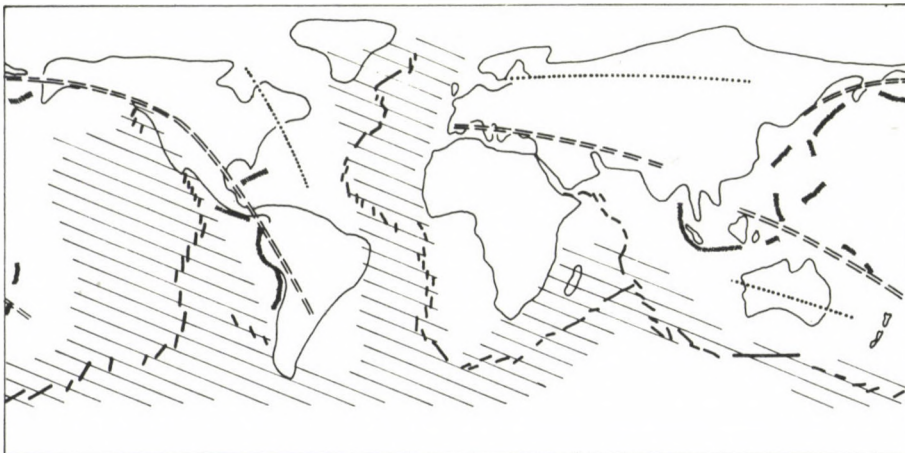


Fig. 19. Geoid anomalies at the surface of the Earth. The distance between contour lines is 10 m



- |   |                                   |   |          |   |                                     |
|---|-----------------------------------|---|----------|---|-------------------------------------|
|  | central line of the oceanic ridge |  | positive |  | central line of the geoid anomalies |
|  | island arc                        |  | negative |  | area of small geoid anomalies       |

Fig. 20. Geoid anomalies and the big tectonic lines of the Earth

If this form composed of rotation-symmetrical components is subtracted from the entire geoid, the remaining residual part represents the influence of inhomogeneities near the surface as due to the isostasy of the middle and deep mantle, no major mass inhomogeneities are existing there. The inhomogeneities near the surface are — on the other hand — in close connection with the relief, respectively with the dynamics of the surface masses forming it; one can also suppose that these and only these are reflected in the residual geoid (Fig. 20).

In fact, the two big mountain systems of the Earth, the Alp-Himalaya and the chain of Cordilleras and Andes present themselves as positive stripes in the residual picture. Scandinavia-Siberia form a negative zone which can be explained by the effect of ice cover accumulated during the ice age. The ice cover pressed in the material of the crust and upper mantle and an isostatic equilibrium resulted. After a quick melting of the cover a mass deficit has been brought about and a slow compensating process started.

In addition, it is remarkable that the zero line of the residual anomalies approximately follows the line of the oceanic ridges. This is an interesting coincidence, as the material of the ridges is probably in an isostatic equilibrium due to intense movements occurring there. Observations, however, lead to other considerations, too. The ridges can be considered generally as geologically symmetrical structures on their both sides. But if the zero line of the residual geoid picture coincides with them, then we find on the one side of the lines positive, on the other negative geoid regions, i.e. the plates on the two sides of the ridge are of different structure. This phenomenon should be further studied and interpreted.

This study is also indicating possible directions of further investigations. It would be desirable to reduce further the residual geoid anomalies in relation with relief influences; this could lead to a further separation of effects due to statically balanced and unbalanced masses, these latter trying to get into an equilibrium, thus further data could be obtained concerning the dynamics of the Earth's core.

At the beginning of the present gravity investigations it was concluded — based on the eccentric structure of the magnetic field of the Earth — that there existed an eccentric mass distribution in the Earth's core. Starting from this it was recognized that the main part of the geoid figure (its two third part about) is the sum of two rotation-symmetrical forms, while its minor (about third) part is due to the effect of irregular surface inhomogeneities. The directions of the axes of the rotation-symmetrical forms — as mentioned above — are in good agreement with the main directions of the magnetic field of the Earth. Supposing that this agreement is not of an accidental character, but it indicates the existence of a physical connection, the intersection points of these axes should be shifting towards west in the same manner as those of the magnetic dipole do. For the shift of the gravitational sources with the same speed the value of secular gravity change at the surface was computed. The change is very small and unfortunately the civilized regions coincide with areas of a small change (Fig. 21).

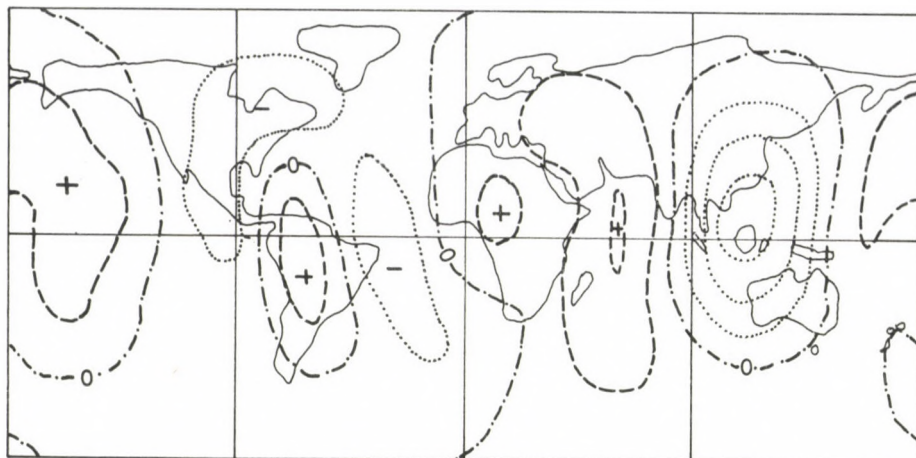


Fig. 21. Supposed secular gravity variation. Change of the  $g$  during a year. The distance between contour lines is  $20 \mu\text{gal}$

A detection of this secular change is very difficult, but it is perhaps not hopeless if modern laser technics is applied in the measurements. In the case if the value of  $g$  does not change due to some compensation setting in during the rearrangement of masses, a similar westward drift would be detected in the change of the geoid form, too. The detection of this would furnish a decisive proof of the connection of the gravity and magnetic fields, but at present it is only a hypothesis based on the closeness of characteristic points.

The place of gravity points can be computed theoretically with any accuracy, in practice, however, the disturbing effect of surface inhomogeneities cannot be fully eliminated and their effect on the measurements, respectively on the computations cannot be cancelled. For the magnetic points the occurrence of errors is more probable. Even Adolf Schmidt knew when he gave the place of the best approximating dipole for the magnetic field based on spherical harmonic coefficients (the determination involved the reduction of the number of second order members of the spherical harmonics from 5 to 1 applying certain coordinate transformations) that the new concept is somewhat of a hypothetical character so that he put always in inverted commas the term "the magnetic centre of the Earth". His successors did not observe the inverted commas so that the emphasis on the hypothetic character of the concept faded.

All these features of the definition, the measurement and approximation procedure cause the occurrence of errors in the determination of the characteristic magnetic as well as gravity points. Therefore, beyond the proving force of coincidence it is to be investigated, if the gravity field presents a secular variation and if a westward drift could be detected in it. In case if this holds the logical connection can be accepted as a physical one and conclusions can be drawn concerning the physical properties of

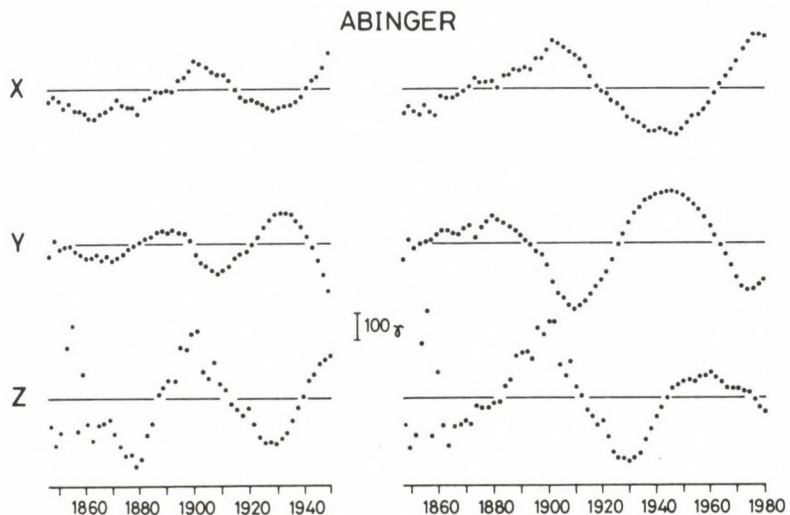
the Earth's core, the mechanical energies can be connected with the energy processes of the interior of the globe and an energetical background would be provided for a few well known phenomena (e.g. the terrestrial magnetic dynamo, secular magnetic variation).

### Possible research directions and objectives

In the investigations a few data systems were studied in connection with the Earth. Conclusions were drawn from the similarities, respectively from divergences, using some results of geophysical, geodetical and astronomical observations. We have generally made use of Legendre polynomials — spherical harmonics. It is of interest that the mathematical treatment — beyond its role as a tool of quantitative description — furnished in some cases the basis for statements setting up real limits for the possibilities.

According to Le Minh Triet's (1983) magnetohydrodynamic computations the internal core of the Earth oscillates freely in the material of the outer core, the period is supposing conventional material parameters (density, viscosity, etc.) about 67 years, which agrees rather well with the period detected in magnetic series more than 30 years ago.

It seems that this period of a half century has a basic importance in the interpretation of the processes of the Earth's core and its study promises important results. The previous investigations have been namely closed using data series up to 1950. Since then these series has became longer by 30 years and many new



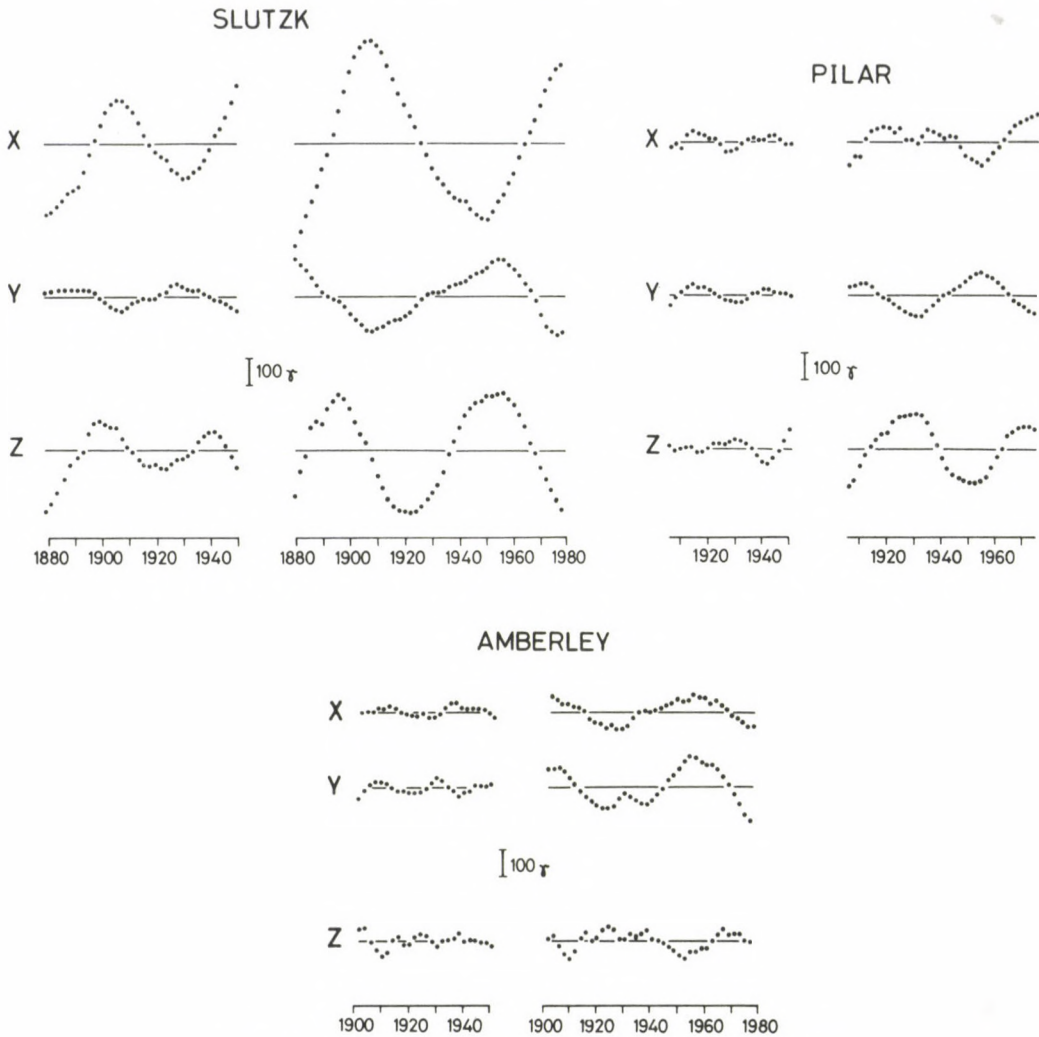


Fig. 22. The superimposed wave at various observatories till 1980

observatories present well usable data series of significant length and the number of unobserved areas has decreased.

Many new informations can be obtained by means of a repeated computation using series longer by 30 years. The first data obtained from it indicate that the helix is developing further. Modern computers enabled a more detailed investigation of these space curves and provided material for a very accurate comparison of them. Thus the curves show more details of the physical processes bringing about the secular variation (Fig. 22).

The appearance of the 50 years period and its further tracking in the rotational and displacement processes of the Earth may be the source of further considerations, but the supposition of the existence of connections is still a hypothetical one. The corroboration of this hypothesis depends mainly on the determination of the existence of a secular variation of the geoid figure and for this purpose long lasting and tenacious efforts in measuring and computing are needed.

The inner core happens to be in a zero gravity domain, thus the buoyancy law does not fix its place. But till now it has been impossible to take into account the mutual influence of the individual mass domains. Although according to the potential theory the gravity field inside a homogeneous spherical shell vanishes, the value of this effect is unknown in a system of confocal ellipses, especially if the homogeneity of the outer mass domains cannot be unambiguously postulated. It would be also desirable to find the position of the inner core based on the known structural elements of the outer core and of the mantle-crust, as well as on the deviation from the spherical structure, using also a full appreciation of the mutual effects of the mass domains.

In any case a globe of asymmetrical structure possesses more degrees of freedom, therefore it provides us a more extended research domain and more flexible reasoning possibilities than the central-symmetrical way of thinking. The supposition of a complete central symmetry excludes from the research possibilities a score of possible changes. The surface observations are definitely in contradiction to an exact central symmetry, but even in a great depth we must not adhere to it — maybe for reasons of comfort or symmetry —, because two of the force fields prove clearly and in a measurable way the existence of asymmetry and enable to compute its amount.

In the future it will be perhaps possible to approximate better the solution of this difficult, but for the geophysics very important problem applying more accurately defined approximation ideas and by carrying out a continuous study of all the features of the geoid figure.

## Appendix I

The geoid undulation can be computed from the spherical harmonic coefficients of the gravity potential of the Earth; it is the radial difference of two surfaces connected with the same potential value: the geoid and the best fitting ellipsoid. Thus, this is a surface of potential character in essence, due to a part of the mass distribution of the globe, which deviates from the regular one.

The values of the geoidundulation-function can be calculated at various distances from the origin, too; the values of the function computed for an individual distance determine the figure of level surfaces characterizing the mass anomalies of the Earth. At a sufficiently great distance from the surface of the globe, the influence of the surface irregularities is evidently rather small, but the oscillation of the level surface does not diminish at the same rate. E.g. at a height of 6000 km from the surface the maximum estimated effect of the surface irregularities is about 1 m, while the maximum of the undulation values is 35 m. According to it the surface series can be divided into the sum of two functions. One of them describes the mass anomalies at the surface; its value diminishes rapidly with the height. The other part is caused evidently by sources of much bigger mass situated at great depth; this should be called the main part of the geoid. Within the geoidal configuration this corresponds in essence to the six big anomalies.

It has been proved by computations that any level surface of the main part of the geoid can unequivocally be represented as the radial sum of two cylinderymmetrical surfaces. In theorem of Appendix II it will be proved that only the level surface series of a cylinderymmetrical mass distribution can itself be a cylinderymmetrical one. Thus it can be stated that the main part of the geoid is caused by two cylinderymmetrical sources. This representation is unequivocal, i.e. if the formation of the main part of the geoid is to be explained by the supposition of more than two sources, this can only be made by a redistribution of the original two cylinderymmetrical sources into parts.

Thus, according to the present calculations, the main part of the geoid is the radial sum of two cylinderymmetrical surfaces. This statement has not been based on a simple approximative computation. Namely, the sum of zonal spherical harmonic series describing cylinderymmetrical surfaces chosen accordingly, approximates the geoidundulations with a surprisingly small error. Owing to the additive character of the potential we could not formulate yet concrete statements based only on the fact above, not mentioned that the fit of an approximation can variously be improved by means of numerical methods (e.g. by choosing a better series of functions, by increasing the number of the terms of the series etc.). But the radial sum of two cylinderymmetrical surface possesses the unique property that its equation is unequivocally determined by the function describing the plane section of it on the plane of the symmetry axes. This property has been detected by Barta (1971) in his studies concerning the geoid.

In what follows I will give a proof of this property.

The plane polar angle is denoted by  $\vartheta$ . Let  $g_1$  be the plane curve symmetrical to the  $\vartheta_1$  direction and  $g_2$  the same for the direction  $\vartheta_2$ ; both should be closed curves (Fig. A-1).

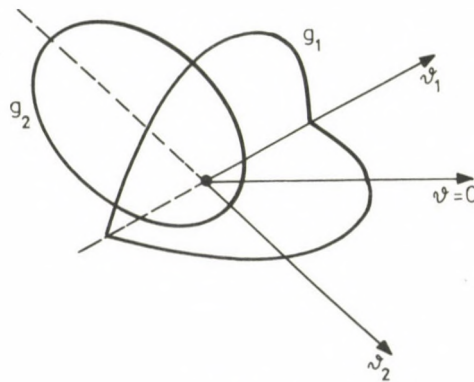


Fig. A-1

$g_1$  and  $g_2$  should represent equations of the curves in plane polar coordinates. Owing to the symmetry the cosines of the angles  $\vartheta - \vartheta_1$ , and  $\vartheta - \vartheta_2$  can be chosen as independent variables. The equations describing the curves are:

$$g_1 = g_1 [\cos (\vartheta - \vartheta_1)],$$

$$g_2 = g_2 [\cos (\vartheta - \vartheta_2)].$$

Let  $g$  be the radial sum of the two curves. Its equation in polar coordinates is:

$$g = g_1 [\cos (\vartheta - \vartheta_1)] + g_2 [\cos (\vartheta - \vartheta_2)].$$

The curves  $g_1$  and  $g_2$  should be chosen so that the domain bounded by  $g$  should be a simply connected one.

Let us rotate in the space both curves around their own symmetry axis. We get two cylinderymmetrical surfaces which are unequivocally determined by the functions  $g_1$  and  $g_2$ . If the spherical

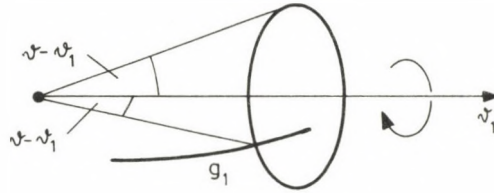


Fig. A-2

cosines of the solid angles measured from the  $\vartheta_1$  and  $\vartheta_2$  directions are chosen then as independent variables both surfaces are obviously described by the same function as the corresponding plane curves (Fig. A-2).

Therefore the equation of the surface expressed as the radial sum of the two surfaces with these specially chosen solid angle variables is the same as the equation of the curve  $g$  as function of the corresponding plane angles.

The sum-surface itself is obviously reflectionsymmetrical to the plane given by the directions  $\vartheta_1$  and  $\vartheta_2$ . The surface given by  $g_1$ , namely, is symmetrical to every plane containing the direction  $\vartheta_1$ , and this holds also for  $g_2$  and  $\vartheta_2$ . Thus the plane containing  $\vartheta_1$  and  $\vartheta_2$  is really the symmetry plane of the sum-surface.

Since  $g$  is encircling a closed and simply connected part of the plane, as a consequence the cylindersymmetrical surface is also a limiting surface of a simply connected domain of the space.

Thinking over the generating process of the sum-surface it is obvious that the above statement may hold in case of three curves and of the three surfaces corresponding to them. If the three symmetry axes are lying in a plane and if the three straight lines intersect just in the origin, then the equation of the sum-surface agrees with the equation of the curve of intersection lying in the symmetry plane, when suitable angle variables are applied. Nevertheless, there is an essential mathematical difference between the intersection-curves lying in the symmetry plane. According to our supposition  $g$  is bounded and continuous on the  $[0, 2\pi]$  interval, therefore its Fourier series represents the curve  $g$  at least almost in all points. Thus  $g$  can be represented in the form

$$g(\vartheta) = \sum_{n=0}^{\infty} a_n \cos n \vartheta + \sum_{n=1}^{\infty} b_n \sin n \vartheta .$$

This can easily be transformed into a series in the terms of the system

$$\{1, \cos n(\vartheta - \vartheta_1), \cos n(\vartheta - \vartheta_2)\}_{n=1}^{\infty} ;$$

in case of suitable  $\vartheta_1, \vartheta_2$  angles, the members of the system are linearly independent. Thus the sum of two symmetrical plane curves can unequivocally be written as function of the arguments

$$\cos n(\vartheta - \vartheta_1), \quad \cos n(\vartheta - \vartheta_2) .$$

In case of three curves this does not hold any more, as the functions

$$\cos n(\vartheta - \vartheta_1), \quad \cos n(\vartheta - \vartheta_2), \quad \cos n(\vartheta - \vartheta_3)$$

are linearly dependent for any fixed  $\vartheta_1, \vartheta_2, \vartheta_3$  and for all positive integers  $n$ . This can be expressed so that the sum of three (and in consequence no matter of how many) symmetrical plane curves — where the symmetry axes intersect in the origin — can always be written as the sum of two curves of such a character.

Let us summarize the statements concerning the radial sum of cylindersymmetrical surfaces.

Let the equation of a closed surface in a direction passing through any point  $P$  of the unit sphere be (using the notations in Fig. A-3):

$$g(P) = g_1(\cos \delta_1) + g_2(\cos \delta_2) ,$$

where  $\cos \delta_1$ , and  $\cos \delta_2$  are the spherical cosines subtended with two fixed spatial directions. This equation obviously agrees with the equation of the intersection-curve falling into the plane of the fixed directions. At a spherical point  $Q$  of the symmetry plane we have:

$$g(Q) = g_1(\cos \alpha_1) + g_2(\cos \alpha_2) ,$$

where  $\alpha_1$  and  $\alpha_2$  are angles in the plane.

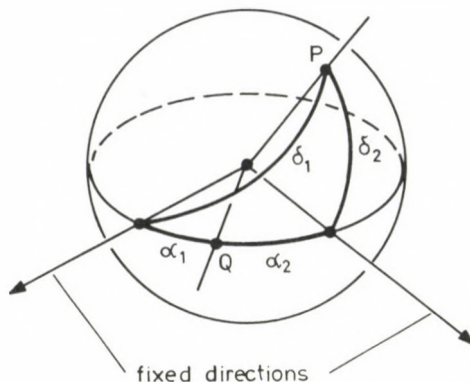


Fig. A-3

The surface determined by the function  $g$  is the radial sum of two cylindrically symmetrical surfaces. Based on what was said above, it is obvious that this surface alone has the property that the equation of one plane section of it determines the whole surface itself.

The main part of the geoid has this property. This has been verified by computing the numerical coefficients of two zonal spherical harmonic series applying two different approximations. With one of them the whole data system of the geoid was adjusted, while with the other only the part of the spherical harmonic series falling into the plane of the symmetry axes was treated. If the geocentric coordinates of the directions of the symmetry axes are  $(74^\circ, 59.5^\circ)$ , respectively  $(90^\circ, 163.5^\circ)$ , then the numerical coefficients obtained for the two approximations agree. Thus, the main part of the geoid is really unequivocally determined by a unique plane section of it.

Based on the following theorem a similar statement can be made for the sources too: the main part of the geoid is brought about by two cylindrically symmetrical sources.

### Appendix II

*Theorem:* The gravity potential function of a body is cylindrically symmetrical if and only if the body itself shows a cylindrically symmetrical mass distribution.

For notations see Fig. A-4.

The spherical coordinates of an internal point of a gravitational source are:  $(r, \varphi, \lambda)$ , those of a point outside the source:  $(R, \Phi, \Gamma)$  according to Fig. A-4.

The  $T$  gravity source is determined by two functions:

1.  $\sigma = \sigma(r, \varphi, \lambda)$ , the density function of  $T$ ,
2.  $\rho = \rho(\varphi, \lambda)$ , the equation of the surface covering  $T$ .

Let  $U$  be the gravity potential function of  $T$  in the points of the space outside  $T$ .

*Statement:* The potential function  $U$  is cylindrically symmetrical if and only if the source  $T$  is cylindrically symmetrical itself, i.e.

$$U(R, \Phi, \Gamma) = U(R, \Phi)$$

holds if and only if

$$\sigma(r, \varphi, \lambda) = \sigma(r, \varphi),$$

$$\rho(\varphi, \lambda) = \rho(\varphi).$$

*Proof:*

1. If the source is cylindrically symmetrical, the statement is obvious.
2. To prove the inverse statement, the spherical function series of the potential of the source  $T$  being dependent of  $\lambda$  too should be used. Taking into account the cylindricity of the function series, the statement can be obtained using the integrals giving the values of the numerical coefficients of the series.

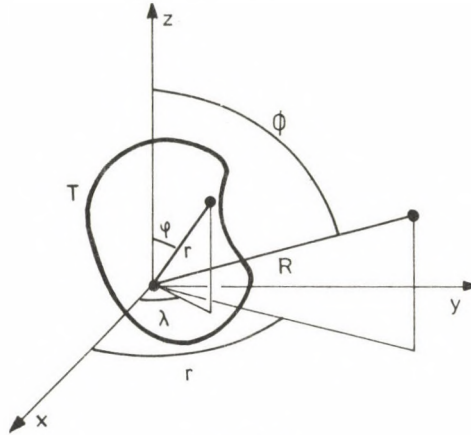


Fig. A-4

The potential of  $T$  determined by  $\sigma$  and  $\rho$  is in spherical coordinates:

$$U(R, \Phi, \Gamma) = \int_{\lambda=0}^{2\pi} \int_{\varphi=0}^{\pi} \int_{r=0}^{\rho(\varphi, \lambda)} \frac{\sigma(r, \varphi, \lambda) \cdot r^2 \sin \varphi \, dr \, d\varphi \, d\lambda}{\sqrt{r^2 + R^2 - 2rR(\cos \varphi \cos \Phi + \sin \varphi \sin \Phi \cos(\lambda - \Gamma))}}.$$

Obviously, it can be supposed that the functions  $\sigma$  and  $\rho$  possess all the necessary analytical properties (e.g.  $\sigma$  is continuous,  $\rho$  is simply connected, the integration domain is a normal one etc.), since the potential is an additive function. In case of a source  $T$  with unfavourable properties it can be divided into parts as long as all the parts satisfy the conditions.

The integrand contains just the generator function of the spherical harmonics series, therefore one has:

$$U(R, \Phi, \Gamma) = \int_{\lambda=0}^{2\pi} \int_{\varphi=0}^{\pi} \int_{r=0}^{\rho(\varphi, \lambda)} \sigma(r, \varphi, \lambda) \cdot \sin \varphi \cdot \sum_{n=0}^{\infty} \sum_{m=0}^n \frac{r^{n+2}}{R^{n+1}} \cdot P_{nm}(\cos \varphi) \cdot P_{nm}(\cos \Phi) \cdot \cos m(\lambda - \Gamma) \, dr \, d\varphi \, d\lambda.$$

The order of summation and integration can be interchanged, since the integrand is given by a uniformly convergent function series, thus one has:

$$U(R, \Phi, \Gamma) = \sum_{n=0}^{\infty} \sum_{m=0}^n \frac{1}{R^{n+1}} \cdot P_{nm}(\cos \Phi) \cdot [I_{nm} \cos m\Gamma + I_{nm}^* \sin m\Gamma],$$

where

$$I_{nm} = \int_{\lambda=0}^{2\pi} \int_{\varphi=0}^{\pi} \int_{r=0}^{\rho(\varphi, \lambda)} \sin \varphi \cdot \sigma(r, \varphi, \lambda) \cdot r^{n+2} \cdot P_{nm}(\cos \varphi) \cos m\lambda \, dr \, d\varphi \, d\lambda,$$

$$I_{nm}^* = \int_{\lambda=0}^{2\pi} \int_{\varphi=0}^{\pi} \int_{r=0}^{\rho(\varphi, \lambda)} \sin \varphi \cdot \sigma(r, \varphi, \lambda) \cdot r^{n+2} \cdot P_{nm}(\cos \varphi) \sin m\lambda \, dr \, d\varphi \, d\lambda.$$

According to the supposition, the potential function is cylindrically symmetrical:

$$U(R, \Phi, \Gamma) = U(R, \Phi).$$

Therefore, only the coefficients of the zonal terms of the series do not vanish:

$$U(R, \Phi, I) = \sum_{n=0}^{\infty} \frac{1}{R^{n+1}} \cdot P_n(\cos \Phi) \cdot I_{n0},$$

i.e.  $I_{nm} = 0,$  if  $m \neq 0,$   
 $I_{nm}^* = 0.$

Thus, from the cylindersymmetry of  $U$  it follows:

$$\int_{\lambda=0}^{2\pi} \cos m\lambda \int_{\varphi=0}^{\pi} \int_{r=0}^{\rho(\varphi, \lambda)} \sin \varphi \cdot P_{nm}(\cos \varphi) \cdot r^{n+2} \cdot \sigma(r, \varphi, \lambda) \, dr \, d\varphi \, d\lambda = 0,$$

$$\int_{\lambda=0}^{2\pi} \sin m\lambda \int_{\varphi=0}^{\pi} \int_{r=0}^{\rho(\varphi, \lambda)} \sin \varphi \cdot P_{nm}(\cos \varphi) \cdot r^{n+2} \cdot \sigma(r, \varphi, \lambda) \, dr \, d\varphi \, d\lambda = 0.$$

The internal double integral, therefore, as the function of  $\lambda$  is orthogonal to the elements of the system:

$$\{\cos m\lambda, \sin m\lambda\}_{m=1}^{\infty}.$$

From this and from the completeness of the trigonometric system it follows that:

$$\int_{\varphi=0}^{\pi} \sin \varphi \cdot P_{nm}(\cos \varphi) \int_{r=0}^{\rho(\varphi, \lambda)} r^{n+2} \cdot \sigma(r, \varphi, \lambda) \, dr \, d\varphi = C_{nm}$$

is constant for  $n, m = 1, 2, \dots$ . Therefore, the value of the inner integral may depend only on  $\varphi$ :

$$\int_{r=0}^{\rho(\varphi, \lambda)} r^{n+2} \cdot \sigma(r, \varphi, \lambda) \, dr = D_n(\varphi).$$

It is to be proved only the independence of  $\sigma$  and  $\rho$  on  $\lambda$ , therefore the designation of the dependence on  $\varphi$  is omitted for sake of simplicity.

Thus, as a consequence of cylinder-symmetry of  $U$  the following identity results:

$$\int_{r=0}^{\rho(\lambda)} r^{n+2} \cdot \sigma(r, \lambda) \, dr = D_n$$

this being constant for  $n = 1, 2, \dots$

According to the lemma (to be proved later) this can hold if and only if

$$\sigma(r, \lambda) = \sigma(r),$$

$$\rho(\lambda) = \rho \quad \text{constant},$$

i.e. the source body is a cylindersymmetrical one.

**Lemma:**

Let  $r$  and  $\lambda$  be the polar coordinates of a point of the plane. Let  $\rho$  be a closed continuous curve for which (Fig. A-5)

$$0 < \rho(\lambda) < 1, \quad \lambda \in (0, 2\pi).$$

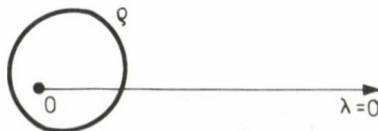


Fig. A-5

Let  $\sigma$  be a continuous function in the domain bounded by  $\rho$ . Let  $f_n$  be the following function:

$$f_n(\lambda) = \int_{r=0}^{\rho(\lambda)} r^n \cdot \sigma(r, \lambda) dr, \quad n = 1, 2, \dots \quad (1)$$

*Statement:*  $f_n$  is a constant independent of  $\lambda$  for every positive integer  $n$  if and only if  $\rho$  is just a circle and  $\sigma$  is a cylindersymmetrical function, i.e.

$$f_n(\lambda) = D_n \quad \text{constant} \quad (2)$$

if and only if

$$\begin{aligned} \sigma(r, \lambda) &= \sigma(r) & \text{and} \\ \rho(\lambda) &= \rho \quad \text{constant.} \end{aligned} \quad (3)$$

*Proof:*

From the fulfillment of the two conditions (3) it follows evidently that Eq. (2) is satisfied.

Now we will prove that also from Eq. (2) it follows the validity of Eq. (3). It is obvious that from the two statements of Eq. (3) it is sufficient to prove one and the other one follows from it. Therefore we will prove that, if

$$\int_0^{\rho(\lambda)} r^n \cdot \sigma(r, \lambda) dr = D_n, \quad n = 1, 2, \dots,$$

then

$$\rho(\lambda) = \rho \quad \text{constant.}$$

Let the primitive function of Eq. (1) be denoted by  $G$ :

$$G(r, \lambda) = \int r^n \cdot \sigma(r, \lambda) dr.$$

$G$  as a function of  $r$  is not identically constant, since

$$\frac{\partial G(r, \lambda)}{\partial r} = r^n \cdot \sigma(r, \lambda) \neq 0. \quad (4)$$

According to the supposition:

$$G(r, \lambda)|_{r=\rho(\lambda)} - G(r, \lambda)|_{r=0} = D_n.$$

Since the value of  $G$  at the lower limit is just  $G_0$ , the value of the function at the origo, one has

$$G[\rho(\lambda), \lambda] = D_n + G_0 = A \quad \text{constant,}$$

i.e. the primitive function is constant along the  $\rho$  curve.

Let us compute the integral of order  $n+1$  — using  $G$  — by partial integration:

$$\begin{aligned} D_{n+1} &= \int_0^{\rho(\lambda)} r \cdot r^n \cdot \sigma(r, \lambda) dr = [r \cdot G(r, \lambda)]_0^{\rho(\lambda)} - \int_0^{\rho(\lambda)} G(r, \lambda) dr = \\ &= \rho(\lambda) \cdot A - \int_0^{\rho(\lambda)} G(r, \lambda) dr, \end{aligned}$$

from which

$$\int_0^{\rho(\lambda)} G(r, \lambda) dr = \rho(\lambda) \cdot A - D_{n+1}. \quad (5)$$

Similarly to what was said above in connection with  $G_0$ , the value at the lower limit of the integral (5) is also independent from  $\lambda$ , i.e. constant, therefore the primitive function  $G^*$  of Eq. (5) is:

$$G^*(r, \lambda) = A \cdot r.$$

Hence one has:

$$G(r, \lambda) = \frac{\partial G^*(r, \lambda)}{\partial r} = A \quad \text{constant,}$$

in contradiction to the statement given (4); therefore the curve  $\rho$  cannot depend on  $\lambda$ , i.e. it represents a circle.

Thus it is proved that a group of cylindersymmetrical level surfaces can only be caused by a source with cylindersymmetrical mass distribution.

## References

- Barta Gy 1954: On the 44 years period of the secular variation of the terrestrial magnetic field (in Hungarian). *Geofizikai Közlemények*, 3, 2–24.
- Barta Gy 1956: A 40–50 year period on the secular variation of the geomagnetic field. *Acta Geol. Acad. Sci. Hung.*, 4, 15–42.
- Barta Gy 1957: On the secular variation of the terrestrial magnetic field (in Hungarian). *Geofizikai Közlemények*, 6, 29–35.
- Barta Gy 1958a: Transversal and longitudinal effect of the secular variation of the terrestrial magnetic field (in Hungarian). *Geofizikai Közlemények*, 7, 3–31.
- Barta Gy 1958b: Über die Säkularbewegung des magnetischen Zentrums und der magnetischen Pole der Erde. *Zeitschrift für Geophysik*, 24, 197–209.
- Barta Gy 1959: On the drifting in time of the magnetic poles and centre of the Earth (in Hungarian). *Geofizikai Közlemények*, 8, 3–17.
- Barta Gy 1962a: Der Zusammenhang der Exzentrizität des erdmagnetischen Feldes mit der Dreiachsigkeit der Erde. Deutsche Akad. der Wiss. zu Berlin, Geomagn. Inst. Potsdam, 29, 12–21.
- Barta Gy 1962b: Longitudinal and transversal effect of the secular magnetic variation computed on the basis of the observations of the San Miguel observatory. In: *Publ. comemorative do 50 aniversario do Obs. Magnético de S. Miguel, Acores, Lisboa*, 81–87.
- Barta Gy 1962c: The connection between the eccentricity of the terrestrial magnetic field and the triaxiality of the Earth (in Hungarian). *Geofizikai Közlemények*, 10, 45–62.
- Barta Gy 1967: The asymmetric structure of the Earth and its secular processes. Proc. of the Int. Symposium "Figure of the Earth and Refraction", Vienna 1967, *Zeitschrift f. Vermessungswesen*, 77–79.
- Barta Gy 1971: On the secular variation and distortion of the force fields of the Earth. *MTA X. Oszt. Közl.*, 2–4, 91–103.
- Barta Gy 1973a: Zu den physikalischen Zusammenhängen des asymmetrischen Baus des Erdkörpers. *Gerlands Beiträge Geophysik*, Leipzig, 82, 257–266.
- Barta Gy 1973b: Physical background of the geoidal figure. *Nature*, 243, 156–158.
- Barta Gy 1974: Satellite geodesy and the internal structure of the Earth. *Space Res.*, 16, 2–11.
- Barta Gy, Hajósy A 1981: Recent results of the study of physical background of the geoidal figure. *Space Res.*, 1, 195–202.
- Le Minh Triet 1983: Some new contributions to the magnetohydrodynamic theory of the secular short-period variations in the Earth's magnetic field. Thesis for a Doctor's degree. Ho Chi Minh City, Vietnam



## NEW POINTS OF VIEW FOR DETERMINING THE PARAMETERS OF THE REFERENCE ELLIPSOID OF THE EARTH

A HAJÓSY<sup>1</sup>

[Manuscript received February 13, 1984]

The paper — in connection with Barta's (1985) paper — deals with the determination of the parameters of the reference ellipsoid based on Barta's hypothesis on the internal structure of the Earth.

**Keywords:** geoid; internal structure of the Earth; reference ellipsoid; rotation-symmetrical density distribution

The level surface of the gravity field of the Earth coinciding with the average sea level is called the figure of the Earth or geoid. This surface is characterized by geoidal heights being the radial deviations of the geoid from the reference ellipsoid.

The reference ellipsoid is a very good approximation of the figure of the Earth being assumed to be rotation-symmetrical and showing a hydrostatic equilibrium state. The figure of the Earth is very similar to a rotation ellipsoid indeed, indicated also by the fact that the second degree harmonic coefficient of the gravity potential function of the Earth is about one thousand times greater than those of higher degrees. Therefore the reference ellipsoid can be taken as the niveau surface of a liquid-like globe rotating in its own gravity field. Thus, it is brought about by the rotation-symmetrical part of the mass distribution of the Earth as well as by the rotation of it, the symmetry axis being the rotation axis of the Earth having a fixed position. Because the internal mass distribution of the Earth is unknown, only approximating values of the parameters of the ellipsoid can be determined by some indirect way.

Thus, the irregular surface given by the geoid heights (i.e. the radial difference between the geoid and the reference ellipsoid) is caused by density differences deviating from a rotational symmetry. From the gravity potential function describing these differences the parameters of the ellipsoid can simply be calculated. Subtracting namely the potential function characterizing the geoid heights from the well known gravity potential of the Earth, just the reference ellipsoid is obtained as the level belonging to the difference function. This paper deals with the determination of the ellipsoid parameters on this way.

<sup>1</sup> Institute of Geophysics, University Lorand Eötvös, Budapest, Kun Béla tér 2, H-1083

Barta (1985) discusses the structure of source factors bringing about the geoid heights. He states that these sources can be divided into two groups. Owing to this separation the surface characterizing geoid heights can be divided into two parts. One of them is of a simple structure and it is probably due to density differences present within the core of the Earth. The other part is brought about by surface, respectively nearsurface inhomogeneities. The effect of these latter is rapidly diminishing with increasing distance from the Earth's surface. E.g. the undulation of the surface anomaly due to a layer of a thickness 1 km and 1 unit density difference having an extension as Hungary is about 0.1 m at a distance of 1 Earth radius. The maximum of the geoid height map at this distance is about 35 m, the average of the absolute values is 7 m. Thus at a sufficiently great distance the geoid heights reflect only the effect of deep seated density differences. In what follows we will call this the essential part of the geoid.

Niveau surfaces of the essential part of the geoid are very interesting surfaces from a geometric point of view: they can be represented unequivocally as sums of two cylinder-symmetrical surfaces. Of course, the symmetry axes of these deviate one from another as well as from the rotation axis of the Earth. Behind the geometrical point of interest there is a very important physical factor: the source itself is also of a similar character, i.e. the essential part of the geoid is brought about by two masses of cylinder-symmetrical distribution. One can prove, namely, that only a cylinder-symmetrical mass distribution can be the source of a cylinder-symmetrical series of niveau levels.

Let us construct the niveau surface of the potential function of the Earth's gravity at a sufficiently great distance from the globe. Owing to what was said above this can be splitted into two parts. One of them is a rotation ellipsoid representing the rotation-symmetrical part, the other represents the essential part of the geoid. This latter can also be described by means of a simple functional connection, because it reflects the effect of two masses of cylinder-symmetrical distribution. This functional connection can be determined in an indirect way since the internal mass distribution of the Earth is unknown.

The computation procedure is well known from Barta's paper (1985): the data system of the geoid heights is approximated by the sum of two series of zonal spherical harmonics. The numerical coefficients of the series depend — in case of a given computing method (method of least squares) and a given degree — obviously on two factors. One of them is the spatial position of the symmetry axes of the cylinder-symmetrical surfaces described by the spherical harmonics, the other is the data system itself. The numerical values of the geoid heights, namely, depend not only on the well known harmonic coefficients of the gravity potential of the Earth, but on the choice of the reference ellipsoid, too. Barta (1985) has shown that there exists an unequivocal solution of the problem, its numerical error is negligibly small. Thus, the essential part of the geoid is caused by two cylinder-symmetrical sources and this representation is unequivocal, i.e. if the essential part of the geoid were to be interpreted by assuming the existence of several sources this could be done only by dividing further the two sources

determined above. This unicity has also the consequence that the ellipsoid has been separated from the level surface series of the gravity potential function of the Earth so that it should really represent the rotation-symmetrical part of the mass distribution of the Earth. In what follows we will deal with the determination of this ellipsoid.

For the computations we have chosen the level surface at a height of 6000 km. For the calculation of the equation defining the geoid height map at this level we will use the data of SAO III (Gaposchkin 1973). (Data of the more recent geoids do not deviate essentially from the numerical values of SAO III (Gaposchkin 1980).)

The gravity potential of the Earth is as follows:

$$U = \frac{fM}{r} \sum_{n,m} \left(\frac{a}{r}\right)^n [C_{nm} \cos m\lambda + S_{nm} \sin m\lambda] P_{nm}(\cos \varphi),$$

where  $fM = 3.986013 \cdot 10^4 \text{ m}^3 \text{ s}^{-2}$ , a high precision constant,  
 $a = 6\,378\,140 \text{ m}$ , mean radius of the equator,  
 $r \approx a + h$ ,  $h = 6000 \text{ km}$ ,  
 $C_{nm}, S_{nm}$  harmonic coefficients,  
 $\varphi, \lambda$  spherical coordinates,  
 $P_{nm}$  spherical function.  
 The harmonic coefficients

$$C_{10} = C_{11} = S_{11} = C_{21} = S_{21} = 0$$

due to mechanical considerations. The value of  $C_{20}$  is about a thousand times greater than the other coefficients.

The geoid height is (Fig. 1):

$$\Delta r = \frac{U(r_e) - V}{g},$$

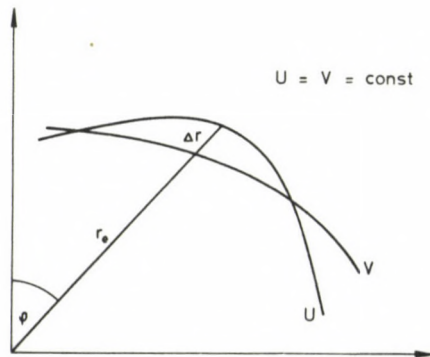


Fig. 1

where we suppose that the potential  $V = \text{constant}$  of the ellipsoid agrees with the potential value  $U$  of the geoid, and the gravity acceleration  $g$  between the surfaces given by  $U$  and  $V$  does not depend on the distance from the origin:

$$g = g_{\text{ellipsoid}}.$$

For the potential of the ellipsoid an approximation of fourth order is already sufficiently accurate:

$$V = \frac{fM}{r_e} \left[ 1 + K_2 \left( \frac{a}{r_e} \right)^2 P_2(\cos \varphi) + K_4 \left( \frac{a}{r_e} \right)^4 P_4(\cos \varphi) \right],$$

where

$$r_e = \frac{A}{\sqrt{1 + E^2 \cos^2 \varphi}}, \quad A = a + h.$$

Let us estimate the error of the approximation. From the fourth order approximation of the binomial series of the ellipsoid one has:

$$r_e = A \cdot \sum_{n=0}^2 \binom{-1/2}{n} \cdot (E^2 \cos^2 \varphi)^n + H_4.$$

At the distance chosen  $|H_4| < 2.5 \cdot 10^{-3}$  m. As computed from the terrestrial harmonic coefficients, the values of  $V_n$  diminish according to Table I.

Table I

$n$	$V_n (\text{m}^2/\text{s}^2)$
0	$3.22 \cdot 10^7$
2	$9.25 \cdot 10^3$
4	3.67
6	0.34

Since  $V$  is constant on the ellipsoid, the numerical coefficient of  $\cos^2 \varphi$ , respectively of  $\cos^4 \varphi$  should be zero in the expression of V Köhlein. Lundquist (1966) in his review study dealing with the Smithsonian geoid has computed — based on these two conditions — connections for the parameters, and he has given approximative solutions for them (the equations do not contain the rotation speed of the Earth any more, due to the height 6000 km):

$$0 = \frac{fM}{2} \left[ \frac{E^2}{A} + \frac{3K_2}{a} \left( \frac{a}{A} \right)^3 \left( 1 - \frac{E^2}{2} \right) - \frac{15K_4}{2a} \left( \frac{a}{A} \right)^5 \left( 1 - \frac{E^2}{4} \right) \right],$$

$$0 = \frac{fM}{4} \left[ \frac{E^2}{2A} + \frac{3K_2 E^2}{a} \left( \frac{a}{A} \right)^3 \left( 3 - \frac{E^4}{4} \right) + \frac{35K_4}{2a} \left( \frac{a}{A} \right)^5 \right],$$

where  $A$ ,  $E^2$ ,  $K_2$ ,  $K_4$  are unknowns to be determined:

$A$ ,  $E^2$  parameters of the reference ellipsoid,

$K_2$ ,  $K_4$  mass functions of the ellipsoid.

Thus — due to the equality of the potentials — two equations exist between the four unknown quantities, therefore, one has some freedom in choosing two parameters. (If a higher order development into series of the potential  $V$  is used, the number of equations will be naturally higher, but also the number of unknown mass functions  $K_{2n}$  will increase. The number of connections deducible from the equality of potentials is always less by two than the number of unknowns.)

For the satellite geoids the obviously most practical ellipsoid (the so-called best fitting ellipsoid) is chosen as follows:

$$K_2 = C_{20},$$

$$A = a + h,$$

and the geoid heights computed on this basis have accordingly small absolute values.

In case of this choice the parameters of the reference ellipsoid are at a height of 6000 km:

$$A = 12\,378\,140 \text{ m},$$

$$E^2 = 8.6309 \cdot 10^{-4}, \quad (f = 1/2328),$$

$$K_2 = -1.0826370 \cdot 10^{-3},$$

$$K_4 = 2.1119 \cdot 10^{-6}.$$

At such a great distance from the Earth, the change of  $g$  with geocentric latitude is as follows:

$$2.6019 \leq g \leq 2.6030 \quad (\text{m/s}^2),$$

so that with a high approximation one gets

$$\frac{fM}{gr_e} = A.$$

This simplification does not cause an error more than 1 cm. Even smaller is the error from the following simplifying supposition:

$$\frac{a}{r_e} = \frac{a}{A}.$$

Thus, the series of functions of the geoid height is:

$$\begin{aligned} \Delta r(\varphi, \lambda) = A \left\{ (C_{22} \cos 2\lambda + S_{22} \sin 2\lambda) \left(\frac{a}{A}\right)^2 P_{22}(\cos \varphi) + \right. \\ \left. + \sum_{n=3}^N \sum_{m=0}^n (C_{nm} \cos m\lambda + S_{22} \sin m\lambda) \left(\frac{a}{A}\right)^n P_{nm}(\cos \varphi) \right\}, \end{aligned}$$

where

$$C_{40} = C_{40}^* - K_4,$$

$C_{40}^*$  being the harmonic coefficient of the gravity potential, and the other numerical coefficients  $C_{nm}$ ,  $S_{nm}$  of the series are the harmonic coefficients of the gravity potential. Thus, the series of functions describing geoid heights at a given height is to be treated as a spherical surface harmonic. Introducing the quantities (of the dimension length):

$$X_{nm} = \frac{a^n}{A^{n-1}} C_{nm}, \quad Y_{nm} = \frac{a^n}{A^{n-1}} S_{nm},$$

the spherical surface harmonics can be written in the form:

$$\begin{aligned} \Delta r(\varphi, \lambda) = & (X_{22} \cos 2\lambda + Y_{22} \sin 2\lambda) P_{22}(\cos \varphi) + \\ & + \sum_{n=3}^N \sum_{m=0}^n (X_{nm} \cos m\lambda + Y_{nm} \sin m\lambda) P_{nm}(\cos \varphi). \end{aligned}$$

Therefore, the series of function  $\Delta r$  is a series where the coefficients of surface harmonics of zero, respectively first degree vanish, while among the second degree terms only those of the second order coefficients are different from zero.

Barta following the publication of the first satellite geoids arrived to the idea that the essential part of the geoid could be supposed as the sum of two zonal spherical harmonics developments. Nevertheless, in the course of his approximating computations he could get appropriate results only when applying a reduction depending on geometric latitude. It was therefore a reasonable idea that a physical explanation of the reduction should be looked for in a variation of the flattening of the ellipsoid.

The surface described by a sum of the two zonal harmonics is

$$\Delta r^*(\varphi, \lambda) = \sum_{n=1}^N \{A_n P_n(\cos \delta_1) + B_n P_n(\cos \delta_2)\},$$

where  $\cos \delta_1 = \cos \varphi \cos \Phi_1 + \sin \varphi \sin \Phi_1 \cos(\lambda - A_1)$ ,

$\cos \delta_2 = \cos \varphi \cos \Phi_2 + \sin \varphi \sin \Phi_2 \cos(\lambda - A_2)$ ,

$\left. \begin{array}{l} \Phi_1, A_1 \\ \Phi_2, A_2 \end{array} \right\}$  are the symmetry axes of the spherical harmonics and the geocentric coordinates of their intersection on the unit sphere.

In the approximating computations the unknown values  $A_n, B_n, \Phi_1, A_1, \Phi_2, A_2$  have been determined so that the condition

$$\Delta r = \Delta r^*$$

should be fulfilled with a negligible error. Of course, the task was not only a simple calculation of the approximating function. Barta (1985) has shown that  $\Delta r^*$  computed on the basis of the complete data system of geoid heights agrees with the approximating function, whereby the function to be approximated is the system of geoid heights belonging to the main circle of the points  $(\Phi_1, A_1), (\Phi_2, A_2)$ . The agreement between the

two approximating functions is the basis for the statement that the essential part of the geoid is the sum of two cylinder-symmetrical surfaces.

The computations indicated that for the solution of the problem the parameters of the ellipsoid are to be changed slightly in the function  $\Delta r$  to be approximated. Another experience gained from the computations was that among the parameters of the approximating function the first degree coefficients and one of the second degree coefficients vanish. Taking this into account the function  $\Delta r^*$  can be written as follows:

$$\Delta r^* = \sum_{n=2}^N A_n P_n(\cos \delta_1) + \sum_{n=3}^N B_n P_n(\cos \delta_2).$$

The fact that  $A_1 = B_1 = 0$ , is a consequence of that in the function defining the geoid heights the first degree coefficients have also zero values. But the condition  $B_2 = 0$  is already a significant feature of the function  $\Delta r^*$  describing the sum of two cylinder-symmetrical surfaces.

Based on this, one can determine the geocentric coordinates  $\Phi_1$ ,  $A_1$ , the coefficient  $A_2$  as well as the amount of change of the ellipsoid. Using namely the addition theorem of spherical functions the spherical expansion of  $\Delta r^*$  can be obtained. Because we would like to fulfil the condition  $\Delta r \approx \Delta r^*$ , the computation of the unknowns could be carried out by comparing the numerical coefficients of the two series.

The second degree term of  $\Delta r^*$  is according to the addition theorem of spherical harmonics

$$\begin{aligned} A_2 P_2(\cos \delta_1) &= A_2 P_2(\cos \varphi) P_2(\cos \Phi_1) + \\ &+ \frac{2}{3!} A_2 P_{21}(\cos \varphi) P_{21}(\cos \Phi_1) \cos(\lambda - A_1) + \\ &+ \frac{2}{4!} A_2 P_{22}(\cos \varphi) P_{21}(\cos \Phi_1) \cos(\lambda - A_1). \end{aligned}$$

By comparing it with the second degree member of  $\Delta r$ , the following equalities are obtained

$$\begin{aligned} X_{20} &= A_2 P_2(\cos \Phi_1), \\ X_{21} &= \frac{1}{3} A_2 P_{21}(\cos \Phi_1) \cos A_1, \\ Y_{21} &= \frac{1}{3} A_2 P_{21}(\cos \Phi_1) \sin A_1, \\ X_{22} &= \frac{1}{12} A_2 P_{22}(\cos \Phi_1) \cos 2A_1, \\ Y_{22} &= \frac{1}{12} A_2 P_{22}(\cos \Phi_1) \sin 2A_1. \end{aligned}$$

The second and third equalities yield, since  $X_{21} = Y_{21} = 0$ ;

$$0 = \frac{1}{3} A_2 P_{21}(\cos \Phi_1) \cos A_1,$$

$$0 = \frac{1}{3} A_2 P_{21}(\cos \Phi_1) \sin A_1.$$

Here one has obviously  $A_2 \neq 0$ . Because the two equations  $\cos A_1 = 0$  and  $\sin A_1 = 0$  cannot be fulfilled simultaneously, one has:

$$P_{21}(\cos \Phi_1) = \frac{3}{2} \sin 2\Phi_1 = 0,$$

$$\Phi_1 = 90^\circ.$$

The equation has also a solution  $\Phi_1 = 0^\circ$ , but it is no solution of the problem, as it would mean that the symmetry axis of the cylinder-symmetrical source body coincides with the rotation axis of the Earth. Thus, the comparison of the second degree first order coefficients shows that the axis of the cylinder-symmetrical source body is lying in the plane of the equator.

The comparison of the second degree second order coefficients furnish the value of  $A_2$  and the angle  $A_1$ . Let us compute at first the coefficients  $X_{22}$ ,  $Y_{22}$  in the expansion of geoid heights:

$$X_{22} = \frac{a^2}{A} C_{22} = \frac{a^2}{A} 1.5362 \cdot 10^{-6} = 5.0488 \text{ m},$$

$$Y_{22} = \frac{a^2}{A} S_{22} = -\frac{a^2}{A} 8.815 \cdot 10^{-7} = -2.8970 \text{ m}.$$

Taking into account that  $P_{22}(\cos 90^\circ) = 3$ , one has the following equations:

$$5.0488 = \frac{1}{4} A_2 \cos 2A_1,$$

$$-2.8970 = \frac{1}{4} A_2 \sin 2A_1.$$

Hence:

$$A_1 = 165.1^\circ,$$

$$A_2 = 23.2833 \text{ m}.$$

As regards the zonal (zero order) terms it is obvious that the series  $\Delta r$  of the geoid heights must be completed by the zonal term in the expression of  $\Delta r^*$  in order that the relation  $\Delta r \approx \Delta r^*$  should be valid at all. That involves a slight change of the  $K_2$  mass

function of the ellipsoid. As

$$X_{20} = A_2 P_2(\cos \Phi_1) = -11.6417,$$

the numerical coefficient in the function  $\Delta r$  describing the geoid heights is:

$$C_{20}^* = X_{20} \frac{A}{a^2} = -3.5423 \cdot 10^{-6}.$$

Thus we choose for the  $K_2$  mass function the value:

$$K_2 = C_{20} - C_{20}^* = -1.0826370 \cdot 10^{-3} + 3.5423 \cdot 10^{-6} = -1.0790947 \cdot 10^{-3}.$$

From the Köhnelein-equations and from the conformity of volumes it follows

$$E^2 = 8.6026 \cdot 10^{-4}, \quad (f = 1/2326),$$

$$A = 12\,378\,134.2 \text{ m}.$$

The change of the equatorial great axis can be explained by the following calculation. The zonal term is:

$$\rho(\lambda, \varphi) = 23.3 P_2(\cos \delta_1),$$

where

$$\cos \delta_1 = \cos \varphi \cos 90^\circ + \sin \varphi \sin 90^\circ \cos(\lambda - 165.1^\circ).$$

Its equatorial intersection is:

$$\begin{aligned} \rho(\lambda)|_{\varphi=90^\circ} &= 23.3 \left[ \frac{3}{4} \cos 2(\lambda - 165.1^\circ) + \frac{1}{4} \right] = \\ &= 17.5 \cos 2(\lambda - 165.1^\circ) + 5.8. \end{aligned}$$

The so-called equatorial ellipsis described by the second degree second order terms is:

$$\begin{aligned} e(\lambda) &= (X_{22} \cos 2\lambda + Y_{22} \sin 2\lambda) P_{22}(\cos 90^\circ) = \\ &= 3 \sqrt{X_{22}^2 + Y_{22}^2} \cos 2(\lambda - \lambda_0), \end{aligned}$$

where

$$\operatorname{tg} 2\lambda_0 = Y_{22}/X_{22},$$

$$e(\lambda) = 17.5 \cos 2(\lambda - 165.1^\circ).$$

As Fig. 2 shows the two functions describe the same curve, thus  $K_2$  and together with it the parameters of the ellipsoid are chosen so that the effect of the equatorial ellipsis on the poles is taken into account.

Finally, the parameters of the two ellipsoids will be compared relative to the Earth's surface (Table II).

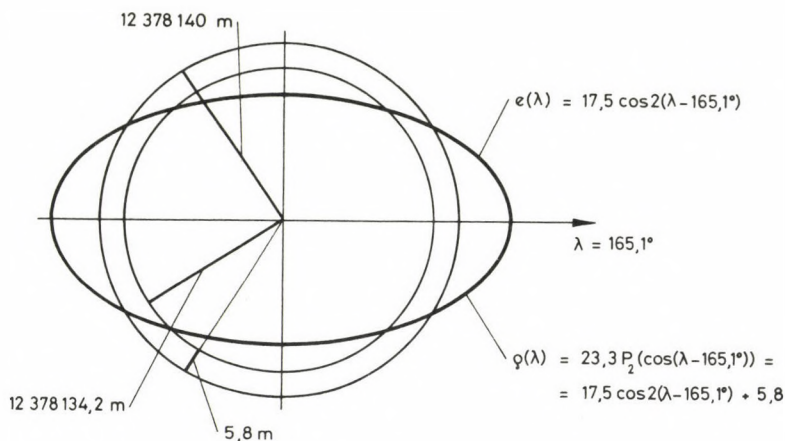


Fig. 2.

Table II

	Best fitting ellipsoid	The ellipsoid computed by us
$A$	6 378 140 m	6 378 128,4 m
$E^2$	$6.7395 \cdot 10^{-3}$ ( $f = 1/298.256$ )	$6.7287 \cdot 10^{-3}$ ( $f = 1/298.732$ )
$K_2$	$-1.0826370 \cdot 10^{-3}$	$-1.0790947 \cdot 10^{-3}$
$K_4$	$2.3841 \cdot 10^{-6}$	$2.3660 \cdot 10^{-6}$

## References

- Barta G 1985: The presumable connection between the internal structure of the Earth and geodynamics. *Acta Geod. Geoph. Mont. Hung.* (present issue)
- Gaposchkin E M ed. 1973: Smithsonian Standard Earth (III). Spec. Rep. 353, Smithsonian. Astrophys. Observ., Cambridge, Mass.
- Gaposchkin E M 1980: Global gravity field to degree and order 30 from geos 3 satellite altimetry and other data. *J. Geophys. Res.*, B85, 7221-7234.
- Lundquist C A ed. 1966: Geodetic parameters for a 1966 Smithsonian Institution Standard Earth. Spec. Rep. 200, Smithsonian. Astrophys. Observ., Cambridge, Mass.

## GEOPHYSICAL ASPECTS IN THE SELECTION OF A GEODYNAMIC TEST AREA IN TRANSDANUBIA (WESTERN HUNGARY)\*

CONTRIBUTION TO THE INTERNATIONAL LITHOSPHERE PROGRAMME

A ÁDÁM<sup>1</sup>

[Manuscript received January 5, 1984]

Tectonic-geophysical considerations are presented which resulted in the selection of the Ukk-Türje seismoactive region for geodynamic investigations as a Hungarian contribution to the International Lithosphere Programme.

**Keywords:** geodynamic test area; Transdanubia; Ukk-Türje region

The selection of a test area for geodynamic investigations in Transdanubia was based on the following considerations:

1. Tectonic lines of first or second orders were looked for among the longitudinal and transversal fractures along which significant displacements occurred in the *geological past*.
2. A tectonically active area was to be selected where earthquakes were observed in the second half of this century.
3. The fractures here can be well distinguished from their environment by different physical parameters.
4. Industrialization including the opening of a new mine is planned in this area in the near future and prediction of hazards is of great human and economic interest.
5. The area selected for a geodynamic study should lie possibly near to the geodynamic observatory of the Geodetic and Geophysical Research Institute in Sopronkertváros to shorten the expenses of the geodetic measurements connecting regularly the test area to the geodetic basic network.

These requirements are met by the longitudinal and transversal fractures of the Ukk and Türje region. The shallow sedimentary basin was broken into blocks by these tectonic elements (Fig. 1) and an earthquake with a magnitude of  $M = 4.3$  and intensity of  $I_0 = 6.5$  MSK occurred on September 13, 1953.

\* Read on May 19, 1982 in Veszprém at the session of the Committee of Geosciences of the Veszprém Academic Branch

<sup>1</sup> Geodetic and Geophysical Research Institute of the Hungarian Academy of Sciences, H-9401 Sopron, POB 5, Hungary

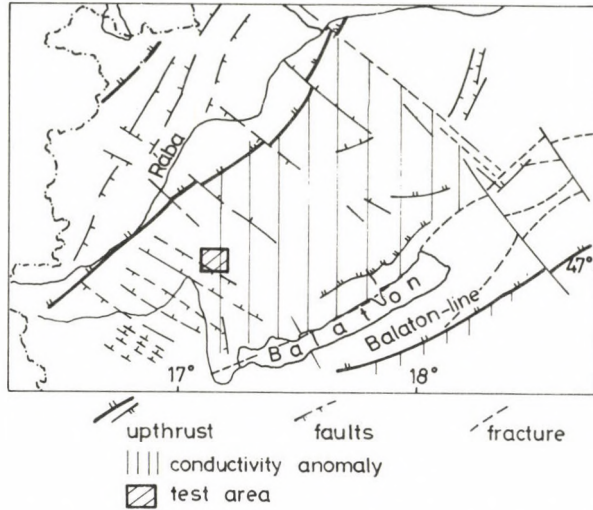


Fig. 1. Geodynamic test area between Ukk and Túrje shown in the tectonic map of West Hungary

To support our selection, some geological geophysical results will be presented in the followings.

### Tectonics

A tectonic map of this area was recently constructed by Haas (see it in Fig. 2, personal communication of Haas). This new tectonic map by Haas shows a complicated basement block-structure in a depth range below sea-level between 100 and more then 800 m bounded by longitudinal and significant transversal fractures. A detailed MTS profile measured on this area hinted also at this feature of the basement.

The filtered gravity map from the Geophysical Research Enterprise (Fig. 3, personal communication by F Kovács) reflects also the main features of Haas's map. Haas took into account the gravity data analyzing the basement relief.

### Seismicity

The macroseismic data of the Ukk-Túrje earthquake (September 13, 1953) were published by Kiss (1954). The data were reinterpreted by Zsiros (1982) at our request in 1982.

The seismic intensities are shown in Fig. 4. The greatest intensity values appeared along the transversal faults near Ukk and Túrje. After Kiss the epicenter of the earthquake is connected to the transversal fault of Túrje.

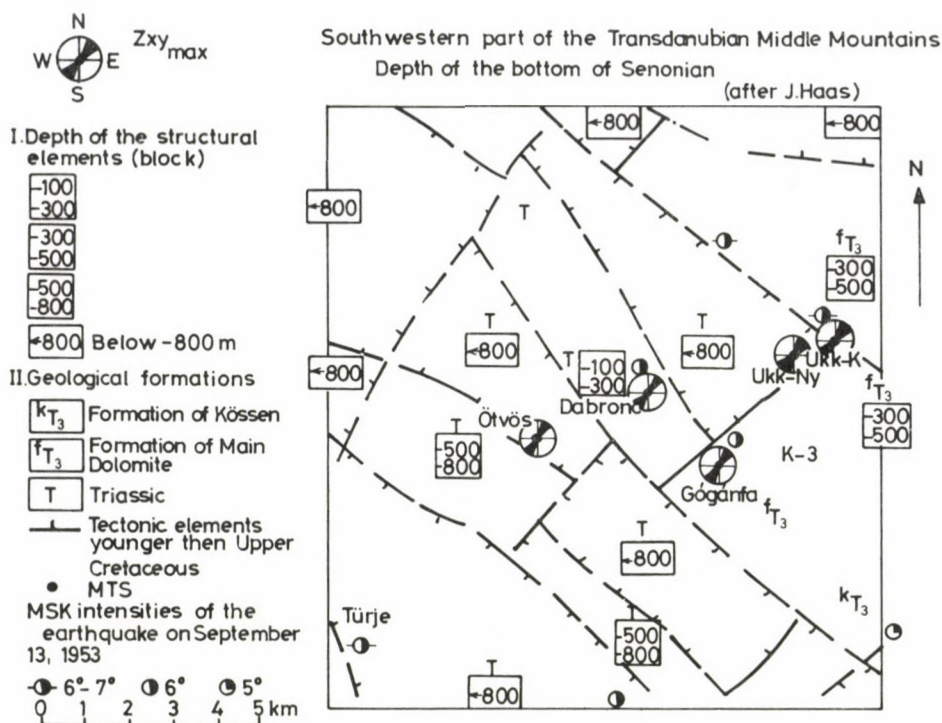


Fig. 2. Depth of the formation below Senonian (after Haas) and earthquake intensities after Zsíros (1982) on the test area with direction of the magnetotelluric maximum impedance values ( $Z_{xy\max}$ )

The focal depth estimation by Zsíros based on the isoseismals gives 6 km for the depth of the earthquake focus in agreement with an earlier calculation by Csomor and Kiss (6.4 km).

According to these authors the magnitude of the earthquake was about  $M = 4.3$ .

After Geller's formula (1976) an area of about 3.8 km<sup>2</sup> was affected by the earthquake. An average displacement of 5–6 cm was calculated by Zsíros on the basis of the above magnitude using Ohnaka's relations. He supposes that the 200–300 m height difference of the Cretaceous basement along the Túrje fault can be deduced by 4000–6000 similar seismic events in case of the same earthquake source mechanism. (He did not take into account the denudation.) 4000–6000 earthquake represent a low occurrence frequency since the end of the Cretaceous era (70 m years) but even these phenomena are not equidistant in time.

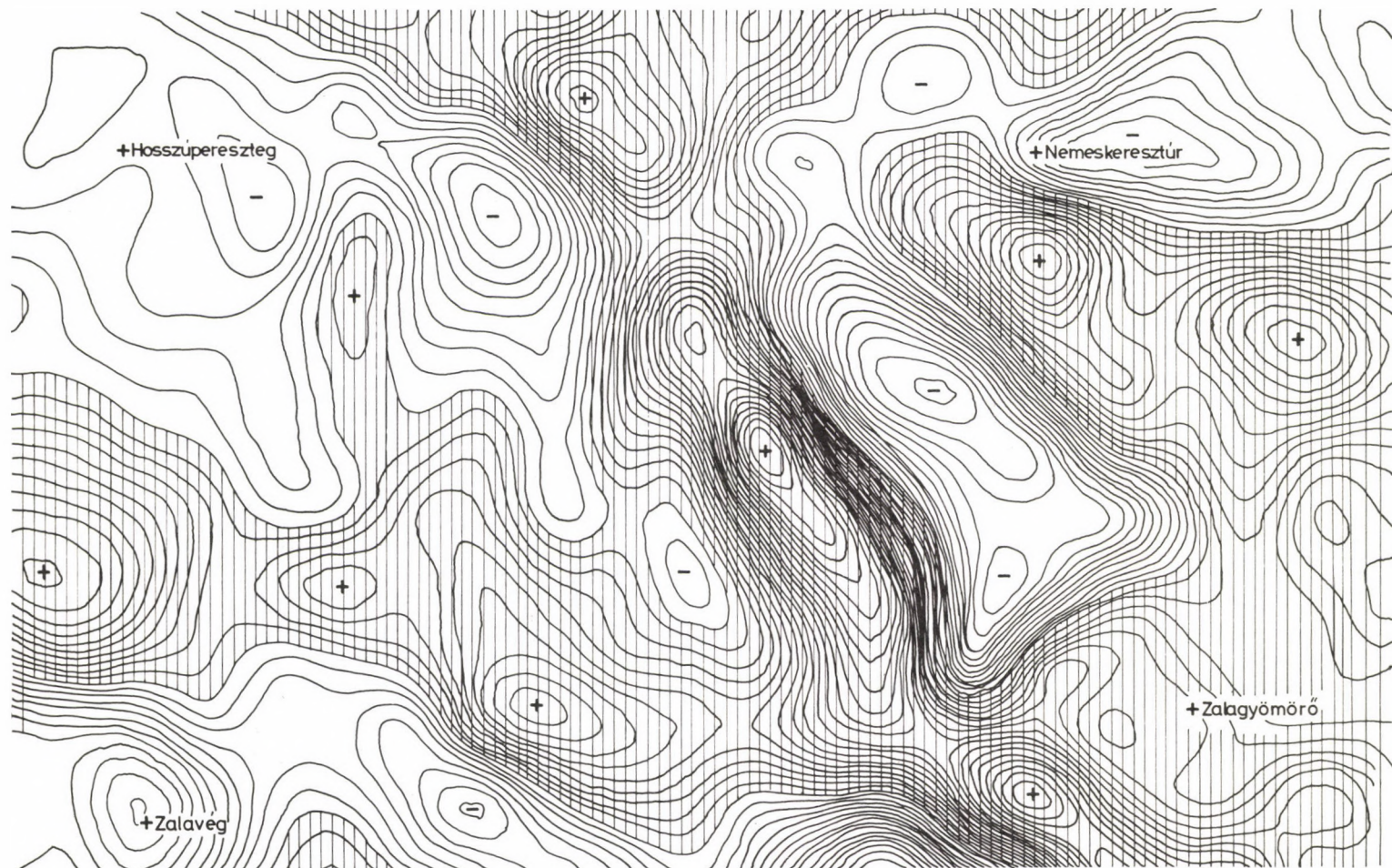


Fig. 3. Filtered gravity map on the test area (after Kovács, Geophysical Research Enterprise)

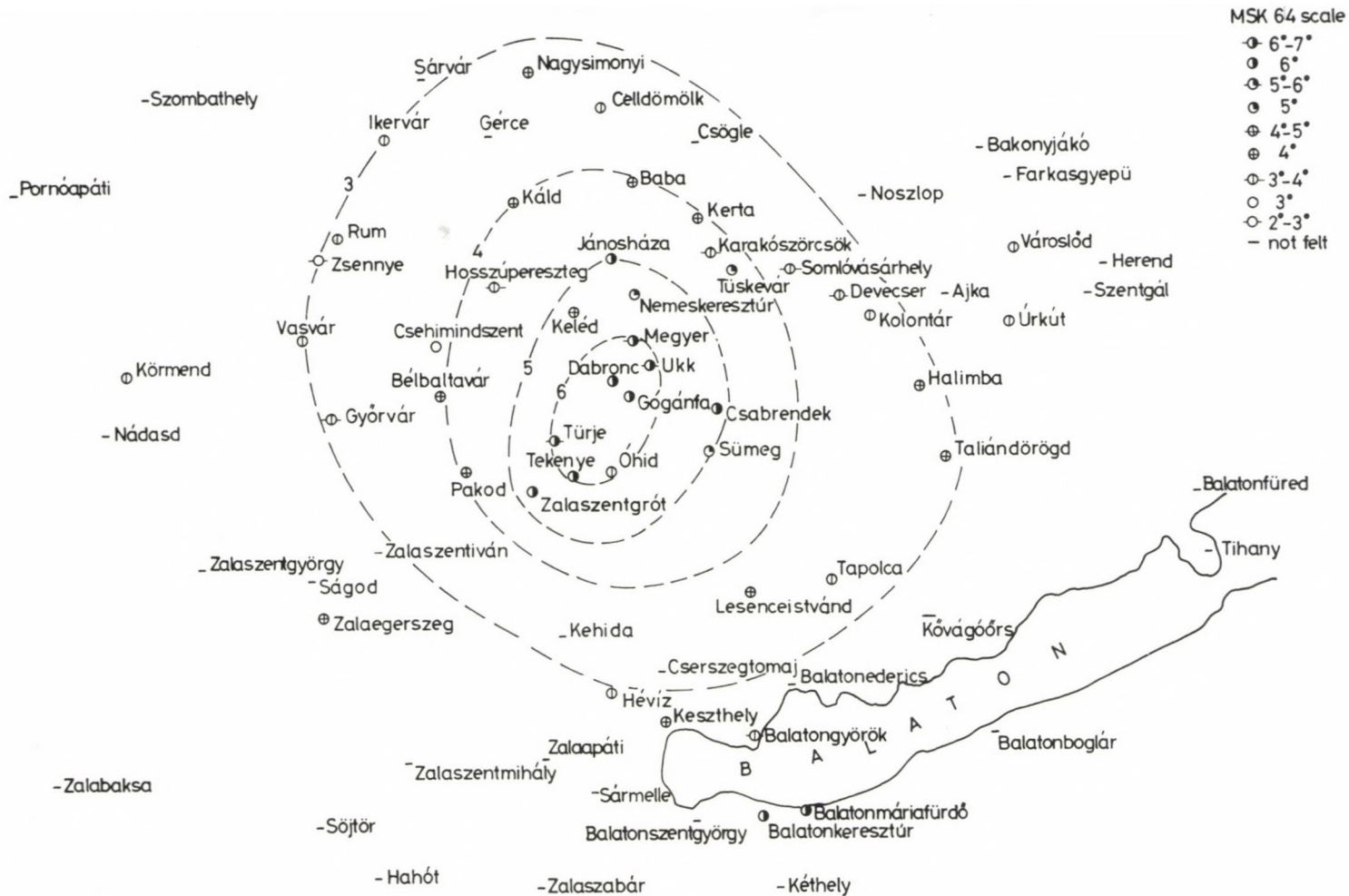


Fig. 4. Distribution of the felt intensity of Ukk-Türje earthquake on September 13, 1953 (Zsíros 1982)

### Recent crustal movements

Joó et al. (1979) presented a recent vertical crustal movement map of the Carpatho-Balkan region at the IUGG General Assembly in Canberra. A mean square error of  $\pm 0.28$  mm/year was given for the territory of Hungary.

As stated a slight elevation occurred in the Carpathians including the Carpathian basin during the last decades. According to this map the Ukk-Türje region lies between the isolines 0 and +1.0 but somewhat nearer to the 0-line.

### Geothermics

Heat flow values were determined in the cities Keszthely (105 NHFU) and Pápa (88 NHFU) nearest to the area studied. These heat flow values are near to the average of the Hungarian Basin which is much higher than values measured outside of the Basin.

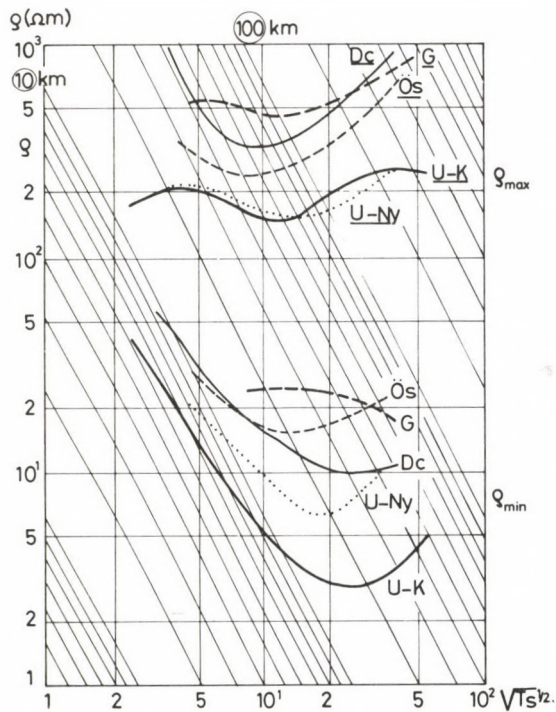


Fig. 5. Magnetotelluric  $\rho_{\min}$  and  $\rho_{\max}$  sounding curves

### Electromagnetic soundings

The magnetotelluric and geomagnetic deep soundings of the GGRI carried out along a profile crossing the area between Ukk and Ötvös with short (1–3 km) distances between measuring sites indicated here in seismoactive fractures the conducting formations of the Transdanubian crustal anomaly (Ádám 1981). These fractures differ from their environments by their low resistivity.

The directions of the maximum value of the MT impedance ( $Z_{xy\max}$ ) are perpendicular to the *transversal* fractures indicating the connection of the resistivity distribution here with the fracture zones (see Fig. 2). On the basis of this relation a geoelectric model was developed to represent these fractures. A 2-D numerical modelling showed that the most reliable layer parameters can be obtained by the  $\rho_{\min}$  curves measured in the epicentral point of the fracture zone.

The  $\rho_{\min}$  curves of the profile split into two groups (Fig. 5). The strongest indication of the resistivity decrease appears at the site Ukk-K (see the longest decreasing branch of the sounding curve here). The depth of the conducting formation is about the same (= 6 km) as that of the earthquake focus. The minimum  $\rho$  values of the isoresistivity profile in Fig. 6 vs. the period ( $T$ ) of EM variations (which is proportional to the penetration depth of telluric currents) show the location of the fractures.

### Conclusion

The Ukk–Türje region is proposed for a geodynamic test area first of all on the basis of its seismo-active fracture zones in which the electric conductivity increases just in the depth of the earthquake focus. This relation yields information about the earthquake mechanism and may enable its prediction, too.

The industrial importance of the selection of this area for geodynamic investigations is underlined by the establishment (opening) of a new deep coal mine (so-called Ajka II) at the end of the eighties in a distance of only some km-s from this tectonically active zone. The security, needed for a mine in connection with coal-dust and methane outbursts, water in-flow triggered by tectonic events and accompanied by great human and material loss, can be the main practical task of a geodynamical observation net besides its scientific value.

Thus, geodynamic investigations in the Ukk–Türje region serve at the same time economic and scientific purposes, the latter as expressed by the International Lithosphere Programme.

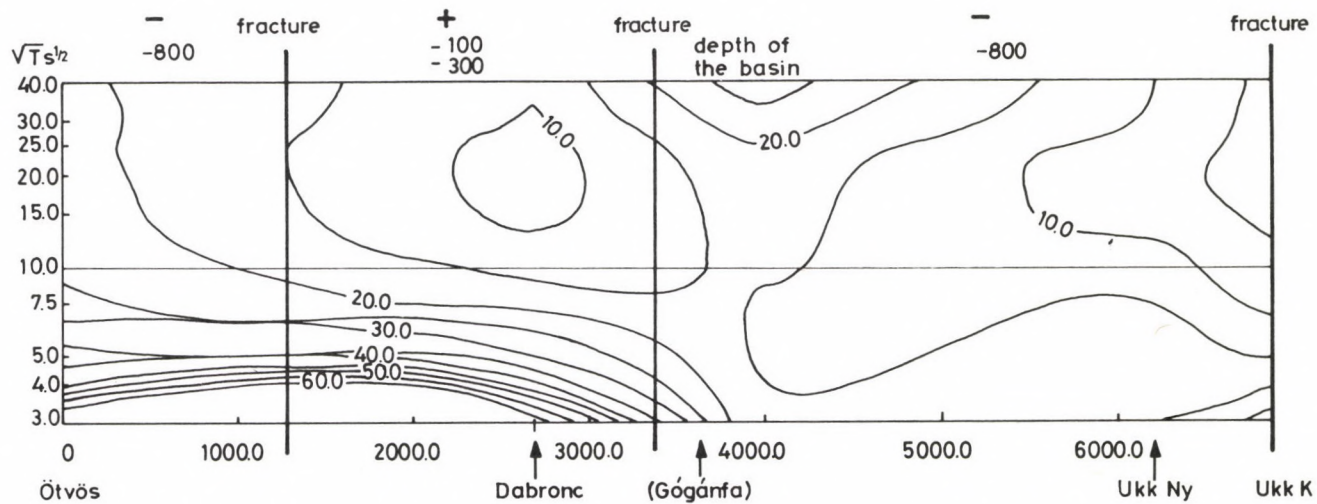


Fig. 6. Isohm lines as function of square root of the period of the MT variations between Ukk and Ötvös

### References

- Ádám A 1981: Statistische Zusammenhänge zwischen elektrischer Leitfähigkeitsverteilung und Bruchtektonik in Transdanubien (Westungarn). *Acta Geod. Geoph. Mont. Hung.*, 16, 57–113.
- Geller R J 1976: Scaling relations for earthquake source parameters and magnitudes. *Bulletin of the Seismological Society of America*, 1501–1523.
- Joó I, Csáti E, Janovič P, Popescu M, Somov V I, Thurm H, Thury J, Totomanov I N, Vanko J, Wyrzykowski T 1979: Recent vertical crustal movements of the Carpatho–Balkan Region (Manuscript). Budapest
- Kiss Z 1954: Earthquakes in Hungary in 1953 (in Hungarian). Országos Földrengésvizsgáló Intézet Kiadványa, Budapest
- Ohnaka M 1976: Focal parameters and earthquakes magnitudes. Programme and Abstracts. Seismol Soc. Japan, No 2.
- Zsíros T 1982: Earthquake in Ukk and Türje (Manuscript).



## MEASUREMENT OF THE PLASMA PARAMETERS IN THE IONOSPHERE BY NIGHT WITH RETARDING POTENTIAL ANALYZERS ON BOARD OF THE GEOPHYSICAL ROCKET VERTICAL-10

P BENCZE<sup>1</sup>, K KOVÁCS<sup>1</sup>, I SZEMEREY<sup>2</sup>, V V AFONIN<sup>3</sup>, V V BEZRUKIH<sup>3</sup>

[Manuscript received February 22, 1984]

Two retarding potential analyzers looking in and opposite to the flight direction were attached to the container of the geophysical rocket Vertical-10, which was launched December 21, 1981, 21. 35 Moscow time. The plasma parameters have been determined by curve fitting. The profile of the ion temperature shows fluctuations above 600 km hinting at some height dependent source of energy. Such irregular behaviour of the ion temperature was already found previously during the flight of Vertical-6 in 1977.

**Keywords:** plasma parameters in the ionosphere; retarding potential analyzer; rocket measurements

The measurements with plane-gridded retarding potential analyzers carried out previously by day on board of the geophysical rockets Vertical-6 and Vertical-9 were repeated on Vertical-10 by night. Vertical-10 was launched December 21, 1981 21. 35 Moscow time from the midlatitude area of the European part of the USSR.

The sensing part of the equipment consisted of two planegridded ion traps. The ion traps were prepared in the Institute for Space Research, Academy of Sciences of the USSR, Moscow. During ascent the ion flux was analyzed by the upwards looking ion trap, while in course of the descent the downwards looking analyzer worked. Thus, during both the ascent and the descent there was an ion trap on the container looking into the flight direction.

The electronic units were constructed using the experiences obtained during previous experiments. The evaluation of the data has shown that at low altitudes the sensitivity of the amplifier (positive ion current) is not high enough for a reliable determination of the positive ion composition (concentration of molecular ions). Therefore, the sensitivity of the amplifier has been increased. In the previous experiments the amplifier had three different ranges of measurement with automatic change of the ranges. The first range extended from  $5 \cdot 10^{-11}$  to  $3 \cdot 10^{-9}$  A, the second range from  $1 \cdot 10^{-9}$  to  $6 \cdot 10^{-8}$  A and the third range from  $2 \cdot 10^{-8}$  to  $1 \cdot 10^{-6}$  A.

<sup>1</sup> Geodetic and Geophysical Research Institute, Hungarian Academy of Sciences, H-9401 Sopron, Pf. 5, Hungary

<sup>2</sup> Central Institute for Physics, Hungarian Academy of Sciences, H-1525 Budapest, Pf. 49, Hungary

<sup>3</sup> Institute for Space Research, Academy of Sciences of the USSR, Moscow, Profsoiuznaia ul. 88. U.S.S.R.

The instrument on Vertical-10 had the following ranges of measurement:  $2.8 \cdot 10^{-13} - 9.1 \cdot 10^{-11}$  A,  $9.1 \cdot 10^{-11} - 2.6 \cdot 10^{-9}$  A and  $2.6 \cdot 10^{-9} - 9.6 \cdot 10^{-8}$  A in order of decreasing sensitivity. As it can be seen, the sensitivity of the amplifier was now an order of magnitude higher, than in case of the previous equipments.

Further in case of the previous instruments in altitudes, where only light, atomic ions ( $\text{He}^+$ ,  $\text{H}^+$ ) collected at small retarding potentials are present, the number of measurements per sweep was small. Thus, in this case the characteristic curve was not sufficiently determined and the ion composition could not reliably enough be found by means of curve fitting. Therefore, the range of the retarding potential and the period of the saw-tooth voltage were diminished. In the preceding equipments the retarding potential (amplitude of the saw-tooth voltage) changed from +18 V to -2 V (compared to the potential of the body) its period being 3 s. In case of the instrument flown on Vertical-10 the saw-tooth voltage changed from +16 V to -2 V in 2.5 s. Thus, the number of measurements determining the current-voltage curve increased both in low and high altitudes. The electronic units were constructed in the Central Institute for Physics, Budapest.

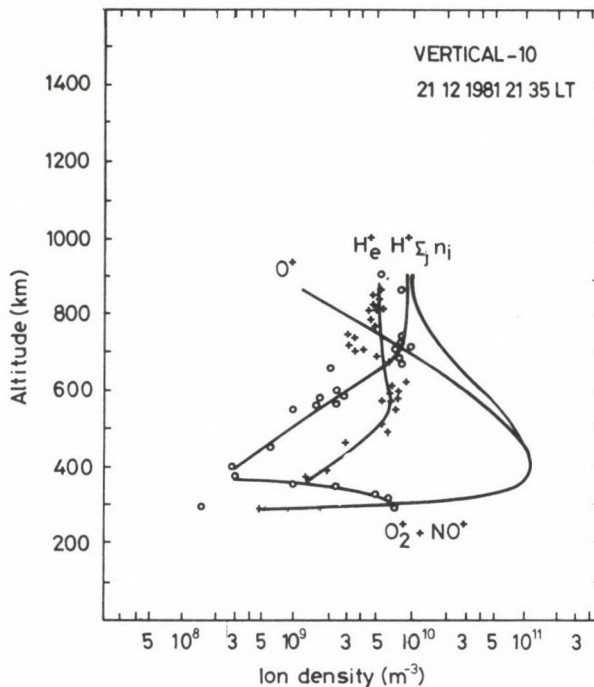


Fig. 1. Height variations of the total positive ion density and the concentrations of the ions  $\text{O}_2^+ + \text{NO}^+$ ,  $\text{O}^+$ ,  $\text{He}^+$ ,  $\text{H}^+$  during descent

The characteristic curves were evaluated by curve fitting (Knudsen 1966, Moss and Hyman 1968, Hanson et al. 1970, Bencze et al. 1984). The unknowns determined during the processing of the data were the total ion density, the ion composition, the ion temperature and the potential of the container. The curve fitting has been carried out so that the types of ions, the concentration of which had to be determined, were different in different height regions. The data processing has been done in the Geodetic and Geophysical Research Institute, Hungarian Academy of Sciences, Sopron.

As regards the geophysical conditions at the time of the flight the relative sunspot number was 72, the daily solar flux at 2800 MHz was 142.2, the three-hourly planetary geomagnetic index  $K_p = 2^-$ . Thus, the rocket was launched in rather quiet geophysical conditions.

In Fig. 1 the total positive ion density profile measured during the descent is shown. Because of night and quiet geomagnetic conditions the concentration of ions is small. In Fig. 1 the height variations of the ions  $O_2^+ + NO^+$ ,  $O^+$ ,  $He^+$  and  $H^+$  are also plotted.

In Fig. 2 the height variation of the ion temperature during descent is shown. The ion temperature is low because of night and quiet geomagnetic conditions, as in case of the positive ion density. The profile indicated fluctuations of the ion temperature above

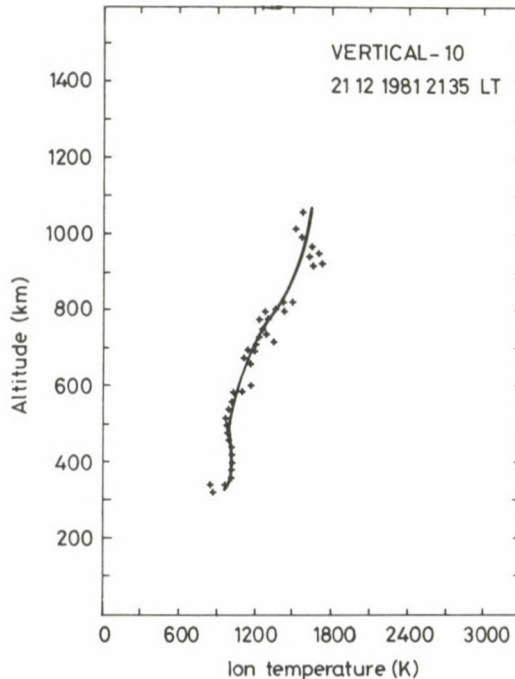


Fig. 2. The ion temperature profile determined for the descending part of the orbit

600 km. The reliable determination of the ion temperature profile is aggravated by the significant variation of conditions during a single sweep of the retarding potential, too. This makes impossible to evaluate the characteristic curves and thus, some data determining the profile are missing.

Previous measurements may prove that these strange variations are not errors due to the equipment or to the evaluation of the data. Namely, similar temperature fluctuations have been found during the flight of Vertical-6, in October, 1977 (Apáthy et al. 1981). It is assumed that this behaviour of the ion temperature might be due to charge exchange and to the counterstreaming of ions in this region.

### References

- Apáthy I, Szemerey I, Bencze P, Kovács K, Afonin V, Bezrukih V, Gringauz K, Shutte N 1981: Comprehensive investigation of the basic parameters of the upper atmosphere at the time of the flight of the geophysical rocket "Vertical-6". *Adv. Space Res.*, 1, 101-105.
- Bencze P, Kovács K, Szemerey I, Afonin V V, Bezrukih V V 1984: Methodology of evaluation of the data measured by retarding potential analyzers. *Acta Geod., Geoph. Mont. Hung.*, 19, 467-474.
- Hanson V B, Sanatani S, Zuccaro D, Flowerday T W 1970: Plasma measurements with the retarding potential analyzer. *J. Geophys. Res.*, 75, 5483-5501.
- Knudsen W C 1966: Evaluation and demonstration of the use of retarding potential analyzers for measuring several ionospheric quantities. *J. Geophys. Res.*, 71, 4669-4678.
- Moss S J, Hyman E 1968: Minimum variance technique for the analysis of ionospheric data acquired in satellite retarding potential analyzer experiments. *J. Geophys. Res.*, 73, 4315-4323.

# ELASTODYNAMICS EXPRESSED IN TERMS OF MAXWELL'S THEORY OF ELECTRODYNAMICS, CYLINDRICAL WAVE PROPAGATION AND ELASTIC WAVE PROPAGATION IN INHOMOGENEOUS MEDIA

O FÖRTSCH<sup>1</sup> and E KOCH<sup>2</sup>

[Manuscript received February 27, 1984]

In electrodynamics, most theoretical deductions are based on Maxwell's theory. It is applied by the introduction of Maxwell's quantities **K** and **P**. Using **K** and **P** we can describe more clearly energy and energy flow of a wave. To profit by Maxwell's theory with regard to different fields of physics it is tried in this paper to transfer Maxwell's theory to elastodynamics, i.e. to the propagation of elastic waves in solid bodies.

In seismology the so-called modulated waves are especially important. Here, the maximum amplitudes vary on the wave-fronts according to a sinusoidal function. In our paper we discuss the effect of this phenomenon upon the phase and energy velocities.

The traditional transformation of the Laplacian operator from Cartesian coordinates into cylindrical ones leads to Bessel's differential equation. But the solution of this equation is not in accordance with the observations.

Finally, wave propagation in an inhomogeneous medium is discussed. Hereby density and elastic properties of the medium depend on site. A solution can be achieved using Maxwell's theory. The calculations lead to a wave that is composed of a travelling and a stationary part. The energy transfer is caused by the travelling wave part only. We can perceive the occurrence of a stationary part if we consider that wave energy is continually reflected in both directions because of the local change of velocity. Thus, a stationary wave is finally generated.

In conclusion we should like to note that the occurrence of a stationary wave part in addition to a travelling wave part can be attributed to a phase shift between Maxwell's quantities **K** and **P**.

**Keywords:** cylindrical waves; elastodynamics; extended Laplacian operator; Maxwell's quantities; Maxwell's theory; modulated elastic waves; waves in inhomogeneous media

## 1. Introduction

It is well known that, in physics, the broad field of electrodynamics is based on Maxwell's theory and its equations. Most phenomena of electromagnetism can be simply and clearly described by these equations. Therefore Sommerfeld (1949) says about them in the foreword of his textbook: "Die wundervolle Einfachheit und Schönheit der Maxwellschen Gleichungen, die besonders aus deren relativistischer Formulierung für das Vakuum hervorleuchtet, führen zu der Überzeugung, daß diese Gleichungen zusammen mit den Gleichungen der Gravitation Ausfluß einer

<sup>1</sup> Fürstenfeldbruck, Theodor Heuss-Str. 16, Federal Republic of Germany, D-8080

<sup>2</sup> Denkhof b. Büchlberg, Büchlberger Str. 11, Federal Republic of Germany, D-8391

umfassenden Weltgeometrie sein müssen."<sup>1</sup> Four decades earlier Schaefer (1908) praised Maxwell's equations in the conclusion of his book: "Diese kritischen Bemerkungen nehmen der Maxwell'schen Theorie nichts von ihrer Bedeutung; im Gegenteil müssen sie die Bewunderung dafür erregen, wie mit einfachen Mitteln diese Theorie die Mannigfaltigkeit der elektromagnetischen Phänomene, sofern es sich um nicht zu rasche Vorgänge handelt, zu beherrschen imstande ist."<sup>2</sup>

These statements lead to the question whether it may be possible to transfer Maxwell's theory, a theory of such great importance for electromagnetism, to different fields of physics for the purpose attaining progress and better understanding in these fields. In this connexion the authors, who are seismologists, especially consider the field of elastodynamics and the propagation of elastic waves. Definition and application of Maxwell's theory for elastodynamics is the subject of this treatise.

In the treatises on Maxwell's theory one may find the note that Maxwell's equations are valid only for Cartesian coordinate systems, not for curvilinear systems. This indeed is surprising. Why should a law of nature only be valid for a special coordinate system? In this treatise we will enter into the particulars of that matter as well. In this connexion we will consider the propagation of cylindrical waves. According to theory, the propagation of these waves is usually described in terms of cylindrical functions, whereas observations in seismology show that these waves can be described by the simple wave equation  $s = (S/\sqrt{r}) \cos(\omega t - kr)$ . How can this contradiction be explained?

Elastic waves generated by earthquakes propagate in the earth's interior. The terrestrial body chiefly represents a medium where the velocity of the seismic waves varies with depth. The problem of wave propagation in such a medium will be discussed in the last chapter of this paper.

## 2. Maxwell's theory of electrodynamics

### 2.1 Maxwell's equations and propagation of electromagnetic waves

To illustrate the coherence of electrodynamics and elastodynamics, we present Maxwell's well-known equations. We can restrict this to their differential notation that is most commonly used. Using vector notation we have the following two equations valid for an isotropic insulator at rest:

$$-(\mu/c) \partial \mathbf{H} / \partial t = \text{curl } \mathbf{E}; \quad (\varepsilon/c) \partial \mathbf{E} / \partial t = \text{curl } \mathbf{H}. \quad (1)$$

<sup>1</sup> "The wonderful simplicity and beauty of Maxwell's equations, especially shining out of their relativistic formulation for a vacuum, lead to the conviction that these equations, together with the equations for gravitation, must be an emanation of a comprehensive geometry of the world."

<sup>2</sup> "These critical remarks don't detract from the importance of Maxwell's theory; on the contrary they ought to cause admiration if one appreciates by which simple means it is possible to handle the variety of electromagnetic phenomena using this theory, except for processes which are too fast."

We use the following symbols:

$\mathbf{E}$  = electric field,  $\mathbf{H}$  = magnetic field,  $t$  = time,  $\varepsilon$  = dielectric constant,  $\mu$  = permeability,  $c$  = speed of light in vacuum. Using the components of  $\mathbf{E}$  and  $\mathbf{H}$  in the  $x$ ,  $y$ , and  $z$  directions of a Cartesian coordinate system we obtain the following equations:

$$\begin{aligned} -\frac{\mu}{c} \frac{\partial H_x}{\partial t} &= \frac{\partial E_z}{\partial y} - \frac{\partial E_y}{\partial z}, & \frac{\varepsilon}{c} \frac{\partial E_x}{\partial t} &= \frac{\partial H_z}{\partial y} - \frac{\partial H_y}{\partial z}, \\ -\frac{\mu}{c} \frac{\partial H_y}{\partial t} &= \frac{\partial E_x}{\partial z} - \frac{\partial E_z}{\partial x}, & \frac{\varepsilon}{c} \frac{\partial E_y}{\partial t} &= \frac{\partial H_x}{\partial z} - \frac{\partial H_z}{\partial x}, \\ -\frac{\mu}{c} \frac{\partial H_z}{\partial t} &= \frac{\partial E_y}{\partial x} - \frac{\partial E_x}{\partial y}, & \frac{\varepsilon}{c} \frac{\partial E_z}{\partial t} &= \frac{\partial H_y}{\partial x} - \frac{\partial H_x}{\partial y}. \end{aligned} \quad (1a)$$

With regard to our purpose, it is important that we can easily deduce the differential equations of electromagnetic waves from these equations. Differentiating the first equation of (1) with respect to  $t$  and taking the curl of the second one, we get:

$$\frac{\varepsilon\mu}{c^2} \frac{\partial^2 \mathbf{E}}{\partial t^2} = \Delta \mathbf{E}; \quad \frac{\varepsilon\mu}{c^2} \frac{\partial^2 \mathbf{H}}{\partial t^2} = \Delta \mathbf{H} \quad (2)$$

by using the relations:  $\text{curl curl } \mathbf{E} = \text{grad div } \mathbf{E} - \Delta \mathbf{E}$  and  $\text{div } \mathbf{E} = 0$  as well as  $\Delta \mathbf{E} = \partial^2 \mathbf{E} / \partial x^2 + \partial^2 \mathbf{E} / \partial y^2 + \partial^2 \mathbf{E} / \partial z^2$ .

We get the second equation of Eq. (2) by handling Eq. (1) in an analogous way. Calculation leads us to the differential wave equation for each component:

$$\begin{aligned} \frac{\varepsilon\mu}{c^2} \frac{\partial^2 E_x}{\partial t^2} &= \Delta E_x; & \frac{\varepsilon\mu}{c^2} \frac{\partial^2 E_y}{\partial t^2} &= \Delta E_y; & \frac{\varepsilon\mu}{c^2} \frac{\partial^2 E_z}{\partial t^2} &= \Delta E_z, \\ \frac{\varepsilon\mu}{c^2} \frac{\partial^2 H_x}{\partial t^2} &= \Delta H_x; & \frac{\varepsilon\mu}{c^2} \frac{\partial^2 H_y}{\partial t^2} &= \Delta H_y; & \frac{\varepsilon\mu}{c^2} \frac{\partial^2 H_z}{\partial t^2} &= \Delta H_z. \end{aligned} \quad (2a)$$

The equations lead to the conclusion that each component of  $\mathbf{E}$  and  $\mathbf{H}$  will propagate. In the course of wave propagation the components of  $\mathbf{E}$  are connected with the components of  $\mathbf{H}$ . Eqs (2) and (2a) describe all possible kinds of propagating electromagnetic waves, if the wave-fronts are planes; each possible direction, in which the wave may propagate, is included. The condition for validity of this statement, however, is as follows: the orientations of  $\mathbf{E}$  and  $\mathbf{H}$  and the direction of wave propagation are in accordance with the axes of a right-handed coordinate system. The velocity of wave propagation is  $v = c / \sqrt{\varepsilon\mu}$ . Each type of polarized and stationary waves can be described by Eqs (2) and (2a) as well.

As is known, the energy density in the magnetic and electric field of plane electromagnetic waves are:

$$W_h = \frac{\mu}{8\pi} \mathbf{H}^2; \quad W_e = \frac{\varepsilon}{8\pi} \mathbf{E}^2. \quad (3)$$

The vector of radiation, i.e. Poynting's vector of energy flow is defined as follows:

$$\mathbf{S} = \frac{c}{4\pi} [\mathbf{E} \cdot \mathbf{H}]. \quad (4)$$

Using its components we can write:

$$\mathbf{S} = \frac{c}{4\pi} [(E_y H_z - E_z H_y) \mathbf{i} + (E_z H_x - E_x H_z) \mathbf{j} + (E_x H_y - E_y H_x) \mathbf{k}] \quad (4a)$$

$\mathbf{i}$ ,  $\mathbf{j}$  and  $\mathbf{k}$  are the rectangular unit vectors having directions of the positive  $x$ -,  $y$ - and  $z$ -axis of a rectangular coordinate system. The equation shows that two waves propagating in the directions of each of the three axes are possible.

## 2.2 The electromagnetic wave in a conductor

In those textbook chapters dealing with electromagnetism, generally the propagation of electromagnetic waves is treated in media, where the conductivity  $\sigma$  is not equal to zero. We are going to consider this theory once more, but with regard to different aspects. Maxwell's equations in such a medium (according to Joos 1934 for example) are as follows:

$$-\frac{\mu}{c} \frac{\partial \mathbf{H}}{\partial t} = \text{curl } \mathbf{E}; \quad \frac{\varepsilon}{c} \frac{\partial \mathbf{E}}{\partial t} + \frac{4\pi\sigma\mu}{c} \mathbf{E} = \text{curl } \mathbf{H}. \quad (5)$$

From this equation, we can deduce the following differential wave equations:

$$\frac{\varepsilon\mu}{c^2} \frac{\partial^2 \mathbf{E}}{\partial t^2} + \frac{4\pi\sigma\mu}{c^2} \frac{\partial \mathbf{E}}{\partial t} = \Delta \mathbf{E}; \quad \frac{\varepsilon\mu}{c^2} \frac{\partial^2 \mathbf{H}}{\partial t^2} + \frac{4\pi\sigma\mu}{c^2} \frac{\partial \mathbf{H}}{\partial t} = \Delta \mathbf{H}. \quad (6)$$

To illustrate the solutions of these differential equations and to facilitate analyzing them, we confine ourselves to a simple plane wave but without losing essential information. Let the wave propagate in the  $x$ -direction and have the components  $E_y$  and  $H_z$ . The differential equations are in this case:

$$\begin{aligned} \frac{\varepsilon\mu}{c^2} \frac{\partial^2 E_y}{\partial t^2} + \frac{4\pi\sigma\mu}{c^2} \frac{\partial E_y}{\partial t} &= \frac{\partial^2 E_y}{\partial x^2}; \\ \frac{\varepsilon\mu}{c^2} \frac{\partial^2 H_z}{\partial t^2} + \frac{4\pi\sigma\mu}{c^2} \frac{\partial H_z}{\partial t} &= \frac{\partial^2 H_z}{\partial x^2}. \end{aligned} \quad (6a)$$

To solve these equations, we try the following formula for  $E_y$ :

$$E_y = A e^{-\kappa x} \cos \omega(t - x/v). \quad (7)$$

$\kappa$  denotes the absorption coefficient,  $\omega$  denotes the angular frequency,  $v$  the phase velocity of the wave.

Calculating the differential quotients with respect to  $E_y$  and substituting them in the first equation of Eq. (6a) we find:

$$\left[ \frac{\omega^2}{v^2} - \frac{4\pi^2 \sigma^2 \mu^2 v^2}{c^4} - \frac{\omega^2}{v_0^2} \right] \cos \omega \left( t - \frac{x}{v} \right) + \left[ 2\kappa \frac{\omega}{v} - \frac{4\pi\sigma\mu}{c^2} \right] \sin \omega \left( t - \frac{x}{v} \right) = 0. \quad (8)$$

The condition that the terms in parenthesis must be equal to zero leads to the formula:

$$\frac{c}{v} = \sqrt{\frac{\mu}{2} \left[ \varepsilon + \sqrt{4 \frac{4\pi^2 \sigma^2}{\omega^2} + \varepsilon^2} \right]}.$$

We use the notations  $T = 2\pi/\omega =$  wave period,  $v_0 = c/\sqrt{\varepsilon\mu} =$  phase velocity for  $\sigma = 0$  and  $N = \sqrt{1/4 + \sigma^2 T^2/\varepsilon^2}$ , thus we can rewrite the equation above and the equation of the absorption coefficient  $\kappa$ :

$$\frac{v_0}{v} = \sqrt{N + \frac{1}{2}}; \quad (9)$$

$$\kappa = \frac{\omega}{v_0} \sqrt{N - \frac{1}{2}} = \frac{2\pi}{\lambda_0} \sqrt{N - \frac{1}{2}} = \frac{2\pi}{\lambda} \sqrt{N - \frac{1}{2}} / \sqrt{N + \frac{1}{2}} = 2\pi M/\lambda.$$

$\lambda$  denotes the wave-length in the case of  $\sigma \neq 0$ ;  $\lambda_0$  denotes the wave-length in the case of  $\sigma = 0$ , and  $M = \sqrt{N - 1/2} / \sqrt{N + 1/2}$ .

We can deduce the component  $H_z$  from the first equation of Eq. (5). In the considered case we have the equation:

$$\frac{\partial H_z}{\partial t} = \frac{c}{\mu} \frac{\partial E_y}{\partial x}.$$

Solving this equation for  $H_z$ , we find:

$$H_z = \sqrt{\frac{\varepsilon}{\mu}} \sqrt{2N} A e^{-2\pi M x/\lambda} \cos [\omega(t - x/v) - \varphi]. \quad (10)$$

The phase angle  $\varphi$  is defined by  $\varphi = \arctan M$ . The magnetic field and the electric field in a conductor differ by a phase shift of the angle  $\varphi$ , whereby the magnetic field will have a phase delay.

As  $N$  is a function of  $T$ , both  $v$  and  $\kappa$  depend on frequency. Therefore dispersion occurs. A signal consisting of a group of several frequencies ("wave package") will be distorted with regard to phase and amplitude while propagating in a conductor.

Now, we consider the energy density  $W$ . For the electric and the magnetic field respectively they are:

$$W_e = \frac{\varepsilon}{8\pi} E_y^2 = \frac{\varepsilon}{8\pi} A^2 e^{-4\pi Mx/\lambda} \cos^2 \omega(t-x/v), \quad (11)$$

$$W_h = \frac{\mu}{8\pi} H_z^2 = \frac{\varepsilon}{8\pi} 2N A^2 e^{-4\pi Mx/\lambda} \cos^2 [\omega(t-x/v) - \varphi].$$

For our further calculations the energy densities averaged over one period  $T$  or one wave-length  $\lambda$  are of importance:

$$\bar{W}_e = \frac{\varepsilon}{16\pi} A^2 e^{-4\pi Mx/\lambda}, \quad \bar{W}_h = \frac{\varepsilon}{16\pi} 2N A^2 e^{-4\pi Mx/\lambda}. \quad (12)$$

$\bar{W}_h$  exceeds  $\bar{W}_e$ . We should like to describe this fact more clearly:

$$\bar{W}_h = \frac{\varepsilon}{16\pi} \left[ 1 + 2 \left( N - \frac{1}{2} \right) \right] A^2 e^{-4\pi Mx/\lambda} = [1 + 2(\kappa^2/k_0^2)] \bar{W}_e. \quad (12a)$$

The first part of  $\bar{W}_h$  being equal to  $\bar{W}_e$  participates in the wave motion effectively. The second part goes into Joule heating by the conductivity  $\sigma$ .

Now, we calculate the radiation vector  $\mathbf{S}$ . It is:

$$S_x = \frac{c}{4\pi} E_y H_z. \quad (13)$$

By substituting the corresponding terms we get:

$$S_x = \frac{\varepsilon}{4\pi} v_0 \sqrt{N + \frac{1}{2}} A^2 e^{-4\pi Mx/\lambda} \left[ \cos^2 \omega \left( t - \frac{x}{v} \right) + M \sin \omega \left( t - \frac{x}{v} \right) \cos \omega \left( t - \frac{x}{v} \right) \right]. \quad (13a)$$

As for  $W$  we are interested in the average flow of energy per unit area per second. We can write it at once:

$$\bar{S}_x = \frac{\varepsilon}{8\pi} v_0 \sqrt{N + \frac{1}{2}} A^2 e^{-4\pi Mx/\lambda} = \frac{\varepsilon}{8\pi} \frac{v_0^2}{v} A^2 e^{-4\pi Mx/\lambda}. \quad (14)$$

The energy sharing in the wave motion is  $2\bar{W}_e$ . But the total energy is  $2(N + 1/2)\bar{W}_e = 2(v_0^2/v^2)\bar{W}_e$ .

The energy per unit area per period  $T$  is  $\bar{S}_x T$ . Suppose that the wave has to travel the distance  $L$  until it reaches the unit area. Thus, the wave has accumulated the energy  $\bar{W}L$ , when it reaches the area. If we define  $L$  appropriately, the energy  $\bar{S}_x T$  will be equal to  $\bar{W}L$ . In a way,  $L$  is the wave-length of the energy velocity  $u$ , and we get  $u = L/T = \bar{S}_x/\bar{W}$ . There are two alternatives for defining  $\bar{W}$  now: We can choose the energy

sharing in the wave motion or the total energy. Thus, we get  $u_1$  or  $u_2$ :

$$u_1 = v_0^2/v \quad \text{or} \quad u_2 = v. \quad (15)$$

$u_1$  defines the energy velocity correctly. As for  $u_2$ , the joule heating shares in this parameter, but it does not affect the wave mechanism in the considered segment  $dx$  (the wave propagates in the  $x$ -direction). According to Eq. (9)  $v_0$  exceeds  $v$ , whereas  $u_1$  exceeds  $v_0$ . Thus, anomalous dispersion occurs. Anomalous dispersion is caused, because there is a term containing  $\partial/\partial t$  in the differential equation. From the term  $\partial/\partial x$  normal dispersion results.

According to Sommerfeld (1945) the connexion between  $u$  and the energy transport in a wave was already mentioned by Osborne Reynolds and Lord Rayleigh in the last century. They considered a volume  $V=q\lambda$  ( $q$ =cross-section perpendicular to the direction of wave propagation). The amount of energy  $S_x^+$  flowing through  $q$  per period  $T=\lambda/v$  is equal to  $\bar{S}_x q \lambda/v$ . In the volume  $V$  the amount of energy  $E_x^+ = \bar{W} q \lambda$  is stored. Thus, the ratio  $S_x^+/E_x^+ = \bar{S}_x q \lambda / \bar{W} q \lambda v = u/v = L/\lambda$ .

In physics, usually the group velocity, being equal to the energy velocity defined above, is the derivative of  $\omega$  with respect to  $k$ :  $u = d\omega/dk$ . The quantity  $k = 2\pi/\lambda$  is called wave number. The notation "group velocity" has been derived from the deduction of the formula just mentioned. Suppose that there are two waves at slightly different frequencies travelling in the same direction. A maximum amplitude being modulated sinusoidally results from their superposition. The loop antinodes of the maximum amplitude travel with the velocity  $u$  (the group velocity is the speed at which modulated signals are transmitted). Hence the conclusion is often drawn that energy can only be transported by a wave train, not by a wave having only one certain frequency. But this conclusion is erroneous; just the opposite is correct. It must not be forgotten that — as is manifested by the relation  $u = d\omega/dk$  — we have to let the slightly different frequencies approach each other in the above calculation and that we have to calculate the limit. Thus, there is only one frequency left. The formula for  $S$  and  $W$  includes only one frequency  $\omega$ , hence the misleading notation "group velocity" should be removed from notations of physics and should be substituted by the more significant notation "energy velocity".

Using the formulas  $v = v_0/\sqrt{N+1/2}$  and  $u = d\omega/dk = v \left( 1 + \frac{T}{v} \frac{dv}{dT} \right)$  we find for the energy velocity:

$$u = v_0^2/v \left( \frac{1}{2} + N - \sigma^2 T^2 / 2N\epsilon^2 \right).$$

This expression for  $u$  is different from the equation above. And indeed it is not correct, because the identity  $u = d\omega/dk$  is only valid for waves having a constant maximum amplitude, i.e. for waves without loss of energy.

The exponent of the exponential function describing absorption (Eqs 7 and 10) includes the quotient  $x/\lambda$ . We can rewrite the wave function  $\cos \omega(t - x/v)$ , as it has

often been done before:  $\cos 2\pi(t/T - x/\lambda)$ . These relations also include the terms  $x/\lambda$  and  $t/T$ . This means that the wave has a "system of measurement" of its own. The units of this system are the wave-length instead of metres and the period  $T$  instead of seconds, because wave-length and period are the "natural units" of the wave. This perception is not a new one, and it will be of good value, as we shall see later.

Consideration of the equations above leads to defining two more quantities. We call them "Maxwell's quantities"  $\mathbf{K}$  and  $\mathbf{P}$  and define them as follows:

$$\mathbf{K} = \sqrt{\frac{\mu dV}{4\pi}} \mathbf{H}; \quad \mathbf{P} = \sqrt{\frac{\epsilon dV}{4\pi}} \mathbf{E}. \quad (16)$$

$\mathbf{K}$  and  $\mathbf{P}$  are vectors with the components  $K_x, K_y, K_z$  and  $P_x, P_y, P_z$  respectively. Substituting them in Maxwell's equations, we find:

$$-\frac{\partial \mathbf{K}}{\partial t} = v_0 \text{curl } \mathbf{P}; \quad \frac{\partial \mathbf{P}}{\partial t} = v_0 \text{curl } \mathbf{K}. \quad (1b)$$

Using  $\mathbf{K}$  and  $\mathbf{P}$  we achieve perfect symmetry of Maxwell's equations. We find for these equations using component notation:

$$-\frac{\partial K_x}{\partial t} = v_0 \left[ \frac{\partial P_z}{\partial y} - \frac{\partial P_y}{\partial z} \right]; \quad \frac{\partial P_x}{\partial t} = v_0 \left[ \frac{\partial K_z}{\partial y} - \frac{\partial K_y}{\partial z} \right]. \quad (1c)$$

Cyclic permutation of the indices leads to the equations of  $\frac{\partial K_y}{\partial t}, \frac{\partial K_z}{\partial t}, \frac{\partial P_y}{\partial t}$  and  $\frac{\partial P_z}{\partial t}$ .

The differential equations of  $\mathbf{K}$  and  $\mathbf{P}$  have the same structure as for  $\mathbf{H}$  and  $\mathbf{E}$ . The equations of the energy density  $W$  and the energy  $E$  stored in the volume element  $dV = dx dy dz$  are:

$$\begin{aligned} W_h &= \frac{1}{2} \mathbf{K}^2/dV; & W_e &= \frac{1}{2} \mathbf{P}^2/dV, \\ E_h &= \frac{1}{2} \mathbf{K}^2; & E_e &= \frac{1}{2} \mathbf{P}^2. \end{aligned} \quad (3a)$$

$E$  with or without indices  $h$  and  $e$  respectively is the symbol for the energy. The radiation vector is:

$$\mathbf{S} = v_0 \mathbf{K} \mathbf{P} / dV. \quad (4b)$$

Suppose that the energy flows parallel to the  $x$ -axis. Thus, we can rewrite Eq. (4b):

$$\bar{S}_x dV = v_0 \bar{K} \bar{P} \quad \text{or} \quad \bar{S}_x q T = \frac{v_0}{v} \bar{K} \bar{P} = S_x^+. \quad (4c)$$

As the product of  $\mathbf{K}$  and  $\mathbf{P}$  has the unit of energy,  $\bar{S}_x dV$  is equal to the product of energy and energy velocity. Therefore  $\bar{S}_x$  is equal to the product of energy density and energy velocity.

The factor  $dV$  within  $\mathbf{K}$  and  $\mathbf{P}$  is not necessary for Cartesian coordinate systems, because  $dV$  does not depend on the coordinates. Some authors treating the theory of electromagnetism say that Maxwell's theory is only valid for Cartesian coordinate systems. This is surprising. As we shall show in the following chapters, we have to add  $\sqrt{dV}$  when treating Maxwell's theory in terms of curvilinear coordinates, because — for example in the case of cylindrical coordinates — the volume element  $dV = r dr d\varphi dz$  is a function of  $r$ .

It is known from the literature on electromagnetism that  $\mathbf{H}$ ,  $\mathbf{E}$ ,  $\mathbf{K}$  and  $\mathbf{P}$  respectively can be deduced from a "potential". As  $\mathbf{H}$  is proportional to the partial derivative of the charge density with respect to time ( $\partial Q/\partial t$ ) and  $\mathbf{E}$  is proportional to the partial derivative of the charge density with respect to  $n$  ( $\partial Q/\partial n$ ), where  $n$  is the notation for any given direction, we have to consider the charge density  $Q$  as a potential function. In the theory of elastodynamics the potential function is still more important.

### 3. "Maxwell's theory" of elastodynamics

#### 3.1 Association of terms of electrodynamics with those of elastodynamics

It is not difficult to transfer Maxwell's theory of electrodynamics to the theory of elastodynamics. The propagation of waves is the focus of both theories. The basic differential equations describing wave propagation are similar in both theories. All we need to do is to associate the quantities of elastodynamics with the quantities of electromagnetism. For electric and elastic oscillations the equivalent quantities have already been associated with each other (ref. to Wagner 1947). This book includes Maxwell's equations of mechanical oscillations, but without reference to the analogy to Maxwell's equations of electrodynamics.

The quantities particle velocity  $\mathbf{V}$  and elastic stress  $\mathbf{T}$  in the theory of elastodynamics correspond to the magnetic and electric fields in electrodynamics. Similarly, the quantities  $\mu/c$  and  $\epsilon/c$  in electrodynamics correspond to the density of a medium  $\rho$  and the reciprocal elastic constant  $1/q$ . Let us call the elastic displacement of a particle  $\mathbf{s}$  and its components  $s_1$ ,  $s_2$  and  $s_3$  in the directions of the  $x$ -,  $y$ - and  $z$ -axis, respectively; thus we get for the particle velocity  $\mathbf{V} = \partial \mathbf{s} / \partial t$ .  $\mathbf{V}$  is a vector. As is known the stress  $\mathbf{T}$  is a tensor having nine components. The elastic constant  $q$  depends on the kind of wave and on the conditions of wave propagation. As Förtsch and Kardeván (1974) have shown, in the case of shear (transverse) waves we find  $q = 2\mu = E/(1 + \sigma)$  instead of  $E/2(1 + \sigma)$ , as one will find in the traditional theory of elastodynamics. Note that we use the following symbols:

$$\begin{array}{ll} E = \text{modulus of elasticity,} & \mu = \text{modulus of shearing,} \\ k = \text{bulk modulus,} & \sigma = \text{Poisson's ratio.} \end{array}$$

Considering the propagation of a longitudinal wave we can deduce  $q$  as follows:

- a)  $q = E$  for a thin rod
- b)  $q = E/(1 - \sigma)$  for a thin plate
- c)  $q = E/(1 - 2\sigma) = 3k$  for a solid body.

In the traditional theory one will find for a thin plate  $q = E/(1 - \sigma^2)$  instead of (b) and for the solid body  $q = E(1 - \sigma)/(1 + \sigma)(1 - 2\sigma)$  instead of (c), but Förtisch and Kardeván (1974) have proved that these formulas are wrong.

Now, let us enter into particulars of the constant  $3k$ . The constant  $3k$  is only valid in the case of volume change without change of the shape of the volume element, i.e. in the case that the volume is changed by uniform dilatational or compressional strain, where the strain is symmetrical in all three directions. This case can be realized by hydrostatic pressure. In elastodynamics, in the case of compression or dilatation in one direction, a different constant is valid. In the case of longitudinal waves propagating in solids we have compression and dilatation in one direction only. But nevertheless, we find  $q = 3k$ . The reason is as follows: While the particles rhythmically vibrate back and forth in the course of wave propagation, strength and inertia of the solid prevent that a deformation — compression or dilatation — transverse to the direction in which the wave travels comes into existence. Thus, parts of stress cannot produce a deformation. Förtisch and Kardeván (1974) have called this stress "Restspannung" (= remaining stress). Therefore for the ratio of stress and deformation we get  $3k (= q)$ . In the case of wave propagation in a thin rod a deformation transverse to the direction of wave travel can occur in two directions. Therefore we have  $q = E$  according to definition. In the case of a thin plate the transverse deformation is prevented in one direction; therefore we find  $q = E/(1 - \sigma)$ . As just mentioned, in solids a transverse deformation cannot occur, and therefore we have  $q = E/(1 - 2\sigma)$ .

As Förtisch and Kardeván (1974) have also shown, the tensor of deformation (tensor of strain) can be divided into the tensor of pure change of volume (without change of shape) and the tensor of pure shear strain (change of shape without change of volume). Change of volume and change of shape, where one excludes the other, may be called basic deformations. The tensor of stress can be divided similarly as the tensor of deformation. We choose the following notation:

$$\begin{aligned} t &= \text{components of stress (with indices)} \\ e &= \text{components of strain (with indices) (deformation)} \\ \tau &= (t_{xx} + t_{yy} + t_{zz})/3; \quad \varepsilon = (e_{xx} + e_{yy} + e_{zz})/3, \end{aligned}$$

thus we get:

$$\begin{vmatrix} \tau & 0 & 0 \\ 0 & \tau & 0 \\ 0 & 0 & \tau \end{vmatrix} = 3k \begin{vmatrix} \varepsilon & 0 & 0 \\ 0 & \varepsilon & 0 \\ 0 & 0 & \varepsilon \end{vmatrix},$$

$$\begin{vmatrix} t_{xx} - \tau & t_{yx} & t_{zx} \\ t_{xy} & t_{yy} - \tau & t_{zy} \\ t_{xz} & t_{yz} & t_{zz} - \tau \end{vmatrix} = 2\mu \begin{vmatrix} e_{xx} - \varepsilon & e_{yx} & e_{zx} \\ e_{xy} & e_{yy} - \varepsilon & e_{zy} \\ e_{xz} & e_{yz} & e_{zz} - \varepsilon \end{vmatrix}. \quad (17)$$

### 3.2 Maxwell's equations of elastodynamics

Now, we shall turn to Maxwell's equations. According to Eq. (1) we find in our case:

$$\rho \frac{\partial \mathbf{V}}{\partial t} = \frac{\partial \mathbf{T}}{\partial n}; \quad \frac{1}{q} \frac{\partial \mathbf{T}}{\partial t} = \frac{\partial \mathbf{V}}{\partial n}. \quad (18)$$

As is known from the theory of elasticity,  $\mathbf{T} = q\mathbf{D}$ , where  $\mathbf{D}$  is the symbol for deformation; therefore we can rewrite Eq. (18):

$$\rho \frac{\partial \mathbf{V}}{\partial t} = q \frac{\partial \mathbf{D}}{\partial n}; \quad \frac{\partial \mathbf{D}}{\partial t} = \frac{\partial \mathbf{V}}{\partial n}; \quad (18a)$$

As  $\mathbf{D} = \partial \mathbf{s} / \partial n$ , we can rewrite Eqs (18) and (18a) once more:

$$\rho \frac{\partial^2 \mathbf{s}}{\partial t^2} = q \frac{\partial^2 \mathbf{s}}{\partial n^2}; \quad \frac{\partial^2 \mathbf{s}}{\partial t \partial n} = \frac{\partial^2 \mathbf{s}}{\partial t \partial n}. \quad (18b)$$

We know the first of both equations from the law of forces. It means that the inertial force acting on an unit volume is equal to the force acting on an unit area, where this force results from the local change of stress and deformation per unit length respectively. The second equation is an identity in homogeneous media; i.e. the change of deformation per time is expressed in terms of the stress  $\mathbf{T}$  on the left side of the equation and in terms of the velocity  $\mathbf{V}$  on the right side.

Above we have learnt that the charge density  $Q$  is the potential function in electrostatics. As one may learn from this chapter, the particle motion  $\mathbf{s}$  in the course of wave propagation is the potential function in elastodynamics.

Now, we are going to introduce Maxwell's quantities  $\mathbf{K}$  and  $\mathbf{P}$  to elastodynamics. We find:

$$\mathbf{K} = \sqrt{\rho dV} \mathbf{V}, \quad \mathbf{P} = \sqrt{qdV} \mathbf{D} = \sqrt{dV/q} \mathbf{T}. \quad (19)$$

Using  $\mathbf{K}$  and  $\mathbf{P}$  we can rewrite Maxwell's equations:

$$\sqrt{\rho dV} \frac{\partial \mathbf{K}}{\partial t} = \sqrt{qdV} \frac{\partial \mathbf{P}}{\partial n}; \quad \sqrt{\rho dV} \frac{\partial \mathbf{P}}{\partial t} = \sqrt{qdV} \frac{\partial \mathbf{K}}{\partial n}. \quad (18c)$$

Hereby we find perfect symmetry as well.

### 3.3 The nature of elastic waves

Elastic transverse waves involve vibrations of particles of matter *s* perpendicular to the direction in which the waves travel; their velocity is  $b = \sqrt{2\mu/\rho}$ . The velocity of elastic longitudinal waves that involve back and forth vibrations of particles of matter in the same direction as that in which the wave travel depends on geometrical conditions. The velocity in a thin rod is  $a_r = \sqrt{E/\rho}$ . Suppose that the rectangular rod is increasing in one direction to form a thin plate. Now consider the velocity  $a$  of the wave: it increases also, because the transverse deformation is prevented the more the plate is increasing. Finally, we find  $a_{pl} = \sqrt{E/\rho(1-\sigma)}$ . Now let the plate increase in the third dimension to form a solid volume. Thus the transverse deformation is decreasing more and more. Finally, we find the velocity of the wave in a solid  $a_{so} = \sqrt{3k/\rho}$ . Here we have the explanation for another phenomenon, too. The velocity  $a_{so}$  of the waves in a solid decreases the more, the nearer to the surface of the solid the waves propagate; at the surface the velocity turns into  $a_{pl}$ . In a beam with a large cross-section we find the following velocities of the longitudinal waves:

$$\begin{aligned} &a_{so} \text{ in the interior of the beam,} \\ &a_{pl} \text{ at its surface,} \\ &a_r \text{ at its edges.} \end{aligned}$$

Förtsch and Kardeván (1974) calculated this change of the velocities  $a_{so}$ ,  $a_{pl}$  and  $a_r$  into one another. Now, the surprising phenomenon that a medium is inhomogeneous with regard to a longitudinal wave, although the density and the elastic constants are constant and do not vary with the site in the medium. The reason is the transverse deformation. Such a medium is always homogeneous with regard to a transverse wave.

Now let us use the symbol  $\gamma$  for the wave velocity in a medium.  $\gamma$  can be either  $a$  or  $b$ .

The first equation of Eq. (18b) is the differential wave equation for the displacement  $s$ ; the velocity  $\gamma$  is equal to  $\sqrt{q/\rho}$ . The same differential equation can be deduced from Eqs (18) and (18a) for  $V$ ,  $T$  and  $D$ . The multiplicity of solutions, i.e. the multiplicity of waves that can be deduced from the differential equation is even greater in elastodynamics than in electrodynamics. In addition, there are two kinds of transverse waves and one kind of longitudinal wave. We find the same kinds of elastic waves, namely travelling waves, stationary waves and furthermore waves, where the maximum amplitudes vary on the wave fronts. The last mentioned case is more important in elastodynamics than in electrodynamics; it is especially important in the field of seismology. For example, surface waves important in seismology belong to this type of waves. There are two kinds of surface waves: the Love Wave, a transverse wave, and the Rayleigh Wave that is composed of a longitudinal and a transverse component; both components superpose each other in a special manner.

$T$  and  $D$  are tensors, therefore it is helpful to rewrite Eq. (18) using component notation:

$$\begin{aligned}\rho \frac{\partial V_x}{\partial t} &= \frac{\partial t_{xx}}{\partial x} + \frac{\partial t_{yx}}{\partial y} + \frac{\partial t_{zx}}{\partial z}, \\ \rho \frac{\partial V_y}{\partial t} &= \frac{\partial t_{xy}}{\partial x} + \frac{\partial t_{yy}}{\partial y} + \frac{\partial t_{zy}}{\partial z}, \\ \rho \frac{\partial V_z}{\partial t} &= \frac{\partial t_{xz}}{\partial x} + \frac{\partial t_{yz}}{\partial y} + \frac{\partial t_{zz}}{\partial z},\end{aligned}\tag{18d}$$

$$\begin{aligned}\frac{1}{q} \frac{\partial}{\partial t} (t_{xx} + t_{yx} + t_{zx}) &= \left( \frac{\partial}{\partial x} + \frac{\partial}{\partial y} + \frac{\partial}{\partial z} \right) V_x, \\ \frac{1}{q} \frac{\partial}{\partial t} (t_{xy} + t_{yy} + t_{zy}) &= \left( \frac{\partial}{\partial x} + \frac{\partial}{\partial y} + \frac{\partial}{\partial z} \right) V_y, \\ \frac{1}{q} \frac{\partial}{\partial t} (t_{xz} + t_{yz} + t_{zz}) &= \left( \frac{\partial}{\partial x} + \frac{\partial}{\partial y} + \frac{\partial}{\partial z} \right) V_z.\end{aligned}$$

The first index of  $t_{\nu\mu}$  indicates the direction of the principal normal to the area, on which  $t_{\nu\mu}$  is acting; the second index indicates the direction, in which the force is acting. These two indices — alone or in combination — determine the direction  $n$  in which the wave will travel.

If we are going to use deformation components  $e_{\nu\mu}$  instead of the stress components  $t_{\nu\mu}$ , we have to multiply the right side of the first set of equations and the left side of the second set by  $q$ .

We can also specify the energy densities of elastic waves now at once. Using the following symbols:

- $W_k$  = kinetic energy density of the longitudinal and transverse wave,
- $W_{pl}$  = potential energy density of the longitudinal wave,
- $W_{pt}$  = potential energy density of the transverse wave,

we find:

$$W_k = \frac{\rho}{2} V^2; \quad W_{pl} = \frac{3k}{2} D^2 = \frac{1}{2 \cdot 3k} T^2;$$

$$W_{pt} = \frac{2\mu}{2} D^2 = \frac{1}{2 \cdot 2\mu} T^2.$$

Herein we have:

$$V^2 = V_x^2 + V_y^2 + V_z^2,$$

$$T^2 = t_{xx}^2 + t_{yx}^2 + t_{zx}^2 + t_{xy}^2 + t_{yy}^2 + t_{zy}^2 + t_{xz}^2 + t_{yz}^2 + t_{zz}^2,$$

$$D^2 = e_{xx}^2 + e_{yx}^2 + e_{zx}^2 + e_{xy}^2 + e_{yy}^2 + e_{zy}^2 + e_{xz}^2 + e_{yz}^2 + e_{zz}^2.$$

The radiation vector in elastodynamics is defined by the equation:

$$\mathbf{S} = -\mathbf{T}\mathbf{V} = -q\mathbf{D}\mathbf{V}. \quad (20)$$

The three components of  $\mathbf{S}$  are:

$$S_x = -(t_{xx}V_x + t_{xy}V_y + t_{xz}V_z),$$

$$S_y = -(t_{yx}V_x + t_{yy}V_y + t_{yz}V_z),$$

$$S_z = -(t_{zx}V_x + t_{zy}V_y + t_{zz}V_z).$$

One may already find this vector in the books of Love (1926, 1944), where it is called "Flux of Energy". But its relationship to Poynting's vector was not mentioned.

### 3.4 Absorption of elastic waves

In Chapter 2 we have treated waves propagating in a conductor. Thereby absorption of wave energy occurs, caused by the conductivity of the medium. In elastodynamics it is possible to find equations that are in accordance with Maxwell's equations (5) and the differential wave equations (6) and (6a). Some authors have presented these equations. According to them, absorption is caused by an elastic after-effect. But the results of theory are not in accordance with the results of experiments, with regard to observations of absorption. If we suppose that an elastic after-effect causes absorption, we ought to find in our experiments that the absorption coefficient decreases while the wave frequency increases, but this result was not found.

Other authors tried to explain the absorption of elastic waves by assuming that a solid keeps part of its viscosity after solidification. The differential equation (18b first Eq.) does not include a term with regard to absorption. In order to take absorption by viscosity into account, we have to add a term. Thus, we find the following differential wave equation:

$$\rho \frac{\partial^2 \mathbf{s}}{\partial t^2} = q \frac{\partial^2 \mathbf{s}}{\partial n^2} + q' \frac{\partial}{\partial t} \frac{\partial^2 \mathbf{s}}{\partial n^2}, \quad (21)$$

$q'$  is the symbol for the viscosity constant.

The theory of visco-elasticity was popular among seismologists until the 1950's. But nevertheless the results of experiments were not in accordance with the theory. According to the theory, the absorption coefficient increases with increasing wave frequency. But this led to the conclusion that a wave could not occur any longer if the frequency attains a certain value, because the maximum amplitude would decrease too much. But experiments have shown that supersonic waves occur.

Even if the term in the differential equation that causes absorption were proportional to  $\partial s / \partial t$ , the absorption coefficient  $\kappa' = 2\pi M$  (the dot indicates that the

coefficient  $\kappa'$  is defined per wavelength  $\lambda$ ) would depend on the wave frequency, as, according to Eq. (9) in Chapter 2,  $M$  is a function of the frequency. The absorption would decrease with increasing frequency.

The analysis of many observations about travelling waves by Förtsch (1940, 1953) has shown that  $\kappa'$  does not depend on frequency. The data analyzed by Förtsch represent a frequency spectrum that reaches from 0.05 to 40 cycles per second. Förtsch has also evaluated the results of measurements of some other authors who have investigated wave propagation and natural vibrations, especially with regard to rock rods. The logarithmic decrement of natural vibrations  $\delta' = \delta T_d$  ( $T_d$  = period of the damped natural vibration) is equal to the absorption coefficient  $\kappa'$ , because natural vibrations can be defined as stationary waves. The experiments show that one always gets the same absorption coefficient, if one considers the same material, although the coefficient is deduced from observations of propagation with regard to longitudinal, transverse or surface waves, and from longitudinal or torsion vibrations or vibrations of a bent beam respectively.

Born (1941) has been the first who has had the idea that the observed law with regard to the absorption coefficient can only be explained by taking sliding, i.e. Coulomb's friction, into account. Förtsch (1956) has also studied this problem and more extensively. In order to solve the problem, we define the term describing the absorption in the differential wave equation so that it includes a differential quotient of odd order with regard to  $t$  and  $n$ ; thus we have an absorption coefficient that depends on frequency. A term describing energy dissipation and including a differential quotient of even order can only be deduced, as Wiechert (1903) has shown treating the theory of seismographs with friction of the writing mechanism, if sliding friction — as a

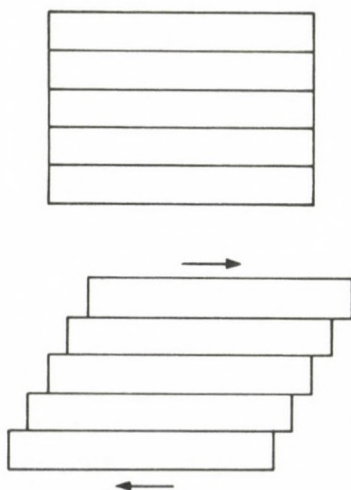


Fig. 1. Diagram of sliding friction occurring in the case of shear

third force — is added to the differential equation. The law of Coulomb's friction is  $R = \pm r|K_r|$ .  $R$  is the symbol for the frictional force.  $K_r$  is the symbol for the force, by which the surfaces of two bodies are pressed against each other.  $r$  is the symbol for the coefficient of friction; it is dimensionless. We have to choose the sign in such a way that the sign of  $R$  is always opposite to the sign of the velocities at that the bodies move relative to each other.

Let us consider a square body composed of many sheets. Now, let this body be distorted, as shown in Fig. 1; the sheets are shifted with respect to each other by the torsion. Now, let us suppose that an elastic wave propagates in such a body. In the course of wave propagation, we have shifting of the sheets and thus sliding friction with varying sign. In order to describe this phenomenon we have to consider elastic stress connected with  $K_r$ ; the stress is  $T = q \partial s / \partial n$ . Now, the differential wave equation is, according to Förtisch (1956):

$$\rho \frac{\partial^2 \mathbf{s}}{\partial t^2} = q \frac{\partial^2 \mathbf{s}}{\partial n^2} \pm r q \left| \frac{\partial^2 \mathbf{s}}{\partial n^2} \right|. \quad (22)$$

We cannot treat the solution of this differential equation in particular in this paper. A particular solution can only be found with respect to half a wavelength. At the points where the frictional force changes the sign — these points are identical with the points of maxima and minima of the ground motion  $\mathbf{s}$  — the maximum amplitudes have to be accommodated to each other. Note that according to theory the ratio of two succeeding maximum amplitudes is:  $A_x / A_{x+\lambda} = 1 / (1 - 2r)$  ( $\lambda$  = wave-length). The ratio does not depend on the frequency, as the observations require. The maximum amplitudes are determined by the exponential functions  $\pm e^{-\kappa' x / L}$ . As  $r \ll 1$ , and  $e^{-\kappa' x} \approx (1 - \kappa' x)$ , we find  $\kappa' = 2r$ . Thus, the observations of absorption and damping phenomena yield an "internal" friction coefficient of the media. The notation "internal" refers to the interiors of solid bodies. The "external" friction coefficient is far greater than the "internal" one. The "external" coefficient can be deduced from calculating the relative motion of two bodies, the surfaces of which are pressed against one another.

Note that the function describing absorption does not include  $\lambda$ , as one may expect, but the wave-length  $L$  with respect to the energy velocity. The results of experiments of Förtisch (1953) support this statement. This is understandable, because we treat a phenomenon of energy absorption.

### 3.5 Maxwell's quantities of elastodynamics

We have already introduced Maxwell's quantities  $\mathbf{K}$  and  $\mathbf{P}$  and the corresponding equations (see chap. 3.2, Eqs (19) and (18c)). We have mentioned the symmetry of Eq. (18c) as well. Remember that we have multiplied the differential quotient  $\partial / \partial t$  ( $t$  = time) by the factor  $\sqrt{\rho dV}$  and  $\partial / \partial n$  ( $n$  = site) by the factor  $\sqrt{q dV}$ . Thus, we have so-called standardized quotients.

Using  $\mathbf{K}$  and  $\mathbf{P}$  we find the same basic equations in elastodynamics, as we find in electrodynamics with regard to the energy densities and the energies stored in a volume element  $dV$ :

$$W_k = \frac{1}{2} \mathbf{K}^2/dV; \quad W_p = \frac{1}{2} \mathbf{P}^2/dV, \quad E_k = \frac{1}{2} \mathbf{K}^2; \quad E_p = \frac{1}{2} \mathbf{P}^2. \quad (19a)$$

Of course the quantities are different, but the basic equations have the same structure.

Using  $\mathbf{K}$  and  $\mathbf{P}$  again, we find for the vector of radiation  $\mathbf{S}$ :

$$\mathbf{S} = - \sqrt{\frac{q}{\rho}} \mathbf{K}\mathbf{P}/dV = -\gamma \mathbf{K}\mathbf{P}/dV. \quad (20b)$$

Considering a medium where wave energy is absorbed by Coulomb's friction, we find the following differential equations for  $\mathbf{K}$  and  $\mathbf{P}$ :

$$\rho \frac{\partial^2 \mathbf{K}}{\partial t^2} = q \left[ \frac{\partial^2 \mathbf{K}}{\partial n^2} \pm r \left| \frac{\partial^2 \mathbf{K}}{\partial n^2} \right| \right], \quad \rho \frac{\partial^2 \mathbf{P}}{\partial t^2} = q \left[ \frac{\partial^2 \mathbf{P}}{\partial n^2} \pm r \left| \frac{\partial^2 \mathbf{P}}{\partial n^2} \right| \right]. \quad (23)$$

Solving these equations we find that the phase velocity of the wave is equal to the medium velocity  $\gamma = \sqrt{q/\rho}$ . We can illustrate this: During one period the influences of the last term in the above equation upon the phase velocity are nearly compensated by each other because of the change of sign that occurs each time the amplitudes reach their maxima.

#### 4. Modulated waves

In physics, the modulated wave is of less importance, but in seismology this kind of wave is found as a surface wave in connexion with every earthquake. A wave is modulated, if the maximum amplitude is not constant on the wave front but depends on site. The simplest kind of modulated waves is generated when a plane wave is continually totally reflected between two parallel horizontal boundary planes, whereby the wave hits the planes at a certain inclined angle. Hereby we have a superposition of two waves, one of them propagates from the plane above to the plane below by a certain inclined angle, and the other one propagates from the plane below to the plane above by the same inclined angle. We can describe this phenomenon:

$$a = \frac{A}{2} [\cos(\omega t - kx \sin \alpha - kz \cos \alpha) + \cos(\omega t - kx \sin \alpha + kz \cos \alpha)] = \\ = A \cos(kz \cos \alpha) \cos(\omega t - kx \sin \alpha).$$

$\alpha$  is the angle of incidence between the direction of propagation of the first wave and the  $z$ -axis. We find for the corresponding angle of the second wave:  $180^\circ - \alpha$ . The maximum amplitude is modulated by a cosine-function. Note that the travelling and the

stationary waves result from the modulated wave described above as a limit case. Letting  $\alpha = 90^\circ$  we have a travelling wave in the  $x$ -direction; letting  $\alpha = 0^\circ$  we have a stationary wave in the  $z$ -direction. In a way, the modulated wave corresponds to the transfer of a travelling wave into a stationary one.

#### 4.1 The modulated SH-wave

In seismology, we call a wave a SH-wave, if the vector of vibration is perpendicular to the plane of incidence. Suppose that the wave is modulated in the direction of the  $z$ -axis and that the plane of incidence is parallel to the  $xz$ -plane. Then we can describe the plane wave by the formula:

$$s_2 = S_2 \cos k_z z \cos(\omega t - k_x x). \quad (24)$$

Suppose that the modulation of the wave determined by  $k_z$  is known. Equation (24) has to satisfy the differential wave equation (18b, first equation), where  $\partial^2 s / \partial n^2$  denotes the Laplacian operator. As we have  $q = 2\mu$  in our case, we get the following equation in order to calculate  $k_x$ :

$$\frac{\omega^2}{b^2} = k_b^2 = k_x^2 + k_z^2, \quad \text{or} \quad k_x = \sqrt{k_b^2 - k_z^2}. \quad (25)$$

$k_b$  is the wave number belonging to the medium velocity  $b$ . As one can realize, the modulation must be less than  $k_b$ , as otherwise  $k_x$  will be imaginary. The intervals of wave nodes and loop antinodes must not succeed each other too fast in the  $z$ -direction. Equation (25) also leads to the conclusion that the wave travels in the  $x$ -direction with the following velocity:

$$v_x = 1 / \sqrt{\frac{1}{b^2} - \frac{k_z^2}{\omega^2}} = b / \sqrt{1 - k_z^2/k_b^2} = b / \sin \alpha. \quad (26)$$

$v_x$  exceeds  $b$ . According to Eq. (25) we get:  $k_z = k_b \cos \alpha$  and  $k_x = k_b \sin \alpha$ , where  $\alpha$  is defined as mentioned above in the introduction to Chapter 4. Letting  $k_z = 0$ , we get  $\alpha = 90^\circ$  and  $v_x = b$ . Thus, we have a plane wave travelling in the  $x$ -direction. Letting  $k_z = k_b$  we get  $\alpha = 0^\circ$  and  $v_x = \infty$ . All phases are equal in the  $x$ -direction; thus only the stationary wave in the direction of the  $z$ -axis is left over.

Equation (25) leads to the energy velocity  $u_x = d\omega/dk$  that can be calculated as follows:

$$u_x = b^2/v_x. \quad (27)$$

Note that we have had a similar result, when we considered the propagation of electromagnetic waves in a conductor. Hereby we found  $u_1 = v_0^2/v$  (refer to Eq.(15)).

The connexion between phase velocity and energy velocity as described above is illustrated in Fig. 2. A plane wave travels towards the ground surface, where the

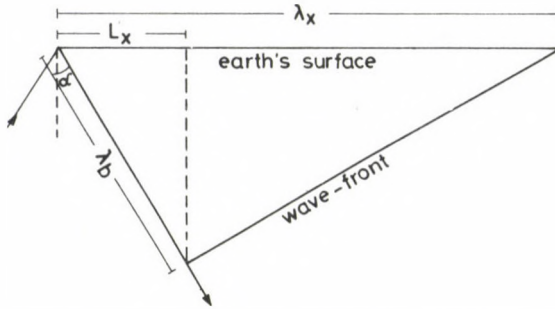


Fig. 2. Illustration of the connection between medium wave-length  $\lambda_m$ , phase wave-length  $\lambda_x$  and energy wave-length  $L_x$

observer is situated; the wave being at an inclination to the surface is reflected when striking the surface. Figure 2 illustrates the connexion of the wave-lengths  $\lambda_b$ ,  $\lambda_x$  and  $L_x$ .  $\lambda_b$  relates to the wave velocity of the medium  $b$ ,  $\lambda_x$  relates to the wave velocity  $v_x$  with which the wave travels virtually along the ground surface, and  $L_x$  relates to the energy velocity  $u_x$  of the wave travelling along the ground surface.  $u_x$  is also a virtual velocity along the ground surface.

Now, we are going to consider Maxwell's quantities of the modulated wave:

$$K_x = -\sqrt{\rho dV} \omega S_2 \cos k_z z \sin(\omega t - k_x x),$$

$$P_{xx} = \sqrt{2\mu dV} k_x S_2 \cos k_z z \sin(\omega t - k_x x),$$

$$P_{zx} = -\sqrt{2\mu dV} k_z S_2 \sin k_z z \cos(\omega t - k_x x).$$

The kinetic energy in a volume element  $dV$  is:

$$E_k = \frac{1}{2} K_x^2 = \frac{1}{2} \rho \omega^2 dV S_2^2 \cos^2 k_z z \sin^2(\omega t - k_x x).$$

The potential energy in a volume element  $dV$  consists of two parts corresponding to the travelling and stationary waves respectively:

$$E_p = E_{px} + E_{pz} = \frac{1}{2} (P_{xx}^2 + P_{zx}^2),$$

$$E_p = \frac{1}{2} 2\mu dV k_x^2 S_2^2 \cos^2 k_z z \sin^2(\omega t - k_x x) + \\ + \frac{1}{2} 2\mu dV k_z^2 S_2^2 \sin^2 k_z z \cos^2(\omega t - k_x x).$$

The radiation vector is:

$$\mathbf{S} = S_x i + S_z k.$$

Here  $i$  and  $k$  denote the unit vectors on the  $x$ - and  $z$ -axis respectively. We find:

$$S_x = -bK_x P_{xx} = b^2 \rho \omega^2 \frac{1}{v_x} dV S_2^2 \cos^2 k_z z \sin^2 (\omega t - k_x x),$$

$$S_z = -bK_x P_{zx} = -b^2 \rho \omega k_z dV S_2^2 \sin k_z z \cos k_z z \sin (\omega t - k_x x) \cos (\omega t - k_x x).$$

We are interested in the average energy amounts that are stored in the volume element  $dV$  during one period:

$$\bar{E}_k = \frac{1}{8} \rho \omega^2 dV S_2^2; \quad \bar{E}_p = \frac{1}{8} 2\mu (k_x^2 + k_z^2) dV S_2^2.$$

Referring to Eq. (25) we can write for  $\bar{E}_p$ :

$$\bar{E}_p = \frac{1}{8} 2\mu k_b^2 dV S_2^2 = \frac{1}{8} \rho \omega^2 dV S_2^2.$$

As one can realize the kinetic energy is equal to the potential energy in the case of the modulated wave as well. The parts of  $\bar{E}_k$ , being equal to  $\bar{E}_{px}$ , and  $\bar{E}_{px}$  are the driving energies of the wave, they cause the wave propagation. The other parts of  $\bar{E}_k$ , being equal to  $\bar{E}_{pz}$ , generate the stationary wave. They do not share in the wave propagation. On the contrary they impede the propagation. Thus  $u$  is reduced. Using the notation  $\sin \alpha$  for the ratio  $\bar{E}_{px}/\bar{E}_k$ , we get:

$$\text{phase velocity } v_x = b/\sin \alpha,$$

$$\text{energy velocity } u_x = b \sin \alpha.$$

Furthermore we can calculate the average radiation:

$$\bar{S}_x = \frac{b^2}{v_x} \frac{1}{4} \rho \omega^2 dV S_2^2, \quad \bar{S}_z = 0.$$

We can calculate the energy velocity from the ratio  $\bar{S}_x/\bar{E}$  as well, where  $\bar{E}$  denotes the total average energy  $\bar{E} = 2\bar{E}_k$ :

$$u_x = \frac{b^2}{v_x} = b \sin \alpha = b \sqrt{1 - k_z^2/k_b^2}.$$

#### 4.2 The modulated SV-wave

Once again we consider a transverse wave as in Chapter 4.1, but now the vector of vibration is parallel to the  $z$ -axis. Suppose that the modulation is also parallel to the  $z$ -axis. This type of wave can be described by the formula:

$$s_3 = S_3 \cos k_z z \cos (\omega t - k_x x). \quad (28)$$

Suppose again that  $k_z$  is known,  $k_x$  must also not be too large in this case. The most important difference between the SH- and SV-waves is that the stationary SV-wave in the  $z$ -direction has the nature of a longitudinal wave. Substituting the formula (28) in the differential wave equation (18, first equation), we get:

$$\rho\omega^2 = 2\mu k_x^2 + 3k k_z^2. \quad (29)$$

This equation leads to  $k_x$ :

$$k_x = \sqrt{\frac{\rho}{2\mu}\omega^2 - \frac{3k}{2\mu}k_z^2} = \frac{\omega}{b} \sqrt{1 - \frac{3k}{2\mu}(k_z/k_b)^2}. \quad (30)$$

Here we use the notation  $k_b = \omega/\sqrt{2\mu/\rho} = \omega/b$ . We can deduce the phase and energy velocities from Eqs (29) and (30):

$$v_x = b \sqrt{1 - \frac{3k}{2\mu}(k_z/k_b)^2}, \quad u_x = b \sqrt{1 - \frac{3k}{2\mu}(k_z/k_b)^2}. \quad (31)$$

As for the SV-wave, the phase velocity is slightly greater than in the case of the SH-wave and therefore the energy velocity less. Furthermore,  $P_{zx}$  is greater by the factor  $\sqrt{3k/2\mu}$  as in the case of the SH-wave. Note that  $k_z$  must not exceed  $\sqrt{2\mu/3k} k_b$ .

#### 4.3 The modulated $P$ -wave

In seismology, longitudinal waves are called  $P$ -waves, as at the earthquake observing stations they are recorded first of all the vibrations produced by an earthquake. Their velocity exceeds the velocities of transverse and surface waves. Suppose that the vector of vibration of a  $P$ -wave is parallel to the  $x$ -axis and its modulation parallel to the  $z$ -axis; thus we can write:

$$s_1 = S_1 \cos k_z z \cos(\omega t - k_x x). \quad (32)$$

Once more we suppose that  $k_z$  is known, but must not increase too much. Furthermore, the nodes and loop antinodes of the wave must not succeed too fast. The stationary wave in the  $z$ -direction is of a transverse nature. Substituting Eq. (32) in (18b) (first equation) we get:

$$\rho\omega^2 = 3k k_x^2 + 2\mu k_z^2. \quad (33)$$

We can deduce  $k_x$  from this equation:

$$k_x = \sqrt{\frac{\rho}{3k}\omega^2 - \frac{2\mu}{3k}k_z^2} = \frac{\omega}{a} \sqrt{1 - \frac{2\mu}{3k}(k_z/k_a)^2}. \quad (34)$$

Using the denotation  $k_a = \omega / \sqrt{3k/\rho} = \omega/a$  we get:

$$v_x = a \left/ \sqrt{1 - \frac{2\mu}{3k} (k_z/k_a)^2} \right. \quad (35)$$

As one can realize,  $k_z$  must not exceed the quantity  $\sqrt{3k/2\mu} k_a$ . Furthermore, the energy velocity  $u_x$  is given by the formula:  $u_x = a^2/v_x$ .

#### 4.4 The generalized Laplacian operator

In Chapters 4.2 and 4.3 we have hold back that — properly speaking — we must not substitute the formulas above in Eq. (18b) (first equation) without further reflexions. This differential equation is:

$$\rho \frac{\partial^2 \mathbf{s}}{\partial t^2} = q \frac{\partial^2 \mathbf{s}}{\partial x^2} + q \frac{\partial^2 \mathbf{s}}{\partial y^2} + q \frac{\partial^2 \mathbf{s}}{\partial z^2} \quad (18e)$$

On the right side of this equation each differential quotient is multiplied by the same factor  $q$ . But remember the equations of the *SV*- and *P*-waves: the factors are different; they can be  $2\mu$  or  $3k$  depending on whether the wave is of transverse or longitudinal nature. This result leads us to extend the traditional Laplacian operator. We have to write:

$$\Delta_e \mathbf{s} = g_1 \frac{\partial^2 \mathbf{s}}{\partial x^2} + g_2 \frac{\partial^2 \mathbf{s}}{\partial y^2} + g_3 \frac{\partial^2 \mathbf{s}}{\partial z^2} \quad (36)$$

The factors  $g_1$ ,  $g_2$  and  $g_3$  may be called the weights of the differential quotients.

Let us consider some examples for  $\Delta_e \mathbf{s}$ :

1. We can write the extended Laplacian operator for a *SH*-wave being modulated in the  $y$ - and  $z$ -direction:

$$\Delta_e s_2 = 2\mu \frac{\partial^2 s_2}{\partial x^2} + 3k \frac{\partial^2 s_2}{\partial y^2} + 2\mu \frac{\partial^2 s_2}{\partial z^2}.$$

The phase velocity is:

$$v_x = b \left/ \sqrt{1 - \left( \frac{3k}{2\mu} k_y^2 + k_z^2 \right)} \right/ k_b^2.$$

2. We consider a *SV*-wave being modulated in the  $y$ - and  $z$ -direction. We find:

$$\Delta_e s_3 = 2\mu \frac{\partial^2 s_3}{\partial x^2} + 2\mu \frac{\partial^2 s_3}{\partial y^2} + 3k \frac{\partial^2 s_3}{\partial z^2}.$$

The phase velocity is:

$$v_x = b \sqrt{1 - \left( k_y^2 + \frac{3k}{2\mu} k_z^2 \right)} / k_b^2.$$

3. The extended Laplacian operator for the modulated *P*-wave is:

$$\Delta_e s_1 = 3k \frac{\partial^2 s_1}{\partial x^2} + 2\mu \frac{\partial^2 s_1}{\partial y^2} + 2\mu \frac{\partial^2 s_1}{\partial z^2}.$$

We find for the phase velocity:

$$v_x = a \sqrt{1 - \frac{2\mu}{3k} (k_y^2 + k_z^2) / k_a^2}.$$

Above we used the symbols:  $k_b = \omega/b$  and  $k_a = \omega/a$ . In the formulas describing the phase velocities, the numbers in the roots always have to be positive. We have to choose  $k_y$  and  $k_z$  in accordance with this conditions.

In the conclusion of this chapter we will answer the question whether the extended Laplacian operator is only of theoretical importance or whether it is of practical interest. We must answer this question in the affirmative. Let us consider tectonic earthquakes. They are caused by the sudden displacement of crustal blocks along a fault. An earthquake gives rise to seismic (elastic) waves. Briefly, the amount of energy emitted depends on the direction in which the wave leaves the focus (we cannot describe the phenomenon more extensively in this treatise). This leads to the conclusion that the maximum amplitudes on the wavefronts depend on site; here, the sign may vary. In nature the general distribution of the maximum amplitudes is divided into amplitude fields for modulated waves (as described above) according to Fourier's theorem; the modulated waves travel with the corresponding phase and energy velocities. The seismologist knows that this — among other things — is the reason why vibrations that are generated by an impulse are expanded to the wave trains.

## 5. The propagation of cylindrical waves

### 5.1 Observation results with regard to cylindrical waves

In the chapters above we have treated plane waves. The condition for plane waves is that they are emitted from each point of a plane in a synchronous way. In the case of cylindrical waves the synchronous emission occurs at each point of a straight line. Spherical waves are generated by a point source. In the case of plane waves the wave-fronts are also planes. In the case of cylindrical waves the wave-fronts are cylindrical surfaces. And in the case of spherical waves they are spherical surfaces. In

Chapter 1, we have already mentioned that it has not yet been possible to explain the propagation of cylindrical waves in a satisfactory way.

First we will illustrate the requirements of the observation results with regard to theory. There are two examples that we will consider for explanation. In seismic experiments for exploring surface conditions, particular machinery was used to generate surface waves — Rayleigh waves — in the uppermost layer under the earth's surface. The waves propagating radially and horizontally from the machinery were pure cylindrical waves. This could be verified by evaluating the observations of the decrease of the maximum amplitudes with increasing distance  $r$ . Furthermore, the phase differences between the machinery and the observation points were determined. Figure 3 shows one example of measurement. On the abscissa the distance of the observation points from the machinery are marked, while the travel times of the loop antinodes from the machinery to these points are marked on the ordinate. The travel times correspond to the phase differences. The graph shows that the measurement results, without exception, lie on a straight line from the origin of the coordinate system. The phase velocity is  $v = 170$  m/s in our example, the frequency is 10 cycles per second. Hence we can calculate the wave-length; it is  $\lambda = 17$  m. As the Rayleigh wave is composed of a modulated longitudinal wave and a modulated transverse wave — this is caused by the condition of wave reflections at the boundary planes of the uppermost layer — dispersion occurs. Figure 3 especially illustrates the fact that the phases travel with constant velocity after having passed the first measurement point at a distance of 5 m from the machinery.

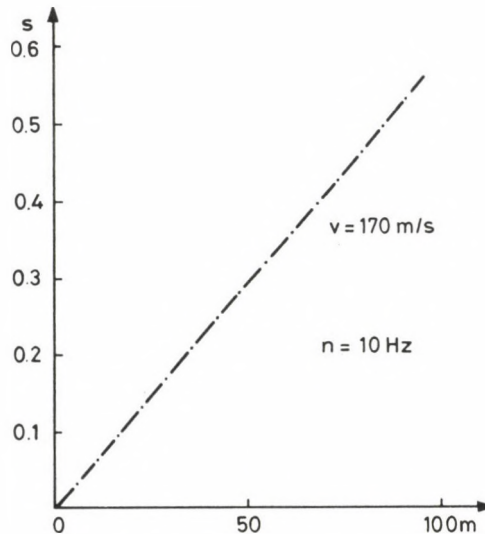


Fig. 3. Measurement of phase velocity in the case of cylindrical wave propagation

The analysis has also shown that the product of measured maximum amplitude and root of the distance is constant over the entire measuring range.

For our second example we remind of an experiment that can be performed by everybody every day. A water drop falling on to a surface of water generates a surface wave that will propagate in a circular way. This surface wave can be classed among the cylindrical waves. The experiment shows that — as in our first example — the wave travels with a constant velocity from the source. It also shows that the deformation of the surface of the water caused by the wave motion is preserved from the source to large distances. In our experiment the wave motion has impulse character, in this case the deformation can only be preserved, if there is no dispersion occurring, i.e. if all frequencies travel with the same velocity.

### 5.2 Description of the propagation mechanism of cylindrical waves—theoretical conceptions

#### 5.21 Cylindrical functions

In Cartesian coordinates, the differential equation of the plane wave can be deduced from the principle: sum of inertial force and elastic force is equal to zero. This differential equation describes the ground displacement  $\mathbf{s}$  (Eq. (18b), first equation); hereby  $\Delta \mathbf{s} = \partial^2 \mathbf{s} / \partial n^2 = \partial^2 \mathbf{s} / \partial x^2 + \partial^2 \mathbf{s} / \partial y^2 + \partial^2 \mathbf{s} / \partial z^2$  is the Laplacian operator. Transferring this operator into cylindrical coordinates  $r, \varphi, z$ , we get the well-known formula:

$$\begin{aligned} \Delta \mathbf{s} &= \frac{\partial^2 \mathbf{s}}{\partial r^2} + \frac{1}{r} \frac{\partial \mathbf{s}}{\partial r} + \frac{1}{r^2} \frac{\partial^2 \mathbf{s}}{\partial \varphi^2} + \frac{\partial^2 \mathbf{s}}{\partial z^2} = \\ &= \frac{1}{r} \frac{\partial}{\partial r} \left( r \frac{\partial \mathbf{s}}{\partial r} \right) + \frac{1}{r^2} \frac{\partial^2 \mathbf{s}}{\partial \varphi^2} + \frac{\partial^2 \mathbf{s}}{\partial z^2}. \end{aligned} \quad (37)$$

We assume that the sum of the forces mentioned above does not depend on the  $z$ -coordinate, thus we can rewrite the sum as follows:

$$\frac{\partial^2 \mathbf{s}}{\partial r^2} + \frac{1}{r} \frac{\partial \mathbf{s}}{\partial r} + \frac{1}{r^2} \frac{\partial^2 \mathbf{s}}{\partial \varphi^2} - \frac{1}{\gamma^2} \frac{\partial^2 \mathbf{s}}{\partial t^2} = 0. \quad (37a)$$

It is known that the solution of this differential equation is composed by the product of three functions, one of these functions depends on the coordinate  $r$  only, one depends on the coordinate  $\varphi$ , and the third one depends on time  $t$ :  $s = s_r \cdot s_\varphi \cdot s_t$ .  $s_r$  is proportional to  $e^{i\omega t}$  (function of time  $t$ );  $s_\varphi$  is proportional to  $e^{in\varphi}$ , where  $n$  has always to be an integer in the case of cylindrical waves. Using  $k_0 = \omega/\gamma$  we can rewrite the differential equation above:

$$\frac{\partial^2 \mathbf{s}}{\partial r^2} + \frac{1}{r} \frac{\partial \mathbf{s}}{\partial r} + \left( k_0^2 - \frac{n^2}{r^2} \right) \mathbf{s} = 0. \quad (38)$$

This equation is the noted Bessel's differential equation. Its solutions are functions of  $r$ , they are the cylindrical functions. They are divided in Bessel's, Neumann's and Hankel's functions of first and second kind. These functions are not very clear and of little practical value, and it is difficult to treat them. But it is especially important that these functions are not in accordance with the observed results on cylindrical waves that have been described above. Equation (37) does not describe the propagation of cylindrical waves.

### 5.22 Application of Maxwell's theory

In order to explain the propagation mechanism of cylindrical waves we consider Maxwell's theory as a further concept. Suppose that — in accordance with our observation examples — the wave propagates radially and does not depend on the  $\varphi$ - and  $z$ -coordinates. Thus, Maxwell's equations are — according to Eq. (18c) — whereby we have to replace  $n$  by  $r$ , and  $K$  and  $P$  relate to the component of the ground displacement  $s_1$ :

$$\sqrt{\rho dV} \frac{\partial K}{\partial t} = \sqrt{q dV} \frac{\partial P}{\partial r}; \quad \sqrt{\rho dV} \frac{\partial P}{\partial t} = \sqrt{q dV} \frac{\partial K}{\partial r}. \quad (39)$$

In order to get the differential wave equation for  $K$ , we multiply the first equation by the operator  $\sqrt{\rho dV} \partial/\partial t$  and the second equation by the operator  $\sqrt{q dV} \partial/\partial r$  and get:

$$\begin{aligned} \rho dV \frac{\partial^2 K}{\partial t^2} &= \sqrt{\rho q} dV \frac{\partial^2 P}{\partial t \partial r}, \\ \sqrt{\rho q dV} \frac{\partial}{\partial r} \left( \sqrt{dV} \frac{\partial P}{\partial t} \right) &= q \sqrt{dV} \frac{\partial}{\partial r} \left( \sqrt{dV} \frac{\partial K}{\partial r} \right). \end{aligned}$$

Noting that  $dV$  is a function of  $r$  we differentiate the terms in the second equation. Furthermore, we substitute the terms for  $\partial^2 P/\partial t \partial r$  and  $\partial P/\partial r$ , that we have deduced from the first equation and Maxwell's equation, in the second equation as well; thus we get:

$$\sqrt{\rho q} dV \sqrt{\frac{\rho}{q}} dV \frac{\partial^2 K}{\partial t^2} + \sqrt{\rho q} dV \frac{1}{2r} \sqrt{\frac{q}{\rho}} \frac{\partial K}{\partial r} = q dV \frac{\partial^2 K}{\partial r^2} + q dV \frac{1}{2r} \frac{\partial K}{\partial r}.$$

We can rewrite this equation in a simpler form:

$$\frac{\partial^2 K}{\partial t^2} = \gamma^2 \frac{\partial^2 K}{\partial r^2}. \quad (40)$$

It is known that the solution of this differential equation is:

$$K = K_0 \cos(\omega t - k_r r). \quad (41)$$

We can deduce  $P$  from Maxwell's equations as well and get the same result.  $K_0$  is the maximum amplitude of  $K$ . Equation (41) means that in the case of propagation of

cylindrical waves in the average each volume element  $dV$  contains the same amount of energy. We try the following formula for the ground motion, whereby  $s$  may be directed radially ( $s_1$ ) or perpendicular to this direction ( $s_2$  or  $s_3$ ):

$$s = S \sin(\omega t - k_r r). \quad (41a)$$

Thus, we have  $K = \sqrt{\rho dV} \omega S \cos(\omega t - k_r r)$  and  $P = -\sqrt{q dV} k_r S \cos(\omega t - k_r r)$ ; as we have  $\sqrt{\rho} \omega = \sqrt{q} k_r$ , in the case of cylindrical waves  $K$  and  $P$  also have the same magnitude, but opposite signs. As  $K_0 = \text{const} = \sqrt{\rho dV} \omega S$ ,  $S$  has to decrease by the factor  $1/\sqrt{r}$ :  $S = S_0 \sqrt{r_0/r}$ .  $S_0$  is the maximum amplitude at the site  $r_0$ . The description of cylindrical waves that has been deduced from Maxwell's theory is in complete accordance with the observed results. Dispersion does not occur. This means that the distribution of wave energy on to larger spaces or spaces that are reduced more and more does not affect the mechanism of wave propagation. Later on in this treatise we shall enter into the particulars of a peculiarity with regard to the radial propagation of a longitudinal wave with the ground motion vector  $s_1$ .

### 5.3 Modulated cylindrical waves

Now, let us consider modulated cylindrical waves. First we will study a transverse wave that propagates radially and shows displacement  $s_3$  in the  $z$ -direction. Suppose that it is modulated in the  $z$ -direction also. In this case, we find the following differential equation:

$$\frac{\partial^2 K}{\partial t^2} = b^2 \frac{\partial^2 K}{\partial r^2} + a^2 \frac{\partial^2 K}{\partial z^2}. \quad (42)$$

As the following identities are valid:

$$\partial^2 K / \partial t^2 = -\omega^2 K, \quad \partial^2 K / \partial r^2 = -k_r^2 K, \quad \partial^2 K / \partial z^2 = -k_z^2 K,$$

we find the following expression for the phase velocity:  $v_r = b / \sqrt{1 - 3k k_z^2 / 2\mu k_b^2}$  according to Eq. (26) and  $u_r = b^2 / v_r$  according to Eq. (27).

Now, we will consider the modulation of our wave in the direction of the coordinate  $\varphi$ . Hereby  $k_\varphi = 2\pi/\lambda_\varphi$  has to satisfy the condition  $2\pi r = n\lambda_\varphi$ , where  $2\pi r$  is the circumference and  $n$  is an integer. Therefore we have:  $k_\varphi = 2\pi/\lambda_\varphi = 2\pi n/2\pi r = n/r$ . Thus, the modulation decreases radially by the factor  $1/r$ . The phase velocity can be determined by the equation  $v_r = b / \sqrt{1 - n^2/r^2 k_b^2}$ . According to this relation we find  $v_r = \infty$  for  $r_{\min} = n/k_b$ . In this distance  $r_{\min}$  measured from the origin only a stationary wave in the  $\varphi$ -direction occurs. In the case that  $r$  exceeds  $r_{\min}$  we find a travelling wave and a stationary one. In the case of  $r = \lambda_b$  there is practically only a wave travelling radially left over, because the relations above are functions of  $r^2$ . For  $n = 1$  we find  $r_{\min} = 0.16 \lambda_b$ . In practice it is difficult to produce such a wave. As  $v_r$  is a function of  $r$ , a stationary wave occurs in addition to the travelling one.

Similar results as described above for the waves with the displacement  $s_3$  can be deduced for transverse waves propagating radially, where the displacements  $s_2$  are parallel to the  $\varphi$ -direction.

Cylindrical coordinates will certainly be used only in those cases that cylindrical waves and cylindrical vibrations are treated. We have discussed these waves in detail above. But now we want to ask the additional question whether there are waves occurring that propagate in the direction of the coordinates  $\varphi$  and  $z$ . In the case of waves propagating in the  $\varphi$ -direction the wave-fronts ought to be planes. These planes would include the axis of the cylinder and rotate around it. As the circuits on which the waves would travel increase when  $r$  increases, the wave-length would have to increase as well, and the period  $T$  also, so that the phase velocity would become equal to the medium velocity. But this condition cannot be performed in experiment or practice. A wave with an appropriate frequency can travel only in a thin-walled hollow cylinder. Such a cylinder rings, when hit. A thick-walled cylinder only gives a dull sound, a solid cylinder doesn't sound at all.

For waves propagating in the direction of the cylinder axis  $z$  only waves can occur with maximum amplitudes which are constant or modulated (in a way as it was discussed using Cartesian coordinates) in the planes of the wave-fronts, i.e. in the cross-section planes of the cylinder. A modulation in the  $\varphi$ - and  $r$ -direction would not generate a travelling wave.

#### 5.4 The propagation of the longitudinal cylindrical wave

There is a peculiarity that should be noted for a longitudinal wave propagating radially from the origin. As already mentioned there is a displacement  $s_1$  in the direction of  $r$  connected with Maxwell's quantities  $K_r$  and  $P_{rr}$ . We try the formulation  $s_1 = (S_1/\sqrt{r}) \sin(\omega t - k_r r)$ . Besides the force  $3k \, dV \partial^2 s_1 / \partial r^2$  resulting from the changes of the elastic stress and from the inertial force  $-\rho \, dV \partial^2 s_1 / \partial t^2$  there is a third force existing that acts in the radial directions as well. Figure 4 illustrates that the displacement  $s_1$  will cause an extension of the volume element  $dV$  in the  $\varphi$ -direction by  $dv = s_1 \, d\varphi$ . Note that there is an angle  $d\varphi$  between the areas  $dr \, dz$ , whereby the areas are orientated in the  $\varphi$ -direction. Therefore, the force  $k_{\varphi\varphi}$  has a component  $k_{r\varphi}$  acting in the direction of  $r$ . The extension having the length 1 m on the circuit is  $\partial s_2 / \partial r$ . The extension also is  $2\pi s_1 / 2\pi r = s_1 / r$ . Thus, the strain force  $3k (s_1 / r) \, dr \, dz$  is acting on the area  $dr \, dz$ . The component acting in the  $r$ -direction is  $-3k (s_1 / r^2) \, dV$ . Thus, we find the following differential wave equation:

$$\rho \frac{\partial^2 s_1}{\partial t^2} = 3k \left( \frac{\partial^2 s_1}{\partial r^2} - \frac{s_1}{r^2} \right). \quad (43)$$

Because of the connection of  $s_1$  with  $K_r$  and  $P_{rr}$  we can rewrite Eq. (43) using  $K_r$  and  $P_{rr}$  instead of  $s_1$ .

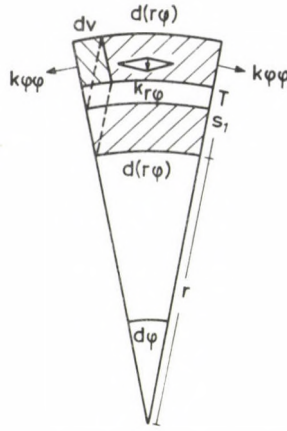


Fig. 4. Illustration of transverse deformation caused by radial cylindrical displacement

As usual we try the following formulation in order to solve Eq. (43):  $s_1 = S_1 \sin(\omega t - k_r r)$ . Note that the maximum amplitude  $S_1$  decreases by the factor  $1/\sqrt{r}$  as we have shown above.

From Eq. (43) we get:

$$-\omega^2 = -a^2 \left( k_r^2 + \frac{1}{r^2} \right).$$

Hence, we can calculate the phase velocity  $v_r = \omega/k_r$  and the energy velocity  $u_r$ :

$$v_r = a / \sqrt{1 - \frac{1}{(k_a r)^2}}, \quad u_r = d\omega/dk_r = a^2/v. \quad (44)$$

Here the law of dispersion is the same as in the case of a transverse wave propagating radially and being modulated in the  $\varphi$ -direction (modulation  $n = 1$ ). In the case of the modulated transverse wave we have a stationary wave in addition to the travelling transverse wave, this stationary wave is of transverse nature with regard to the displacement  $s_3$ , of longitudinal nature with regard to the displacement  $s_2$ . As for the radial longitudinal wave there occurs a radial stationary wave of longitudinal nature besides the travelling longitudinal wave. How can we explain the occurrence of that wave? Suppose that a plane wave hits the boundary between two media at an angle of  $0^\circ$ , suppose further that the medium velocities are different in the two media. As is known one part of the wave energy goes from one medium into the other one, the other part (the remaining energy) is reflected. This effect also occurs in the case that the medium velocity does not change, but the phase velocity changes. In this case, energy is also reflected. A stationary wave is generated in the case that a wave with corresponding energy will be reflected back and forwards between two mirrors. In our

case reflections occur continually, and in both directions. Thus, a stationary wave is produced. But as the gradient of the phase velocity is not constant, the distances of wave nodes and loop antinodes vary. We find  $r_{\min} = 1/k_a = \lambda_a/2\pi$  as in the case of the wave modulated in the  $\varphi$ -direction for  $n=1$ .  $r_{\min}$  is small again. Therefore the stationary wave occurs only in a narrow region in the inner space.

Now, we calculate Maxwell's three quantities:

$$K_r = \sqrt{\rho \, dV} \, \omega S_1 \cos(\omega t - k_r r),$$

$$P_{rr} = -\sqrt{3k \, dV} \, k_r S_1 \cos(\omega t - k_r r),$$

$$P_{r\varphi} = \sqrt{3k \, dV} \, \frac{1}{r} S_1 \sin(\omega t - k_r r).$$

The total energy is:

$$E = \frac{1}{2} (\rho \omega^2 + 3k k_r^2) dV S_1^2 \cos^2(\omega t - k_r r) + \\ + \frac{1}{2} 3k \frac{1}{r^2} dV S_1^2 \sin^2(\omega t - k_r r).$$

Hence we can calculate the average energy:

$$\bar{E} = \frac{1}{4} \left( \rho \omega^2 + 3k \left( k_r^2 + \frac{1}{r^2} \right) \right) dV S_1^2.$$

The vector of radiation with regard to this wave is:

$$\bar{S}_r = a \sqrt{\rho 3k} \, \omega k_r \, dV S_1^2 \cos^2(\omega t - k_r r) + \\ + a \sqrt{\rho 3k} \, \frac{1}{r} \, \omega \, dV S_1^2 \sin(\omega t - k_r r) \cos(\omega t - k_r r).$$

The average is:

$$\bar{S}_r = \frac{1}{2} a^2 \rho \omega^2 \frac{1}{v_r} dV S_1^2.$$

We need not enter into particulars of longitudinal waves being modulated in the  $\varphi$ - and  $z$ -direction. The deduction is similar to that of modulated transverse waves. The formulas for the phase and energy velocities are of corresponding structure.

### 5.5 The propagation of spherical waves

As is known, the differential wave equation for spherical waves is:

$$\frac{1}{\gamma^2} \frac{\partial^2 s}{\partial t^2} = \frac{\partial^2 s}{\partial r^2} + \frac{2}{r} \frac{\partial s}{\partial r} + \frac{1}{r^2 \sin^2 \vartheta} \frac{\partial^2 s}{\partial \varphi^2} + \frac{1}{r^2} \frac{\partial^2 s}{\partial \vartheta^2} + \frac{\text{ctg } \vartheta}{r^2} \frac{\partial s}{\partial \vartheta}.$$

If we neglect a dependence on  $\varphi$  and  $\vartheta$ , we find the spherical wave propagating radially and having constant maximum amplitudes on the wave-fronts. It is known that the solution of the differential equation is:

$$s = \frac{S_0 r_0}{r} \sin(\omega t - k_r r).$$

This solution meets all requirements. It especially satisfies the condition that the average amount of energy is constant in every volume element. We gain the same results, too, if we deduce the spherical wave using Maxwell's theory.

## 6. The propagation of plane waves in inhomogeneous media

In the last chapters we have discussed the propagation of different kinds of waves in homogeneous media. In the case of elastic waves we call a medium a homogeneous one, if both its density and its elastic properties do not depend on site. Otherwise, we call it an inhomogeneous medium. Thus we have  $\rho = \rho(x, y, z)$ ,  $3k = 3k(x, y, z)$  and  $2\mu = 2\mu(x, y, z)$ . Therefore we get  $a = a(x, y, z)$  and  $b = b(x, y, z)$ . In 3.1 we have specified that in the case of a longitudinal wave a homogeneous medium is transformed into an inhomogeneous medium by the wave's geometrical feature. In the following considerations we will confine ourselves to a medium whose properties vary in the  $x$ -direction only. Furthermore, let us suppose that the plane waves propagate in the  $x$ -direction only, i.e. in the directions of the gradients.

There is no solution existing for the equation of wave propagation in such a medium, although this solution would be of great importance, especially in seismology. The vibrations produced by earthquakes travel through the solid earth. Density and elastic properties of the minerals and rocks generally increase with depth. Our seismographs record the motions of the waves having travelled through an inhomogeneous medium. In order to be able to draw conclusions from the wave propagation with regard to the medium's structure we must be able to describe the propagation correctly. In this chapter, we would like to give a first contribution for solving this problem.

### 6.1 The differential wave equation for inhomogeneous media

In traditional physics, the differential equation for elastic waves — as described above — deduced from the principle: inertial force + force resulting from the change of the elastic stress along  $dx$  ( $dx$  = length of the volume element  $dV$ ) is equal to zero. We can deduce the equation for inhomogeneous media from the above principle as follows:

$$\rho \frac{\partial^2 s_1}{\partial t^2} = \frac{\partial}{\partial x} t_{xx} = \frac{\partial}{\partial x} \left( q \frac{\partial s_1}{\partial x} \right) = q \frac{\partial^2 s_1}{\partial x^2} + \frac{\partial q}{\partial x} \frac{\partial s_1}{\partial x}.$$

Until now a solution to this differential equation could not be found. Especially the formula for the plane wave propagating in the  $x$ -direction does not lead to a satisfaction of the above equation. It is important to state that we cannot describe the effect of density change upon propagation velocity by the above equation and — as we will learn later on — that the effect of the change of the elastic properties is less important than would seem from this equation, because the medium velocity is a function only of the roots of the elastic properties. Therefore we have to find a different solution for the wave equation with regard to inhomogeneous media.

Once more — as in the case of the cylindrical waves — we find the solution by using Maxwell's theory. Maxwell's equations (18c) are our basis. As we are going to consider plane waves, the Cartesian coordinate system is the most appropriate one for our purpose. In this case, we have  $dV$  being constant always; therefore we can omit  $dV$  from Maxwell's quantities  $K$  and  $P$ .

Maxwell's equations are:

$$\sqrt{\rho} \frac{\partial K}{\partial t} = \sqrt{q} \frac{\partial P}{\partial x}, \quad \sqrt{\rho} \frac{\partial P}{\partial t} = \sqrt{q} \frac{\partial K}{\partial x}. \quad (45)$$

We calculate the first derivative of the first equation with respect to  $\sqrt{\rho} \frac{\partial}{\partial t}$  and the second one with respect to  $\sqrt{q} \frac{\partial}{\partial x}$  and get:

$$\begin{aligned} \rho \frac{\partial^2 K}{\partial t^2} &= \sqrt{\rho q} \frac{\partial^2 P}{\partial t \partial x}, \quad \sqrt{\rho q} \left[ \frac{\partial \sqrt{\rho}}{\partial x} \frac{1}{\sqrt{\rho}} \frac{\partial P}{\partial t} + \frac{\partial^2 P}{\partial t \partial x} \right] = \\ &= q \left[ \frac{\partial \sqrt{q}}{\partial x} \frac{1}{\sqrt{q}} \frac{\partial K}{\partial x} + \frac{\partial^2 K}{\partial x^2} \right]. \end{aligned}$$

From this equation the following differential equation results for  $K$ :

$$\frac{\rho}{q} \frac{\partial^2 K}{\partial t^2} = \frac{\partial^2 K}{\partial x^2} + \left( \frac{\partial \sqrt{q}}{\partial x} \frac{1}{\sqrt{q}} - \frac{\partial \sqrt{\rho}}{\partial x} \frac{1}{\sqrt{\rho}} \right) \frac{\partial K}{\partial x}. \quad (46)$$

Using the notations  $\gamma = \sqrt{q/\rho}$  and  $\beta = \left( \frac{\partial \sqrt{q}}{\partial x} \frac{1}{\sqrt{q}} - \frac{\partial \sqrt{\rho}}{\partial x} \frac{1}{\sqrt{\rho}} \right)$  we get:

$$\frac{1}{\gamma^2} \frac{\partial^2 K}{\partial t^2} = \frac{\partial^2 K}{\partial x^2} + \beta \frac{\partial K}{\partial x}. \quad (46a)$$

We find a similar differential equation for  $P$ :

$$\frac{1}{\gamma^2} \frac{\partial^2 P}{\partial t^2} = \frac{\partial^2 P}{\partial x^2} + \beta \frac{\partial P}{\partial x}. \quad (46b)$$

As  $K$  and  $P$  are connected with the ground displacement  $s$ , the following formula is valid for  $s$ , too:

$$\frac{1}{\gamma^2} \frac{\partial^2 s}{\partial t^2} = \frac{\partial^2 s}{\partial x^2} + \beta \frac{\partial s}{\partial x}. \quad (46c)$$

Using  $\gamma = \sqrt{q/\rho}$  we get

$$\frac{\partial \gamma}{\partial x} = \frac{\partial \sqrt{q}}{\partial x} \frac{1}{\sqrt{\rho}} - \frac{\partial \sqrt{\rho}}{\partial x} \frac{\sqrt{q}}{\rho} = \gamma \left( \frac{\partial \sqrt{q}}{\partial x} \frac{1}{\sqrt{q}} - \frac{\partial \sqrt{\rho}}{\partial x} \frac{1}{\sqrt{\rho}} \right) = \gamma \beta, \quad \beta = \frac{\partial \gamma}{\partial x} \frac{1}{\gamma}$$

is the relative change of the medium velocity  $\gamma$ .

### 6.2 The solution of the differential wave equation for inhomogeneous media

Now we try to solve the differential equation (46). We can write:

$$\frac{1}{\gamma^2} \frac{\partial^2 y}{\partial t^2} = \frac{\partial^2 y}{\partial x^2} + \beta \frac{\partial y}{\partial x}. \quad (46d)$$

The wave "measures" length in terms of wave-length  $\lambda$  and time in terms of period  $T$  (refer to Chapter 2). We mark the quantities measured in terms of  $\lambda$  and  $T$  by a dot. We have:

$$\omega t = 2\pi \frac{t}{T} = 2\pi t', \quad kx = 2\pi \frac{x}{\lambda} = 2\pi x'; \quad y' = \frac{y}{\lambda}; \quad Y' = \frac{Y}{\lambda}; \quad \gamma' = \frac{\gamma}{v}, \quad \beta' = \beta \lambda.$$

Now we transform the differential equation (46d) into our new  $\lambda - T$ -unit system and get:

$$\frac{1}{\gamma'^2} \frac{1}{\lambda} \frac{\partial^2 y'^2}{\partial t'^2} = \frac{1}{\lambda} \frac{\partial^2 y'}{\partial x'^2} + \frac{\beta'}{\lambda} \frac{\partial y'}{\partial x'} \quad \text{or} \quad \frac{1}{\gamma'^2} \frac{\partial^2 y'}{\partial t'^2} = \frac{\partial^2 y'}{\partial x'^2} + \beta' \frac{\partial y'}{\partial x'} \quad (46e)$$

In the MKS-system we try the solution:

$$y = Y(x) \cos(\omega t - k_x x). \quad (47)$$

In our  $\lambda - T$ -system the corresponding equation is:

$$y' = Y'(x) \cos 2\pi(t' - x'). \quad (47a)$$

Calculating the required differential quotients from this equation and substituting them in (46e), we find:

$$\left[ \frac{1}{\gamma'^2} 4\pi^2 - 4\pi^2 + \frac{d^2 Y'}{dx'^2} + \beta' \frac{dY'}{dx'} \right] \cos 2\pi(t' - x') + \left[ 2 \frac{dY'}{dx'} 2\pi + \beta' Y' 2\pi \right] \sin 2\pi(t' - x') = 0.$$

The terms in parantheses have to be equal to zero. Thus the second term leads to the equation:

$$\frac{dY'}{dx'} + \frac{1}{2} \beta' Y' = 0.$$

The solution of this differential equation is:

$$Y' = Y'_0 e^{-\int \beta' dx'/2}.$$

The velocity  $\gamma'$  results from the first term being equal to zero:

$$\gamma' = 1 / \sqrt{1 + \frac{1}{4\pi^2} \left( \frac{1}{2} \frac{d\beta'}{dx'} + \frac{1}{4} \beta'^2 \right)}.$$

We have to rewrite this equation using the MKS-system and find:

$$v = \frac{\omega}{k_x} = \frac{\lambda}{T} = \gamma \sqrt{1 + \frac{\lambda^2}{4\pi^2} \left( \frac{1}{2} \frac{d\beta}{dx} + \frac{1}{4} \beta^2 \right)}.$$

We solve this equation for  $\lambda$  and divide  $\lambda$  by  $T$ , thus we get:

$$v = \gamma / \sqrt{1 - \frac{\gamma^2 T^2}{4\pi^2} \left( \frac{1}{2} \frac{d\beta}{dx} + \frac{1}{4} \beta^2 \right)}. \quad (48)$$

Again we calculate the energy velocity from  $d\omega/dk_x$ . According to the equation above we find:

$$\omega = \gamma \sqrt{k_x^2 + \frac{1}{2} \frac{d\beta}{dx} + \frac{1}{4} \beta^2}.$$

From this equation we can deduce  $u$ :

$$u = 2\gamma k_x / 2 \sqrt{k_x^2 + \frac{1}{2} \frac{d\beta}{dx} + \frac{1}{4} \beta^2} = \gamma^2 / v. \quad (49)$$

We shall discuss the solution of the differential wave equation in inhomogeneous media later on, first we are going to note the quantities being important for wave propagation. Here, we use the notation  $\delta = e^{-\int \beta dx/2}$ . Again we consider a longitudinal wave propagating in the  $x$ -direction.

Ground motion amplitude:

$$s_1 = S_1 \delta \cos(\omega t - k_x x),$$

Particle velocity:

$$V_x = \frac{\partial s_1}{\partial t} = -\omega S_1 \delta \sin(\omega t - k_x x),$$

Maxwell's quantity  $K_x$ :

$$K_x = \sqrt{\rho dV} V_x = -\sqrt{\rho dV} \omega S_1 \delta \sin(\omega t - k_x x),$$

Deformation  $D_{xx}$ :

$$D_{xx} = \frac{\partial S_1}{\partial x} = k_x S_1 \delta \sin(\omega t - k_x x) - \frac{\beta}{2} S_1 \delta \cos(\omega t - k_x x),$$

Maxwell's quantity  $P_{xx}$ :

$$P_{xx} = \sqrt{q dV} D_{xx} = \sqrt{q dV} k_x S_1 \delta \sin(\omega t - k_x x) - \sqrt{q dV} \frac{\beta}{2} S_1 \delta \cos(\omega t - k_x x),$$

Kinetic energy:

$$E_k = \frac{1}{2} K_x^2 = \frac{1}{2} \rho \omega^2 dV S_1^2 \delta^2 \sin^2(\omega t - k_x x),$$

Potential energy:

$$\begin{aligned} E_p &= \frac{1}{2} (P_{xx}^2 + P_{xx}'^2) = \\ &= \frac{1}{2} q k_x^2 dV S_1^2 \delta^2 \sin^2(\omega t - k_x x) + \frac{1}{2} q \frac{1}{4} \beta^2 dV S_1^2 \delta^2 \cos^2(\omega t - k_x x), \end{aligned}$$

Vector of radiation:

$$\begin{aligned} S_x &= -\gamma K_x P_{xx} = \gamma \sqrt{\rho q} dV \omega k_x S_1^2 \delta^2 \sin^2(\omega t - k_x x) - \\ &- \gamma \sqrt{\rho q} dV \omega \frac{\beta}{2} S_1^2 \delta^2 \sin(\omega t - k_x x) \cos(\omega t - k_x x). \end{aligned}$$

The first term on the right side of the last equation describes the active radiation component, the second one describes the reactive radiation component.

Again we write down the average energies stored in the volume element  $dV$  and the average energy flow:

$$\begin{aligned} \bar{E}_k &= \frac{1}{4} \rho \omega^2 S_1^2 \delta^2 dV, \quad \bar{E}_p = \frac{1}{4} q \left( k_x^2 + \frac{1}{4} \beta^2 \right) S_1^2 \delta^2 dV, \\ \bar{E}_p &= \bar{E}_k \left( k_x^2 + \frac{1}{4} \beta^2 \right) \left/ \left( k_x^2 + \frac{1}{4} \beta^2 + \frac{1}{2} \frac{d\beta}{dx} \right) \right., \\ \bar{E} &= \bar{E}_k + \bar{E}_p = 2\bar{E}_k \left( 1 - \frac{\frac{1}{4} \frac{d\beta}{dx}}{k_x^2 + \frac{1}{4} \beta^2 + \frac{1}{2} \frac{d\beta}{dx}} \right), \\ \bar{S}_x &= \frac{1}{2} \gamma \sqrt{\rho q} dV \omega k_x S_1^2 \delta^2 = \frac{1}{2} \gamma^2 \frac{\rho}{v} \omega^2 S_1^2 \delta^2 dV = 2\bar{E}_k \gamma^2 \frac{1}{v}. \end{aligned}$$

From this equation we can deduce the energy velocity  $u$ :

$$u = \bar{S}_x / \bar{E} = \gamma^2 \frac{1}{v} \left/ \left( 1 - \frac{(1/4) d\beta/dx}{k_x^2 + \frac{1}{4} \beta^2 + \frac{1}{2} \frac{d\beta}{dx}} \right) \right. \quad (50)$$

### 6.3 Discussion of wave propagation in inhomogeneous media

When we considered the modulated wave, we found that in the case of a sinusoidal change of the maximum amplitude perpendicular to the propagation direction the phase velocity exceeded the medium velocity and the energy velocity was less than the medium velocity. The entire wave is composed by a travelling part and a stationary part. The latter can be perceived as "ballast" in the course of energy transfer.

We found the same phenomenon in the case of longitudinal cylindrical waves propagating radially. Hereby the phase velocity varies with radius  $r$ , if the medium velocity is constant. At a certain  $r_{\min}$  the phase velocity is infinite; it quickly approaches the medium velocity  $\gamma$  with increasing  $r$ . The energy velocity is equal to zero at  $r_{\min}$ , increases with increasing  $r$  and thus approaches the medium velocity from below. At  $r_{\min}$  the stationary part of the wave is equal to the total energy amount. It decreases swiftly with increasing  $r$  and becomes equal to zero after a short distance.

The statements above lead to the conclusion that it is not a simple propagating wave which we have to do with in the case of inhomogeneous media. We will start our discussion considering a special case, namely that case, where  $\beta$  is constant. From  $\beta = (d\gamma/dx)/\gamma = \text{constant}$  results, that  $\gamma$  has to increase in the  $x$ -direction according to the law  $\gamma = \Gamma e^{\beta x}$ . In this case, we have  $\delta = e^{-\beta x/2} = \sqrt{\Gamma/\gamma}$ . Here, we find for the phase and energy velocities:

$$v = \gamma / \sqrt{1 - \beta^2 / 4k_m^2}, \quad u = \gamma \sqrt{1 - \beta^2 / 4k_m^2}, \quad (48a)$$

where  $k_m = \omega/\gamma$ . Thus once more we find the relations for the velocities that we know from the modulated waves. The potential energy is divided into two parts: one part with regard to the travelling wave motion and one part with regard to the stationary wave motion. The sum of the average amounts of potential energy is equal to the kinetic energy. Furthermore, we also find an active radiation component and a reactive one that compose the energy radiation. For the average active radiation component we get  $\bar{S}_x = \bar{E}\gamma^2/v$ . Hence we can deduce the above formula for the energy velocity.

Of course  $\beta$  can also be negative or the wave is travelling in the opposite direction. The medium velocity decreases with increasing distance; according to this fact the maximum amplitude increases with increasing  $\delta$ . Thus, the average energy density increases as well. But as we have to add up the amount of energy along a wavelength, we find that the sum remains constant, because  $\lambda$  and  $\gamma$  decrease with  $\delta^2$ . In the

formula of the active radiation component the exponential functions compensate each other. The active radiation component is determined by the factor  $\sqrt{1 - \beta^2/4k_m^2}$ , i.e. by the energy velocity.

As one can see from that formula, the ratio  $\beta/k_m$  must not exceed 2, otherwise the wave velocities will become imaginary. That means that  $\gamma$  must not be equal to or exceed  $2\omega/\beta$ . In the limit case, only the stationary part of the wave is left over, and that in the distance  $x = (1/\beta) \cdot \ln(2\omega/\Gamma\beta)$  (here, we have  $\gamma = \Gamma e^{\beta x}$ ). Here the phase wave-length  $\lambda$  is infinite, the energy wave-length  $L$  is equal to zero. As we know from stationary waves, in our case particles adjacent in the  $x$ -direction have the same phases. Thus, the travelling wave motion ceases.  $\delta$  receives the value  $\sqrt{\Gamma\beta/2\omega}$ . The active radiation component becomes equal to zero. Obviously the energy is reflected totally in this case and travels back. A stationary wave is generated for each frequency, if the wave motion is in a certain condition. Let us call it "transient state" in analogy to telecommunications. As a discontinuous change of the medium velocity does not occur in the critical distance, we must not expect that an abrupt reflexion occurs at this point. To some extent the reflection is brought about the farther the wave propagates. Finally, total reflexion occurs. It is easy to perceive that the critical distance varies with frequency. The unit of measurement, i.e. the wave-length, has a different value for each frequency. Thus,  $\partial v/\partial r$  has a different value for each frequency as well. Although the medium is supposed as being distinct, it has different conditions for waves with different frequencies. That is the reason for the following phenomenon: Suppose that wave energy radiation is produced by an impulse. Firstly the ground motion has impulse character as well. But because of the fact described above the impulse character is not perceived. The observations of vibrations produced by earthquakes or explosions verify the theory. Here, we already refer to Fig. 5 that will be explained in detail later on in this paper.

In the case that a wave travels in the direction where the medium velocity decreases at an exponential function and finally becomes equal to zero,  $k_m$  increases greatly and therefore the phase and energy velocity will approach the medium velocity and thus become equal to zero as well. The maximum amplitudes also increase very much. Relative to the wave, the propagation phenomenon does not show any disturbance, but in the observations an enormous compression of wave energy occurs that leads to the destruction of the material. In nature, velocities as extreme as those in the described two limit cases are seldom observed.

Now, we turn to the general case. In a medium where the medium velocity varies facultatively, wave propagation is principally similar to that just described. The relative change of the medium velocity, that is determined with regard to the actual site, defines the phase and energy velocity. The additional term in the roots,  $(1/2)(d\beta/dx)$ , is of little importance and always small in practice. In a way, at different sites different exponential functions are valid for the medium velocity. Therefore the additional addend causes a continual transition from one medium velocity to the other one. Here,

the entire potential energy that is always slightly less than the kinetic energy has to be adapted to the desired value. With regard to this adaptation the energy velocity (according to Eq. (50)) has to be increased by a small amount relative to the energy velocity according to Eq. (49). Equation (49) is only valid for compensated wave propagations where the sum of the potential energy amounts is always equal to the kinetic energy. Equation (50) is of more general character.

The factor  $\delta$  included in the maximum amplitude describes the intense interaction between the travelling part of the wave motion and the stationary one occurring at each site. The exponent of  $\delta$ ,  $-\int \beta dx/2$ , means that the maximum amplitude decreases continually, if  $\beta$  is positive. The reason is that the medium velocity and thus the wave-length increase in this case. Thus, an energy amount being constant with regard to each wave-length is caused. Suppose that the medium velocity remains constant, if a certain distance  $x'$  from the origin is exceeded. In this case, the value of the integral will remain constant as well because of the condition  $\beta=0$ , and thus the maximum amplitude remains constant too: we have the wave propagation in a homogeneous medium. Now suppose that the medium velocity decreases, if a certain distance  $x''$  is exceeded. In this case  $\beta$  will become negative and the integral and the maximum amplitude will increase. Finally suppose that after all the medium velocity achieves the value again that the wave has had at its origin. In this case, the integral in the exponent of  $\delta$  will become equal to zero. Thus the maximum amplitude regains its original value as well.

Apart of few exceptions, the seismologist is generally confronted with inhomogeneous media. The earth interior consists of materials, the elastic properties and densities of which vary with site. This fact leads to the conclusion that phase and energy velocities generally differ in the course of wave propagation, and that in the case of vibrations generated by events as earthquakes on a large scale or hammer blows on a small scale. The improved recording instruments have verified this conclusion in the last decades. We would like to illustrate this using a seismogram montage that we have borrowed from a paper of Allam (1970). On the vertical axis we have marked the distances of the observation points from the source where the vibrations are generated. Note that the vertical axis is plotted from the top towards the bottom. On the horizontal axis we have marked the time since generation of the vibrations.

In the experiments a flat beam (length 2 m, width 0.3 m, thickness 0.04 m) was placed on the ground at the source. Furthermore, the beam was weighted. In order to generate vibrations it was hit by a heavy hammer at one of its front surfaces. At a distance of 5 m from the beam, measured perpendicularly to its longitudinal axis, and than every one metre a geophon was placed. In Fig. 5 we have plotted the ground motion recorded by these geophones.

Figure 5 shows that the impulse character of the hammer blow cannot be identified, it is lengthened to wave trains. In a distance of 5 to 10 m the vibrations are relatively weak. With increasing distance a vibration train having a large amplitude in

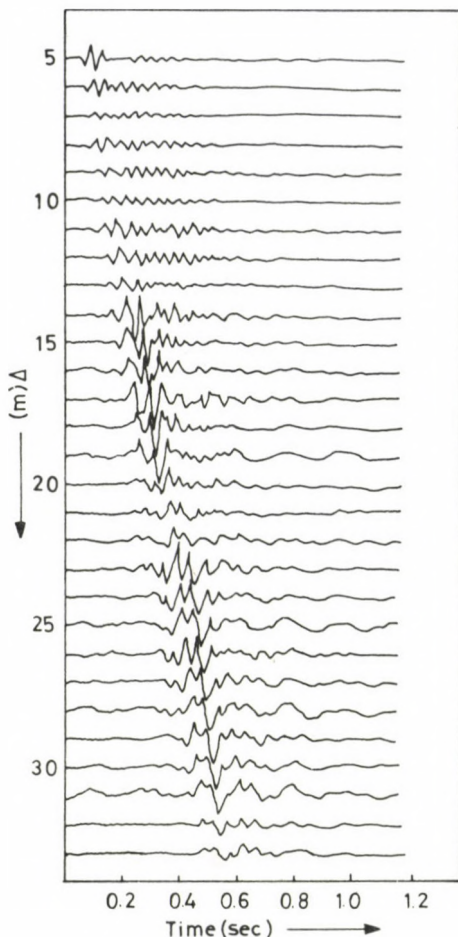


Fig. 5. Examples of seismograms obtained by hitting the ends of a wooden plate horizontally (surface observation) (according to Allem 1970)

its centre is generated. From a distance of 20 m it does not occur any longer. The phase velocity can be deduced from the phenomenon that the large amplitudes show an increasing delay with increasing distances; the phase velocity is 12 m/s. In a distance of 20 to 22 m the ground motions are weak again. Thereafter a new vibration train with a large amplitude in its centre is originated. The second wave train is delayed by 0.08 s compared with the first one. Now, let us plot a connecting line from one of the central amplitudes to the other one. As one can see at once, if extended, the line goes through the origin. From its inclination we can calculate the velocity (55 m/s). Obviously this value corresponds to the energy velocity. Further observations would probably have shown a third delayed wave train. In our experiment dispersion occurs. The velocity

values mentioned above obviously are valid for the frequency that contributes mostly to the oscillation with the largest amplitude.

In our experiment the medium velocity increases with depth, but the wave propagates chiefly in horizontal direction. The conditions for the calculations above are not given, but the phenomena described above in connexion with Fig. 5 can be expected in the case of wave propagation in the vertical direction as well. We must leave the calculation of wave propagation in horizontal direction to later theoretical treatises.

Normally, seismologists believe that the elastic waves propagate with the medium velocity. We hope that we could show with this treatise that normally in seismology medium velocity, phase velocity and energy velocity are different. Only in special cases they are equal.

In conclusion we should like to note that the occurrence of a stationary wave part in addition to a travelling part can be attributed to a phase shift between Maxwell's quantities  $\mathbf{K}$  and  $\mathbf{P}$ . The greater the shift, the more the stationary wave part will increase. If the shift is equal to  $90^\circ$ , only the stationary part exists. The shift is caused by a local change of the phase velocity in the course of wave propagation. There is no energy loss connected with the shift. In the case of an electromagnetic wave propagating in a conductor, the electric conductivity causes an energy loss that is caused by a phase shift as well.

### Acknowledgements

The authors thank Dr. J Brandt, Essen, for revising the translation of the treatise.

### References

- Allam A M 1970: An investigation into the nature of microtremors through experimental studies of seismic waves. *Bull. intern. Inst. Seismology and Earthquake Engineering*, 7, 1–59.
- Born W T 1941: The attenuation constant of earth materials. *Geophysics*, 6, 132–148.
- Förtsch O 1940: Ableitung des von der Frequenz unabhängigen Absorptionskoeffizienten aus Maschienen-schwingungen. *Z. Geophys.*, 16, 57–84.
- Förtsch O 1953: Deutung von Dispersions- und Absorptionsbeobachtungen an Oberflächenwellen. *Gerl. Beitr. Geophys.*, 63, 16–58.
- Förtsch O 1956: Die Ursachen der Absorption elastischer Wellen. *Ann. di Geofisica*, 9, 469–524.
- Förtsch O, Kardeván P 1974: Die Kontinuumstheorie der Elastizität fester Körper und die Ausbreitung elastischer Wellen in ihnen. *Acta Geod., Geoph., Mont. Hung.*, 9, 385–448.
- Frank Ph, v. Mises R 1961: Die Differential- und Integralgleichungen der Mechanik und Physik. Bd. I u. II. Nachdr. d. 2. Aufl. Verl. Vieweg & Sohn, Braunschweig
- Hort W 1950: Die Differentialgleichungen der Technik und Physik. 5. Aufl., neu bearbeitet v. Thoma. Joh. Ambros Barth Verl., Leipzig
- Joos G 1934: Lehrbuch der theoretischen Physik, 2. Aufl., Akad. Verlagsges., Leipzig
- Love A E H 1944: A treatise on the mathematical theory of elasticity. 4. ed., Dover Publication, New York

- Schaefer C 1908: Einführung in die Maxwellsche Theorie der Elektrizität und des Magnetismus. Verl. v. B. G. Teubner, Leipzig und Berlin
- Sommerfeld A 1945: Vorlesungen über theoretische Physik. Bd. II: Mechanik der deformierbaren Medien. Akad. Verlagsges., Leipzig
- Sommerfeld A 1949: Vorlesungen über theoretische Physik. Bd. III: Elektrodynamik. Akad. Verlagsges., Leipzig
- Wagner K W 1947: Einführung in die Lehre von den Schwingungen und Wellen. Dietrichsche Verlagsbuchhandlung, Wiesbaden
- Wiechert E 1903: Theorie der automatischen Seismographen. Abhandl. d. Ges. d. K. Wiss. zu Göttingen, Math.-Phys. Kl., Neue Folge Bd. II, 1–128, Weidmannsche Buchh., Berlin



## CONNECTION BETWEEN THE INTERPLANETARY MEDIUM AND PULSATIONS OF THE GEOMAGNETIC FIELD WITH PERIODS 1–600 s

L HOLLÓ<sup>1</sup>

[Manuscript received March 15, 1984]

The connection between the activity of the geomagnetic pulsations with periods of 1–600 s and some parameters of the interplanetary medium (magnitude and direction of the interplanetary magnetic field, IMF, and solar wind velocity) has been studied on the basis of the records from the years 1971–1973 of the Nagycenk observatory. The activity of the pulsations with periods less than 30 s increases when the IMF magnitude increases as described by the hyperbolic connection between the two quantities. The maximum activity has been found for periods below 30 s at a cone angle of 30°, while the maximum for longer periods lies at 0°. The increase of the amplitudes due to increasing solar wind velocity is the strongest for periods of 15–30 s.

**Keywords:** geomagnetic pulsations; IMF direction; IMF intensity; solar wind

### Introduction

Fairfield (1969) presented data from Explorer 34 measurements which indicated the presence of magnetohydrodynamic waves with periods of 20–100 s in the pre-magnetopause portion of the interplanetary medium. These waves correspond according to Kovner et al. (1976) to waves observed on ground, the regularities of their appearance in function of the azimuth of the IMF were similar to those on ground. As soon as the first data on the interplanetary medium, mostly on the solar wind velocity became available, comparisons with the amplitudes of the pulsations were carried out. The first comparison was made by Gringauz et al. (1971). Later investigations indicated that pulsations may originate from the extramagnetospheric space. Data published for the years 1963–1974 (King 1977) — including IMF parameters, solar wind velocities etc. — gave new impetus to researches. Results in this field were summarized in several reviews since then (Golikov et al. 1980, Greenstadt et al. 1981) which summarized results in this field. Most data published hitherto refer to periods of 20–120 s.

<sup>1</sup> Geodetic and Geophysical Research Institute, Hungarian Academy of Sciences Sopron, H-9401 Sopron, P.O. Box 5, Hungary

### Results of the investigations

The investigation of the connection between geomagnetic pulsation activity and solar wind velocity began in our Institute slightly after other groups (Verő 1975). Researches were promoted by the long uninterrupted series of pulsation records in the Nagyecenk observatory ( $\Phi = 47.2^\circ$ ,  $\Lambda = 98.3^\circ$ ,  $L = 1.9$ ) where pulsation recording was started in 1957. This data quantity enabled to carry out investigations concerning a statistical analysis of the connection between pulsations and interplanetary medium. The processing of the Nagyecenk pulsation records is based on 12 period ranges between 1 and 600 s (Holló et al. 1972) where amplitudes are given in half-hourly intervals for the most characteristic part of the record. These data were compared with the magnitude and cone angle (determined from the azimuth and inclination of the IMF vector) of the IMF, as well as with solar wind velocities for the years 1972, 1973 and 1974 (Holló 1982).

#### a) IMF intensity and the pulsations

Gul'elmi (1974) found a hyperbolic connection between IMF magnitude and pulsation periods based on ground observations which can be described as  $T = 160/B$ , where  $T$  is the period of the pulsations,  $B$  the IMF magnitude. Greenstadt and Olson (1976) found that the correlation between the two quantities depends on geomagnetic

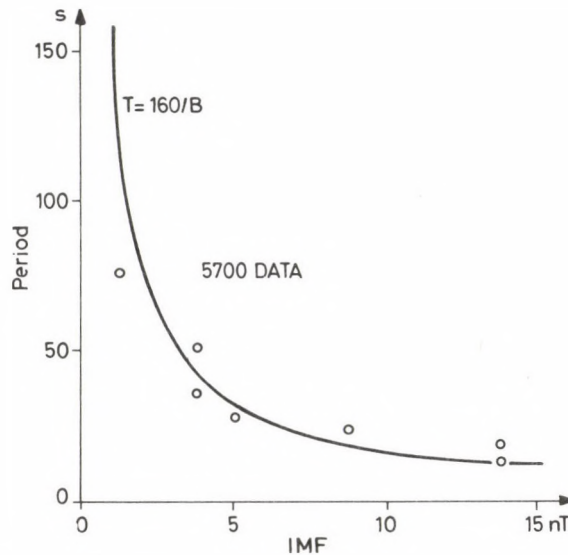


Fig. 1. Period of the geomagnetic pulsations in function of the IMF magnitude: the curve represents the hyperbolic approximation  $T = 160/B$

activity. The existence of such a hyperbolic connection was denied by Arthur and McPherron (1977) on the basis of ATS-6 data, Russel and Fleming (1976) proposed some correction. Earlier own investigations have confirmed Gul'elmi's formula. In these investigations the 5-step daily indices P1-P12 were used (referring to different period ranges) for the year 1971. Similar results were obtained when using the higher time resolution data of the year 1973 (Fig. 1). We suppose that contradictory results may be partly the consequence of a lower data number and on the other hand, most deniers of the hyperbolic dependence came from satellite investigators, because of the *B*-dependence of the pulsation periods is absent in satellite data most likely due to the very enhanced presence of a local resonant line, hampering the appearance of the *B*-dependent periods.

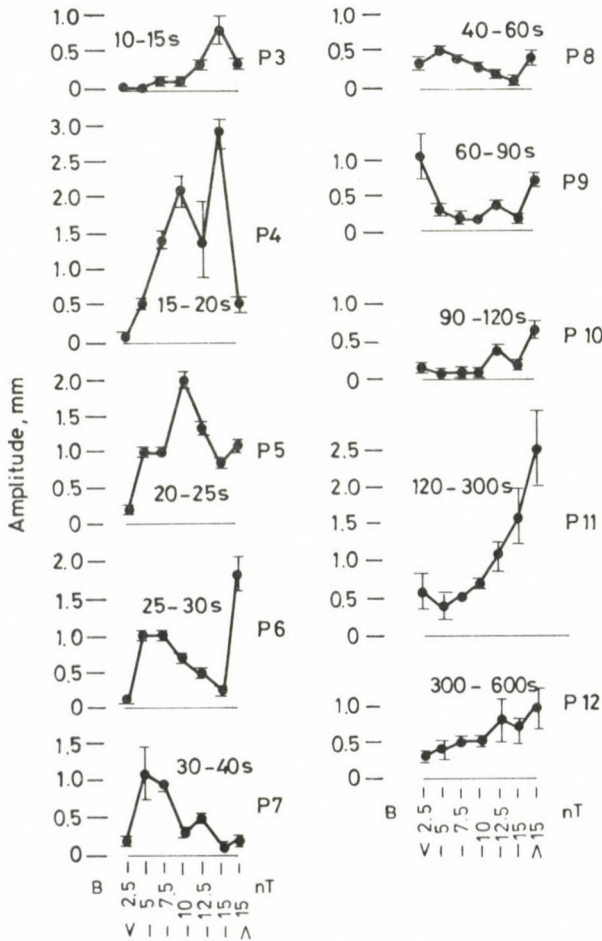


Fig. 2. Amplitudes of the geomagnetic pulsations vs. IMF magnitude

The average amplitudes of the period ranges *vs.* IMF magnitude shows higher correlations for the period range of 15–30 s (taking the hyperbolic dependence also into account), and for periods of 120–300 s, too (Fig. 2).

*b) IMF direction and pulsations*

The greatest differences in the ideas of different groups exist about the effect of the direction of IMF. At first, the effect of the IMF longitude ( $\vartheta$ ) and latitude was looked for. So e.g. Troitskaya et al. (1971) found maximum activity of the pulsations at longitudes of  $90^\circ$  (and  $270^\circ$ ). Generally, a more expressed change was found with changing longitude than with changing latitude. According to our own investigations, at least for Pc 1, the inclination has a greater effect on the activity. In the Irkutsk observatory lying at a geomagnetic latitude similar to that of Nagycenk ( $\Phi = 40.8^\circ$ ,  $\Lambda = 174.5^\circ$ ) Vinogradova (1973) analysed Pc 1 occurrences for the year 1972 in function of the IMF latitude and longitude. She found occurrence frequencies related to the total number of the occurrence of the given direction being a maximum when the IMF has a southward component (Fig. 3).

The cone angle of the IMF can be computed as  $\cos \Theta = \cos \vartheta \cdot \cos i$ ; the cone angle is the angle between the direction of the IMF and the normal of the magnetopause. On the basis of theoretical considerations Kovner (1974) expected maximum activity at cone angles of  $30^\circ$  based. Many experiments, including Greenstadt and Olson's (1976) yielded maximum pulsation activities at cone angles of  $0^\circ$ , i.e. when the IMF is exactly perpendicular to the normal of the magnetopause.

If the average amplitudes of the pulsations are compared to values of the cone angles, the maximum is found in the period range of 15–30 s for the cone angles of  $20^\circ$ – $40^\circ$ , i.e. at values around  $30^\circ$ . In the period range of 30–60 s, the maximum activity is found for cone angles around  $0^\circ$  (Fig. 4).

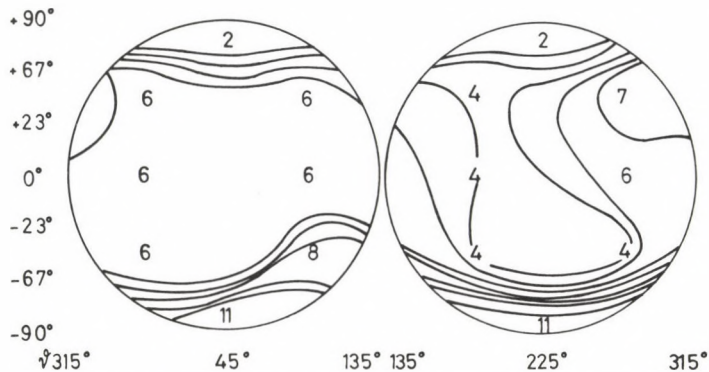


Fig. 3. Occurrence frequency of Pc 1 pulsations *vs.* longitude and latitude of IMF in percents of the occurrence of the corresponding sectors

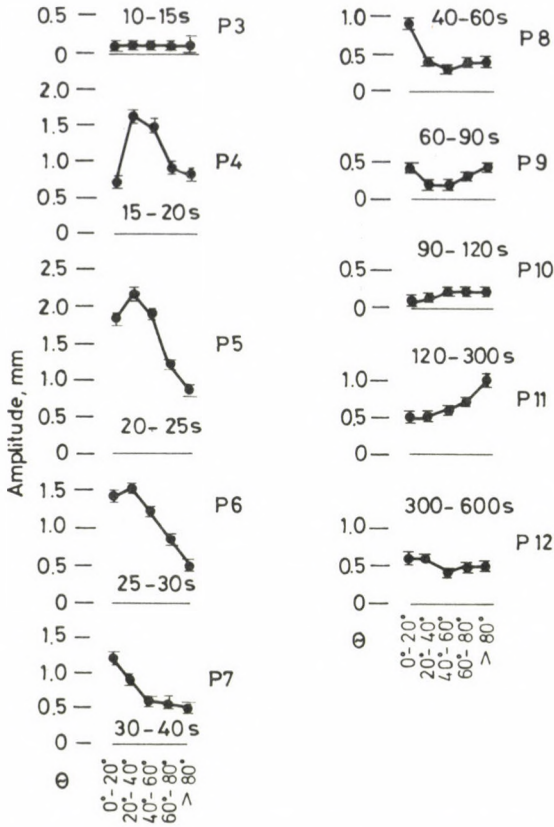


Fig. 4. Geomagnetic pulsation amplitudes in function of the cone angle

A part of the differences may be caused by the rather rough period resolution of Pc 3, as a single frequency group in most investigations. In such a wide range the maximum may be at 0°. Verő et al. (1984) found, however, that in Irkutsk even for the shorter period part of Pc 3, the activity peak lies at 0°. The reason of this difference is yet unknown.

c) Solar wind velocity and pulsations

At present there is no more doubt about significant changes of the pulsation amplitudes with solar wind velocity (Greenstadt et al. 1981, Takahashi et al. 1981, Golikov et al. 1980). This connection means a connection between pulsation activity and the energy transported by the solar wind.

The average amplitudes of the pulsations with different periods for the year 1973 show a most pronounced increase of the pulsation amplitudes with increasing solar

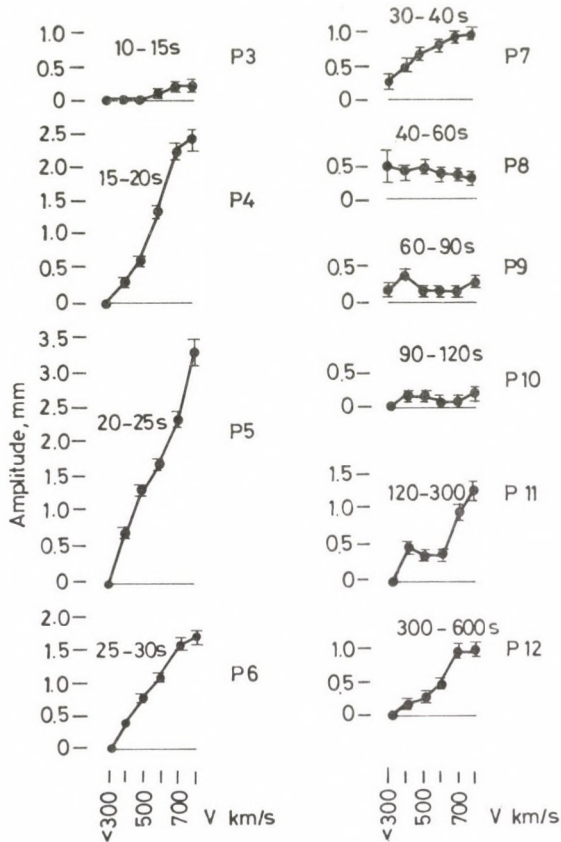


Fig. 5. Pulsation amplitudes vs. solar wind velocity

wind velocity for periods of 15–30 s. The correlation between the two quantities decreases quite strongly for periods longer than 30 s, it reaches a minimum (even of negative coefficients) for the range of 1–2 min, than for periods longer than 2 min the correlation is again positive and getting stronger with increasing periods (Fig. 5).

The connection between pulsation amplitudes and solar wind velocity can be described by  $A = c \cdot V^x$ , where  $A$  is the average pulsation amplitude,  $V$  the solar wind velocity,  $c$  a constant for a period range and  $x$  an exponent to be determined. According to theoretical investigations (Kovner 1974) the exponent has a value of 2 or more.

The exponent  $x$  has been determined for each period range for different values of the cone angle (Fig. 6). The value of the exponent  $x$  is about 2 or more for the periods shorter than 30 s, then the exponent decreases, between 1 and 2 min, its value lies around 0 or slightly negative. For variations of longer period, the exponent increases

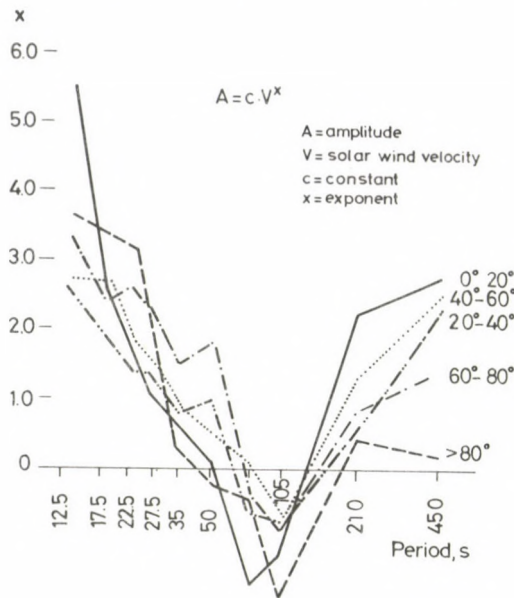


Fig. 6. Value of the exponent  $x$  in the connection between pulsation amplitudes and solar wind velocity in function of period and cone angle

again, but the highest values are obtained if the cone angle is small. This shows once again that both solar wind velocity and cone angle control the pulsation activity in different period ranges, but these controls are quite different for different ranges.

### Conclusions

The connections between interplanetary medium and pulsation parameters depend on the period of the latter. So e.g. the increase of the intensity of the IMF is accompanied by an increase of the amplitude of pulsations with periods less than 30 s. The influence of the IMF direction on the pulsations can be described as a maximum activity at cone angles of  $30^\circ$  for periods less than 30 s, for longer periods the maximum activity is found at a cone angle of  $0^\circ$ . The effect of the solar wind velocity is strongest for periods between 15 and 30 s and for 300–600 s; in the latter case the exponent of the connection depends on the cone angle, too, while in the former it does not.

All these facts confirm the existence of some physical difference between pulsations with periods less than 30 s and those with periods longer than 30 s, at least for observing sites at the latitude of the Nagycenk observatory.

## References

- Arthur C W, McPherron R 1977: Interplanetary magnetic field conditions associated with synchronous orbit observations of Pc 3 magnetic pulsations. *J. Geophys. Res.*, 82, 5138–5142.
- Fairfield D H 1969: Bow shock associated waves observed in the far upstream interplanetary medium. *J. Geophys. Res.*, 74, 3541–3553.
- Golikov Y Y, Plyasova-Bakounina T A, Troitskaya V A, Chernikov A A, Puststovalov V V, Hedgecock P C 1980: Where do solar wind controlled micropulsations originate? *Planet. Space Sci.*, 28, 535–543.
- Greenstadt E W, Olson J V 1976: Pc 3–4 activity and interplanetary field orientation. *J. Geophys. Res.*, 81, 5911–5920.
- Greenstadt E W, McPherron R L, Takahashi K 1981: Solar wind control of daytime, midperiod geomagnetic pulsations. *J. Geomag. Geoelectr.*, 32, 89–110.
- Gringauz K I, Solomatina E K, Troitskaya V A, Schepetnov R V 1971: Variations of solar wind flux observed by several spacecrafts and related pulsations of the Earth's electromagnetic field. *J. Geophys. Res.*, 76, 1065–1069.
- Gul'elmi A V 1974: Diagnostic of the magnetosphere and interplanetary medium by means of pulsations. *Space Sci. Reviews*, 16, 331–345.
- Holló L 1982: Connection between the interplanetary magnetic field and variations of the geomagnetic field. Thesis.
- Holló L, Tátrallyay M, Verő J 1972: Experimental results with the characterization of geomagnetic micropulsations. I. The methods of characterization used in the investigations. *Acta Geod. Geoph. Mont. Hung.*, 7, 155–160.
- King J H 1977: Interplanetary medium data book. National Space Data Center, NASA
- Kovner M S 1974: Pulsacii Pc 2–4 nizkочастotnűje kolebania v solnechnom vetre pered frontom udarnűj volnű. *Geomagn. Aeron.* 14, 680–684.
- Kovner M S, Lebedev V V, Plyasova-Bakounina T A, Troitskaya V A 1976: On the generation of low-frequency waves in the solar wind in the front of the bow-shock. *Planet. Space Sci.*, 24, 261–268.
- Russel C T, Fleming K B 1976: Magnetic pulsations as a probe of the interplanetary magnetic field: a test of the Borok B index. *J. Geophys. Res.*, 81, 5882–5886.
- Takahashi K, McPherron R L, Greenstadt E W, Neely C A 1981: Factors controlling the occurrence of Pc 3 magnetic pulsations at synchronous orbit. *J. Geophys. Res.*, 86, 5472–5484.
- Troitskaya V A, Plyasova-Bakounina T A, Gul'elmi A V 1971: Szvjaz pulsacii Pc 3–4 mezhplanetnűm magnitnűm polum. *Doklādű AN SSSR*, 197, 1312–1313.
- Verő J 1975: Determination of the solar wind velocity from pulsation indices. *J. Atm. Terr. Phys.*, 37, 561–564.
- Verő J, Holló L 1978: Connections between interplanetary magnetic field and geomagnetic pulsations. *J. Atm. Terr. Phys.*, 40, 857–865.
- Verő J, Holló L, Potapov A S, Polyuskhina T N 1984: Analysis of the connections between solar wind parameters and dayside geomagnetic pulsations based on the data of the observatories Nagycenk (Hungary) and Uzur (USSR) *J. Atm. Terr. Phys.* (in press)
- Vinogradova V N 1973: Pc 1 pulsations catalogue. Issledovaniya po geomagnetizmu, aeronomii i fizike solnca. *Irkutsk. Vűpusk* 24, 272–295.

## TELLURIC AND MAGNETOTELLURIC INFORMATION ABOUT THE GEOLOGICAL STRUCTURE OF TRANSDANUBIA

L NEMESI<sup>1</sup>, J HOBOT<sup>1</sup>, G VARGA<sup>1</sup>

[Manuscript received March 17, 1984]

Geoelectric reconnaissance surveys (corresponding to a scale 1:200 000) in basin areas of Hungary started at the beginning of the sixties, with some delay to seismic and gravimetric measurements. They were interrupted almost totally at the end of the seventies although maps were compiled for hardly more than fifty percent of explorable areas (Fig. 1). In this paper it is attempted to illustrate by several examples from the Transdanubian region in Hungary the importance of geological information obtained from a comparison of geoelectric results with seismic and gravimetric information which cannot be achieved by any of the methods alone. Thus, the authors suggest that it would be worth completing the reconnaissance telluric-magnetotelluric survey, as in combination with other methods this would yield a basis for up-to-date seismic and electromagnetic prospecting. The costs of the suggested survey are minute as compared to expenses involved in seismic and electromagnetic operations.

**Keywords:** conductivity anomaly; geoelectric survey; magnetotellurics; tellurics; Transdanubia

First experimental telluric measurements in the Transdanubian area were made at the beginning and middle of the fifties. These measurements were carried out by the Geophysical Department of the Section Geodesy at the Budapest Technical University (at present Geophysical Department of the Miskolc University for Heavy Industry) and by the Geophysical Research Laboratory of the Hungarian Academy of Sciences (at present Geodetic and Geophysical Research Institute, GGKI). The Eötvös Loránd Geophysical Institute (ELGI) measured its first experimental profile in the second half of the fifties, along the profile Sopron-Celldömök.

Quasi-network-like measurements were started by the ELGI crew in the area of the southern-Transdanubian town Szigetvár in 1961 and lasted in Transdanubia only till 1964 when the prospection activity was shifted to the Great Hungarian Plain. Somewhat later the Geophysical Research Company of the Hungarian Oil and Gas Trust (OKGT) also established an Electric Section which made its first measurements in a network in the counties Somogy and Zala. The measurements have been made since about 1960 with instruments of the type T-9 and T-14 using Picard-galvanometers and photorecording. Processing was made manually using the method

<sup>1</sup> Eötvös Loránd Geophysical Institute, H-1145 Budapest, Columbus u. 17-21, Hungary

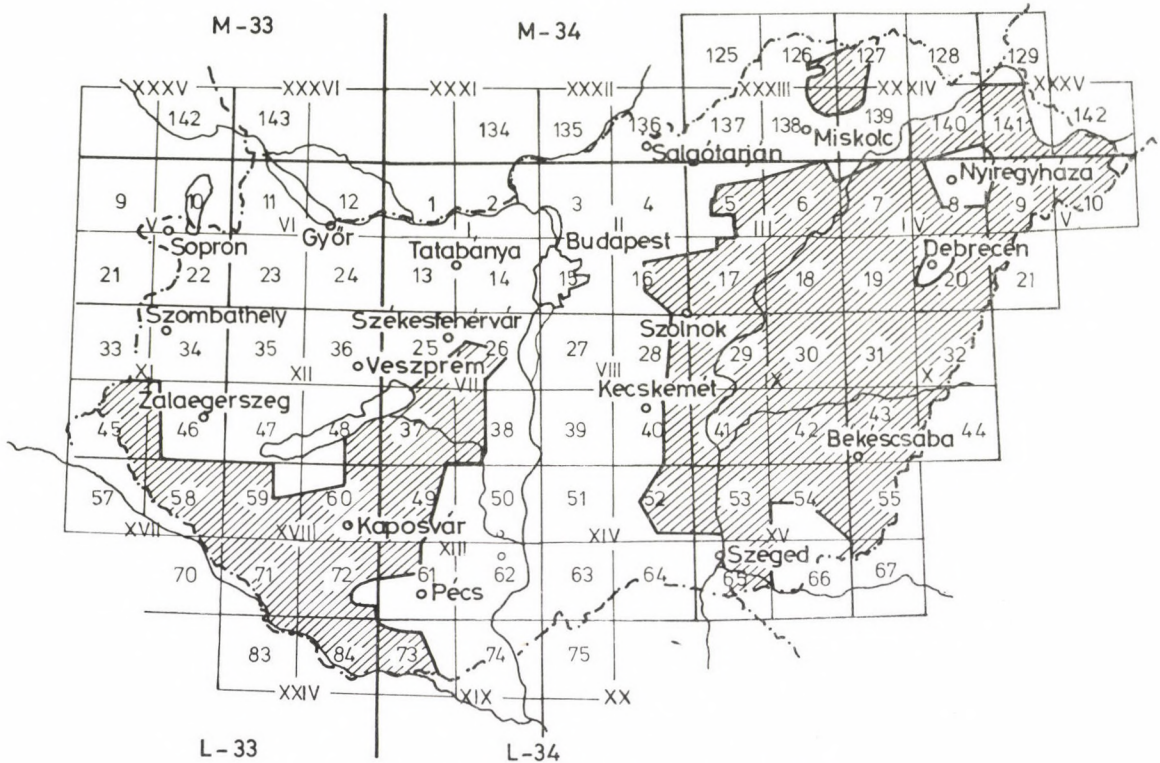


Fig. 1. Areas covered by telluric survey, January 1982

of relative ellipses, the straight lines method and the total method which all contained many subjective elements. These methods were improved in many respects during the following years, mainly by the introduction of programmable HP-calculators and the apparatus for the determination of the total ellipse which eliminated a great part of the subjective elements. In the instrumentation the decisive change occurred, however, only in 1981 when the digital equipment TEM-80 developed in ELGI was introduced. These instruments contain already filters which enable the recording of a frequency range adapted to the exploration task and to the geological structure of the area. The built-in microprocessor starts the processing simultaneously with the measurements, too. In addition using a desktop computer HP-9845 processing methods were introduced which enable the determination of parameters which were earlier computed only in some experimental magnetotelluric (MT) measurements (direction depending conductivity data, map of the anisotropy ellipses describing geological models etc.) (Fig. 2).

This short historic review has shown that data produced by telluric measurements in Transdanubia are very inhomogeneous, both the reliability and the density of coverage are highly variable. These setbacks are even more increased by many



problems in the interpretation. In the Great Hungarian Plain the causes of the anomalies are (statistically in at least 90 percent of cases) changes in the horizontal conductivity of the low-resistivity sedimentary complex, i.e. in its thickness and specific resistivity. The same holds only in very limited areas of Transdanubia. The role played by the conducting sedimentary complex may be important for telluric anomalies in deep basin formations such as the Little Hungarian Plain (in the NW-corner of Transdanubia) and the southern basin. *Vice versa*, there are great areas where the telluric anomalies are caused by changes in the pre-Tertiary basement, sometimes in considerable depths. Such information can be obtained by comparing telluric results with seismic or gravimetric ones or by borehole data. Last but not least magnetotelluric measurements play also a most important role in the interpretation of telluric results.

In the following a study is given on results obtained in the interpretation of telluric measurements in the Transdanubian area. It should be emphasized that telluric and MT measurements have an important role in the exploration of the geological structure in Transdanubia. Most significant results were obtained in connection with the pre-Tertiary basement which have at present already importance for the immediate raw material exploration.

The first comparative interpretation was made in 1964 by Szénás et al. They found significant differences in the depth of electric and seismic basements (the electric basement was determined mainly from telluric measurements). In certain areas the electric "basement" lies deeper, in others the seismic one. The reason for such differences was unknown in 1964, nevertheless Szénás has emphasized: "This phenomenon results in the important general conclusion that both methods (the seismic and the geoelectric) cannot fully substitute each other. Their combined application yields more geologic information than each of them alone." This principle has been often rejected, or forgotten. Concerning the southern part of Transdanubia, since then the borehole Felsőszentmárton-1 has been drilled, and its logging detected one cause for the differences: the specific resistivity of the thick Miocene sediments in the Dráva Valley and the lowermost part of the Pannonian is by nearly one order of magnitude higher than that of the upper Pannonian sediments, thus, in lower Pannonian layers the geoelectric "basement" on the 1964 map contains depth values near to the top of the Miocene.

In the mid-seventies Kassai (1983) dealt with the problem of the different depth data from seismic and geoelectric surveys. Figure 3 is from his paper representing the differences in the depths of the seismic and geoelectric basements. Several boreholes deepened or re-interpreted in the mid-seventies revealed an other cause for the differences, too. To the North of the Dráva Valley, in the area of the villages Bogádmindszent, Darány, Kalmánca, Szulok there is a graben in the lower Paleozoic rocks covered by Carboniferous sediments which contain in a comparatively small amount organic material of very low resistivity with a very high rate of carbonization.

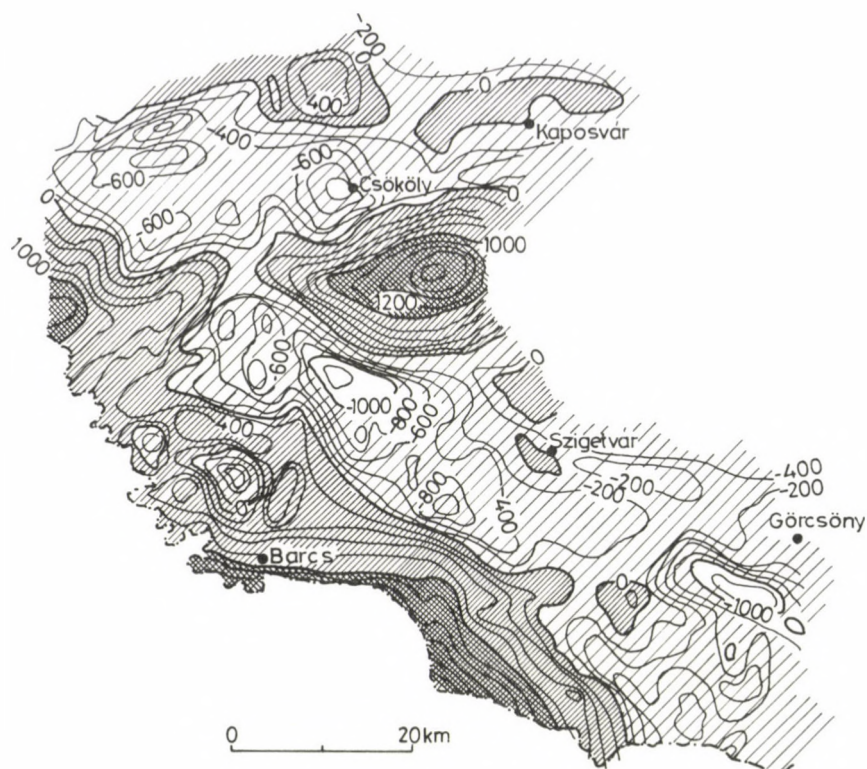


Fig. 3. Differences in the depth of the seismic and electric "basement" ( $H_s - H_e$ ) after Kassai

In consequence the average specific resistivity of the Carboniferous complex is 1–10  $\Omega\text{m}$ , in spite of the preponderance of sandstones with specific resistivities of 60–100  $\Omega\text{m}$ . Thus, the greater depths of the geoelectric basement in this area can be explained by the presence of low-resistive Carboniferous sediments which could not be separated by geoelectric methods from the Pannonian sediments, as their specific resistivities nearly coincide. The Carboniferous-Pannonian boundary is, however, a clear velocity contrast in seismic measurements. It should be noted nevertheless that Carboniferous formations are not impermeable for up-to-date seismic measurements, as well as the top of Miocene for up-to-date telluric and MT measurements. Though in both cases there are boundaries which are for one of the methods first-order horizons, while for the other those of less importance. Therefore, a complex survey and interpretation remains even today inevitable as such comparisons may yield important additional information and help correct interpretations.

In any case, schemata should be avoided. The differences between the depths of the seismic and geoelectric basements represented in Fig. 3 should not be interpreted



Fig. 4. Bouguer anomaly map



Fig. 5. Telluric isoareal map

quite formally so that where thick Carboniferous sediments occur the geoelectric basement lies deeper, and where the seismic basement lies deeper, the Miocene complex influences the telluric data. The common interpretation of seismic and MT measurements is general and profitable in the research programmes of Geologic Basic Profiles. At present, however, less expensive, but only qualitative methods are being compared. Reconnaissance gravimetric and geomagnetic maps are at disposal for the whole territory of Hungary, and even telluric measurements cover great areas in spite of a significant decrease in the telluric measurements activity during the last decade. Let us compare from such a point of view the map of Bouguer anomalies and the telluric map of ELGI covering an area of about 8.5 thousand km<sup>2</sup> in southern Transdanubia (Figs 4 and 5). The two maps have for a first glance many similarities. This result is important and differs from experiences gained in the area east of the river Tisza. There Bouguer and telluric maps have generally nothing in common and the basement depths are better reflected in the telluric maps. The global explanation for this difference is most likely the smaller thickness of the Neogene southern Transdanubia. Experiences have shown that in the Great Hungarian Plain, too, the correlation between the two maps is generally high in case of basement depths below 2000 m. Another likely reason for this difference can be that the pre-Tertiary basement of the area east of the river Tisza has more and clearer density-inhomogeneities than that of the corresponding Transdanubian area. A consequence of the rather high correlation of the Bouguer map and the depth of the pre-Tertiary basement in Transdanubia is that the cause of the differences between the telluric and gravimetric maps should be looked for in the inhomogeneities of the conductivity in the basement itself. As first examples, let us consider differences in the two smaller areas, being very expressive: in the area of the village Magyarmecske and in the area Zselicség. In both areas, MT soundings have been recently made and seismic profiles are also at disposal, and in Zselicség, near the village Gálosfa there is also a deep borehole. In both cases the gravimetric anomalies reflect the pre-Tertiary basement relief. According to the MTS measurements (Fig. 6), the specific resistivity of the basement in Magyarmecske is about 1  $\Omega$ m, lying in a depth of about 400–500 m, immediately below the Pannonian, it has rather high density and relatively high velocity. Based on the nearby borehole of Bogádmindszent, this complex has been interpreted as Carboniferous remarking that the content of highly carbonized organic material in southern Transdanubia is the highest just here. The complex starts below the Pannonian in depths of 300–500 m and has a thickness of about 1000 m. Its horizontal extent is unknown, but according to the measurement network with station distances of 1.5–2 km, it could cover an area of about 60–80 km<sup>2</sup>. Taking into account all these facts, it would be advisable to complete a borehole into this complex to explore its exact nature and economic value.

In the Zselicség area, it was similarly supposed that Carboniferous sediments cause the telluric minimum, but MT measurements excluded this possibility by yielding a 9–11 km depth for the conductive formation causing the telluric minimum.

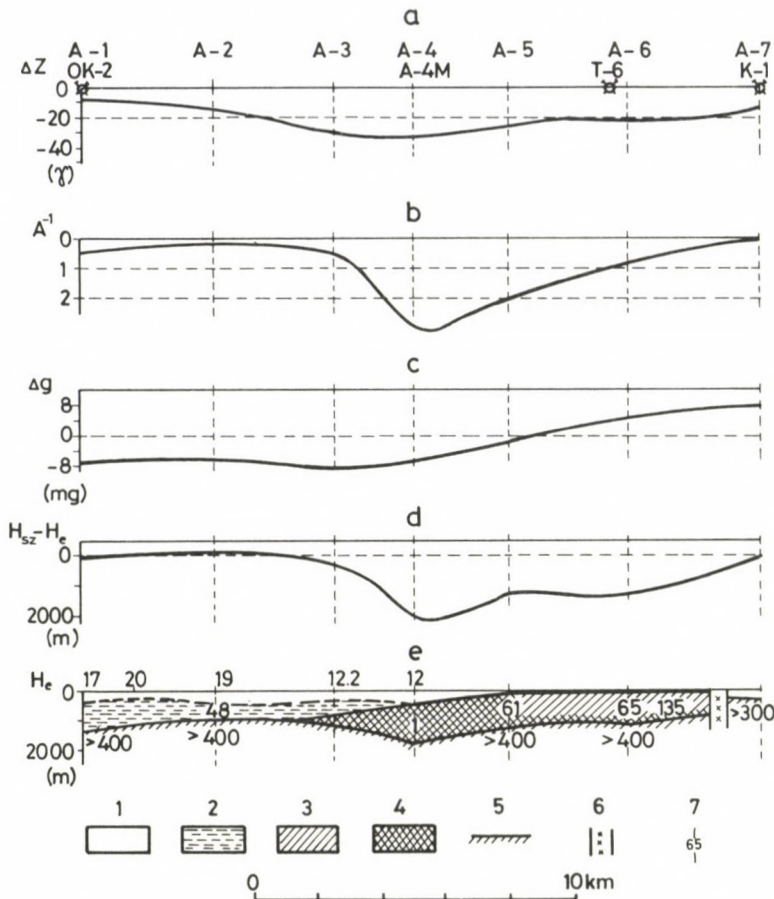


Fig. 6. Geophysical investigation of the telluric minimum complex at Magyarmecske

a) magnetic  $\Delta Z$  plot; b) telluric  $A^{-1}$  diagram; c) gravity Bouguer anomaly curve; d) difference in the depth of seismic and electric "basement"; e) geological model of the section according to magnetotelluric measurements. 1 — Holocene, Pleistocene, upper Pannonian complex; 2 — Carboniferous complex with medium resistivity; 3 — Carboniferous complex with medium resistivity; 4 — Carboniferous complex with very low resistivity; 5 — lower Paleozoic formation with high resistivity; 6 — zone of outpinching (fractures); 7 — resistivity of electric beds

This can hardly be Carboniferous, and in the near future it does not promise any economic profit. It may have, however, an importance from a tectonic or plate tectonic point of view, as it is known that deep fractures are accompanied by conductivity anomalies. For such a conclusion, however, the few existing MT measurements are insufficient.

Having presented these two examples, let us discuss the comparison of telluric and gravimetric results in the whole area of 8500 km<sup>2</sup> presented in Figs 7 and 8. Figure

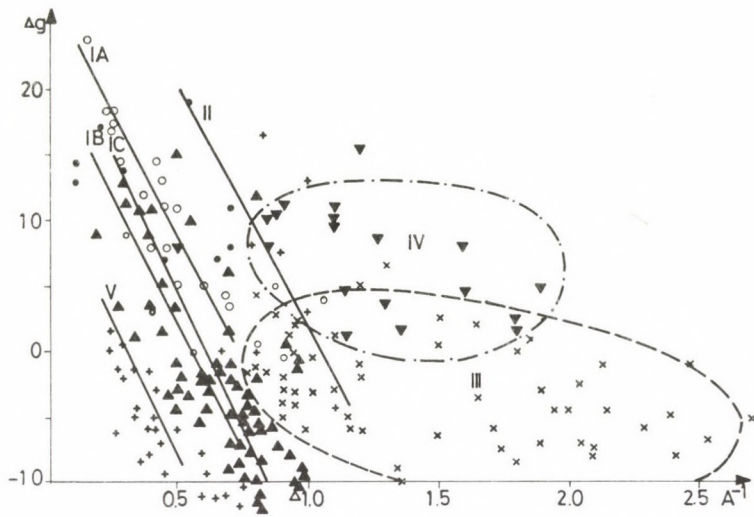


Fig. 7. Function  $A^{-1} = f(\Delta g)$  for the Transdanubian area

7 shows values in the nodal points of a  $5 \times 5$  km network from Bouguer and telluric isoarea maps, with the values  $\Delta g$  represented in function of  $A^{-1}$ . The result is a quite disordered set of points, but can be divided into subsets to be approximated by straight lines which seem to express connections valid for different geologic units. The straight lines 1A, 1B and 1C correspond to data from the southern shore of the Lake Balaton, from the area Kaposvár–Kaposő and from the area Mágocs, respectively, where it is known from boreholes that the young sedimentary complex of low-resistivity, and low-density is underlain by lower Paleozoic crystalline rocks having higher resistivities and densities as the young sediments according to the function  $A^{-1} = f(\Delta g)$ .

Straight line II refers to the area Igal. It is parallel shifted with respect to the previous ones. Such a shift can result neither from resistivity inhomogeneities nor from density inhomogeneities in the sediments. It could be the consequence of low resistivity formations within the high density basement, but this possibility is excluded by the MT measurements. Thus, only one possibility remains: the difference is caused by anomalously high densities in the basement of the area. The gravimetric anomaly cannot be explained alone by the known uplift of the Mesozoic carbonate surface of the basement.

The characteristic straight line V refers to the Dráva Valley and in general to basin formations of Miocene or Permian age. This line lies nearest to the origin what means, e.g. in comparison with the lines I that the electric basement lies above the high density Paleozoic basement (thus the telluric value is low for the corresponding



Fig. 8. Types of geological structures for the southern part of the Transdanubian area as suggested by a comparison of gravity and telluric results (Fig. 7)

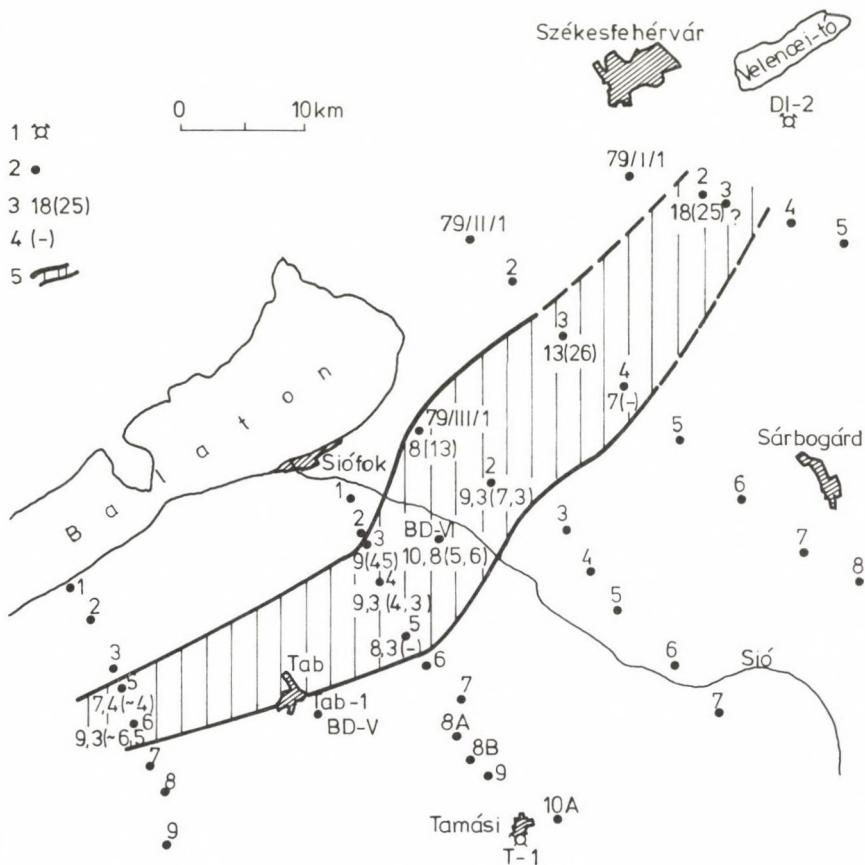


Fig. 9. Deep conductivity anomaly related to the Balaton line according to MTS measurements. 1 — deep well, 2 — MTS measuring point, 3 — true depth of the conducting bed from the "E" polarization curve, in brackets: apparent depth of the conductive bed from the "H" polarization curve, 4 — the "H" polarization curve does not indicate the conductive bed, 5 — area where conductivity anomalies were observed

gravimetric basement depth). The density of the Miocene and Permian rocks is also lower than that of the crystalline rocks.

The areas III and IV can be rather clearly separated, but here is a rather loose connection between the results of the two methods. A quite disordered set of points characterizes both areas in Fig. 7 and their main characteristics are that the conductivities are much higher than it would follow from the basement depths of the gravimetric results. This means anyway that conductors should be present within the high density basement. More detailed and accurate MT measurements are at disposal from area III. The region has been crossed by five MT profiles. It is worth mentioning that within this area two different reasons were found for the differences. In the

northern part of the area, MT measurements indicate a conductor in depths of 8–10 km (Fig. 9). This zone coincides with a zone indicated on tectonic maps, i.e. with the so-called Balaton line. Up to now, this is the only tectonic line known in Hungary which can be unambiguously identified with a conductivity anomaly. It is not excluded that a similar case is present in the Zselicség-anomaly, moreover the conductivity anomaly in the area of Bakony Mountains can also be partly connected with fracture zones, but in the latter case many near-surface distortion effects and other complicated geologic formations, e.g. those being similar to the conducting Carboniferous formations in southern Transdanubia, can play a certain role.

To the South from this fracture zone, but within type III the "high resistivity basement" has conductivities of only 40–60  $\Omega\text{m}$ , hinting at Paleogene or upper Paleozoic sedimentary formations, i.e. these sediments have rather low resistivities respective to their densities. The areas I and III are crossed by the profiles MK–5 between Ságvár and Tamási, by MK–2 between Karád and Igal, and in both profiles there are low resistivity layers of 5–10  $\Omega\text{m}$  below the main reflections in depths of about 1000 m. The complicated, unusual structure of these areas, the probably great thickness of the Paleogene and upper Paleozoic sediments indicate the possibilities for the comparison of two cheap, quick methods, i.e. of telluric and gravimetric maps.

In the last years, the measurements reached within the framework of the Geologic Base Profiles programme the area of the Little Hungarian Plain — Bakony Mountains. The measurements here also consisted of seismic and magnetotelluric measurements and only small scale experiments were made with telluric measurements. The most interesting result of these measurements is also the detection of low conductivity formations within the basement rocks. On the basis of measurements made by the GGKI group, A Ádám reported several times on this conductivity anomaly below the Bakony Mts as detected by MT measurements. This anomaly appeared in the southern parts of the profiles MK–3, DK–1, MK–1. The source of the anomaly is not clear. A Ádám and O Ádám supposed fracture lines, but the presence of conductive layers is also likely. In the profile MK–1 the low conductivity layer is pinching out in the vicinity of the Rába line, where the Mesozoic complex is also wedging out. The existence of the anomaly is absolutely clear, about its explanation, however, we have only hypotheses so far. It should be added that a few telluric profiles consisting of a low number of stations has also been measured in the boundary zone between the Little Hungarian Plain and the Bakony Mts. These profiles include the magnetotelluric profiles MK–1 and MK–3. Relative telluric areas and Bouguer anomalies follow rather well the topography of the pre-Tertiary basement: where Mesozoic rocks lie at the surface, high Bouguer anomalies are found (Fig. 10). The relative conductivity is, however, increasing in the direction of the Bakony Mts as compared to the sediment thickness. As there is only a very thin sedimentary layer, the conductivity can only be due to conductive formations below the high resistivity limestone. A comparison of the results of the two methods enables to outline the

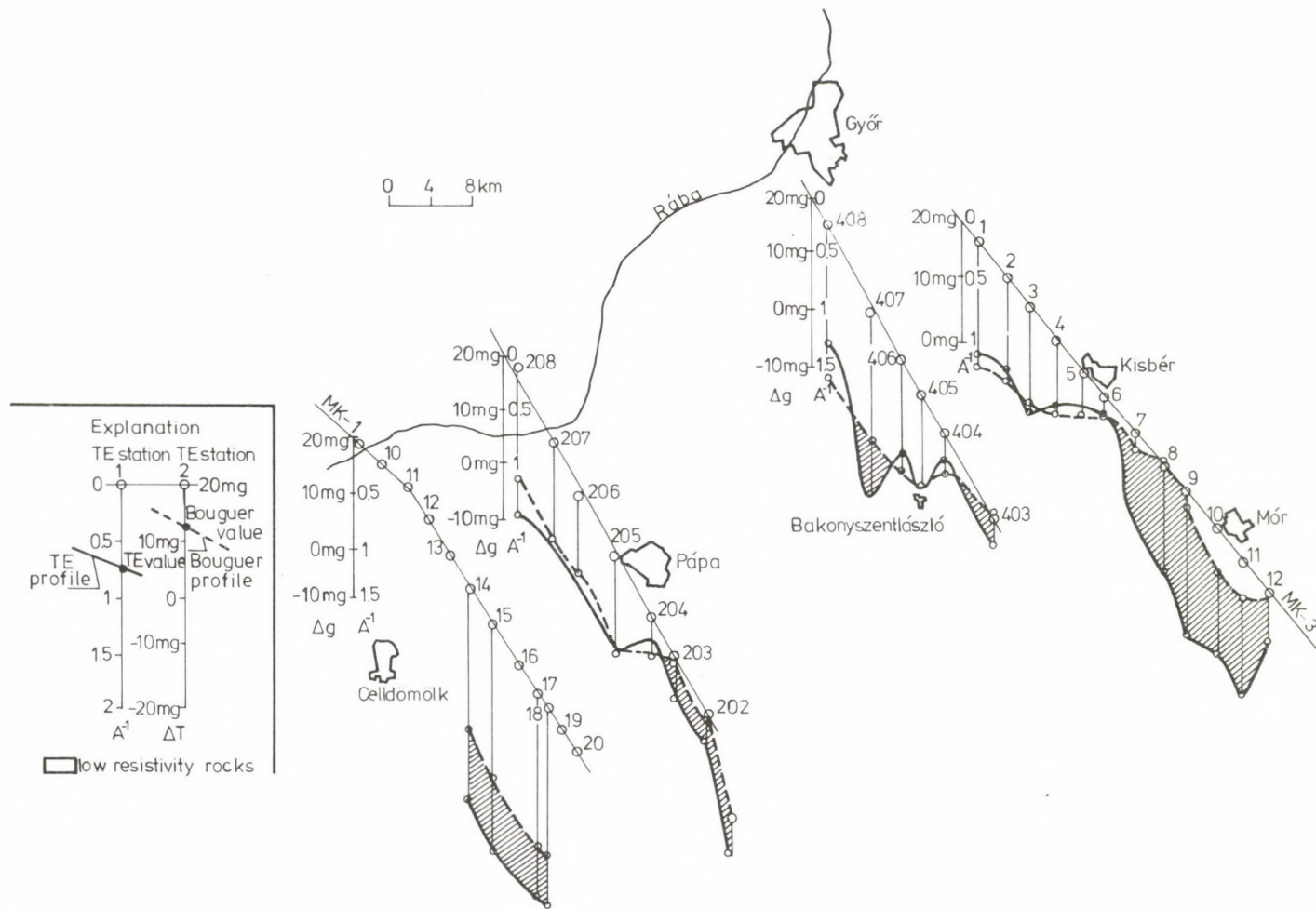


Fig. 10. Comparison of telluric and Bouguer anomaly values at the border of the N Bakony Mts and the NW Little Hungarian Plain (hatched parts of the section indicate deep low resistivity formations)

anomalous areas. This is confirmed by MT measurements made along the MT profiles MK-3 and DK-1 and the accordance with the telluric results is acceptable.

As a conclusion, electric methods have an important role in the prospection of both the pre-Tertiary basement and the earlier formations and tectonic lines. Reconnaissance results can be obtained from a comparison of gravimetric and telluric results, hinting at interesting areas. More quantitative results can be obtained from a comparison of seismic and MT results. It is not aimed here to discuss the problems of detailed surveys, but it should be emphasized that when planning controlled source frequency soundings and magnetotelluric measurements the data of the previous reconnaissance geoelectric information should be considered. It is proposed, too, that in places of important anomalies, more dense measurement networks would be necessary, because — as the previous examples prove — the results to be received from them cannot be replaced by great-scale gravimetric or seismic measurements.

Reconnaissance telluric and MT measurements should be naturally carried out before detailed seismic measurements, but a part of the previous examples shows that in the exploration of conductive formations within the basement, electric measurements can yield important information, even after up-to-date seismic measurements. Methodology and station density is, however, a much discussed problem in geophysics. The problem of time and expenses is seldom considered when discussing problems of the choice between tellurics and magnetotellurics, or station density. It cannot be denied that most information could be obtained in the pre-exploration phase from MT measurements in a network of  $2 \times 2$  km. Such high station density was used in Hungary up to now only in a few limited areas of the detailed surveys of OKGT. At present, there are not much more than thousand up-to-date MT stations, measured by digital instruments. The measurement capacity of ELGI and OKGT is about 200 points pro year at present. If the basin areas of Hungary, where these measurements have an economic importance, is supposed to be  $75\,000\text{ km}^2$ , then about 90 years would be needed for the completion of an MT reconnaissance network. Even about 40 years would be needed with the present rate of work if only areas should be covered, where at present no telluric or MT measurements exist. They include the Little Hungarian Plain, the area between the rivers Danube and Tisza, the SE part of Transdanubia, etc. Magnetotelluric measurements on the latter areas would cost about 530 million Ft at present prices. At the same time, a digitally equipped telluric crew consisting of the same number of vehicles and personnel as a MT crew could measure about one thousand stations a year. Such a group could cover the basin area of Hungary without telluric measurements in a network of  $2 \times 2$  km within 9 years with an expenditure of about 30 million Ft. A resulting telluric map, together with the gravimetric and magnetic maps could serve as a basis for the preliminary planning of expensive up-to-date methods.

In the knowledge of the possibilities and results of the MT method the telluric method alone seems to us somewhat outdated. We had the same opinion 20 years ago;

then tellurics was combined with dipole electric soundings. Similarly, a combination of telluric and MT measurements seems to us as a realistic programme nowadays. More concretely, in the first phase MT measurements would help to define the frequency range to be used for the telluric measurements. In the Little Hungarian Plain e.g. this aim can be reached by the MT measurements carried out in the framework of the Geologic Basic Profiles programme and by the measurements of the OKGT.

In the second phase telluric measurements are to be carried out by digital equipment, using a methodology which enables a secondary processing. In the third phase MT measurements are carried out in a 15–20 times wider network than that of the telluric measurements in order to find the causes of the telluric anomalies. This latter means an expense of about 30 million Ft, too. The total expense of the combined telluric-MT measurements would be so about 60 million Ft, about 11 percent of the dense MT measurements. All the measurements could be made by one telluric and one MT crew within 9–10 years.

### References

- Ádám A 1971: Determination of Paleozoic graphitic schists below screening layers by magnetotelluric method in the Hungarian Basin and some genetic conclusions. (In Hungarian) *MTA X. Oszl. Közl.*, No. 2–4, 297–308.
- Ádám A 1982: Fractures as conducting dykes and corresponding 2-D models. (In Hungarian) *Magyar Geofizika*, 23, 166–177.
- Ádám O 1977: Deep structure of the Transdanubian Middle Mts and its foreground as shown by geophysical measurements. Research Report, MÁFI
- Kassai M 1983: Distribution and raw material perspectives of the upper Carboniferous in southern Transdanubia. (In Hungarian) *Földtani Kutatás*, 26, No. 2–3, 53–56.
- Szénás Gy et al. 1964: Results of geophysical exploration in Mecsek and Villány Mts. MÁELGI-Year-book, Vol. I. Műszaki Könyvkiadó, Budapest

## INTRODUCTION TO THE SERIES “CONDUCTING CRUSTAL ANOMALIES IN GEOTHERMALLY ACTIVE AREAS”

The number of sites occupied by magnetotelluric measurements has increased significantly in the last decade, mainly due to a higher technical level of the instrumentation. In addition to near-surface structures, there is an increasing quantity of geoelectric information about crustal and upper mantle depths. It is well known that the determination of near-surface distorting effects needs utmost carefulness. It seems, however, to us that the interpretation of the anomalies cleaned from distortions got a task of secondary importance. It is often the case that investigations end in the selection of distortionfree data, and the construction of models and interpretation are omitted. On the basis of petrophysical measurements in laboratory and theoretical investigations, several possibilities are open for the interpretation of the conductive crustal anomalies. The only possible way is to confront these ideas with the geologic-tectonic structure of the corresponding areas in order to obtain unique solutions.

These considerations led us to the idea to start a series in *Acta Geodaetica, Geophysica et Montanistica Hungarica* on a selected, well-limited group of geoelectric anomalies, i.e. on conducting crustal anomalies in geothermally active areas and to present them in their geophysical-geological surroundings. Readers will see experiments to interpret the anomalies and they can take a choice to get nearer to the solution of their own problem.

We intend to publish the series — after publication in the *Acta* — in form of a book. We call for further contributions on this field and thank to the authors of the papers published in this issue for their contributions.

*A. Ádám, H. Fournier, J. Verő*



## MAGNETOTELLURIC RESULTS IN NORTH-EAST ICELAND — ELECTRICAL CONDUCTIVITY, TEMPERATURE, CRUST- AND MANTLE STRUCTURE\*

M BEBLO<sup>1</sup> and A BJÖRNSSON<sup>2</sup>

[Manuscript received February 13, 1984]

A high-conductivity layer, about 10  $\Omega\text{m}$ , marking the transition between crust and upper mantle is detected in North-East Iceland. It shows a distinct uplift within the Neovolcanic area and indicates some basaltic melt fraction at temperatures around 1.000 °C.

**Keywords:** basaltic melt; crustal conductivity anomaly; Iceland; mid-oceanic rift; magnetotellurics

The electrical conductivity of the Earth's interior depends mainly on temperature. It is also strongly related to chemical composition. From magnetotelluric data we get information about the electrical conductivity in correlation to the temperature distribution and the multiphase rock-systems with the aim of geodynamic modelling of crust and mantle.

In 1977 and 1980 magnetotelluric surveys in North and East Iceland were realized in a joint effort of the University of Munich, Germany, and the National Energy Authority of Iceland. A total of 38 magnetotelluric sites were distributed over the main geological structures, the Neovolcanic zone and the adjoining older Tertiary flood basalt areas (Fig. 1).

### *The results from magnetotelluric measurements*

A high-conductivity layer, about 10  $\Omega\text{m}$ , is detected throughout the surveyed area. The high-conductivity layer shows a distinct uplift within the Neovolcanic areas (Fig. 2). Its depth increases from 10 km to 20–30 km depth at a 50–100 km distance from the rift axis. The high-conductivity layer indicates some basaltic melt fraction and temperatures around 1.000–1.200 centigrades.

<sup>1</sup> Institut für Allgemeine und Angewandte Geophysik, Universität München, Theresienstraße 41/IV, D-8000 München 2

<sup>2</sup> National Energy Authority, Grensasvegi 9, 108 Reykjavík Iceland

\* Paper given at the IUGG Interdisciplinary Symposium 3. Crustal Accretion in and around Iceland, August 16–18, 1983, Hamburg, FRG

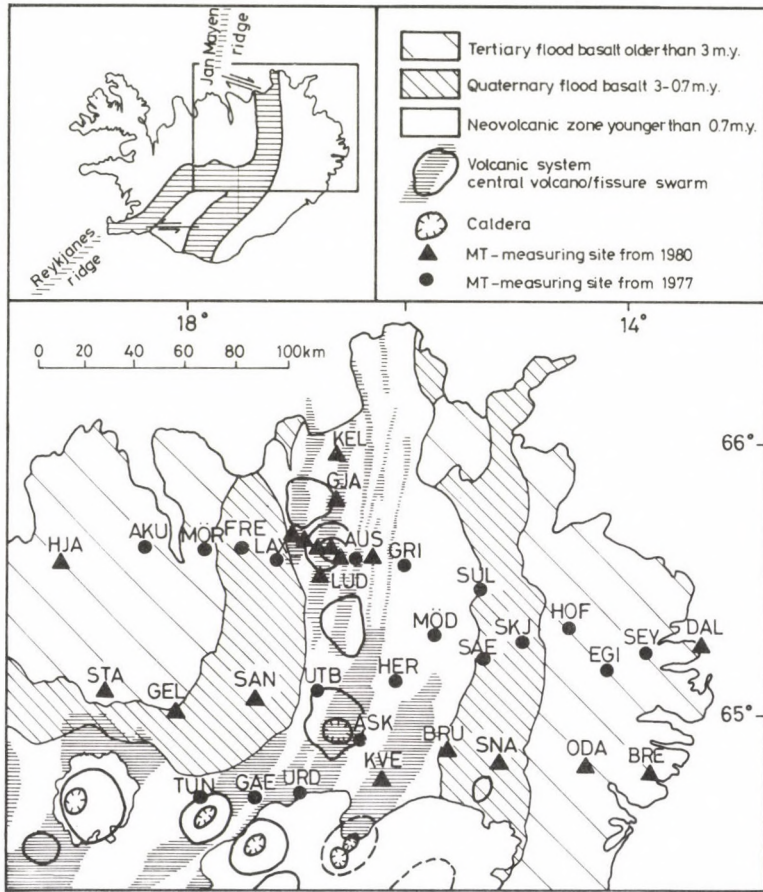


Fig. 1. Simplified geological map of northeast Iceland, showing locations of magnetotelluric sites (after Beblo et al. 1983)

The basaltic high-conductivity layer is interpreted as the base of the crust, formed by upward migration of basaltic melt from parent ultrabasic mantle material.

If we assume, the basaltic material to extend below the high-conductivity layer, the decreased average conductivity of  $100 \Omega\text{m}$  up to 100 km depth would indicate a decrease in temperature. This would not be in agreement with the geodynamic processes. In rifting zones an upward flow of material is connected with an upward dragging of isotherms, therefore an increase in temperature with depth is expected.

Consequently, the change in conductivity is a result of change in chemical composition of the rock-system.

We conclude that the material below the high-conductivity layer is of ultrabasic composition, depleted of the basaltic component. The conductivity values give even

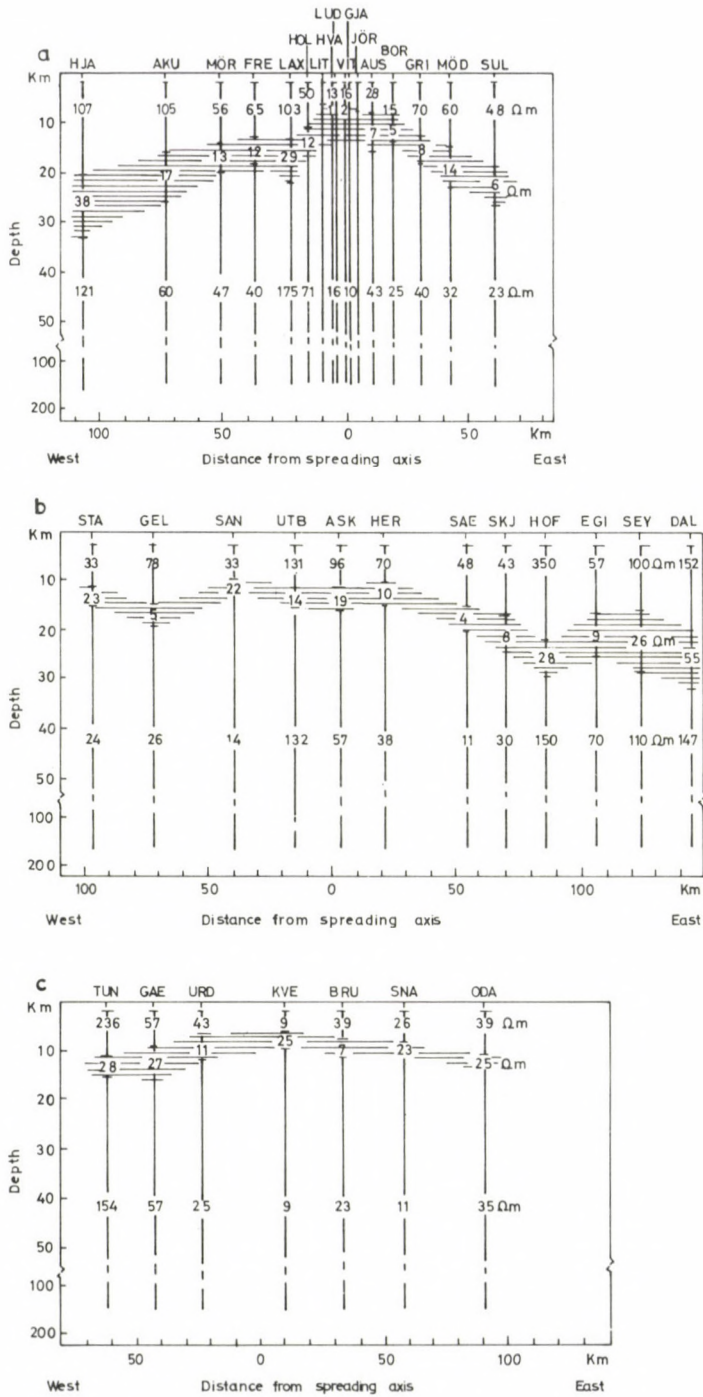


Fig. 2a-c. Models of one-dimensional conductivity distribution at all sites, calculated from apparent resistivities and phases of the TE-mode, and assembled into profiles. The hatched areas show a continuous high conductivity layer. The numbers indicate resistivities in Ωm. These east-west magnetotelluric cross-sections are perpendicular to the strike and centered at the spreading axis showing significant updoming of the high conductivity layer within the Neovolcanic zone (after Beblo et al. 1983)

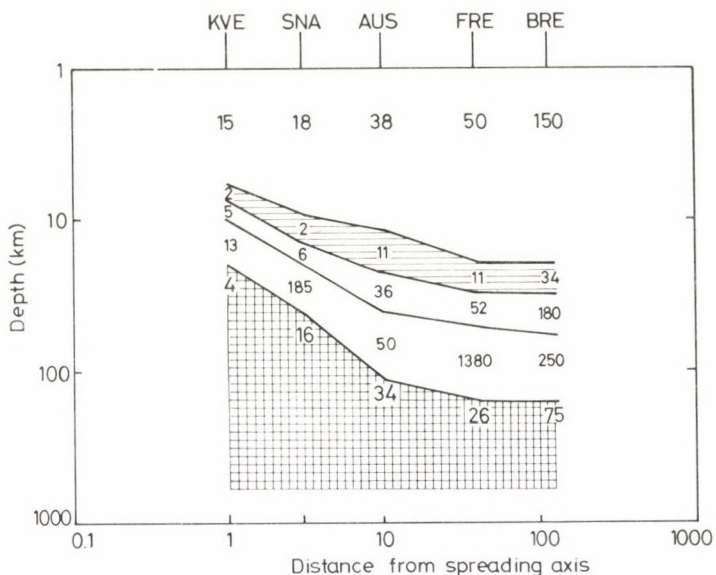


Fig. 3. Crust and mantle resistivity structure depending on the distance from spreading axis. The numbers indicate resistivities in  $\Omega\text{m}$ . A significant record increase in conductivity can be seen at about 100km depth

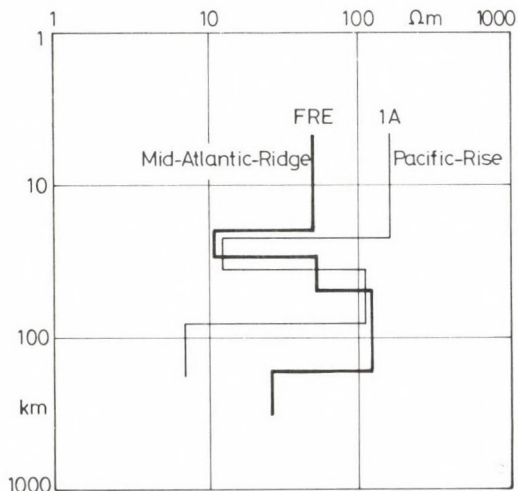


Fig. 4. The Mid-Atlantic-Ridge conductivity model for Iceland compared to MT results in the Pacific-Rise-Crest (Filloux 1981, 1982). The conductivity models are shown for site FRE (Iceland) and station 1A (Pacific Rise). These sites are at the same distance from the spreading axis (after Beblo et al. 1983)

more temperatures around 1.000–1.200 centigrades with some melt content. The melt content is highest in the basaltic high-conductivity layer and decreases with increasing depth within the upper mantle.

Magnetotelluric results for longer periods show a significant second increase in conductivity for the asthenosphere at around 100 km depth (Fig. 3).

It is interesting to compare our results for Iceland to MT measurements in the Pacific-Rise crest. Both conductivity models are quite similar. They show the high-conductivity layer at the base of the crust and a second increase in conductivity for the asthenosphere (Fig. 4).

### Conclusion

The crust beneath Iceland is similar to the oceanic crust. No significant lateral changes in electrical conductivity could be found, normally expected for mid-oceanic-rift systems at crustal depths.

The crust-mantle interface beneath Iceland is characterized by significant increase in electrical conductivity and decrease in seismic P-wave velocity. This can be explained by a diapiric updoming of the asthenosphere and a diminishing thickness of lithosphere (Fig. 5).

Diapiric updoming of the asthenosphere leads to partial fusion of parent ultrabasic mantle material, resulting in segregation and upward migration of a basaltic melt. The melt fraction tends to escape due to its lower viscosity and higher mobility as compared to the solid phase. Consequently, a chemical differentiation between melt fraction and rock matrix occurs.

*We conclude*, the upper mantle contains cracks, filled with high-conductive melt. The cracks are electrically isolated. It seems to be plausible, these cracks — filled with high-conductive melt — will rise and create a zone of magma accumulation at the top

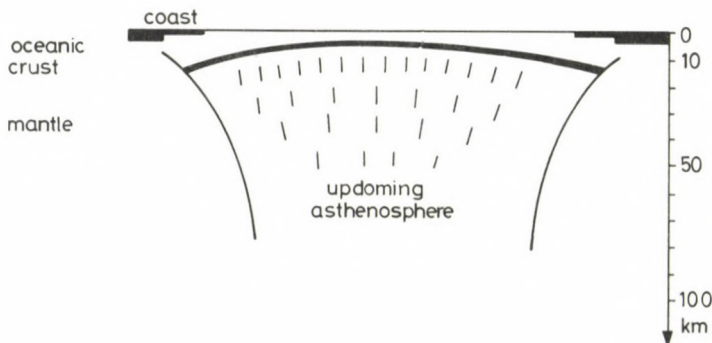


Fig. 5. Simplified model of the upper mantle below Iceland. Diapiric updoming of the asthenosphere leads to partial fusion at the base of the crust

of the asthenosphere. This zone forms the Icelandic basaltic crust, thickening away from the ridge with increasing age.

The diapiric updoming asthenosphere is in its uppermost parts depleted of the basaltic component, the effect for the low conductivity in these depths. At about 100 km depth the segregation of melt from the olivine-ultrabasic-basalt multiphase rock-system of the mantle seems to be finished. For this reason the increase in conductivity to normal conductivity-values of the deeper asthenosphere is explainable.

### References

- Beblo M, Björnsson A, Arnason K, Stein B, Wolfgram P 1983: Electrical conductivity beneath Iceland- Constraints imposed by magnetotelluric results on temperature, partial melt, crust- and mantle structure. *J. Geophys.*, 53, 16–23.
- Filloux J H 1981: Magnetotelluric exploration of the North Pacific: Progress report and preliminary soundings near a spreading ridge. *Phys. Earth Planet. Int.*, 25, 187–195.
- Filloux J H 1982: Electrical conductivity structure of the seafloor beneath the North Pacific. Proceedings Symp. on Electromagn. in the Transition zone between ocean and continent. Earthquake Res. Institute. The University of Tokyo

## THE HOT DOME OF TACO RALO, IN THE NW OF ARGENTINE

N VATIN-PERIGNON<sup>1</sup>, C POMPOSIELLO<sup>2</sup>, M MAMANI<sup>3</sup>, A MAIDANA<sup>3</sup>  
M KELLER<sup>4</sup>, J C GASCO<sup>2</sup>, H FOURNIER<sup>5</sup>, J FEBRER<sup>2</sup>

[Manuscript received June 15, 1984]

The Nazca plate subduction process beneath the South American continent has sections with different behaviour. One of the transition zones between sections occurs aligned with the 27°S–28°S parallel, with its greatest development in the Argentine North-West. The area is seismically inactive.

The geophysical magnetotelluric study shows a thinning of the continental lithosphere in coincidence with the transition area. The measured lithospheric thickness is about 6–30 km in comparison with the surrounding measured value of 70–80 km. The lithospheric thickness allows us to infer a geothermal regional gradient between 3.5 and 4 times its normal value. This region is a geothermal anomaly of great dimension and intensity with an important accumulation of energy in the thin zones of the lithosphere. A new thermogenic mechanism associated with the weakness lines of the oceanic plates and the accentuation of the heat flux is proposed.

**Keywords:** Argentina; geothermal field; magnetotellurics; Nazca plate; plate collision

### Geographic position

The hot dome of Taco Ralo is situated between 26°–30° South and between 64°–68° West. The interesting part of the dome has a diameter of 150 km. The eastern part is composed mostly of great plains producing sugarcane with a mean altitude of 400 m. The central part consists of the Aconquica NS tertiary mountain chain with summits up to 5500 m. The western part comprises the desert of Pipanaco having a diameter of 100 km and an altitude of 800 m. As we have seen, this topography, at the east border of the Cordillera de los Andes, is very diversified.

### Geological situation

The eastern part is composed mostly of Tertiary continental sediments produced by the erosion of the Tertiary Aconquica mountains chain. The desert of Pipanaco (western part) seems to be a circular graben.

<sup>1</sup> Laboratoire de Volcanologie de l'Institut Dolomieu, Grenoble, France

<sup>2</sup> Comisión Nacional de Investigaciones Espaciales, Avda. Mitre 3100 San Miguel, 1663, Argentina

<sup>3</sup> Instituto de Investigaciones Aplicadas de Ciencias Espaciales, cc. 131, Mendoza, 5500 Argentina

<sup>4</sup> Instituto Antártico Argentino, Cerrito 1248, Buenos-Aires, Argentina

<sup>5</sup> Instituto de Investigaciones Aplicadas de Ciencias Espaciales, cc. 131, Mendoza, 5500, Argentina

The interesting fact is the presence of numerous and important massifs of granite (acidic rocks in general) in the environment of the hot dome of Taco Ralo. See the "*Mapa Metalogenetico de la Rep. Argentina*".

There are no deep borehole data available for this region. The western part is tectonically very perturbed: general compressed zone first, followed by some distention period, producing the relatively unimportant graben.

### Geophysical data

There exists in the hot dome of Taco Ralo region a great number of hot springs and aquiferous hyperthermal layers, and, of course, thermal stations, over more than 26 000 km<sup>2</sup>. The geothermic gradient is in the range of three to four times the normal one.

Barazangi and Isaks (1976) have proposed in 1976 one seismic triangular silent zone, extending below the region of the hot dome of Taco Ralo. At the East of the triangle, the focus of the earthquakes are situated in the range of 500 to 600 km depth.

For Bonatti et al., in 1977, this region of Belen-Taco Ralo is the hypothetic end of the continental hot line prolongation Easter Island, San Felix and San Ambrosio Island.

In 1979, Baldis et al. interested by these results on one hand, and by the programme of the National Geothermic Inventory of Argentine on the other hand, proposed a magnetotelluric investigation over the silent seismic triangular zone.

### Electromagnetic induction data

Within the frame of the programme of the National Geothermic Inventory of Argentine, four magnetotelluric campaigns have been done from 1980 through 1983 in the NW of Argentine over a region of 300 km diametre. Twenty deep MT soundings were made, using fluxgate magnetometers, classical core coiled magnetic variometers and audiomagnetic variometers.

The main results are presented in Fig. 1: eight more characteristic MT curves obtained with the telluric line parallel to the regular NS tectonic direction. The general interpretation of these eight curves gives a very conductive sedimentary basin of a few km thickness followed by a more resistive layer of 4 to 12 km according the site of the sounding, then a highly conductive layer, 5 km thick, down to 0.3  $\Omega\text{m}$  below Taco Ralo, then a last layer, more resistant, of 50  $\Omega\text{m}$  or more.

Figure 2 shows a map giving the position of the sounding sites, the general trend of the isodepths of the top of very conductive layer forming the dome, meanwhile Fig. 3 gives the NS section Frias (8) Leales (3) of this conductive dome.

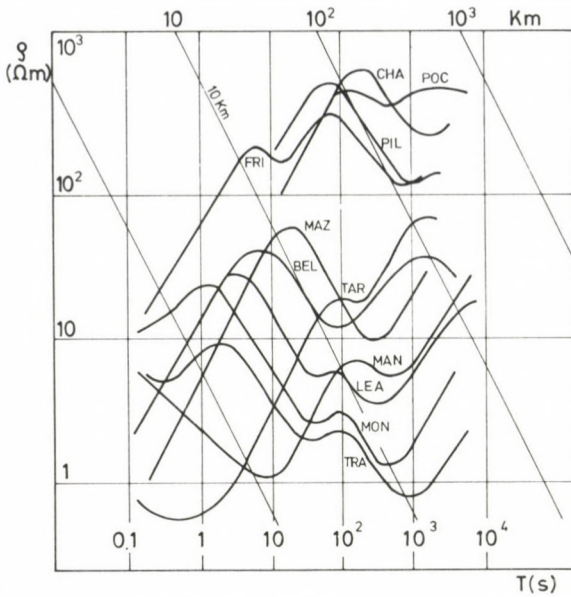


Fig. 1. 8 MT curves obtained with the use of the telluric component parallel to the NS regular direction. T.RA=1 Taco Ralo, MON=2 Monteagudo, LEA=3 Leales, MAN=4 Mansupa, TAR=5 Taruqa Pampa, BEL=6 Belen, MAZ=7 Mazan, FRI=8 Frias. The curves cited: PIL Pilar, CHA Chemical and POC Pocito (San Juan) concern the 32° S parallel MT study described by Baldis et al. (1983). These curves do not show a conductive layer in the crust. We can see that the upper crust conductive layer phenomenon is not general in the NW of Argentine

### Interpretation

The results given in the review of Haak (1980) permit us to suggest that this highly conductive layer situated in the upper crust is composed of partially molten rocks having a temperature of about 900° to 1000 °C in the central zone of the dome at least. Below this very conducting and supposedly very hot layer our actual results do not permit us to know if the other layers are also at a very high temperature because of the strong screening effect of the conductive layer and the fact that our interval of periods used to do the soundings is too short at high temperatures. This high temperature is, however, possible according to the results proposed in the review of Haak (1980).

The quasi absence of volcanic rocks and, on the contrary, the presence of numerous granite massifs around the hot dome region may allow us to propose that this is an acidic rocks-region in the generating phase at a depth of only a few km below the surface, which is somewhat exceptional.

The origin of the heat is probably the breaking of the Nazca plate into two parts having different plunging dip angles, suggested by Barazangi and Isacks (1976). This

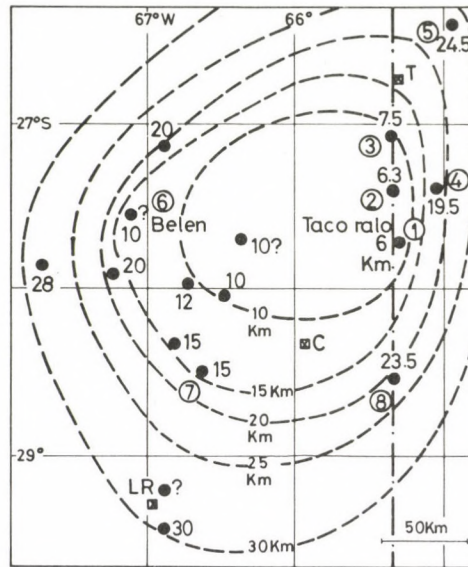


Fig. 2. Map of the isodepth of the top of the very conductive layer. T = San Miguel de Tucuman; C = San Fernando del Valle de Catamarca; LR = La Rioja — for the number of sites see the legend of Fig. 1. The map indicates the provisionary isodepths of the top of the very conductive layer situated in the upper crust. We can easily see the importance of this newly found geothermal field. It seems probable that the diameter of the workable surface is approximately 100 km. A similar silent triangle exists in Peru

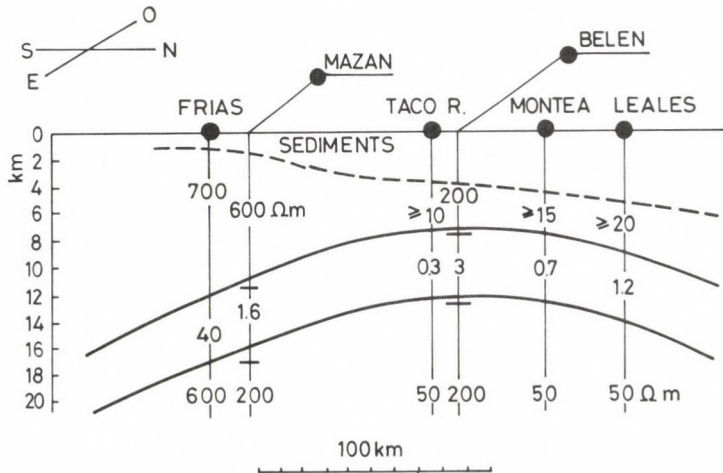


Fig. 3. Cross section along the NS direction passing by Leales, Monteagudo, Taco Ralo and Frias stations. We see the general trend of the section of the dome delimited by the top of this very conductive layer having a dip angle of approximately 8 to 10%. It is impossible to give true values of the resistivity of the underlying layer because the strong screening effect generated by this conductive layer does not permit it

frictional effect produces heat and dehydration. This water, going to the surface, on the way, makes a partially molten state with the acidic upper crust rocks.

It seems, that we have found below the Taco Ralo region a kind of new geodynamic phenomenon, which we have named a "hot dome".

It is possible that the same hot dome exists below the seismic silent triangle of Peru, for the same symmetrical type of breaking of the Nazca plate.

### References

- Baldis B, Demicheli J, Febrer J, Fournier H, Triep E, Trivedi N 1979: Confirmation magnetotellurique sur le prolongement de la plaque de Nazca et complément d'information possible par la même méthode sur deux secteurs de silence sismique délimités par des foyers de séismes de plus en plus profonds d'W en E au Nord et au Sud de l'Altiplano. 7<sup>e</sup> Réunion Annuelle des Sciences de la Terre, Lyon, Avril. Soc. Geol. Fr. édit. Paris
- Baldis B, Demicheli J, Febrer J, Fournier H, Garcia E, Gasco J C, Mamani M, Pomposiello M C 1983: Magnetotelluric results along a 1200 km long deep profile with an important geothermal area at its North-West end in the provinces of Tucuman and Santiago del Estero in Argentina. *Acta Geod. Geoph. Mont. Hung.*, 18, 489–499.
- Barazangi M, Isacks B 1976: Spatial distribution of earthquakes and subduction of the Nazca plate beneath South America. *Geology*, 4, 686–692.
- Bonatti E, Harrison C G A, Fisher D E, Honnorez J, Schilling J-G, Stipp J J, Zentilli M 1977: Easter Volcanic chain (Southeast Pacific): A mantle hot line. *J. Geophys. Res.*, 82, 2457–2478.
- Haak V 1980: Relations between electrical conductivity and petrological parameters of the crust and upper mantle. *Geophysical Surveys*, No 4, 57–69.
- Mapa Metalogenetico de la República Argentina 1969: Compilado y publicado por la Dirección Nacional de Geología y Minería., Escala 1 : 2 500 000



## MAGNETOTELLURIC EXPLORATION IN THE MEAGER MOUNTAIN GEOTHERMAL AREA, CANADA\*

C FLORES<sup>1</sup>, R D KURTZ<sup>2</sup>, J DELAURIER<sup>3</sup>

[Manuscript received March 31, 1984]

Seven MT soundings were measured along an east-west traverse crossing the geothermal anomaly designated South Reservoir near Meager Creek 150 km north of Vancouver (Canada).

Positive correlations have been observed between an increased temperature gradient at a depth of about 200 m, the MT layered model and the drilling results.

**Keywords:** Canada; geothermal area; magnetotellurics; Meager Mts

### Introduction

Meager Mountain, located at lat 50° 34' N, long 123° 23' W, or 150 km north of Vancouver (Fig. 1), is recognized as an important geothermal prospect in Canada. Since 1973 a program of geothermal energy evaluation in this region has been conducted by the Department of Energy, Mines and Resources, Canada and by contractors to the British Columbia Hydro and Power Authority. One of the three possible geothermal zones, designated South Reservoir (Fairbank et al. 1981) has been outlined near Meager Creek in Fig. 1. The margins of this potential reservoir enclose an area of about 6 km<sup>2</sup>. They are defined by measurements of surface D. C. electrical resistivity and temperature in drillholes.

The regional heat flow across the Canadian Cordillera is about 80 mW · m<sup>-2</sup> (Hyndman 1976, Jessop and Judge 1971). Measurements in a drillhole located about 7 km east of Meager Mountain show an anomalous heat flow value of 130 mW · m<sup>-2</sup> (Lewis and Jessop 1981) while over the convective zone in the South Reservoir values from 310 to 1700 mW · m<sup>-2</sup> have been measured (Fairbank et al. 1981).

The basement rocks are part of the Coast Plutonic Complex, a Tertiary and older granitic and metamorphic terrain. In the Meager Creek area, the Complex is

<sup>1</sup> Geophysics Division, Department of Physics, University of Toronto, Toronto, Ontario M5S 1A7, Canada

<sup>2</sup> Division of Seismology and Geomagnetism, Earth Physics Branch, Energy, Mines and Resources, Ottawa K1A 0Y3, Canada

<sup>3</sup> Pacific Geoscience Centre, Energy, Mines and Resources, 9860 West Saanich Road, Sidney, B.C. V8L 4B2, Canada

\* Earth Physics Branch Contribution No. 1102

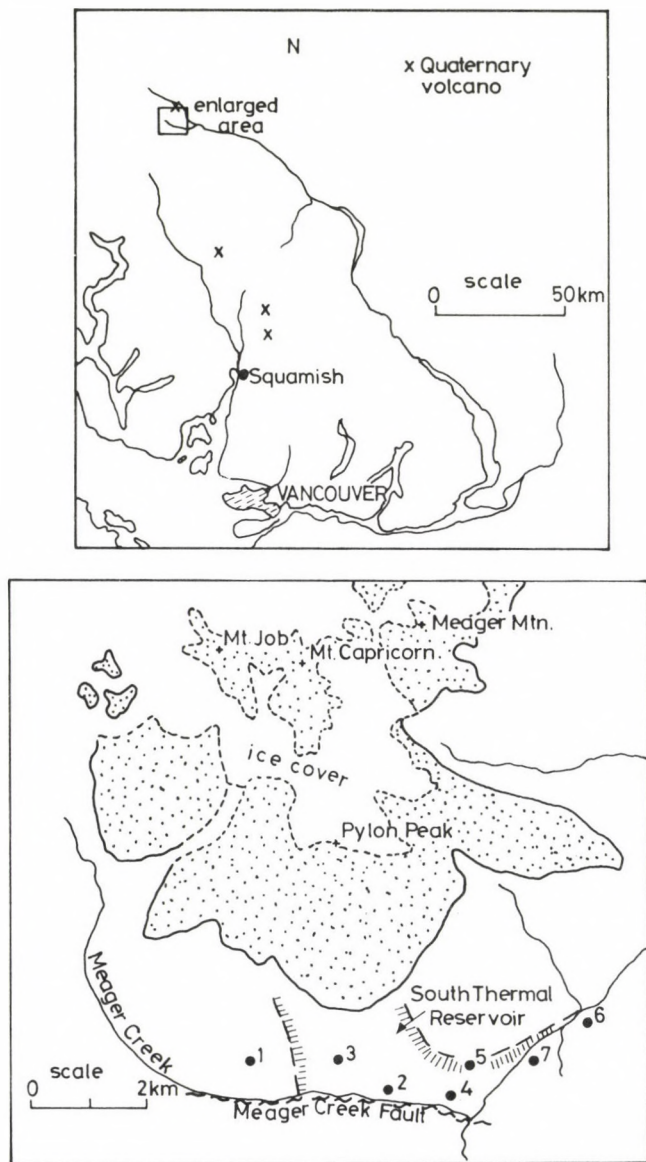


Fig. 1. Meager Mountain location and simplified geology showing volcanic rocks (stippled areas) in the vicinity of the South Reservoir, thermal anomaly and seven magnetotelluric sites (maps adapted from Lewis and Souther 1978)

comprised of fractured granodiorite and associated gneiss, is crossed by a north, northwesterly-trending belt of late Tertiary and Quaternary plutons and a north-south belt of Quaternary volcanoes (the Garibaldi belt) of andesite-dacite composition (Lewis and Souther 1978). The most recent eruption of Meager Mountain was approximately 2440 years before the present (Nasmith et al. 1967). Pleistocene alluvium of volcanic origin overlay both basement and volcanic material.

The South Reservoir is located in an alluvium plateau of gentle slope, limited to the north by the steep slopes of the Meager Mountain volcanic edifice with a relief of 1500 m and to the south by the fault scarp of Meager Creek Fault, with an associated relief of about 500 m.

### Previous electrical and electromagnetic surveys

There are a number of other D. C. and electromagnetic (EM) studies in the area:

- a) Six dipole-dipole resistivity traverses (Shor 1975).
- b) Two lines of Magnetometric-Resistivity (MMR) data (Scintrex 1981).
- c) Two magnetotelluric (MT) stations in the close vicinity of the thermal anomaly (Pham Van Ngoc 1978) and four other stations in the high relief areas on the volcano (Pham Van Ngoc 1980).
- d) Twenty two stations of horizontal-loop EM soundings using frequencies from 3 up to 1000 Hz (Gómez-Treviño and Edwards 1983).

### The survey

Seven MT sites were located along an east-west traverse crossing the thermal anomaly (Fig. 1) using a Phoenix Geophysics Ltd. real-time MT system (DeLaurier et al. 1982). The three magnetic and two telluric field components were observed at forty frequencies from 0.00055 to 384 Hz. Apparent resistivities and phases were obtained during the field survey by rotating the impedance tensor into the principal directions using standard methods (Vozoff 1972). Other MT earth response parameters that were determined are: single-station vertical magnetic transfer functions, dimensionality indices (skew and ellipticity), impedance polar diagrams and ellipticity, degree and angle of polarization of the telluric field.

### Results

All the sites showed a strong anisotropy. In general, the skews were low ( $<0.3$ ) for frequencies larger than about 3 Hz at all locations. This suggests that the resistivity distribution is approximately two-dimensional only for shallow depths. The real induction arrows (rotated  $180^\circ$ ) point towards current concentrations within the boundaries of the geothermal anomaly.

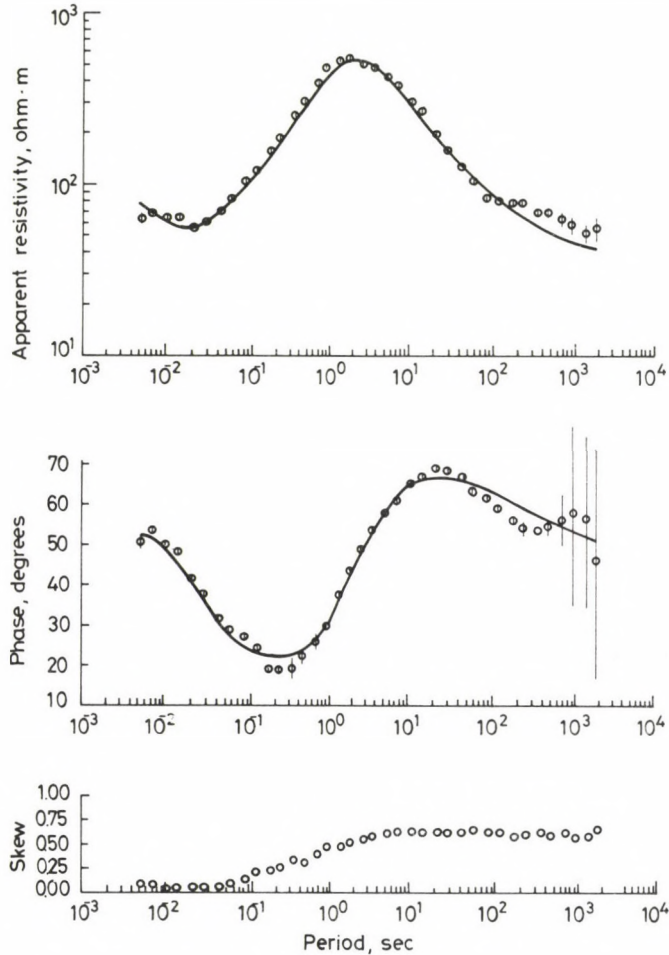


Fig. 2. MT response curves for site 2. Solid curves are computed responses of the corresponding layered model in Fig. 3. Error bars are plus/minus one standard deviation of the mean when larger than the plotting symbol

### Layered earth inversions

Reddy and Rankin (1972) showed that the conductivity variation with depth can be estimated by interpreting the  $E$ -polarization ( $E$  parallel to strike) apparent resistivity curve for locations in the centre of a conducting two-dimensional graben. In order to select this polarization in the Meager data, the angles of polarization of the telluric ellipse, the impedance polar diagrams and the strike from the real induction arrows were used. The  $E$ -polarization orientation was northwest-southeast.

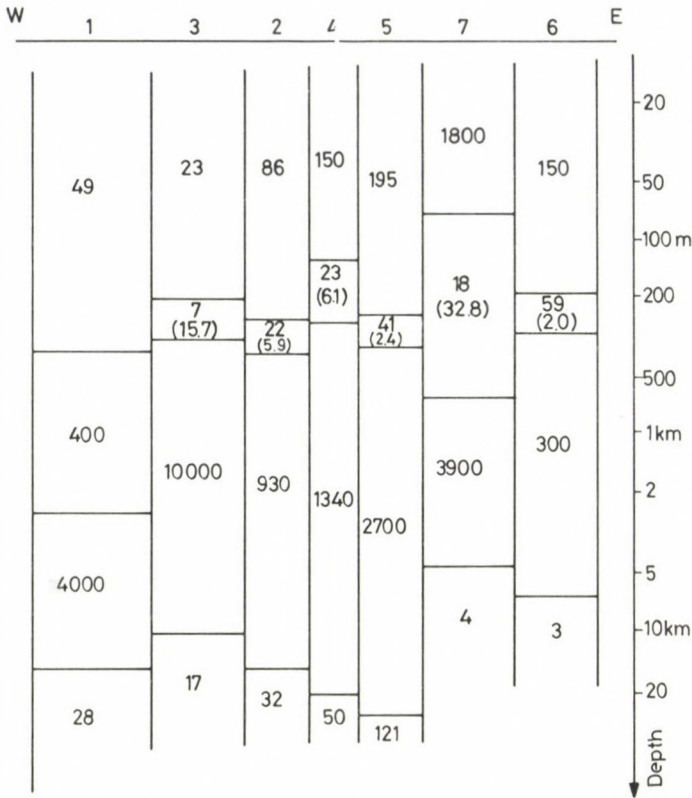


Fig. 3. Resistivity section inferred from layered models. Resistivities in ohmm. Bracketed numbers are the conductivity-thickness product of the second layer in siemens. Station numbers are given across the top of the figure

As a first step in determining the resistivity distribution, a joint inversion of apparent resistivities and phases for a layered earth was performed using the generalized linear inversion algorithm of Jupp and Vozoff (1975). An uncertainty of plus/minus one standard deviation was used in the measured apparent resistivities and phases. The only constraint applied was the requirement that the number of layers be kept to a minimum.

At all stations a three-layer earth over a halfspace sequence was derived. The fits between the observed and the computed responses from the inverted models were good, especially for the apparent resistivity curve. Figure 2 shows the computed and observed responses at site 2. With the exception of location 1, all sites rendered a sequence, from top to bottom, of resistive-conductive-resistive-conductive (Fig. 3). The H-polarization curves were used to obtain the layered model at site 1, because for a

location on the resistive side of a lateral inhomogeneity, a one-dimensional interpretation of the *H*-polarization curve gives a structure with correct interface depths but over-estimated resistivities (Wright 1970, Jones and Hutton 1979).

In order to assess which model parameters are well determined, an eigensolution analysis was undertaken (Edwards et al. 1981). The best resolved parameters were the thickness of layer 3 and the conductivity-thickness product of layer 2. However, model parameters are open to question for depths below the second layer because of strong three-dimensional effects.

The topographic relief in the vicinity of the MT sites may lead to doubts on the validity of the model parameters of Fig. 3. The topographic effect on the apparent resistivity curve was estimated using a two-dimensional topographic model reproducing the Meager relief within 4 km from the centre of the thermal anomaly (the actual topography is nearly two-dimensional within this range). The modeling technique is described by Swift (1971). Using this model with a homogeneous resistivity of 200 ohmm, the apparent resistivities for the *E*-polarization were computed at frequencies from 1 to 100 Hz. The topographic effect causes a decrease in apparent resistivities with respect to the constant value of 200 ohmm, with a maximum discrepancy of 10 percent of a decade at a frequency of 30 Hz. Consequently, the MT response is not produced entirely by the topography, but indicates a second conductive layer.

### Discussion

The drilling results and the D. C. resistivity pseudosections suggest that the eastward extension of the thermal anomaly is produced by an outward plume derived from the main thermal anomaly. Based on this evidence, the presence of the second conductive layer at sites 5, 6 and 7 seems to be produced by lateral effects of this plume. The temperature measurements in the main thermal anomaly show an increased temperature gradient at a depth of about 200 m, which correlates well with the MT, D.C. and EM controlled source interpretations. The MMR data define clearly the west and east boundaries of the conductive body, agreeing with those of the main thermal anomaly.

Further positive correlations between the drilling results and the MT layered model have been observed. For example, a drillhole located 500 m, north of site 1 entered a zone of increased rock competency at a depth of 310 m, which may correspond to the increase in resistivity from the first to the second layer in this site. An integrated interpretation of the drilling, geological and geophysical data is currently in progress.

## Acknowledgements

This project was funded by the Pacific Geoscience Centre. We thank Dr. R N Edwards for his support and for providing his inversion routine. One of the authors (C.F.) was financially supported by the Consejo Nacional de Ciencia y Tecnología, Mexico.

## References

- DeLaurier J, Kurtz R, Flores C 1982: A magnetotelluric survey over the Meager Mountain Southern Geothermal Reservoir. A Survey Report, Pacific Geoscience Centre Internal Report 82-5.
- Edwards R N, Bailey R C, Garland G D 1981: Conductivity anomalies: lower crust or asthenosphere? *Phys. Earth and Planet. Int.*, 25, 263-272.
- Fairbank B D, Reader J F, Openshaw R E, Sadlier-Brown T L 1981: 1980 Drilling and Exploration Program, Meager Creek Geothermal Area, upper Lillooet River, British Columbia. Rept. to B.C. Hydro and Power Authority
- Gómez-Treviño E, Edwards R N 1983: An electromagnetic survey at the Meager Mountain Geothermal Resource. British Columbia. Unpublished internal report, University of Toronto
- Hyndman R D 1976: Heat flow measurements in the inlets of southwestern British Columbia. *J. Geophys. Res.*, 81, 337-349.
- Jessop A M, Judge A S 1971: Five measurements of heat flow in southern Canada. *Can. J. Earth Sci.*, 8, 711-716.
- Jones A G, Hutton R 1979: A multi-station magnetotelluric study in southern Scotland — I. Fieldwork, data analysis and results. *Geophys. J. R. astr. Soc.*, 56, 329-349.
- Jupp D L B, Vozoff K 1975: Stable iterative methods for the inversion of geophysical data. *Geophys. J. R. astr. Soc.*, 42, 957-976.
- Lewis T J, Souther J G 1978: Meager Mountain, B.C. A possible geothermal energy resource. *Earth Physics Branch, Energy, Mines and Resources, Ottawa, Geothermal Series No. 9.*
- Lewis J F, Jessop A M 1981: Heat flow in the Garibaldi volcanic belt, a possible Canadian geothermal energy resource area. *Can. J. Earth Sci.*, 18, 366-375.
- Nasmith H, Mathews W H, Rouse G E 1967: Bridge River ash and some other recent ash beds in British Columbia. *Can. J. Earth Sci.*, 4, 163-170.
- Pham Van Ngoc 1978: Magneto-telluric prospecting in the Mount Meager Geothermal Region (British Columbia). Report of the Earth Physics Branch, Open File 78-6E
- Pham Van Ngoc 1980: Magneto-telluric survey of the Mount Meager region and of the Squamish Valley (British Columbia). Report of the Earth Physics Branch, Open File 80-8E
- Reddy I K, Rankin D 1972: On the interpretation of magnetotelluric data in the plains of Alberta. *Can. J. Earth Sci.*, 9, 514-527.
- Scintrex 1981: Report on: Magnetometric-Resistivity (MMR) Survey, Meager Mountain Geothermal Resource, by Scintrex Ltd., Concord, Ontario
- Shor G 1975: Deep resistivity surveys and supplementary geophysics at Meager Creek selected area. Pemberton, B.C., Deep Grid Analysis Ltd.
- Swift C M 1971: Theoretical magnetotelluric and Turam response from two-dimensional inhomogeneities. *Geophys.*, 36, 38-52.
- Vozoff K 1972: The magnetotelluric method in the exploration of sedimentary basins. *Geophys.*, 37, 98-141.
- Wright J A 1970: Anisotropic apparent resistivities arising from non-homogeneous two-dimensional structures. *Can. J. Earth Sci.*, 7, 527-531.



# ELECTRIC CONDUCTIVITY INCREASES IN THE EARTH'S CRUST IN TRANSDANUBIA (W-HUNGARY)

A STATUS REPORT

A ÁDÁM<sup>1</sup>

[Manuscript received June 20, 1984]

After describing the geographical and geological position of two crustal conductivity anomalies in Transdanubia, two hypotheses on their origin (graphitic schist or electrolyte in the pores and cracks of fractures) are discussed taking into account the distortions of the electromagnetic field in connection with tectonics, geochemical and geothermal relations. The Transdanubian anomalies are compared to the Alpine crustal anomalies to illuminate the geothermal effects.

**Keywords:** conductivity anomaly; crust; fractures; graphite; Transdanubia

## Geographical and geological positions

In the western part of the Pannonian Basin, in Transdanubia two crustal conductivity anomalies have been observed. One of them, the so-called "Transdanubian conductivity anomaly" occupies a larger area extending to the Bakony Mts and its NW foreground (Fig. 1). The second one is connected to the Balaton fracture and represents a 10 km wide highly conducting zone in some kms depth around it (Fig. 2).

The Transdanubian anomaly was detected by relative telluric frequency soundings in the early sixties (Ádám and Verő 1964). It was further investigated by magnetotelluric and geomagnetic deep soundings (Takács 1968, Ádám 1981, Albu et al. 1983). The Balaton-line anomaly was observed by magnetotellurics (Varga 1980).

The Transdanubian anomaly crops out towards northwest at the Rába fracture line together with the Mesozoic basement carbonates of the Kisalföld sedimentary basin. The Rába-line, a tectonic zone of first order is recently interpreted as the continuation of the Insubric lineament of the Alps (Kovács 1983) which separates the unmetamorphosed Southern Alps from the metamorphosed Eastern and Western Alps. Northwest of the Rába line only a weak remote effect of the anomaly can be found on the (*E* polarized?)  $\rho_{\min}$  MT sounding curves. The SE-border of the anomaly coincides with the outcrops of the upper Paleozoic formations near the northwestern shore of Lake Balaton (Balatonfelvidék). This boundary is indicated by the opposite

<sup>1</sup> Geodetic and Geophysical Research Institute of the Hungarian Academy of Sciences, H-9401 Sopron, Pf. 5.

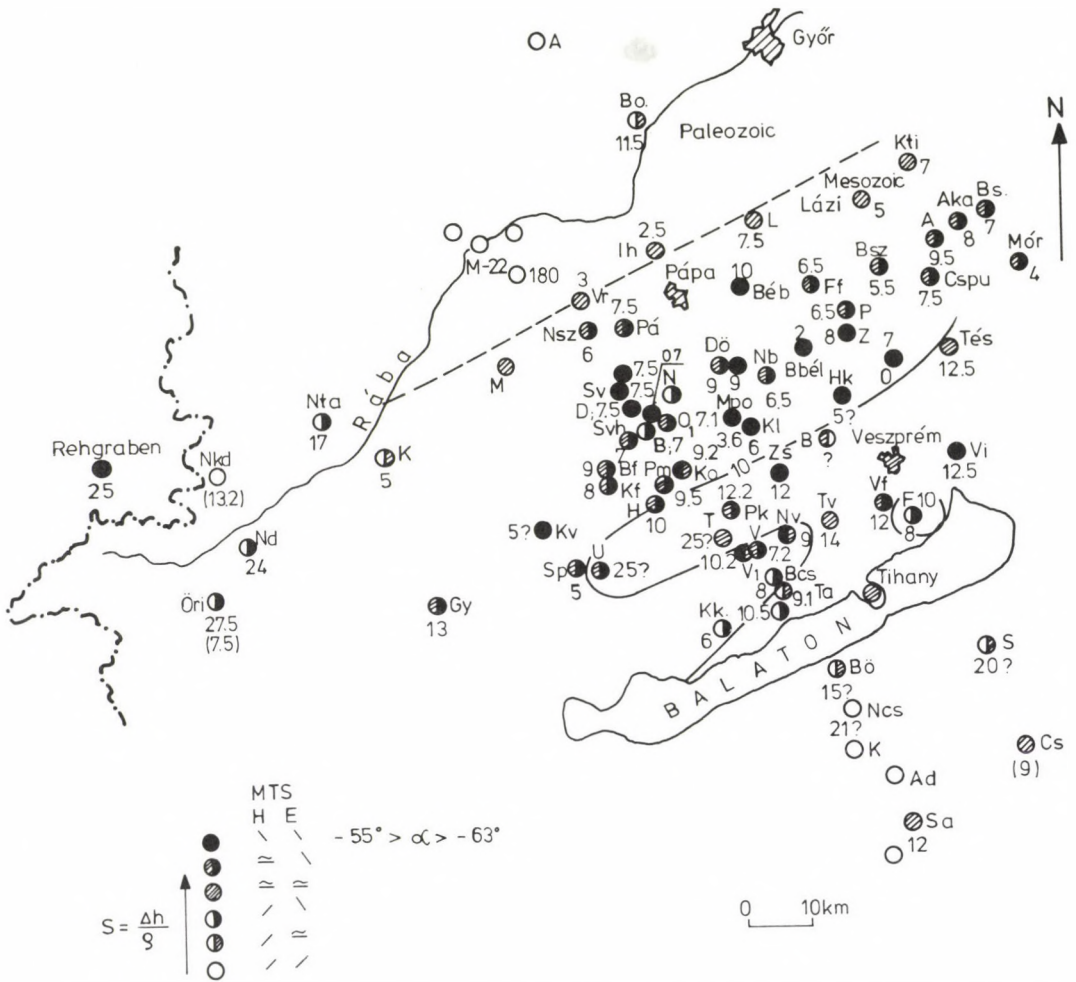


Fig. 1. The map of the Transdanubian crustal conductivity. The circles indicate the measuring sites and the numbers next to the circles give the depth to the highly conducting layer. The shading of the circles shows the character of the sounding curve (see the symbols below on the left corner)

tendency of the  $\rho_{\min}$  and  $\rho_{\max}$  sounding curves. To the east, the extent of the anomaly is not well determined.

The conducting formation is included into Paleozoic or Precambrian layers overlain by some km thick Mesozoic carbonates and Neogene sediments. The lithological connection of unknown character between the conductivity anomaly and the Mesozoic carbonates could illuminate the material origin of the anomaly.

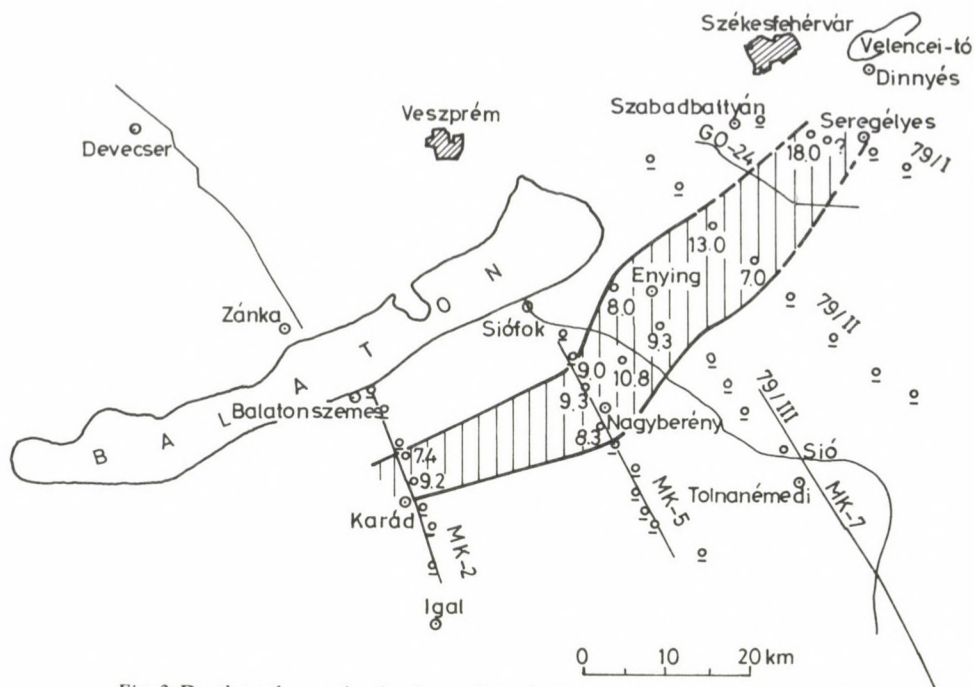


Fig. 2. Depth to the conducting layer along the Balaton fracture line (Varga 1980)

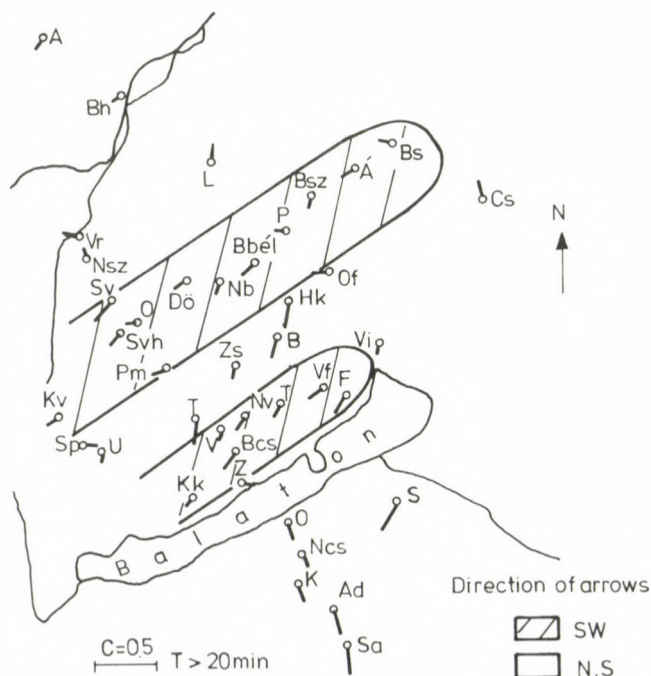


Fig. 3. Wiese induction arrows showing the fine structure of the Transdanubian conductivity anomaly (Wallner 1977)

The extent and inner structure of the Transdanubian crustal anomaly is also shown by the Wiese induction arrows (Ádám and Wallner 1975, Wallner 1977). Although in the Pannonian Basin the Wiese-arrows are generally southwards directed, in the area of the Transdanubian anomaly there are two characteristic stripes parallel to the Balaton-line where the direction of the arrows is mainly west-southwest. The arrow length in these stripes is smaller than 0.1 for periods  $T > 20$  minutes. At the boundary of the anomaly the arrows point outwards, i.e. towards the formations of high resistivity (Fig. 3). (No geomagnetic deep sounding has been carried out along the Balaton-line anomaly.)

### Geophysics of the anomaly area

In the Pannonian Basin heat flow values of about  $80\text{--}110 \text{ mWm}^{-2}$  were measured, being higher in comparison to the other surrounding great tectonic units, specially to the East European (Russian) Platform. Heat flow values measured nearest to the anomalies are: 105, 97 and  $88 \text{ mWm}^{-2}$  (Dövényi et al. 1983).

The crust is thin in the basin. It averages around 27 km but just below the Transdanubian conductivity anomaly it reaches 37 km, the highest value of the Basin (Posgay et al. 1981). According to the mantle diapir theory, the crust thinned out from below (Stegen et al. 1975).

In the area of the anomaly, alkaline basalt volcanoes erupted in the Neogene and Quarternary periods across extensional longitudinal (NE-SW) and transversal (NW-SE) fractures. The regional character of the electric resistivity anisotropy is determined mainly by the fractures of these directions in the Pannonian basin (Ádám 1969).

### Magnetotelluric deep soundings

The MT sounding sites on the Transdanubian anomaly are represented in Fig. 1 by small circles. According to the key these circles characterize the increasing or decreasing tendency of the  $\rho_{\min}$  and  $\rho_{\max}$  curves (in case of a 2-D structure, the  $E$  and  $H$  polarized curves). The depths to the conducting layer are given next to the circles.<sup>2</sup>

<sup>2</sup> On the area of the Transdanubian conductivity anomaly MT soundings were carried out by the Geodetic and Geophysical Research Institute (GGRI) and by the Hungarian Geophysical Institute Lorand Eötvös (MÁELGI), the latter one measuring mainly along basic geological profiles. The period range of the electromagnetic variations used by MÁELGI is 0.05–100 s, and that of the GGRI is about 10–15 000 s. According to these period ranges, MÁELGI has more precise data inversion for the upper part of the geoelectric section. The maximum difference between the depth values to the crustal conducting formation as got by the two institutes may be 1–2 km due to its approximation from the upper (MÁELGI) or the lower part (GGRI) of the geoelectric section using the mentioned different period ranges. In some cases, mainly in the Bakony Mts covered by very thin sediments, the depth values differ from each other if two measurements are not done exactly at the same site and so the effect of the local near-surface inhomogeneities is different. In this paper the depth values by GGRI are used.

The depth values for the Balaton line anomaly are also given after Varga (1980) in Fig. 2.

In Fig. 4 a depth profile is shown across the Transdanubian anomaly. The conductance is added numerically in each measuring point. The main features of this profile are the outcrops of the formation in NW and SE and its deepening below the Bakony Mts. An outcrop appears as an apparent increase in the depth of the conducting body with decrease of its conductance when moving away from its boundary. These phenomena are due to the induction i.e. side effect of the conducting body on the E polarized sounding curves. The increase in depth of the formation below the Bakony Mts is at least partly caused by the S-effect of the thinning sediments on the highly resistive crystalline rocks. Although the depth to the conducting formation is determined after Berdichevsky and Dmitriev (1976) from sounding curves best approximating the E polarization, the 3-D effect cannot be perfectly excluded therefore the S effect appears on the quasi-E polarized curves, too.

In the SE part of the anomaly the E polarization is unambiguously represented by the  $\rho_{\min}$  curves as it was proven by a statistical investigation of the distortion effects (Ádám 1981). The direction of the  $\rho_{\min}$  curves lies mainly in the common strike of the basement and the longitudinal fractures. The role of transversal fractures is somewhat less, nevertheless, in some cases they may influence the polarizations of the soundings

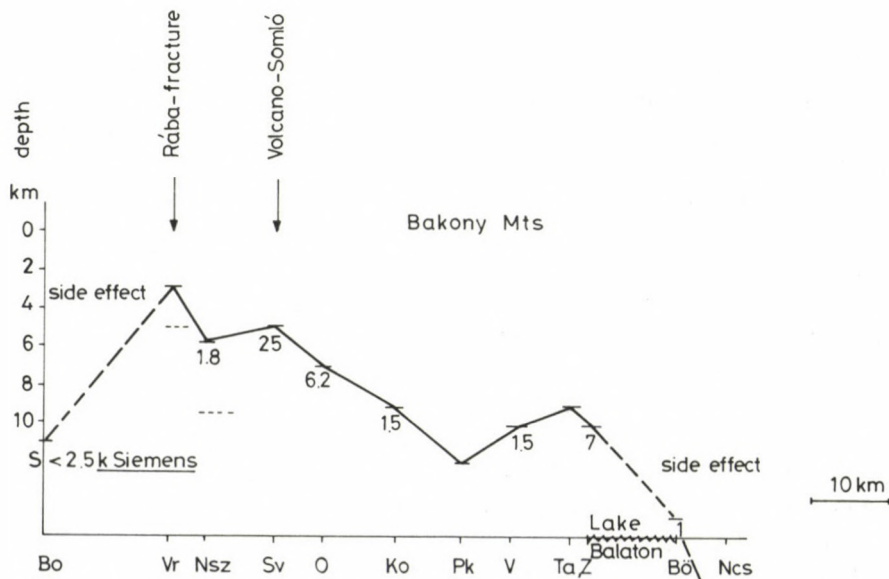


Fig. 4. Depth to the high conductivity layer calculated on the basis of the  $\rho_{\min}$  (E-polarized) curves and its conductance along a NW-SE profile (dotted line: depth values from  $\rho_{\max}$  curves)

and thus turns the MT anisotropy (e.g. in Bakonybél in Fig. 1 Bbél) perpendicularly to the regional strike direction of the basement.

On the northwestern part of the anomaly the thickness of the sedimentary layer increases and here the major axis of the impedance polar diagrams (and so  $\rho_{\max}$ ) turns into the strike of the basement. Here, when looking for the  $E$  polarized curves, a shape of the conducting formation is unavoidably to be supposed.

Having no boreholes deep enough for sampling the conducting material, we have two hypotheses:

1. The conducting formation consists of *graphitic shales*, schists in Paleozoic or Precambrian rocks as it was supposed at the beginning of the seventies by Ádám (1971). The graphitic schists form (electrically) a conducting layer. If this would be true, the  $\rho_{\max}$  curves should be used as  $E$  polarized ones in the NW part of the anomaly where the sedimentary basin deepens to determine the parameters of the conducting layer. On the basis of this hypothesis the MÁELGI profile shows an abrupt increase in the depth of the conducting formation from 5–6 km to 8–10 km where the  $\rho_{\min}$  and  $\rho_{\max}$  curves change their polarization.

A proof for this graphitic model should be the coincidence of the surface of some seismic horizons with the top of the conducting formation in some (but not all) basic geological profiles (see e.g. Fig. 41 in Albu et al. 1983 on the profile MK–3/77). Nemesi et al. (1985) support this idea by a Paleozoic graphitic formation found in a borehole in S-Transdanubia (Magyarmecske) but it lies much shallower, in a depth of some hundred meters.

2. The Transdanubian anomaly can be deduced from a *series of fractures* (Ádám O 1977, Ádám 1982) similarly to the narrow conductive zone along the Balaton-line. In the fractures the conductivity increase belongs to the electrolytes which fill the pore volume being enlarged by the tectonic events. This hypothesis can be supported by the followings:

- a) There is a lithological connection unexplained until now between the Mesozoic limestones and the conducting formation. An increase in the concentration of the electrolyte can be expected below these carbonates.
- b) The directions of the major impedances ( $Z_{xy\max}$ ) are perpendicular to the fractures strike both in case of the longitudinal as well as of the transversal fractures (Fig. 5).
- c) According to Quist et al. (1970) the maximum conductivity of an electrolyte appears at about 300 °C. This temperature can be expected under the geothermal conditions of the Hungarian Basin (Dövényi et al. 1983) just in an average depth of 7 km corresponding to the conducting formation. Calculations by Hermance (1973) using solutions of different concentration, pore pressures and geothermal gradients led to the same conclusions.

In case of a narrow (about 10 km) wide conducting body (i.e. dyke), the numerical modelling (with the finite difference method) unambiguously shows that the  $E$  polarization is represented by the  $\rho_{\min}$  curves (Tátrallyay 1977). An indication for this

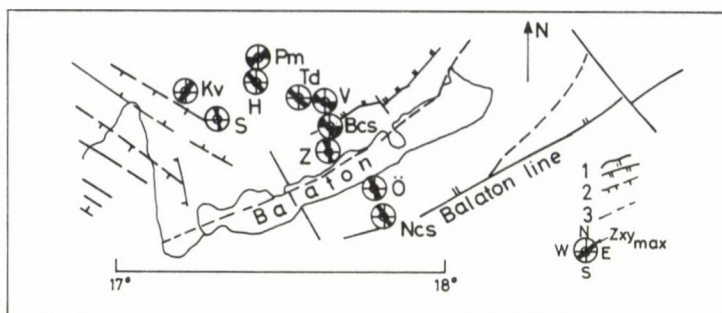


Fig. 5. The main tectonic lines around Lake Balaton and the direction of major axis of the  $Z_{xy}$  polardiagrams ( $Z_{xy\max}$ ). Keys: 1 — upthrust; 2 — normal faults; 3 — fractures

model may be the perpendicularity of the  $Z_{xy\max}$  direction to the fractures (Fig. 5). If this model is valid for the whole anomaly area, including its north-western part, too, the  $E$  polarization character of the  $\rho_{\max}$  curves is questionable. The model may be, nevertheless, more complicated if the strike of the basement and the dyke lie in different directions, and there is a thick sedimentary cover above the conducting fracture, etc.

Even if a graphite layer does exist, an electrolytic conductivity increase can be expected at least in the Rába-line similarly to the Eulaton-line and to the Insubric (Periadriatic) lineament (Ádám et al. 1984).

### Comparison of the Transdanubian and Alpine crustal conductivity anomalies

As to the role of the deep temperature in the origin of the crustal conductivity anomalies, new aspects can be expected if we compare the parameters of anomalies observed under similar and different geothermal conditions in the Pannonian Basin and the Eastern Alps (in Austria).

MT soundings were carried out in two areas of the Eastern Alps:

1. Along the crustal deep seismic profile, mainly in the Lavantal where convective heat-transport increases the surface heat flow across seismic active fractures to a value of  $100 \text{ mWm}^{-2}$ . This area approximates well the geothermal conditions of Transdanubia.
2. Along the Periadriatic line (Gail-valley and Karawanken-lineament) continuation of which towards East is identified with the Balaton line by Kovács (1983). Around the Periadriatic line Čermák and Hurtig's map (1979) shows heat flow values by  $30\text{--}40 \text{ mWm}^{-2}$  lower than in Lavantal and in Transdanubia.

The conducting zone was observed in Lavantal similarly to the Transdanubian anomaly in depths of 6–9 km (Ádám et al. 1981, Fig. 6), while it lies along the

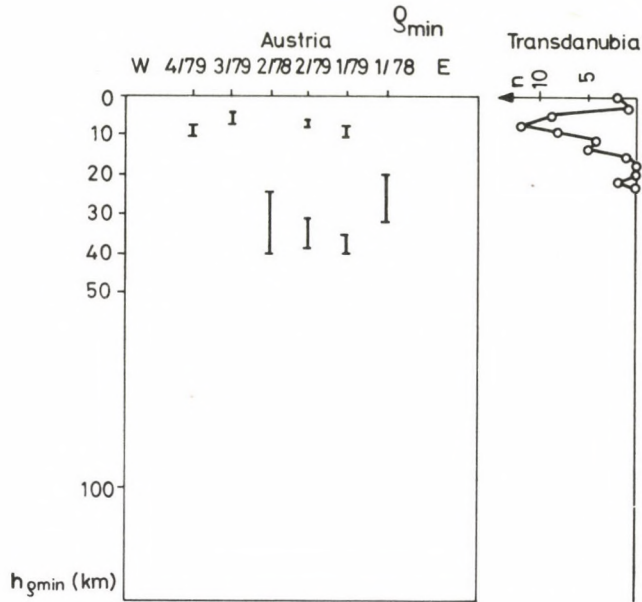


Fig. 6. Depth of conducting bodies in the Styrian Alps with their error limits calculated on the basis of  $\rho_{min}$  curves. For comparison, the occurrence frequencies of  $h_{\rho_{min}}$  are also shown for Transdanubian anomaly (after Ádám et al. 1981)

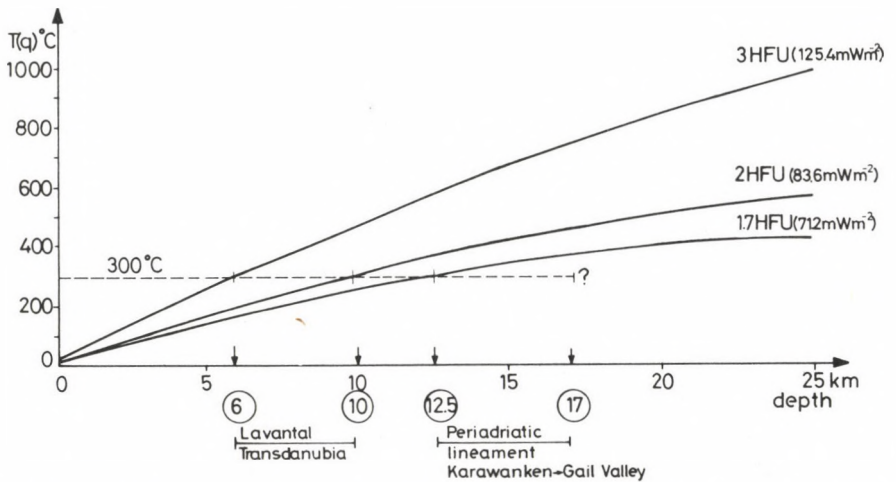


Fig. 7. Temperature depth curves in case of different surface heat flow after Haenel (1970) and the depth of the conductive layers in Transdanubia and the Eastern Alps

Periadriatic lineament much deeper, in 12.5–17 km (Ádám et al. 1984). In these depths the temperature is about 300 °C according to Haenel's temperature *vs.* depth function deduced from the different surface heat flows (Fig. 7). It is interesting to note that the depth to the conducting formation is greater in the Gail-valley than in the Karawanken lineament, in accordance with their heat flows. Of course, this result is only poorly supported by the sparse measurements.

At the present state of the research, none of the hypotheses can be unambiguously accepted on the basis of the mentioned arguments, nevertheless, in case of the Balaton-line (and the Periadriatic lineament), the probability of an electrolytic model is much greater.

### References

- Albu I, Ádám O, Majkuth T, Nemesi L, Tátrai M, Ráner G, Varga G 1983: Investigation of the main geologic profiles (in Hungarian). In: *Magyar Állami Eötvös Loránd Geofizikai Intézet 1982. évi jelentése*, 66–71.
- Ádám A 1969: Appearance of electrical inhomogeneity and anisotropy in the results of the complex electrical exploration of the Carpathian Basin. *Acta Geod. Geoph. Mont. Hung.*, 4, 187–197.
- Ádám A 1971: Determination of Paleozoic graphitic formations under electrically shading layers in the Hungarian basin using magnetotelluric method and some genetic conclusions (in Hungarian). *Geonómia és Bányászat*, 4, 297–308.
- Ádám A 1981: Statistische Zusammenhänge zwischen elektrischen Leitfähigkeitsverteilung und Bruchtektonik in Transdanubien (Westungarn). *Acta Geod. Geoph. Mont. Hung.*, 16, 97–113.
- Ádám A 1982: Deep fractures, conducting dykes and 2D models (in Hungarian). *Magyar Geofizika*, 23, 166–177.
- Ádám A, Verő J 1964: Ergebnisse der regionalen tellurischen Messungen in Ungarn. *Acta Techn. Hung.*, 47, 63–77.
- Ádám A, Wallner Á 1975: Influence of tectonics on the direction of induction arrows in the Carpathian Basin. *Acta Geod. Geoph. Mont. Hung.*, 10, 199–205.
- Ádám A, Márcz F, Verő J, Wallner Á, Duma G, Gutdeutsch R 1981: Magnetotelluric sounding in the transitional zone between the Eastern Alps and Pannonian Basin. *J. Geophys.*, 50, 37–44.
- Ádám A, Duma G, Gutdeutsch R, Verő J, Wallner Á 1984: Periadriatic lineament in the Alps by magnetotellurics (in Hungarian). *Magyar Geofizika*, 25, 136–150.
- Ádám O 1977: Deep structure of Transdanubian Midmountains and its foregrounds on the basis of geophysical results (in Hungarian). In: *M. Áll. Földtani Int. évi jelentése az 1977 évről*, 269–287.
- Berdichevsky M N, Dmitriev V I 1976: Distortion of magnetic and electric fields by near-surface lateral inhomogeneities. *Acta Geod. Geoph. Mont. Hung.*, 11, 447–483.
- Dövényi P, Horváth F, Liebe P, Gálfi J, Erki I 1983: Geothermal conditions of Hungary. *Geophysical Transactions*, 29, 3–114.
- Haenel R 1970: Interpretation of the terrestrial heat flow in the Rhinegraben. In: *Graben Problems*, Illies J H, Mueller S E eds, E. Schweizerbart'sche Verlagsbuchhandlung, Stuttgart, 116–120.
- Hermance J F 1973: An electrical model for the sub-Icelandic crust. *Geophysics*, 38, 3–13.
- Kovács S 1983: Major tectonic outline of the Alps (in Hungarian). *Általános Földtani Szemle*, 18, 77–135.
- Nemesi L, Hobot J, Varga G 1985: Telluric and magnetotelluric information about geological structure of Transdanubia (in present issue)
- Posgay K, Albu I, Petrovics I, Ráner G 1981: Character of the Earth's crust and upper mantle on the basis of seismic reflection measurements in Hungary. *Earth Evolution Sciences*, 3–4, 272–279.

- Quist A S, Marshal W L, Franck E V, v. Osten M 1970: A reference solution for electrical conductance measurements to 300 °C and 12 000 bars. Aqueous 0.01 demal potassium chloride. *J. Phys. Chem.*, 74, 2241–2243.
- Stegena L, Géczy B, Horváth F 1975: Late Cenozoic evolution of the Pannonian Basin. *Tectonophysics*, 26, 71–90.
- Takács E 1968: Anomalous conductivity of the upper crust in the NW foreground of the Bakony Mountains. *Acta Geod. Geoph. Mont. Hung.*, 3, 155–160.
- Tátrallyay M 1977: On the interpretation of EM sounding curves by numerical modelling. *Acta Geod. Geoph. Mont. Hung.*, 12, 279–285.
- Varga G 1980: Study of geological basic profiles I. Report on telluric and MT measurements in 1979: In: *MÁELGI jelentés*. Manuscript in Hungarian, 10.
- Wallner Á 1977: The main features of the induction arrows on the area of the Transdanubian conductivity anomaly. *Acta Geod. Geoph. Mont. Hung.*, 12, 145–150.

## DEEP ELECTRICAL CONDUCTIVITY IN EASTERN SIBIRIA

A P SHILOVSKY<sup>1</sup>

[Manuscript received July 13, 1984]

Numerous magnetotelluric soundings have been carried out in the last twenty years in Eastern Siberia in the period range of exploration geophysics (0.5–800 s). Merely in Yakutia, in the Baikal rift zone and on the southern slope of the Aldan anticline approximately 2.5 thousand MTS have been performed. The obtained material is generally very inhomogeneous, but the high number of sounding curves enables to use statistical methods of processing to extract information about the deep electrical conductivity.

**Keywords:** Baikal rift zone; Eastern Siberia; crustal conductivity anomaly

The Siberian platform differs from other ancient platforms by the higher apparent resistivity of the sediments there, and this makes Eastern Siberia to a unique area from the point of view of the study of the deep structure of the Earth's crust by electromagnetic methods. The telluric currents flowing in the sedimentary cover shield the effects of deeper layers completely only in the Tunguz- and Lena-Vilyuy-syneclise, where the longitudinal conductivity of the sediments exceeds 500 mho. According to this situation, and the application of modern processing and interpretation methods enabled to investigate the deep structure of the Earth's crust in Eastern Siberia. Just here, on the Northern slope of the Aldan anticline one of the world's first crustal layers with enhanced electrical conductivity was discovered (Berdichevsky et al.). It is to be noted that at the Siberian platform the crustal layer with enhanced electrical conductivity gets the unique object for the investigation by the deep geoelectrics as information about the upper part of the Earth's crust is shielded by the conductivity of the sediments, and information about the weakly developed platform asthenosphere with a summarized longitudinal conductivity of 1000 mho is shielded by the conducting crustal layer.

In Yakutia 14 zones could be separated on the basis of the statistical averaging of the effective curves of the apparent resistivity by combining them according to their shapes which reflect the deep structure. Seven of these zones lie in the unfavourable area (Fig. 1). On the basis of the rest average curve of the apparent resistivity, adjusted for the regional galvanic effect and for the different longitudinal conductivity of the sediments (Fig. 2), the changes of the conductive crustal layer can be traced. From the

<sup>1</sup> I M Gubkin Institute of Petrochemical and Gas Industry, 117296 Moscow, USSR

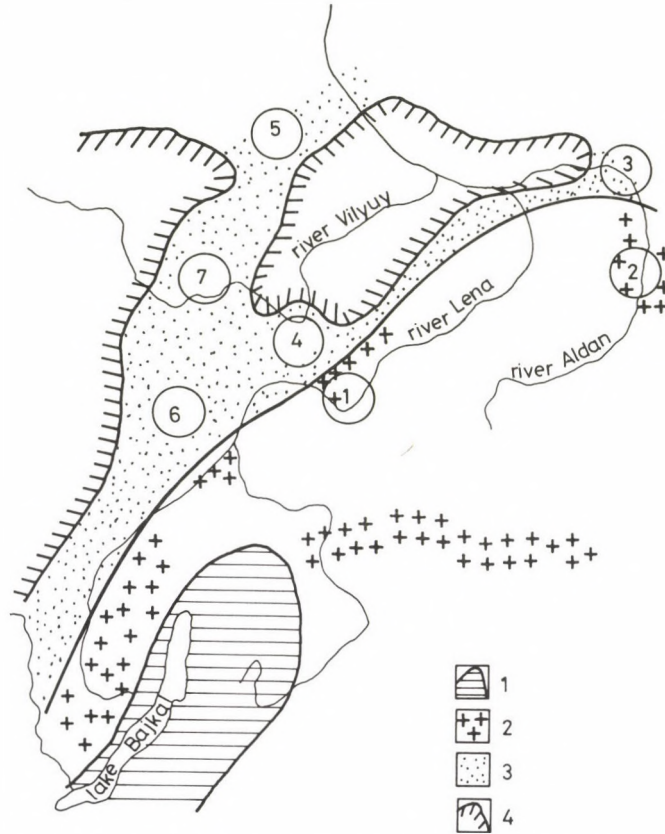


Fig. 1. Areas separated in Eastern Siberia by electromagnetic methods. Average curves for the zones 1-7 see in Fig. 2. 1: 700 mho and more, 2: 300-500 mho, 3: 200-300 mho, 4: unfavourable area

southern part of the area towards north, the summarized conductivity of the crustal layer varies from 600-700 mho to 200-300 mho, and the depth from 20-25 km to 30-35 km.

The schematic diagram representing the distribution of the electrical conductivity of the crustal layer, where, in addition to Yakutia, the Baikal rift zone and the Southeastern edge of the Siberian platform, are also included by published data, convinces on the strict genetic connection between crustal conductivity and tectonic activity. The electrical conductivity decreases when moving away from the Baikal rift zone where the crustal conducting layer has its strongest development (conductivity 1500 mho and depth 15 km). This fact confirms the hypothesis about the hydrothermal origin of the enhanced conductivity which is based on the up-to-date assumption that

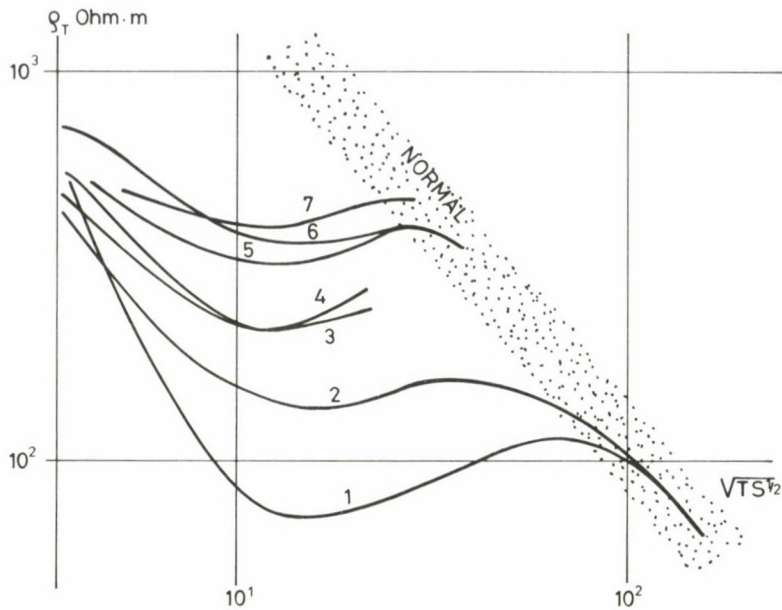


Fig. 2. Typical MTS curves of the areas separated in Fig. 1

there are supercritical fluids in the lower parts of the Earth's crust. In the Baikal rift zone the active asthenosphere is also "looking through" in addition to the crustal conducting layer, the former being in a depth of about 100 km.

### References

- Berdichevsky M N, Borisova V P, Budnov V P, Vanyan L L, Feldman I S, Yakovlev I Y 1969: The anomaly of crustal electric conductivity in Yakutia (in Russian). *Izv. Akad. Nauk SSSR, Fiz. zemli*, No. 10



## PROFESSOR ANTAL TÁRCZY-HORNOCH 85 YEARS



Professor Tarczy-Hornoch reaches his 85th birthday on October 13, 1985. On this occasion the community of Hungarian earth scientists wishes him continuing good health and quiet peaceful years.

Here only the most significant events during his long carrier should be metioned which spans exactly this century. After his universities in Leoben (Austria) he received the degree of mining engineer in 1923, in the next year of engineer of mining survey and of doctor techn, with a dissertation on "Neue Gesichtspunkte zur rechnerischen Lösung der Markscheideraufgaben". He was appointed professor at the High School of Mining, Metallurgy and Forestry in Sopron in 1926. During the half century to follow he initiated a number of projects at the oldest technical Alma Mater in Europe including a foreign language periodical with him acting as editor, the start of higher education in geodesy and geophysics and the foundation of research laboratories for geodesy and geophysics, the predecessors of the present Geodetic and Geophysical Research Institute of the Hungarian Academy of Sciences. He is well known all over the world due to several hundreds of publications and some books. He was awarded

many times both nationally and internationally including the Hungarian State Prize and the Kossuth Prize, Membership of the Hungarian, Austrian, Bulgarian, French and Polish Academies of Sciences, six times Doctor Honoris Causa and many others.

Two generations of earth scientists are happy in Hungary to have learned from Professor Tarczy-Hornoch. His central idea was always that honest work brings his fruits. His work, the Institute he founded, the Chair at the University in Miskolc which he led through many decades and also his one-time pupils will conserve his ideas and instructions.

*J Somogyi*

## PROFESSOR GYÖRGY BARTA 70 YEARS



Professor Barta ordinary member of the Hungarian Academy of Sciences, Head of the Geophysics Department of the Loránd Eötvös University, Budapest celebrates his 70th birthday this year. His numerous contributions to geophysics and to earth sciences, in general, as well as his organizational work and leading role in several international scientific bodies has long made him one of the internationally esteemed representatives of Hungarian science.

Professor Barta was born in Poprad (Slovakia) in 1915. He attended the L. Eötvös University from 1934 to 1939. He obtained his Ph. D. (*summa cum laude*) in geography, physics and mathematics from the University of Debrecen in 1947.

In 1939 he joined the Hungarian Institute of Meteorology and Geomagnetism and worked from 1940 till 1945 in the Ógyalla Observatory of this Institute. In the academic year 1941/42 he visited geomagnetic observatories in Germany and Denmark.

Dr Barta joined the Eötvös Lóránd Geophysical Institute in 1947 and organized first the Geomagnetic Observatory in Budakeszi (1946), then the more complex Geophysical Observatory in Tihany (1953–54). He also directed the new geomagnetic surveying of the country and, beside several papers, he published two books on the geomagnetic field and its variations in the territory of Hungary.

He obtained his C. Sc. and D. Sc. degrees from the Hungarian Academy of Sciences in 1952 and 1956, respectively. He delivered lectures at various Hungarian universities and in 1963 he was appointed a honorary professor of the Lóránd Eötvös University.

Professor Barta's most outstanding contributions concern the magnetic and gravity field of the Earth. He pointed out that the secular change of the magnetic field contains a period of about 50 years, emphasized and explained the asymmetric nature of the geomagnetic field and called attention to its possible connections with the gravity field and the internal structure of the Earth. Later on he postulated a global secular change of the gravity field and that of the geoid. In the 1970's he outlined the physical background of the geoidal figure. Recently he is engaged in the determination of the  $G$  (the gravitational constant). He published over 140 papers in various Hungarian and international periodicals, including such prominent journals as the *Zeitschrift für Geophysik*, *Boll. di Geofisica Teorica ed Applicata*, *Gerlands Beiträge zur Geophysik* and *Nature*.

Professor Barta delivered numerous lectures on his theories at several universities and scientific conferences: in Moscow, Paris, Berlin, Prague, Warsaw, Kiev, Firenze, Genova, Barcelona, Uppsala, Seattle to mention but a few.

The Hungarian Academy of Sciences elected him a corresponding member in 1970 and in 1982 he became an ordinary member. Prof. Barta has also been elected a member of the International Academy of Astronomy.

In 1971 he joined the Lóránd Eötvös University and since then he has been the Head of the Geophysics Department.

Professor Barta held or is holding responsible leading posts in several Hungarian and international scientific organizations, committees and councils. Some of his most important assignments include the 7-member presidential board of COSPAR (1971—1975), the chairmanship of Working Group 6 of the International Geodynamics Project (1971—1980), membership of the IAG Special Study Group No. 4. 21. He also served as chairman of the Geophysical Committee of the Hungarian Academy of Sciences, chairman of the Hungarian COSPAR committee, vice-chairman of the Hungarian KAPG committee and several others. He is on the editorial board of several scientific journals, including the *Acta Geodaetica*, *Geophysica et Montanistica Hungarica*. Professor Barta played an active role in founding the Hungarian Geophysical Society and since 1966 he is an Honorary Member of the Society.

In 1973 Prof. Barta was awarded the State Prize, one of the highest distinctions in Hungary. In addition he was also given the Eötvös medal (in 1966 by the Hungarian Geophysical Society), the Konkoly-Thege medal (in 1973 by the Slovakian Meteorological Society), the Steiner medal (in 1975 by the Hungarian Meteorological Society) and the Gauss and Humboldt medals (in 1977 and in 1984, respectively, both by the Scientific Academy of the GDR).

On behalf of his many associates, students, and friends in Hungary as well as abroad we wish Professor Barta health and fruitful activities for many years to come.

## Book reviews

---

J B MAYNARD: *Geochemistry of Sedimentary Ore Deposits*. Springer Verlag, Berlin, Heidelberg, New York, 1983. 149 figs. XI, 305 pages. Cloth DM 69,—, approx. US \$ 27.40. ISBN 3-540-90783-1.

The book covers according to the usual terminology the field of economic geology, more exactly the description and genetics of ore deposits where up-to-date geochemical principles play an important role. As sedimentary ore deposits — which are especially treated here — are generated by processes in which geochemistry plays a significant role, the choice of the title becomes understandable. Moreover the book does not deal with ore deposits produced by non-chemical processes, e.g. by mechanical breakage or by mainly biologic processes. In contrast, ore deposits of a mixed volcanic-sedimentary origin (e.g. exhalative deposits) are treated also here as chemical processes play a significant role in their formation.

The principle accepted for a rather long time, namely that ore deposits are no exceptional, isolated objects, but they came into being together with their surroundings, is consequently and excellently represented in this book, as in the treatment of different type ore deposits the sedimentological description of the connate complete sediment series is also given. In the geochemical-genetic description the means of the stable isotopic composition (S, C and O) as well as of the equilibrium diagrammes (Eh, pH, temperature and fluid composition as variables) are as much used as only possible, being already unavoidable means of the modern sedimentological interpretation.

For the sake of a uniform treatment, the single chapters (devoted to sedimentary deposits of a metal or of a group of metals) have a uniform structure: mineralogy, geochemistry, petrography, vertical sequence (with examples of existing deposits), theories of origin. The examples of the deposits are selected and concentrated according to types, i.e.

they contain a detailed presentation of the genetic types rather than an enumeration of the single deposits with some short description. The text is clear and easily understandable; it avoids complicated explanations, and if something is not yet understood, it is also said and not suppressed.

Following an introduction on general principles, seven longer chapters deal with the single sedimentary ore deposits according to the mentioned philosophy. These chapters include: iron (in two parts: iron-formations and ironstones); copper and silver (treated together); aluminium and nickel (in a single chapter, but in two different parts); manganese, uranium; lead and zinc (together, but in two sections: carbonate-hosted deposits and clastic-hosted deposits); volcanic-sedimentary deposits (again in two sections: deposits of divergent plate boundaries and deposits of convergent plate boundaries).

There are very few Hungarian references in the book. Only the chapters on aluminium and manganese refer to a few Hungarian explorers.

*P Kisházi*

W E GALLOWAY and D K HOBDDAY: *Terrigenous Clastic Depositional Systems*. Applications to Petroleum, Coal and Uranium Exploration. Springer-Verlag, New York—Berlin—Heidelberg—Tokyo, ISBN 0-387-90827-7; 237 figures, 423 pages. ISBN 3-540-90827-7.

This comprehensive and major study on the terrigenous clastic depositional systems offers the following fourteen chapters:

1. The fuel-mineral resource base.
2. Approaches to genetic stratigraphic analysis.
3. Alluvial-fan systems.
4. Fluvial systems.
5. Delta systems.
6. Clastic shore-zone systems.

7. Terrigenous shelf systems.
8. Terrigenous slope and basin systems.
9. Lacustrine systems.
10. Eolian systems.
11. Depositional systems and basin hydrology.
12. Coal.
13. Sedimentary uranium.
14. Petroleum.

This book is an authoritative study and a definitive account by two prominent internationally recognised experts of the fuel-mineral geology. Such a work is of substantial importance when increasingly sophisticated exploration concepts and technology must be employed to maintain the world's energy requirements. The fuel and mineral resources are bound to sedimentary rocks so any procedure or method to help understand and predict the attributes of the sedimentary units contributes to the discovery of coal, uranium and petroleum resources.

Probably the grouping of coal, uranium and petroleum appears to be somewhat artificial, however, the basic premise is that they are common genetic attributes shared by all three and the sedimentological principles are fundamentally similar and factors are found to be important including deposition and environment characteristics. Reviewing depositional systems with emphasis on field and subsurface recognition, the ground water-flow systems are analysed how they evolve in relation to changing structural configuration and consolidation. In controlling the distribution of fuel-minerals, the paleoenvironment setting, emplacement and subsequent transformations are considered as of primary importance.

This excellent book with many top quality figures will be a highly useful source of reference for all those involved in fuel-mineral exploration. It is directed towards exploration and development geologists and geophysicists as well as interpreters of geological and geophysical sections for an up-to-date stratigraphic analysis.

*I Polcz*

*Dissolved loads of rivers and surface water quantity/quality relationships.* IAHS Publication No. 141. (Hamburg IUGG/IAHS Symposium Proceedings)

In recent years the attention has been directed to the erosion and yield of particulate material. However, it has emerged from many past and present investigations undertaken in earth sciences and related disciplines that solid matter transport represents only one, and sometimes a subordinate, component of river loads and that a comprehensive

discussion of continental erosion should also feature the processes of solute release and the magnitude of dissolved yields.

An opinion has been emerging within IAHS and its commission on Continental Erosion (ICCE) that the time is ripe for a meeting focussed on the dissolved loads problem. Thus the "Dissolved loads of rivers and surface water quantity/quality relationships" IAHS Symposia in the framework of the XVIII General Assembly of International Union of Geodesy and Geophysics (IUGG) provides an opportunity to take stock of recent progress in the study of dissolved loads of rivers.

These proceedings of 35 papers of the Symposia are divided into three major sections. In each one the first paper provides a more general review of the theme. Spatial and temporal variations in dissolved loads and solute concentrations are discussed first and individual papers highlight global, continental, regional and more local spatial variations. Studies in the United States, Africa, India and Europe are reported and findings from contrasting environments, including glaciated mountains and agricultural lowlands, are presented. Within this section, papers also focus on the temporal response of dissolved substances and loads to discharge and other factors which revealed through detailed investigation of individual storm events and by statistical analysis of records from more routine water quality monitoring.

A second group of papers is concerned with sources of dissolved material, solute budgets and denudation. Atmospheric and geological sources of stream solutes are considered and the quantification of weathering reactions, undertaken in one paper for sandstone and shale lithologies, emerges as a particularly worthwhile objective in studies of solute production. The important, but sometimes overlooked influence of biological controls on chemical mass balance is stressed in several papers and the theme of solute budgeting is addressed not only for the river but also for lacustrine and estuarine environments. The magnitude of dissolved and particulate loads and the balance of chemical and mineral denudation are also discussed in this section at countrywide and drainage basin scales.

Application of surface water quantity/quality relationships to the utilization and management of water resources constitutes a third theme, and this group of papers encompasses a discussion of the impact, in general, of hydraulic projects and more specific studies of the consequences of river regulation and the role of stormwater detention basins in quality control. Several papers isolate the impact of

agricultural land drainage on transport of nutrients, especially nitrate, in rivers and numerical solution technique described in one paper and based on the coupling of models of hydrological and chemical behaviour, would seem to offer a very promising method assessing the impact of particular agricultural practices. The use of real time forecasting models is also discussed in the context of other chemicals derived from urban environments. Some attention is given in this section to more general principles underlying the monitoring and calculating strategies which may be employed to determine chemical fluxes. The volume is appropriately concluded by a consideration of longer-term human impacts on water quality as revealed by two studies of the heavy metal content of lake sediments.

After this general summary, some conclusions will be drawn subsequently. In the general review of the first theme Walling and Webb assembled values of mean annual total dissolved loads from 490 rivers located throughout the world and these data have been used to review the general characteristics of dissolved load transport. On the basis of the sample, it may be suggested that the dissolved loads of world rivers typically lie in the range  $5\text{--}100\text{ t km}^{-2}\text{ year}^{-1}$ . The mean load associated with the 490 rivers is  $38.8\text{ t km}^{-2}\text{ year}^{-1}$ . A number of workers have pointed out the general influence of climate embodied in a positive relationship between annual dissolved load ( $D$ ) and mean annual runoff ( $Q$ ). A similar trend is gained from the global data set assembled:  $D = 3.3 \cdot Q^{0.385}$ . Their conclusion is that the production of an acceptable map of global variations in dissolved loads should await the extension of measurement activity to areas of the world for which little or no data are available, and further multivariate analysis of the influence of climate, geology and other physiographic factors would be facilitated by the collection of data from relatively small basins exhibiting essentially homogeneous conditions.

According to Aurada, the average ionic runoff amounts to  $3.6$  or  $4.3 \cdot 10^9\text{ t} \cdot \text{year}^{-1}$  and the average rate of the chemical denudation to  $1.1$  or  $1.3\text{ g s}^{-1}\text{ km}^{-2}$ . The estimated global anthropogenic ionic input of  $0.7 \cdot 10^9\text{ t} \cdot \text{year}^{-1}$  in local cases leads to disturbances of the stability in hydrological design of structures and measures taken to influence processes. Investigating the solute yield from a glacierized high mountain basin Collins showed that the relationship between load and discharge is nonlinear, and middle-range flows accounts for the highest transport of solute load. The annual gross cationic denudation rate was estimated as  $478.1\text{ mg m}^{-2}\text{ year}^{-1}$ , which is significantly higher than

continental average. Basins of various sizes have been compared by Davis and Keller to examine behaviour of chemical and hydrological patterns under different geological and climatic conditions. These were independent of basin size. Cyclical patterns of change was the main behaviour observed in the study basins. The driving mechanism was considered to be the same in small and large areas and is related to seasonal changes which are themselves of a cyclic nature. Fehér concluded that a particular water quality component can be substituted by values computed from regression functions only if the relative error for the comparison of computed and measured data at calibration is less than 10% and the relative standard deviation of errors is less than 10%. Historical data collected at 88 long-term water quality sites were evaluated by Steel and regression relationships between major inorganic constituent concentrations and specific conductance or discharge were developed. Water quality conditions also were related to regional geological features and physiographic provinces.

In the first paper of the second theme Meybeck reviewed the atmospheric input and river transport of dissolved substances topic. He concluded that new estimates of natural world average for rain and river composition can be given for 10 elements and 18 specific forms, and from these the following contributions of natural wet and dry fallout can be calculated to the global river transport to the ocean: Si, 4%; Ca, 6%; Mg, 19%; Na, 53%; K, 27%; Cl, 72%; S, 42%; P, 11%; N, 170%; org C, 41%. Cycles of marine salts contribute to the average natural fallout rates over the exoreic part of the continents as follows: Ca, 40%; Mg, 76%; Na and Cl, 100%; K, 53%; and S, 46%. The remaining part of this fallout is of continental origin. Bennett presents a hybrid one-layer/two-layer kinematic transport model to compute nutrient and sediment budgets for three zones of the tidal Potomac. Hasholt investigated the dissolved and particulate load in Danish water courses. It is concluded that the dissolved component contributes the greatest part of total loads in Danish rivers, and this contribution is largest in the eastern part of the country in spite of lower runoff values. The main trends exhibited by load values are in good accordance with geological background and the landscape evolution.

As the review paper of the third theme Gras, Albigat and Gosse examined the effects of hydraulic projects and their management on water quality. All hydraulic projects, including those to meet quantitative needs (navigation, irrigation, flood control) have a definite effect on the quality of water.

The criteria relating to water quality differ from one use to another, and even for the same application, various criteria may be in conflict. Mathematical models allow these problems to be analysed with respect to the estimation of effects, or to the improvement of the design and selection of proper management. It is useful to include fish resources in the discussion since they provide an overall reflection of environmental quality.

Balland presented different methods for quantifying nutrient loads in rivers. He concluded that the accuracy of load computation is directly dependent on the amount of data available, and the author recommended comparative testing of the different techniques.

Vaussade and Prat propose a numerical model which is based on a conceptual hydrological model and simulates nitrogen transformations and transfers for polycrop basins and non-point source exports. After calibration and validation using experimental data from a small basin in southwest France, the model is used to show the influence of various phenomena on water quality, including leaching, temperature, fertilizer use and crop type.

Kovács and Pintér discussed the evolution and development of observation networks on the volume and quality of water resources in Hungary, and the establishment and modernization of the national quality monitoring network. Research and development has been aimed at evaluating and improving the information content of the data base including correlation of observation parameters, potential completion of records, trend analysis of quality changes, effect of sampling frequency, impacts of surface runoff and flood waves on water quality.

Marivoet compared four methods for forecasting fluoride and chloride concentrations of a safety reservoir used in drinking water supply. The first model was a single ARMA model. The second and third methods were based on dilution relationships. A transfer function-noise model with the reciprocal of river flow as input and the concentration as output was proposed as a fourth. A simple rainfall-runoff model was introduced to forecast future runoffs. The transfer function-noise model yielded the best results for short term forecasts and the dilution models for long term forecasts.

*J Fehér*

R KELLER ed.: *Hydrology of humid tropical regions*. Aspects of tropical cyclones. Hydrological effects of agriculture and forestry practice. (Proceedings of the Hamburg Symposium 1983, organized by the IAHS International Commission on Surface Water and cosponsored by UNESCO) IAHS Publ. No. 140, 1983 468 + XI pages

The book contains fourty papers presented at the Symposium on "Hydrology of Humid Tropical Regions with Particular Reference to the Hydrological Effects of Agriculture and Forestry Practice" during the XVIIIth General Assembly of the Geodesy and Geophysics at Hamburg, 15-17 August 1983. The Symposium was organized by the IAHS International Commission on Surface Water and cosponsored by UNESCO.

The volume is devoted to various principal aspects of hydrology of the humid tropical regions. A concise introduction is given in the heading WMO paper dealing with general features of operational hydrology of these regions. The tropical papers deal with: hydrological aspects of tropical cyclones, hydrological regions of the tropics, relation of land use and hydrology, water balance and regime, inadequate data and hydrological models — composing the five sections of the book.

Since it is not possible to deal with each of the papers individually, only some of the more significant aspects emphasized in various works shall be mentioned. The first group of papers consists of contributions on hydrological aspects of tropical cyclones, originally planned as a special workshop. The second group of papers in this volume deals with the hydroclimatology of humid tropics. The hydrological regional differentiation and basic information given of the five papers of this section can be used in applied studies.

Thirteen papers covering land-use related studies give a wide scope of ecological impact of different human activities. Effects of deforestation and the general role of forest and agricultural practices are tackled and enlightened from many sides.

Less contributions were received for the section dealing with water balance and regime. These papers give additional information on hydroclimate of particular regions.

The title hydrological models unites a large diversity of papers, unquestionably very valuable among them. Some items indicate useful practical

results and suggest water resources development, flood protection and agricultural (irrigation) applications of the models. The reader will not find a clear answer in these thirteen papers for the principal questions, whether there is a difference between the hydrology of the tropics and the hydrology of temperate regions and whether models developed for different climatic conditions can be directly transferred to humid tropical regions.

In the last decades hydrological science has focussed attention on the arid zones rather than on

humid tropical areas. There is therefore little hydrological knowledge about humid tropical regions and any attempt to change this situation is in fact a valuable contribution to the hydrology of these zones and in the same time serves the interests of economic development and cultivation of tropical regions. That is why the Hamburg Symposium and the publication of this volume is welcomed and very much appreciated.

*G Bálint*

PRINTED IN HUNGARY  
Akadémiai Kiadó és Nyomda, Budapest

- treble underlining: bold-face italics
- red underlining: Greek letters
- green underlining: script letters.

Rules for mathematical-physical notations:

- trigonometric, logarithmic, analytic symbols, symbols for units and functions are in roman type (not underlined)
- letter symbols in mathematical and physical formulas, scalars, and subscripts of algebraic and physical quantities are in italics (underlined)
- vectors, matrices, operators in probability theory are in bold-face roman type (double underlining)
- tensors, operators and some special functions are in script letters (green underlining). These cannot be bold.
- Greek letters (red underlining) cannot be bold or extra bold type (thus they cannot be used for vectors or tensors)
- void upper lines e.g. for vectors
- avoid possible confusion between o (letter) and 0 (zero), l (letter) and 1 (one),  $\nu$  (Greek nu) and  $v$ ,  $u$  (letters) etc.
- explain ambiguous or uncommon symbols by making marginal notes in pencil
- be careful about superscripts and subscripts
- formulae must be numbered consecutively with the number in parentheses to the right of the formula. References in text to the equations may then usually be made by the number in parenthesis. When the word equation is used with a number, it is to be abbreviated, Eq. or Eqs in the plural
- the International System of Units (SI) should be used.

Authors are liable for the cost of alteration in the *proofs*. It is, therefore, the responsibility of the author to check the text for errors of facts before submitting the paper for publication.

3. *References* are accepted only in the Harvard system. Citations in the text should be as:

... (Bomford 1971) ... or Bomford (1971)

... (Brosche and Sündermann 1976) ...

... (Gibbs et al. 1976b) ...

The list of references should contain names and initials of all authors (the abbreviation et al. is not accepted here); for *journal articles* year of publication, the title of the paper, title of the journal abbreviated, volume number, first and last page.

For *books* or *chapters in books*, the title is followed by the publisher and place of publication.

All items must appear both in the text and references.

Examples:

Bomford G 1971: *Geodesy*. Clarendon Press, Oxford

Brosche P, Sündermann J 1976: Effects of oceanic tides on the rotation of the earth. Manuscript. Univ. of Bonn

Buntebarth G 1976: Temperature calculations on the Hungarian seismic profile-section NP-2. In: *Geoelectric and Geothermal Studies (East-Central Europe, Soviet Asia)*, KAPG Geophysical Monograph. Akadémiai Kiadó, Budapest, 561–566.

Gibbs N E, Poole W G, Stockmeyer P K 1976a: An algorithm for reducing the bandwidth and profile of a sparse matrix. *SIAM J. Numer. Anal.*, 13, 236–250.

Gibbs N E, Poole W G, Stockmeyer P K 1976b: A comparison of several bandwidth and profile reduction algorithms. *ACM Trans. on Math. Software*, 2, 322–330.

Szarka L 1980: Potenciáltérképezés analóg modellezéssel (Analogue modeling of potential mapping). *Magyar Geofizika*, 21, 193–200.

4. *Footnotes* should be typed on separate sheets.

5. *Legends* should be short and clear. The place of the tables and figures should be indicated in the text, on the margin.

6. *Tables* should be numbered serially with Roman numerals. Vertical lines are not used.

All the illustrations should contain the figure number and author's name in pencil on the reverse.

*Figures* will be redrawn. Therefore the most important point is clearness of the figures, even pencil-drawings are accepted (with a duplicate).

*Photographs* and *half-tone* illustrations should be sharp and well contrasted.

If a specific reduction or enlargement is required, please indicate this in blue pencil on the figure.

The editors will send information to the first author about the *arrival* and acceptance of the papers. A galley proof is also sent to the first author for *correction*. Hundred *offprints* are supplied free of charge.

Periodicals of the Hungarian Academy of Sciences are obtainable  
at the following addresses:

**AUSTRALIA**

C.B.D. LIBRARY AND SUBSCRIPTION SERVICE  
Box 4886, G.P.O., Sydney N.S.W. 2001  
COSMOS BOOKSHOP, 145 Ackland Street  
St. Kilda (Melbourne), Victoria 3182

**AUSTRIA**

GLOBUS, Höchstädtplatz 3, 1206 Wien XX

**BELGIUM**

OFFICE INTERNATIONALE DE LIBRAIRIE  
30 Avenue Marnix, 1050 Bruxelles  
LIBRAIRIE DU MONDE ENTIER  
162 rue du Midi, 1000 Bruxelles

**BULGARIA**

HEMUS, Bulvar Ruszki 6, Sofia

**CANADA**

PANNONIA BOOKS, P.O. Box 1017  
Postal Station "B", Toronto, Ontario M5T 2T8

**CHINA**

CNPICOR, Periodical Department, P.O. Box 50  
Peking

**CZECHOSLOVAKIA**

MAD'ARSKÁ KULTURA, Národní třída 22  
115 66 Praha  
PNS DOVOZ TISKU, Vinohradská 46, Praha 2  
PNS DOVOZ TLAČE, Bratislava 2

**DENMARK**

EJNAR MUNKSGAARD, Norregade 6  
1165 Copenhagen K

**FEDERAL REPUBLIC OF GERMANY**

KUNST UND WISSEN ERICH BIBBER  
Postfach 46, 7000 Stuttgart 1

**FINLAND**

AKATEEMINEN KIRJAKAUPPA, P.O. Box 128 SF-00101  
Helsinki 10

**FRANCE**

DAWSON-FRANCE S. A., B. P. 40, 91121 Palaiseau  
EUROPÉRIODIQUES S. A., 31 Avenue de Versailles, 78170  
La Celle St. Cloud  
OFFICE INTERNATIONALE DE DOCUMENTATION ET  
LIBRAIRIE, 48 rue Gay-Lussac  
75240 Paris Cedex 05

**GERMAN DEMOCRATIC REPUBLIC**

HAUS DER UNGARISCHEN KULTUR  
Karl Liebknecht-Straße 9, DDR-102 Berlin  
DEUTSCHE POST ZEITUNGSVERTRIEBSAMT Straße der  
Pariser Kommüne 3-4, DDR-104 Berlin

**GREAT BRITAIN**

BLACKWELL'S PERIODICALS DIVISION  
Hythe Bridge Street, Oxford OX1 2ET  
BUMPUS, HALDANE AND MAXWELL LTD.  
Cowper Works, Olney, Bucks MK46 4BN  
COLLET'S HOLDINGS LTD., Denington Estate Wellingbo-  
rough, Northants NN8 2QT  
WM. DAWSON AND SONS LTD., Cannon House Folkstone,  
Kent CT19 5EE  
H. K. LEWIS AND CO., 136 Gower Street  
London WC1E 6BS

**GREECE**

KOSTARAKIS BROTHERS INTERNATIONAL  
BOOKSELLERS, 2 Hippokratous Street, Athens-143

**HOLLAND**

MEULENHOF-BRUNA B. V., Beulingstraat 2,  
Amsterdam  
MARTINUS NIJHOFF B.V.  
Lange Voorhout 9-11, Den Haag

**SWETS SUBSCRIPTION SERVICE**

347b Heereweg, Lisse

**INDIA**

ALLIED PUBLISHING PRIVATE LTD., 13/14  
Asaf Ali Road, New Delhi 110001  
150 B-6 Mount Road, Madras 600002  
INTERNATIONAL BOOK HOUSE PVT. LTD.  
Madame Cama Road, Bombay 400039  
THE STATE TRADING CORPORATION OF INDIA LTD.,  
Books Import Division, Chandralok 36 Janpath, New Delhi  
110001

**ITALY**

INTERSCIENTIA, Via Mazzè 28, 10149 Torino  
LIBRERIA COMMISSIONARIA SANSONI, Via Lamarmora 45,  
50121 Firenze  
SANTO VANASIA, Via M. Macchi 58  
20124 Milano  
D. E. A., Via Lima 28, 00198 Roma

**JAPAN**

KINOKUNIYA BOOK-STORE CO. LTD.  
17-7 Shinjuku 3 chome, Shinjuku-ku, Tokyo 160-91  
MARUZEN COMPANY LTD., Book Department, P.O. Box  
5050 Tokyo International, Tokyo 100-31  
NAUKA LTD. IMPORT DEPARTMENT  
2-30-19 Minami Ikebukuro, Toshima-ku, Tokyo 171

**KOREA**

CHULPANMUL, Phenjan

**NORWAY**

TANUM-TIDSKRIFT-SENTRALEN A.S., Karl Johansgatan  
41-43, 1000 Oslo

**POLAND**

WĘGIERSKI INSTYTUT KULTURY, Marszalkowska 80,  
00-517 Warszawa  
CKP-1 W, ul. Towarowa 28, 00-958 Warszawa

**ROUMANIA**

D. E. P., Bucuresti  
ILEXIM, Calea Grivitei 64-66, Bucuresti

**SOVIET UNION**

SOJUZPECHAT — IMPORT, Moscow  
and the post offices in each town  
MEZHDUNARODNAYA KNIGA, Moscow G-200

**SPAIN**

DIAZ DE SANTOS, Lagasca 95, Madrid 6

**SWEDEN**

GUMPERS UNIVERSITETSOKHANDEL AB  
Box 346, 401 25 Göteborg 1

**SWITZERLAND**

KARGER LIBRI AG, Petersgraben 31, 4011 Basel

**USA**

EBSCO SUBSCRIPTION SERVICES  
P.O. Box 1943, Birmingham, Alabama 35201  
F. W. FAXON COMPANY, INC.  
15 Southwest Park, Westwood Mass. 02090  
READ-MORE PUBLICATIONS, INC.  
140 Cedar Street, New York, N. Y. 10006

**YUGOSLAVIA**

JUGOSLOVENSKA KNJIGA, Terazije 27, Beograd  
FORUM, Vojvode Mišića 1, 21000 Novi Sad

# **Acta Geodaetica, Geophysica et Montanistica Hungarica**

**VOLUME 20, NUMBERS 2—3, 1985**

EDITOR-IN-CHIEF

**A TÁRCZY-HORNOCH**

EDITOR

**J VERŐ**

EDITORIAL BOARD

**A ÁDÁM, GY BARTA, B BÉLL, P BIRÓ,  
L KAPOLYI, F KOVÁCS, F MARTOS, A MESKÓ, D RÁCZ,  
J SOMOGYI, J ZÁMBÓ**

**Symposium on Chemistry of Mining  
and Hydrocarbon Recovery**

**Visegrád, 1983**



**Akadémiai Kiadó, Budapest**

AGGM 20 (2—3) 197—374 (1985) HU ISSN 0236-5758

# ACTA GEODAETICA, GEOPHYSICA et MONTANISTICA HUNGARICA

## A Quarterly Journal of the Hungarian Academy of Sciences

---

*Acta Geodaetica, Geophysica et Montanistica (AGGM)* publishes original reports on geodesy, geophysics and minings in English.

AGGM is published in yearly volumes of four numbers by

AKADÉMIAI KIADÓ

Publishing House of the Hungarian Academy of Sciences  
H-1054 Budapest, Alkotmány u. 21.

Manuscripts and editorial correspondence should be addressed to

AGGM Editorial Office  
H-9401 Sopron P.O. Box 5

*Subscription information*

Orders should be addressed to

KULTURA Foreign Trading Company  
H-1389 Budapest P.O. Box 149

## INSTRUCTIONS TO AUTHORS

*Manuscripts* should be sent to the editors (MTA Geodéziai és Geofizikai Kutató Intézet, AGGM Editorial Office, H-9401 Sopron, P.O.Box 5, HUNGARY). Only articles not submitted for publication elsewhere are accepted.

Manuscripts should be typewritten in duplicate, double-spaced, 25 lines with 50 letters each. The papers generally include the following components, which should be presented in the order listed.

1. Title, name of author(s), affiliation, dateline, abstract, keywords
2. Text, acknowledgements
3. References
4. Footnotes
5. Legends
6. Tables and illustrations

1. The *affiliation* should be as concise as possible and should include the complete mailing address of the authors. The *date of receipt* of the manuscript will be supplied by the editors. The abstract should not exceed 250 words and should clearly and simply summarize the most important methods and results. 5–10 significant expressions describing the content are used as *keywords*. Authors may recommend these keywords.

2. The *text* should be generally in English and as short and clear as possible. From Hungarian authors papers are also accepted in Hungarian.

The section heading should *not* be underlined or in capitals.

Please note that underlining denotes special types:

- single underlining: italics
- double underlining: bold-face roman

## CONTENTS

Principia of system-contemplation of the mining chemistry — <i>Bella L, Tóth J</i> .....	199
New dressing technology system of domestic carbonate iron ores — <i>Balla L sen.</i> .....	209
Explosion risk of coal dust (methane) — inert material mixtures — <i>Bánhegyi M, Egyedi J</i> .....	219
Some aspects to the comprehensive interpretation of filtration process-control and reservoir-chemical interactions — <i>Rácz D</i> .....	233
Interfacial and capillary phenomena in the displacement of oil by CO <sub>2</sub> — <i>Bauer K</i> .....	241
Redox method for the investigation of coal quality — <i>Mrs. Milley Tóth J</i> .....	253
Interfacial energy and pore structure — <i>Balla L, Milley Gy, Wagner O</i> .....	261
Rapid pyrolysis of Hungarian brown coals — <i>Gerej J, György I</i> .....	273
Examination of relations between osmotic properties of shales and drilling problems occurring during drill-out — <i>Berlinger H, Molnár J</i> .....	283
Reservoir damage by phase dispersion during multiple gas-water displacements — <i>Kretschmar H J, Colbe P</i> .....	293
Laboratory investigation of residual phase distribution in consolidated sandstones — <i>Weinhardt B, Heinemann Z</i> .....	303
Geochemical components of the effect mechanism of oil displacement with carbon dioxide — <i>Németh E</i> .....	319
Adsorption from binary liquid mixtures on the heterogeneous surfaces of actual solids; excess isotherms and heats of immersion — <i>Rudziński W, Zajac J</i> .....	337
The measurement of capillary pressure at a moving boundary — <i>Rácz G, Ludányi B</i> .....	355
Preparation and application of low solid containing and solid-free drilling fluids — <i>Dormán J</i> ..	365



The present number contains the text of papers presented at the Symposium on Chemistry of Mining and Hydrocarbon Recovery, organized by the Chemical Research Laboratory of Mining of the Hungarian Academy of Sciences in Visegrád, April 20–22, 1983.



## PRINCIPIA OF SYSTEM-CONTEMPLATION OF THE MINING CHEMISTRY

L BELLA<sup>1</sup> and J TÓTH<sup>2</sup>

The topic of Mining Chemistry is defined by the authors as: "The mining chemistry is the field of science consisting of chemical, physico-chemical and physical knowledge promoting the exploration, production and dressing of mineral raw materials."

Attempts have been made to systematize the knowledge and methods included in this definition. As a starting point the physical state of the mineral raw material has been taken, and further that it is expedient to fit the physico-chemical knowledge and methods to the mining activity.

The development of this system-hypothesis showed the different kinds of concrete theoretical and practical promoting role of the chemical science in the mining activities.

The mining chemistry is divided into two large groups:

I. Chemistry for mining of solid minerals

II. Chemistry for fluid mining.

The detailed description of these large groups is given. The authors emphasize that the outlined system-hypothesis of the mining chemistry is considered as an initiative, and reflections from the scientific community are welcome for necessary modifications and developments.

**Keywords:** analytical chemistry for mining; breaking; explosion risk; leaching; mine fire protection; mineral dressing; mining chemistry; mining safety; preparatory activity; thermal treatment; underground gasification

During the last decade we could witness the speedy development of connections between the mining and chemical sciences. This development is determined also today by efforts made to a more effective exploration, production and dressing of mineral raw materials. This statement hints also at the fact that the chemical sciences have an assisting role in mining, and at the same time by playing this function in the scope of applied chemistry specific, individual connections have been found which resulted in the development of a relatively independent sphere of science, of the mining chemistry.

In Hungary this fact was realized already some decades ago, so among others a book with the title "Oil Mining Chemistry" was published by László Gráf in 1951. The further development demanded by the up-to-date knowledges has been formulated in the decision No. 32/1980 by the Presidency of the Hungarian Academy of Sciences as follows:

<sup>1</sup> Central Development Institute for Mining, Budapest, Varsányi I u. 40-44.

<sup>2</sup> Chemical Research Laboratory for Mining of the Hungarian Academy of Sciences, Miskolc-Egyetemváros, H-3515

*“The interdisciplinary connections between the mining and other branches of sciences have to be further developed, in the direction of geological sciences promoting the recognition of mineral resources which give the object of mining activity, and in the direction of physico-chemical sciences promoting the development of mining products . . .”*

According to the above, the concept of mining chemistry can be determined as follows:

*The mining chemistry is the field of science consisting of chemical, physico-chemical and physical knowledge promoting the exploration, production and dressing of mineral raw materials.*

This work attempts to systematize the knowledge and methods included in the above definition. As a starting point the physical state of the mineral raw material has been taken, and further that it is expedient to fit the physico-chemical knowledge and methods to the mining activities. This systematizing principle has the disadvantage that it leads to overlappings and repetitions, but it has the advantage that the mentioned promoting role of chemical sciences will also be manifested, and even better than if mining knowledge would be attached to the already systematized physical chemistry.

The development of this system-hypothesis showed, too, of course, what kind of *concrete* theoretical and practical promoting role chemical sciences have in the mining activities.

According to the above, the mining chemistry itself can be divided into two large groups:

- I. Chemistry for mining of solid minerals
- II. Chemistry for fluid mining.

In Table I to XI the systematization is shown within these two groups and verbal supplements are given only to promote a better understanding. An other significant remark is that the systematization does not strive at completeness, but the efforts served for giving only a frame which could take up the knowledge omitted here or to be discovered later.

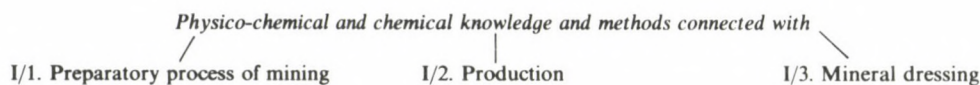
A possible classification of chemistry for mining solid minerals is shown according to the outlined principles in Table I. Within the activity of preparation of mining, the geological research incorporating different phases (exploratory, preliminary, detailed) precedes all other (see Table II).

In the field of analytical chemistry serving geological prospecting, the so called exploratory geochemical activity can be included, used to explore ores and soluble salts: analysis of vadose water, soil, vegetable ash, close-to-surface water. The classical inorganic chemical and quantitative instrumental analysis of different rock samples belongs also to this field. A special feature is here in comparison to other fields of analytical chemistry the necessity to adapt methods to the wide variousness of nature. This variousness appears

- in the variety of elements to be determined;
- in the variety of matrices;
- in wide concentration ranges, from 0.01 ppm to 100%.

**Table I**

## I. Chemistry in mining of solid minerals

**Table II**

## I/1. Preparatory process of mining

I/1.1 Geological exploration → Determination of mineral resources → I/1.2. Mine settlement

Inorganic chemical  
(to a lesser degree organo-chemical),  
classical and instrumental  
quantitative analysis

**Table III**

## I/2. Production

Exploration

Mining

I/2.1 Mining research

I/2.2 Mining safety

I/2.3 Corrosion protection

I/2.4 Breaking

Inorganic (partly organic)  
classical and instrumental  
chemical analysis

Elimination of surfacechemical  
or electrochemical effects  
on metal surfaces by means of  
inhibiting agents effecting  
through adsorption or chemi-  
sorption

More accurate determination  
of mineral resources      Planning of mining

The conditions inspired to develop a number of new methods of analytical chemistry, with special regard to methods permitting the determination of element(s) interesting from the point of view of the investigation, even when disturbing element(s) exist(s) in a concentration range of several orders of magnitude.



- electrochemical oxidation,
- colorimetry,
- change of electric conductivity,  
gas adsorption on the surface of semiconductors following the adsorption of gas from solutions,
- galvanic cell,
- absorption of infrared radiation,
- chemiluminescency.

Water analysis occurs as tracing at water intrushes, in the determination of hydrogeological conditions and in the identification of water reservoirs.

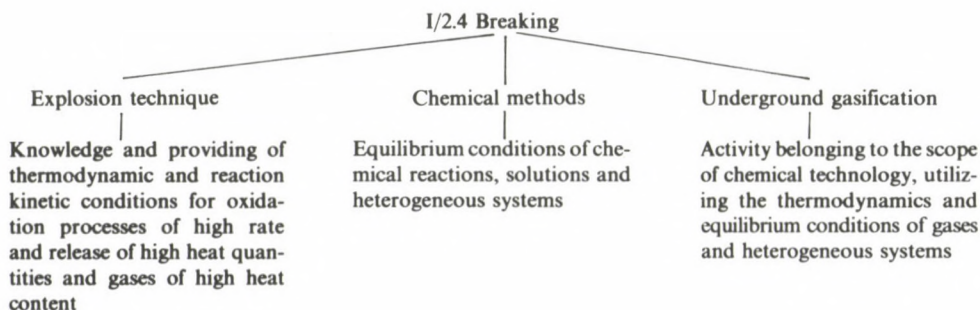
The quantitative analysis of dusts serves the determination of pathogenetic effects.

Within the scope of danger ward-off, the following concrete tasks can be listed:

- solution of rock solidification, supporting and water elimination problems by means of cementing (cement, bitumene, cement slurry), of chemicals (water glass +  $\text{CaCl}_2$  or  $\text{H}_3\text{PO}_4$ , sodium aluminate, *etc.*) and of plastic materials (aminoplast polymers), built up of hydraulic barriers in the defence against the expansion of explosions and mine fires (gypsum, anhydrite, fly ash), use of technologies applied in dust-protection (fixation of dust sediments by salt solutions and aqueous surfactant sprays),
- protection against mine fires of an auto-ignition, endogeneous or of other origin by antipirogene materials and inhibitors, production technology of different foam-extinguishers and determination of their effective mechanism,
- technology of extinguishing by inert gases and heat extraction, and
- elaboration of the rock solidification technology by freezing.

Within the chemical, physico-chemical methods and knowledge of breaking (see Table V), the blasting technique involves the operations of explosive production and control and the technique of shooting.

**Table V**



The chemical leaching and the underground gasification belong to the new "breaking" technologies being under development. Their development is urged by economic demands with special regard to the exploitation of ores and mineral deposits of poor quality being under the minable limit.

The development of chemical leaching technologies supposes the knowledge of equilibrium conditions of chemical reactions, solutions and heterogeneous systems. Some more interesting technologies are:

- the technology of sulfur melting and salt leaching through boreholes are already applied in the practice,
- the recovery of copper from copper ores and oxide ores under the minable limit by sulfuric acid leaching,
- the recovery technology of copper ores by bacterial leaching can be also mentioned here, as bacteria play only the role of a catalisator in the chemical process of leaching,
- the technology of underground gasification can be used mainly for the exploitation of poor quality coal deposits and the remaining coal beds in abandoned mines.

The interconnections of solid mineral mining and fluid mining chemistry is most obvious here, in the scope of breaking by chemical methods.

Activities belonging to mineral dressing, and the responding chemical and physico-chemical problems are summed up in Table VI. It should be remarked only that the same is valid for the analytical chemical methods of product qualification as mentioned concerning the geologic and mining exploration.

The different processes concerning the chemical and physico-chemical knowledge and methods belonging to the mineral dressing are so wide that they are summed up separately in Table VII.

The demands of environmental protection, the complex utilization of mineral resources and the elimination of the import of energy carriers urge the development of methods mentioned in Table VII if simpler solutions do not exist.

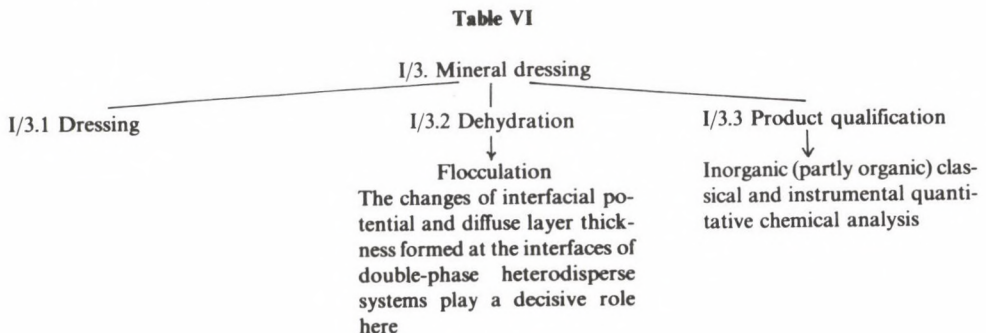


Table VII

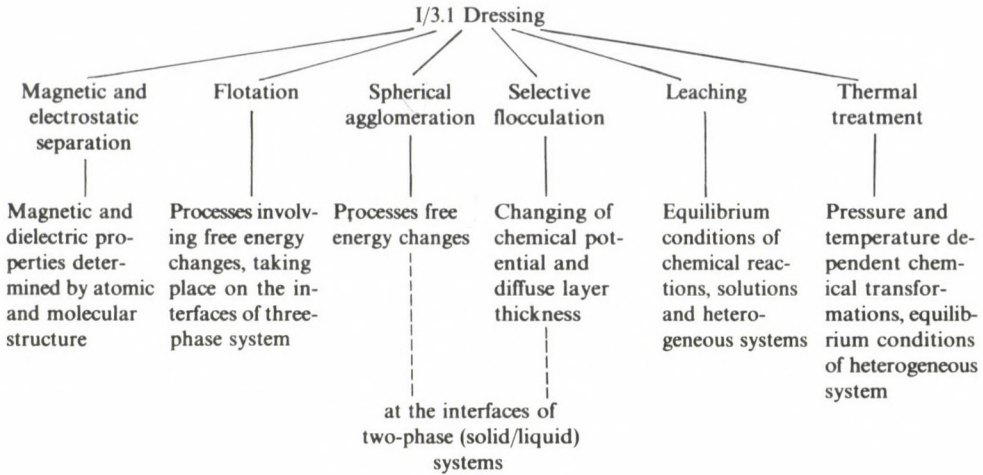
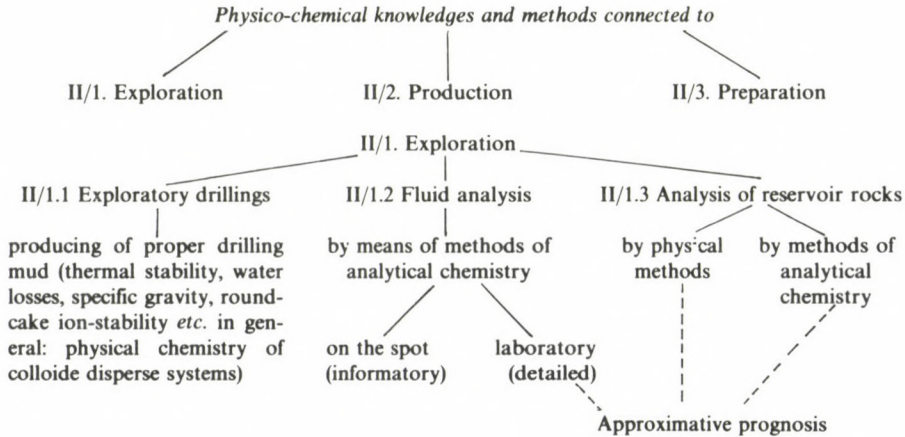


Table VIII

## II. Chemistry for fluid mining

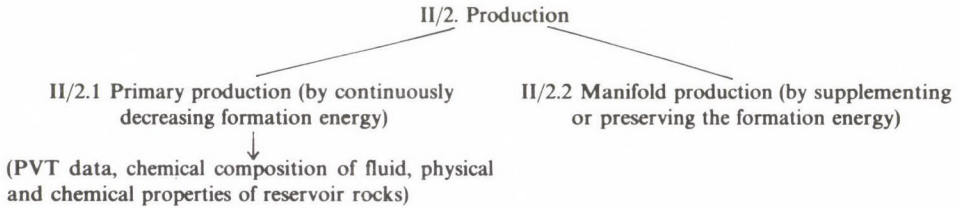


At last technologies based on pressure and temperature dependent chemical reactions are to be mentioned, being partly under development, which belong to the group of thermal processes, as especially the chloridizing roasting, sulfatizing roasting and hydro-thermal pyrite extraction.

The fluid mining chemistry is essentially in connection with two of the most important mineral raw materials, with the mining of crude oil and of deep water. The informatory and detailed chemical analysis of these fluids and the reservoir rocks are

grouped to the exploratory activities (see Table VIII) because these analyses belong chronologically to the first ones and their field of application is very important — together with a number of other geological and geochemical data — in preparing a prognosis of mineral raw materials. The cardinal problems in classifying the fluid mining chemistry are in connection with the production. This is obvious as the necessity of applying physical chemistry is most clearly emphasized just here. The basic principle of the classification was fitted here also to the two large groups of fluid recovery (see Table IX).

**Table IX**



Concerning the manifold (several times repeated) production (see Table X), it is to be remarked that a single or a multiple phase flow is established, of course, in the primary production process, too, but this flow is influenced only by the production process itself (by its rate) so besides hydrodynamical knowledge the need to apply any other field of sciences is only a peripheral one. In case of manifold production, the situation is radically different. The injected system(s) not only supplement(s) or preserve(s) the formation energy but as compared to the primary production, the interfacial energies are also substantially changed, and as a consequence, significant physico-chemical changes take also place in the internal phases. These possible phenomena are outlined in Table X. An important remark belongs here, too, namely that the manifold fluid mining is typically the mining process connected to which the specific, individual rules and relative independency of the fluid mining chemistry emerged. So e.g. only the fluid mining chemistry deals with the problem how the interfacial free energies and chemical potentials may or must be changed in a single or multiphase flow, at reservoir pressure and temperature, in order to make the exploitation of mineral raw material most effective.

At last, in Table XI, the most important problems belonging to the preparatory activities are schematically grouped according to the concrete appearance form of fluid mineral raw materials (gas, oil, water). Processes necessary before the transportation to the customers have been grouped into the sphere of preparatory activities.

At last, it should be emphasized that the outlined system-hypothesis of the mining chemistry is considered only as an initiative, and reflections from the scientific community are welcome for necessary modifications and developments.

**Table X**

II/2.2 Manifold production (by supplementing or preserving the formation energy)

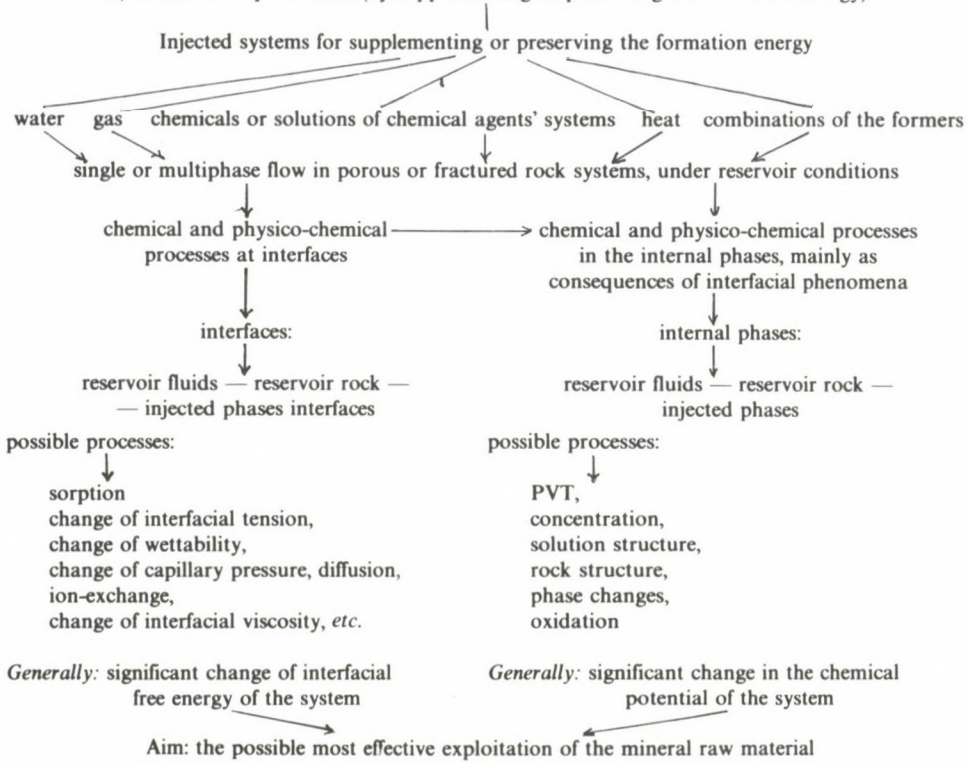
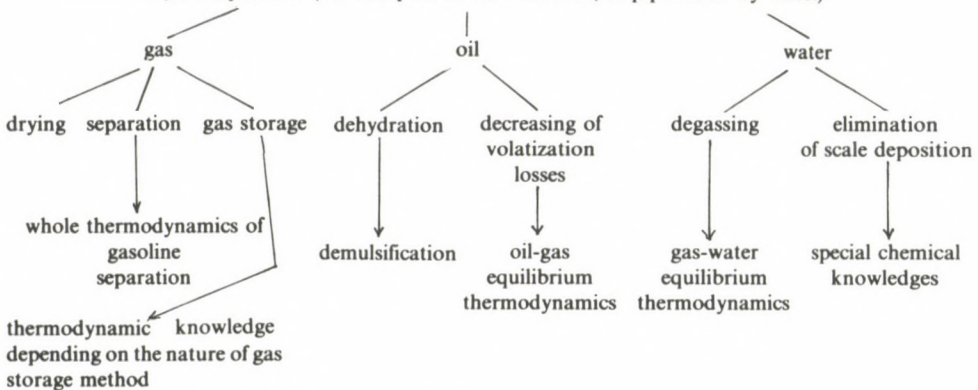


**Table XI**

II/3. Preparation (for transport to the consumer, in pipeline or by wheel)



**References**

Gráf L 1951: Oil Mining Chemistry (in Hungarian). Nehézipari Könyv- és Folyóiratkiadó Vállalat, Budapest



## NEW DRESSING TECHNOLOGY SYSTEM OF DOMESTIC CARBONATE IRON ORES

L BALLA sen.<sup>1</sup>

Recently in mineral dressing, the magnetic separation in enriching iron ores has spread everywhere, where it became possible to separate the strongly magnetic iron ores from that of poorly magnetic ones by means of strong magnetic fields. A particularly essential change happened with the prospect of strong magnetic field separators. Equipments are produced which are capable for a sludge yield of 3000 m<sup>3</sup>/hour and to produce field strengths of 1.5–2.0 Tesla.

Dressing experiments were also made for poorly magnetic carbonate iron ores from Rudabánya (the value of mass susceptibility:  $\kappa < 7.5 \cdot 10^{-6}$  m<sup>3</sup>/kg) by means of magnetic separators of a high field intensity and of a high gradient.

On the basis of research results, a dressing family-tree and a technology can be described which contains the most appropriate alternative in modernizing the domestic iron ore dressing.

**Keywords:** carbonate iron ores; dressing technology; magnetic separation

### Geological environment

The only minable iron ore occurrence in Hungary is at Rudabánya. On the territory of the Rudabánya iron ore locality, siderite (FeCO<sub>3</sub>) containing iron ore (iron spar) was formed by hydrothermal metasomatism of Anisian dolomites belonging to the middle stage of Triassic, this is the primary ore and limonite (Fe<sub>2</sub>O<sub>3</sub> · 1.5H<sub>2</sub>O) containing iron ores (brown ironstones) from the near-to-ground oxidation of siderite (oxidation zone) are the secondary ones.

Siderite containing ores were also found in the dolomite lenses of sandstones belonging to the Lower Triassic. These ores have a basicity index < 1, therefore they were denominated as sour iron spars.

The primary products of the hydrothermal metasomatism were associated at the spot, in the last phase of their formation by sulfide and sulfate type minerals which contained mostly copper, lead, silver and barium.

The exploitation of limonite containing brown ironstones was finished in the early 1980s', and now only the siderite containing iron spars are in a minable quantity at disposal. The names brown ironstone, iron spar, sour iron spar, are of a local origin, and later they were used by other specialists, too. When the quantity of brown

<sup>1</sup> Iron Ore Works, Rudabánya

ironstone diminished and besides iron spar, the sour iron spar has appeared instead of iron spars, the names "basic carbonate iron ore" (basicity index:  $>1$ ) and "sour carbonate iron ore" (basicity index:  $<1$ ) were introduced in Rudabánya on a suggestion of the present author because these names express more accurately the properties and contents of the ores.

### The dressing technology of basic carbonate iron ores

Hungary was the first from socialist countries to carry out at Rudabánya in 1960 the dressing of 22% Fe containing basic carbonate iron ores (at that time the high mass of sour carbonate iron ores had not yet been known) by means of magnetizing roasting and magnetic separation by a low field intensity magnetic induction:  $<0.1 T$ . Up to now, 46% mass and 87% metal yield index have been reached which compared to the data of other mines are acceptable ones. From 460 kt of raw material fed a year, 210 kt concentrate of 42% Fe content was produced.

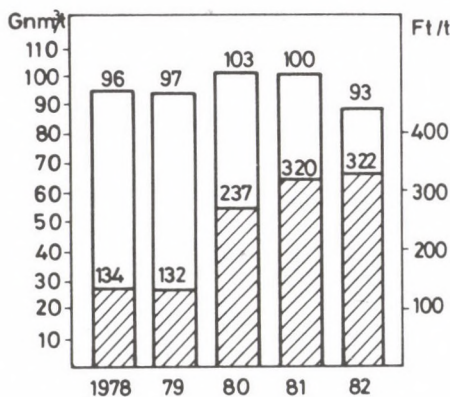


Fig. 1. The trend of natural gas consumption

The heat necessary for the roasting is provided by a natural gas burner. The magnetizing roasting is carried out at 800–900 °C, so the carbonate iron ore decomposes into  $Fe_2O_3/Fe_3O_4$  iron oxides. The fuel consumption is 1500  $Gnm^3/h$  for one furnace.

Due to a constant rise in prices, the use of natural gas became later a disadvantage of the technology considered previously as a modern one.

In Fig. 1 information is given about the natural gas consumption and about expenses of the last 5 years of iron dressing, it shows that the expenses increased significantly at about the same natural gas consumption.

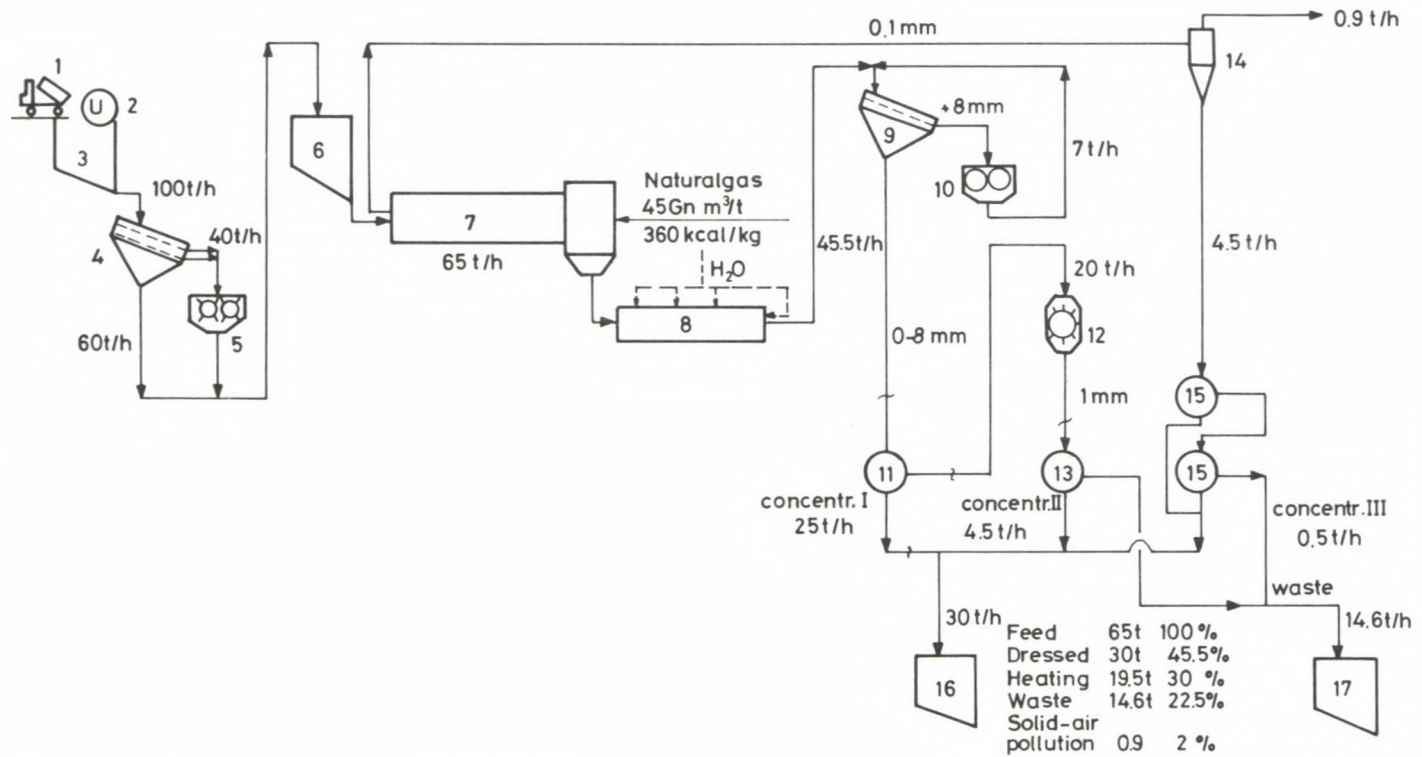


Fig. 2. The suggested family-tree of an iron ore dressing work. 1. Track, 2. Whipper, 3. Raw ore bin, 4. Twin vibrator (100.30 mm), 5. Roller crusher, 6. Raw ore storage bin, 7. Rotary roasting kiln, 8. Cooling cylinder, 9. Free-plate vibrator, 10. After-crusher, 11. Dry magnetic drum separator (0–8 mm product), 12. Prall-mill for middling crushing, 13. Dry magnetic drum separator (– 1 m drum separator), 14. Dust extracting cyclone plant for flue-gas, 15. Dry magnetic drum separator (two-stage flue-dust separation), 16. Product bin (2000 t), 17. Waste bin

The further disadvantages of iron ore dressing by magnetizing roasting can be summed up as follows:

- a) It demands a selective production from the mine, as for the dressing the sour carbonate iron ores of a high  $\text{SiO}_2$  content the method is unsuitable.
- b) The energy demand of the process is extremely high, 80% of the dressing expenses originate from the gas consumption. This fact became intolerable due to a continuous increase of the energy price, especially at present.
- c) Useful additional components of the ore (copper, barite *etc.*) suffer such chemical changes under the effect of heat treatment, that their recovery is problematic, i.e. they would be easier recoverable in their natural state. (At Rudabánya, there is a waste rock pile of about 2 million tons containing 0.2% Cu, 10% Fe and 15%  $\text{BaSO}_4$  produced by the iron ore dressing, from which the recovery of useful components is unsolved up to now.)
- d) The basicity of the dressed ore worsens as compared to the basicity of the fed ore.
- e) The dressed ore contains relatively a high concentration of Cu and  $\text{BaSO}_4$  which are metallurgically damaging components.
- f) The roasting of iron ores pollutes the environment. As an illustration Fig. 2 shows the family-tree of the present iron ore dressing technology.

### **The new technological system of carbonate iron ore dressing**

Initiatives to change the iron ore dressing method were made to enable a complex utilization of domestic iron ores, i.e. besides iron ore enrichment, also copper and barite are to be recovered. They were definitely connected to the existing dissipative heat transfer (roasting) dressing processes.

Essential ideas have been published:

Podányi (1979) who expressed his opinion about the metallurgical value of the dressed ores.

Gagyí Pálffy *et al.* (1963) showed the problems of a new-type iron ore dressing and the ways of developments (modification of roasting furnace masonry, introduction of natural gas heating, *etc.*). They made a proposal to recover the copper and barite from the waste.

Tóth (1965) proposed a combined method for the complex processing and suggested the flotation dressing of sour carbonate iron ores to recover the barite.

Gyurkó (1971) reached significant results on the field of flue dust utilization.

Kiss *et al.* (1978) carried out laboratory and plant experiments to recover barite from the waste rock pile composed of the mixture of separation wastes of flue dust.

Experiments have been carried out since the early sixties for the complex processing of Rudabánya iron ores, in a cooperation of National Ore and Mineral Mines and the Mining Research Institute (one of predecessors of the Central Mining

Development Institute). The present author started in 1976 laboratory experiments aimed at the elaboration of Fe dressing without roasting, and to determine the recoverability of other useful components.

Experiments were carried out in the laboratory of the Department for Mineral Dressing of the Technical University for Heavy Industry (NME), Miskolc, and in the Iron Ore Works of National Ore and Mineral Mines (OÉÁ), semi-plant experiments started in the Sajókeresztúr laboratory of the Research Institute for Iron Industry (VKI), plant experiments in the Iron Dressing Factory of OÉÁ.

The wet magnetic separation experiments were made by means of a high field strength, high gradient laboratory scale magnetic separator at the Department for Mineral Dressing of NME. Experiments were carried out also on dry ways. The results of dry and wet magnetic separation experiments (magnetic induction: 0.2–1.0 Tesla) were of a similar character.

The selection of sour carbonate iron ores by means of high magnetic field intensities can be reached by both ways so that the magnetic product is a concentrate of an enriched iron content, while in the non-magnetic product a material of enriched copper, barite, and perhaps, lead and silver content will be present (Dept. Min. Dressing 1979).

The iron ore concentrates got from the experiments were metallurgically examined. The success of iron ore dressing is decided namely in metallurgy, therefore the products of the roastless magnetic separation, as pre-dressed iron ores were used in the laboratory of VKI to prepare sinters, and the pre-dressed iron ores were tested in the sintering process on the basis of mixture composition used in the Borsod Ore Dressing Works (Research Institute for Iron Industry 1979)

The recovery of copper-sulfide and barite from the non-magnetic part of the products of magnetic separation enriched in copper and barite content, was carried out by means of a flotation process.

On the basis of these results a family-tree and technology of the dressing was suggested which contains the most proper alternative for modernizing the domestic iron ore dressing technology. The proposed technology is unambiguously applicable for the dressing of basic carbonate iron ores, and the basic experiments were also promising for sour carbonate iron ores (Balla 1980).

The experiments show that at least 30% Fe and 10% SiO<sub>2</sub> can be reached in case of properly attacked ores (particle size < 1 mm). The basicity of the dressed ores increases. The enriched copper ore and barite content in the non-magnetic products of the pre-dressing can be simply selected from the waste by means of known flotation methods.

It is not necessary to roast the pre-dressed ore at Rudabánya, it can be transported by rail for further dressing to the Borsod Ore Dressing Works carrying out the sintering, where the pre-dressed ore gets the heat amount necessary for carbonate dissociation on the Dwight-Lloyd line, and so the Fe content of the iron ore formerly

pre-dressed in wet separators increases from 30–33% to 46–50%, at a dressing degree of 1.5.

The most important apparatus of the new technology is the wet magnetic separator of a high intensity and high gradient.

The enrichment of the Fe content in iron ores of low susceptibility and magnetizability, can be carried out only by means of specially constructed devices (Mertins 1980), wet magnetic separators of a high magnetic strength magnetic induction  $\geq 0.1$  Tesla (the basic principle is shown in Fig. 3).

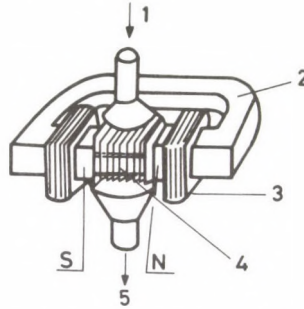


Fig. 3. The basic principle of high field intensity magnetic separators. 1. Sludge feed, 2. Iron core, 3. Coils, 4. Sheet matrix, 5. Sludge outflow

The essence of the device is that a bed formed of magnetizable materials, a special matrix, is placed into the magnetic field, in which the slightly magnetizable solid particles of the flowing sludge adhere while the perfectly unmagnetizable materials flow through. The efficiency of magnetic separation depends on the magnetic field strength, on the local high magnetic gradient got by the matrix formation, on the rate of flow of the material, and on the size of the matrix.

The  $F$  magnetic force can be simply written as:

$$F = \kappa \cdot H \cdot \frac{dH}{dx}$$

where  $F$  = magnetic force

$\kappa$  = a factor depending on particle volume, particle mass and mass-susceptibility

$H$  = magnetic field strength

$\frac{dH}{dx}$  = gradient of magnetic lines of force, i.e. the unidirectional change of magnetic field.

Modern iron ore dressing and complex utilization are unimaginable without the use of high intensities and high gradient magnetic separators. In Hungary there is no



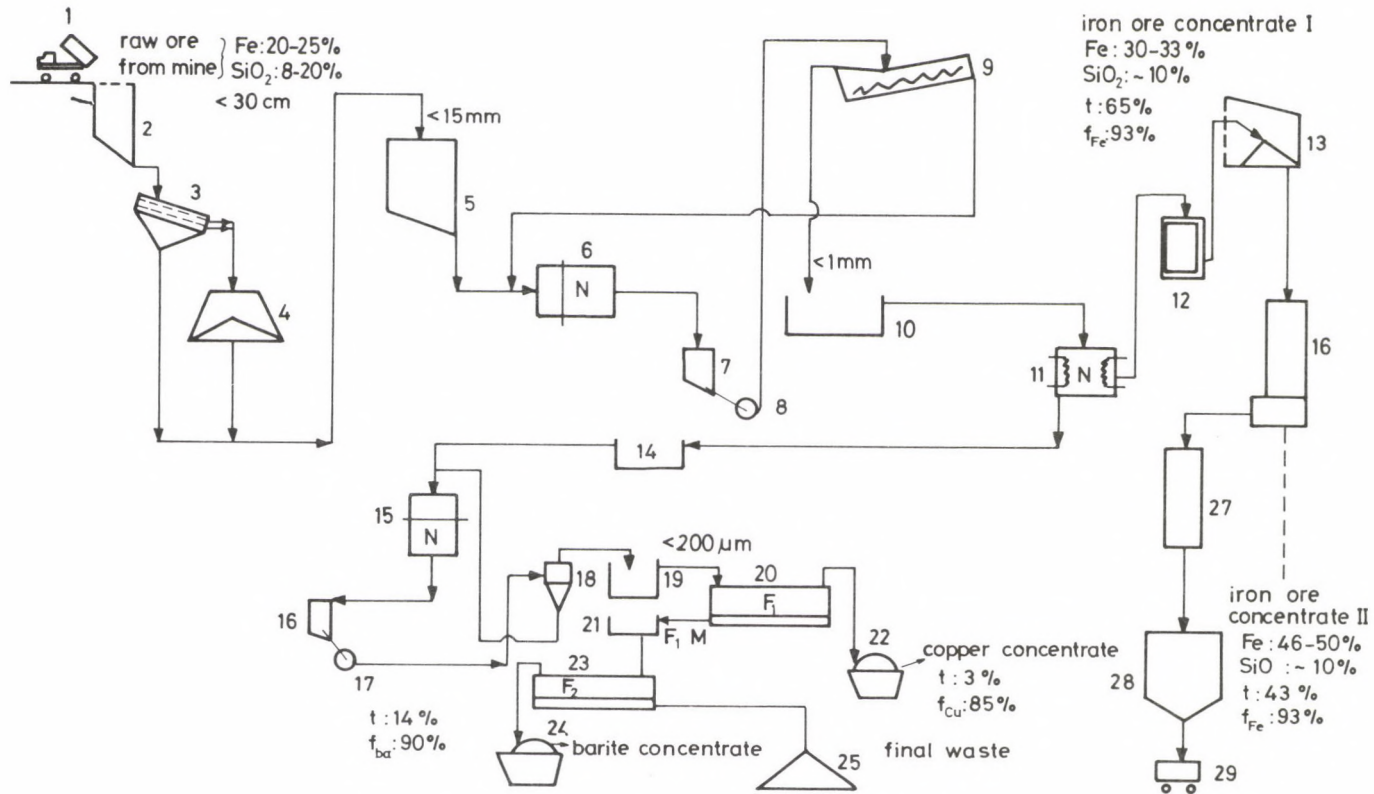


Fig. 5. The principal family-tree of the new technological system of basic and sour carbonate iron ore dressing. 1. Track, 2. Bin, 3. Vibrator, 4. One-crusher, 5. Bin, 6. Rod-mill, 7. Supply tank, 8. Sludge pump, 9. Akins classifier, 10. Container, 11. High field intensity, high gradient, wet magnetic separator, 12. Vibrating centrifuge for dehydration, 13. Iron ore concentrate 1. reservoir, 14. Waste sludge container, 15. Ball-mill, 16. Sludge pump, 17. Sludge pump, 18. Hydro-cyclone, 19. Mixing tank, 20. Flotation cells' line, 21. Tank, 22. Revolving filter, 23. Flotation cells' line, 24. Revolving filter, 25. Waste rock pile, 26. Rostering furnace, 27. Cooling cylinder, 28. Iron concentrate 2. bin, 29. Railway car

Separators can be built in wide capacity ranges. Separators are known for capacities from 0.5 t/h to 300 t/h or even higher (Mertins 1980).

The optimal choice of solid particles in the sludge is a very important criterion of the undisturbed separation process.

Figure 5 shows the suggested family-tree of the new technology system of domestic carbonate iron ore dressing (Balla 1980). The advantages of the new technology are:

- a) It does not demand selective production in the mine.
- b) The iron ore dressing consumes less energy because the roasting is eliminated.
- c) The useful additional components of the iron ore do not suffer change. They are enriched in the non-magnetic product, high purity sulfide and barite concentrates can be produced from them, so a significant surplus return can be reached from sales.
- d) The basicity of the iron ore concentrate varies between 1.8–2.0.
- e) In the concentrate the metallurgically damaging Cu and BaSO<sub>4</sub> contents decrease.
- f) Air pollution is eliminated and the closed system water economics exterminates the water pollution, too.
- g) Machines necessary to the new technology are widely known.
- h) It is not necessary to destroy the machines of older technology, because they can be used for other useful purposes, e.g. the roasting furnaces for roasting the coars-grained, classified aglohematites of poor quality.
- i) The high intensity magnetic separation may be the first ore dressing process when the Rudabánya iron ores would be processed for prerduced furnace-pellets.

As a summary, the modernization and the extension of the ore dressing factory at the only domestic iron ore site is advisable. The Rudabánya ore — in spite of its low quantity — has the great advantage that it contains slag formers necessary to smelting in excess quantity, which otherwise have to take in the mixture in form of Ca- and Mg-carbonate.

The intermittent-duty, 1–3 t/h capacity high gradient magnetic separator manufactured for the Steel Union by the Department of Mineral Dressing of NME could give a significant help to the final elaboration of the plant technology. The results serve not only the fundation of the technology, but the development of a domestic machinetype, too.

## References

- Balla L 1980: Long-term development possibilities of iron ore mining (in Hungarian). *Érc- és Ásványbányászati múzeumi füzetek*, Rudabánya, No 5.
- Dept. for Min. Dressing of the University for Heavy Industry 1979: Dressing of sour spar iron ores of Rudabánya. Final Research Report (in Hungarian), Miskolc
- Gagyí Pálffy A, Pálffy G, Halász A 1963: The dressing of Rudabánya iron spar and getting barite and copper content (in Hungarian). *Bányászati Lapok*, 96, No 8, 505–514.

- Gyurkó L 1971: Utilization of loose dust product of the Rudabánya Iron Ore Dressing Works (in Hungarian). Doctor's Thesis, University for Heavy Industry, Miskolc
- Kiss J, Szuromi B, Lévai I 1978: Getting of barite from the waste stockpile of the Rudabánya Iron Ore Dressing Works (in Hungarian). Manuscript
- Mertins E 1980: Die Magnetscheidung — Ein Verfahren zur Sortierung und Filtration. *Aufbereitungs-Technik*, No 12, 212–218.
- Podányi T 1979: The economic interest of utilization of the Rudabánya Iron Ores (in Hungarian). *BKL-Bányászat*, 112, No 10, 655–662.
- Research Institute for Iron Industry 1979: The effect of dressed carbonate-type iron ores on the Fe-content of the sinter, the basicity and the specific efficiency. Research Report (in Hungarian), Budapest
- Tarján G 1980: Mineral dressing (in Hungarian). Tankönyvkiadó, Budapest
- Tóth G 1965: The complex processing of Rudabánya iron spars with special regard to the planned capacity development of the Iron Ore Dressing Works (comparison of technical alternatives) (in Hungarian). Doctor's Thesis, University for Heavy Industry, Miskolc
- Wenz L, Zabel W H 1973: Die Aufbereitung schwach magnetisierbarer Eisenerze durch nasse Starkfeld-Magnetscheidung. *Aufbereitungs-Technik*, No 3, 66–82.

## EXPLOSION RISK OF COAL DUST (METHANE) — INERT MATERIAL MIXTURES

M BÁNHEGYI<sup>1</sup> and J EGYEDI<sup>1</sup>

The simplest explosive mixtures are formed from oxygen and some kind of flammable materials (gas, steam, dust). These two-component mixtures practically do not occur in the mining practice, as the well-known fire damp itself contains, beside methane and oxygen, also nitrogen, as inert gas, according to the composition of air.

The explosive mixtures occurring in mining always consist of more than two components, flammable and inert materials (CH<sub>4</sub>, CO, H<sub>2</sub>, coal dust, and N<sub>2</sub>, CO<sub>2</sub>, water, rock dust, *etc.*), besides the air.

The resulting properties of mixtures depend on the material characteristics and the ratio of individual components, and can be determined experimentally.

For this reason, the development, expansion and damping of mine bursts can be generally studied on the basis of the characteristics of methane-coal dust-inert material systems which describe the effect of every influencing factor in a mutual relation to each other.

It has been experimentally proved that in this ternary system the range of explosiveness is enveloped by a three-dimensional frame (frame of explosiveness).

Frames of explosiveness for the most frequently occurring mixtures of the mining practice give a possibility to interpret uniformly the development of explosion risk (fire damp, coal dust explosion, mine fire, coal and gas bursts) and its prevention and ward off (staunching blind, rock dust barrier, automatic stop, scattered rock dust belt, *etc.*).

**Keywords:** mine burst; mine fire; hybrid mixture; inertization; methane explosion damping traps; explosion effects; prevention of explosions; explosion risk; three dimensional frame of explosiveness; explosion chamber; fire damp; coal dust

### 1. Experimental part

#### 1.1 *The explosion chamber*

The explosiveness of multi-component mixtures was investigated in an explosion chamber. The explosion chamber is a closed, heavy-walled pressure vessel in which the proper gas-air mixture is at first prepared, followed by the dispersion of coal dust or coal dust-inert dust mixture.

The volume of authors' explosion chamber is 40 litres (Figs 1 and 2). A dust container of a volume of 0.4 litre is connected to the chamber (Fig. 2). A quantity of dust necessary to set the necessary dust concentration is put into the dust container before the

<sup>1</sup> Coal Mines of Mecsek, Research Department, Pécs

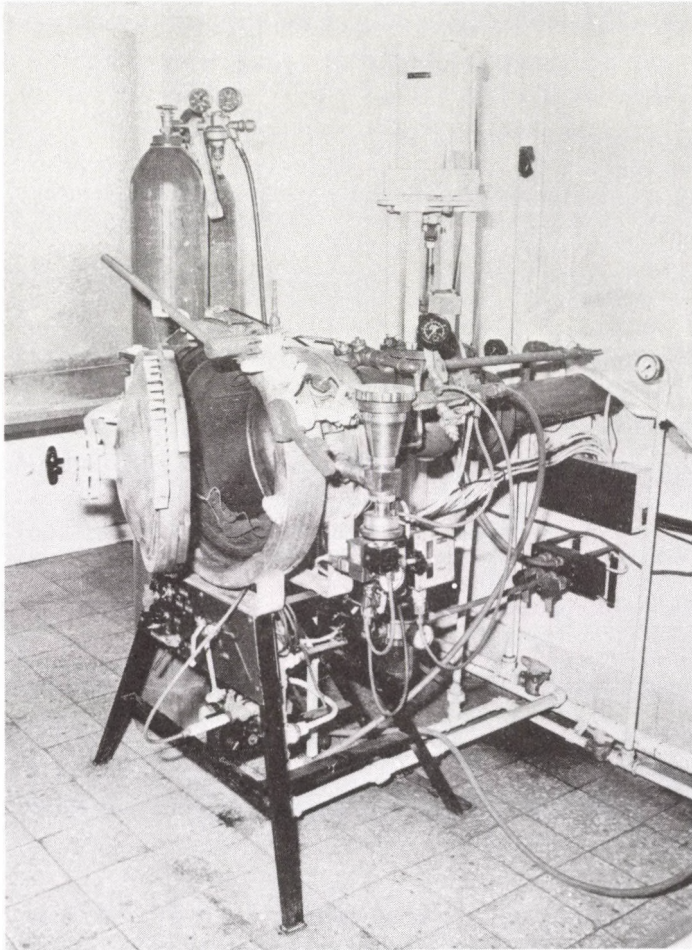


Fig. 1. Explosion chamber of a volume of 40 l

explosion experiments. A gas mixing device is also connected to the explosion chamber by means of which methane-air mixtures of any concentration can be produced.

The dust-gas-air mixture in the chamber space is initiated by a chemical detonator of an energy of 5 kJ.

The capacitance type pressure measuring device is connected to a boring in the wall of the chamber. For the automatic control of the explosion experiments and for the consecutive control of different operations (atomization, ignition, pressure measurement, recording), and for the calculation and display of the explosion parameters, an electronic control- and calculator-unit is added.

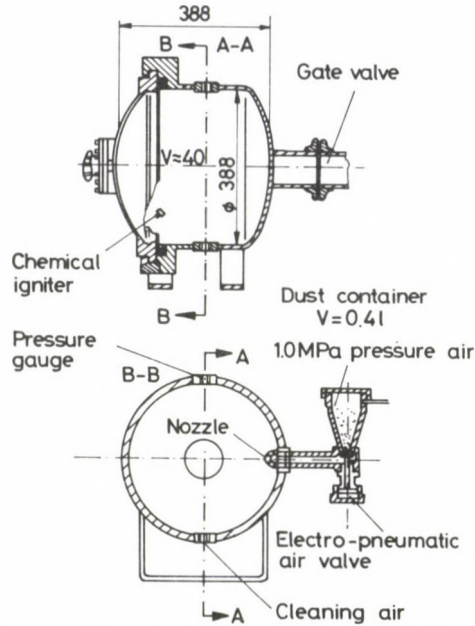


Fig. 2. Sketch of the explosion chamber

### 1.2 Method of investigation

For preparing a given dust mixture (e.g. 100 part coal dust — 0 part rock dust), a quantity of dust sample satisfactory for the given dust concentration is poured into the dust container. Afterwards the necessary methane-air concentration is set in the chamber space. The explosion process following the atomization and initiation is characterized by the explosiveness factor  $k_{ex}$  which is the geometric mean of maximum of velocity pressure increase,  $(dp/dt)_{max}$  and of the average velocity pressure increase,  $p_{max}/\Delta t$  (Fig. 3):

$$k_{ex} = \sqrt{(dp/dt)_{max} \cdot p_{max}/\Delta t}, \text{ MPa/s.}$$

A mixture is considered to be explosive if the average  $k_{ex}$  values of three parallel experiments is at least 8 MPa/s. This limiting value was accepted on the basis of investigations of the "Experimental Drift" in Dortmund-Derne (Landesoberbergamt Nordrhein-Westfalen) being an approximative average  $k_{ex}$  of an undoubtedly non-explosive mixture ( $k_{ex} < 7$  MPa/s) and a surely explosive mixture ( $k_{ex} > 9.5$  MPa/s). This mixture, burning during the continuously expanding explosion, provides a power which ensures that the conditions for further expansion of the explosion (whirling of dust, ignition) are fulfilled. The explosion process of such mixtures can be interrupted only by external intervention, e.g. by means of an explosion damping trap.

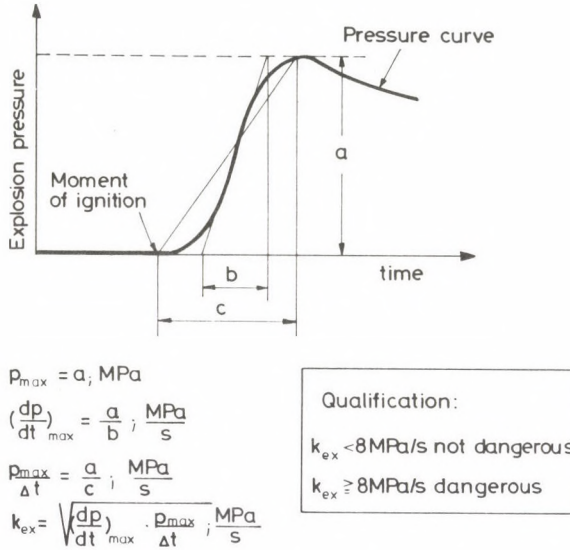


Fig. 3. Evaluation of explosions, explosion parameters

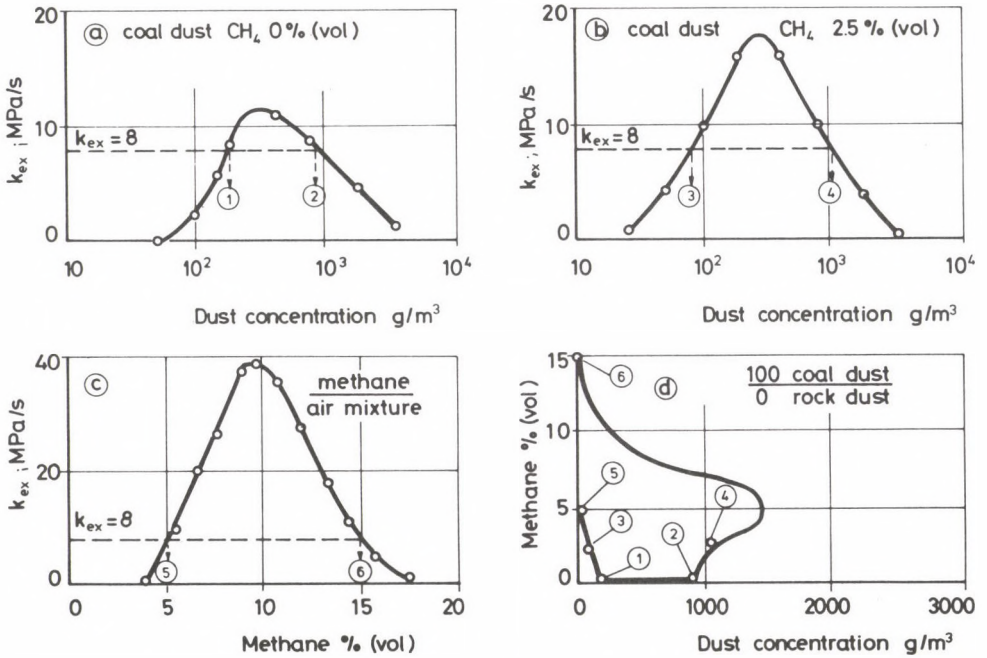


Fig. 4. Method for determining the explosion limits

The explosion properties of mixtures were examined at dust concentrations of 25, 50, 100, 150, 200, 400, 800, 1600, 3200 g/m<sup>3</sup> and at methane concentrations of 0; 0.75; 1.5; 2.5; 5; 7; 8.5; 10; 12 and 15 percent by volume.

How results are plotted, is shown by an example. At the methane concentrations listed above, diagrammes of dust concentration *vs.*  $k_{ex}$  values were constructed (Fig. 4a, b). The upper and lower limiting concentrations for explosion risk were taken from these diagrammes.

All data obtained so were completed with the limiting value for a methane-air mixture and then plotted in the methane *vs.* dust concentration diagramme (Fig. 4c, d). The data points determine a closed area. The points within this area and on its boundaries correspond to explosive risk, and external points are non-explosive mixtures.

## 2. Characteristics of the materials examined

### 2.1 Flammable components

- Coal dust: crushed cutting coal dust from Mecsek  
Ash content ( $A^a$ ) = 8.5%  
Volatile content ( $V^{daf}$ ) = 34.4% (for ashfree and dry coal)  
Humidity content ( $W^a$ ) = 0.8%  
Median value = 18  $\mu$ m
- Methane: natural gas, containing 98–99% by volume CH<sub>4</sub>.

### 2.2 Inert components

- Rock dust: crushed dolomite  
Median value = 43  $\mu$ m
- Fire dust: NaHCO<sub>3</sub> base  
Median value = 20  $\mu$ m

## 3. Results of investigations, plotting of the three-dimensional frame

### 3.1 The explosion risk of methane-coal dust mixtures

The lower limiting values of explosiveness follow the Le Chatelier principle (Le Chatelier and Boudouard 1898), but the upper limits for explosiveness are shifted significantly towards higher dust concentrations compared to that probable according to the Le Chatelier straight line (Figs 5 and 6). This observation agrees with the results of Ishihama et al. (1979). The explosion range is widest at a methane content of 5 percent.

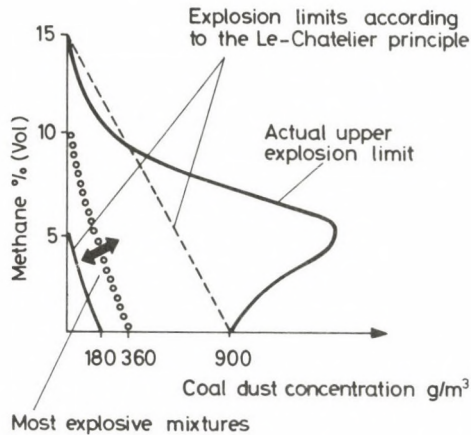


Fig. 5. Explosiveness of hybrid mixtures

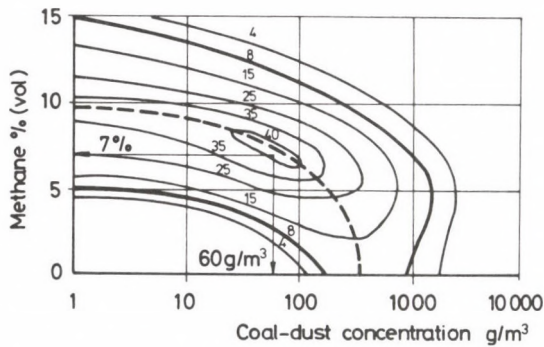


Fig. 6. Explosion risk of methane-coal dust mixtures

The most explosive mixtures fall on the line connecting the optimum methane and coal dust concentration (9.8% and  $360 \text{ g/m}^3$ , respectively, dotted top line). The top line represents the optimum ratio of flammable materials (methane + coal dust) and air, and for the left part of this line, the reduction of explosiveness is caused by the lack of flammable material, while on the right part by the lack of oxygen.

Regarding the whole concentration range, the most violent explosion does not take place at the optimum concentration of the more explosive component (9.8%  $\text{CH}_4$ ). The most violent explosion process — partly because of turbulency caused by the dust particles — develops in a mixture containing 7.0%  $\text{CH}_4$  and  $60 \text{ g/m}^3$  coal dust ( $k_{cx} = 42 \text{ MPa/s}$ ).

### 3.2 The explosiveness of methane-coal dust-rock dust mixtures. The three-dimensional frame

If an inert material is added in increasing ratio to the methane-coal dust system, the explosion limits are modified, and envelop the three-dimensional frame of explosiveness defined previously. At the enveloping surface and within the frame, the mixtures correspond to explosion risk but outside of the frames they are not explosive.

The methane-coal dust-rock dust mixtures were examined in about 1700 explosion experiments. Summarizing the explosion ranges of different coal dust and rock dust ratios, the range of explosiveness of the ternary system, that is, the three-dimensional frame was obtained (Fig. 7). The visible planes of the frame give the explosiveness of the coal dust-methane (1), rock dust-methane (2) and methane-air (3)

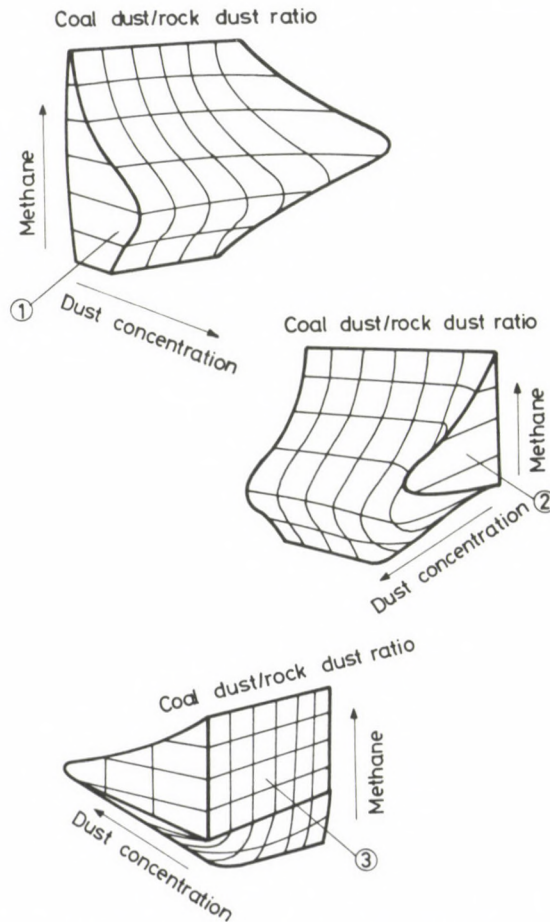


Fig. 7. Explosion limits of coal dust-methane-rock dust mixtures (three dimensional frame of explosion risk)

mixtures. The characteristics of the three-dimensional frame can be seen from the following sections:

- changing coal dust-inert material ratio;
- changing methane content;
- changing dust concentration.

#### 4. Conclusions from the three-dimensional frame

Sections for changing methane content, coal dust-inert material ratio, and dust concentration of a rock dust and a  $\text{NaHCO}_3$  base fire dust are seen in Figs 8, 9 and 10.

By means of frames determined for different flammable-inert material systems — taking into account the limitations of laboratory investigations — the conditions of explosion development and damping, and the relative effectiveness of different damping materials can be interpreted.

##### 4.1 *Prevention of explosion by rock dust spreading*

Because of the serious consequences of mine explosions, efforts are made to assure conditions by means of which the explosions can be prevented and their effect can be restricted. The prevention of explosions means — among others — to neutralize and to hinder the formation of explosive materials and mixtures. One of the tasks is to make the already deposited coal dust harmless. A possible way is the use of rock dust and the creation of rock dust zones. The essence of the method is to mix rock dust to the deposited coal dust in a quantity sufficient to increase the concentration of the inflammable part up to 80%. Such grift section can prevent not only the development of the coal dust explosion, but under certain conditions, can be useful to block an explosion accelerating in a section of high coal dust content. The examination of the sections of the three-dimensional frame gives a possibility to investigate theoretically the rock dust zones and to understand their mechanism.

Thus in the absence of methane, the explosiveness of coal dust is stopped at a coal dust/rock dust ratio of 41/59 (Fig. 11a). As the safety rule prescribes an inert material ratio of 80%, this means that the rock dust used for the unit mass of coal dust is 2.7 times more than the experimentally necessary value.

On the other hand, the 80% inert material ratio gives a protection only below 3%  $\text{CH}_4$  content (Fig. 11b). It is generally true that the lower limit of methane explosion is decreased in a certain degree by the coal dust inertized.

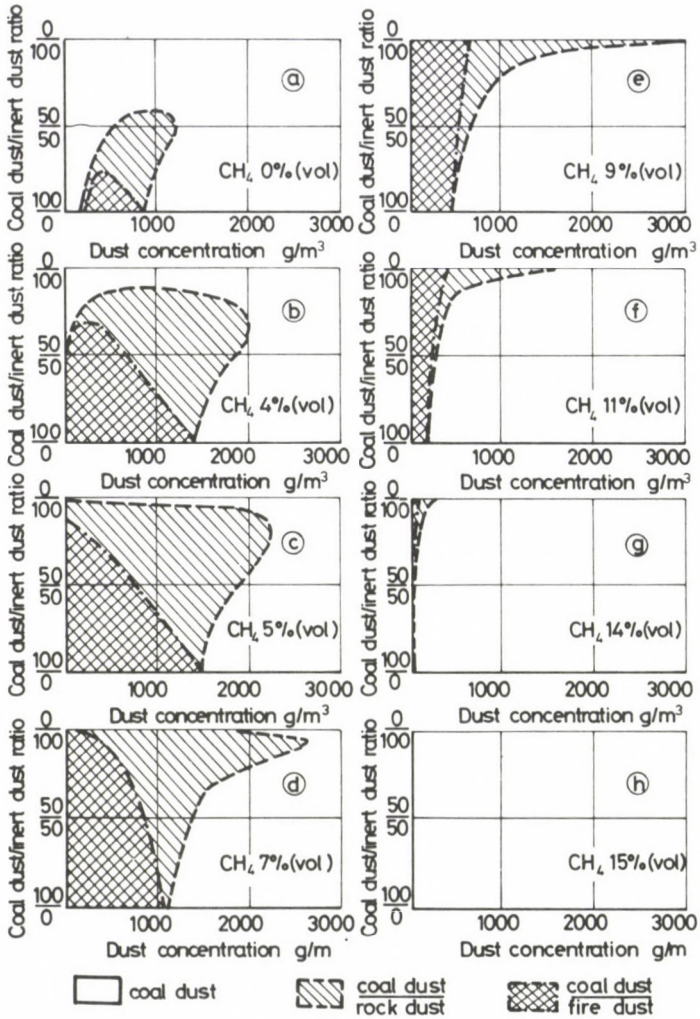


Fig. 8. Sections of three dimensional frame of explosion risk according to the changing methane content

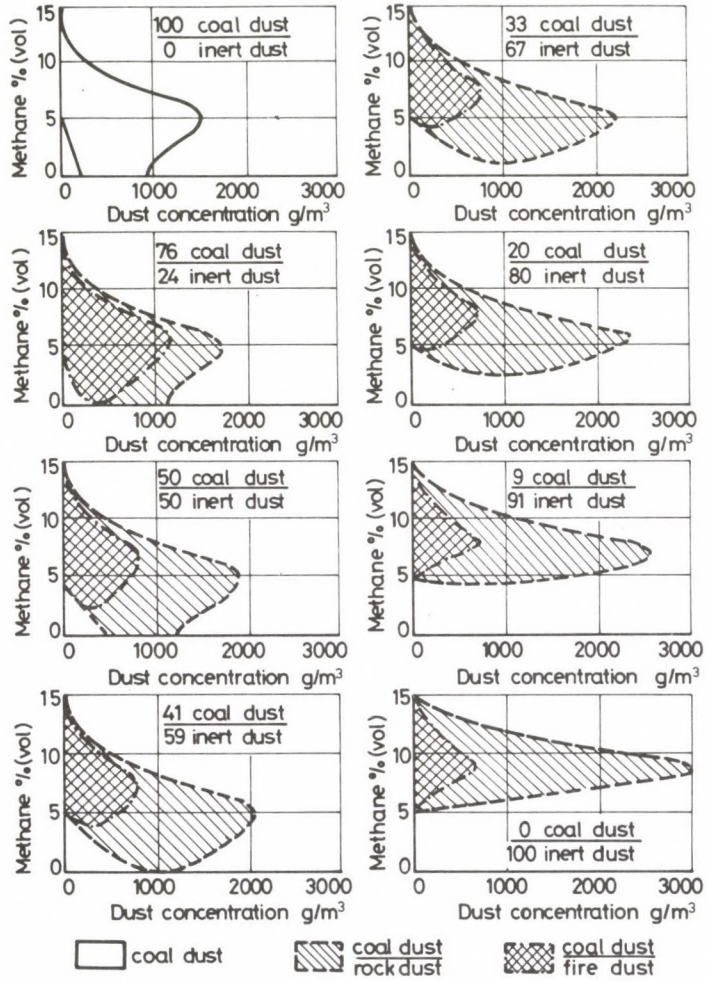


Fig. 9. Sections of the changing coal dust-inert dust ratio

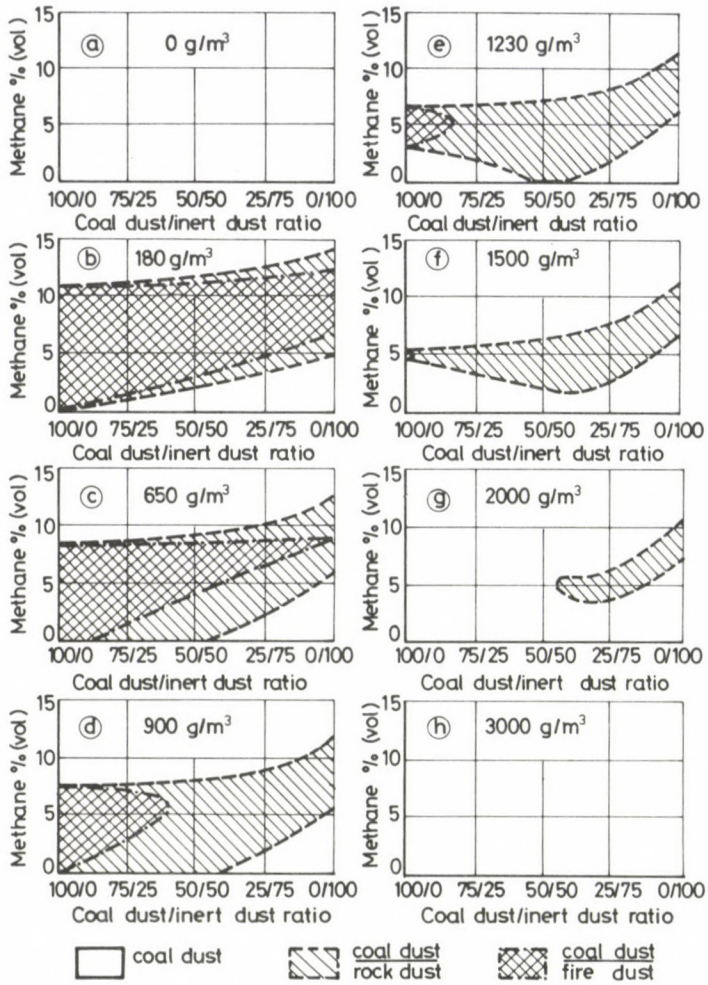
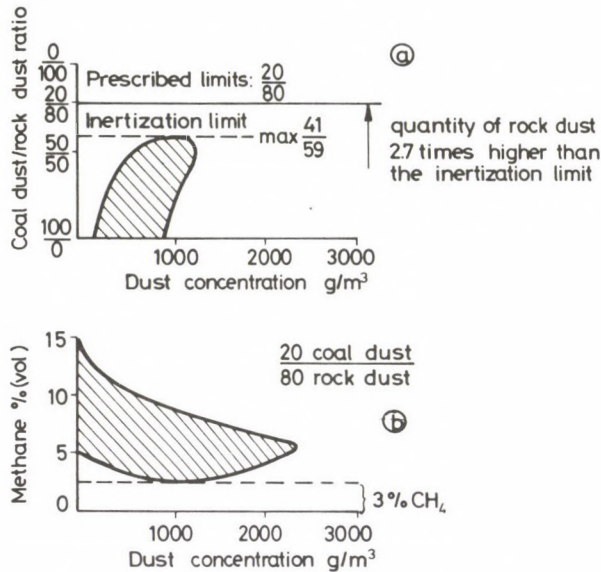


Fig. 10. Sections of three dimensional frame of explosion risk according to the dust concentration



The lower explosion limit of fire damp expanded

Fig. 11. Prevention of explosion by rock dust spreading: a) without  $CH_4$ , b) in the presence of  $CH_4$

#### 4.2 Damping of explosion by rock dust barrier

An important means to prevent explosions under present mining conditions are represented by the explosion barriers. Putting inert material (rock dust or water) or active fire dust at the very moment into the zone where and when the explosion is running through, one can reach that the explosion flame will be extinguished in the neighbourhood of the barriers or at a certain distance behind them.

According to Hungarian safety rules, it is necessary to place in the barrier at least  $400 \text{ kg}/m^2$  rock dust related to the drift section, in a length that the nominal dust concentration should not be lower than  $10 \text{ kg}/m^3$  (Fig. 12a). At any composition of the methane-coal dust mixture, the explosion can be damped with a rock concentration of  $3 \text{ kg}/m^3$  according to the experiments (Fig. 12b). The rock dust barrier fulfils this requirement, until the rock dust is distributed in the case of an explosion along a drift section not longer than 3.3 times the barrier length.

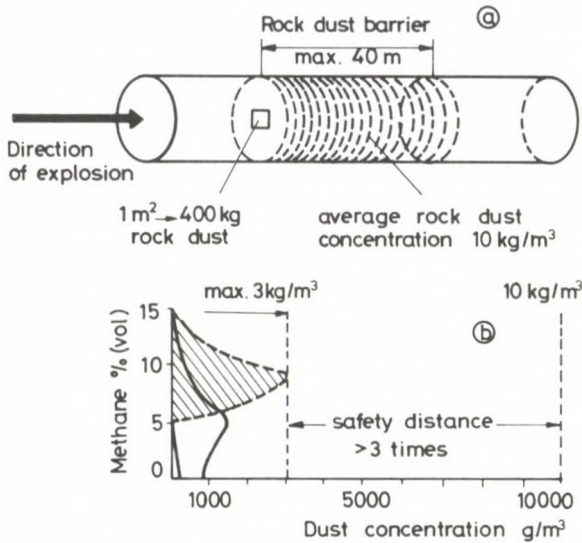


Fig. 12. Damping of explosion by rock dust barrier: a) rock dust quantity according to safety rules, b) experimentally determined necessary rock dust quantity

#### 4.3 Comparison of the damping effect of inert materials

The experimental results are suitable to compare the damping effect of different kind of inert materials. On this basis — by calculating for the necessary amount of damping material for unit mass of coal dust — the coal dust explosion is damped 4.5 times better by fire dust than by rock dust (Fig. 13a).

It is interesting to note that to stop the explosiveness of the most explosive fire damp mixture (9% CH<sub>4</sub> by volume) — in agreement with the above data — 4.6 times more rock dust is necessary than fire dust.

As a further comparison, one can ask for the necessary amount of rock dust or fire dust in a unit volume of the air to eliminate the explosiveness of any coal dust-air mixture containing no methane.

$$\begin{aligned} \text{This value is for rock dust} & 0.55 \cdot 1230 = 680 \text{ g/m}^3 \\ \text{and for fire dust} & 0.24 \cdot 370 = 90 \text{ g/m}^3. \end{aligned}$$

According to the necessary amount of inert material to stop the coal dust explosion, on the contrary to the earlier date,  $680/90 = 7.6$  times more rock dust is necessary than fire dust. It follows from the fact that with the increase of the rock dust ratio, the explosion limits and the optimum concentration of the dust mixtures are shifted to higher values. Independently of the existing coal dust-rock dust ratio, it is true that in the most violently exploding mixture the concentration of pure coal dust is always about  $360 \text{ g/m}^3$ , which, in the same time, is the optimum concentration of the

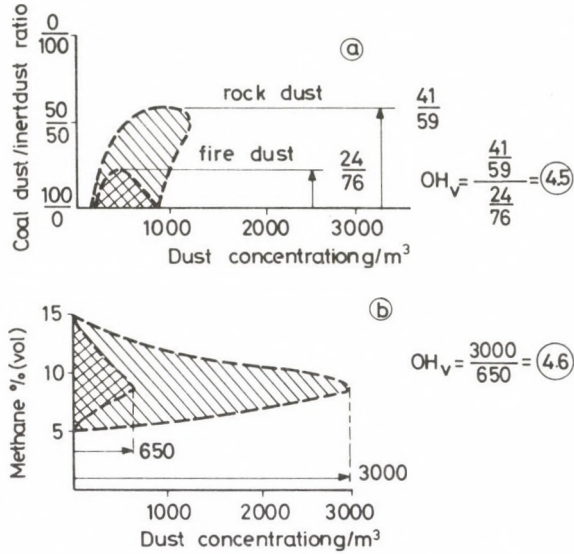


Fig. 13. Comparison of damping effect of inert materials: a) in case of coal dust explosion, b) in case of fire damp

coal dust-air mixture, free from inert materials. On the contrary, the lowest quantity of fire dust already narrows the explosion limits, and in the most violently exploding (most difficultly extinguishable) mixture it is not the concentration of the coal dust, but that of the coal dust + fire dust which remains constant (360 g/m<sup>3</sup>).

## 5. Further plans

The three-dimensional frames of explosiveness for materials used up to now or potentially useful (e.g. water and nitrogen) for inertizing explosive mixtures in mining are processed experimentally. It is expected that they will help to interpret the development of explosion risks of different origins, and they will complete the knowledge necessary to divert the explosion risk.

## References

- Bestimmungen des Landesoberbergamts Nordrhein-Westfalen für die Prüfung und Beurteilung der Explosionsgefährlichkeit von Kohlenstaub (Kohlenstaub-Prüfbestimmungen vom 27. 5. 1974).
- Ishihama W H Takagi H, Enomoto H 1979: Explosion characteristics of coal-methane-air mixture. Internationale Konferenz über wissenschaftliche Forschung auf dem Gebiet der Arbeitssicherheit in der Bergbauindustrie Cavtat, 179–194.
- La Chatelier H, Boudouard O 1898: Sur les limites d'inflammabilité. *Bull. Soc. Chim. (Paris)* 19, 483–488.

## SOME ASPECTS TO THE COMPREHENSIVE INTERPRETATION OF FILTRATION PROCESS-CONTROL AND RESERVOIR-CHEMICAL INTERACTIONS

D RÁCZ<sup>1</sup>

The technical progress, development of new instruments, devices, methods, made it more and more evident that different branches of learning depend on each other. This was particularly urgent in the hydrocarbon recovery based essentially on indirect observations where geological, reservoir engineering, chemical, physical and microphysical phenomena are in such a close connection that the change in any of them results in a change of the whole system.

The investigation of the interaction between reservoir engineering and reservoir-chemistry has a particular importance in developing new recovery methods. It is necessary to consider also phenomena earlier neglected by simplifications, as they may have a determinant role in the effective processing. Such a phenomenon is represented by the secondary phase of the fractional flow because the permeability to water compared to that to oil is significantly higher, therefore in this flow range the role of mobility conditions essentially change.

Several problems of the mutual interaction of mechanical stress and chemistry are to be studied as interrelations in formation treatment and displacement processes.

**Keywords:** chemical effects; displacement; hydrocarbon recovery; mechanical stresses; mobility; physico-chemical effects

The conception is ascribed to Darcy that the description of subsurface filtration processes is more difficult than the revelation of laws of the Cosmic Space. This seems to be unbelievable, but it takes up the specialists' attention, less from the aspect of the description of the Cosmic Space — there the results have been nearly immeasurable — but from the point of view of almost inextricable questions arising again and again in connection with the processes in porous systems.

Darcy, in 1856, determined the empirical relationships merely for the filtration of water through sand which are relevant to a number of respects even now. During the last 150 years the filtration theories developed in an enormous extent.

With respect to crude oil and natural gas, the scientific bases of reservoir engineering were put by Lejbenzon (1934) and Muskat (1937) who published monographs on the underground motion of gases, gaseous fluids, water and oil. After this, the development of reservoir engineering was accelerated. In the last decades a number of specialists dealt with the further development of filtration theories and elaboration of new methods and processes.

<sup>1</sup> Hungarian Hydrocarbon Institute, Százhalombatta

Presently, up-to-date measuring instruments and plenty of information are available for the specialists. Recently the processing of information has extremely quickly developed. In spite of this, an exact description of subsurface processes has not yet been reached, and one cannot influence the flow conditions as it had been supposed. The results of theoretical and laboratory researches are not completely proved in the industrial practice. The recovery efficiency of oil reserves is low. All over the world 70–75% of the reserves in average remains unrecovered, but there are some oil fields where the recovery is only a few percents. Therefore the further development of the filtration theories has a great importance. It is an economic interest to increase the supply of reserves.

The specialists of the oil industry do not believe in any of the radical ideas which — according to political purposes — inspire that the reserves will run out, or on the contrary suppose that reserves are inexhaustible.

The correct question is: what do we do in order to make of underground mineral resources industrial reserves utilizable for the economy? The natural environment and the creative human work are inseparable in this meaning.

A detailed exposition of this topic would lead too far, therefore only two characteristic relations of a potential source-utilization model to be developed will be shown on the basis of world-wide data, but these considerations are valid for all the source-utilization regions and countries, in different dimensions (Fig. 1).

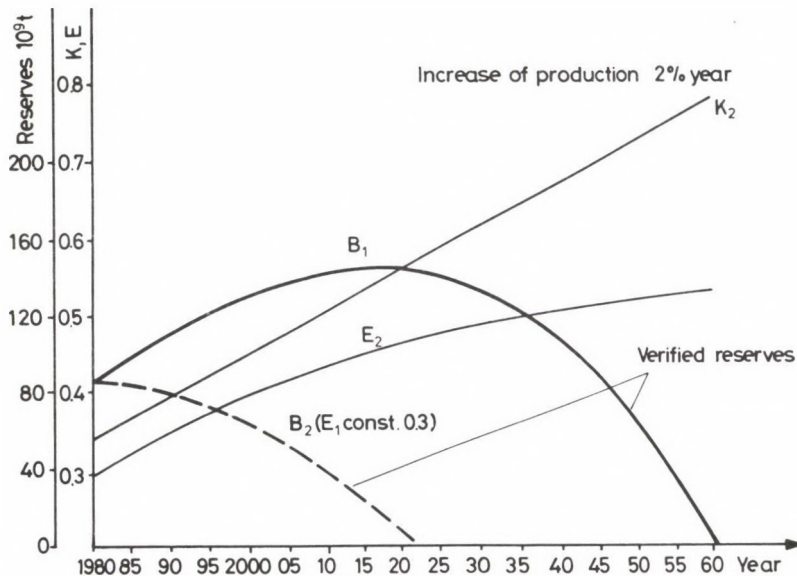


Fig. 1. Change of the verified reserves at different values of the  $K$  and  $E$  indices

The model takes into account that in 1980, in a world-wide scale, the degree of exploration of potential crude oil resources is 34.4% ( $K = 0.344$ ). On the technical development level of 1980, the recovery can be estimated as 30% ( $E = 0.30$ ).

According to the example, until 2060 the degree of exploration reaches a value of 0.780, and it will change along a straight line. Such a level of the exploration-increase seems to be extreme, but this supposition also means that it is practically impossible to reach a higher value. In the same time, according to the supposition, the recovery reaches 55%, which is more reasonable, as during 80 years a 25% increase in efficiency may be expected.

Taking into account a 2% per year increase in recovery, the tendency of verified reserves is shown by curve  $B_1$  in Fig. 1. From this it follows that even at such an enormous exploration rate, a shortage will arise in 2060. If the recovery would remain 30%, the shortage would appear already about 2020 (Curve  $B_2$  in Fig. 1). From these data one can feel the importance of increasing the recovery, but in addition the curves also establish the fact that between 2020 and 2060 a shortage would arise if the recovery development will not be carried out parallel to the exploration. This is evident thinking over that oil fields discovered in more and more complicated, difficult situations increase the geological reserves, nevertheless, if they are poorly recoverable, a high percent of crude oil remains in the reservoirs, and the necessary degree of supply cannot be provided. For this reason, the development of oil recovery methods, an introduction of new processes can be postponed in no country.

Similarly to the Fig. 1 shown, one can calculate with different versions of exploration and recovery, and different production rates can be taken into account.

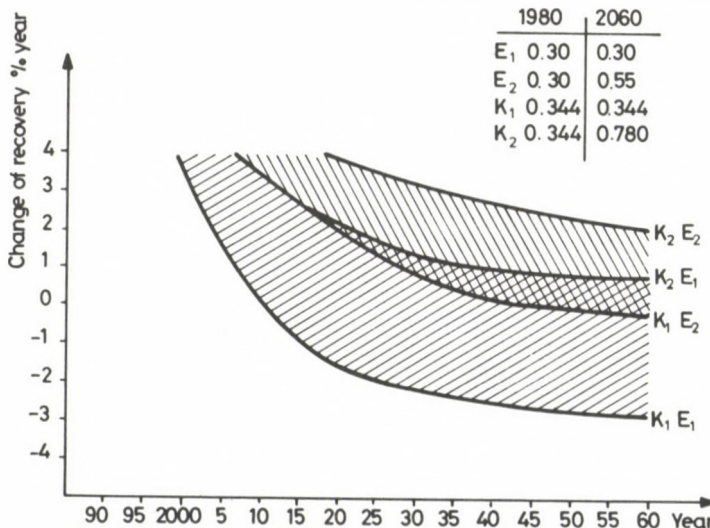


Fig. 2. Exhaustion of reserves and the appearance of shortage at different production rates in function of  $K$  and  $E$

Figure 2 represents the exhaustion of reserves and appearance of shortage at different values of the indexes  $K$  and  $E$ . The curve  $K_1E_1$  shows that unrealistic situation when neither geological and drilling explorations, nor production-development are carried out. At the recovery rate of 1980, the reserves will indeed run out by 2010. The reserves will run out at a lower production rate later, at a higher one earlier.

Such a situation cannot be supposed, but since 1973–1974 argumentations starting out from this base situation have been often heard, and ideas about the exhaustion of reserves were arisen mainly when an increase of prices was striven at.

The importance of recovery development is directly emphasized by the relation  $K_1E_2$  as it shows the significant role played by the development of recovery methods in the increase of reserves, and what a prolongation of the crude oil supplies can be provided if the recovery efficiency is increased. For recovery values between 55% and 30%, one can conclude from points in the area closed by the curves  $K_1E_1$  and  $K_1E_2$ . It is obvious that an intensive geological and drilling exploration gives good results ( $K_2E_1$  curve), but the result is the best when the development of exploration and recovery is carried out simultaneously, according to the curve  $K_2E_2$ .

In the area between the curves, the effect of changes in  $K$  and  $E$  can be calculated by several methods. However, the production rate should be followed with special attention, as the supply for a longer period can be provided only at a lower production rate. It follows that the development of recovery methods will remain a basic duty of crude oil mining, as many problems raised in the last decades are yet unsolved in a number of aspects. In the future, the recovery of oil fields discovered in more and more complicated geological conditions is to be solved, and significantly higher recovery values must be obtained.

It should be accounted for that the nature resists to an upsetting of the underground equilibrium established during many million or billion years. A change in the conditions of equilibrium results in a series of mechanical, chemical and hydrodynamical changes.

In addition to more and more sophisticated theoretical and laboratory researches, a reservoir model is required which interpretes the geological, physical, chemical and mechanical conditions and their mutual interactions. On this basis, one should arrive at the application of more perfect simulation methods to describe more completely the processes.

On the basis of structural, lithophysical, tectonical analyses, the geological model describes statistically the reservoir system in which the accumulation of oil, gas and water had taken place. Compared to this, the reservoir model is more complete because it includes the reservoir engineering evaluation, too. This is a dynamic interpretation of the uniform system where and how the process takes place. In such a system it should be calculated with the properties of the reservoir rock and reservoir fluids predominating during the recovery. These are: wettability properties, perme-

ability conditions, capillary effects, hydrodynamical relations, changes of state caused by the interactions of water-oil-gas-rock, changes in mechanical stresses, *etc.*

The concept of the model — in addition to the earlier — is to be extended at the development of new methods when those factors should be especially emphasized which are necessary for the introduction and development of new methods. Such a model is also the underground combustion reservoir based on the laws of reaction kinetics (Fig. 3) as in the combustion the reservoir is to be considered as an underground reactor, too. The kinetic characteristics of this underground reactor essentially affect the combustion process and the mechanism of displacement. In the combustion reservoir model — besides the geological circumstances — the physico-chemical properties of the rock and fluids, their thermal characteristics, the hydrodynamical circumstances may be evaluated only together, and the relationships should be carefully analysed.

If the processes of the underground combustion are separately investigated, no conclusions can be drawn for the expectable results. An analysis of reservoir engineering and reservoir-chemical interactions and of their mutual depending, is required. The underground combustion itself represents a wide problem.

A number of relationships were discovered by these investigations, but there remained a lot of questions to be answered, in spite of hundred years passed since the first mention of the idea of the underground combustion and, during the last 50 years, intensive research works were carried out all over the world.

It is more or less possible to make combustion, but to make a correct combustion and to direct the process suitably requires thorough planning from both the research workers and the industrial specialists. In the combustion reservoir model, the mutual

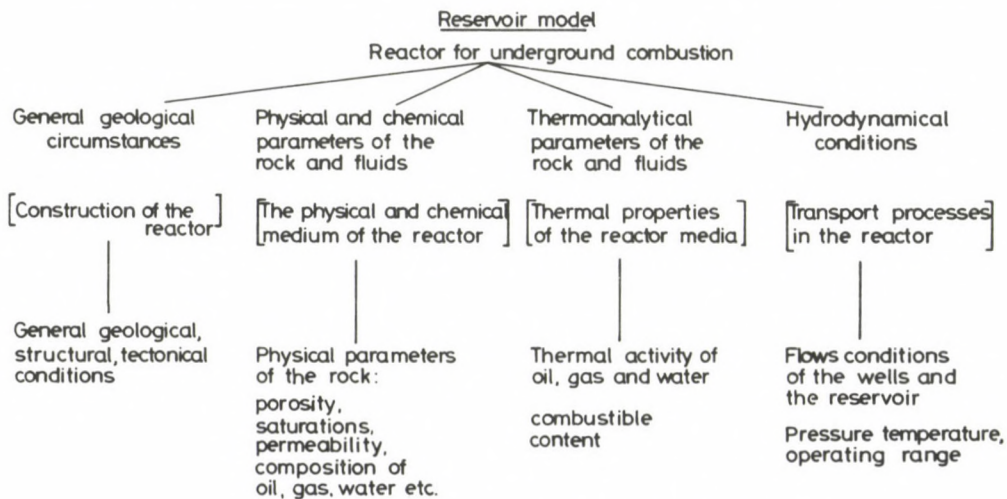


Fig. 3. Reservoir model for the underground combustion

dependence of reservoir engineering and chemistry is evident. The so called chemical recovery methods are similarly complicated and they are based mainly on knowledges from the chemistry. Such methods are e.g. the use of carbon-dioxide, surfactants, *etc.* In these cases a lot of complex relations may be analysed, too. Efforts are to be made to discover the laws of neighboring fields of science, as they may contain knowledges which can help in resolving unclear questions.

There are tendencies to neglect some factors and processes considering them unimportant or already solved by other branches of research.

Such is e.g. the frontal displacement based on Darcy's law, or certain details of the fractional flow. Let us consider for instance the mobility ratio and within this, the role of viscosity ratio as it determines essentially the displacement mechanism.

In recovery planning and in elaborating new methods, the aim is always to reduce the viscosity of the displaced phase and to increase the viscosity of the displacing phase.

Is this point of view correct in every case?

Let us consider this question at such a saturation when the reservoir is exhausted, the wells produce practically water, that is, the permeability to water as compared to that to oil is extremely high ( $k_w \gg k_o$ ).

Let us start from the water-oil fractional flow equation:

$$f_w = \frac{1}{1 + \frac{k_{ro}}{k_{rw}} \cdot \frac{\mu_w}{\mu_o}}$$

and examine the change of  $f_w$  as a function of  $S_w$ :

$$\frac{df_w}{dS_w} = \frac{-\frac{d}{dS_w} \cdot \left(\frac{k_{ro}}{k_{rw}}\right) \cdot \frac{\mu_w}{\mu_o}}{\left(1 + \frac{k_{ro}}{k_{rw}} \frac{\mu_w}{\mu_o}\right)^2}.$$

At high  $S_w$  saturations one has:

$$\frac{df_w}{dS_w} = \frac{A \frac{\mu_w}{\mu_o}}{1 - \frac{k_{ro}}{k_{rw}}}$$

as

$$\frac{d}{dS_w} \left(\frac{k_{ro}}{k_{rw}}\right) \quad \text{and} \quad \frac{k_{ro}}{k_{rw}}$$

are constant, and

$$S_w \approx (1 - S_{or}), \quad \frac{k_{ro}}{k_{rw}} \approx 0$$

whence

$$\frac{df_w}{dS_w} = A \frac{\mu_w}{\mu_o}$$

is obtained.

It follows from this relationship that in case of watered formations, if  $\mu_o$  decreases or  $\mu_w$  increases, the rate of the water portion also increases, so the conditions of watering become more severe and the conditions for the flow of oil are worsening. The formation of an oil bank in the reservoir cannot be expected under such conditions, especially if the heterogeneity of the reservoir is considered.

Therefore, the conditions of oil displacement cannot be improved in such a degree as it would be expected. Processes taking place in the secondary phase of frontal displacement, have basically to be reevaluated, and are to be approached from certain saturation and flow regions, where the concept of displacing and displaced phase are modified. If the permeability to water increased considerably, water displaces that water which contains the dispersed oil drops. The friction resistance of drops in the water stream is to be increased and not to decreased.

The simultaneous flow cannot be based only on Darcy's filtration theory, but it is essential to use Stokes' law and the Einstein-relation as the two-phase flow is influenced by all the parameters incorporated in these equations, i.e. by viscosity, density, degree of dispersion, shape of the dispersed particles, etc.

The complexity of the reservoir model and the interdependence of different branches is more evident when a change of the mechanical potential equilibrium state of the reservoir system is to be described (Fig. 4).

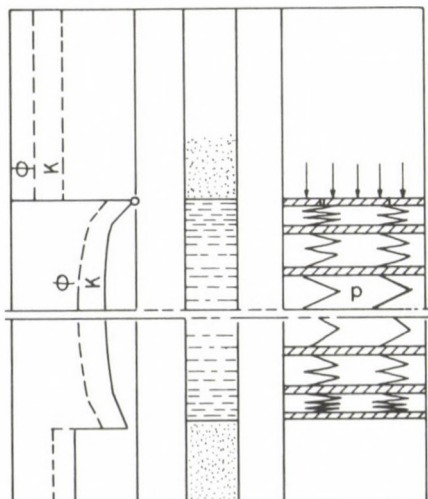


Fig. 4. Hindered compaction model

The compaction model by Terzaghi, Katz and Ibrahim refers to a state when a so called pressure barrier is formed in the Earth' crust in a given depth. In the zone below this pressure barrier, the physical parameters of the formation show anomalous values, meaning that the values of permeability and porosity reach even in greater depths values higher than that determined by regular compaction. The mechanical equilibrium state means that the matrix stress and the pressure of the fluids in the porous system are in equilibrium with the geostatical principal stress. If the system is disturbed during drilling, the mechanical stress conditions will be changed resulting in a change of the chemical equilibrium, too. As a consequence, the filtration conditions will deteriorate around the well. These laws are to be taken into account when examining the fluid flow into the well, and in the development of new methods for formation treatment. Efforts are to be made to eliminate the disadvantageous effects and to strengthen the advantageous ones. This view of reservoirs is to be applied in a greater extent in the case of formation treatment and the application of new recovery methods.

### References

- Buckley S E, Leverett M C 1942: Mechanism of fluid displacement in sands. *Trans AIME*, 146, 107—116.  
Lejbenzon L S 1934: Reservoir Mechanics (in Russian). Gorgeonefteizdat Moskva  
Muskat M 1937: Flow of Homogeneous Fluids Through Porous Media, McGraw Hill Book Co., New York  
RÁCZ D 1980: Földalatti elégetéses művelési módszerek (Subsurface Combustion Recovery Processes).  
Manuscript  
RÁCZ D 1983: Kőolajkészlet-kőolajjellátás. Műszaki gazdasági kilátások. *Magyar Tudomány*, 7—8, 529—537.  
Terzaghi K, Peck R B 1948: Soil Mechanics in Engineering Practice. John Wiley and Sons Inc., New York

## INTERFACIAL AND CAPILLARY PHENOMENA IN THE DISPLACEMENT OF OIL BY CO<sub>2</sub>

K BAUER<sup>1</sup>

The mechanism of CO<sub>2</sub>-flooding is discussed on the basis of literature information and experimental results. It is concluded that during carbon-dioxide flooding the efficiency increasing effect of crude oil swelling and viscosity reduction caused by CO<sub>2</sub> dissolved in the oil can be compensated or strongly spoiled by the increase of useful pore space and by the shifting of rock wettability to oil-wet direction.

**Keywords:** change of wettability; CO<sub>2</sub>-flooding; oil swelling; pore structure modification; role of clay minerals

The temperature conditions of the crude oil reservoirs in Hungary are not advantageous to set up in the formations pressure distributions which would promote the miscible displacement mechanism resulting in a high increase of oil recovery. The original initial formation pressure of the 60–80 °C reservoirs is too low to provide the criteria for miscibility and during CO<sub>2</sub> flood operations the injection of gases of high CO<sub>2</sub> content into exhausted formations to be taken again in production, used to be done at lower pressures.

In the absence of a miscible drive not only the positive effects of the mobility improving oil viscosity reduction and of the oil swelling effects of the CO<sub>2</sub> dissolved in the reservoir fluids among the parameters determining the motion of reservoir fluids and recovery, but also the rock-fluid interfacial properties and the capillary behaviour of the system get a more significant role in controlling the flow of fluids. Changes in these parameters, produced by the effect of the dissolved CO<sub>2</sub> gas, could be especially significant in the case of sand and sandstone reservoirs due to the hydration ability of their mineral components.

### **Rock components of hydration ability and their modifying effect of fluid motion**

In any reservoir the limits of fluid motions are determined by the underlying rock and the cover layer. The macroscopic flow pathes in the productive zone are modified by the vertical and horizontal distribution of permeability and by the settlement beds.

<sup>1</sup> Chemical Research Laboratory for Mining of the Hungarian Academy of Sciences, Miskolc

The microscopic fluid motions are in connection with the submicroscopic silicate minerals (they are macroscopically homogeneous components of the rock texture which show microscopically a disperse distribution), i.e. with their clay mineral fractions being ready for hydration.

This submicroscopic detritus is localized in the sands and already consolidated sandstones around the contact points and in the pore voids formed by quartz or seldom carbonate and other mineral particles giving the frame of the rock, the size of which is significantly larger than 1  $\mu\text{m}$ .

The size fraction of rock particles below 1  $\mu\text{m}$  and the clay minerals able for hydration captured by them, furthermore the permeability modifying effect of the clay particles, were extensively investigated. These investigation fell in the same time period when the artificial water flooding of crude oil reservoirs has been started.

As for the origin of clay minerals in marine deposits, conflicting ideas exist and the standpoints vary among the genetical possibilities of detrital or diagenetical origins and the chemical reactions between the dissolved mineral constituents in the sea water and in the flowed-in water (Nemecz 1973).

The sand and sandstone reservoir rocks have a microscopically disperse distribution, therefore the origin of clay minerals in the pores and at the contact points of particles is essentially detritic in contrast to the clays in the underlying and cover rocks and the impermeable settlement beds, as verified by the investigations of several authors.

Thus, the types of clay minerals in the rock texture are determined rather by the continental source-fields and by the effects of decay during transportation than by diagenetic metamorphosis during the formation of rocks which effect is detectable in sediments older than Mesozoic.

In the Bradford sand, California, of a lower Paleozoic age, the illite is denoted as basic component by Bates et al. (1946), but small amounts of kaolinite and montmorillonite can be observed, too. In California, in the productive sands and sandstone reservoirs of the tertiary period, montmorillonite, illite and kaolinite are found alike, according to investigations by Hughes (1947) and by Nahin et al. (1951).

Morris et al. (1959) showed the montmorillonite to be dominant clay mineral in the productive layers of Californian oil fields. Dodd et al. (1955) found in about 90 rock samples of different ages and sources different quantities of illite, chlorite, kaolinite and miscellaneous clay minerals susceptible to swelling, and they pointed out that in Permian sands of West-Texas the clay minerals of montmorillonite type able to hydration can be found in higher quantities than in Mesozoic sands.

Nevertheless, it can be accepted as a general rule according to Grim (1958) that in sediments older than Mesozoic the proportion of montmorillonite decreases. The sands and sandstones of crude oil reservoirs are predominantly marine deposits. The rock frame consisting mainly of quartz particles are deposited next to the sea shore from the aqueous suspension of submicroscopic detritic materials washed together

with them into the sea. During deposition the larger particles closed certain parts of the suspension between themselves, too. An aggregation of the accumulated drift took place and particle contacts were formed until a given state, determined by the shape and particle size distribution of the larger frame particles.

The aqueous suspension of submicroscopic detritus was trapped in the pores and around the contact points of the frame forming particles, therefore inside the pores the compaction and diagenetic metamorphosis could not be initiated by an increase of the lithostatic load caused by sinking, until the start of plastic deformation of the frame forming particles, be it according to Riecke's rock particle dissolution concept.

Taylor (1950) examined the particle deformation at the particle contact points and in his opinion the pore size reduction caused by particle deformation can reach a level below 2000–3000 m depth where the detritus within the pores gets under increasing load which together with the increasing temperature helps the atomic diffusion, i.e. the equilibrium of energy differences (montmorillonite-illite transformation).

The fluid flow experiments carried out on sands and sandstones, included the investigations of the effect of polar and nonpolar fluids, gases and waters of different salinity. Bates et al. (1946) drew attention with their investigations to the rock permeability modifying effect of waters of different salinity.

Baptiste and Sweney (1955) investigated the effect of the quantity of particles below 2  $\mu\text{m}$  and the effect of the ratio of different clay minerals. Finally they concluded that in the control of flow and in the change of permeability the presence of montmorillonite type mixed clay minerals plays an essential role.

The investigations by Dodd et al. (1955) gave similar results. In their opinion the rock is sensitive to water, if the particle size fraction below 45  $\mu\text{m}$  contains 5–10% clay minerals, the effective permeability to water is then lower by 60% than the extrapolated permeability to gas.

Several authors investigated beside the effect of salt concentration, the effect of salt quality in connection with the water flooding.

Novak and Krueger established already in 1951 that the dissolved polyvalent cations play a more important role in the conservation of rock permeability than the monovalent ones.

Von Engelhardt and Tunn (1954) systematically investigated mixtures of quartz sand and 4% of different clays able for hydration and found that changes in permeability, as a function of NaCl, occur even when the clay mixed to the sand is not montmorillonite. The qualitative order of the clay minerals in the decreasing of the permeability is: montmorillonite > illite > kaolinite. (Fig. 1).

The effect of the pH of water was investigated by Hughes (1947). As Fig. 2 shows the change of permeability vs. pH of the solution is reversible.

Jordan's (1949) investigations are very important regarding the adsorption of hydrocarbons on clay minerals. According to his results, the surface of clay minerals is

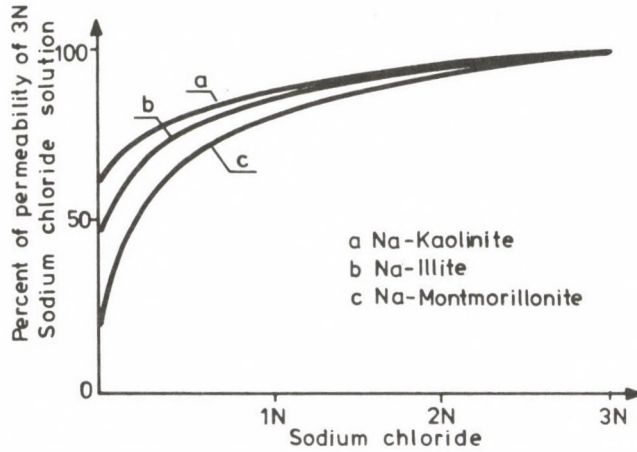


Fig. 1. Change of the permeability of mixtures made of quartz sand and 4% Na-clay with the NaCl concentration of water. After Von Engelhardt and Tunn (1954)

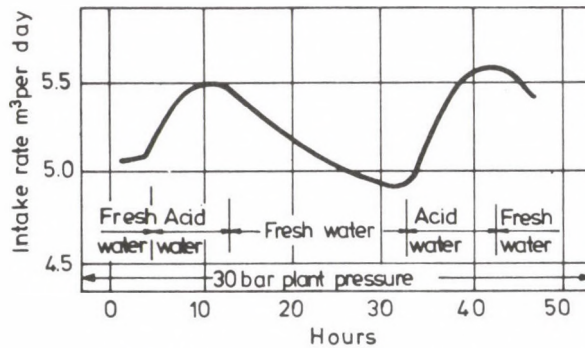


Fig. 2. Change of the permeability during cyclic injection of surface and acidic water with the injection rate at constant pressure after Hughes (1947)

modified by the adsorption and by the chemisorption of ionic and polar organic molecules being present in the crude oil and in the brine.

The presence of such organic components in the aqueous solution may decrease or increase the adsorption of hydrocarbons and promote or restrain the dispersion of the clay minerals.

The effect of the NaCl concentration in water and the montmorillonite contained in the quartz sand for the rock properties, were investigated in detail by Jacquin (1965). The changes of porosity, permeability and capillary behaviour were determined (Fig. 3

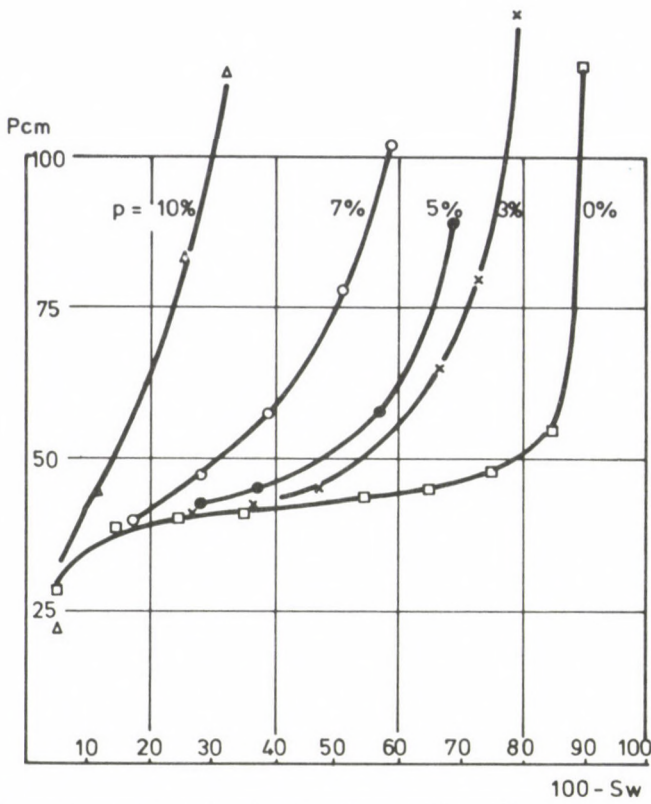


Fig. 3. Capillary pressure curves for quartz sands containing different percents of montmorillonite determined for air and for 50 g/l aqueous solution of NaCl. After Jacquin (1965)

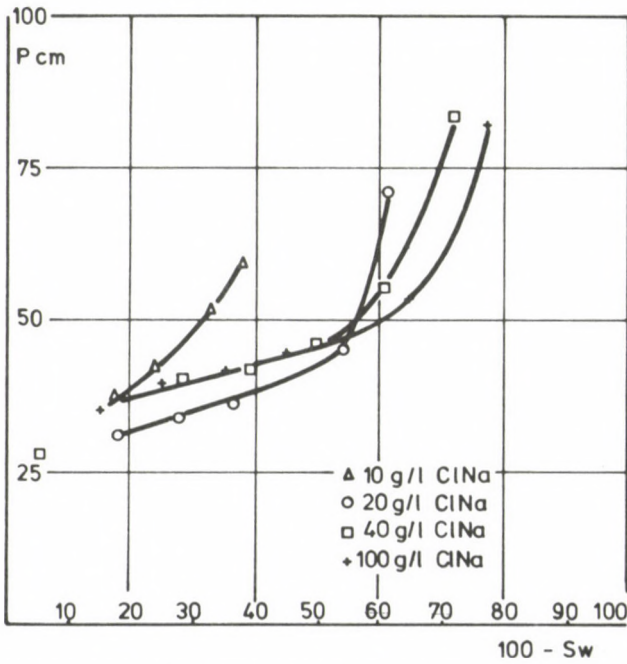


Fig. 4. Capillary pressure curves of quartz sand and 3% montmorillonite mixtures, determined for air and aqueous NaCl solutions of different concentrations. After Jacquin (1965)

and Fig. 4). The existence of a limit concentration was established, at higher concentrations the change of the measured rock properties is systematic and continuous with changing salt concentration, while at lower concentrations the clay closed in the pores gets into an instable, disperse state.

### **One possible basis of the change of physico-chemical properties of rocks**

The clay minerals closed into the pores of rocks are composed of a mixture of different silicate fragments produced by decay at the continental source and during the flow transportation, can also form loose structured agglomerations as it is shown in Fig. 11.

On the surface of particles water molecules can be adsorbed, independently of their internal structure. The effective volume of these agglomerations depends — besides the state of particles — firstly on the quantity of water adsorbed. The adsorbed water molecules are in an oriented position and connected to the surface by hydrogen bonds. This water layer behaves like the solid particle itself on which the water is adsorbed. The orientation of water molecules decreases with the distance of the particle surface, and beyond a given distance they get into the normal state of water. The arrangement of particles in the agglomeration is determined by this distance.

All the fragments of layered silicates contain oriented adsorbed water, but in different quantities. The montmorillonite contains the largest quantity of water and at the same time is capable to the highest adsorption. The cations adsorbed on the mineral surface, influence significantly the adsorbed water and determine — besides its layer thickness — also the nature of the transition from the oriented state to the free bulk water.

In case of monovalent cations, especially of the  $\text{Na}^+$  adsorption, this transition is gradual, the adsorbed layer is thicker than for polyvalent cations where the transition is sharp. E.g. the adsorbed water of Ca-montmorillonite is built up of 5 molecular layers and has a thickness of  $\sim 30 \text{ \AA}$  in contrary to the Na-montmorillonite, where this layer is several times thicker, and in a physical meaning there is no boundary between the bounded and free water, as stated by Pirson (1958). The cation-set adsorbed on the particles can be replaced. Generally, the polyvalent cations are bounded more strongly, so it requires a higher concentration of monovalent cations to replace them by the latter ones. The process of replacement can be modified by the pH of the intrinsic water. The pH-decrease is favourable to the adsorption of polyvalent cations and  $\text{H}^+$  ions and at the same time affects in the direction of compaction of the agglomeration, i.e. in the direction of increasing the free pore volume. The pH-increase results in an excess of  $\text{Na}^+$  in the water and promotes the exchange for  $\text{Na}^+$ , thus increasing the thickness of the adsorbed water layer around the particles and causes a loosening in the agglomeration and a reduction in the pore volume.

### The role of clay minerals in the efficiency of CO<sub>2</sub> gas flooding

The results of investigations with CO<sub>2</sub> containing reservoir fluids were presented by Bauer (1983), thus data of capillary pressure and relative permeability measurements, determined by means of a device developed just for this purpose (Bauer 1978).

The comparison of values measured on sandstone reservoir rocks and synthetic rocks containing no components of a hydration ability (Figs 5–10 and Table I.), led to the conclusion that the interfacial and capillary behaviour of natural rocks significantly changes under the effect of CO<sub>2</sub> containing reservoir fluids.

On the basis of the investigations, these changes indicated by a gradual decrease of the slope of drainage  $P_c$ -curves and by a decrease of the irreducible water saturation (Figs 5 and 7) and by an increasing residual oil saturation in the imbibition direction (Figs 6 and 8) are caused by the 2–4% clay mineral content of rocks. With an increasing amount of dissolved CO<sub>2</sub> gas in the water, i.e. with a decrease of the water pH, the effective volume of clay mineral agglomerations decreases in the pores, the originally adsorbed Na<sup>+</sup> ions are at first exchanged for H<sup>+</sup> ions, and afterwards — with the

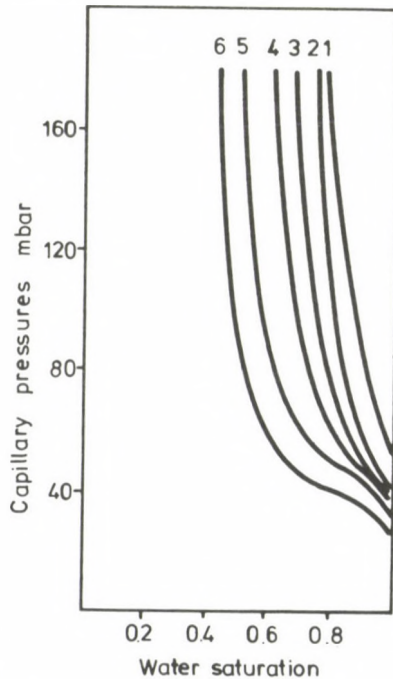


Fig. 5. Drainage capillary pressure curves measured under reservoir conditions (82 °C, 100 bars) on Lovászi sandstone — distilled water-Lovászi crude oil system, Curve 1: The fluids do not contain CO<sub>2</sub> gas. Curves 2–6: CO<sub>2</sub> gas saturation pressures at 82 °C: 5, 20, 40, 60 and 80 bars

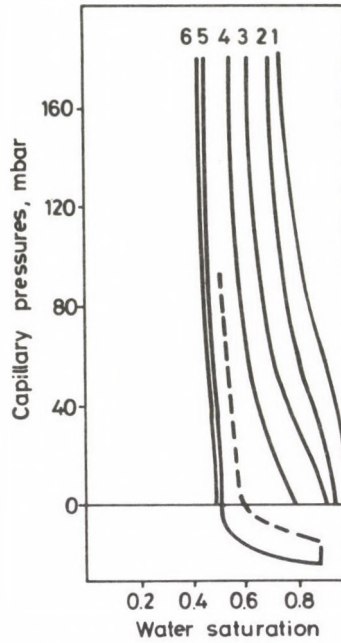


Fig. 6. Imbibition capillary pressure curves measured on the system of Fig. 5

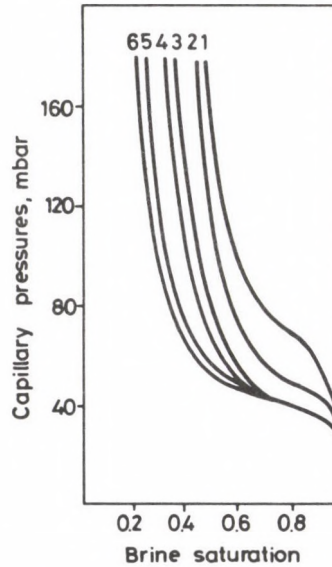


Fig. 7. Drainage capillary pressure curves measured under reservoir conditions (62 °C, 100 bars) on Zala sandstone-Zala reservoir fluids. Curve 1: The fluids do not contain CO<sub>2</sub> gas. Curves 2-6: CO<sub>2</sub> gas saturation pressures at 62 °C: 5, 20, 40 60 and 80 bars

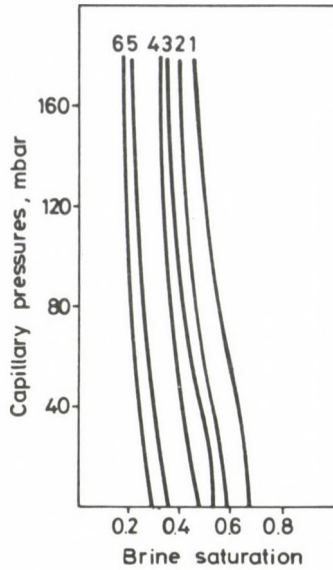


Fig. 8. Imbibition capillary pressure curves measured on the system of Fig. 7

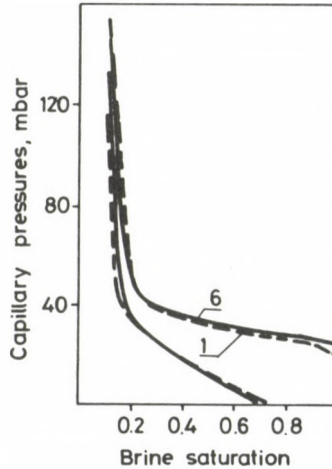


Fig. 9. Drainage and imbibition capillary pressure curves measured under reservoir conditions (82 °C, 100 bars) on sintered pyrex glass powder-Lováski reservoir fluids system. Curve 1: The fluids do not contain CO<sub>2</sub> gas. Curves 2–6: The fluids are saturated with CO<sub>2</sub> gas at 82 °C and a pressure of 80 bars

increase of the carbonate component — for Ca<sup>++</sup> and Mg<sup>++</sup> ions. This process takes place in the direction of drainage, i.e. that of oil accumulation, so the incorporation of natural surfactants contained by the oil produces an organic integration resulting also in a gradual development of an oil-wet rock character.

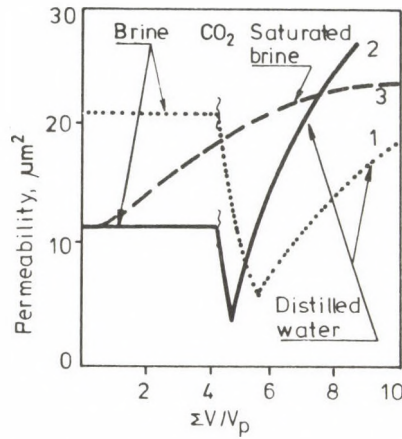


Fig. 10. Permeability changes of the Lovászi reservoir rock vs. cumulated volume of the injected fresh fluids (Zala brine and then distilled water) measured by injection and back-flow. Curve 1: temperature 20 °C, liquid phase pressure 10 bars. Curve 2: temperature 62 °C, liquid phase pressure 100 bars. Curve 3: Zala brine with high dissolved CO<sub>2</sub> concentration at 62 °C and 100 bars

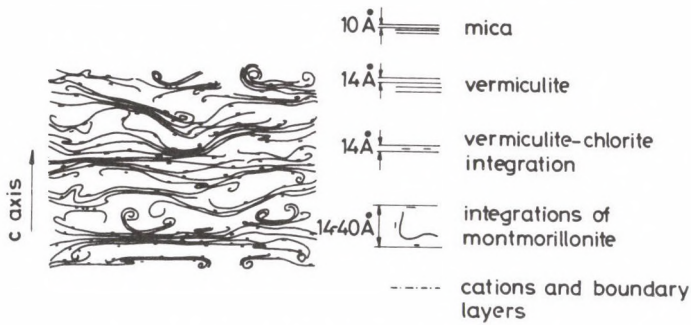


Fig. 11. Representative silicate-clay associations. After Bear (1964)

Table I

Average permeabilities ( $k_i$ , $\mu\text{m}^2$ ) and porosities ( $\phi$ ) of rock samples			Interfacial tensions of liquid pairs ( $\gamma_{wo}$ , $\text{mN} \cdot \text{m}^{-1}$ ) at different CO <sub>2</sub> saturating pressures ( $p_s$ , bar)					
$k_{\infty, N_2}$	$k_b$	$\phi$	0	5	20 $p_s$	40	60	80
Lovászi sandstone			Temperature 82 °C					
			Dist. water — Lovászi crude oil					
65	8	0.165	11.2	12	13	13.5	14	14.5
Sintered Pyrex glass			1237	1206	0.372			
Zala sandstone			Temperature 62 °C					
			Zala formation water-form, oil					
74	11	0.212	11.5	11.6	12	12.6	13.2	14

In connection with the effectiveness of CO<sub>2</sub> flooding, the followings may be established:

1. In reservoirs flooded already with surface water, depending on the quality of the water used, the hydration of clay minerals in the rock pores is already increased when the CO<sub>2</sub> gas injection starts.

2. In the system of reservoir fluids driven by CO<sub>2</sub> gas, the CO<sub>2</sub> containing water precedes the motion of the later mobilized oil, therefore its later accumulation takes place already in the part of rock having an increased useful pore-space.

3. During the accumulation of oil, the changes of the rock-fluid interface to an oil-wet direction, increases the residual oil saturation during the driving oil-bank.

4. On the basis of the above mentioned facts, the efficiency increasing effect of crude oil swelling and viscosity reduction, caused by CO<sub>2</sub> dissolved in the oil, can be compensated or strongly spoiled by the increase of useful pore space and by the shifting of rock wettability to oil-wet direction.

### References

- Baptiste O, Sweney S A 1955: Effect of clays on the permeability of reservoir sands to various saline waters. U.S. Bur. Mines Rept. Invest. 5180
- Bates T, Gruver R M, Yuster S T 1946: Influence of clay content on water conductivity of oil sands. *Oil Weekly*, 10, 48–50.
- Bauer K 1978: Results of capillary pressure-cycles measurements applying CO<sub>2</sub> saturated formations fluids under reservoir conditions. Report. Parts 1, 2.
- Bauer K 1983: Capillary behaviour of rock-fluid systems in presence CO<sub>2</sub>. Int. Symp. on CO<sub>2</sub> Enh. Oil. Rec. Hung. 3 (8–11) LS-8, 1–10.
- Bauer K, Tálas M, Bajor L 1975: Measuring process for determining the fluid saturation distribution in porous systems. Pat. No. 167–140.
- Bear F E 1964: Chemistry of the Soil. Reinhold Publ. Co. New York
- Dodd C G, Conley R F, Barnes P M 1955: Clay minerals in petroleum reservoir sands and water sensitivity. *Natl. Acad. Sci. Publ.* 395, 221–238.
- Grim R E 1958: Concept of diagenesis in argillaceous sediments. *Bull. Am. Assoc. Petrol. Geologists*, 42, 246–253.
- Hughes R V 1947: Importances of clay studies in water flood operations. *Producers Monthly* 11, No. 4. 13–16.
- Hughes R V, Pfister R I 1947: Advantages of brines in secondary recovery of petroleum by water flooding. *Trans. AIME*, 170, 187–201.
- Jacquin C 1965: Etude des ecoulements et des equilibres de fluids dans les sables argileux. *Revue de l'Inst. Franc. du Petr.* Tom. 20.
- Jordan J W 1949: Organophylic bentonites. T: Swelling in organic liquids. *J. Phys. Coll. Chem.*, 53, 294–306.
- Morris F C, Aune Q A, Gates G L 1959: Clays in petroleum reservoir rocks. U.S. Bur. Mines, Rept. Invest. 5425
- Nahin P G, Merrill W C, Grenall A, Grog R S 1951: Mineralogical study of California oil-bearing formations. *AIME, J. Petroleum Technol.*, 192, 151–158.
- Nemecz E 1973: Clayminerals. *Hung. Acad. Sci. Publ.* 471–481.
- Novak T I, Krueger R F 1951: The effect of mud filtrates and mud particles on the permeabilities of cores. *Drill. and Prod. Pract.*, 164–181.
- Pirson S J 1958: Oil Reservoir Engineering. Mc Graw-Hill Co. New York
- Taylor I M 1950: *Bull. Am Assoc. Petr. Geologists.*, 34–701.
- Von Engelhardt W, Tunn W M 1954: The flow of fluids through sandstones. *Heidelberger Beitr. Mineral u. Petrog.*, 2, 12–25.



## REDOX METHOD FOR THE INVESTIGATION OF COAL QUALITY

MRS. MILLEY J TÓTH<sup>1</sup>

The scope of this work is a quick measuring method requiring simple instruments, the essence of which is that the coal is treated with the aqueous solution of a strong oxidizing agent, and by measuring and recording the change of electrode potential against a saturated calomel electrode vs. time; a characteristic curve is given related to the chemical and physical state of coals, using which one may conclude to the degree of carbonization and to the geological history of coals, namely, it is possible to classify and qualify the coal samples.

**Keywords:** coal qualification; redox potential

### *Symbols*

$E$	electrode potential against a saturated calomel electrode,
$E_0$	standard redox potential
$\frac{(ox)}{(red)}$	the ratio of the activities of the oxidized and reduced forms,
$n$	number of equivalents,
$R$	universal gas constant = $8.31 \frac{\text{Joule}}{\text{mol. K}}$ ,
$T$	absolute temperature, K,
$F$	Faraday's number, 96500 coulomb

The knowledge of coal-chemical and coal-mineralogical features of coals of different origin is very important from the point of view of scientific and practical applications. A lot of laboratory analyses is necessary to classify and qualify exactly a given kind of coal on the basis of its physical and chemical properties (CHNS analysis, determination of volatile, ash and humidity content, measurement of vitrinite reflexion and other chemical and mineralogical components, *etc.*).

Only having determined the physical and chemical features (a tedious and tiresome work) is it possible to classify and qualify the coal sample into a characteristic group. From the point of view of the everyday practice, a quicker investigation method would be necessary. At the present time, however, the chemical and physical methods cannot assure quick, exact and reproducible information.

<sup>1</sup> Chemical Research Laboratory for Mining of the Hungarian Academy of Sciences, Miskolc-Egyetemváros, POB 2, Hungary, H-3515

The redox potential measurements were applied first by Krumbein and Garrels (1948), Pustovalov and Sokolova (1957) to determine rock characteristics in sediment petrology. In Hungary, Szádeczky-Kardoss (1952) emphasized the importance of redox potential in sediment geology.

The general equation for the redox potential was formulated by Nernst:

$$E = E_0 + \frac{RT}{nF} \ln \frac{(\text{ox})}{(\text{red})}.$$

For redox potential measurements, Pt or Au, and calomel electrodes were used, which were put into wetted rockpowder and the change of the redox potential was measured vs. time until the equilibrium was reached.

In Hungary, Bod and Bárdossy (1959) introduced a new method using a strong oxidizing agent, by means of which a general picture about the oxidizing process has been obtained. As oxidizing agent potassium bichromate + sulfuric acid was used. In this case the whole redox process is:



and the electrode potential:

$$E = E_0 + \frac{0.058}{6} \log \frac{(\text{Cr}_2\text{O}_7^-)(\text{H}^+)^{14}}{(\text{Cr}^{3+})^2}.$$

By this method the change of potential of the potassium bichromate system due to the rock material is measured. The change is the greater the higher the degree of reduction of the sample is, i.e. from the potential change one may conclude to the oxidation state of the rock.

This method was used first by Kossuth (1982) in Hungary to investigate the coals. She could conclude from these measurements to the general state of different coals (genesis, age, degree of carbonization, etc.).

The measuring technique of the redox potential has been improved and refined in the Chemical Research Laboratory for Mining (Hungary), thus it became applicable for the general qualification of coals of different state. The precision and reproducibility have been increased so that distinctions can be made between chemically and/or physically treated coal samples even in the case when they originated from the same source and are of the same geological age.

### Experimental part

The measurements were carried out with an OP-208 Precision Digital pH Meter (Radelkis) and an OH-814/1 Potentiometric Recorder (Radelkis) using saturated calomel and Pt electrodes as reference and measuring ones, respectively.

The oxidizing agent was a sulfuric acidic solution of  $K_2Cr_2O_7$ .

The chemicals were of analytical grade.

The measurements were carried out in a closed vessel of double wall to assure constant temperature and it had three tube connections for the electrodes and to feed the sample. For the thorough mixing of the solvent-coal suspension during the measurement a magnetic stirrer was used. The coal samples were ground and sieved to a given particle size.

### Discussion

As a first step, three coals of different age and source were examined to indicate differences in the redox potential *vs.* time curves, as it is shown in Fig. 1. Figure 1 shows that the time required for oxidation increases with the degree of maturity (carbonization), i.e. it decreases the degree of reduction.

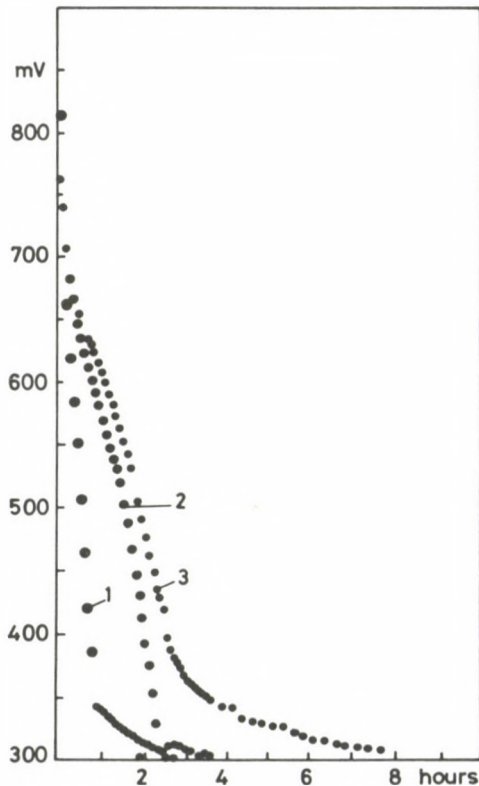


Fig. 1. Curve 1: young lignite from Gyöngyösvisonta, Curve 2: brown coal of a Miocene age from Lyukóhánya, Curve 3: brown coal of an Eocene age from Tatabánya

Figure 2 shows the curves of a certain coal for different particle sizes. From these data it follows that the time of oxidation increases with increasing particle size. This phenomenon can be explained by two effects: 1. the specific surface area decreases with increasing particle size, so the effect of the oxidizing agent decreases; 2. difference in the mineral composition of the grain size fractions. To eliminate their disturbing effect, the grain size fractions under  $63\ \mu\text{m}$  were used in the following for each treatment and measurement. In Fig. 3 the effect of the ash content decreasing chemical treatment is shown. The ash contents of coal samples corresponding to curves 1 to 3 are 20.1; 3.2 and 1.5% by weight, respectively. The C contents from CHNS analysis data were 49.6; 58.5 and 68.6% by weight, respectively.

In the further experiments special attention was paid to the so-called mechanochemical effects, i.e. to the kind of changes which take place during the joint grinding of different coals with different materials. These mechanochemical effects were earlier investigated from an other point of view by Tóth and Milley (1982). Figure 4

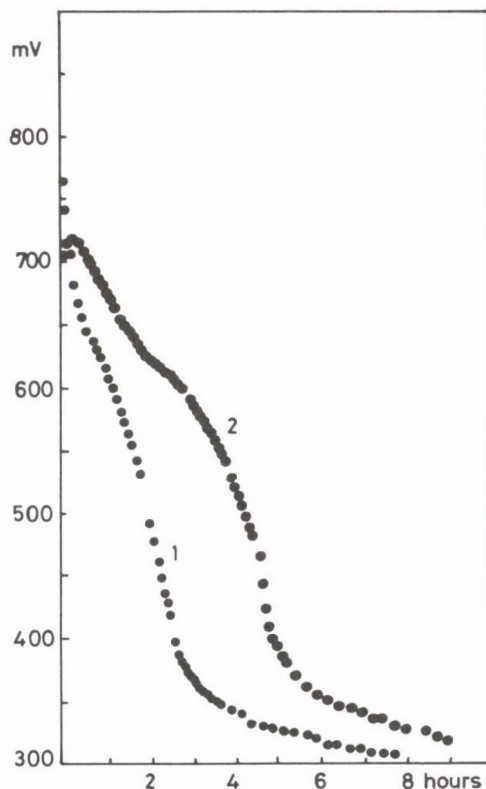


Fig. 2. Curve 1: particle size below  $63\ \mu\text{m}$ , Curve 2: particle size fraction  $63\text{--}100\ \mu\text{m}$

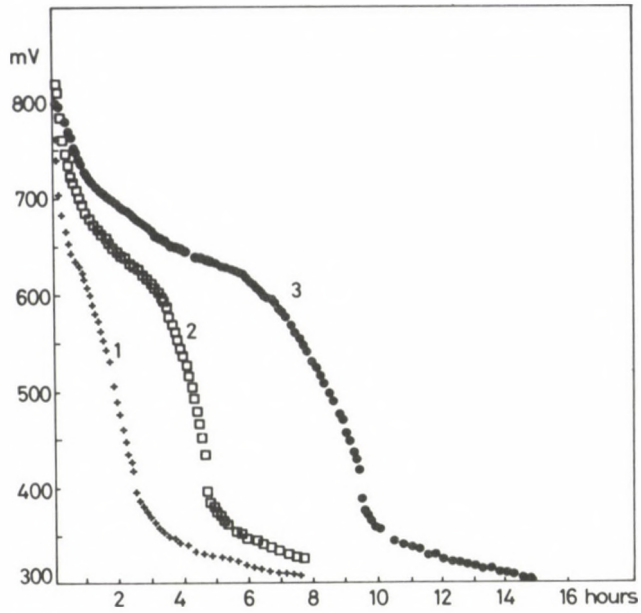


Fig. 3. Curve 1: washed coal from Tatabánya, Curve 2: the same coal after percolation, Curve 3: percolated coal treated with HCl

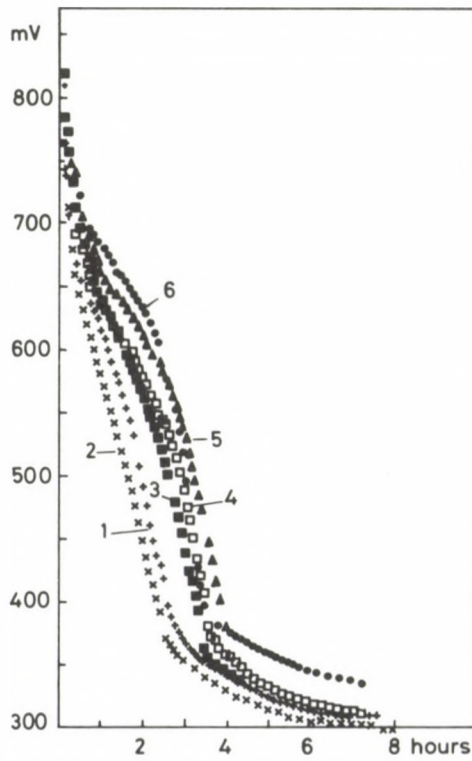


Fig. 4. Curve 1: washed coal from Tatabánya, Curve 2: the same coal ground with 30% water, Curve 3: ground with 7.5% fuel oil, Curve 4: ground with 15% fuel oil, Curve 5: ground with 20% fuel oil, Curve 6: ground with 30% fuel oil

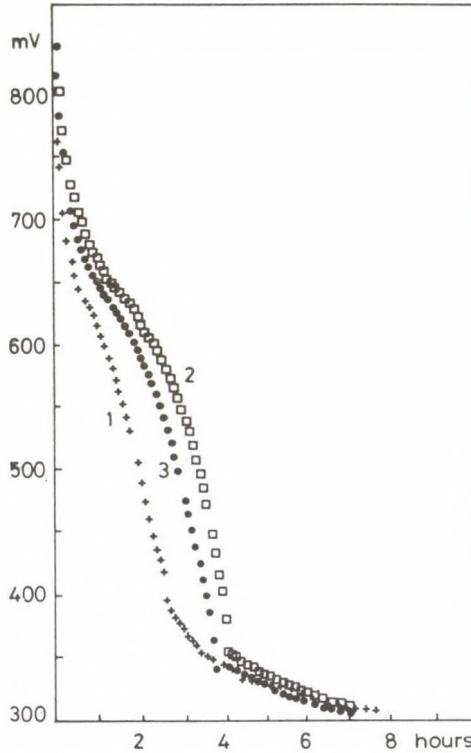


Fig. 5. Curve 1: washed coal from Tatabánya, Curve 2: the same coal ground with 20% fuel oil for one hour, Curve 3: ground with 20% fuel oil for two hours

shows the results of these investigations when a certain coal was jointly ground for 1 hour with water and with different quantities of fuel oil. On the basis of Fig. 4 the conclusion can be drawn that the grinding with water made the coal "younger" (curve 1 is below the curve of the original coal), but the grinding with fuel oil made it "older". These results show the direction of changes. The changes are connected to the wettability, too, as the higher carbonization makes the coal less water-wet and *vice versa*. According to these measurements the desired quantity of fuel oil can be chosen, as different quantities of oil result in different changes. At the same time it is not profitable to increase the oil quantity by more than 30% by weight, as the change between 20 and 30% is already negligible.

Figure 5 shows the effect of the grinding time with the same quantity of oil. After one hour the carbonization process turns back. Thus the ideal grinding time can be determined.

The next step was to investigate the efficiency of grinding. Figures 6 and 7 show the effect of grinding tools and grinding methods. In Fig. 7 the intermittent grinding

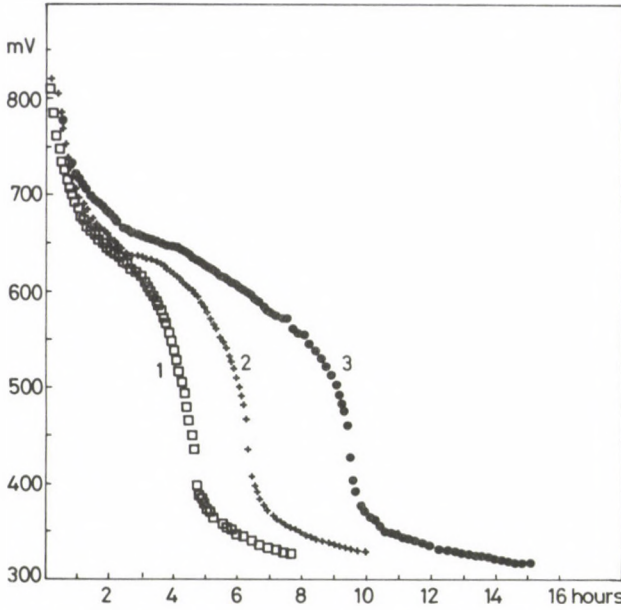


Fig. 6. Curve 1: percolated coal from Tatabánya, Curve 2: the same coal homogenized with fuel oil in a homogenizer for ten minutes, Curve 3: ground in a ball mill with 15% fuel oil for one hour

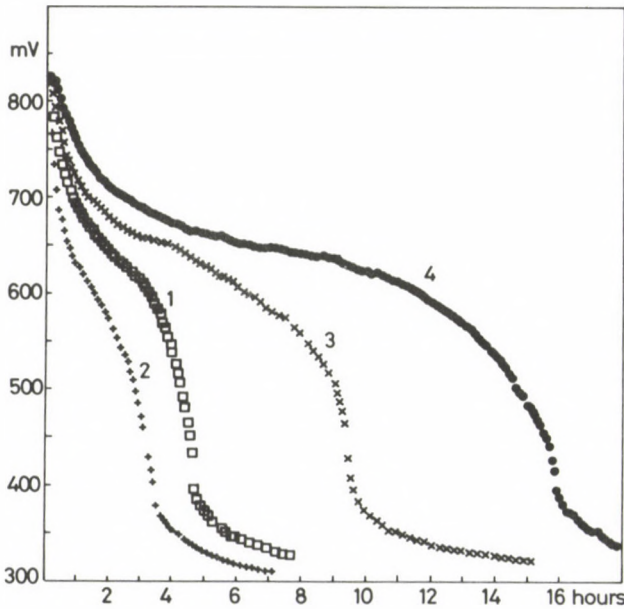


Fig. 7. Curve 1: percolated coal from Tatabánya, Curve 2: washed coal from Tatabánya ground with 15% fuel oil for one hour, Curve 3: the same coal ground with 15% fuel oil for one hour, Curve 4: ground with 15% fuel oil for 4 × 15 minutes (intermittent grinding)

means that in every 15 minutes the mill was opened and the coal was mixed to assure fresh particle surfaces. These figures show that the greatest change took place in the case of intermittent grinding in a ball mill.

The experiments described above were the most typical ones to illustrate some possibilities for the redox potential curves in coal chemistry, but, in addition to these, there may be a number of fields where this method can be applied and is to be developed.

### Conclusions

Experiments show that the redox potential curves give useful information about the chemical and physical state of coals, e.g. about their source, genesis, age, change of their character during or after chemical and physical treatment, wettability, *etc.* The method yields detailed information about coals, if the different characters of the curves are taken into consideration. The curves have sections of different slopes, integral values, different maxima on the differential curve, *etc.*, and these values are related to the chemical and/or mineral composition, physical and chemical state, *etc.* Comparing specific coal characteristics (as known from detailed analysis) to the characteristic features of the redox potential curves, it is possible to use these curves as the "fingerprints" of coals. In order to develop the proposed method in an absolute one, further experimental and analytical work is necessary, and these investigations are already going on.

### Acknowledgements

The author wishes to express her gratitude to Dr. J Tóth and to Dr. Gy Milley, for their interest in this research and for their help given by assuring the proper samples and instrumentation.

A special thank is due to Mrs. G Kossuth for her initiatives and valuable information.

### References

- Bod M, Bárdossy Gy 1959: A new method to determine the redox conditions of sedimentary rocks. (In Hungarian) *Geofizikai Közlemények*, 8, 53–64.
- Kossuth G 1982: Personal communication.
- Krumbein W C, Garrels R M 1948: Origin and classification of chemical sediments in term of pH and oxidation-reduction potentials. *Journal of Geol.*, 56, 13–19.
- Pustovalov L V, Sokolova E I 1957: Methods to determine pH and Eh in sedimentary rocks (in Russian). In: *Metodi izucheniya osadochnikch porod. Gosgeoltekhizdat, Moscow*, 112.
- Szádeczky-Kardoss E 1952: New ideas in the classification of sedimentary rocks. (In Hungarian) *Földtani Közlöny*, 2, 12–27.
- Tóth J, Mrs. Milley Tóth J 1982: Possible role of mechanical effects in crude oil generation and geochemical investigation of hydrocarbons. *Acta Geod. Geoph. Mont. Hung.*, 17, 447–454.

## INTERFACIAL ENERGY AND PORE STRUCTURE

L BALLA<sup>1</sup>, GY MILLEY<sup>1</sup>, O WAGNER<sup>1</sup>

The microscopic properties of the porous medium and particularly the role of pore structure and interfacial energy are dealt with.

It is shown that the knowledge of the pore size distribution gives more information for the pore structure than the average permeability value.

It was found that it is expedient to determine the pore size distribution and the specific interfacial energy from the imbibition because of the dynamic characteristic of the process.

**Keywords:** average permeability; imbibition; interfacial energy; pore size distribution; pore structure

### *Symbols*

<i>A</i>	cross sectional area, m <sup>2</sup>
<i>D</i>	deviation, dimensionless
<i>E</i>	specific interfacial energy, Nm <sup>-1</sup>
<i>f</i>	pore size distribution function, dimensionless
<i>g</i>	gravitational acceleration, ms <sup>-2</sup>
<i>h</i>	height of capillary rise, m
<i>k</i>	absolute permeability, m <sup>2</sup>
<i>K</i>	relative permeability function, dimensionless
<i>L</i>	length, m
<i>n</i>	homogeneity number, dimensionless
<i>P</i>	pressure, Pa
<i>r</i>	radius, m
<i>S</i>	saturation, dimensionless
<i>t</i>	time, s
<i>V</i>	volume, m <sup>3</sup>
$\alpha$	angle of the slope of the capillary tube
$\sigma$	interfacial tension, Nm <sup>-1</sup>
$\Gamma$	gamma function, dimensionless
$\mu$	dynamic viscosity, Pa · s
$\rho$	density, kg · m <sup>-3</sup>
$\Phi$	porosity, dimensionless
$\Theta$	contact angle, grade

<sup>1</sup> Chemical Research Laboratory for Mining of the Hungarian Academy of Sciences, Miskolc-Egyetemváros, POB 2. Hungary, H-3515

## Subscripts

<i>a</i>	average	<i>n</i>	nonwetting phase
<i>c</i>	capillary	<i>r</i>	relative
<i>e</i>	equivalent	<i>w</i>	wetting phase
<i>i</i>	irreducible	*	normalized

The efficiency of the combined oil recovery methods is mainly determined — besides the exploitation system — by the geometric and physico-chemical properties of the porous media of reservoir rocks. This paper deals only with the microscopic properties of the porous medium, emphasizing the role of pore structure and interfacial energy.

The porous system, the saturation and distribution of residual oil, the dispersion and reaction of the chemicals used, are significantly determined by the pore structure and the interfacial energy. An acceptable picture is given about the pore structure and the interfacial energy — according to the present knowledge of measuring technique by the saturation-capillary pressure curves, being in connection with the flow process in the porous media, as in the case of different pore extraction methods the interfacial energy deviates from the real conditions. For this reason, the investigations are based on the evaluation of saturation-capillary pressure measurements.

### Characterization of the pore size distribution

For the mathematical simulation and laboratory investigations, measured saturation-capillary pressure values are to be approximated by mathematical functions. However, among the mathematical functions only those could be useful to draw proper conclusions which have parameters of physical meaning.

The processed literature data and the results of our laboratory measurements have confirmed that — in most cases — the measured capillary pressure *vs.* saturation data can be described by the following function (Milley and Wagner 1975):

$$P_c = P_{ac} (-\ln S_w^*)^{\frac{1}{n}} \quad (1)$$

where

$$S_w^* = \frac{S_w - S_{wi}}{1 - S_{wi} - S_{ni}}$$

Changing the  $P_{ac}$  and  $n$  parameters in Eq. (1), the capillary pressure-saturation range shown in Fig. 1 can be described. Applying the Laplace equation

$$P_c = \frac{2\sigma \cos \Theta}{r} \quad (2)$$

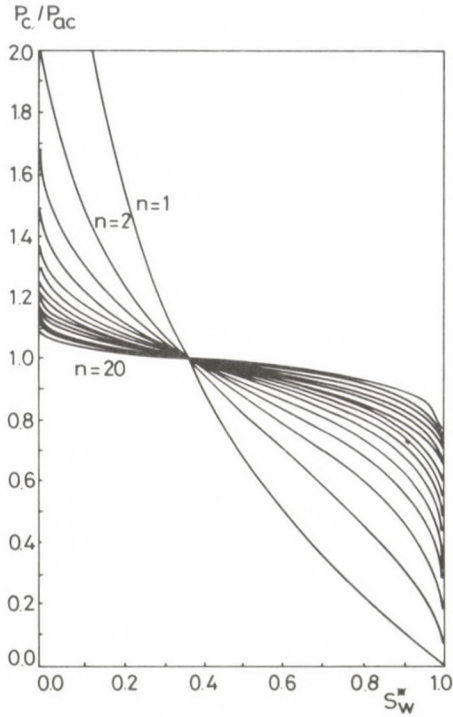


Fig. 1. The capillary pressure function

and the Scheidegger-relation

$$\frac{\int_0^r r^2 f(r) dr}{\int_0^\infty r^2 f(r) dr} = S_w^* \tag{3}$$

the following relative pore size distribution can be derived (Balla 1982):

$$f(r) = \frac{n \left(\frac{r}{r_{ac}}\right)^{-(n+3)} \exp\left[-\left(\frac{r}{r_{ac}}\right)^{-n}\right]}{\Gamma\left(1 + \frac{2}{n}\right)} \tag{4}$$

where

$$r_{ac} = \frac{2\sigma \cos \Theta}{P_{ac}} \tag{5}$$

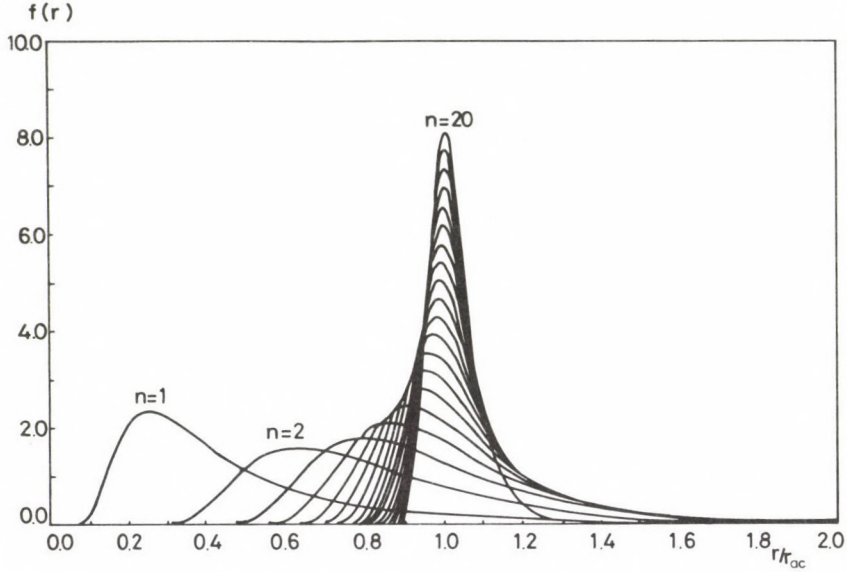


Fig. 2. The pore size distribution function

For the  $f(r)$  distribution function it is valid:

$$\int_0^{\infty} f(r) d\left(\frac{r}{r_{ac}}\right) = 1. \tag{6}$$

In Fig. 2 the  $f(r)$  pore size distribution function is seen at different values of  $n$ . The range of the pore size distribution which decreases as the homogeneity number,  $n$ , increases, is characteristic for the homogeneity of pore sizes: the lower the  $n$  is, the more homogeneous is the pore structure.

The relative pore size distribution function defined in Eq. (4) is characterized by its average value:

$$r_{ra} = \frac{\Gamma\left(1 + \frac{1}{n}\right)}{\Gamma\left(1 + \frac{2}{n}\right)}, \quad r_{ra} = \frac{r_a}{r_{ac}} \tag{7}$$

the variance of which is

$$D^2 = \frac{1}{\Gamma\left(1 + \frac{2}{n}\right)} - \left[ \frac{\Gamma\left(1 + \frac{1}{n}\right)}{\Gamma\left(1 + \frac{2}{n}\right)} \right]^2 \tag{8}$$

and the relative deviation is:

$$D_r = \left\{ \left[ \frac{\Gamma\left(1 + \frac{2}{n}\right)}{\Gamma\left(1 + \frac{1}{n}\right)} \right]^2 / \Gamma\left(1 + \frac{2}{n}\right) - 1 \right\}^{1/2} \tag{9}$$

In Fig. 3, Eqs (7), (8) and (9) are represented in the function of  $n$ .

Figure 4 shows the relative deviation in the function of  $1/n$ . The relation with and acceptable accuracy can be supposed to be linear so

$$D_r \cong \frac{1}{n} \tag{10}$$

that is, the value of  $1/n$  is approximately the relative deviation of the pore size distribution. The relative deviation is directly characteristic for the pore size distribution range, therefore  $1/n$  characterizes the homogeneity of the pore structure.

To find the physical meaning of the parameter  $P_{ac}$  in the capillary pressure function, let us constitute its integral according to the saturation. It means an energy term relating to the unit pore volume, necessary to exert from outside or by the system, to displace the fluid in the pore space by an other one. The work is made against the specific interfacial energy being defined by the  $\sigma \cos \Theta$  relation.

Into the energy relation

$$E = \int_0^1 P_c \cdot dS_w^* \tag{11}$$

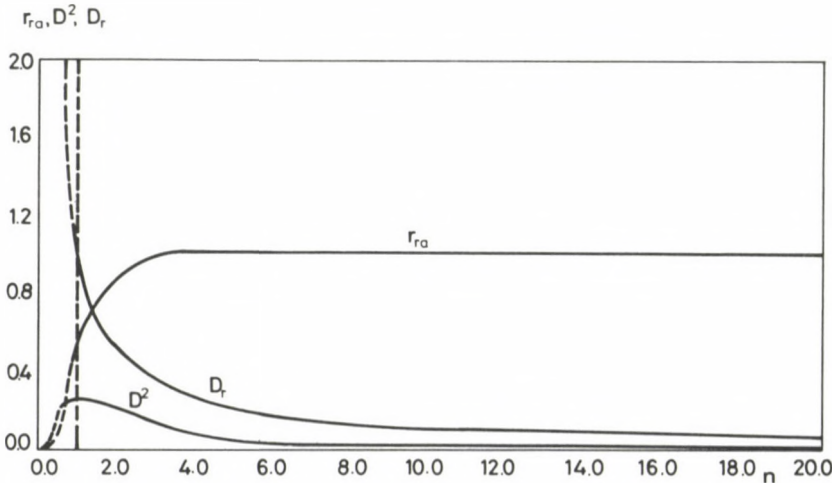


Fig. 3. Characteristics of the pore size distribution

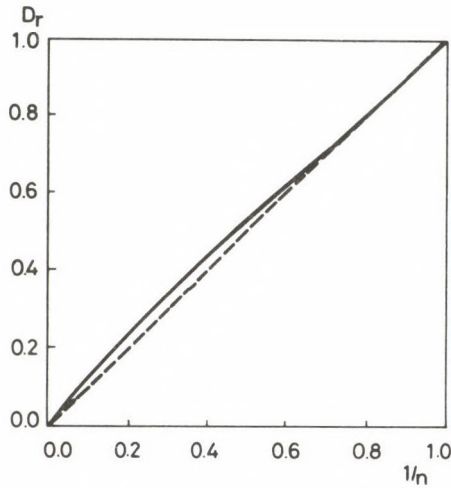


Fig. 4. The function  $D_r - 1/n$

let us insert the capillary pressure function defined by Eq. (1). After integration, the following equation is got:

$$E = P_{ac} \cdot \Gamma\left(1 + \frac{1}{n}\right). \quad (12)$$

In Fig. 5 function  $\Gamma\left(1 + \frac{1}{n}\right)$  is represented as a function of  $n$ . If  $n \geq 1$ , which is valid according to Eq. (1), we get:

$$\Gamma\left(1 + \frac{1}{n}\right) \cong 1 \quad (13)$$

that is

$$E \cong P_{ac} \quad (14)$$

so  $P_{ac}$  represents the energy related to the pore volume.

It follows that the parameters  $P_{ac}$  and  $n$  in Eq. (1) have a certain physical meaning. The theoretical conclusions were verified experimentally, on the basis of experimental data published by Calhoun et al. (1949) and by the data of experimental measurements carried out in the Chemical Research Laboratory of Mining (CRLM). In both series of experiments the relative deviation of the pore size distribution can be supposed as constant within permissible limits with a high probability, because Calhoun et al. (1949) used identical but regenerated core samples, while in the CRLM, consolidated bodies were prepared from glass beads of different diameters, but of the same distribution.

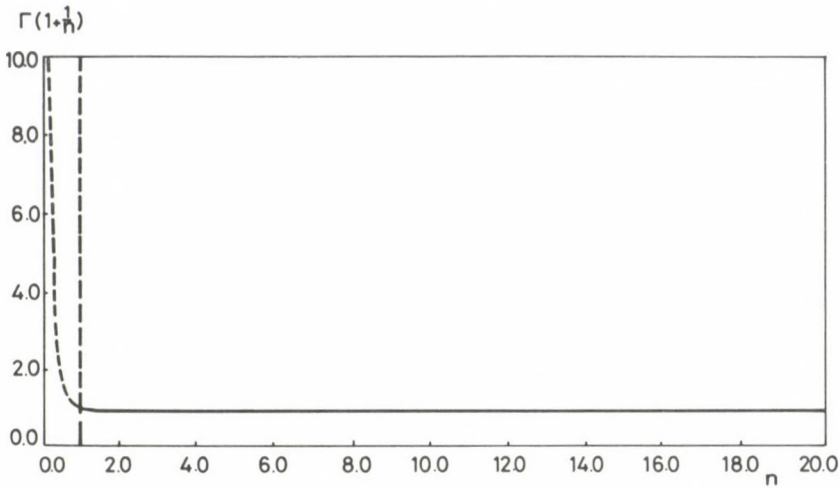


Fig. 5. The function

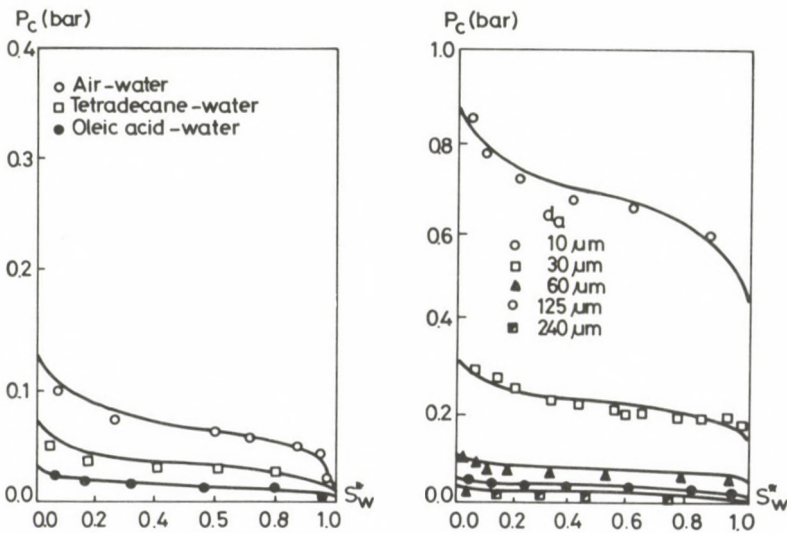


Fig. 6. Calculated and measured values of  $P_c$

In Calhoun et al's experiments the specific interfacial energy was changed at constant pore structure, while in our laboratory experiments the average pore size was changed at constant interfacial energy and relative pore size deviation.

The results of the measurements and the capillary pressure functions adjusted to them are shown in Fig. 6.

The constancy of the values  $n$ , verifying the physical meaning of  $n$ , was within 10% accuracy. The insignificant difference originates from differences in the technology of core regeneration and core preparation.

In Fig. 7 calculated values of  $P_{ac}$  are compared to the measured specific interfacial energies, i.e. to the square root of the measured permeability being directly proportional to the pore size. The linear relations verify the Laplace equation, and by it the physical meaning of  $P_{ac}$ .

Thus, it is proved both theoretically and experimentally that the parameters of the capillary pressure function have a well defined physical content, so they can be applied for further theoretical and experimental investigations.

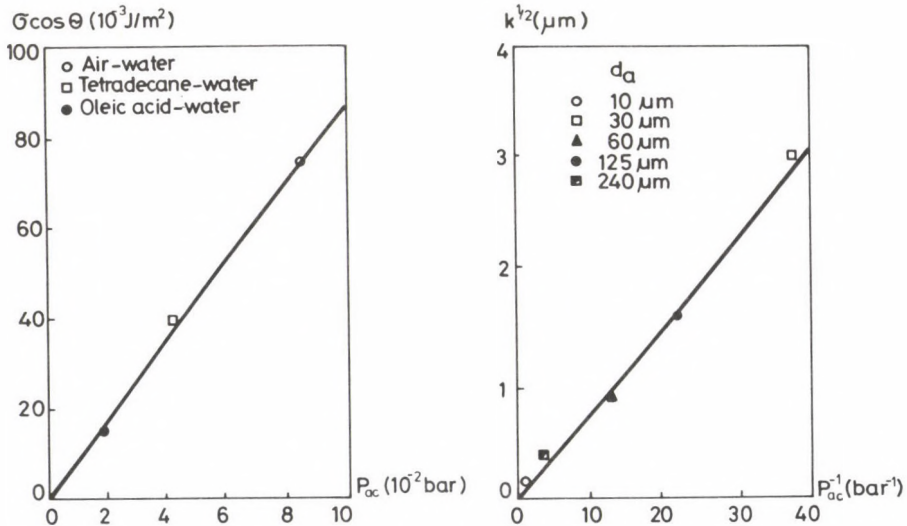


Fig. 7. Comparison of calculated  $P_c$  values to measured ones

### The applicability of the pore size distribution

The most general investigation method of flow processes in porous media is the laboratory linear displacement experiment.

The two-phase, immiscible, incompressible, isotherm, Darcy-type fluid flow is described by the Buckley-Leverett theory, if it is supposed that the interfacial energy is zero.

For the calculations the normalized relative permeability functions are used which are based on the Burdine's relations and give a sufficient accuracy for the theoretical investigations:

$$K_w^* = S_w^{*2} \int_0^{S_w^*} \frac{dS_w^*}{P_c^2} \bigg/ \int_0^1 \frac{dS_w^*}{P_c^2}$$

(15)

and

$$K_n^* = (1 - S_w^*)^2 \int_{S_w^*}^1 \frac{dS_w^*}{P_c^2} \bigg/ \int_0^1 \frac{dS_w^*}{P_c^2}$$

The normalized relative permeability functions calculated using the capillary pressure function (1) are shown in Fig. 8.

Let us suppose that experiments are carried out on linear cores of the same lengths and permeabilities using immiscible, incompressible fluids of the same mobility ratio, under isothermal conditions, at constant injection rate. Figure 9 shows the saturation distributions ( $S_w^*$ ) calculated for the cases when  $n=2$  and  $n=10$ , at identical values. The difference between the two saturation distributions is significant seen also at the time of breakthrough.

It follows that it is necessary to take into account not only the permeability of the porous core, when evaluating and planning laboratory experiment, but also the homogeneity of the pore structure is to be considered, as a significant factor.

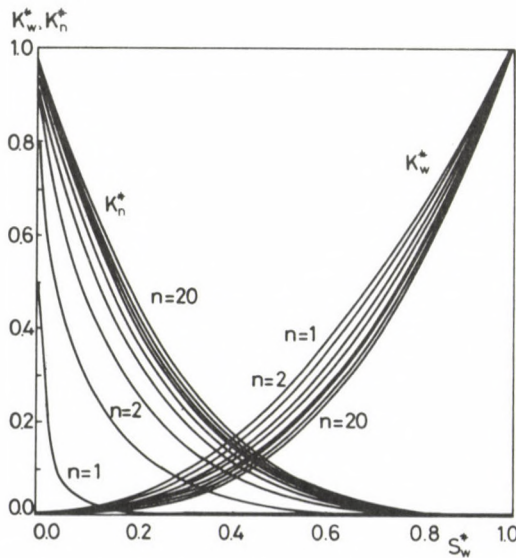


Fig. 8. The normalized relative permeability functions

The process of free imbibition in a porous medium is characteristic for its structure, therefore if the information got from a measurement is properly processed, valuable data can be obtained concerning the pore structure.

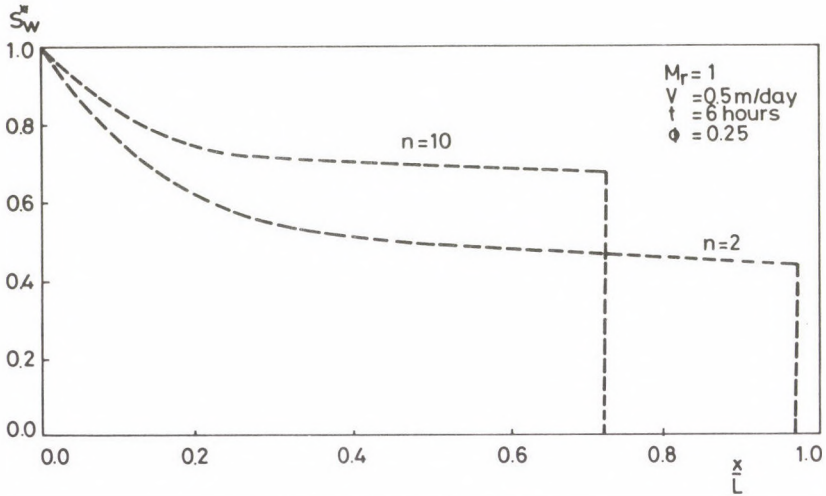


Fig. 9. The saturation distribution

The imbibition process is characterized by the flow system introduced earlier. Until now, for interpreting the process, the Washburn-equation was generally used (Levine and Neale 1975):

$$\frac{dh_w}{dt} = \frac{r_e^2}{8\mu_w} \left( \frac{2\sigma \cos \Theta}{r_e \cdot h_w} - (\rho_w - \rho_n)g \cdot \sin \alpha \right) \tag{16}$$

where the equivalent pore size,  $r_e$ , can be determined from the following equation:

$$\frac{k}{\Phi} = \frac{r_e^2}{8} \tag{17}$$

Using the pore size distribution function (4), and supposing the applicability of the capillary-bundle model, the liquid quantity imbibed during a time  $t$  by a prism of a cross sectional area  $A$ , porosity  $\Phi$  and height  $L$ , is:

$$V(t) = A \cdot \Phi \frac{\int_0^\infty r^2 h_w(r, t) f(r) dr}{\int_0^\infty r^2 f(r) dr} \tag{18}$$

where the value of  $h_w(r, t)$  is calculated by means of Eq. (16).

Figure 10 shows the calculated and measured results of an imbibition process carried out on a synthetic, consolidated core. The experiment was made under isothermal conditions, using a water-air system and absolutely water-wet medium, so the value of the specific interfacial energy  $\sigma \cos \Theta$  was known.

The calculated values  $r_{ac}$  and  $n$  fitting best the experimental results are real ones, and the value calculated by them are in agreement with the measured results what supports the applicability of the model based on the pore structure.

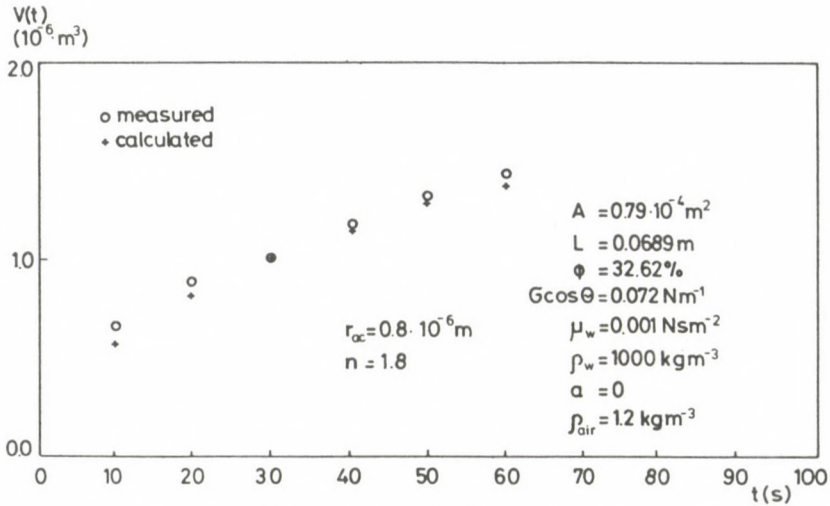


Fig. 10. The quantity of imbibed fluid

## Conclusions

The fluid flow processes in porous media cannot be studied in most cases with proper accuracy using the average hydrodynamic characteristics and the permeability of the porous system, but it is necessary to take into account also other characteristics of pore size distribution.

The knowledge of the pore size distribution, even if it is approximative, gives more information for the pore structure than the average permeability value.

It is expedient to determine the pore size distribution and the specific interfacial energy from the imbibition process, as in this case it is characteristic for the dynamic conditions.

Knowing the pore structure, the oil displacement processes can be more realistically evaluated, and the planning of new combined oil recovery processes can be made more accurate.

## References

- Balla L 1982: Study of modelling possibility of fluid flow in porous media. (In Hungarian) Doctor's Thesis, University for Heavy Industry, Miskolc
- Calhoun J C, Lewis M, Newman R C 1949: Experiments on the capillary properties of porous solids. *Transactions of AIME*, 186, 189–196.
- Levine S, Neale G 1975: Theoretical aspects of the rate of wetting of a porous medium. In: *Int. Conf. on Colloid and Surface Sci.*, Akadémiai Kiadó, Budapest, 761–768.
- Milley Gy, Wagner O, 1975: The theoretical and practical solution of producing porous bodies from monodisperse spheres and the study of these systems. (In Hungarian) Candidate's Thesis, Budapest

## RAPID PYROLYSIS OF HUNGARIAN BROWN COALS

J GEREJ<sup>1</sup> and I GYÖRGY<sup>1</sup>

A Hungarian brown coal and a lignite were subjected to rapid pyrolysis at 400–800 °C using a laboratory scale (100 g/h) entrained bed reactor. The Heinze-assay performed on product chars indicated that the coals had undergone pyrolysis with a high conversion at the low residence times used. The yield of tar was shown to diminish at higher temperatures with both coals. Acidic and basic extraction as well as gas-chromatographic simulated distillation methods were used to characterize tars. The fraction of phenolic and basic components decreases strongly with increasing temperature, whereas the fraction of saturated, aromatic and polyaromatic compounds increases.

**Keywords:** brown-coal pyrolysis; tar formation

### Introduction

A number of coal conversion procedures have been developed which utilize decomposition of powdered coals using high heating rates ( $10^3 - 10^4$  K/s). The COED, COALCON, Chukhanov, IGI, Garrett, Kellogg and Toscoal methods use gaseous or solid (burning coke, melted metals and salts, ceramic balls) heat carrier for rapid heating (CEP 1974, Howard–Smith and Werner 1976). Though these methods achieved up to now rather different stages of development, they all promise economic feasibility by employing continuous operation of high-capacity reactor units to produce low-sulfur char, fuel gas and oil of high calorific value as well as a valuable light-oil fraction which can be subjected to further refining (Durai–Swamy et al. 1979, Schonfeldt et al. 1981).

Among the various processes of coal conversion, pyrolysis is of special importance, as it is the primary process of all the others taking place in hydrogenation, gasification combustion, *etc.* Though the pyrolysis of coal has long been studied and the subject has seen a revival of interests particularly in recent years, the main efforts have still been concentrated on studying devolatilization or the evolution of gaseous products (Anthony and Howard 1976). The formation of tars, as well as their characterization, upon rapid or flash pyrolysis have received less attention.

This work reports on the rapid pyrolysis of brown coals carried out in a bench scale entrained bed reactor. Emphasize was put on the formation and structure of tar and char products.

<sup>1</sup> Institute of Isotopes of the Hungarian Academy of Sciences H-1525 Budapest, P.O.B. 77

## Experimental

The scheme of the pyrolysis apparatus is shown in Fig. 1. The 1000 mm long silica reactor tubing had an internal diameter of 24 mm. External heating of the reactor was supplied by a temperature controller of 2200 Watt power output. Coal powder ( $\sim 100$  g/h) was fed into a preheated stream of high-purity nitrogen ( $20$  l/h). The temperature of the char pot was maintained at  $0^\circ\text{C}$  throughout this work. The gas-stream was fed into water-cooled condensers, dry and oil-filters, a gas sampling device and a wet test meter.

Coal samples and their analyses (Table I) were supplied by the Central Institute for the Development of Mining (Budapest). The coals were ground to  $0\text{--}0.1$  mm and stored under argon.

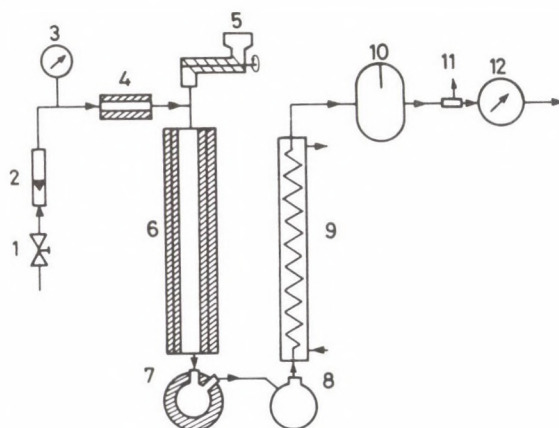


Fig. 1. Scheme of pyrolysis apparatus. 1. Valve; 2. Flow meter; 3. Pressure gauge; 4. Preheater; 5. Coal feeder; 6. Reactor; 7. Char pot; 8. Condensates; 9. Water-cooling system; 10. Filter; 11. Gas-sampling device; 12. Wet test meter

Table I. Coal samples and their analyses (as received, %) (Central Institute for the Development of Mining, Budapest)

	Tatabánya brown coal	Visonta lignite
Moisture	12.0	8.9
Ash	21.7	12.4
Volatiles	36.7	43.0
Calorific value, MJ/kg	17.4	18.4
Carbon	46.5	48.9
Hydrogen	3.2	4.0
Sulfur	3.8	1.4
Nitrogen	1.3	0.8
Oxygen (by difference)	11.5	23.6

In order to perform a highly constant rate of coal-feeding, sand was admixed to the coal in a ration of 3:1. A narrow fraction of sand (0.1–0.315 mm) was treated with hydrochloric acid, then washed with distilled water and finally heated at 900 °C for 2 hours. The coal + sand mixtures were dried in a stream of argon at 105 °C for 1 hour prior to each experiment.

The effect of heating rate on product yields could be elucidated by applying a constant rate of heating to the coals in a Heinze type arrangement of the same reactor. The reactor was loaded with 20 small silica boats, each of them containing 1 g of coal, and the temperature was programmed linearly with a rate of 8 °C/min to 800 °C.

The gaseous products were analyzed by a Chrom 31 type chromatograph equipped with a 2.5 m long column filled with Molecular Sieve 5A and a thermal conductivity detector.

Tars were collected from the condensers by washing them with dichlormethane. The char was extracted in a Soxhlet-apparatus using the same solvent. Having removed the dichlormethane by distillation, the weight of tar was measured. Dilute dichlormethane solutions of tar were subjected to further analysis.

The method of gas-chromatographic simulated distillation developed originally to the analysis of heavy crude-oil fractions, was adapted to the characterization of tars (Eggersten et al. 1960, Green et al. 1964, Schweighardt et al. 1982). Analyses were carried out using a 2.5 m column of 10% SP-2100/Supelcoport loaded into a gas-chromatograph, type Chrom 4, equipped with a flame-ionization detector. The temperature was programmed from 60 to 240 °C at a rate of 8 °C/min. The yield of fractions having different boiling ranges (light-oil: –180 °C, middle-oil: 180–230 °C, heavy oil: 230–270 °C, anthracene oil: 270–340 °C) as well as the corresponding temperatures in the chromatogram were determined using adequate calibration standards.

The yields of acidic, basic and neutral fractions of tars were determined by extraction of tar solutions with 10% sodium-hydroxid, 10% sulfuric acid solutions and concentrated sulfuric acid. Between each step the corresponding simulated distillation profiles were determined.

The char samples were subjected to detailed analysis in the laboratories of the Central Institute for the Development of Mining (Budapest).

## Results and discussion

The rapid pyrolysis of a Tatabánya brown coal and a Visonta lignite (0–0.1 mm) was studied in the entrained flow apparatus. If the stream of carrier gas is maintained at a rate of 20 l/h, a coal particle having a diameter of 0.1 mm will fall approximately freely. The residence time at this particle size is a few tenths of a second, according to Stokes' equation (Scaroni et al. 1981), whereas the calculated residence time of the gas is

about 50 s. Chen and Wen (1980) suggest that a 1.0 mm coal particle will be heated up at a rate of  $10^3$  Ks upon falling into a gas at  $1000^\circ\text{C}$ . Chukhanov (1956) estimated that not more than 0.01 s is needed for a 0.1 mm coal particle to reach a temperature of  $1000^\circ\text{C}$  when dropped into a gas stream at atmospheric pressure.

The major gaseous products of pyrolysis are: hydrogen, methane, carbon-monoxid and carbon-dioxid. The yields of gaseous products formed upon slow and

**Table II.** Yields of gaseous products under slow and rapid heating (dry coal %)

Coal	Tatabánya (brown)			Visonta (lignite)		
Temperature, $^\circ\text{C}$	520	600	800	520	600	800
Heating rate	slow	rapid	rapid	slow	rapid	rapid
Products:						
Hydrogen	0.1	0.1	0.6	0.1	0.2	0.5
Methane	1.5	1.6	2.5	1.1	1.5	1.8
Carbon-monoxide	1.4	2.9	8.8	1.6	5.0	7.0
Carbon-dioxide	4.2	5.8	6.3	5.8	9.7	15.8
Total	7.2	10.4	18.2	8.6	16.4	25.1

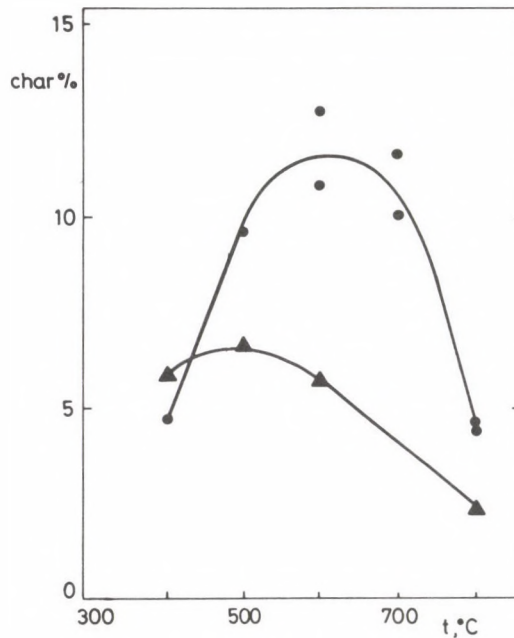


*Fig. 2.* Temperature dependence of tar yields (dry coal %)   
 ● Tatabánya coal      ▲ Visonta lignite

rapid heating are compared in Table II. The total yield of gaseous products and among them those of hydrogen and carbon-monoxide, strongly increase with the temperature. Although the data do not refer strictly to the same temperature, yet it seems that at the much higher rate of heating the yield of carbon-monoxide is preferentially increased.

The yield of tar is shown in Fig. 2 as a function of the temperature. A maximum is observed in the tar yields both of Tatabánya and Visonta coals at about 600 and 500 °C, respectively. According to Durai-Swamy et al. (1979) the loss of tar found at higher temperatures could be interpreted by thermal and/or catalytic cracking of tar

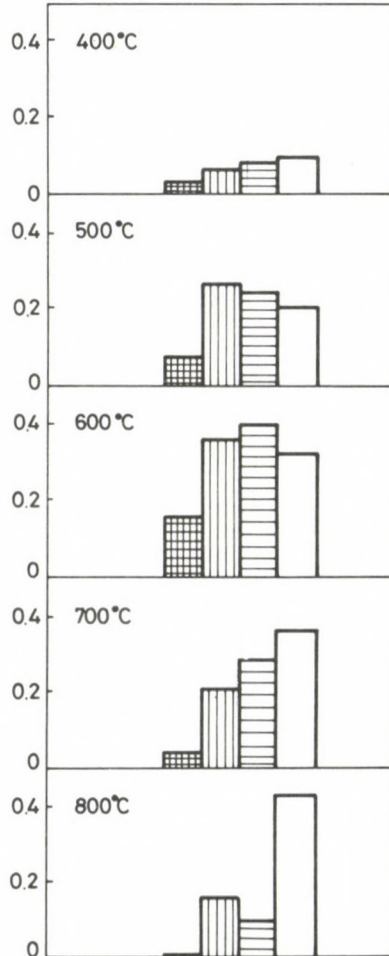


Fig. 3. Yield of tar fractions (dry coal %) formed from the pyrolysis of a Tatabánya brown coal at various temperatures

- ▣ light oil (-180 °C)
- ▤ middle oil (180-230 °C)
- ▥ heavy oil (230-270 °C)
- ▦ anthracene oil (270-350 °C)

taking place on the char (and sand) particles. The data compare well with the gaseous product yields, which show a strong increase in the high temperature region.

Using the method of gas- chromatographic simulated distillation, the yields of light ( $-180^{\circ}\text{C}$ ), middle ( $180\text{--}230^{\circ}\text{C}$ ), heavy ( $230\text{--}270^{\circ}\text{C}$ ) and anthracene oil ( $270\text{--}350^{\circ}\text{C}$ ) distillates were determined. The yields of tar fractions obtained from the Tatabánya coal are shown in Fig. 3. The total yield as well as the yields of fractions

**Table III.** Composition of tars formed under slow (to  $800^{\circ}\text{C}$ ) and rapid (at  $800^{\circ}\text{C}$ ) heating (%)

Coal	Tatabánya (brown)		Visonta (lignite)	
	slow	rapid	slow	rapid
Heating rate				
Products:				
Phenols	39	9	43	13
Bases	13	9	14	12
Unsaturated	37	43	33	37
Saturated + aromatics	11	39	10	38
Total	100	100	100	100

boiling beyond  $270^{\circ}\text{C}$  reach their maxima at about  $600^{\circ}\text{C}$ , whereas the highest-boiling fraction, i.e. anthracene oil shows a monotonous increase with the temperature.

Similar conclusions are valid for the pyrolysis of Visonta lignite (not shown).

Table III shows the composition of tar produced during rapid and slow pyrolysis at a temperature of  $800^{\circ}\text{C}$ . It is tempting to say that the yields referring to the same heating rate for the two types of coal are less different than those referring to the same coal at different heating rates. The phenol-type (acidic) compounds appear with considerable yields among the products upon slow heating, while their amount is much smaller in case of rapid pyrolysis. On the other hand, about four times as much saturated and aromatic products are formed in rapid pyrolysis, than in the slow pyrolysis. This tendency might be important if the processing of tars by hydrogenation or hydrocracking is considered.

As gas-chromatographic analyses indicated, the phenolic compounds formed from Tatabánya coal appear mainly in the light and middle oil fractions. With pyrolyses performed at  $600$ ,  $700$  and  $800^{\circ}\text{C}$ , the relative yields of phenolic compounds in the tar were 20, 14 and  $<10$  percent, respectively, indicating a strong diminution when going to the higher temperatures. These results are in accordance with the gaseous product yields. It was shown that the yield of carbon-monoxide, the most important gaseous product of decomposition of phenolic compounds, strongly increases with the temperature. Our results are in agreement with those of Furfari and Cypres (1982) who showed that the concentration of phenolic OH-groups found in product cokes decreases with increasing temperature.

Some important tar components were identified and their yields measured by gas-chromatography. The variation of their yields as a function of temperature of rapid pyrolysis might be helpful in an understanding of the mechanism of tar formation and decomposition in the system. We had to limit our analysis on the pentane-soluble fraction of tars, i.e. the maltenes, in order to avoid contamination of the chromatographic column with very high-boiling components. Table IV shows yields of some

**Table IV.** Major components of maltene fractions (maltene — %) formed in the pyrolysis of Tatabánya brown coal at various temperatures

Temperature	600 °C	700 °C	800 °C
Naphtalene/middle-oil	37	93	98
Cresols/middle-oil	35	9	2
1- and 2-Methylnaphtalene/heavy-oil	60	45	2
Acenaphten + acenaphtylene/heavy-oil	16	37	69
Fluorene/anthracene-oil	1	20	1.5
Phenantrene + anthracene/anthracene-oil	1	51	90

important product compounds formed at various temperatures, the yields being expressed in percent of the corresponding fraction of tar distillates. The percentage of naphtalene, acenaphtene + acenaphtylene and anthracene + phenantrene increases with the temperature, while the percentage of cresols and methylnaphtalenes decreases, whereas that of fluorene exhibits a maximum at 700 °C. A generalized picture which arises from the results implies that higher temperatures favor the formation of aromatics and detachment of substituent groups, as well as the decomposition of heteroatomic rings.

The yield of char is shown in Fig. 4 as a function of the temperature. The variation of yields at the lower temperatures indicates that in that region devolatilization takes similar routes with both coals. At higher temperatures, however, char yields from the Tatabánya coal exhibit a minimum which is not the case with the Visonta lignite. We may assume that the higher yield of char from Tatabánya coal at higher temperatures is related to the strongly decreasing yield of tar observed in the same range of temperatures. The interaction of tar with, or within the char particles can lead to the formation of a heavy, pitch-like substance which is insoluble in dichloromethane and therefore contributes to the char product in our analysis. This process is seemingly less effective in the case of Visonta lignite than with the bituminous Tatabánya brown coal. An inspection of product yields from the lignite suggests that the higher temperatures give rise mainly to an abundant formation of gaseous products at similar conditions. Ample evidences were submitted in the literature on the pressure and particle size dependence observed with tar/devolatilization yields which

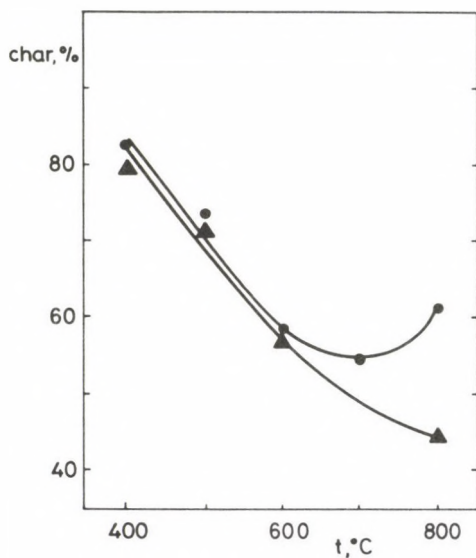


Fig. 4. Yield of char as a function of temperature

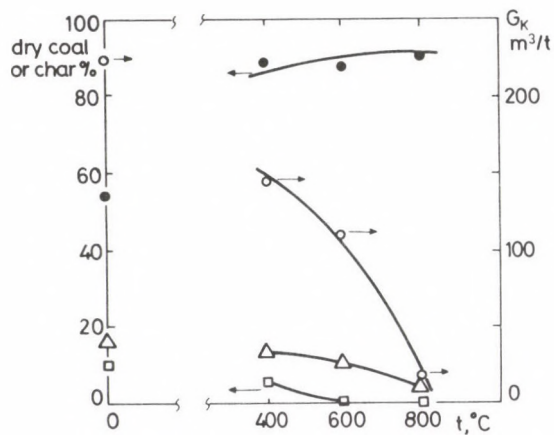


Fig. 5. Yields of Heinze-assay (top temperature = 800°C) performed on chars produced at various temperatures from a Visonta lignite

● Tatabánya coal      ▲ Visonta lignite  
 ● char                  △ liquor  
 □ tar                    ○ gas

demonstrate that these processes are controlled by mass-transfer in case of bituminous coals, as opposed to lignites (Anthony and Howard 1976, Hedden et al. 1979, Russel et al. 1979, Scaroni et al. 1981).

In order to obtain a more quantitative picture on the extent of carbonization at various temperatures using the very short residence times, the Heinze-assay was performed on both coals and their char products uniformly up to a top-temperature of

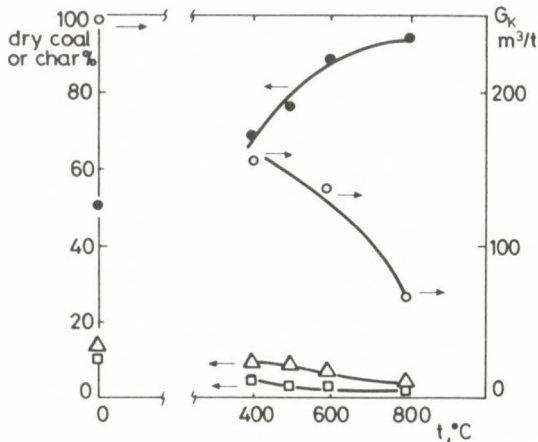


Fig. 6. Yields of Heinze-assay (top temperature=800 °C) performed on chars produced at various temperatures from Tatabánya brown coal

- char
- △ liquor
- tar
- gas

800 °C. These analyses were made in the Laboratory of the Central Institute for the Development of Mining. The yields of main products of Heinze-assay are shown in Figs 5 and 6 for the Visonta and Tatabánya coals, respectively. The negligible yields of tar and apparent constancy of char yields found with Visonta lignite above about 600 °C suggest that heating-up of particles and, consequently, devolatilization has nearly been completed (Fig. 5). The residual yields of tar and, mainly gaseous products indicate, however, an incomplete carbonization in case of the bituminous Tatabánya coal (Fig. 6) which might be traced back, again, to the heavy fraction of tars retained by the char. While mass-transfer processes may be controlling devolatilization at short residence times in the latter case, the lignite which is more “fragile” due to the substantially higher content of oxygen, may readily decompose to gases, mainly carbon-oxides, thus performing evidence on chemical control of carbonization.

It is hoped that a more detailed examination of product formation in the rapid pyrolysis of a wide range of coals, under way among others in our Laboratory, may contribute to a better understanding of their behaviour in thermal coal conversion processes.

### Acknowledgements

The Authors are indebted to Mrs. I Pallos, Drs. P Takács and Gy Wolf (Central Institute for the Development of Mining) for helpful discussion and the analyses of coal and char samples.

### References

- Anthony D B, Howard J B 1976: *A. I. Ch. E. Journal*, 22, 625  
CEP 1974: *Coal Processing Technology*, Technical Manual, American Institute of Chemical Engineers, New York  
Chen L H, Wen C Y 1980: *Am. Chem. Soc. Div. Fuel Chem. Prepr.*, 141  
Chukhanov Z F 1956: *Brennstoff-Chemie*, 37, 234.  
Durai-Swamy K, Che S, Knell E, Green N W, Zahradnik R 1979: *Fuel Chem. Symp. Preprints*, Honolulu  
Eggersten F T, Groennings S, Holst J J 1960: *Anal. Chem.*, 32, 904  
Furfari S, Cypres R 1982: *Fuel*, 61, 453  
Green L E, Schmanch L J, Worman J C 1964: *Anal. Chem.*, 36, 1512  
Hedden K, Hauk R, Huber L 1979: *Erdöl und Kohle, Erdgas, Petrochemie*, 32, 423  
Howard-Smith I, Werner G J 1976: *Coal Conversion Technology*, Noyes Data Corporation, Park Ridge, NJ  
Russel W B, Saville D A, Greene M I 1979: *A. I. Ch. E. Journal*, 25, 65  
Scaroni A W, Walker P L Jr, Essenhigh R H 1981: *Fuel*, 60, 71.  
Schonfeldt H von, Durai-Swamy K, Che S, Deslate W 1981: In: *ASMF Publ., Industrial Power Conference Preprints*  
Schweighardt F K, Hoover D S, Kingsley I S, Kamzelski A Z, Rappe G C 1982: In: *Proc. V. Int. Conf. on Coal Science*, Düsseldorf

## EXAMINATION OF RELATIONS BETWEEN OSMOTIC PROPERTIES OF SHALES AND DRILLING PROBLEMS OCCURRING DURING DRILL-OUT

H BERLINGER<sup>1</sup> and J MOLNÁR<sup>1</sup>

During drill-out of shales often occur so called layer difficulties which may result in a collapse of liner-free drilled hole, or, in an extreme case, in the constrained abandoning of the drill point.

The reason for these occurrences may be related to the hydration and swelling of clay minerals in the shales and to the osmotic phenomena occurring due to the statement above. Because of the importance of the scope, intensive research work has been carried out in the last decade to clarify the processes taking place in the drill hole between the drilling fluids and the drilled out shales. Although a number of questions remained yet open, the experimental data show that not the montmorillonite is responsible for the hydration and osmotic properties in the water-susceptible rocks, but the transient mixed networked montmorillonite/illite minerals produced during reversals of genetic series.

**Keywords:** clay minerals; illite; osmotic phenomena; montmorillonite; reversal of genetic series; swelling of clays; transient montmorillonite/illite minerals

During drill-out of shales so called layer difficulties occur in many cases which may result in stuck-pipe, in a collapse of the drilled hole without a liner or in unwilling abandoning of the drill point in an extreme case. The reason for these occurrences may be related to hydration and swelling of clay minerals in the shales and to osmotic phenomena occurring due to the statement above. Considering the importance of the issue, intensive research has been started in the last ten years to clarify the processes taking place in the drill hole between drilling fluids and shales drilled out.

Due to the complexity of the problem — although many methods offering favourable solutions to the drilling processes have been invented — a theoretical solution to all issues has not yet been provided. The reasons for this lie first of all in the following:

- a) the composition of the shales is extremely variable,
- b) there is no way to bring rock samples to the surface without a change in the original stress conditions or characteristic properties of the rocks,
- c) the execution of model experiments under conditions simulating drill hole conditions is extremely expensive.

<sup>1</sup> Hungarian Hydrocarbon Institute, Százhalombatta

The drill hole instability can be related to hydration of shales and to changes occurring due to it. Thus, the research aimed at understanding the hydration and osmotic conditions of these types of rocks. In the present paper the wetting and osmotic properties were mainly studied. The processes taking place in the shales upon contact with water can be grouped at a first approach as follows:

### Surface hydration

The surface hydration depends on two factors; the charge density on the surface of the clay crystal and the hydration energy of its interlaminar cations. This water uptake by the rock takes place theoretically in two steps by means of two different mechanisms. The primary process is a water uptake due to the hydration energy of the clay minerals. This water uptake can be explained by the fact that water is partially or fully removed from the clays due to compaction processes when they are in greater depths. An absorption potential of limited extent is formed enabling repeated water uptake in the minerals thus dehydrated and partially altered. Due to the nature of the process, the quantity of the water uptake is relatively small. However, since the released network energy of the clay minerals initiates this water uptake, it takes place with great intensity. This process is followed by the hydration of interlaminar cations. The relatively small quantity of water take-up in these two ways may be the cause of important shale instability problems, although it does not cause noticeable swelling. The estimation of the so called surface hydration for chalky clays can be made by considering the compaction forces acting in a subsurface burying. The actual compacting force effecting the chalky clay can be described by the formula (Darley 1969)

$$\sigma = S - P \quad (1)$$

where

$\sigma$  = intergranular stress or matrix stress

$S$  = overburden pressure

$P$  = pore pressure.

Since the matrix stress balances the actual compaction force, it can be deduced that the surface hydration power of a subsurface shale is:

$$a_w = S - P.$$

It follows from this that

- a) the deeper the shale is, the greater is the surface hydration power,
- b) the greater the pore pressure is in the shale, the smaller is the surface hydration power.

In the moment the shale is released from the lateral pressure due to the drilling, the surface hydration power causes adsorption when in contact with water. The surface hydration is, however, not the only force that can initiate the shales to become instable.

### Osmotic hydration

The clay minerals (layer silicates) in the shales are able to take up water and to show osmotic properties due to their structure. The minerals that are able to do this — the smectites in the first place — will swell during water uptake and the result is that they behave as closing layers in the direction of axis *C*, while they have membrane properties perpendicular to axis *C*. So when drilling out shales where the ionic concentration of water in the drilling fluid is smaller than in the water inclusions of the shale, an osmotic hydration force is formed. But the clay minerals in the shale keep this property only for a short time, then lose it as the process continues and also the dissolved ions can permeate. When drilling shales with water-based fluids, both the surface and osmotic hydration occur. With drilling fluids made with water of small salt content, both forces act towards hydration and expansion of shales. With drilling fluids of high salt content the osmotic force helps the dehydration to take place. However, the experiments indicate that the osmotic dehydration force never prevents the surface hydration. It would be useful if the osmotic force could be acceptably estimated and related to the surface hydration forces estimated on the basis of the above calculations. Unfortunately such determinations cannot be performed. That means the shale does not behave like a thin semi-permeable layer separating the water based drilling fluid and the water inclusions.

Instead of that an ion concentration gradient is formed that seems to limit the osmotic hydration to a relatively small magnitude.

It follows from this calculation method that the surface hydration force exceeds the osmotic dehydration for a shale of normal compactness and lying below a depth of 610 metres. Thus, it can be expected even with drilling fluids having a high salt content that hydration does occur in the case of most shales and clays rather than dehydration.

### Study of wetting and osmotic processes

Experiments have been carried out for 8 years in the Mud Research Department of the Hydrocarbon Institute at Nagykanizsa in relation to wetting and osmotic properties of shales. The published experiments of this type were conducted with so called recombined rock samples, i.e. with samples ground and settled in a solution of known salt concentrations, then artificially compacted by high known pressures. Contrary to these models, we formed the samples necessary to the examinations from natural rock cores.

Their advantage is that the original structure of the shales is undisturbed, thus we suppose that more realistic conclusions can be drawn from the results obtained.

Figure 1 shows the equipment used.

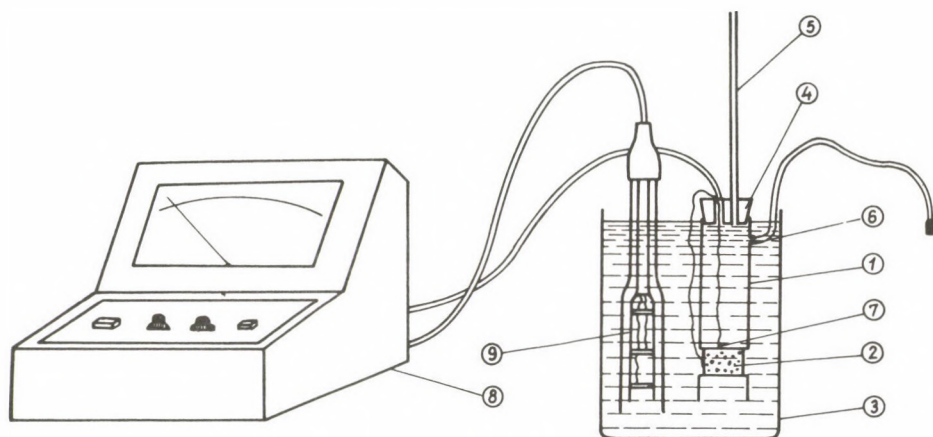


Fig. 1. Experimental apparatus (I). 1. Plexi-glass tube; 2. Shale sample; 3. Glass container; 4. Seal; 5. Level indicator; 6. Fill nozzle; 7. Electrode; 8. Conductometer; 9. Measuring electrode

The following processes were studied on the samples:

- wetting,
- osmotic and ion-transport processes.

### Wetting

The determination of the wetting process for the shales was based on the conductivity data. The shales have a high resistance in dry state, i.e. they have little conductivity. However, it is not the conductivity of the shale that was measured in the experiments, as it would be somewhat difficult, but the so called resultant conductivity value which can be defined by a suitable mathematical relation (Molnár and Berlinger 1977):

$$K_e = \frac{1}{R_v + R_m + R_0}, \quad (2)$$

where

$K_e$  = the resultant conductivity value,

$R_v$  = lateral resistance between the outer surface of the shale and the surface of the outer electrode,

$R_m$  = resistance of the shale,

$R_0$  = resistance of the electrolyte between the inner surface of the shale and the surface of the inner electrode.

As the water front advances, the resistance decreases in the shale, i.e. its conductivity increases. As soon as the sample has been completely wetted, the osmosis starts and the solvent enters the inner space diluting the concentrated electrolyte solution contained there and this results in the decrease of the conductivity. Since the change in the first two terms in Eq. (2) is negligible compared to that of the third one, the wetting of the shale can be related to the conductivity value where its decrease begins.

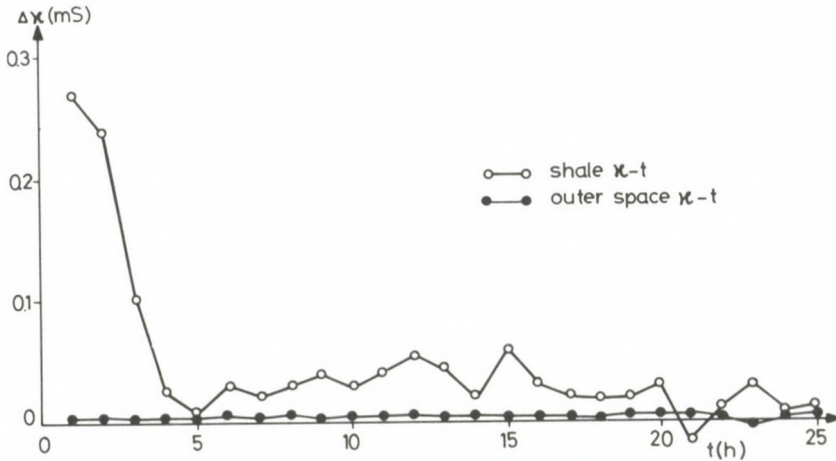


Fig. 2. Examination of wetting in shale samples based on conductivity measurements

Plotting graphically the differences ( $\Delta k$ ) of conductivity value vs. time ( $h$ ), the point of wetting can suitably be plotted (Fig. 2). The decrease in conductivity is temporary as an increase follows the decrease. The explanation is that the dissolved ions flow from the inner space to the outer space via the measuring space. Since the solvent molecules in the measuring space are exchanged for dissolved ions due to the diffusion, the conductivity starts to increase again. The conductivity values measured later are influenced by the relation of diffusion and solvent flow. The rate of progress of the water front in the chalky clay is fast in the initial stage then gradually slows down. The whole process has a nearly hyperbolic run.

### Osmosis and ion transport

After the shale has wetted, the osmosis begins. It is attributed to clay minerals in the shale. The extent of osmosis depends on:

- a) clay minerals in the shale,
- b) the original structure of the shale,
- c) correct preparation of the sample.

In the case of an undisturbed rock, i.e. in a rock having no natural cracks or cracks made during sample preparation, the osmotic pressure may be rather high and the process itself may take a long time. Osmosis and ion transport are processes working against each other; it depends on the dominant process whether osmosis occurs. The clay mineral content in the shales allows the development of the osmosis, the heterogeneous structure of the shale — or the cracks caused by sample preparation — work against it, since they support the ionic transport. As time proceeds, the clay minerals lose their semi-permeable properties and this leads to the stopping of osmosis.

In case of wrong sample preparation the great hydration stress due to the swelling of shale could break the seal and spoil the examination.

### Measuring results and evaluation

The conductivity values of the sample or the changes in them are recorded on the one hand, and the conductivity values of the outer space (see Fig. 1) on the other. The daily changes in the liquid level in the measuring tube are also recorded, for it is a characteristic value of the osmosis rate. While preparing the test cores, we tried to obtain at least 4 useful samples from the same depth. The measurements up to now were carried out by having filtrates of 3 mole  $\text{CaCl}_2$ , 0.7 mole KCl solutions and  $\text{K}^+$ -humate mud (0.7 mole KCl + 0.07 kg/kg K-humate) in the inner space while distilled water is in the outer space. The method can be applied naturally in all concentration conditions or electrolyte solutions. In most experiments with shales from different drilling depths, the wetting times showed fairly great differences. The wetting time is significantly effected by the compactness, porosity conditions, clay mineral content and other mineral parameters. According to the results the wetting time depends in the case of cores having the same structure and composition on the type and concentration of the ion in the wetting medium and on the substances of great molecular volume in the system. According to our findings the effect of the first two factors is considerably greater in this process than that of the third one. The longest wetting times were obtained with the 3 mole  $\text{CaCl}_2$  system, while approximately the same times were experienced with the 0.7 mole % KCl or  $\text{K}^+$ -humate systems. After wetting the process begins if the sample is susceptible for osmosis. As mentioned above, the development and extent of osmosis depends on the clay mineral content in the shale. This is why the mineral composition is important together with the quality and quantity of clay minerals. The mineral composition in the shales was determined using the X-ray diffractometric analysis. On the basis of these semi-quantitative results certain conclusions can be drawn regarding the osmotic processes and clay minerals in the shale. Based on the results obtained so far (in case of the  $\text{CaCl}_2$  system) the following marginal cases or clay groups can be identified:

Group A: The clay mineral content is low, below 0.03 kg/kg for the crystalline phase. In the shales classified into this group, a slight or no osmosis takes place or the process is overcompensated by the ionic transport.

Group B: High clay mineral content thus a significant osmotic pressure develops.

Group C: Significant osmotic pressure is experienced even with a relatively smaller clay mineral content. For each of these shales high *X*-ray amorphous content was measured. The significant osmosis can be very likely explained by the fact that the small clay mineral content determined by the *X*-ray applies only to the crystalline phase. The composition of that phase being in *X*-ray amorphous is unknown and may also contain a great amount of clay minerals.

Group D: Small osmotic pressure was measured at a high clay mineral content. This can be traced probably back to the failure of the sample. A crack can develop as a result of high pressure in the shale due to the relatively fastly initiating osmotic process. Because of the crack the process of osmosis stops in one day or two.

The development of the osmosis pressure in the different types of shales is illustrated in Fig. 3. Examining the effects of different ions in the wetting medium as regards the osmosis, it is found that the highest osmotic pressure occurred in systems with  $\text{CaCl}_2$  content.

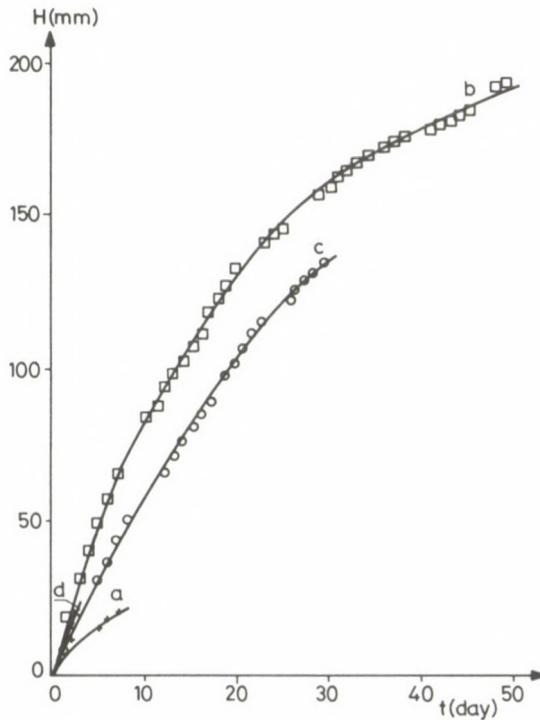


Fig. 3. Development of the osmotic pressure in case of different types of shales

In the KCl system no osmosis occurred in any case. On the contrary, the osmosis developed in the system of  $K^+$ -humate only after a so called "delay time". The fact that no osmosis develops in the system of KCl is connected to the specific effect of the  $K^+$  ion. The  $K^+$  ion built into the laminar space of materials practically "pulls together" the layers. Thus it is even more surprising to experience osmosis in case of systems with  $K^+$  humate. The extent of the osmotic pressure is, however, far less than in case of systems with  $CaCl_2$ . So the  $K^+$  humate system is midway between the  $CaCl_2$  system producing high osmotic pressure and the pure KCl system eliminating osmosis. With the  $K^+$  humate system a further difference is that in our experience the effect of the  $K^+$  ion is dominant in wetting while in the development of osmosis the humic acid ion of a relatively great mole volume may play a role. This seems to be verified by the fact that if the measuring is continued in such a system for a longer time after the wetting the osmosis begins in a few days time. This observation corresponds to remarks in the literature that the potassium-humate systems do not completely stop the instability for certain types of shales, they delay only its development thus providing time for securing the dangerous layers with liners.

So the presence of humate ions in some cases seems to be a disadvantage.

At the same time the results of experiments with the extent of dispersion for the rock samples supported the fact that the humate ion practically forms a protecting coat on the shale. The shale coated by the humate disperses to a lesser extent than those without such a protecting effect (the comparisons were made with a so called gypsum mud). As regards clay stability, the direction of osmosis is critical and it is dependent of the salt concentration of the shale or mud and in the development of which the humate content may also play a role. The aim in all cases is to dehydrate the shale and this requires the salt content of the mud to be set to a greater value than the salt content of the shale or of the water in it. For this the salt concentration in the water of the shale should be known. The soluble salt content of the shale was determined by extraction.

It was concluded on the original moisture content on the basis of the moisture content in the parts drilled from inside the rock cores. Since the permeability and porosity of shales is very small, the values obtained this way may be considered as a good approximation of the original moisture content even if the clay was used only after a longer storage. By doing this, the salt concentration can be given and an optimum mud salt concentration can be provided for a shale susceptible for osmosis. The instability problems can be prevented or minimized with such muds.

When examining the osmotic properties of shales, it is useful to determine the temperature and pressure functions of the osmosis. For this purpose a new apparatus (Fig. 4) has been developed. The original measuring principle has been conserved for the new apparatus. From the measurements at 25 °C, 50 °C and 75 °C and pressures of 1 and 15 bar only a few data are available to give the role of pressure and temperature exactly. However, based on the available data of a relatively small amount, it seems that the effect of the temperature on the osmosis is considerably greater than that of the pressure.

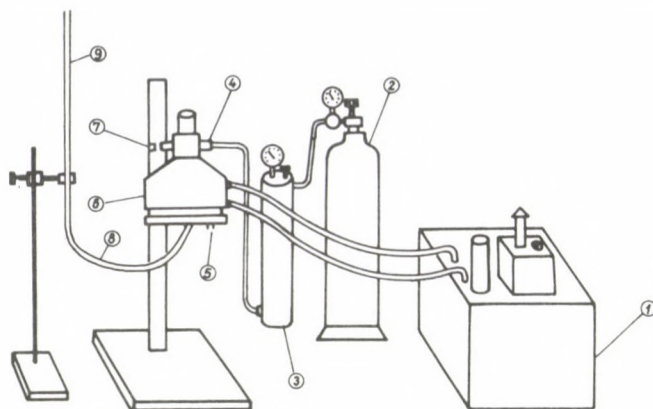


Fig. 4. Experimental apparatus (II). 1. Thermostat; 2. Air cylinder; 3. Buffer container; 4. Pressure connection; 5. Fill opening; 6. Casing; 7. Vent; 8. Plastic connecting tube; 9. Level indicator

Besides knowing the temperature and pressure dependence, it is at least as much important to find out what minerals and to what extent are responsible for the development of osmosis. For this an exact qualitative and quantitative identification of the clay minerals in the shale are required (the *X*-ray data are not sufficient). For the purpose of qualitative and quantitative identification, the clay minerals have to be separated from the other components in the shale. To obtain the optimum clay mineral content the optimum preparation technique needs to be at first developed.

The selected shales were ground in a ball mill after rough chopping. The optimum grinding time for a weighted quantity had previously been determined. When an appropriate quantity of the sample had been available, the peptization experiments were started using  $\text{Na}_2\text{CO}_3$ ,  $\text{Na}_3\text{PO}_4$  and "water glass" as peptizer. From the data obtained it has been quite obvious that the  $\text{Na}_2\text{CO}_3$  is the most effective peptizer.

The shales were peptized at an optimum  $\text{Na}_2\text{CO}_3$  concentration then they were fractionated by means of the Stokes equation. Then the fractions were identified by the derivatographic method. It could be established that only the clay minerals had enriched and this allowed their separation from the other components. The wetting and immersion-heat examinations conducted at the Colloid Chemistry Dept. of the József Attila University contributed significantly to the identification of the clay minerals responsible for osmosis.

Based on the *X*-ray data no montmorillonite or only its traces were found in the shales examined. Nevertheless, the literature relates the osmotic properties mainly to this mineral. American authors (Jones 1981, Darley 1969) give e.g. always high montmorillonite content in all cases of shales susceptible for osmosis. Here the explanation of the osmotic properties logically follows from that fact. Thus according to that concept no osmotic properties should be present in the shales examined by us. Whereas collapses, stuck-pipe or falls occurring in the Hungarian practice prove the

contrary and the laboratory results are also supporting it. In these rocks no montmorillonite but significant amounts of illite content could be detected in all cases. The literature also contains references (Roloff 1965) to minerals that seem to be illites by X-raying whereas neither the  $K^+$  content nor other properties correspond to illites. This is why these clay minerals are referred to as illite-like minerals. By a more detailed analysis it can be determined that these are practically montmorillonites in which the transformation process due to higher temperatures and pressures has already started. They have released most of their hydration water and the migration of small-sized ions ( $H^+$ ,  $H_3O^+$ ) is about to begin in the empty octahedral positions. But this mineral of transient character being in a metastable state, is able to take up again its hydration (surface or ionic) water on contact with water. As stated before, the change in energy during the process is extremely great.

Based on the measured data up to now and on the results of sorption experiments it can be stated that it is not the montmorillonite mineral that is responsible for the hydration and osmotic properties in the so called water-susceptible rocks, but the transient mixed-networked montmorillonite/illite minerals produced during reversals of the genetic series.

### References

- Darley A G H 1969: Physical and chemical factors affecting borehole stability. AIME, Forth Conference of Drilling and Rock Mechanics, University of Texas
- Jones R D 1981: Troublesome shale formations require inhibitive mud. *Oil and Gas Journal*, 55
- Molnár J, Berlinger H 1977: Study of wettability and osmosis of shales (in Hungarian). *Technical Scientific Publications of the Hungarian Hydrocarbon Institute*, 13, 100–108.
- Roloff G 1965: Über die Rolle glimmerartiger Schichtsilicate bei der Entstehung von Erdöl und Erdöllagerstätten. Dissertation. Heidelberg

## RESERVOIR DAMAGE BY PHASE DISPERSION DURING MULTIPLE GAS-WATER DISPLACEMENTS

H J KRETZSCHMAR<sup>1</sup> and P CZOLBE<sup>1</sup>

Laboratory tests, theoretical research and field experience gained so far have indicated the occurrence of reservoir engineering restrictions during multiple gas-water displacement. Cyclic displacement leads to an increased dispersion of gas and water which form a "mechanical" mixture during the flow process. Due to this foaming phenomenon especially if tensides are applied — an intensive gas sorption occurs within the pore spaces and the gas mobility undergoes a reduction. The formation of dead gas can strongly influence the operational efficiency of aquifer gas storage facilities or gas fields.

**Keywords:** cyclic gas-water displacements; dispersion effect; foam formation; gas mobility reduction; tensides; underground gas storage

### 1. Formulation of the problem

Formation of dead gas and internal gas volume losses (Fig. 1), respectively, which are observed particularly in aquifer gas storage systems and in heterogeneous gas fields cause problems in the domestic gas industry and in the gas industries of other countries as well; they are attributed to two significant phenomena occurring in pore spaces, i.e.

- decrease of gas mobility (gas phase permeability), and
- occurrence of a marked gas sorption.

The dominant cause of these phenomena appears to be a dispersion of the two flowing phases — i.e. gas and water — in the form of foaming. As a result, the two phases are no longer continuous but become discontinuous.

In addition to looking for the cause of the above-mentioned phenomena, the mobilization of gas volumes which have become primarily inactive due to pressure variations is a problem of particular importance to the gas industry. Consequently, the possibilities of the planned secondary influences, by means of tensides, on mobility conditions during gas-water flow have been examined by laboratory tests which have established close parallels with the process of tenside-water flooding of oil fields. The scientific concept developed for such a secondary oil recovery within the last few years includes the following steps:

- formation of micellar slugs or microemulsions of oil-in-water by means of tensides to mobilize residual oil,

<sup>1</sup> Fuel Institute, Freiberg, German Democratic Republic

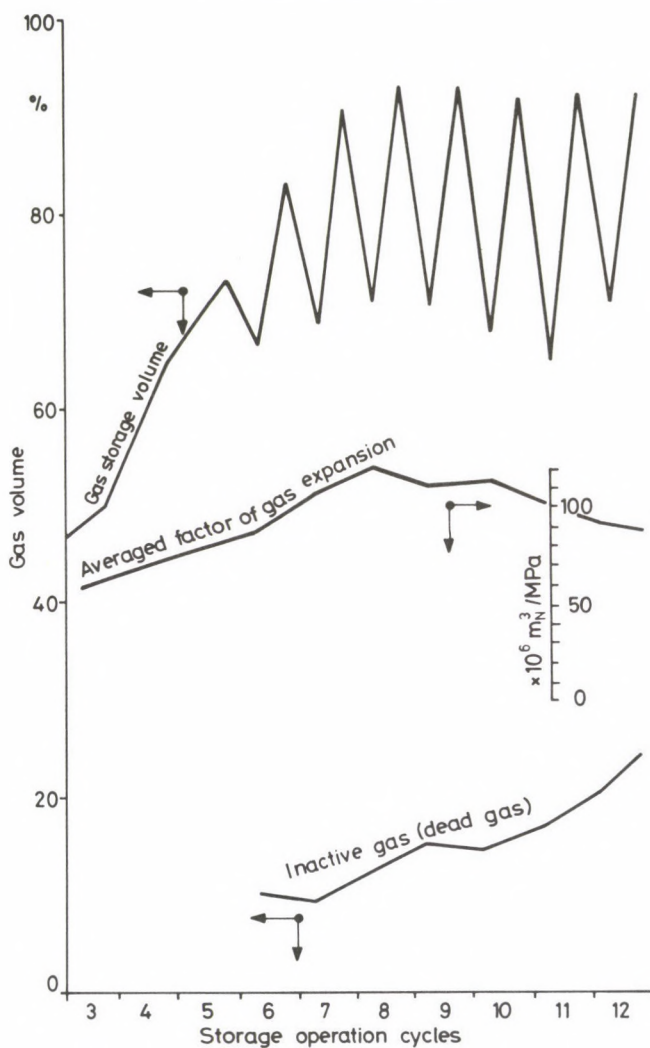


Fig. 1. Development of gas storage parameters and dead gas volumes in an aquifer gas storage facility

— subsequent formation of a flowing oil bank from the oil-water dispersion employing a controlled phase inversion temperature of the tenside water.

The thermodynamical and reservoir engineering fundamentals of the above concept are similar to those of the gas-water phase dispersion.

Consequently, the use of tensides in a two-phase flow which was based on empirical principles in the past, may cause flooding damages as well.

Accordingly, it will be necessary in future projects to pay more attention to the bivalency of tenside treatments in aquifer gas storage systems.

## 2. Mobility — phase permeability

As to gas-water flow without the addition of tensides, the following basic characteristics of phase dispersion have been derived from several laboratory tests.

Cyclic operation (i.e. periods of injection and withdrawal) which is typical of aquifer gas storage facilities, involves constantly changing directions of gas-water displacement.

The development of mobility in the course of three displacement cycles is presented in Fig. 2 for a comparatively low flow rate, and in Fig. 3, for a comparatively high flow rate.

At low gas flow rates, the mobility of gas decreases due to the constantly changing directions of displacements; at the same time, the gas saturated pore volume increases as a result of subsequent water displacements during the cycles. It must be mentioned, however, that this increase in storage capacity cannot be taken into account under actual conditions because the reservoir space is filled in part with a gas-water phase mixture blocking any flow. In an aquifer gas storage system, such an increase in reservoir space results in an increase of the amount of cushion gas. The mobility trend described above actually occurred in the aquifer gas storage near Ketzin which is characterized by a comparatively low flow rate in the zone of the gas-water contact.

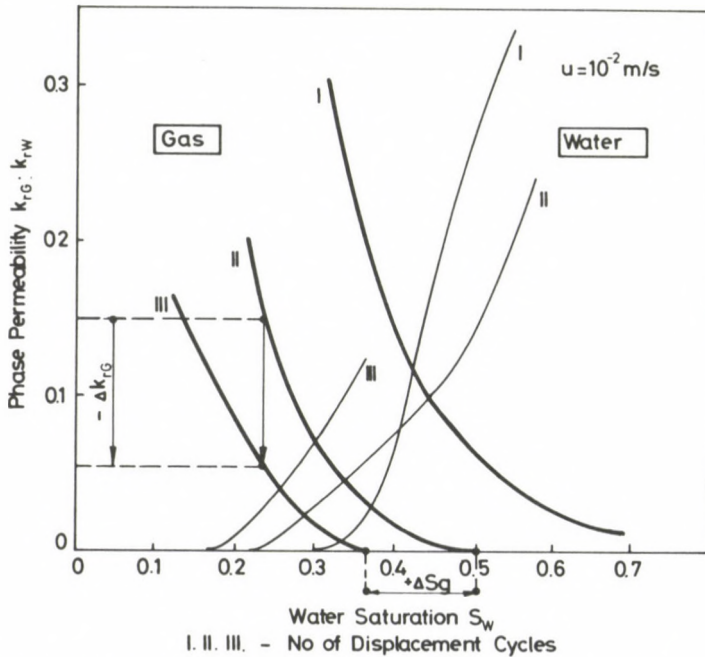


Fig. 2. Variations of phase permeability functions during three displacement cycles at a relatively low flow rate

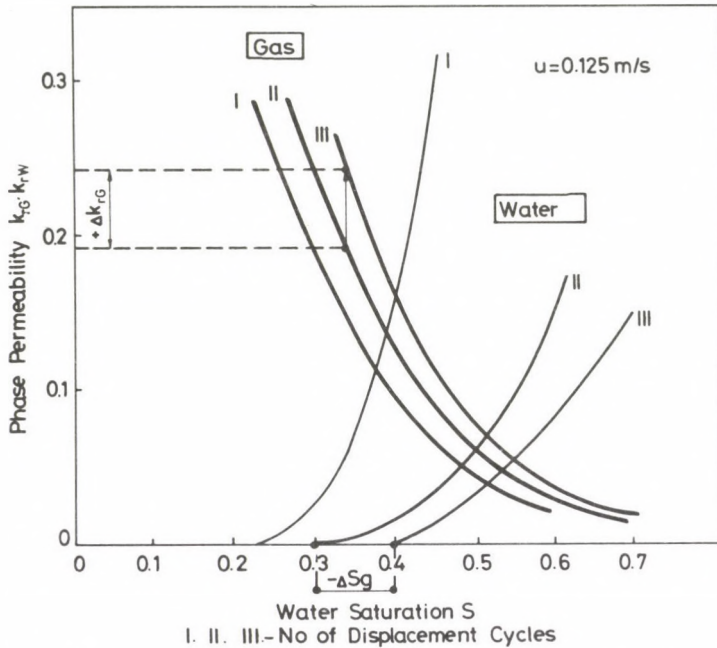


Fig. 3. Variations of phase permeability functions during three displacement cycles at a relatively high flow rate

A comparatively high flow rate causes gas mobility to increase during a number of cycles; this process, in turn, is connected with a reduction of the gas saturated pore volume and, consequently, an increase in residual gas saturation. Thus the gas flows in "preferred gas channels", and water steadily infiltrates into pore spaces which are small in size. As compared with processes characterized by lower flow rates, there is a higher degree of separation of gas and water and thus a reduced phase dispersion. In storage operation, the percentage of cushion gas volume in the total reservoir volume decreases but the latter cannot be increased considerably. The "channel flow" described above which is accompanied by a reduction of phase dispersion has been observed in the aquifer storage near Buchholz.

### 3. Gas sorption

Intensity data of sorption processes in pore systems of individual reservoir rocks have been derived from single lab-scale gas-water/water-gas displacement cycles. The sorption volumes obtained (see Fig. 4) assume comparatively large proportions ranging between 50 and 70% of the pore space theoretically accessible to gas at the

pressure differences selected for the test. It is hardly conceivable that such large amounts of gas enclosed subsequent to water flooding should be present in continuous phase in a pore system having an irregular structure. On the contrary, the milky coloration of the water flowing out of the core of reservoir rock during pressure decrease, the initially delayed process of gas release, and the large amount of gas remaining within the core at atmospheric pressure are indications of an intensive phase dispersion (Fig. 4).

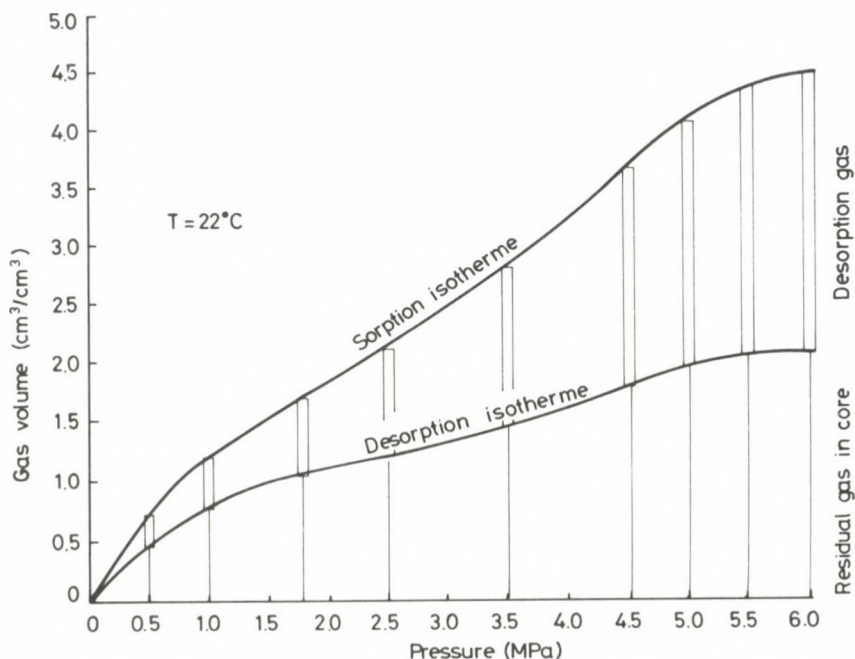


Fig. 4. Isothermal curve of gas sorption within an argillaceous sandstone; desorption gas during expansion down to atmospheric pressure, and residual gas remaining within the core of reservoir rock

#### 4. Thermodynamical characteristics of the dispersion process

According to thermodynamical laws, phase dispersion is characterized by a loss of technically usable energy. As shown in Fig. 5, the laws of thermodynamics describe the energy state within a reservoir.

In accordance with these laws,  $U = TS$  is a process of energy transformation which is reversible and thus free of losses; actually, this process cannot be realized because the interfacial free energy  $dF = \sigma dA$  is lost from the energy system of the reservoir. The  $dF$  expression shows that this energy loss — which should be minimized — is controlled by means of the two factors covered below.

### Interfacial Free Energy — Laws of Thermodynamics

2nd Law:

$$dI \leq T dS \quad \left\{ \begin{array}{l} < \text{Irreversible} \\ = \text{Reversible} \end{array} \right.$$

Enthalpy      Entropy

1st Law:

$$dI = dU + V dp$$

Internal      External  
Energy      Energy

From the above, Gibbs' fundamental equation can be derived, i.e.

$$dU = T dS - V dp.$$

Subsequent to separation of the work required for interface extension from the external energy, the formula which is relevant in terms of reservoir mechanics will be as follows:

$$dU = T dS + \sigma dA - V dp.$$

The term of external energy represents the mode of operation of the reservoir non-recurrent gas production or cyclical storage operation.

An ideal energy balance of a reservoir would be

$$U = TS.$$

$T$  — temperature;  $V$  — volume;  $p$  — pressure;  $\sigma$  — interfacial tension;  $A$  — interface

Fig. 5. Data of interfacial free energy derived from the laws of thermodynamics

#### a) Interfacial tension $\sigma$

Naturally, the  $\sigma$  parameter of the gas-water flow is an established one, i.e.  $\sigma = 74$  mN/m. It may be reduced by injecting tensides into the pore space, but the minimum value attained is only  $\sigma \approx 35$  mN/m. By such a procedure energy losses may be cut down to 50% at best.

#### b) Change of interface $dA$

The phase dispersion observed during laboratory tests leads to an extension of the interface —  $dA$  — the factor of which is much greater than 2. Consequently, the adverse influence of  $dA$  is stronger than the  $\sigma$  action. A special method of determining  $dA$  has been developed.

If the objective of activities is to reduce phase dispersion and at the same time to enhance gas mobility in a reservoir, input of chemical energy by adding tensides is efficient only in those cases when an extension of the interface can virtually be prevented.

It is to be studied in the course of laboratory tests whether such an approach will be feasible.

## 5. Lab-scale examination of the effects of tensides

For laboratory test purposes, five suitable grades have been selected from a wide range of tensides.

In the tests, the tenside concentrations used were ranging between the micellar concentration and 0.3 wt.-%.

The following generalized results may be derived from flow tests carried out with various tenside concentration ranges.

The addition of tensides during gas-water flow leads to an intensive foam formation. Accordingly, the part of the pore space which is available for gas storage is blocked by this phase dispersion, and there is an increase in space blocking with an increase in the number of cycles. Thus, there is virtually a loss of active storage space; finally the remaining amount of gas flow channels is relatively small (see Fig. 3).

In the first stage, gas mobility undergoes a decrease. At a gas flow within the pores which is sufficiently high, resistance to gas flow is reduced if foaming effects within gas flow channels are eliminated or if there are changes in wetting. Under field conditions, a sufficiently high gas velocity can be attained in gas wells, but not in the reservoir areas between wells which constitute the major part of the storage capacity and in which internal gas volume losses occur in the first place.

Thus, the phase dispersion initiated by natural phenomena within the pores is intensified by tensides. From a thermodynamical point of view, a planned process of energy transformation by means of tensides with a view to reducing losses of interfacial free energy is not feasible. The positive effect of a decrease of  $\sigma$  is superimposed by a substantial, and negatively acting, increase of  $dA$ . The extension of the gas-water interface is an irreversible process and inevitably leads to a less favourable energy state, a decrease of gas compression energy and an increased blocking of gas volumes.

There is one particular field in which phase dispersion may have a positive effect, i.e. as a foaming process causing a temporary blocking of zones adjacent to wells in case of high water inflow during gas production. As to this, field tests using tensides have already been carried out. A transfer and scale-up of such effects to an entire reservoir has been described by some authors (supplementary flow tests have not been carried out in this respect) but it is to be refused taking into consideration the information and experience gained so far.

The process of phase dispersion during gas-water flow (with or without tensides) may be compared to the adverse phenomenon of emulsification during oil-water flow.

### 6. Reservoir-engineering calculation methods

Although, it is hardly possible under field conditions to prevent gas-water dispersion, efforts should be made, however, to develop calculation methods relating to such a process.

#### Modification of the fractional flow equation

According to latest findings, the Buckley–Leverett theory should not be applied to calculations relating to multiple displacement and phase dispersion; its base of calculation should not be rejected at present, however, but should be modified as shown in Fig. 6.

*Fraction Flow Equation* (modified BUCKLEY–LEVERETT theory)

$$f_g(S_g, S_{im}); p_c(S_g, S_{im}); k_r(S_g, S_{im}) S_{im}(t)$$

*Gas Phase Differential Equation*

$$\underbrace{\text{div } T_g(S_g, S_{im}) \text{ grad } (p_g - F_G)}_{\substack{\text{Transmissibility} \\ \text{(dispersion-related} \\ \text{modification)}}} = \Phi \frac{\partial}{\partial t} \underbrace{(\rho_g S_g - S_{So})}_{\substack{\text{Sorption/Accumulation} \\ \text{(dependent on pressure)}}$$

*Energy Balance of Reservoir*

$$\Sigma E_i = 0$$

Continuous

Phase

Discontinuous

$$E_{con} = E_p - E_c \quad E_{disc} = E_p - (E_c + E_{Ad} + E_{disp})$$

Potential Energy
Capillary Energy
Adsorption Energy
Dispersion Energy

$$E_c = \frac{1}{l} V \sigma \cos \theta; \quad E_{disp} = A \sigma; \quad E_{Ad} = \epsilon \ln^{-1/2} V_{So}/V$$

$$E_{con} \geq E_{disc}$$

*f* — fraction flow; *S* — saturation; *p<sub>c</sub>* — capillary pressure; *k<sub>r</sub>* — relative permeability; *F* — gravity force; *t* — time;  $\Phi$  — porosity;  $\rho$  — density; *r* — pore radius;  $\theta$  — wettability angle;  $\epsilon$  — adsorption factor. Indices: im — immobile; g — gas; So — sorption

Fig. 6. Reservoir-mechanical calculation methods relating to gas-water phase dispersion

#### Extension of phase differential equations

The established differential equations relating to gas-water displacement should be extended using supplementary terms which take into account a balance of forces more general than the Darcy formula. Figure 6 includes a presentation of a gas differential equation within the framework of a numerical model.

### *General energy balance*

The loss of energy due to phase dispersion becomes more obvious if an energy balance is formulated instead of the common reservoir-engineering balance of forces. The formulas presented in Fig. 6 have been applied successfully to the interpretation of laboratory test results. Similar energy formulas have been developed at the Miskolc Laboratory of the Hungarian Academy of Sciences.

### References

- Czolbe P, Kretzschmar H J, Kühnel G 1982: Reservoirmechanische Untersuchungen zur Gas-Wasser-Strömung in Gasspeichern. *Zeitschr. f. angew. Geol.*, Part I-2, 66-72, Part II-3, 126-132.
- Heilmann M, Richter W 1978: Verbesserung der Reservoireigenschaften in UGS durch Einsatz oberflächenaktiver Stoffe. *Mitteilungen des Brennstoffinstitutes Freiberg*, 9, 19-32.
- Karimov M F, Odegov A I, Sadykov V A 1978: Intensification of the underground gas storage process by physico-chemical methods (in Russian). *Gazov. Prom.*, 4, 46-47.
- Karimov M F 1979: Intensification of gas recovery from underground gas storages by cyclic method (in Russian). *Gazov. Prom.*, 3, 29-32.
- Kosswig K 1980: Möglichkeiten der Anpassung von Tensiden an die Lagerstättenbedingungen beim Tensidfluten. *Erdöl-Erdgas-Zeitschr.*, 9, 318-323.
- Maksimov V M, Filinov M V 1976: Quantitative evaluation of the efficiency of surface active agents in the exploitation of underground gas storages (in Russian). *Neft i Gaz*, 9, 72-78.
- Neumann H J 1981: Zur Entölung beim Tensidfluten. *Erdöl und Kohle-Erdgas-Petrochemie*, 11, 497-499.
- Neumann H J 1982: Grundlagen des Mechanismus der Restölmobilisierung beim Tensidfluten. *Erdöl-Erdgas-Zeitschr.*, 3, 96-99.
- Peters E J, Flock D J 1981: The onset of instability during two-phase immiscible displacement in porous media. *Soc. Petr. Eng. Jour.*, 4, 249-258.



## LABORATORY INVESTIGATION OF RESIDUAL PHASE DISTRIBUTION IN CONSOLIDATED SANDSTONES

B WEINHARDT<sup>1</sup> and Z HEINEMANN<sup>1</sup>

Before an actual enhanced oil recovery (EOR) project can be envisaged, certain laboratory investigations have to ascertain the depletion of the oil under process conditions. The method of choice used to be a linear displacement on models. However, the laboratory model differs from the reservoir in at least 3 fundamental points: (i) the pore structure, (ii) the 3-dimensional extension, and (iii) the displacement velocity.

Both own results recently published and detailed experimental work done by another group have established that the distribution of the residual oil phase depends on the pore structure of the model. This paper examines again how the residual phase is distributed after waterflooding, and discusses how it depends on the core dimension and the displacement velocity, i.e. the pressure gradient in the case of preferentially water-wet rock. This should give some better understanding, in howfar the distribution of residual oil is simulated by laboratory conditions and which data have been used to assess the recovery efficiency of planned field trials. Moreover, the results should give a better insight into field reality.

A convenient method to determine the distribution of the residual phase after waterflooding, developed in our Leoben Laboratory, foresees the oil phase to be replaced by styrene monomer which is polymerized in situ into a solid state. The polystyrene particles are classified according to their largest diameters with an automatic particle size analyser.

The residual phases of any segment of the same core do not show any systematic variation in their distribution functions even 1.2 m distant from the injection zone. On the contrary: the distribution curves of different core segments of different runs are in satisfactory agreement if test conditions are comparable.

We have mainly used a core diameter  $D = 0.03$  m, but no effect could be noticed at core diameters above 0.03 m.

The paper also discusses how the distribution of the residual phase depends on the pressure gradient applied.

**Keywords:** core dimensions; enhanced oil recovery; linear displacement tests; residual phase distribution; pressure gradient; water-wet porous medium

### *Symbols*

$D$	diameter, l
$f$	multipore oil filament length to radius ratio = $\Delta L/a$ , dimensionless
$k$	water (1 wt % NaCl) permeability, l <sup>2</sup>
$k_{rw}$	relative permeability to the wetting phase (water), dimensionless
$L$	length, l
$N_{Le}$	Leverett number = $J_d \sqrt{k/\Phi}$ , dimensionless

<sup>1</sup> Institute of Reservoir Engineering, Mining University, A-8700 Leoben, Austria

$N_{vc}(S)$	viscous/capillary number $u\mu/\sigma = kk_r V\Phi/\sigma$ , dimensionless
$p$	pressure, $\text{ml}^{-1}\text{t}^{-2}$
$p/L$	pressure gradient, $\text{ml}^{-2}\text{t}^{-2}$
$S_0$	initial styrene saturation, dimensionless
$S_r$	residual styrene saturation, dimensionless
$u$	Darcy velocity $= q/A$ , $\text{lt}^{-1}$
$\Phi$	porosity, dimensionless
$\sigma$	interfacial tension, $\text{mt}^{-2}$
$\psi$	geometrical factor for curvature of the front and back of trapped oil mass, dimensionless

## 1. Introduction

Waterflooding is a widely used secondary recovery technique during which parts of the oil in place — the so called mobile oil — and all of the resident brine are displaced from the contacted regions. In the case of preferentially water-wet payrock, there is every reason to assume that the immobile residual oil is trapped by capillary forces in the form of microscopically tiny drops or filaments surrounded by rock and isolated by water. The validity of this concept has already been proved by electroscan micrographs (Reed and Healy 1977, Swanson 1979, Morrow and Chatzis 1981, Chatzis et al. 1983) on a series of residual oil specimen.

For modelling such a two-phase displacement process, certain dimensionless groups — often cited as “capillary number” (Taber 1980) have been suggested to describe the influence of the ratio of the capillary/viscous forces. The standard capillary number is defined as

$$N_{vc}(S) = \frac{u \cdot \mu}{\sigma}. \quad (1)$$

In the system described above, the residual oil is mobilised only by an immiscible drive, if  $N_{vc}$  is raised by a factor of at least  $10^3$ . This can be achieved by a significant decrease of the interfacial tension  $\sigma$  in combination with mobility control. An adequate effect can be produced if suitable chemical compounds are added to the drive water (Larson et al. 1982). Then the fundamental problem of residual oil mobilization is to replace the original water in contact with these residual oil volumes by the reactive water phase.

During the investigations of the displacement mechanism by an immiscible drive, microstructural effects have received much recently attention. In this context Stegemeier (1977) discusses the mechanism of oil entrapment and mobilization in porous media and classifies the parameters exerting influence on  $N_{vc}$ :

$$N_{vc}(S) = \frac{u\mu}{\sigma} \geq [\Phi N_{Le}^2(S)] \cdot [k_{rw}(S)\psi^2(S)] \cdot [1/2f]. \quad (2)$$

The first term of the inequality defines the geometry of the rock pore network and is independent of the fluid types present. The second term defines the fluid/rock interactions, whereas the third term is a constant geometric fluid property which is

independent of the pore structure. According to the definition in Fig. 1, the third term is the dimensionless length of a residual oil filament. From this postulate a homogeneous distribution pattern could be deduced.

Despite the well established correlation between the desaturation curve calculated by use of Eq. (2) and experimental data on the Berea sandstone (1977), well-founded doubts remained whether the hypothesis of a homogeneous residual oil

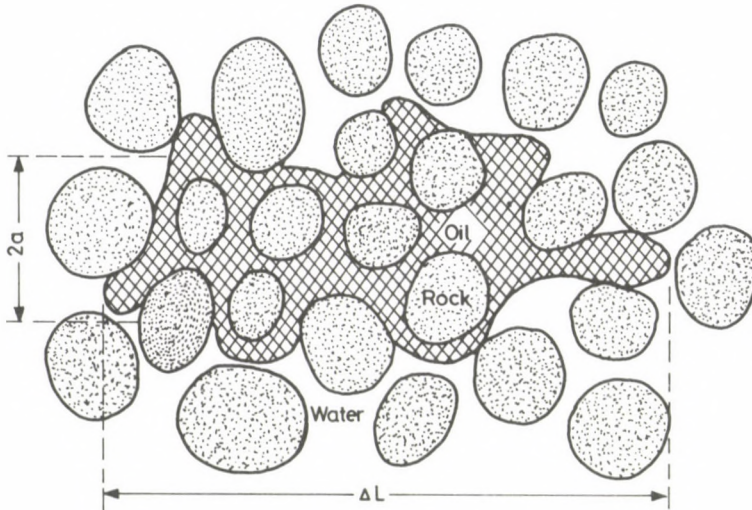


Fig. 1. Multiple residual oil filament (Stegemeier 1976)

distribution pattern without any influence of the pore network geometry reflects the reservoir reality at all. These doubts originated from older microscopic observations, where even synthetic porous media — made of spheres — show variations in respect to residual oil filament volumes (Chatenever and Calhoun 1952). Indeed, some of our own new research results support that the distribution of the residual phase depends on the pore structure (Weinhardt and Heinemann 1982). Chatzis et al. (1983) show in a comprehensive investigation of magnitude and fine structure of residual oil saturation that the distribution function of the residual oil is effected by the size distribution of the pores, but to a larger extent by the spatial arrangement of the pores.

## 2. Scope

Many enhanced oil recovery methods based on the addition of chemicals to the drive water try to mobilize the residual oil trapped in the pores of the flooded zones. The assumption is obvious, that the viscous forces required to release a residual oil

filament, must be a function of its volume related to the pore structure of the trap. The viscous forces required are expected to be inversely proportional to the ganglia length (Melrose and Brandner 1974, Ng et al. 1977, Morrow 1979). The fast mobilization of larger filaments followed by coalescence with still entrapped smaller oil volumes could cause further release and — last, but not least — faster development of an oil bank. A spread in the size distribution of residual oil volumes should decrease the chemical requirements in low interfacial tension flooding.

Before any EOR method can be applied to a pilot project, certain efficiency tests, e.g. linear displacement runs, have to be carried out in laboratory. Usually, the laboratory model differs from the reservoir conditions in at least three fundamental points:

- (i) the pore structure of the porous medium (use of reference rock or sand packs),
- (ii) the 3-dimensional extension,
- (iii) the displacement velocity (linear instead of radial flow).

Some preliminary results of residual phase distribution as a function of the pore structure have already been published (Weinhardt and Heinemann 1982). In addition to these results, we wanted to investigate if and to what extent the core dimension as well as the displacement velocity/pressure gradient influence the distribution of the residual phase in a preferentially water-wet porous medium. This should lead to a better understanding, in how far the distribution function is subject to laboratory conditions.

### 3. Measuring technique

A convenient method to determine the distribution of the residual phase after waterflooding has already been described (Weinhardt and Heinemann 1982). Basically, our method is comparable to that developed by Morrow and Chatzis (1981) concurrently. By this method the oil phase is replaced by styrene monomer. Both core preparation and laboratory equipment correspond with the procedure in the case of an oil/water/sandstone system. Under this laboratory conditions a spontaneous undesired polymerization of styrene is excluded even at elevated temperature. This can be shown by a continuous measurement of styrene viscosity and density at certain elevated temperature levels which show their theoretical inverse proportionality to the temperature over a long period of time.

After waterflooding the residual styrene phase must be polymerized *in situ* into a solid state. The *in vitro* polymerisation of styrene is induced by heat, light and radiation. We suppose that thermal *in situ* polymerisation, as suggested by Morrow and Chatzis (1981), has obvious shortcomings. Apart from a possible coalescence of neighbouring residual volumes due to the initial significant thermal expansion of styrene, the marked difference between the density of styrene heated-up and that of polystyrene, may break

some of the particles during the polymerisation process. However, we prefer *in situ* polymerisation initiated by X-ray radiation of the core, followed by an additional thermal treatment at 60 °C.

After the *in situ* polymerisation of styrene, 0.02 m thick parts both from the core inlet and outlet are discarded. Then the remaining core material is divided in segments 0.04 m long which are solved separately in concentrated hydrofluoric acid at 50 °C. The remaining solid material which includes polystyrene particles, non-volatile fluorides and undissolved sand grains is suspended with distilled water. After this treatment the polystyrene particles which have been proved to be no water-wet are decanted. With each polystyrene sample obtained in this way, a particle size analysis is carried out repeatedly.

We have used an automatic particle size analyzer working with the light blockage principle (HIAC 724-121). After an exposure to ultrasonic waves, a very diluted and constantly stirred suspension is sucked through a sensor. During the flow, the particles are orientated with their longest axis parallel to the stream. In the sensor (measuring range: 10–600  $\mu$ ) the light reduction triggers a voltage pulse which is directly proportional to the maximum projected area of each individual particle. The pulse is then expressed as a circle area. By classifying the counts in 24 classes, a volume distribution curve based on this assumption of circle areas is produced. Finally, both the mean diameter and the 50%-value of all particles are calculated.

## 4. Experimental

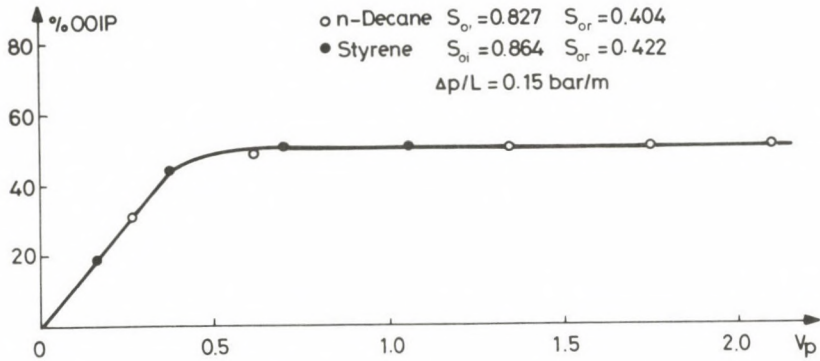
### 4.0 Material

The porous medium used has been a German reference sandstone (Lower Cretaceous) with well-known characteristics: porosity between 0.18 and 0.23; water (1.0 wt.% NaCl) permeability about  $10^{-12}$  m<sup>2</sup>. Generally, the core length amounts to about 0.2 m. The run data are summarized in Table I.

We wanted to demonstrate once more that there is no difference in the displacement by waterflooding between styrene monomer and an oil phase of comparable viscosity like *n*-Decane (Fig. 2).

### 4.1 Core length

The residual phase does not show any systematic variation in its distribution for samples drawn from different regions of the same core even at  $L = 1.2$  m. Therefore the data of a respective run were averaged appropriately and standard deviations were calculated. The following distribution curves are based on these averages, and in some

Fig. 2. Styrene and *n*-Decane replaced by waterTable I. Summary of run data according to the decrease of  $S_r$ 

RUN	$L$ [m]	$D$ [m]	$\Phi$	$k$ $10^{-12}$ [m <sup>2</sup> ]	$u$ [m/day]	$\Delta p/L$ [bar/m]	$S_0$	$S_r$
125	0.18	0.03	0.23	1.82	0.02	<0.05	0.83	0.44
128	0.18	0.03	0.21	1.43	0.02	<0.05	0.79	0.43
130	0.20	0.03	0.20	1.53	0.15	0.15	0.86	0.42
152	0.20	0.03	0.18	1.15	0.02	0.25	0.75	0.41
151	0.20	0.03	0.18	1.00	0.02	0.20	0.75	0.40
155	0.20	0.03	0.17	1.08	0.42	0.30	0.75	0.40
150	0.20	0.03	0.17	0.89	0.43	0.31	0.77	0.39
139	0.18	0.02	0.23	1.67	0.99	0.90	0.81	0.38
138	0.19	0.02	0.21	1.38	1.02	0.95	0.81	0.38
133	0.19	0.06	0.23	1.78	0.43	0.30	0.70	0.38
162	0.20	0.03	0.22	2.39	19.47	4.95	0.73	0.37
161	0.20	0.03	0.23	2.43	22.16	5.42	0.76	0.37
163	1.20	0.03	0.21	0.68	23.42	7.18	0.72	0.37
402	0.20	0.03	0.19	0.78	0.25	0.70	0.76	0.35
160	0.20	0.03	0.22	1.58	2.26	0.77	0.75	0.35
137	0.19	0.06	0.23	1.78	1.14	0.90	0.75	0.34
143	1.18	0.03	0.23	1.79	1.15	0.95	0.71	0.34
148	0.18	0.06	0.21	1.55	1.03	0.90	0.78	0.34
124	0.20	0.03	0.23	1.67	0.97	0.99	0.87	0.34
132	0.19	0.03	0.19	1.25	0.73	1.16	0.74	0.34
400	0.19	0.06	0.23	1.68	1.12	1.08	0.73	0.34
164	0.50	0.03	0.23	1.55	9.65	3.07	0.72	0.34

cases the standard deviations are expressed as shaded areas. On the contrary the distribution curves originating from different core lengths are in satisfactory agreement, if all other test conditions are the same (Figs 3, 4).

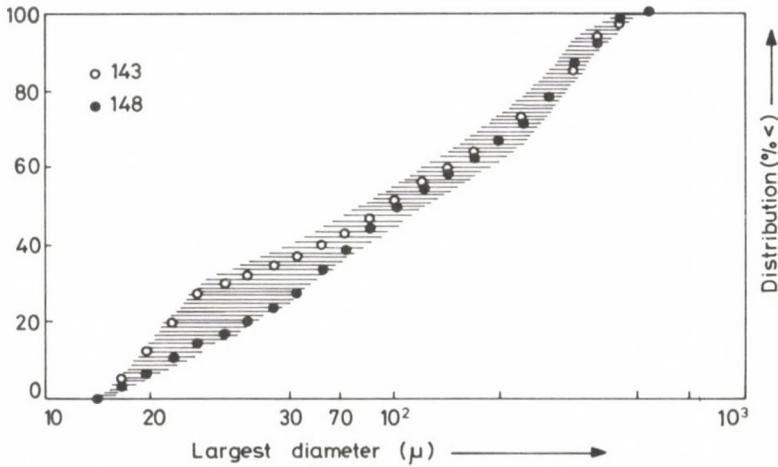


Fig. 3. Residual phase distribution at different runs and core lengths

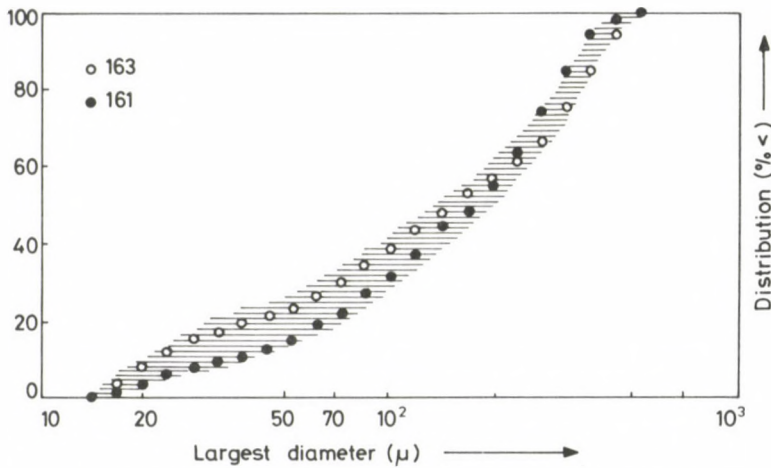


Fig. 4. Residual phase distribution at different runs and core lengths

## 4.2 Core diameter

The residual phase distribution as a function of the core diameter has been examined within the constraints

$$D: 0.02 \text{ m, } 0.03 \text{ m, } 0.06 \text{ m}$$

$$\Delta p/L \text{ about } 1 \text{ bar/m.}$$

At this level of  $\Delta p/L$ , the residual phase saturation does not depend any more on the pressure gradient applied, and minor variations in the displacement velocity do not

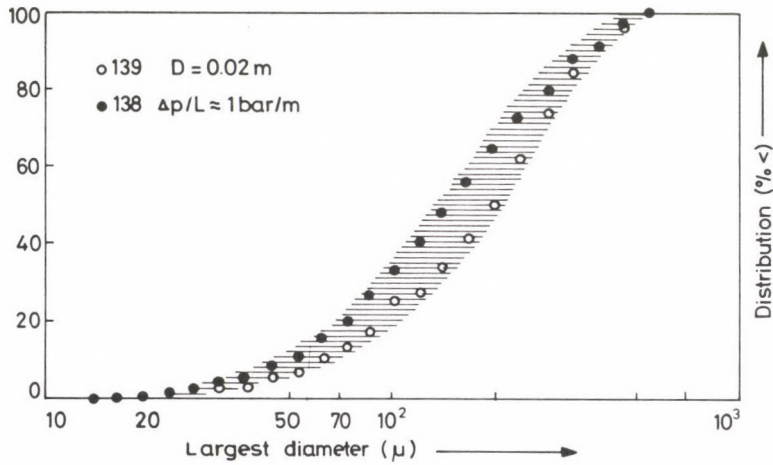


Fig. 5. Reproducibility of the residual phase distribution at constant conditions

Table II. Residual phase saturation as a function of the core diameter  
 $\Delta p/L \approx 1 \text{ bar/m}$

RUN	$D$ [m]	$S_r$	$d(\text{mean}) \pm S. D.$ [ $\mu$ ]		$d(50) \pm S. D.$ [ $\mu$ ]	
138	0.02	0.38	150.8	25.3	131.8	31.1
139	0.02	0.39	174.7	19.3	165.1	23.9
124	0.03	0.34	97.3	14.3	58.8	6.1
132	0.03	0.34	102.3	15.6	72.7	13.1
137	0.06	0.35	134.8	15.5	90.0	16.8
148	0.06	0.34	131.4	8.3	87.7	12.5
400	0.06	0.34	122.5	10.8	97.9	10.4

influence the comparability of the results. The distribution curves of different runs correspond in an excellent way (Figs 5, 6, 7), indicating that this method generates reproducible data. The mean diameters and the 50%-values are summarized in Table II. It should be noted that only the distribution curves of  $D=0.02$  m are outside the standard deviation.

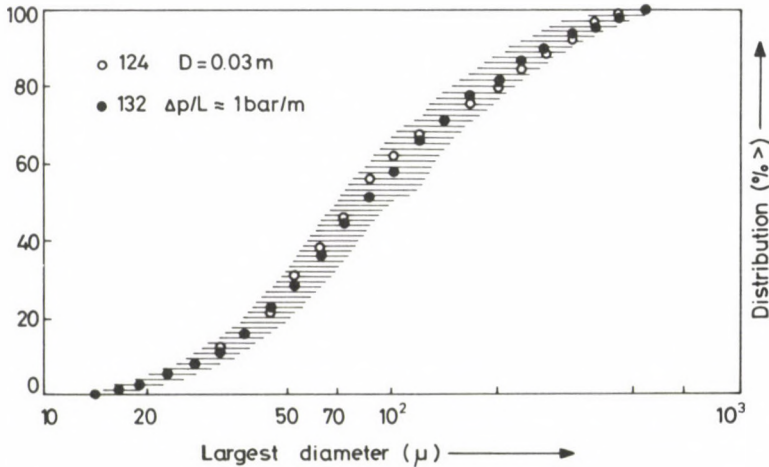


Fig. 6. Reproducibility of the residual phase distribution at constant conditions

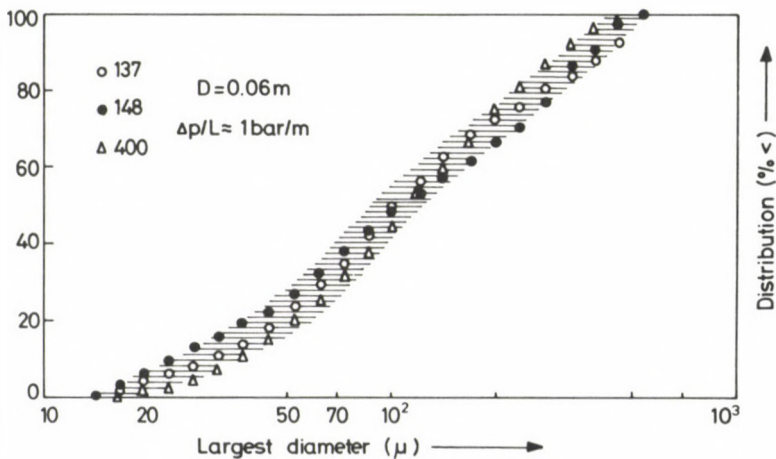


Fig. 7. Reproducibility of the residual phase distribution at constant conditions

## 4.3 Displacement velocity

Figure 8 shows how dramatically the distribution curve of the residual phase can change, if the displacement velocity, i.e. the pressure gradient is increased. The results which are grouped in Table III refer to the priority of the pressure gradient. Meanwhile Fig. 9 presents some distribution curves after waterflooding with distinct injection rates

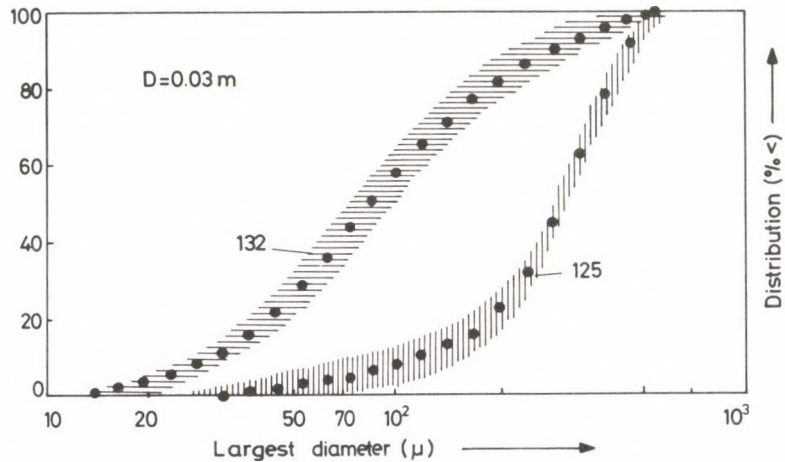


Fig. 8. Residual phase distribution as a function of displacement velocity

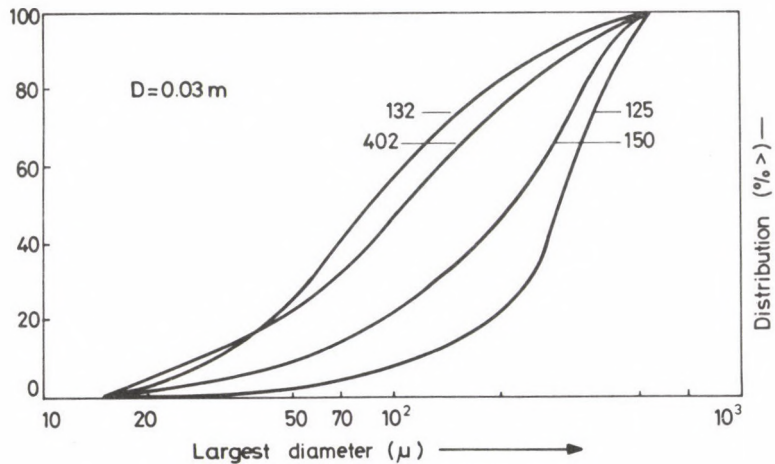


Fig. 9. Residual phase distribution as a function of pressure gradient

**Table III.** Residual phase saturation as a function of the pressure gradient  
 $u=0.02$  m/day

RUN	$\Delta p/L$ [bar/m]	$S_r$	$d(\text{mean}) \pm S. D.$ [ $\mu$ ]		$d(50) \pm S. D.$ [ $\mu$ ]	
125	0.05	0.44	243.5	9.4	244.3	6.0
128	0.05	0.43	218.8	38.8	220.4	44.9
151	0.20	0.40	197.5	16.6	200.7	23.8
152	0.25	0.41	179.3	12.6	177.9	19.1

**Table IV.** Residual phase saturation as a function of the pressure gradient

RUN	$\Delta p/L$ [bar/m]	$S_r$	$d(\text{mean}) \pm S. D.$ [ $\mu$ ]		$d(50) \pm S. D.$ [ $\mu$ ]	
125	<0.05	0.44	243.5	9.4	244.3	6.0
128	<0.05	0.43	218.8	38.8	220.4	44.9
130	0.15	0.42	194.8	21.6	188.2	25.7
152	0.25	0.41	179.3	12.6	177.9	19.1
151	0.20	0.40	197.5	16.6	200.7	23.8
155	0.30	0.40	184.3	11.0	181.6	16.7
150	0.31	0.39	183.8	13.2	179.9	18.6
162	4.95	0.37	190.0	16.7	194.9	25.8
161	5.42	0.37	159.5	15.4	151.9	20.7
163	7.18	0.37	166.1	10.0	104.3	26.8
402	0.70	0.35	125.1	17.7	91.5	12.5
160	0.77	0.35	182.0	24.0	176.0	43.8
143	0.95	0.34	126.8	20.9	86.9	24.1
124	0.99	0.34	97.3	14.3	58.8	6.1
132	1.16	0.34	102.3	15.6	72.7	13.1
164	3.07	0.34	135.6	14.4	107.0	24.7

at  $D=0.03$  m, all respective investigations of residual phase distribution as a function of  $\Delta p/L$  are summarized in Table IV.

The results of displacements by high injection rates have been somewhat unexpected. However, they could be confirmed by a control run (Figs 4 and 10).

Figure 11 indicates that the distribution of the residual phase is still a function of the pressure gradient even at a core diameter as large as  $D=0.06$  m.

*Note:* As possible end effects 0.02 m thick segments both from the core inlet and outlet were not taken into account, as they had been discarded before the remaining core material was analysed.

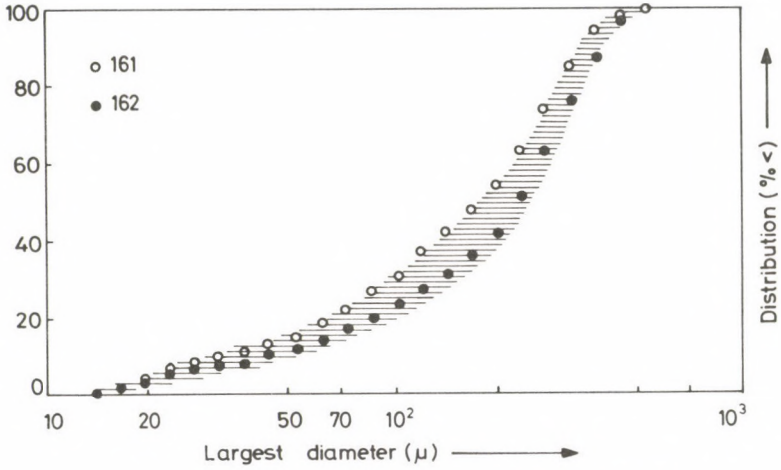


Fig. 10. Residual phase distribution at high pressure gradient

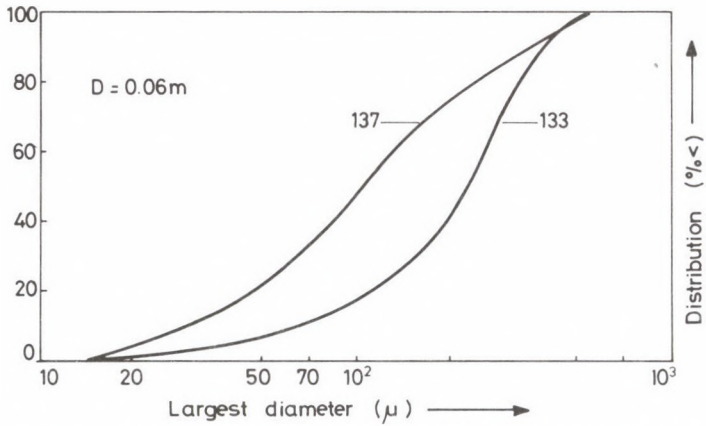


Fig. 11. Residual phase distribution as a function of the pressure gradient

## 5. Discussion

The established independence of the distribution functions on both the distance from the core inlet and the core length, as well as the fact that the boundary regions have some important experimental implications in the case of small core diameters, correspond to the recent computation of capillary displacement and percolation in porous media done by Chandler et al. (1982). Though the capillary number working during our experiments has been much higher than in the case of water imbibition by capillary forces, we are convinced that the conception which concerns residual phase distribution as a function of the core diameter, is valid even for the comparative investigations presented in Figs 5–7 and in Table II. This may be interpreted as follows: while the oil phase is displaced by the drive water, the oil/water interface moves in a very irregular fashion with strong local variation in velocity. The displacement process proceeds with considerable fingering and trapping of the displaced phase at all length scales. Large residual oil filaments result when a region is pinched off by long fingers. If the core diameter is small in comparison with the number of pores on the cross-section, this fingering results in an excess of trapped larger oil blobs pinned against the impermeable sides.

Consequently, laboratory case studies could seriously overestimate the residual oil saturation at low  $N_{vc}$ . This, in turn, may have biased the evaluation data for the EOR method investigated in the laboratory. However, it should be noted that our results do not indicate any effect if the core diameter is larger than  $D=0.03$  m, which diameter is usually applied in our laboratory.

To minimize outlet end effects in the laboratory, water is injected at a rate where viscous forces are large compared to capillary forces. This implies a much higher Darcy velocity of the displacing water phase than in the reservoir, though at extremely high pressure gradients (about 90 bar/m in strongly water-wet cores) reductions in residual oil are usually observed (Moore and Slobod 1956, Jenks et al. 1968). However, laboratory waterflooding pressure gradients are normally 1/10 to 1/1000 of this value. While some authors e.g. Handy and Datta (1966) suggest that extremely low rates lead to higher oil recovery, Rathmell et al. (1973) are convinced that this effect may only rarely be observed.

Our experiments with the system styrene monomer /water/ preferentially water-wet sandstone confirms that the residual phase saturation depends on the pressure gradient applied at relatively low injection rates, but this dependence is negligible at higher pressure gradients. The results which are summarized in Table IV can be interpreted as follows: (i) At first the residual phase saturation is inversely proportional to the pressure gradient, later it becomes independent within a certain range of higher pressure gradients, but increases again if relatively high injection rates are applied. (ii) In the system described above, the relation between the residual saturation and its distribution function is significant: A lower saturation coincides with a smaller mean

diameter and a lower 50%-value. (iii) At low injection rates the pressure gradient becomes paramount to the Darcy velocity. Therefore it is obvious that higher pressure gradients prevent relatively large filaments to be entrapped as a residual phase. High injection rates, on the other hand, achieve that the water is conveyed at a locally different speed through the heterogeneous microstructure of the porous network. Consequently, the displacement process is characterised by enhanced fingering and trapping of larger filaments.

If the force required for release of a residual oil filament is indeed a function of its volume related to the pore structure of its trap, this result should give a fresh stimulus to the existing laboratory practice. As the distribution of the residual phase can be described as a function of the pore structure, this is in itself an argument against the uncritical modelling of EOR trials by linear displacements.

The possible influence of the pore structure as well as the pressure gradient of the driving water on the recovery efficiency has to be quantified by an analysis of the residual phase volumes. This work will be carried out in our laboratory. It is our intention to establish a method by which porous media can be produced which are comparable to the pore structure of the respective reservoir. By doing so, the water drive and the subsequent chemical flooding can be realised under conditions which are controlled by the Darcy velocity of the field displacement front without any efficiency falsification due to end effects, because the core length is large enough.

Moreover, our results should give a better insight into field reality. For an economic evaluation of any EOR process, data of residual oil saturation are required, but these data obtained from specialised logging techniques and laboratory investigations after coring are drawn from a relatively small section of the reservoir adjacent to the wellbore. This region, however, has been subjected to a radial flow and consequently, to a pressure gradient and a displacement velocity much higher than the reservoir. Therefore both the quantity and the size distribution of the oil retained may differ in the zone close to the wellbore from that trapped in the swept reservoir. Morrow and Chatzis (1981) indicate that capillary number relationships can be used to relate the pressure gradient around the wellbore and the associated overbalance pressure to estimate the residual oil saturation in the reservoir. We will also study the impact of the radial flow on the saturation with residual oil and the respective size distribution.

## 6. Summary

1. All experiments show a satisfactory — and often excellent — reproducibility of the distribution curves.

2. The advantages of the automatic particle size analysis, are inter alia (i) the measuring technique is simple and quick, (ii) one count is based on a very large population, (iii) the particles are classified according to the largest diameter of each

particle, outweigh the only real disadvantage that no information on the real shape of the particle volumes is given.

3. The existing laboratory practice of modelling EOR processes by linear displacements with relatively high injection rates during the preceding water drive should be reconsidered in the light of our results.

4. The results should improve the understanding of field reality and provide accurate data of residual oil saturation which are essential for an economic evaluation of any EOR project.

5. The relation between the residual oil saturation as a function of the respective flow conditions and the volume distribution data is significant: a lower saturation corresponds to a smaller mean diameter and a lower 50%-value.

6. The results recommend the use of a core diameter  $D=0.03$  m, because larger core diameters are inefficient.

7. The length of the laboratory model does not influence the distribution curve. On the contrary: if the test conditions are about equal, the distribution curves originating from different runs and core lengths are in satisfactory agreement.

### Acknowledgement

The investigations have been part of the research project No. 2173 sponsored by the Jubilee Fond of the Austrian National Bank via Joanneum Research Society.

### References

- Chandler R, Koplik J, Lerman K, Willemsen J F 1982: Capillary displacement and percolation in porous media. *J. Fluid Mech.*, 119, 249–267.
- Chatenever A, Calhoun I C jr. 1952: Visual examination of fluid behaviour in porous media, Part 1. *Trans AIME*, 195, 149–156.
- Chatzis I, Morrow N R, Lim H T 1983: Magnitude and detailed structure of residual oil saturation. *Soc. Pet. Eng. J.*, 23, 311–326.
- Handy L L, Datta P 1966: Fluid distributions during immiscible displacements in porous media. *Soc. Pet. Eng. J.*, 6, 261–266.
- Jenks L J, Huppler J D, Morrow N R jr., Salathiel R A 1968: Fluid flow within a porous medium near a diamond bit. SPE paper 6824, pres. at 19th Annual Tech. Meeting of the Pet. Soc. of CIM, Calgary
- Larson R G, Davis H T, Scriven L E 1982: Elementary mechanisms of oil recovery by chemical methods. *J. Pet. Techn.*, 34, 243–258.
- Melrose J C, Brandner C F 1974: Role of capillary force in determining microscopic displacement efficiency for oil recovery by water flooding. *J. Can. Pet. Techn.*, 13, 42–48.
- Moore T F, Slobod R L 1956: The effect of viscosity and capillarity on the displacement of oil by water. *Prod. Monthly*, 20, 20–24.
- Morrow N R 1979: Interplay of capillary, viscous and buoyancy forces in the mobilization of residual oil. *J. Can. Pet. Techn.*, 18, 35–46.
- Morrow N R, Chatzis I 1981: Measurement and correlation for entrapment and mobilization of residual oil. Report DOE/BETC 3251-12, Contr. No. DE-AC03-79ET3251.
- Ng K M, Davis H T, Scriven L E 1977: Visualization of blob mechanics in flow through porous media. *Chem. Eng. Sci.*, 33, 1009–1013.

- Rathmell J J, Braun P H, Perkins T K, 1973: Reservoir waterflood residual oil saturation from laboratory tests. *J. Pet. Techn.*, 25, 175–185.
- Reed R L, Healy R N 1977: Some physicochemical aspects of microemulsion flooding: Review. In: *Improved oil recovery by surfactant and polymer flooding*. D O Shah and R S Schechter eds, Academic Press, Inc., 383–437.
- Stegemeier G L 1977: Mechanisms of entrapment and mobilization of oil in porous media. In: *Improved Oil Recovery by Surfactant and Polymer Flooding*. D O Shah and R S Schechter eds, Academic Press, Inc., 55–91.
- Swanson B F 1979: Visualizing pores and nonwetting phase in porous media. *J. Pet. Tech.*, 31, 10–18.
- Taber J J 1980: Research and enhanced oil recovery: Past, present and future. *Pure Appl. Chem.* 52, 1323–1347.
- Weinhardt B, Heinemann Z 1982: Evaluation of residual phase distribution in consolidated sandstones. *Erdöl-Erdgas-Zeitschr.*, 98, 393–399.

## GEOCHEMICAL COMPONENTS OF THE EFFECT MECHANISM OF OIL DISPLACEMENT WITH CARBON DIOXIDE

E NÉMETH

A method developed at the end of the '60s in the fields of South-Zala which aimed at the increase of oil recovery by means of carbon dioxide, has already been applied universally in a large-scale industrial extent. The article describes the history and results of the field experiment that serves as the basis of the method. It analyses the mechanism of oil displacement, the factors which exert an influence on the results. Further, it deals with the physico-chemical processes occurring in the CO<sub>2</sub>-oil-water-rock system, pointing out their role and importance which affect the efficiency of the method.

**Keywords:** carbon dioxide injection; displacement mechanism; dissolving effect of CO<sub>2</sub>; field experiment; ion-exchange; oil swelling

### Symbols

$B$	formation volume factor
$CH$	hydrocarbon
$u$	viscosity, mPa s
$\eta$	recovery, a fraction
$v$	displacement velocity, cm sec <sup>-1</sup>
$S_{orf}$	saturation, a fraction
$\sigma$	interfacial tension, m <sup>3</sup> /m <sup>2</sup>
$R_s$	solution gas, m <sup>3</sup> /m <sup>3</sup>
$T$	temperature, °C
$k$	permeability, $\mu\text{m}^2$
$k_r$	relative permeability
$p$	pressure, MPa
$V$	volume, m <sup>3</sup>
$V_p$	pore volume, m <sup>3</sup>
$\rho$	density, kg/m <sup>3</sup>
$Q$	production, m <sup>3</sup> /day
$N$	cumulative production, m <sup>3</sup>
$Q_{ginj}$	gas injection, m <sup>3</sup> /day
$Q_{winj}$	water injection, m <sup>3</sup> /day
$F_w$	water content of the produced fluid, %
<i>Index-1:</i>	
$o$	oil
$w$	water
$g$	gas
<i>Index-2:</i>	
$r$	residual
$i$	initial

<sup>1</sup> Oil and Natural Gas Mining Enterprise, Nagykanizsa

## Introduction

The classical forms of secondary production, gas- and water injection have become ineffective from the middle of the '60s in the fields of South-Zala as regards to displacement — as they had been applied according to the then known methods. In order to reduce the reserves left behind in the reservoirs, the application of new displacing agents has become imperative by means of which an additional oil recovery could be ensured. Based on laboratory results, the carbon dioxide method proved to be one of the most promising from the new methods that were covered by research, the more so, as in Hungary the developed gas reservoirs containing carbon dioxide offered a real possibility for the field application of the carbon dioxide method.

Until the mid '60s the Hungarian explorations were oriented to the application of pure CO<sub>2</sub> gas — having at least 96 mole % CO<sub>2</sub> content. A special problem arose from the fact that the strongly heterogeneous reservoirs showing poor petrophysical parameters were depleted, and they contained a significant amount of CH<sub>4</sub> gas dissolved in the oil, in a free state and in the shape of gas caps. Under such conditions even the pure CO<sub>2</sub> gas would have diluted, and according to our knowledge it would have lost something from its effect. Bearing in mind the peculiar characteristics of the reservoirs in South-Zala, the experiments were directed from 1967 on towards utilization of the gas that had been developed in the deep horizon of the Budafa Field, which gas contained 81 mole % CO<sub>2</sub>. Thus it came the turn for performing a field experiment in the lense K-2 of the Upper-Lispe sequence.

### Description of the pilot reservoir and its state

The middle sandstone lense, No 2 of the Upper-Lispe sequence at Budafa is a reservoir with a boundary in form of a fault and out-pinchings, with the exception of its SE part which has hydrodynamic connection also with the aquifer (Fig. 1). The reservoir rock is of a Lower-Pannonian quartz sandstone with brownish-yellowish grey colour having mediocre fine grained tight cementing material of varying hardness. The intercalation of marl layers makes the reservoir a layered one.

More important data of the pilot reservoir:

Depth, m	1100
Bed thickness, m	5.6
Porosity, %	21.5
Permeability, $\mu\text{m}^2$	10–40
Formation temperature, °C	68
Initial reservoir pressure, MPa	10.0
Saturation pressure, MPa	9.8

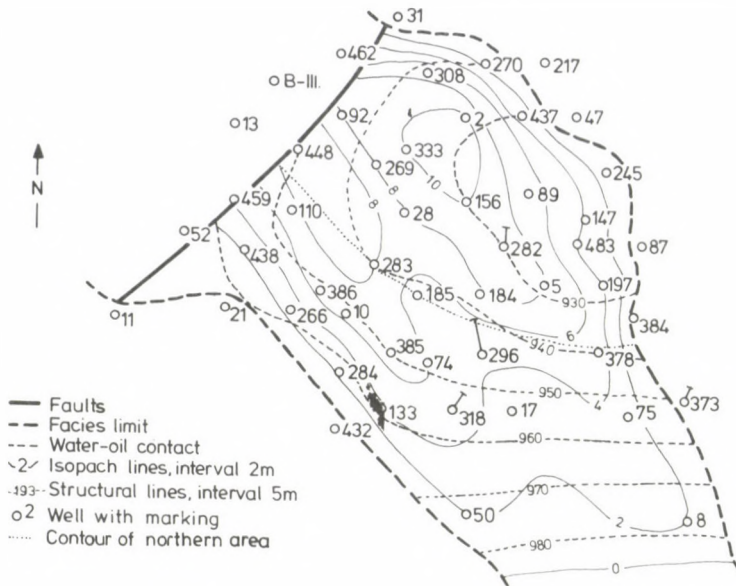


Fig. 1. Structural and isopachous map of the Lense K-2 of Upper-Lispe

Solution gas, $R_{si}$ , $m^3/m^3$	71.5
Viscosity of reservoir fluids, $mPa \cdot s$	
Oil	1.16
Gas	0.018
Water	0.41
$B_{oi}$	1.224
$S_{wi}$ , %	30.0

The stored crude oil is of intermediary-paraffinic nature, its density on 20 °C is 834  $kg/m^3$ , its white product content (up to 275 °C) is 52–55 mass %.

The formation water is the typical Pannonian water: its pH is 8.0–8.5, its NaCl content 1–3 g/l, with a total salt content of 4–5 g/l.

The natural displacing energy was decisively supplied by the solution gas. The effect of edge water was only locally present. Later, in the course of secondary processes at first the CH gas displacement in the higher part of the structure, then water displacement in its lower part constituted the dominant mechanism. Effectiveness and results of these processes are shown by the data of Table I.

For the purpose of evaluating the carbon dioxide experiment, a careful analysis was made on the state of the reservoir at the initiation of experiment. Based on this, it could be determined that in the northern part of the reservoir having a greater thickness the gas saturation followed by gas injection was dominant and typical, while

**Table I.** Performance data of the experimental reservoir preceding the CO<sub>2</sub>-gas injection

	Produced oil, m <sup>3</sup>	Recovery factor, %	Quantity of injected agent, m <sup>3</sup>
With original energy system of the reservoir	150 962	22.63	—
With gas injection	58 555	8.78	94 234 000
With water injection	25 053	3.76	507 000
Total with gas- and water injection	83 608	12.54	—
Total	234 570	35.12	—

**Table II.** Pressure and saturation data of the experimental reservoir preceding the CO<sub>2</sub>-gas injection

	Northern part	Southern part	Lense, total
Distribution of crude oil resources, %	59.5	40.5	100.0
Production, m <sup>3</sup>	124 680	109 890	234 570
Pr, MPa	2.75	5.10	4.0
Saturation, %			
Oil	43.35	38.25	41.30
Gas	14.47	2.45	9.37
Water	42.18	50.30	49.33
Recovery, %	31.43	40.62	35.10

in its thinner part divided by many marl streaks, the high water saturation which followed the water injection was characteristic (Németh 1970). Corresponding to this regional division, Table II summarizes the typical production and saturation data characteristic of the start of gas injection containing carbon dioxide, and the values of the recovery factor as well.

### History of the experiment

The pressure and the fluid distribution of the lense at the beginning of CO<sub>2</sub>-gas injection are visible in Fig. 2. Figure 3 shows the boundaries of reservoir parts covered by the experiment. Zones I, II and III correspond to reservoir parts which have high gas saturation, which are just getting watered-out and which already got watered-out. Since the production of zones II and III has shown identical characteristics, they came to evaluation as an aqueous zone by drawing them together. The main basic data are summarized in Table III.



**Table III.** Main basic data of the reservoir parts contacted by the CO<sub>2</sub> exploitation of the experimental reservoir

	Gaseous zone	Aqueous zone	Zone of experiment
Rock volume, 10 <sup>3</sup> m <sup>3</sup>	1 390	2 170	3 560
Crude oil resources, 10 <sup>3</sup> m <sup>3</sup>	170	273	443
Produced oil, m <sup>3</sup>	51 500	99 500	151 000
Pr, MPa	2.35	4.30	3.50
Saturations, %			
Oil	43.34	40.32	41.90
Gas	19.0	7.0	11.6
Water	37.66	52.68	46.90
Recovery, %	30.3	36.5	34.1

Injection of gas having a carbon dioxide content was started in July 1969 into three zones having different reservoir pressure and degree of watering-out in Wells B-2, -269 and -110, as it is visible in Fig. 2 (Németh 1977). The rate of injection was 30–50-times higher than that of production. Thus, by means of the injected gas the reservoir pressure could be increased by 10–20% above the original values (Fig. 3). Due to the influence of the high rate injection around the injection well vaporization, farther away from it condensation conditions have come into being, helping the formation of an oil bank. The forming oil bank, behaving like a dynamic impact barrier, has brought about in the reservoir part contacting the injected gas a higher pressure than that one which was dominant in the entity of the reservoir, helping thus a better dissolution of CO<sub>2</sub>, and the stabilization of the oil bank (Fig. 5, Curve 5). The reservoir pressure measured in the responding well did not increase at an even rate. After the gas injection was started, there was not any measurable change in the responding well for six weeks. Then in 2–3 days the formation pressure increased from 1.8 MPa to 8.0 MPa, during which time also the production rate of the well increased rapidly, almost leapwise (Fig. 5, Curve 4). The daily oil production rates have become multiplied. The spectacular results in the wells of the gaseous zone lasted for more than two years. Almost simultaneously with the increase of oil production rates the injected CO<sub>2</sub> appeared in the gas of the producing well (Fig. 4). In the phase of pressure increase also gas breakthroughs have soon occurred. The gas channels brought about by means of shut-in of the producing well in the course of water injection have ceased to exist in 6–12 months, and the production afterwards could be renewed continuously and steadily with a low GOR (Fig. 5). The production history of the pilot area is illustrated by Fig. 6.

The characteristic production parameter of the experiment is the increase of the recovery factor obtained. In Table IV the increases of the recovery factor of reservoir parts of differing initial stage and the specific utilization indexes of the injected agents are summarized. For the whole lense the increase of recovery was 10.03%, but that of

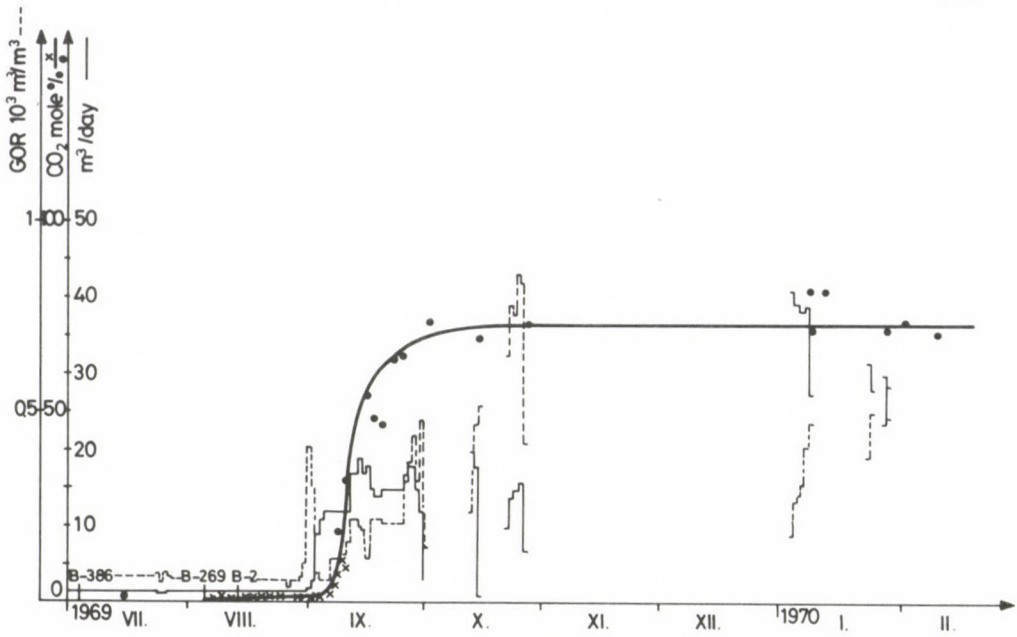


Fig. 4. Break-through of CO<sub>2</sub> gas into the well B-156

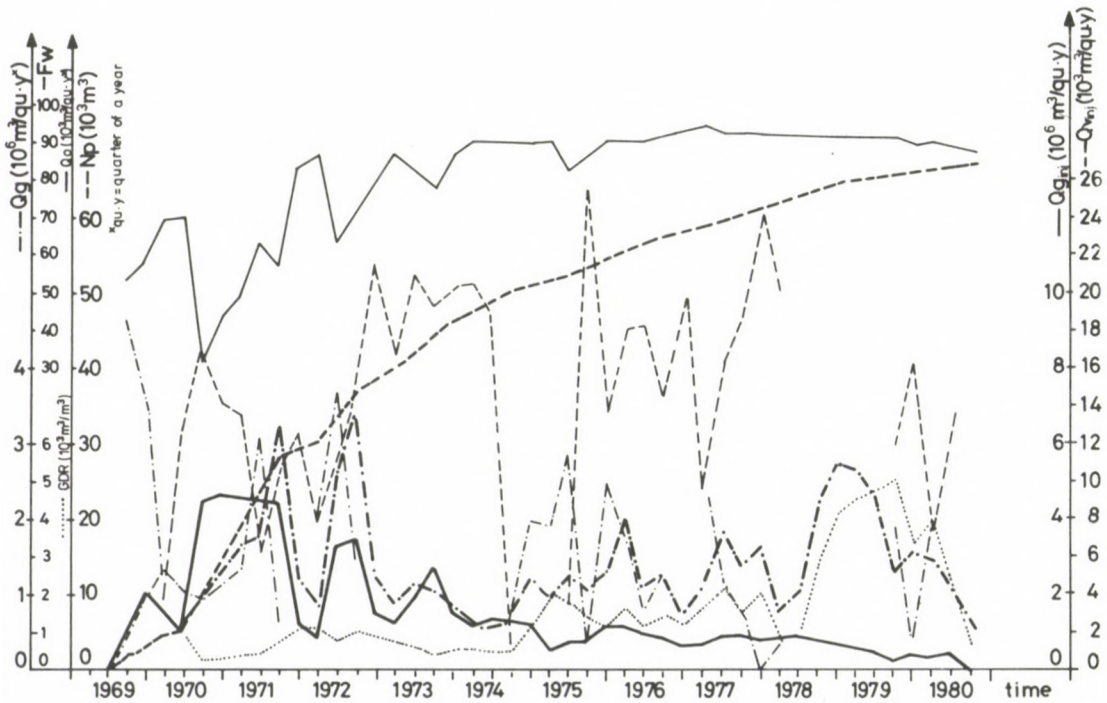


Fig. 5. Production history of the pilot area based on quarterly averaged data

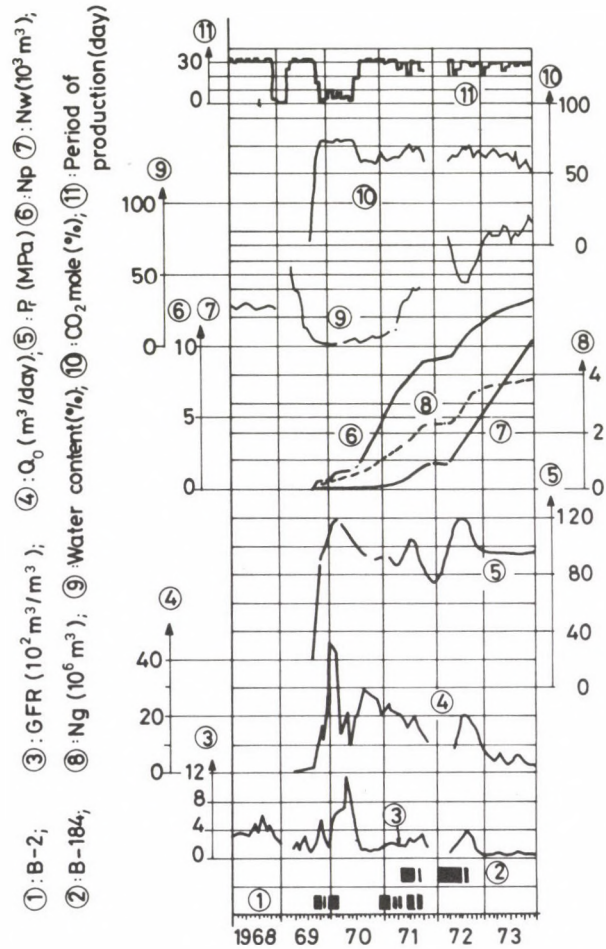


Fig. 6. Production history of the well B-165. 1. Injection into well B-2, 2. Injection into well B-184, 3. GFR,  $10^2 \text{ m}^3/\text{m}^3$ , 4. Oil production,  $\text{m}^3/\text{day}$ , 5. Formation pressure, MPa, 6. Cumulative oil production,  $10^3 \text{ m}^3$ , 7. Cumulative water production,  $10^3 \text{ m}^3$ , 8. Cumulative gas production,  $10^6 \text{ m}^3$ , 9. Water content, mole %, 10. CO<sub>2</sub> content, mole %, 11. Number of producing days, day

the reservoir part affected by the experiment was 15.10%. At the onset of the experiment the increase of the recovery factor is threefold with respect of the average, while that of the aqueous zone is only one third/a quarter. The reason of the difference lies in the diversity between the volumetric efficiency and the efficiency of displacement.

**Table IV.** Recovery factors and specific indices of the CO<sub>2</sub> experiment

	$\eta(\%)$	$Q_{\text{inj}}/V_p$ (m <sup>3</sup> /m <sup>3</sup> )	$Q_{\text{winj}}/V_p$ (m <sup>3</sup> /m <sup>3</sup> )
<i>Until 30.6.1974</i>			
Experimental	10.93	58.4	0.33
Gaseous	24.78	74.4	0.54
Aqueous	3.30	48.3	0.20
Lense, total	7.26	39.2	0.22
<i>From 1.7.1974 until 31.7.1980</i>			
Experimental	4.17	59.5	0.33
Gaseous	8.00	70.2	0.49
Aqueous	1.78	52.8	0.22
Lense, total	2.77	40.0	0.22
<i>Until 31.7.1980</i>			
Experimental	15.10	117.9	0.66
Gaseous	32.78	144.6	1.03
Aqueous	4.08	101.1	0.42
Lense, total	10.03	79.2	0.44

### Factors of the effect mechanism

In the displacement of oil the CO<sub>2</sub>, and the gas containing CO<sub>2</sub>, respectively, exert their effect corresponding to the given conditions by means of the following factors, namely they:

- swell the oil,
- reduce the viscosity of the oil,
- enhance the oil density,
- dissolve well in water,
- exert an acidic dissolving effect on the rock,
- vaporize and extract the crude oil components,
- get chromatographically transported through the porous rock,
- decrease superficial, interfacial tension,
- bring about favourable geochemical processes in the water-rock system.

The extent of the effects listed above is influenced by the following reservoir characteristics:

- properties of the reservoir fluids,
- reservoir temperature,
- reservoir pressure,
- saturation conditions of the reservoir,
- material and structure of the reservoir rock.

In the effect mechanism the factors that influence the displacement efficiency are directly or indirectly pressure and temperature dependent. One of the most important

parameters is the swelling of the oil that depends on the extent of the CO<sub>2</sub> dissolution, this latter depending on the amount of CH gases present in the reservoir, moreover on the formation temperature.

The excellent dissolution of carbon dioxide in the oil makes evident the validity of the miscible displacement process. The reservoir conditions, however, hardly make possible its clear form, e.g. just because of the presence of a high reservoir temperature and/or CH gases. In the process of exploitation, however, steps can be taken which would make the efficiency of the parameters more favourable. In case of a given reservoir an effect may be exerted by influencing the increase of reservoir pressure and the rates of gas injection on all factors that are functions of the pressure and the composition of gas (Németh 1977).

The production data of the experiment, and those of the recovery factor increase, respectively, show a close relationship between the effect mechanism of carbon dioxide and its application technology in a lot of cases *assuming* each other.

#### *High rate gas injection*

When performing a pressure increase, a high rate gas injection was realized, the volume of which surpassed many times the volume drawn. The relationship between the injection velocity and the residual oil is shown by the following laboratory data:

$v(\text{m/day})$	%	$S_{\text{orf}}, \%$
0.50	58.0	29.02
2.92	62.2	26.11
12.91	66.1	23.42
64.56	70.3	20.50

where:

$S_{\text{orf}}$  is the surface volume of the residual oil saturation. The effect of the displacement velocity is given by  $\pi = \frac{\sigma}{\mu_g \cdot v} \left( \frac{\mu_0}{\mu_g} \right)^n$  and the dependence of  $S_{\text{or}}$  on the parameter  $\pi$ , respectively (Prey 1968). Based on experiments with oils of the lense K-2 of Upper-Lispe and Algyő, the change of  $S_{\text{or}}$  with  $\pi$  is shown in case of  $n=0.25$  by Fig. 7. From the data and the figure the advantage of the greater displacement velocity is clearly visible.

#### *Effects of gas saturation*

In the course of the experiment the injection rate was determined in such a way that up to a well radius of 10 m the flow velocity of gas was 100 m/day, at a well radius of 100 m it was 16 m/day. The high velocity gas flowing astray from the injection well entrains with itself the C<sub>3</sub>—C<sub>30</sub> components of residual oil vaporizing them. Enriched

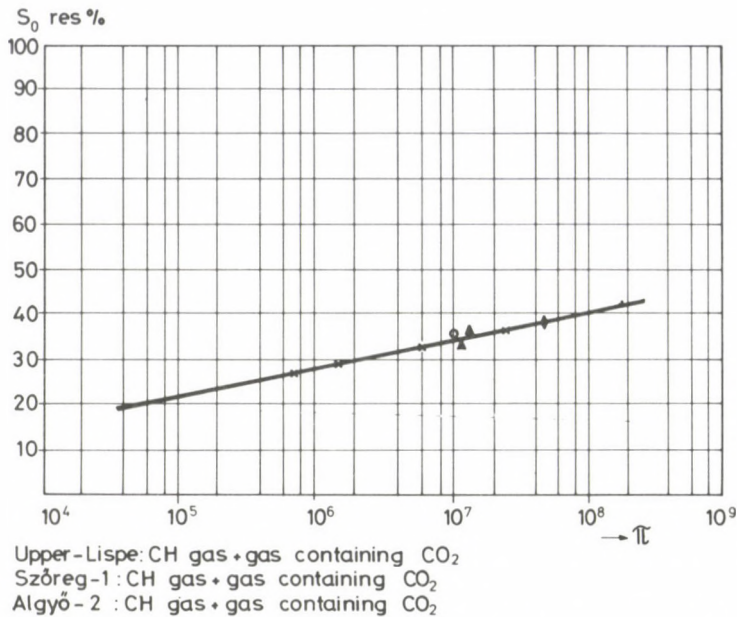


Fig. 7. Change of the residual oil saturation with a  $\pi$  parameter depending on the velocity of the gas displacement

in them they become slower at the front, and the lighter components condense in the oil. From the reservoir part having a 75–100 m radius around the injection well, the gas extracts as much oil as at condenses at the front so that it should form an oil bank.

The oil bank being formed at a distance of 50–100 m from the injection well, it will consume pressure energy. On two sides of the front an essential pressure difference is developing. The space between the oil ring and the injection well is filled up with high pressure gas, thus increasing the dissolution of CO<sub>2</sub> in oil, the result of which is swelling and further oil displacement, enhancing in this way the displacement efficiency.

By means of a high rate gas injection in a reservoir — reservoir parts — possessing gas saturation, the displacement can be made such as to assume a miscible character. At such a time, however, there exists an increasing danger of break-through of the gas, which in the course of the experiment has duly occurred. In such cases the producing wells had been kept shut-in so long as the gas-channel, under the effect of the continued pressure build-up ceased to exist.

#### *Effect of mobile water saturation*

In the aqueous zone, as the data of the experiment showed, the high rate gas injection has given a modest result. The decisive difference lies in the fact that the mobile phase in the pores is the water, while the oil and the gas are immobile. During

gas injection, the gas first displaces the water, then displaces that portion of residual oil which becomes mobilizable because of the swelling of the oil (Fig. 8). It has a high pressure demand to set into motion the forming water ring, and its movement is very slow. From the gas injected a high pressure zone comes into existence around the injection well. (A reservoir pressure of 14.0–15.0 MPa has developed during the experiment in the injection well that had been placed in the aqueous zone, while in the

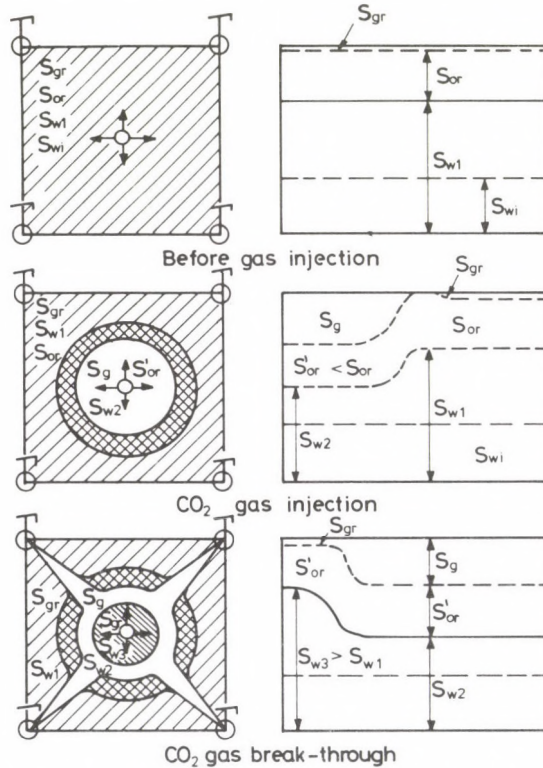


Fig. 8. Process schemes of the displacement of mobile water with gas

gaseous zone this pressure was 11.0–12.0 MPa). This high pressure gas around the well moves ahead the water ring through which, because of the unfavourable mobility, the gas breaks through across a narrow, almost needle-like channel into the producing well. At the same time this is the reason of the low volumetric efficiency as well. As a consequence, it is unpractical to perform a high rate injection in the zone of mobile water saturation, it should be as large as the rate of the water displacement. Corresponding to this, the initial gas injection rate could have been 100–200 m<sup>3</sup>/day/well up to a fill-up to a well radius of 20–50 m.

In a reservoir having mobile water saturation, strictly speaking, water displacement is performed by means of carbon dioxide. It means another disadvantage because the  $\text{CO}_2$  from the water redissolves into the oil. As oil dissolves 8–10 times more  $\text{CO}_2$  than water, the water loses its carbon dioxide content and flows as ordinary water.

*Effect of the  $\text{CO}_2$ -CH component ratio of gas in the reservoir*

In the oil displacement mechanism of  $\text{CO}_2$ , a factor that significantly decreases dissolution is the CH gas existing either dissolved or in free phase. In the course of the experiment a gas having 81 mole %  $\text{CO}_2$  was injected, and there was some CH gas dissolved in the oil in the reservoir as well, and the mobile gas saturation in the gas phase in the pilot reservoir part was some  $8.6 \text{ Mm}^3$ . In the period of pressure increase by means of  $18.1 \text{ Mm}^3$  gas containing carbon dioxide, the  $\text{CO}_2$ -CH component ratio in the reservoir was 1.25, and the percent ratio of  $\text{CO}_2$  was 55.5%, respectively. Due to the later performed pressure maintaining injections this ratio was 55–70 mole % at a reservoir pressure 10.0–12.0 MPa. The  $\text{CO}_2$  content in the gas of the producing wells was again 55–70% as it is visible in Fig. 6 as well. Where the volumetric efficiency was suitable, there the  $\text{CO}_2$  content in the produced gas remained throughout constant. In case of a low volumetric efficiency the  $\text{CO}_2$  mole % of the produced gas has decreased after a short time below 50 mole %, and the effect of  $\text{CO}_2$ , viz. the oil production, too, began to decline, and in its totality it remained slight. The  $\text{CO}_2$  content of the produced gas served, therefore, as a good indicator.

Supported by PVT measurements, it was determined that the pressure of the reservoir should be increased with gas containing carbon dioxide to a value — but at least to 10.0 MPa — at which the  $\text{CO}_2$ -CH component ratio of gases in the reservoir was at least 0.50. It means that the applied  $\text{CO}_2$  gas need not have 0.96 mole %  $\text{CO}_2$  content, with other words, the gas having 0.81 mole %  $\text{CO}_2$  content need not be purified in order to realize a successful exploitation by means of carbon dioxide if we stick to those controllers which guide the operation:

- by taking into account the  $\text{CO}_2$ -CH component ratio in the reservoir, the danger could be avoided that even if pure  $\text{CO}_2$  is injected, the eventual high CH gas content of the reservoir might spoil the planned result because the pressure of the operation had been determined in a way that would correspond to pure  $\text{CO}_2$ ,
- the reservoir pressure, if there is no other obstacles in the way, — e.g. well construction, shallow depth, etc. — can be increased to such a high value that even in case of a high CH content the exploitation remains successful by means of  $\text{CO}_2$ ,
- by increasing the reservoir pressure a more favourable  $\text{CO}_2$ -CH component ratio can be assured, moreover even a carbon dioxide gas can be applied which has 65 mole %  $\text{CO}_2$  content as a minimum.

### Effect of reactions of the $\text{CO}_2$ -water-rock system

Water analysis data of the experiment have shown that  $\text{CO}_2$  comes into reaction with the reservoir rock not only in the presence of mobile water phase (Fig. 9) but even in case of irreducible water (Fig. 10).

The carbon dioxide water reactions with  $\text{CaCO}_3$  are well known. Under the influence of a gas injection having a carbon dioxide content, the changes of the  $\text{Ca}^{++}$ ,  $\text{Cl}^-$ ,  $\text{HCO}_3^-$  and  $\text{Na}^+$  values are shown in Fig. 9 and 10. The water break-through can be seen well in Fig. 10 which is indicated by the NaCl content. In spite of the dilution of the fossil (formation) water,  $\text{Na}^+$  and  $\text{HCO}_3^-$  have not decreased, on the contrary, they have increased. Also Fig. 9 illustrates this phenomenon.

The calcium hydrocarbonate forms only a smaller portion of the carbonate hardness of water, the greater portion is formed by  $\text{NaHCO}_3$ . Its developed equilibrium value is about 5–7 g/l. The increase of  $\text{HCO}_3^-$  is only possible when  $\text{Ca}^{++}$ -s “disappear” from the solution, and in their place a new cation,  $\text{Na}^+$ -s “enter” the solution. The source of the surplus-sodium which is necessary to this are the sodium base clay, marl grains, and minute marl lenses contaminated with clay.

The cations adsorbed at the surface of clay particles may be replaced according to the base-exchange phenomenon. The sodium clay will be converted to calcium clay by means of the base-exchange. This is very advantageous, because the calcium clay has

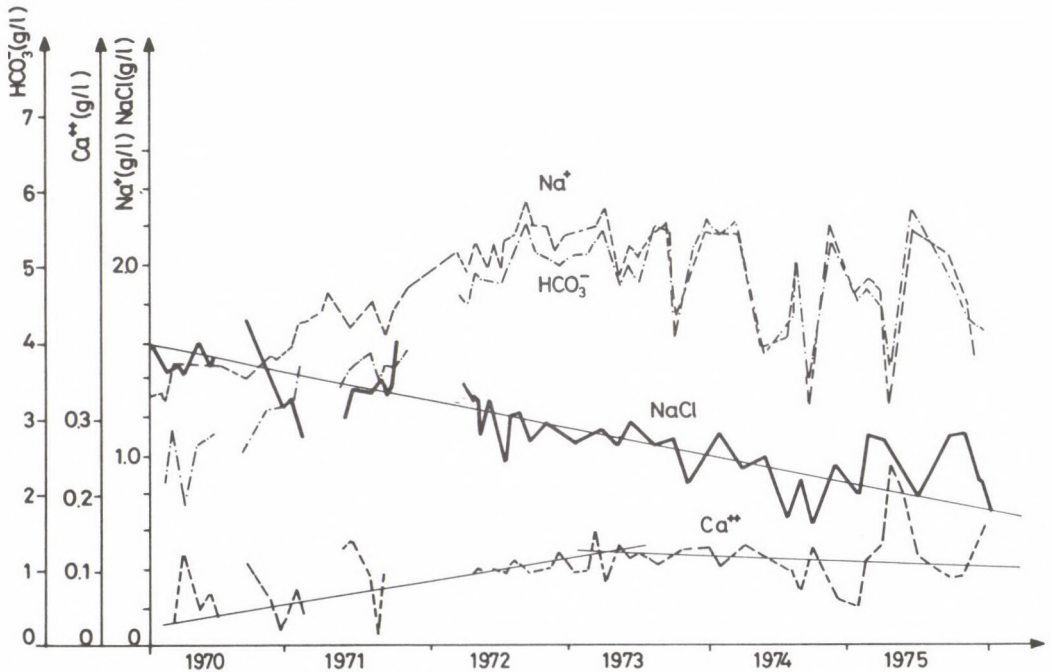


Fig. 9. Change of typical water analysis data with time of the well B-28

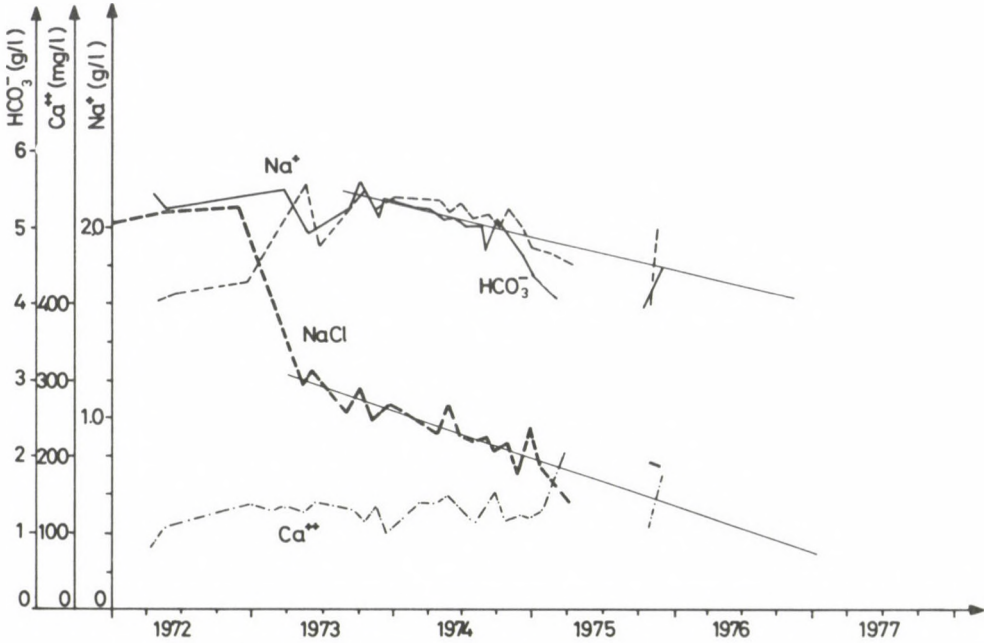


Fig. 10. Change of typical water analysis data with time of the well B-156

a smaller volume — the clay shrinks — and by that improves the efficiency of volumetric flooding.

The replacing  $\text{Ca}^{++}$  originates from the dissolution of  $\text{CaCO}_3$ . Due to the base-exchange, 5–6-times more  $\text{CaCO}_3$  will be dissolved than without base-exchange calculated from the water composition data. Thus, by means of dissolution of  $\text{CaCO}_3$  in the pore-throats the constriction of latter will significantly be enlarged, and by that:

- the permeability increases,
- through the larger pore-throat the flow resistance is lower, the displacement velocity is higher, and the value of residual oil thus decreases,
- by means of the crossflow flooding covers newer space parts.

As a result of cross-sectional enlargement of the pore-throat, the decrease of residual oil is shown by the shift of the relative permeability ratio curves towards lower oil saturation (Fig. 11).

The enlargements of the pore-throat, and the permeability increase of practical value, respectively, are reflected in 3–9-fold increases of the productivity factor. Under the effect of water injection following carbon dioxide gas, the oil content will be greater in the subordinate phase of watering-up. In the process of watering-up the increase of the water content is slow. The increases are followed by decreases the same way as the

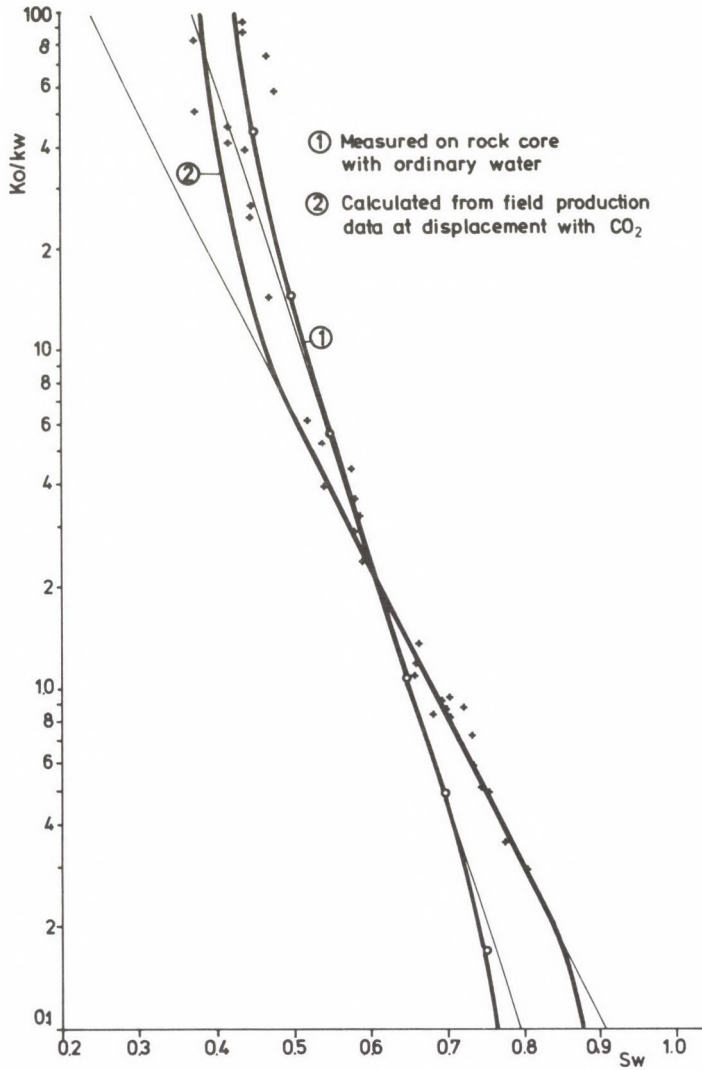


Fig. 11. Relative permeability ratio curves showing the effect without carbon dioxide and with carbon dioxide

oil in form of crossflows gets into the fluid flow from the individual formation-streaks (Fig. 12).

Evaluating the experimental data got for the effect of carbon dioxide on the rock, 50% of the production could be originated from the zone having mobile water saturation, and some 10–15% comes from the gaseous zone.

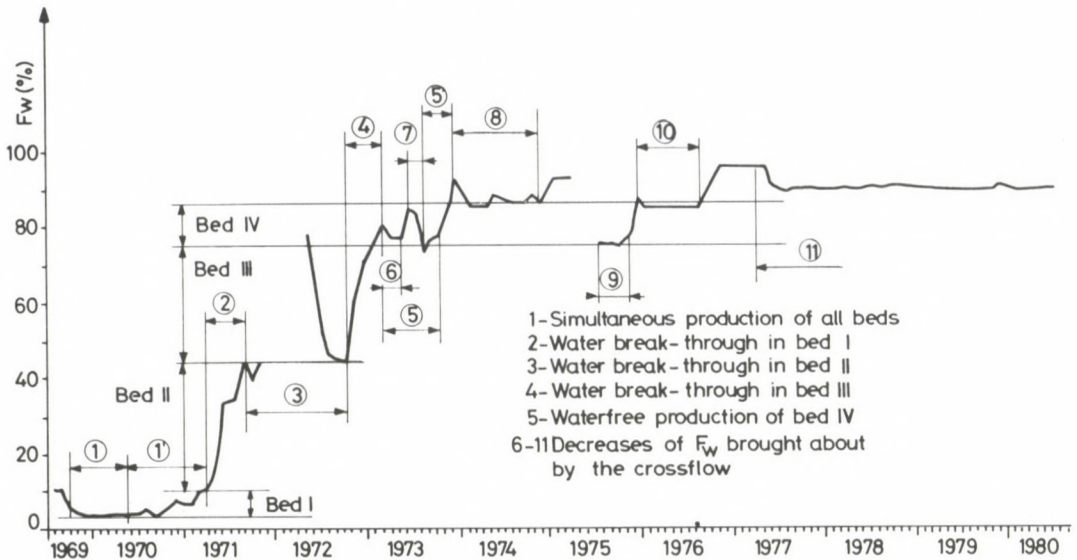


Fig. 12. Change of  $F_w$  values of the well B-156 reflecting crossflow

### Conclusions

1. The most effective form of displacement with carbon dioxide, *viz.* the realization of miscible displacement, is often frustrated by the high reservoir temperature and/or by the high original CH gas content in the reservoir. Namely, the temperature and the CH gas content impair the extent of dissolution, thus increasing the value of the miscibility pressure.

2. The saturation distribution of the reservoir exerts also an influence on the efficiency of the carbon dioxide gas injection. The initial mobile water saturation evokes unfavourable conditions, while gas saturation ensures favourable initial conditions.

3. The effectivity of exploitation by means of carbon dioxide gas, by means of increasing the reservoir pressure can be influenced:

- a) by means of increasing the reservoir pressure with a gas that contains carbon dioxide to a value that the  $\text{CO}_2$ -CH component ratio of gases present in the reservoir should be at least 50%, and the pressure at least 10 MPa,
- b) by means of a high rate injection of gas that contains carbon dioxide.

4. In the course of pressure increase the break-through of gas, based on the mole % of the produced gas and on the GOR criteria can be stopped by production control of the responding wells.

5. The geochemical reactions of the carbon dioxide-water-rock system are favourable to the effectivity of exploitation: by increasing the volumetric efficiency via crossflow, by decreasing the residual oil saturation through the enlargement of pore constrictions, and finally, by increasing the specific productivity factor.

### References

- Avar B 1971: Corrosion experiences during injecting gases of high CO<sub>2</sub>-content. (In Hungarian) *Kőolaj és Földgáz*, 4, 10–14.
- Németh E 1970: Carbon dioxide experiments in Budafa, in the middle lense of the reservoir Upper-Lipse No. 2. (In Hungarian) *Kőolaj és Földgáz*, 3, 235–237.
- Németh E 1974: Oil displacement by gas, water and carbon dioxide in the lense K-2 of Upper-Lipse. (In Hungarian) *Kőolaj és Földgáz*, 7, 225–231; 7, 261–270.
- Németh E 1977: Increasing the oil recovery factor with carbon dioxide in reservoirs having layered systems. Candidate Thesis
- Németh E 1983: Evaluation of the exploitation experiment by means of carbon dioxide in the lense K-2 of the Upper-Lipse sequence in Budafa Field. Symposium on the use of CO<sub>2</sub> for oil recovery. Budapest
- Prey E J 1968: Déplacements non miscibles dans les milieux. Influence des parametres interfaciaux sur les permeabilités relatives. IIIe. Colloque A. R. T. F. P. Pau, 32ème publication

# ADSORPTION FROM BINARY LIQUID MIXTURES ON THE HETEROGENEOUS SURFACES OF ACTUAL SOLIDS; EXCESS ISOTHERMS AND HEATS OF IMMERSION

W RUDZIŃSKI<sup>1</sup> and J ZAJĄC<sup>1</sup>

The previous theoretical approach to the problem of surfaces heterogeneity in adsorption from binaries composed of molecules of different sizes is extended on systems in which the surface phase exhibits a regular solution behaviour whereas the bulk solution behaviour is unrestricted. Equations for the excess isotherms and the heats of immersion are derived for both patchwise and random surface topography. The systems showing the Freundlich and the Dubinin-Radushkevich behaviour are taken into account.

**Keywords:** adsorption; immersion heat; isotherms of adsorption; surface heterogeneity

## 1. Introduction

The concept of an energetic heterogeneity of the solid surfaces in an actual solid/solution adsorption system was published many years ago. Schuchovitzky (1938) was the first who tried to explain the change in the sign in some excess adsorption isotherms as an effect of the energetic surface heterogeneity. Nowadays, many authors have confirmed the importance of this effect in solution adsorption (Hansen and Mai 1957, Delmas and Patterson 1960, Coltharp and Hackerman 1973a, 1973b). Everett (1964, 1965) suggested that it could be a dominant source of imperfection in the surface phase. However, almost thirty years have passed until the first attempt has been made by Rudziński et al. (1973) to describe the effect quantitatively.

At the beginning, all the methods used to describe this effect quantitatively were based on the Sips's procedure developed from the method of the Stieltjes transform and translated next into the language of solution adsorption (Ościk et al. 1974, Dabrowski et al. 1979, Dabrowski and Jaroniec 1980a). By means of this procedure the "liquid" counterparts of appropriate "gaseous" empirical isotherm equations were derived; the "Freundlich" (Rudziński et al. 1973, Dabrowski et al. 1979, Dabrowski and Jaroniec 1979, 1980a, Borówko et al. 1979), the "Dubinin-Radushkevich" (Dabrowski and Jaroniec 1979, 1980b, Borówko et al. 1979, Jaroniec et al. 1983) and the "Tóth"

<sup>1</sup> Department of Theoretical Chemistry, Institute of Chemistry UMCS, 20-031 Lublin, Nowotki 12, Poland

(Jaroniec and Deryło 1982) equations. However, there exist some limitations in their application to describe experimental data in the whole region of concentration. For example, all of them except Tóth's equation, do not reduce correctly to Henry's law at small concentrations of one of the components. The method of the Stieltjes transform cannot be applied in the case of binaries composed of molecules of different sizes. Further, this method cannot be used in general to develop the related equations for the heats of immersion.

Simultaneously, other "gaseous" methods were adopted to describe the solid/solution adsorption, e.g. the "Condensation Approximation" (Ościk et al. 1975, Dabrowski et al. 1979, Rudziński et al. 1982b, 1983) and its modifications (Rudziński et al. 1982b, 1983). Later on methods have been developed which were applied only to describe the adsorption at the solid/solution interface (Waksmundzki et al. 1975, House 1978, Jaroniec 1978, Rudziński and Partyka 1981, Rudziński et al. 1982a, 1983, Dabrowski 1983).

Quite recently, Rudziński et al. (1981, 1982a, 1982b) have discussed for the first time the effect of the energetic surface heterogeneity on both the excess isotherm and the heat of immersion. Such a simultaneous analysis of both the experimental excess isotherms and the related heats of immersion yields a more reliable information about the nature of a solid/solution interface. However, there are only a few papers in which both the experimental excess and the related heats of immersion are reported.

The present paper is a review but also a continuation of the previous works by Rudziński et al. (1981, 1982a, 1982b, 1983) on the effect of the energetic heterogeneity of the actual solid/solution interfaces on both the experimental excess isotherms and the heats of immersion.

## 2. Theory

### 2.1 General relationships

We adopt here a model of monolayer adsorption from binaries composed of molecules *A* and *B* which may have different sizes in the bulk phase and may occupy different areas on the solid surfaces. Further, we accept here a model of a localized adsorption. By an adsorption site, we define the position of a local minimum in the potential energy of adsorbent-adsorbate interactions. This minimum value is a measure of the adsorption energy of a single molecule *A* or *B*. To make further considerations clear and easier, we introduce a quantity  $\varepsilon$  which is closely connected with the adsorption energies of the single molecules *A* and *B*,  $\varepsilon_A$  and  $\varepsilon_B$ ,

$$\varepsilon = \varepsilon_{A_s} - r\varepsilon_{B_s} \quad (1a)$$

$$\varepsilon_{A_s} = \varepsilon_A + RT \ln (q_{A_s}/q_{Ab}) \quad (1b)$$

$$\varepsilon_{B_s} = \varepsilon_B + RT \ln (q_{B_s}/q_{Bb}), \quad (1c)$$

where  $q_b$  and  $q_s$  denote the molecular partition functions in the bulk phase and in the adsorbed state, respectively. Further,  $r$  is the ratio of the surface areas occupied by the molecules  $A$  and  $B$ . We will call further  $\varepsilon$  the adsorption energy. It represents the difference between the interactions of the molecules  $A$  and  $B$ , associated with the surface area corresponding to one adsorption site. Because of the local variation in the stoichiometry and crystallography of the outermost part of the actual solid surfaces, the adsorption energy will be different on different adsorption sites. To describe the problem quantitatively, we define the function  $\chi(\varepsilon)$  which is the differential distribution of adsorption sites among various values of the adsorption energy  $\varepsilon$ , normalized to unity:

$$\int_{\Omega} \chi(\varepsilon) d\varepsilon = 1. \tag{2}$$

In Eq. (2),  $\Omega$  is the physical domain of the adsorption energy  $\varepsilon$ . To comply with the physical meaning, it should be a closed interval  $[\varepsilon_{\min}, \varepsilon_{\max}]$ , or a set of such intervals. Following previous publications (Rudziński and Partyka 1981, Rudziński et al. 1982a, 1982b, 1983), we will accept  $(-\infty, +\infty)$  as the integration interval  $\Omega$  for the purpose of mathematical convenience. This assumption was transferred from the theories of gas adsorption on heterogeneous solid surfaces (see e.g. Rudziński et al. 1982c). We have shown already (Rudziński et al. 1982b, 1982c, 1983) that the problem of the integration limits becomes essential only when the concentration of one of the components is very small.

The most important observables in the description of adsorption at the solid/solution interface are the excess adsorption isotherms and the heats of wetting (immersion). First, we shall define these quantities for a hypothetical homogeneous surface and then present the way of their generalization to the case of the actual adsorption systems with the energetically heterogeneous solid surfaces.

Let the solid surface be homogeneous, i.e., all adsorption sites have the same value of  $\varepsilon$ . Let further  $\varphi_A^s$  denotes the surface fraction of  $A$  which is in equilibrium with the bulk liquid mixture of volume fraction  $\varphi_A^b$ . The adsorption equilibrium constant  $K$  may be defined (Everett 1964, 1965) as follows,

$$K = (\varphi_A^s \gamma_A^s / \varphi_A^b \gamma_A^b) (\varphi_B^s \gamma_B^s / \varphi_B^b \gamma_B^b)^{-r}, \tag{3}$$

where the symbols “ $\gamma$ ” are used to denote the activity coefficients in the surface (s) and in the bulk phase (b). The equilibrium constant  $K$  is related to the adsorption energy  $\varepsilon$  (Rudziński and Partyka 1981, Rudziński et al. 1982a, 1982b) as:

$$K = \exp(\varepsilon/RT). \tag{4}$$

The excess adsorption isotherm,  $n_A^e$ , is defined as follows,

$$n_A^e = M_0 [\varphi_A^s - (\varphi_A^s + r\varphi_B^s)x_A^b], \tag{5}$$

where  $x_A^b$  is the mole fraction of  $A$  in the equilibrium bulk phase and  $M_0$  is the number of the adsorption sites in the adsorbed phase, i.e. the surface capacity for the component with smaller molecules ("the monomer").

The other observable, i.e. the heat of immersion,  $Q_w$ , is given by

$$Q_w = M_0(\varphi_A^s Q_{wA} + r\varphi_B^s Q_{wB}) + \beta, \quad (6)$$

where  $Q_{wA}$  and  $Q_{wB}$  are the molar heats of wetting by pure liquids  $A$  and  $B$  whereas  $\beta$  is the excess of the energy of mixing due to the formation of a solid/solution interface. In a good approximation the variables  $Q_{wA}$  and  $Q_{wB}$  may be identified with the adsorption energies  $\varepsilon_A$  and  $\varepsilon_B$ . Consequently, Eq. (6) can be rewritten in the following form:

$$Q_w = Q_B + M_0\varphi_A^s\varepsilon - M_0\varphi_A^s\lambda + \beta. \quad (7)$$

$Q_B$  denotes the heat of immersion of the whole solid sample in the pure component  $B$  and  $\lambda$  is defined as follows:

$$\lambda = RT \ln [(q_{As}/q_{Ab})(q_{Bb}/q_{Bs})^r]. \quad (8)$$

We assume the monolayer surface solution to be a quadratic mixture in the sense of the Flory-Huggins approach. With this assumption one arrives to the following formula for the function  $\beta$ ,

$$\beta = M_0[a_p\varepsilon_p\varphi_A^s\varphi_B^s + a_v\varepsilon_v(\varphi_A^s\varphi_B^b + \varphi_A^b\varphi_B^s - \varphi_A^b\varphi_B^b)]. \quad (9)$$

Then, by an appropriate differentiation of  $\beta$ , the related surface activity coefficients are obtained:

$$\gamma_A^s = \exp \{ (RT)^{-1} [a_p\varepsilon_p(\varphi_B^s)^2 + a_v\varepsilon_v(\varphi_B^b)^2] \}, \quad (10a)$$

$$\gamma_B^s = \exp \{ (RT)^{-1} r^{-1} [a_p\varepsilon_p(\varphi_A^s)^2 + a_v\varepsilon_v(\varphi_A^b)^2] \}. \quad (10b)$$

In the above equations  $a_p$  and  $a_v$  are the numbers of the nearest neighbours-adsorption sites in the direction parallel ( $p$ ) to the solid surface and in the direction vertical ( $v$ ) to the surface.  $\varepsilon_p$  and  $\varepsilon_v$  denote appropriate "exchange energy" terms which may differ from their bulk counterparts due to perturbations in the adsorbate-adsorbate interactions caused by the presence of the solid phase. Similarly, the lattice parameters  $a_p$  and  $a_v$  are to be assumed as being different from their bulk counterparts. This difference is an effect of the perturbations in the structure of the surface solution, compared to its structure in the equilibrium bulk phase. We denote further the products  $a_p\varepsilon_p$  and  $a_v\varepsilon_v$  by the symbols  $A_p$  and  $A_v$ , respectively. Further, we replace the products  $\varphi_A^b\gamma_A^b$  and  $\varphi_B^b\gamma_B^b$  by appropriate bulk activities of the component  $A$  and  $B$ ,  $a_A^b$  and  $a_B^b$ .

Now, let us assume that the adsorption energy on various adsorption sites may have different values, i.e. the solid/solution surface is energetically heterogeneous. Then, the quantity  $\varphi_A^s$  in Eq. (5) must be replaced by its average value,  $\varphi_{At}^s$ ,

$$\varphi_{At}^s = \int_{\Omega} \varphi_A^s(\varepsilon)\chi(\varepsilon) d\varepsilon. \quad (11)$$

Because of the interactions between the adsorbed molecules, the spatial correlation of the adsorption sites having the same adsorption energy becomes a very important factor. This spatial correlation is usually called the "topography of surface". Following previous publications (Rudziński et al. 1981, 1982a, 1982b), we shall consider two extreme models of the surface topography.

The first one is the "patchwise model", where the adsorption sites of equal adsorption energies are assumed to be grouped into patches. The patches are large enough to use statistical thermodynamics to describe their behaviour and to neglect the states of the whole system when two molecules located on different patches can interact effectively. In other words, the whole adsorption system is considered as a collection of independent subsystems being only in thermal and material contact. The potential of the average force acting on a molecule adsorbed on a certain patch will depend only on the surface concentration on that patch. Thus, the surface activity coefficient,  $\gamma_{Ap}^s$ , associated with this patch, is given by the formula:

$$\gamma_{Ap}^s = \exp \{ (RT)^{-1} [A_p(1 - \varphi_A^s(\epsilon))^2 + A_v(\varphi_B^b)^2] \}, \tag{12}$$

where the subscript  $p$  denotes the patchwise topographical model. Also, the excess of the energy of mixing  $\beta$  is related to the local concentration  $\varphi_A^s(\epsilon)$  on this patch. Taking this into account, we write the equation for  $Q_{wr}$  in the following form:

$$Q_{wp} = Q_B + M_0 \int_{\Omega} \varphi_A^s \epsilon \chi \, d\epsilon - M_0 \varphi_{At}^s \lambda + \int \beta \, d\epsilon. \tag{13}$$

The slight dependence of  $q_{As}$  and  $q_{Bs}$  on  $\epsilon_A$  and  $\epsilon_B$  is usually neglected.

The second extreme model of the heterogeneous surfaces assumes that adsorption sites having different adsorption energies are distributed on the solid surface completely at random. In other words, the adsorption system is considered as a thermodynamic entity. For this reason, any local microscopic concentration on such a surface is equal to the average surface concentration. The surface activity coefficient  $\gamma_{Ar}^s$  and the excess of mixing energy  $\beta_r$  should therefore be written as follows,

$$\gamma_{Ar}^s = \exp \{ (RT)^{-1} [A_p(\varphi_{Bt}^s)^2 + A_v(\varphi_B^b)^2] \}, \tag{14}$$

$$\beta_r = M_0 [A_p \varphi_{At}^s \varphi_{Bt}^s + A_v(\varphi_{At}^s \varphi_B^b + \varphi_A^b \varphi_{Bt}^s - \varphi_A^b \varphi_B^b)], \tag{15}$$

where the subscripts  $r$  refer to the random topographical model. This leads to the following equation for the heat of immersion:

$$Q_{wr} = Q_B + M_0 \int_{\Omega} \varphi_A^s \epsilon \chi \, d\epsilon - M_0 \varphi_{At}^s \lambda + \beta(\varphi_{At}^s). \tag{16}$$

The integral equations (11), (13) and (16) are of a general validity. To investigate the behaviour of a solid/solution interface with the aid of them, one has first to evaluate appropriate integrals having accepted the function  $\chi(\epsilon)$  adequate for the adsorption system studied. For practical reasons, relatively simple analytical formulas should be

striven at. However, this is a difficult problem in general. The form of  $\chi(\varepsilon)$  in the actual solid/solution interface systems is a very complicated function. To make the problem tractable, this function is approximated usually by a smooth analytical function. Such an approximation will reflect only some basic features of the actual energy distribution and will contain a small number of parameters describing its shape. The latter property is very important in a numerical analysis of the experimental data because the above-mentioned parameters appear finally to be best-fit parameters in such an analysis. Of course, one could accept a more realistic form of  $\chi(\varepsilon)$  but it seems doubtful whether the accuracy of the present standard experiment makes the use of such a function reasonable.

In spite of all the difficulties, some *a priori* conclusions can be made about the analytical approximation for  $\chi(\varepsilon)$ . The formation of the real solid surfaces is influenced by many independent factors acting during the preparation of an adsorbent. Therefore for statistical reasons, the dispersion of  $\varepsilon$  should be of a Gaussian type in a first crude approximation. Keeping it in mind, we will consider here the following two distribution functions:

$$\chi_1(\varepsilon) = c^{-1} \exp [c^{-1}(\varepsilon - \varepsilon_0)] \{1 + \exp [c^{-1} \cdot (\varepsilon - \varepsilon_0)]\}^{-2} \quad (17)$$

$$\chi_2(\varepsilon) = 2B(\varepsilon - \varepsilon_l) \exp [-B(\varepsilon - \varepsilon_l)^2]. \quad (18)$$

The function  $\chi_1$  in Eq. (17) represents a near Gaussian distribution function of the adsorption energy centered about  $\varepsilon = \varepsilon_0$ . The spread of this function is characterized by the parameter  $c$  which is a quantitative measure of the surface heterogeneity. When  $c \rightarrow 0$ , the expression (17) degenerates into a Dirac distribution  $\delta(\varepsilon - \varepsilon_0)$ . In such a hypothetical case, we would have to deal with an ideally homogeneous surface described by the adsorption energy  $\varepsilon_0$ .

The distribution  $\chi_2$  in Eq. (18) is the well-known Skew-Gaussian energy distribution. The parameter  $\varepsilon_l$  is the lowest adsorption energy and  $B$  has a similar meaning to that of the parameter  $c$  in Eq. (17).

Now, we are going to discuss a mathematical approach that would let  $\varphi_{At}^s$  and  $Q_{wt}$  be expressed by simple analytical formulas, accurate enough to make a quantitative analysis of the experimental data possible. We shall consider two types of solid/solution interfaces the description of which involves two different mathematical procedures to be used:

The first is the slightly heterogeneous surface type, where the surface heterogeneity may be considered as a kind of "perturbation" from a homogeneous surface behaviour. In such systems the energy distribution is well approximated by Eq. (17).

The second type is a solid/solution interface where the surface heterogeneity is the predominant factor governing the behaviour of the whole adsorption system. There exist some adsorption systems for which it seems reasonable to assume the energy distribution from Eq. (17). For other systems the energy distribution function from Eq. (18) may be more adequate.

2.2 Adsorption at slightly heterogeneous solid/solution interfaces

First, we shall consider the adsorption isotherm  $\varphi_{A_t}^s$ . The starting point will be the simplest case of an ideal surface solution of molecules occupying the same surface areas. The partial derivative of the adsorption isotherm ( $\partial\varphi_{A_t}^s/\partial\varepsilon$ ) takes then the following form:

$$(\partial\varphi_{A_t}^s/\partial\varepsilon) = (RT)^{-1} \exp [(RT)^{-1}(\varepsilon_c^0 - \varepsilon)] \{1 + \exp [(RT)^{-1}(\varepsilon_c^0 - \varepsilon)]\}^{-2}, \tag{19}$$

where

$$\varepsilon_c^0 = -RT \ln (a_A^b/a_B^b). \tag{20}$$

Thus, the derivative ( $\partial\varphi_{A_t}^s/\partial\varepsilon$ ) has essentially the same form as the adsorption energy distribution in Eq. (17). This derivative is centered about  $\varepsilon = \varepsilon_c^0$ , and its spread is given by the value of  $RT$ . When  $RT > c$ , or even  $RT \gg c$ , the function  $\varphi_{A_t}^s(\varepsilon)$  may be considered as a slowly-varying function of  $\varepsilon$ , compared to  $\chi(\varepsilon)$ . In such a case, it is to be expected that the expansion of the kernel  $\varphi_{A_t}^s(\varepsilon)$  around  $\varepsilon = \varepsilon_0$  should be an effective way of evaluating the integral (11):

$$\varphi_{A_t}^s = \varphi_{A_0}^s + 2 \sum_{n=0}^{+\infty} [(\pi c)^{2n}/(2n)!] (2^{2n-1} - 1) \cdot B_n D_0^{(n)}, \tag{21}$$

where

$$D_0^{(n)} = (\partial^n \varphi_{A_t}^s / \partial \varepsilon^n)_{\varepsilon = \varepsilon_0}. \tag{22}$$

Neglecting the terms of an order higher than  $\circ (c/RT)^2$  in the expansion (21), we arrive at the following equation for  $\varphi_{A_t}^s$ :

$$\varphi_{A_t}^s = \varphi_{A_0}^s + (\pi c)^2 D_0^{(2)}/6. \tag{23}$$

The second term on the right hand side of Eq. (23) is a correction term, describing the perturbation in the behaviour of the adsorption isotherm due to surface heterogeneity.

In a similar way, we evaluate the integral

$$\int_{-\infty}^{+\infty} \varphi_{A_t}^s \varepsilon \chi \, d\varepsilon = \varphi_{A_0}^s \varepsilon_0 + (\pi c)^2 (\varepsilon_0 D_0^{(2)} + 2D_0^{(1)})/6 \tag{24}$$

appearing in Eqs (13) and (16). Equations (21) and (24) are of general validity, i.e. they apply to the case when  $\gamma_{A,B}^s \neq 1$  and  $r \neq 1$ .

The influence of the surface topography is reflected in the explicit form of the derivative  $D^{(2)}$ . The first derivative is evaluated according to the equation,

$$D^{(1)} = (\partial\varphi_{A_t}^s/\partial\varepsilon) = -(\partial F/\partial\varepsilon)_{\varphi_A^s} (\partial F/\partial\varphi_A^s)^{-1}, \tag{25}$$

where  $F$  is defined as follows:

$$F = K - (\varphi_A^s \gamma_A^s / \varphi_A^b \gamma_A^b) (\varphi_B^b \gamma_B^b / \varphi_B^s \gamma_B^s)^{-r}. \tag{26}$$

The second derivative is to be calculated by means of the following formula:

$$\begin{aligned} D^{(2)} &= (\partial^2 \varphi_A^s / \partial \varepsilon^2) = \partial(\partial \varphi_A^s / \partial \varepsilon) / \partial \varepsilon = \\ &= [\partial(\partial \varphi_A^s / \partial \varepsilon) / \partial \varphi_A^s] (\partial \varphi_A^s / \partial \varepsilon). \end{aligned} \quad (27)$$

After performing appropriate differentiations, we obtain:

1. for the patchwise surface topography,

$$D_p^{(1)} = (RT)^{-1} \{ [1 + (r-1)\varphi_A^s] [\varphi_A^s(1-\varphi_A^s)]^{-1} - 2(A_p/RT) \}^{-1} \quad (28)$$

and

$$\begin{aligned} D_p^{(2)} &= (RT)^{-2} \{ [1 + (r-1)\varphi_A^s] [\varphi_A^s(1-\varphi_A^s)]^{-1} - \\ &\quad - 2(A_p/RT) \}^{-3} [1 - 2\varphi_A^s + (1-r)(\varphi_A^s)^2] \cdot [\varphi_A^s(1-\varphi_A^s)]^{-2}. \end{aligned} \quad (29)$$

2. for the random surface topography,

$$D_r^{(1)} = (RT)^{-1} \varphi_A^s(1-\varphi_A^s) [1 + (r-1)\varphi_A^s]^{-1} \quad (30)$$

and

$$D_r^{(2)} = (RT)^{-2} \varphi_A^s(1-\varphi_A^s) [1 - 2\varphi_A^s + (1-r)(\varphi_A^s)^2] \cdot [1 + (r-1)\varphi_A^s]^{-3}. \quad (31)$$

Hence, from Eqs (13), (23) and (24), the heat of immersion  $Q_{wt}$  of the heterogeneous surfaces with the patchwise topography, should be expressed as follows,

$$\begin{aligned} Q_{wp} &= Q_B + M_0 \varphi_{A0}^s \varepsilon_0 + M_0 (\pi c)^2 6^{-1} (D_{p0}^{(2)} \varepsilon_0 + 2D_{p0}^{(1)}) - \\ &\quad - M_0 \varphi_{At}^s \lambda + \beta_p, \end{aligned} \quad (32)$$

where

$$\begin{aligned} \beta_p &= M_0 \{ A_p [\varphi_{A0}^s \varphi_{B0}^s + (\pi c)^2 6^{-1} (D_{p0}^{(2)} (\varphi_{B0}^s - \varphi_{A0}^s) - \\ &\quad - 2(D_{p0}^{(1)})^2)] + A_v (\varphi_{At}^s \varphi_B^b + \varphi_A^b \varphi_{Bt}^s - \varphi_A^b \varphi_B^b). \end{aligned} \quad (33)$$

In the case of the random surface topography,  $Q_{wr}$  takes the following form,

$$\begin{aligned} Q_{wr} &= Q_B + M_0 \varphi_{A0}^s \varepsilon_0 + M_0 (\pi c)^2 6^{-1} (D_{r0}^{(2)} \varepsilon_0 + 2D_{r0}^{(1)}) - \\ &\quad - M_0 \varphi_{At}^s \lambda + \beta_r, \end{aligned} \quad (34)$$

where the last term on the right hand side of Eq. (34) is defined as follows,

$$\beta_r = \beta(\varphi_{At}^s). \quad (35)$$

### 2.3 Adsorption at strongly heterogeneous solid/solution interfaces

The essential point in the mathematical procedure applied by us in this case is the integration by parts (Rudziński et al. 1982c),

$$\varphi_{At}^s = \varphi_A^s X \int_{-\infty}^{+\infty} - \int_{-\infty}^{+\infty} (\partial \varphi_A^s / \partial \varepsilon) X(\varepsilon) d\varepsilon, \quad (36)$$

where

$$X(\varepsilon) = \int \chi(\varepsilon) d\varepsilon. \tag{37}$$

Because of the infinite integration limits, the first term vanishes on the right hand side of Eq. (36). In the case of strongly heterogeneous surfaces, i.e., if we have to deal with the reverse situation than previously, the spread of  $\chi(\varepsilon)$  is large compared to the spread of the derivative  $(\partial\varphi_A^s/\partial\varepsilon)$ . The derivative  $(\partial\varphi_A^s/\partial\varepsilon)$  is evaluated by expanding the function  $X(\varepsilon)$  into its Taylor series around  $\varepsilon = \varepsilon_c$ . The value of  $\varepsilon_c$  is found from the following obvious condition:

$$(\partial^2\varphi_A^s/\partial\varepsilon^2)_{\varepsilon=\varepsilon_c} = 0. \tag{38}$$

Thus, the integral from Eq. (36) takes now the following form,

$$\int_{-\infty}^{+\infty} (\partial\varphi_A^s/\partial\varepsilon)X(\varepsilon) d\varepsilon = \sum_{n=0}^{+\infty} (RT)^n/n! A_n \cdot (\partial^n X/\partial\varepsilon^n)_{\varepsilon_c} \tag{39}$$

where

$$A_n = \int_{-\infty}^{+\infty} (\partial\varphi_A^s/\partial\varepsilon) [(\varepsilon - \varepsilon_c)^n/(RT)^n] d\varepsilon. \tag{40}$$

As we have mentioned it in the previous section, the form of the derivative  $(\partial^2\varphi_A^s/\partial\varepsilon^2)$  depends on the model of surface topography. Consequently, we obtain two different formulas for the function  $\varepsilon_c$ :

1. for the patchwise surface topography,

$$\begin{aligned} \varepsilon_c^p = RT \ln [(1 + \sqrt{r})^{r-1}/(\sqrt{r})^r] + RT \ln a_{AB} + A_p [(r-1)/(1 + \sqrt{r})^2] + \\ + A_v [(\varphi_B^b)^2 - (\varphi_A^b)^2]. \end{aligned} \tag{41}$$

2. for the random surface topography,

$$\begin{aligned} \varepsilon_c^r = RT \ln [(1 + \sqrt{r})^{r-1}/(\sqrt{r})^r] + RT \ln a_{AB} + A_p [(\varphi_{Bt}^s)^2 - (\varphi_{At}^s)^2] + \\ + A_v [(\varphi_B^b)^2 - (\varphi_A^b)^2], \end{aligned} \tag{42}$$

where  $a_{AB} = (a_B^b)^r/a_A^b$ .

Retaining only the first term in expansion (39), we arrive at the following expression for the adsorption isotherm  $\varphi_{At}^s$ :

$$\varphi_{At}^s = -X(\varepsilon_c). \tag{43}$$

Now, let us analyse the equation for the heat of immersion  $Q_{wt}$  related to the isotherm equation (43). Let the symbol  $\eta(\varepsilon)$  denote the following integral:

$$\eta(\varepsilon) = \int \varepsilon\chi d\varepsilon. \tag{44}$$

While evaluating the first integral on the right hand side of Eqs (13) and (16), we use the same approximation which led us to Eq. (43),

$$\int_{-\infty}^{+\infty} \varphi_A^s \varepsilon\chi d\varepsilon = -\eta(\varepsilon_c). \tag{45}$$

Now, we shall derive the form of  $\beta_p$  and  $\beta_r$  in terms of the approximation accepted in this section. In the case of the random surface topography,  $\beta$  has the same form as in Eq. (15). For the patchwise surface topography, the following integral  $\gamma(\varepsilon)$  is to be evaluated:

$$\gamma(\varepsilon) = \int \varphi_A^s \varphi_B^s \chi \, d\varepsilon. \quad (46)$$

First, it is easy to check that when  $r = 1$ ,

$$\varphi_A^s \varphi_B^s = RT(\partial \varphi_A^s / \partial \varepsilon) \quad (47)$$

therefore,

$$\int \varphi_A^s \varphi_B^s \chi \, d\varepsilon = RT \int (\partial \varphi_A^s / \partial \varepsilon) \chi \, d\varepsilon \quad (48)$$

and finally:

$$\int_{-\infty}^{+\infty} \varphi_A^s \varphi_B^s \chi \, d\varepsilon = RT \chi(\varepsilon_c). \quad (49)$$

Further, we assume that the relation (49) is approximately valid when  $r \neq 1$ . Then, the equation for  $\beta_p$  takes the form:

$$\beta_p = M_0 [A_p RT \chi(\varepsilon_c) + A_v (\varphi_{A_t}^s \varphi_B^b + \varphi_A^b \varphi_{B_t}^s - \varphi_A^b \varphi_B^b)]. \quad (50)$$

Now, we are able to write the whole explicit form of the equations for the heat of immersion. For the patchwise surface topography, we have:

$$Q_{wp} = Q_B - M_0 \eta(\varepsilon_c) - M_0 \varphi_{A_t}^s \lambda + M_0 [A_p RT \chi(\varepsilon_c) + A_v (\varphi_{A_t}^s \varphi_B^b + \varphi_A^b \varphi_{B_t}^s - \varphi_A^b \varphi_B^b)], \quad (51)$$

while for the random topography, we obtain:

$$Q_{wr} = Q_B - M_0 \eta(\varepsilon_c) - M_0 \varphi_{A_t}^s \lambda + M_0 [A_p \varphi_{A_t}^s \varphi_{B_t}^s + A_v (\varphi_{A_t}^s \varphi_B^b + \varphi_A^b \varphi_{B_t}^s - \varphi_A^b \varphi_B^b)]. \quad (52)$$

Thus, the problem of evaluating the integrals (11) and (13) is reduced to that of finding three functions  $\chi(\varepsilon_c)$ ,  $X(\varepsilon_c)$  and  $\eta(\varepsilon_c)$ . Now, we are going to evaluate these functions for the energy distribution functions from Eqs (17) and (18).

Let us consider first the function (17). The fundamental integrals  $X(\varepsilon)$  and  $\eta(\varepsilon)$  take then the following explicit forms:

$$X_1(\varepsilon) = \{1 + \exp[(\varepsilon - \varepsilon_0)/c]\}^{-1} \quad (53)$$

and

$$\eta_1(\varepsilon) = -\varepsilon \{1 + \exp[(\varepsilon - \varepsilon_0)/c]\}^{-1} - c \ln \{1 + \exp[(\varepsilon_0 - \varepsilon)/c]\}. \quad (54)$$

Hence, from Eq. (43),

$$\varphi_{A_t}^s = \{1 + \exp[(\varepsilon_c - \varepsilon_0)/c]\}^{-1}. \quad (55)$$

Equation (55), combined with Eq. (41) or (42), gives

$$\varphi_{A_t}^s / \varphi_{B_t}^s = K_0 (a_{AB})^{-RT/c} \zeta \quad (56)$$

where

$$K_0 = [(\sqrt{r})^r(1 + \sqrt{r})^{(1-r)}]^{RT/c} \exp(\varepsilon_0/c). \tag{57}$$

In Eq. (56),  $\xi$  is a function arising from the nonideality of the adsorbed phase and its form depends on the model of the surface topography. In the case of the random topography, we have

$$\xi_r = \exp \{ - A_p c^{-1} [(\varphi_{Bt}^s)^2 - (\varphi_{At}^s)^2] - A_v c^{-1} [(\varphi_B^b)^2 - (\varphi_A^b)^2] \} \tag{58}$$

whereas in the case of the patchwise topography, we obtain:

$$\xi_p = \exp \{ - A_p c^{-1} (r-1)(1 + \sqrt{r})^{-2} - A_v c^{-1} [(\varphi_B^b)^2 - (\varphi_A^b)^2] \}. \tag{59}$$

When the adsorbed phase is ideal, i.e.  $\xi = 1$ , and the adsorbed molecules occupy equal surface areas, i.e.  $r = 1$ , Eq. (56) reduces to the so-called “generalized Freundlich isotherm” which has often been used to analyse experimental data quantitatively (Rudziński et al. 1973, 1982b, Dąbrowski et al. 1979, Dąbrowski and Jaroniec 1979, 1980a). Equation (55) may be rearranged as follows:

$$\varepsilon_c = \varepsilon_0 + c \ln(\varphi_{Bt}^s / \varphi_{At}^s). \tag{60}$$

After inserting  $\varepsilon_c$  from Eq. (60) into Eq. (54), we obtain:

$$-\eta_1(\varepsilon_c) = \varphi_{At}^s \varepsilon_0 - c(\varphi_{At}^s \ln \varphi_{At}^s + \varphi_{Bt}^s \ln \varphi_{Bt}^s). \tag{61}$$

The form of the third function  $\chi_1(\varepsilon_c)$  may be derived from Eqs (17) and (60):

$$\chi_1(\varepsilon_c) = c^{-1} \varphi_{At}^s \varphi_{Bt}^s. \tag{62}$$

Having combined all the above results, we arrive at the final form for the heat of immersion at the strongly heterogeneous solid/solution interfaces characterized by the distribution function from Eq. (17). In the case of the patchwise surface topography, we have:

$$Q_{wp} = Q_B + M_0 \varphi_{At}^s (\varepsilon_0 - \lambda) - c M_0 (\varphi_{At}^s \ln \varphi_{At}^s + \varphi_{Bt}^s \ln \varphi_{Bt}^s) + M_0 [A_p R T c^{-1} \varphi_{At}^s \varphi_{Bt}^s + A_v (\varphi_{At}^s \varphi_B^b + \varphi_A^b \varphi_{Bt}^s - \varphi_A^b \varphi_B^b)], \tag{63}$$

while in the case of the random topography, we obtain:

$$Q_{wr} = Q_B + M_0 \varphi_{At}^s (\varepsilon_0 - \lambda) - c M_0 (\varphi_{At}^s \ln \varphi_{At}^s + \varphi_{Bt}^s \ln \varphi_{Bt}^s) + M_0 [A_p \varphi_{At}^s \varphi_{Bt}^s + A_v (\varphi_{At}^s \varphi_B^b + \varphi_A^b \varphi_{Bt}^s - \varphi_A^b \varphi_B^b)]. \tag{64}$$

Now, let us consider the solid/solution interface systems whose energetic heterogeneity is described by the function (18). Then, the integrals  $X(\varepsilon)$  and  $\eta(\varepsilon)$  take the forms,

$$X_2(\varepsilon) = \exp[-B(\varepsilon - \varepsilon_l)^2] \tag{65}$$

and

$$\eta_2(\varepsilon) = -\varepsilon \exp[-B(\varepsilon - \varepsilon_l)^2] + 2^{-1}(\pi/B)^{1/2} \text{ERF}([B^{1/2}(\varepsilon - \varepsilon_l)]), \tag{66}$$

where  $\text{ERF}(x)$  is the well-known error function defined by

$$\text{ERF}(x) = 2\pi^{-1/2} \int_x^{+\infty} e^{-t^2} dt. \quad (67)$$

The excess adsorption isotherm takes now the form:

$$\varphi_{At}^s = \exp[-B(\varepsilon_c - \varepsilon_l)^2]. \quad (68)$$

After inserting Eq. (41) or (42) into Eq. (68), we obtain:

$$\varphi_{At}^s = \exp\{-B(RT)^2[\ln a_{AB} - \varepsilon_l^0 - \ln \zeta]^2\}, \quad (69)$$

where

$$\varepsilon_l^0 = (\varepsilon_l/RT) + \ln[\varepsilon_l(\sqrt{r})^r(1 + \sqrt{r})^{(1-r)}], \quad (70)$$

$$\zeta_p = \exp\{-A_p(RT)^{-1}(r-1)(1 + \sqrt{r})^{-2} - A_v(RT)^{-1}[(\varphi_B^b)^2 - (\varphi_A^b)^2]\} \quad (71)$$

and

$$\zeta_r = \exp\{-A_p(RT)^{-1}[(\varphi_{Bt}^s)^2 - (\varphi_{At}^s)^2] - A_v(RT)^{-1}[(\varphi_B^b)^2 - (\varphi_A^b)^2]\}. \quad (72)$$

$\zeta$  is a quantitative effect of the non-ideality of the adsorbed phase, similarly as  $\zeta$  in Eq. (56). Equation (69) reduces to the "generalized Dubinin-Radushkevich" isotherm in the case when the adsorbed phase is ideal, i.e.  $\zeta = 1$ , and when surface areas occupied by the two kinds of molecules are equal, i.e.  $r = 1$ . After rearranging Eq. (68), we obtain:

$$\varepsilon_c = \varepsilon_l + [B^{-1} \ln(1/\varphi_{At}^s)]^{1/2}. \quad (73)$$

After having combined Eqs (76) and (73), we arrive at the following formulas:

$$-\eta_2(\varepsilon_c) = \varepsilon_l \varphi_{At}^s + 2^{-1}(\pi/B)^{1/2} \{2\pi^{-1/2} \varphi_{At}^s \cdot [\ln(1/\varphi_{At}^s)]^{1/2} - \text{ERF}([\ln(1/\varphi_{At}^s)]^{1/2})\} \quad (74)$$

$$\chi_2(\varepsilon_c) = 2\varphi_{At}^s B^{1/2} [\ln(1/\varphi_{At}^s)]^{1/2}. \quad (75)$$

A combination of Eqs (74), (75) and (52), (51) leads to the final explicite expression for the heat of immersion in the adsorption systems whose surface heterogeneity is characterized by Eq. (18). In the case of the patchwise topography, we have:

$$Q_{wp} = Q^B + M_0 \varphi_{At}^s (\varepsilon_l - \lambda) + 2^{-1} M_0 (\pi/B)^{1/2} \{2\pi^{-1/2} \cdot \varphi_{At}^s [\ln(1/\varphi_{At}^s)]^{1/2} - \text{ERF}([\ln(1/\varphi_{At}^s)]^{1/2})\} + M_0 \{2RT A_p B^{1/2} \varphi_{At}^s [\ln(1/\varphi_{At}^s)]^{1/2} + A_v (\varphi_{At}^s \varphi_B^b + \varphi_A^b \varphi_{Bt}^s - \varphi_A^b \varphi_B^b)\} \quad (76)$$

whereas in the case of the random topography, we obtain:

$$Q_{wr} = Q^B + M_0 \varphi_{At}^s (\varepsilon_l - \lambda) + 2^{-1} M_0 (\pi/B)^{1/2} \{2\pi^{-1/2} \varphi_{At}^s [\ln(1/\varphi_{At}^s)]^{1/2} - \text{ERF}([\ln(1/\varphi_{At}^s)]^{1/2})\} + M_0 [A_p \varphi_{At}^s \varphi_{Bt}^s + A_v (\varphi_{At}^s \varphi_B^b + \varphi_A^b \varphi_{Bt}^s - \varphi_A^b \varphi_B^b)]. \quad (77)$$

### 3. Numerical results and discussion of experimental data

Many papers report experimental excess isotherms. However, only few of them report in addition the related heats of immersion.

Searching for suitable experimental data, we have focused our attention on the very interesting work presented by Tideswell during the "BP Symposium on the Significance of the Heats of Adsorption at the Solid/Liquid Interface" in March 1971 (Groszek 1971). There, the experimental heats of immersion of Graphon in the (*n*-Hexadecane + *n*-Heptane) system are reported. The heats of immersion were measured using a LKB 8700 precision calorimetry system at three temperatures. The author analysed their behaviour in the whole range of concentration. He suggested that, in the neighbourhood of a graphite surface, liquid *n*-alkanes adopt an ordered structure and that the properties of this structured layer are markedly temperature dependent. Consequently, there are two contributions to the enthalpy of immersion: the first a temperature-independent term representing the energy of interaction between a graphite surface and the hydrocarbons fluid, and the second which is strongly temperature dependent, is a configurational term arising from structuring of the hydrocarbon molecules close to the surface. That is why the observed heats are visibly temperature dependent, especially at higher bulk concentration.

For the purpose of the numerical analysis, we have taken into consideration the heats of immersion measured at three temperatures, 298 K, 308 K and 318 K. Now, let us consider the character of the adsorption system in more details.

Among various solid surfaces, surfaces of graphites are believed to be the most homogeneous ones. Nevertheless, the presence of chemical impurities in natural graphites or structural defects in thermally graphitized carbons is a source of a residual surface heterogeneity. This residual heterogeneity was detected in various experiments with gas adsorption on graphite surfaces. Systems with patchwise surface topography are relatively rare, but it is reasonable to include graphites among this class of adsorbents (Ross and Olivier 1964). Liquid molecules adsorb mainly on basal graphite planes and therefore the adsorbent-adsorbate interaction on each plane may be approximately characterized by the same value of adsorption energy. This energy value changes on moving from one plane to the other because the planes have various dimensions. Therefore, we have accepted the model of a slightly heterogeneous surface characterized by a patchwise topography, for the purpose of our theoretical analysis.

The bulk equilibrium solution (*n*-Hexadecane(*A*) + *n*-Heptane(*B*)) exhibits a small negative deviation from Raoult's law. The components have similar properties and the interaction between molecules *A* and *B* does not differ much from those between the same molecules. Therefore, we have accepted here a regular solution model

(in the sense of the Flory-Huggins approach) for the bulk phase. Then, the bulk activity coefficients are given by the following expressions,

$$\gamma_A^b = \exp [(\alpha_{AB}/RT) (\varphi_B^b)^2], \quad (78a)$$

$$\gamma_B^b = \exp [(\alpha_{AB}/RT) (\varphi_A^b)^2], \quad (78b)$$

where  $\alpha_{AB}$  is the regular solution interaction parameter.

Further, we assume that also the surface solution (*n*-Hexadecane(*A*)+*n*-Heptane(*B*)) on the Graphon surface obeys the behaviour of the regular solution. The parameters of the surface lattice and the mutual interaction between admolecules may, in general, be different from their bulk counterparts. The surface activity coefficients are evaluated by means of Eqs (10a) and (10b).

It is not easy to choose an appropriate value for the ratio *r*. In the monograph "Adsorption from Solutions of Non-Electrolytes", Kipling (1965) argues that the alkanes form layers of flatly orientated molecules over any adsorbent surface. Similar conclusion results from Groszek's work (1970, 1971): long-chain *n*-alkanes adsorbed from very dilute solutions lie parallel to the graphite surface. Ash et al. (1968) have shown that in some cases the orientation of adsorbed molecules may change with the composition of the bulk solution. However, for the purpose of our first quantitative analysis, we assumed the ratio *r* was fixed during the whole adsorption process.

We performed the numerical investigation assuming various values of *r*. First, we accepted *r* = 1 corresponding with the vertical orientation of admolecules. Secondly, we tested their parallel orientation. In the latter case, the ratio *r* has a value between 2.0 and 3.0. Groszek (1970) has argued that molecules adsorb with their broader sides in contact with the surface, the hydrogen atoms being positioned over the centres of the carbon rings of the Graphon basal planes (appropriate graphical representation can be found in Tideswell's work, Fig. 5). The packing imposed by this model corresponds to the hexagonally close packed structure generally favoured by hydrocarbons at normal temperatures. Then, the ratio of the surface areas occupied by molecules of *n*-Hexadecane and *n*-Heptane is about 16:7.

The strategy of the numerical calculation was following: We fitted Eq. (32), describing the heat of immersion in systems with a slightly heterogeneous surface, to experimental data at three temperatures simultaneously. The following quantities have been accepted as best-fit parameters:

- $A_p$  and  $A_v$  which characterize the structure of the surface solution and the nature of the interaction between admolecules;
- $\varepsilon_0$ , the most probable value of adsorption energy;
- $M_0$ , the monolayer capacity;
- *c*, the heterogeneity parameter.

First, we performed our numerical analysis twice, assuming that *r* = 1 and next *r* = 2.3 (corresponding to Groszek's model of admolecules orientation). The obtained

results are collected in the first two columns in Table I. Part A and part B in Fig. 1 show graphically that the agreement between theory and experiment is rather poor for these values of  $r$ . Further investigation led us to the conclusion that a better fit is obtained in the case when the ratio  $r$  oscillates around a value of 3.0 Part C in Fig. 1 shows the agreement between theory and experiment when  $r=3.0$ . This time, the agreement between theoretical curves and experimental points seems to be good. The corresponding parameters are collected in the third column in Table I.

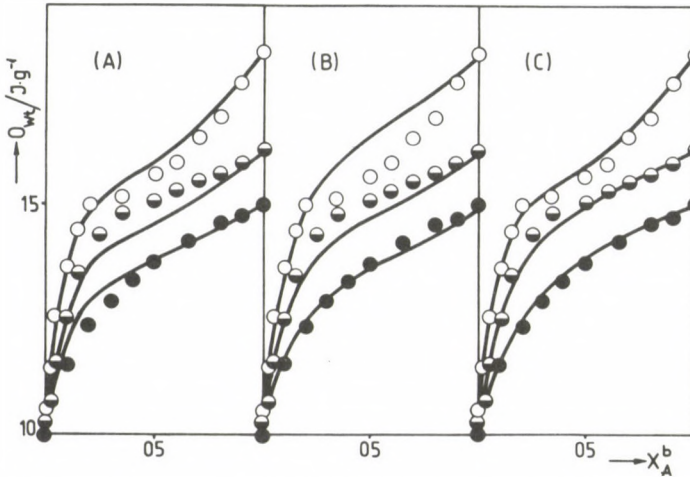


Fig. 1. Comparison between the experimental data for *n*-Hexadecane (A) + *n*-Heptane (B) adsorption on Graphon (Groszek 1971) and the theoretical curves obtained from Eq. (32) using the best-fit parameters reported in Table I. The circles denote the experimental heats of immersion at 298 K ○, 308 K ◐ and 318 K ●. Part A illustrates the effect of the numerical calculations in the case when  $r=1.0$  (column "1" in Table I). Part B corresponds with the column "2" ( $r$  equal 2.3) and part C — with column "3" in Table 1 ( $r$  equal 3.0)

**Table I.** Results of the computer investigation for *n*-Hexadecane(A) + *n*-Heptane(B) adsorption on Graphon (Groszek 1971)

Parameters	1	2	3
1. $r$	1.0	2.3	3.0
2. $M_0/\text{mol g}^{-1}$	0.008	5.1	0.04
3. $A_p/\text{J mol}^{-1}$	58.0	-6.7	-257.6
4. $A_v/\text{J mol}^{-1}$	-96.0	3.8	59.65
5. $\epsilon_0/10^3 \text{ J mol}^{-1}$	1.9	5.1	1.7
6. $c/10^2 \text{ J mol}^{-1}$	19.0	0.5	7.0

## Acknowledgement

One of the authors, W Rudziński wishes to express his warm thanks to Dr. J Tóth for the invitation to participate at the Symposium on Chemistry of Mining and Hydrocarbon Recovery held in Visegrád in 1983.

## References

- Ash S G, Everett D H, Findenegg G H 1968: Multilayer theory for adsorption from solution. *Trans. Faraday Soc.*, 64, 2645–2666.
- Borówko M, Jaroniec M, Rudziński W 1979: Adsorption from multicomponent mixtures on heterogeneous solid surfaces. *Z. phys. Chemis*, 260, 1027–1032.
- Borówko M, Goworek J, Jaroniec M 1982: A model of adsorption at liquid-solid interface involving association in the bulk phase. *Monatshefte für Chemie*, 113, 669–680.
- Coltharp M T, Hackerman N 1973a: Heterogeneity in solution adsorption: Edge carbon and oxide coverages I. *J. Coll. Interface Sci.*, 43, 176–184.
- Coltharp M T, Hackerman N 1973b: Heterogeneity in solution adsorption: Edge carbon and oxide coverages II. *J. Coll. Interface Sci.*, 43, 185–189.
- Dąbrowski A 1983: Theoretical studies on the adsorption from non-ideal binary liquid mixtures on heterogeneous surfaces involving difference in molecular sizes of components. *Monatshefte für Chemie*, 114, 875–890.
- Dąbrowski A, Jaroniec M 1979: Application of Dubinin–Radushkevich and Freundlich equations to characterize the adsorption from non-ideal binary liquid mixtures on heterogeneous solid surfaces. *Acta Chim. Acad. Sci. Hung.*, 99, 255–264.
- Dąbrowski A, Jaroniec M 1980a: Effects of surface heterogeneity in adsorption from binary liquid mixtures. *J. Coll. Interface Sci.*, 73, 475–482.
- Dąbrowski A, Jaroniec M 1980b: Application of Dubinin–Radushkevich type equation for describing the adsorption from non-ideal solutions on real solid surfaces. *Acta Chim. Acad. Sci. Hung.*, 104, 184–191.
- Dąbrowski A, Ościk J, Rudziński W, Jaroniec M 1979: Effects of surface heterogeneity in adsorption from binary liquid mixtures. *J. Coll. Interface Sci.*, 69, 287–300.
- Delmas G, Patterson D 1960: Adsorption from binary solutions of non-electrolytes. *J. Phys. Chem.*, 64, 1827–1830.
- Everett D H 1964: Thermodynamics of adsorption from solution; Perfect systems. *Trans. Faraday Soc.*, 60, 1803–1813.
- Everett D H 1965: Thermodynamics of adsorption from solution; Imperfect systems. *Trans. Faraday Soc.*, 64, 2645–2666.
- Groszek A J 1970: Selective adsorption at graphite/hydrocarbon interfaces. *Proc. Roy. Soc. Lond. A*, 314, 473–498.
- Groszek A J 1971: BP Symposium on the Significance of the Heats of Adsorption at the Solid/Liquid Interface. BP Research Centre, Sunbury-on-Thames
- Hansen R S, Mai U H 1957: Idealized models for adsorption from solution; Van der Waals adsorption from regular solutions. *J. Phys. Chem.*, 61, 573–577.
- House W A 1978: Surface heterogeneity effects in adsorption from solution. *Chem. Phys. Letters*, 60, 169–174.
- Jaroniec M 1978: Kinetics of adsorption from liquid mixtures on heterogeneous solid surfaces. *J. Res. Inst. Catalysis Hokkaido Univ.*, 26, 1–8.
- Jaroniec M, Deryło A 1982: Multi-solute adsorption from dilute solutions on solids. *Chemica Scripta*, 19, 108–115.
- Jaroniec M, Marczewski A W, Einicke W D, Herden H, Schöllner R 1983: Adsorption of 1-tetradecene/dodecane mixtures on different types of zeolites. *Monatshefte für Chemie*, 114, 857–873.
- Kipling J J 1965: Adsorption from solutions of non-electrolytes. Academic Press, London–New-York
- Ościk J, Rudziński W, Dąbrowski A 1974: Quantitative estimation of surface heterogeneity in physical adsorption on heterogeneous solid surfaces. *Ann. Soc. Chim. Polonorum*, 48, 1991–1996.
- Ościk J, Dąbrowski A, Sokółowski S, Jaroniec M 1975: Adsorption on heterogeneous surfaces: Analogy between adsorption from gases and solutions. *J. Res. Inst. Catalysis Hokkaido Univ.*, 23, 91–97.

- Ross S, Olivier J P 1964: On Physical Adsorption. Interscience Publishers, London
- Rudziński W, Partyka S 1981: Adsorption from solutions on solid surfaces. *Trans. Faraday Soc.*, 77, 2577–2584.
- Rudziński W, Oscik J, Dąbrowski A 1973: Adsorption from solutions on patchwise heterogeneous solids. *Chem. Phys. Letters*, 20, 444–447.
- Rudziński W, Narkiewicz–Michalek J, Partyka S 1982a: Adsorption from solutions into solid surfaces; Effects of topography of heterogeneous surfaces on adsorption isotherms and heats of adsorption. *Trans. Faraday Soc.*, 78, 1–8.
- Rudziński W, Narkiewicz–Michalek J, Schöllner R, Herden H, Einicke W D 1982b: Adsorption from binary liquid mixtures on heterogeneous solid surfaces; Analytical approximation for excess isotherms in the case of ideal adsorbed phases. *Acta Chim. Hungarica*, 113, 207–224.
- Rudziński W, Jagiello J, Grillet Y 1982c: Physical adsorption of gases on heterogeneous solid surfaces; Evaluation of the adsorption energy distribution from adsorption isotherms and heats of adsorption. *J. Coll. Interface Sci.*, 87, 478–491.
- Rudziński W, Łajtar L, Zajac J, Wolfram E, Pászli I 1983: Ideal adsorption from binary mixtures on heterogeneous solid surfaces; Equations for excess isotherms and heats of immersion. *Trans. Faraday Soc.* (in press)
- Schuchovitzky A 1938: *Acta Physicochem. USSR*, 8, 531–540.
- Waksmundzki A, Dawidowicz A, Sokolowski S, Jaroniec M 1975: Studies on energetic heterogeneity of adsorbents by means of liquid chromatography. *Chromatographia*, 8, 234–239.



## THE MEASUREMENT OF CAPILLARY PRESSURE AT A MOVING BOUNDARY

G RÁCZ<sup>1</sup> and B LUDÁNYI<sup>1</sup>

In a capillary completely wettable with a surfactant solution, the capillary rise can be measured at dynamic conditions with high reproducibility. The results of the described method characterize well the surface properties of surfactant solutions of technical grade. The measured capillary pressures can directly be used to calculate the flow resistance of two-phase systems. The main characteristics of the liquid-liquid interface and that of the liquid film adhering to the capillary wall were studied, and interrelations were elucidated. From the difference between the capillary pressure measured at a very low wetting phase outflow velocity and the equilibrium capillary pressure, the apparent dilatational surface viscosity of the investigated system can be calculated.

**Keywords:** capillary rise; dynamic capillary pressure; moving boundary

### Introduction

In the planning of tertiary petroleum recovery processes, the interfacial tension of oil-water (or aqueous solution) and its changes during flow are important physico-chemical parameters. Substances being not pure from the aspect of surface chemistry participate in the oil displacement process. It is a well known fact that great difficulties are encountered in the measuring of the equilibrium surface tension of surfactant mixtures (Lunkenheimer and Wantke 1981), and it is to be expected that the interfacial tension changes during flow, depending on the ad- and desorption rate and on the diffusion rate of the components. Thus it seems expedient to measure directly, under dynamic conditions, the surface tension of (model) systems of interest from the point of view of petroleum recovery. The present authors attempted to use the method of capillary rise for the investigation of the dynamic surface properties of surfactant solutions.

### Flow resistance of the liquid-liquid interface

The flow resistance of a liquid moving in a tube means the pressure difference to be established between the ends of the tube to maintain the steady state flow. In a two-phase flow of low velocity flow resistance is the sum of the viscous resistance of sections filled with homogeneous liquid and of the capillary pressures of interfaces completely filling up

<sup>1</sup> Technical University Budapest, Department of Physical Chemistry, Budafoki út 8, Budapest, H-1521 Hungary

the cross-sections. Figure 1 shows the pressure conditions of a two-phase system, moving in a capillary of uniform cross-section. Since the total pressure difference is measurable and viscous resistances can be calculated with Hagen–Poiseuille's equation, the dynamic capillary pressure is as follows:

$$\Delta p_c = \Delta p - \Delta p_o - \Delta p_v, \quad (1)$$

where  $\Delta p_o$  is the viscous resistance of one of the air or oil phases,  $\Delta p_v$  that of the other

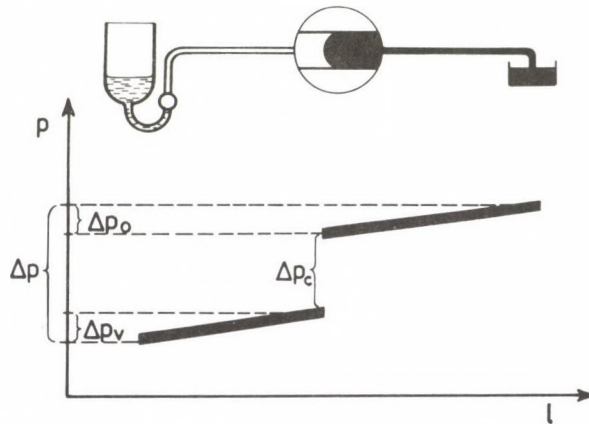


Fig. 1. Moving oil–water boundary in a capillary (meniscus magnified) and schematic course of the pressure drop

(aqueous) phase. The capillary pressure is determined by the curvature of the interface, by its surface tension, and by the three-phase contact angle. In a sufficiently narrow tube (in a capillary) the interface is hemispherical, and hence according to the Young-Laplace equation:

$$\Delta p_c = \frac{2\sigma \cos \Theta}{R}. \quad (2)$$

In general both the interfacial tension ( $\sigma$ ) and the contact angle ( $\Theta$ ) depend on the velocity of the interfacial flow, however, in two particular cases the change of one of the parameters is relevant: in case of a slowly moving boundary of pure, immiscible liquids the tension does not depend on the velocity; in this case the dynamic capillary pressure is determined by the dynamic contact angle alone (Morrow and Nguyen 1982). On the other hand, the contact angle at the water-side of aqueous surfactant solutions well wetting the capillary wall, and that of liquids immiscible with water is zero, independently of velocity, so that capillary pressure depends in this flowing system only on the interfacial tension, and thus, from measurements of the capillary pressure conclusions can be drawn just on changes in surface tension.

### The role of dilatational surface viscosity

If the surface of a surfactant solution is continuously increased, then surface tension will be higher than the equilibrium value. Evidently, a thermodynamic equilibrium between the expanding surface and the solution below cannot be established, as surfactant molecules diffuse at finite velocity to the surface. The process of surface expansion can be characterized by the relative dilatational velocity:

$$\vartheta = \frac{d \ln A}{dt} \quad (3)$$

The change in interfacial tension with respect to the equilibrium value is proportional to  $\vartheta$ :

$$\Delta\sigma = K\vartheta \quad (4)$$

The proportionality coefficient is the dilatational viscosity of the interface. The concept of dilatational viscosity was introduced by Boussinesq (1913), the first readily evaluable measurements were carried out by van Voorst Vader et al. (1964), and recently, Rillaerts and Joos (1982) published an ingenious method. The measuring apparatus generally consists of two main parts: a mechanical device producing a well defined expansion, and an instrument measuring surface tension (usually a Wilhelmy plate).

### Dynamic capillary rise

If the liquid wetting well the wall of the capillary is displaced by an immiscible liquid or by air, then a thin film of the wetting liquid remains on the wall of the capillary. The total surface of the film and meniscus increases in proportion to the displacement rate. When the movement is slow, the film withdrawing from the meniscus does not flow (it adheres to the wall of the capillary), the increase in surface occurs at the meniscus:

$$dA = 2\pi Rv dt \quad (5)$$

$$A = 2\pi R^2 \quad (6a)$$

hence, the relative dilatational velocity of a surface moving at a velocity  $v$  is:

$$\vartheta = \frac{dA}{A dt} = \frac{v}{R} \quad (7a)$$

At a reversion of the flow direction, the liquid wetting well the wall takes up at a uniform rate, the film remains on the wall. Now, the surface decreases at a relative velocity,  $\vartheta = -v/R$ , if the surfactant becoming superfluous at the decreasing surface leaves towards the liquid behind the meniscus, and not towards the film.

The surface tension changed by extension or compression is determined by the measurement of capillary rise in the equipment shown in Fig. 1. Advantages of the method are: the surface-increasing effect and the measurement of surface tension are not separated from each other; the effects of both extension and compression can be investigated; the movement is a steady-state one. The disadvantage of the method is that the relation between flow below the surface and diffusion is complicated, and thus, the process cannot be mathematically analysed.

### Experimental conditions

In the communicating vessels shown in Fig. 1, the heights of the liquid levels were measured with a cathetometer (Wild, Heerbrugg). The average radius of the measuring capillary was  $R = 0.336 \cdot 10^{-3}$  m, its excentricity  $0.005 \cdot 10^{-3}$  m.

#### Reagents used:

*n*-Decane (Fluka A.G.), grade purum, density  $726 \text{ kg} \cdot \text{m}^{-3}$ , viscosity  $0.85 \text{ mPa} \cdot \text{s}$ , at  $25^\circ\text{C}$ .

Dodecylbenzene sulfonic acid, containing 92% sulfonic acid, with about 8% free sulfuric acid impurity. Concentrations given in the text were determined by two-phase titration with the Hyamin measuring solution.

Präwozell ON 100 non-ionic surfactant.

Measurements were carried out at room temperature ( $25 \pm 1^\circ\text{C}$ ).

The length of the capillary was 300 mm.

The average velocity of the meniscus was measured along 20 mm long sections. In the case of moderately changing velocities, the average velocities were taken as equal to the momentaneous velocity at the centre of the measuring section. Knowing this and the length of the tube sections filled with liquid, the viscous pressure losses ( $\Delta p_0$  and  $\Delta p_v$ ) were calculated according to Hagen-Poiseuille's law.

### Capillary pressure at the air-liquid interface

As it was expected, the capillary pressure at the interface of pure acetone and air was independent of velocity and of the direction of movement. The standard deviation of the surface tension calculated from capillary pressure was  $0.2 \text{ mN} \cdot \text{m}^{-1}$ ,  $\sigma$  value corresponded to that published by Timmermans (1950).

The capillary pressure at the interface of the aqueous surfactant solution and air strongly depended on velocity, on the direction of moving, and in the range of dilute solutions on the concentration. Figure 2 shows results measured for the ammonium salt of dodecylbenzene sulfonic acid (DBSN) solutions of various concentrations. The

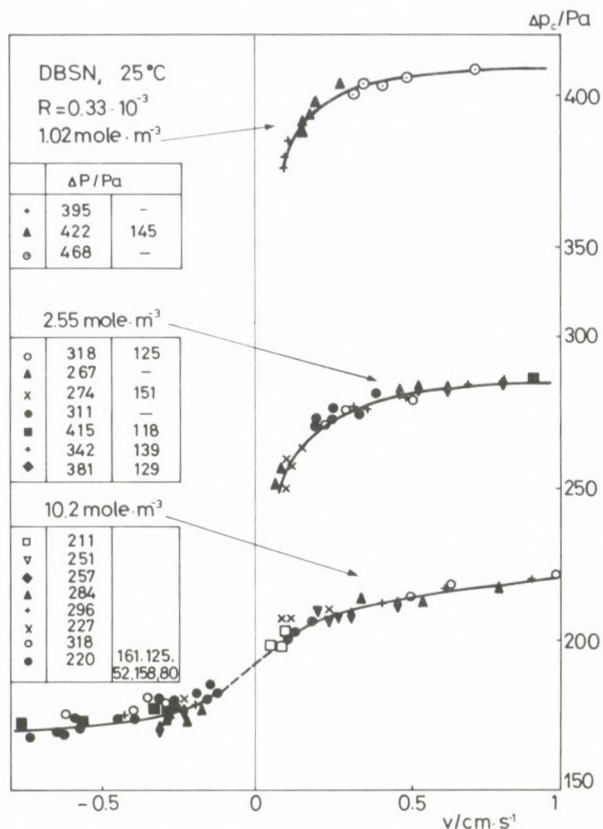


Fig. 2. Capillary pressure at the interface of air and ammonium dodecylbenzene sulfonate as a function of the velocity of the moving meniscus, at three different concentrations. Tables contain the total pressure drop

main characteristics of the curves are: 1. At the compressed surface the capillary pressure is independent of concentration. 2. The change is the greatest in the vicinity of  $v=0$ . 3. In the range of high velocities, the curves become flatter in both directions.

The difference between the capillary pressures of compressed and expanding surfaces does not disappear even in concentrated surfactant solutions. The difference of capillary pressures, measured in aqueous solutions of the sodium salt of technical dodecylbenzene sulfonic acid moving at a velocity of  $5 \text{ mm} \cdot \text{s}^{-1}$  and  $-5 \text{ mm} \cdot \text{s}^{-1}$ , respectively, was independent of concentration ( $30 \pm 7 \text{ Pa}$ ) in the concentration range from 13 to  $53 \text{ mol} \cdot \text{m}^{-3}$ .

### The role of adhering film in the development of capillary pressure at expanding surfaces

The capillary pressure of compressed surfaces depends to a small extent on the velocity at which the film, taken up by the compressed surface, was formed. If the film was formed from a meniscus moving at a low velocity, then the capillary pressure was lower after the inversion of the flow direction than that measured during the compression of the film formed from a meniscus moving at high velocity (Fig. 3).

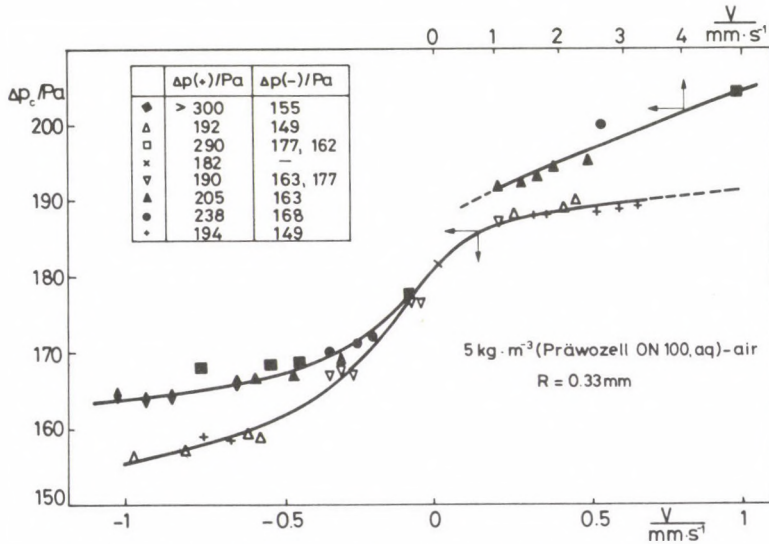


Fig. 3. On a compressed meniscus the capillary pressure depends on pretreatment

The dependence of the film quality on the rate of formation can be explained in the following way. The pressure of air in the tube from which the solution had flown out is everywhere identical. However, in the liquid film the pressure is by  $\Delta p_c = \sigma/R$ , in the liquid behind the meniscus by  $\Delta p_c = 2\sigma/R$  lower than the pressure of air (assuming that  $\sigma$  is everywhere identical). Thus, a pressure difference is established in the liquid which transports the film liquid behind the meniscus. (A similar process takes place in foams between the free films and the Plateau regions attached to the films.) Thereby the film becomes thinner. Outflow from the film remaining on the wall of the capillary is prevented by internal friction. In the formation of the film the direction of which the meniscus moves and the flow direction of the film liquid are the same, thus the film remaining back will be the thicker, the faster the meniscus moves.

At the surface of the film, freshly formed surfactant is continuously adsorbed. Therefore, with growing distance from the meniscus the surface tension of the film decreases. The difference in surface tension initiates surface flow from the film towards

the meniscus which, on one hand, entrains the film liquid, enhancing thereby the film thinning effect, and on the other hand, substance is transported to the meniscus surface, diminishing thereby the surface tension decreasing effect. In other words, in the case of an expanding surface, the higher is the flow rate, the larger is the surface from behind and surfactant is adsorbed at the surface.

For a formal description of compensating effect, let us assume that a section of  $\lambda$  length of the film expands and moves together with the meniscus, so that the combined surfaces of meniscus and film have to be taken into consideration for the calculation of the relative spreading velocity:

$$A = 2\pi R^2 + 2\pi R\lambda \quad (6b)$$

from which and from Eq. (5) one has:

$$\vartheta = \frac{dA}{A dt} = \frac{v}{R + \lambda}. \quad (7b)$$

It is probable that  $\lambda$  and  $v$  are approximately proportional to each other in the velocity range investigated. At a sufficiently low velocity Eq. (7a) is the limiting case of Eq. (7b). At high velocities  $R$  becomes negligible beside  $\lambda$ ,  $\vartheta$  becomes approximately independent of velocity, and thus  $\Delta\sigma$  does not further increase, while the surface tension approaches a limit.

It should be mentioned moreover that at the given test conditions, the film thickness is less than one hundredth of the capillary radius (Székely et al. 1981), therefore the radius of the meniscus curvature can be taken as identical with the capillary radius and independent of velocity.

### Capillary pressure at a slowly moving boundary of oil-aqueous surfactant solution

At a moving boundary of the dilute surfactant solution and *n*-decane, two characteristic changes of the capillary pressure were observed: 1. On inverting the flow direction, the capillary pressure changes suddenly, 2. during the movement it changes continuously in both directions, in a manner impeding the movement. Thus, e.g. in the experiment shown in Fig. 4, the capillary pressure increased to about 70 Pa while the aqueous solution was displaced with *n*-decane. On inverting the flow direction, the capillary pressure suddenly fell to about 30 Pa, then it decreased further to about 10 Pa while displacing oil. Inverting again the flow direction, the pressure jumped up to about 50 Pa, then continuously increased to about 70 Pa.

The phenomenon observed is interpreted by a not complete wetting and by contact angle hysteresis on the one side, and by a continuous change of interfacial tension, on the other.

Let us assume in accordance with solubility conditions that the surfactant dissolved in water is adsorbed less at the glass surface than the same surfactant dissolved in oil. In this case the surfactant is adsorbed along the oil-water-glass three-phase boundary line when oil displaces water and the surfactant is desorbed when water displaces oil. In this process the source or sink of the surfactant is the water-oil interface (Fig. 5).

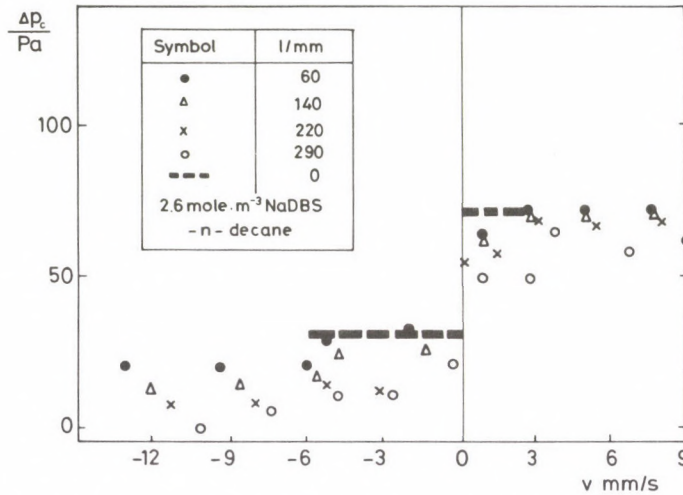


Fig. 4. The interfacial tension of dilute surfactant solution—*n*-decane depends besides velocity also on the covered path (*l*)

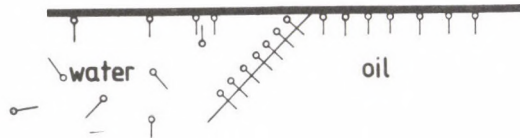


Fig. 5. At wetting the adsorptive saturation of the glass wall changes

At the air-solution interface, similar continuous changes of the capillary pressure *vs.* path were not observed. The difference is caused certainly by the film formation. When film is formed, water flows out together with the surfactant of the bulk phase, and thus steady state is easily achieved. In the case of water displaced by oil, only surfactant flows out from the oil-aqueous dilute surfactant interface, so that surfactant concentration gradually decreases in the zone behind the meniscus, and consequently capillary pressure continuously increases.

At the interface of the concentrated surfactant solution and *n*-decane the capillary pressure is low (at a 26 mol · m<sup>-3</sup> dodecylbenzene-sulfonate concentration, 14 Pa), and is independent of flow direction and velocity.

At the border of concentration ranges called dilute and concentrated, an interesting phenomenon was observed. At oil displacement, at a certain distance before the advancing meniscus, a wavy thickening of the film began, the wave was moving on together with the meniscus. Finally, the wave closed the total cross-section, and tore off drop from the continuous oil filament (Fig. 6). During this process capillary pressure changed continuously to an extent shown in Fig. 7, the formation of a new drop causing no sudden changes in the value of  $\Delta p_c$ . The length of the separating drop depended on the velocity of movement.



Fig. 6. The tearing off of oil drops during oil displacement. The length of drops depends on velocity

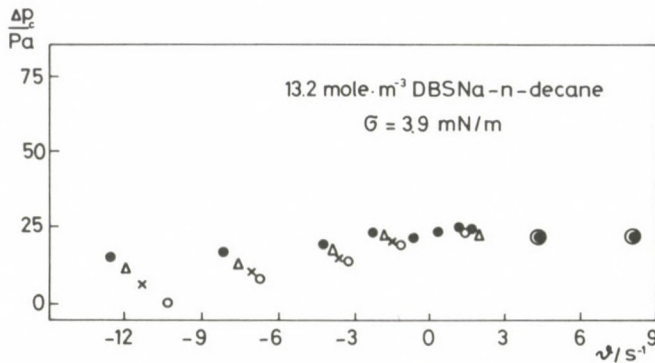


Fig. 7. Capillary pressure in the range of the transitional concentration. Notations are the same as in Fig. 4. In a NaDBS solution of  $26.5 \text{ mol} \cdot \text{m}^{-3}$  concentration, the surface tension is already independent of both path and velocity

The phenomenon is an evident proof of interfacial flow. At the compressed meniscus surface tension is lower than at the film. This difference starts a surface flow from the meniscus towards the film, and the flow entrains the liquid below the surface. In oil displacement the meniscus and surface flow move in the same direction. Surface flow is retarded by the capillary wall, therefore, if the flow rate of the meniscus is increased, surface flow can draw less ahead of the meniscus.

## Conclusions

According to the theoretical finding of Slattery (1974), the efficiency of tertiary oil recovery with surfactants can be increased by decreasing the sum of the surface viscosities, if equilibrium surface tension is less than the critical value in conjunction with pore radius and pressure gradient. The measurement of the interfacial shear viscosity is a task requiring great care, but it has been already solved. However, dilatational viscosity could be measured only with methods very difficult to realize (e.g. Rillaerts and Joos 1982), and only at an air-liquid interface. We think that by the measurement of the dynamic capillary rise the interfacial dilatational viscosity or the  $\Delta p_c - v$  relation, equivalent to it from the point of view of the evaluation of flow resistance, can also be determined at the liquid-liquid interface. In the *n*-decane-sodium dodecylbenzene-sulfonate solution system investigated the apparent interfacial dilatational viscosity is zero, provided that the surfactant concentration is higher than about  $25 \text{ mol} \cdot \text{m}^{-3}$ . More dilute solutions do not wet anymore perfectly the capillary wall, and thereby favourable conditions for the measurement of the dynamic surface tension cease. A dilatational surface viscosity of considerable magnitude was measured in oil-water system containing water-soluble polymers. The measurements will be reported in another communication, because measurements were carried out in an apparatus considerably different from that described in this paper.

## References

- Boussinesq J 1913: Sur l'existence d'une viscosité superficielle, dans la mince couche de transition séparant un liquide d'un autre fluide contigu. *Ann. Chimie Physique*, 29, 349–357.
- Lunkenheimer K, Wantke K D 1981: Determination of the surface tension of surfactant solutions applying the method of Lecomte du Nouÿ (ring tensiometer). *Colloid and Polymer Sci.*, 259, 354–366.
- Miller R, Lunkenheimer K, Kretzschmar G 1979: Ein Modell für die diffusionskontrollierte Adsorption von Tensidgemischen an fluiden Phasengrenzen. *Colloid and Polymer Sci.*, 257, 1118–1120.
- Morrov N R, Mai Dong Nguyen 1982: Effect of interface velocity on dynamic contact angles at rough surfaces. *J. Colloid and Interface Sci.*, 89, 523–530.
- Rillaerts E, Joos P 1982: Measurement of the dynamic surface tension and surface dilatational viscosity of adsorbed mixed monolayers. *J. Colloid and Interface Sci.*, 88, 1–7.
- Székely, E. et al. 1981: A new measuring method determining adherent layer thickness in linear capillaries during immiscible liquid flow. In: *Proceedings of the 3rd Conference on Colloid Chemistry*, Pintér J and Wolfram E eds. Siófok
- Slattery J C 1974: Interfacial effects in the entrapment and displacement of residual oil. *AIChE Journal*, 20, 1145–1153.
- Timmermans J 1950: *Physico-Chemical Constants of Pure Organic Compounds*, Elsevier, New York van Voorst Vader F, Erkens Th F, van der Tempel M 1964: Measurement of dilatational surface properties. *Trans. Farad. Soc.*, 70, 1170–1176.

## PREPARATION AND APPLICATION OF LOW SOLID CONTAINING AND SOLID-FREE DRILLING FLUIDS

J DORMÁN<sup>1</sup>

The effect of drilling fluids on the mechanical rate of drilling and on the characteristics of productive layers was studied. Utilizing the experiences, low solid material containing and solid-free systems were produced and applied in the field (drilling) practice. On the basis of the results with these drilling fluids:

- a favourable chemical medium can be formed for stabilizing the clay minerals;
- the synergism between the hydrophil polymers is well realizable;
- higher drilling rates can be reached;
- the damaging of hydrocarbon bearing layers decreases significantly;
- the environment is protected.

The most important task of today's practice is to extend the application of solid-free systems incorporating the most important elements of modern technology.

**Keywords:** drilling fluid; drilling rate; formation damage; permeability; solid-free drilling fluid; well completion drilling hydraulics

### Introduction

The prospecting and exploration of hydrocarbon bearing reservoir formation — as indirect energy sources — is a most important task. To realize this, significant development is to be reached on two fields, namely

- in the increase of drilling performance (e.g. the rate of drilling), and
- in the preservation of the original permeability of hydrocarbon bearing layers.

It is known that one of the promising possibilities of increasing the drilling rate is to decrease the solid content in the drilling fluids (Murray and Cunningham 1973). Beside a reduction of the differential pressure, this solution gives favourable results concerning also the drilling hydraulics (Eckel 1967, Evans and Gray 1972, Lummus 1974).

The "defence" of hydrocarbon bearing layers, the preservation of the original permeability is, however, a problem as important as the former one. The so called solid-free systems are most suitable to many-sided demand (Paul and Plonka 1973, Rike 1980). This principle is verified by the results of industrial practice, too (Cunningham 1978, Darley 1976).

<sup>1</sup> Hungarian Hydrocarbon Institute, Százhalombatta

### The role of the drilling fluid composition in the efficiency increasing

The results of laboratory (micro-drilling) and field experiments carried out to determine factors influencing the drilling performance and the efficiency of drilling technology, showed that the technology of drilling fluids is an *active* part of the drilling technology and is suitable in itself to increase the drilling performance.

The importance of the following parameters is to be emphasized:

- solid content, i.e. clay content and
- rheological properties, especially viscosity within the bit nozzles.

The positive effect of hydrophil polymers of proper composition (e.g. vinyl acetate-maleic acid anhydride copolymer, partially hydrolyzed polyacrilamide, Na-polyacrilate, polyanionic cellulose, *etc.*) is unambiguously supported by succesful field applications of so called dual-action polymers and selective flocculation agents.

The controlled flocculation in the drilling fluid (Lummus and Field 1968) — beside the advantageous change of rheological properties — enables to decrease significantly the solid content, and so to increase the rate of drilling. The effect of favourable changes in the rheological properties is the most important element of optimization in drilling hydraulics (Lummus 1971).

At the same time, significant damages of the fluid containing layers can occur during both the drilling and well completion operations. Two essential factors of the damaging effect of drilling fluids are:

- the interaction between the filtrate and the reservoir layer components;
- the penetration of solid particles into the pores of the reservoir rock.

Each of the sandstone-type productive layers is more or less water-sensitive because of the existence of clay minerals (Bleakley 1980).

The use of sodium, magnesium and calcium compounds are relatively simple solutions to this problem — coupled with other functions of these applied fluids (Maly 1976).

It proved to be much more effective, however, to use potassium salts in different systems because of the specific adsorption of potassium ions (Steiger 1982). The effect of the zirconium ion and of the hydroxialuminium polycation can be compared to the latter, even it is influenced by several other factors (Blevins et al. 1973).

By a study of the filtration of the drilling fluid under dynamic conditions and of its effect on the drilling rate, information has been obtained about the penetration of solid particles in the porous rock. The experiences showed that particles of colloidal size do not penetrate into the porous rock more than 0.02–0.05 m.

This means at the same time that during drilling the build-up of an “internal filtering layer” is to be taken into account which cannot be destroyed even when the given layer is put into production, i.e. it causes a permanent formation damage.

In addition to reservoir protection at the primary strata opening, i.e. at the penetration of productive layers, attention is to be paid to a proper preparation of the so-called well completion fluids used for testing the layers.

In their choice two essential factors are to be regarded:

- the nature, type and quantity of solid materials insoluble in the fluid phase (if they are necessary indeed);
- the effect of the filtrate — as a chemical medium — on the elements of reservoir rock (clay minerals, rock powder, *etc.*).

These systems have to meet a number of requirements:

- to provide a proper hydrostatic pressure;
- advantageous rheological and filtration characteristics;
- the minimum damage of the productive layer;
- minimum corrosion;
- chemical compatibility to the reservoir components, advantageous hydraulic parameters;
- economical application (regarding all results).

The extremely complex requirements are met above all by the solid-free system, as so the layer damage caused by solid particles can be reduced to a minimum. Obviously, the use of different additives strengthening other functions, may also be necessary depending on the circumstances.

The most frequently used electrolytes, their density, and the attainable maximum fluid density are as follows:

sodium chloride	2.17 gcm <sup>-3</sup>	1190 kgm <sup>-3</sup>
calcium chloride	2.15 gcm <sup>-3</sup>	1400 kgm <sup>-3</sup>
calcium bromide	2.29 gcm <sup>-3</sup>	1800 kgm <sup>-3</sup>
zinc bromide	4.22 gcm <sup>-3</sup>	2290 kgm <sup>-3</sup>

If the improvement of the rheological and/or filtration characteristics of electrolytic solution-based systems is demanded, different nonionic polymers are generally used. Hydroxi ethyl cellulose (HEC) is most frequently used, mainly stabilized by MgO, further biopolymers, guar-gums, starch and polymer combinations.

### The effect of solid content on the drilling rate

The effect of solid content of the drilling fluid on the rate of drilling was studied by applying polymeric flocculant containing systems. In this case, of course, a twin effect arises. On the one hand, the flocculating agents decrease significantly the quantity of colloid size particles, restrain the dispersion of clay minerals (the accumulation of the colloidal fraction), and on the other they make possible to reduce the density of drilling fluid by modifying advantageously the rheological properties.

Results of measurements carried out using 0.15–0.20 kg/m<sup>3</sup> polymeric flocculant (H-FLOC, BEN-EX, DRILLAID-421) in the drilling fluid are shown in Fig. 1 from the start of the drilling of a 0.2159 m diameter bore-hole section.

It is apparent that the rate of drilling increases significantly with the decrease of the density of the drilling fluid, i.e. with that of the solid content. Similar results were obtained also from wells in the other fields.

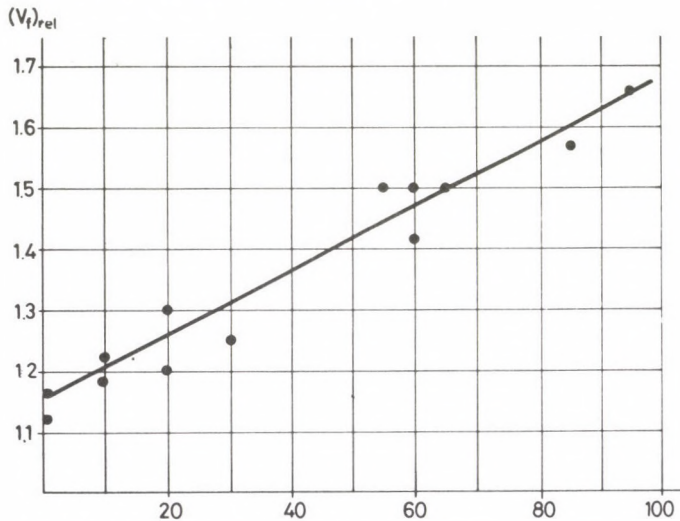


Fig. 1. Increase of the drilling rate vs. decrease of the drilling fluid density

On the basis of an analysis of industrial results, it was found that the following relationship holds between the relative drilling rate and the drilling fluid density in the 1050–1250 kg/m<sup>3</sup> density range if non-weighted drilling fluids treated by flocculants are used when penetrating the Upper- and Lower-Pannonian strata:

$$v = v_0 [1 + k(\rho_0 - \rho)]$$

where  $k = 4.762 \cdot 10^{-3}$

So the results verified the necessity of a solid content reduction. At the same time, however, these results give also evidence that the polymeric flocculants prevent by aggregating the particles of colloidal sizes the formation of a low permeability “internal filter” in the rock layer below the drill. So a more rapid equilibration of the hold-down pressure is provided which helps a more effective bottom-hole cleaning.

As a consequence, the polymeric flocculants promote not only the reduction of the solid content (density) providing thus the realization of the controlled pressure drilling technology, but they are useful in themselves by reducing the quantity of colloid size particles, enabling so an increase of the rate of drilling. This effect can be intensified by means of solid-free systems based on the solutions of hydrophil polymers.

## Experiences with the preparation and application of solid-free drilling fluids

### *The calcium chloride (bromide) based system*

For an effective use of calcium chloride solution as a drilling fluid, a reliable control of the rheological and filtration characteristics is necessary. For this purpose non-ionic hydrophil polymers can be used. The most economic solution is the use of starch. According to the results of tests in the Hydrocarbon Institute, however, starch provides sufficient rheological and filtration properties only up to about 370–390 K. At higher formation temperatures a synthetic polymer of proper effect is also to be used beside the starch.

The thermal stability of the system can be improved using poly-vinyl alcohol (PVA) or poly-vinyl pyrrolidone (PVP) which are in a synergetic interaction with the starch. Although the apparent viscosity of the fluid decreases significantly by the effect of the thermal treatment above 400–410 K, the filtration properties remain satisfactory all the time (Fig. 2).

Experiments show that starch can be effectively replaced by other non-ionic polysaccharide derivatives (e.g. HEC, CMHEC). The synergetic stabilizing effect of synthetic polymers (PVA, PVP) dominates in this case, too.

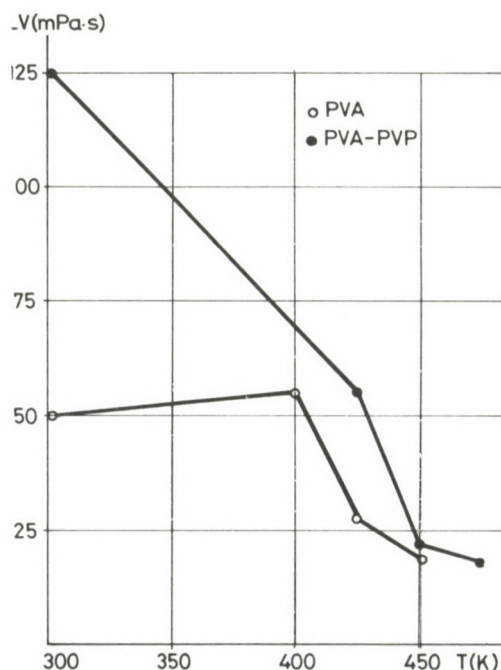


Fig. 2. The apparent viscosity of a  $\text{CaCl}_2$  solution of  $1350 \text{ kg/m}^3$  density stabilized by synthetic polymers, after thermal treatment (hot rolling)

The calcium chloride based drilling fluid has a higher dispersion inhibiting effect than other aqueous systems used today in the drilling practice. By a proper control of the pH the rate of corrosion can be reduced to a convenient level. The industrial application of a solid-free drilling fluid described above (PAC-STAR) was started at the layer tests of two wells in Szank.

The application experiences can be summed up as follows:

- the laboratory results were well reproducible under industrial (field) conditions;
- at a high fluid density (1360–1380 kg/m<sup>3</sup>), the packer operations proved to be unproblematic as the system does not contain any solid material, so there is no sedimentation risk;
- the well-starting was fast and without problems, even after a longer contact with the fluid;
- corrosion problems were not observed.

#### *Hydroxi-aluminium based system*

Using different aluminium salts (chloride, sulfate) and alkali hydroxides, a hydroxi-aluminium compound can be prepared which promotes significantly the stabilization of clay minerals. This system may be a base of a new drilling fluid which enables the joint realization of bore-wall stability and reservoir protection beside an increase of the drilling rate.

For a control of the rheological and filtration characteristics of this system, the already mentioned polymers and their combinations can be applied.

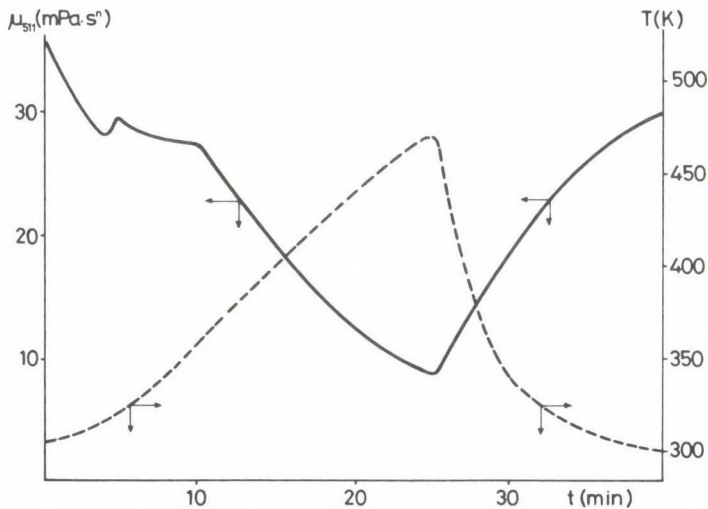


Fig. 3. The viscosity of the SAL-STAR system in the function of temperature

The chemical characteristics of basis fluids enables also the use of anionic polymers (e.g. Na-polyacrilate). Figure 3 shows the viscosity of the hydroxi-aluminium based fluid treated with a combination of starch-poly-acrilate polymer, *vs.* temperature and at the same figure the thermal stability is also indicated.

According to the data determined by a FANN-50 C type viscometer, the system resumes its original rheological properties at the end of the cooling period.

The dispersion inhibiting effect and the density of the new solid-free fluid can be improved by the addition of potassium chloride and sodium chloride or potassium carbonate, respectively.

The field application (drilling, well completion) of the hydroxi-aluminium base drilling fluid (SAL-STAR) produced favourable results.

#### *System gelled by boron compounds*

The gelation of a natural polymer by sodium tetraborate, the so-called guar-gum and its chemically modified hydroxipropylic guar form has been a well known and applied method for a long time. This chemical reaction based on complex formation — in which the OH-groups of the polymer are the functional ones — results in a multiplication of the viscosity of the polymer base solution. Laboratory tests aimed to produce a system free of heavy metal ions and solid material showed that a strong complex formation takes place in the presence of tetraborate or borate ions in aqueous solutions both of the starch and polyvinyl alcohol at proper pH values (8.5–11.5). A strong gelation effect appears at boric acid concentrations above  $6 \text{ kg/m}^3$ , and in this case, excellent rheological and filtration properties can be ensured.

Similar results can be reached using a boric acid and tetraborate combination.

#### **The formation damaging effect of drilling fluids**

The effect of different drilling fluids on the permeability of productive formations, i.e. the so called formation damaging effect was studied on synthetic core samples of permeabilities  $0.10\text{--}0.25 \mu\text{m}^2$ , using the high pressure and high temperature permeability measuring devices developed in the Hungarian Hydrocarbon Institute. In the first measurements the fluid filtration rate was examined at a differential pressure of 0.7 MPa and at temperatures of 293 and 373 K. Thereafter, during the reversed flow of a KCl solution with a concentration of  $20 \text{ g/dm}^3$ , the permeability was determined. The damaging ratio is given by the quotient of the reversed direction ( $k_i$ ) and the original ( $k_0$ ) permeabilities. Consequently, if the damaging ratio is 1.00, the tested rock is undamaged, while 0.00 shows total damaging.

It is obvious that the largest damaging is caused by solid material penetrated into the rock pores.

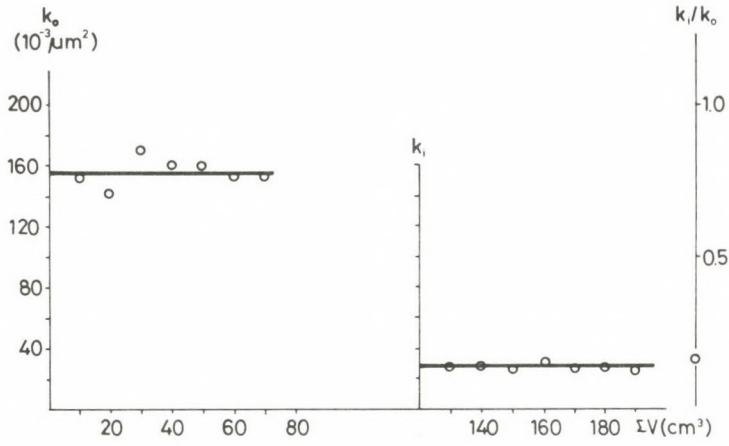


Fig. 4. Damaging fluid: clay-mud,  $k_i/k_0 = 0.173$

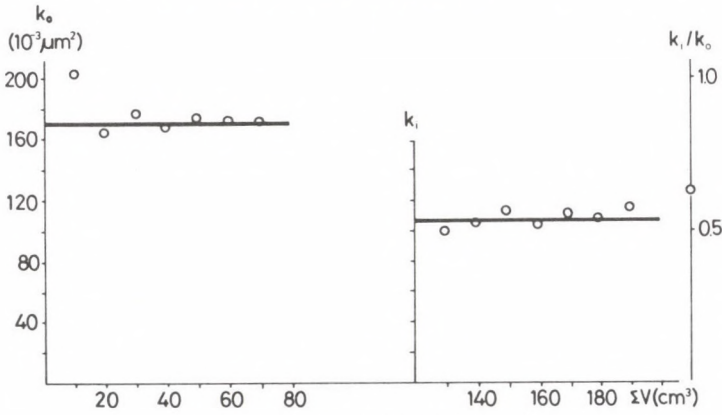


Fig. 5. Damaging fluid: PAC-STAR ( $1360 \text{ kg/m}^3$ ),  $k_i/k_0 = 0.63$

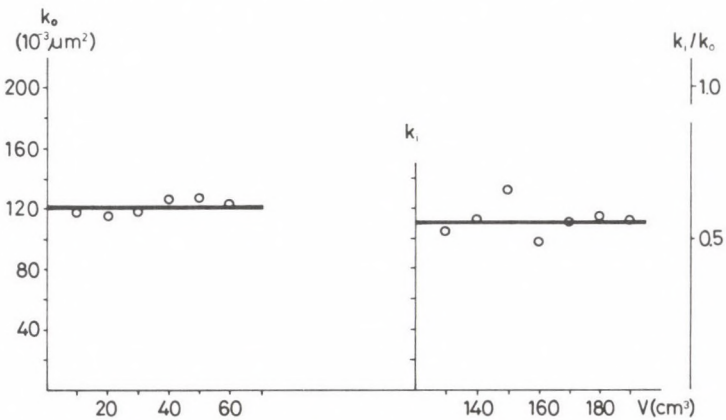


Fig. 6. Damaging fluid: SAL-STAR + 5% limestone powder  $k_i/k_0 = 0.919$

The industrial experiences are verified by the result of an experiment carried out with the so called clay-mud (Fig. 4), when after the flow (at 0.7 MPa and 373 K), only 17.3% of the original permeability was measured.

Solid-free drilling fluids enable essentially more favourable results. In the case of the PAC-STAR system applicable in over-pressure layers, the extent of damaging is 37%, on contrary to the previous value of 82.7% (Fig. 5).

The modern drilling and layer testing technology prefers the utilization of solid-free systems doped with acid-soluble solid materials as "bridge forming" components.

The efficiency of a system of such composition is shown in Fig. 6. Using the SAL-STAR system doped with limestone powder, the damaging is only 8.1%.

The results of laboratory tests have already been verified by a number of practical experiences.

### References

- Bleakley W B 1980: Clear completion and workover fluids — what they are, what they'll do. *Petroleum Engineer*, 19–22.
- Blevins T R, Cotten WR, Dugas E J 1973: OH-AI treatments sustain acid stimulated production. *World Oil*, 26–29.
- Cunningham R A 1978: An empirical approach for relating drilling parameters. *J. Petro. Tec.*, 30,987–92.
- Darley H C H 1976: Advantages of polymer muds. *Petroleum Engineer*, 46–52.
- Eckel J R 1967: Microbit of the effect of fluid properties and hydraulics on drilling rates, *J. Petro, Tec.*, 26, 541–546.
- Evans B, Gray K E 1972: Effect of bentonitic fluid properties on drilling rate. *J. Petro. Tec.*, 28, 657–662.
- Lummus J. L. 1971: Acquisition and analysis of data for optimized drilling. *J. Petro. Tec.*, 28, 1285–1291.
- Lummus J L 1974: Analysis of mud hydraulics interactions. *Petroleum Engineer*, 60–69.
- Lummus J L, Field L J 1968: Non-dispersed polymer mud: a new drilling concept. *Petroleum Engineer*, 27–33.
- Maly G P 1976: Proper fluid selection helps avoid damage. *Oil and Gas Journal*, 73, 68–76.
- Murray A S, Cunningham R A 1973: Effect of mud column pressure on drilling rates. *Soc. Pet. E. J. Preprints*, No. 6, 46–54.
- Paul J R, Plonka J H 1973: Solids-free completion fluids maintain formation permeability. *Soc. Pet. E. J.*, 4655.
- Rike J L 1980: The relationship between clear fluids and effective completions. *Soc. Pet. E. J.*, 22, 9426.
- Steiger R P 1982: Fundamentals and use of potassium/polymer drilling fluids to minimize drilling and completion problems associated with hydratable clays. *Soc. Pet. E. J.*, 23, 11000.

PRINTED IN HUNGARY

Akadémiai Kiadó és Nyomda, Budapest

- treble underlining: bold-face italics
- red underlining: Greek letters
- green underlining: script letters.

Rules for mathematical-physical notations:

- trigonometric, logarithmic, analytic symbols, symbols for units and functions are in roman type (not underlined)
- letter symbols in mathematical and physical formulas, scalars, and subscripts of algebraic and physical quantities are in italics (underlined)
- vectors, matrices, operators in probability theory are in bold-face roman type (double underlining)
- tensors, operators and some special functions are in script letters (green underlining). These cannot be bold.
- Greek letters (red underlining) cannot be bold or extra bold type (thus they cannot be used for vectors or tensors)
- void upper lines e.g. for vectors
- avoid possible confusion between o (letter) and O (zero), l (letter) and 1 (one),  $\nu$  (Greek nu) and  $v$ ,  $u$  (letters) etc.
- explain ambiguous or uncommon symbols by making marginal notes in pencil
- be careful about superscripts and subscripts
- formulae must be numbered consecutively with the number in parentheses to the right of the formula. References in text to the equations may then usually be made by the number in parenthesis. When the word equation is used with a number, it is to be abbreviated, Eq. or Eqs in the plural
- the International System of Units (SI) should be used.

Authors are liable for the cost of alteration in the *proofs*. It is, therefore, the responsibility of the author to check the text for errors of facts before submitting the paper for publication.

3. *References* are accepted only in the Harvard system. Citations in the text should be as:

- ... (Bomford 1971) ... or Bomford (1971)
- ... (Brosche and Sündermann 1976) ...
- ... (Gibbs et al. 1976b) ...

The list of references should contain names and initials of all authors (the abbreviation et al. is not accepted here); for *journal articles* year of publication, the title of the paper, title of the journal abbreviated, volume number, first and last page.

For *books* or *chapters in books*, the title is followed by the publisher and place of publication. All items must appear both in the text and references.

Examples:

- Bomford G 1971: Geodesy. Clarendon Press, Oxford
- Brosche P, Sündermann J 1976: Effects of oceanic tides on the rotation of the earth. Manuscript. Univ. of Bonn
- Buntebarth G 1976: Temperature calculations on the Hungarian seismic profile-section NP-2. In: *Geoelectric and Geothermal Studies (East-Central Europe, Soviet Asia)*, KAPG Geophysical Monograph. Akadémiai Kiadó, Budapest, 561–566.
- Gibbs N E, Poole W G, Stockmeyer P K 1976a: An algorithm for reducing the bandwidth and profile of a sparse matrix. *SIAM J. Numer. Anal.*, 13, 236–250.
- Gibbs N E, Poole W G, Stockmeyer P K 1976b: A comparison of several bandwidth and profile reduction algorithms. *ACM Trans. on Math. Software*, 2, 322–330.
- Szarka L 1980: Potenciáltérképezés analóg modellezéssel (Analogue modeling of potential mapping). *Magyar Geofizika*, 21, 193–200.

4. *Footnotes* should be typed on separate sheets.

5. *Legends* should be short and clear. The place of the tables and figures should be indicated in the text, on the margin.

6. *Tables* should be numbered serially with Roman numerals. Vertical lines are not used.

All the illustrations should contain the figure number and author's name in pencil on the reverse.

*Figures* will be redrawn. Therefore the most important point is clearness of the figures, even pencil-drawings are accepted (with a duplicate).

*Photographs* and *half-tone* illustrations should be sharp and well contrasted.

If a specific reduction or enlargement is required, please indicate this in blue pencil on the figure.

The editors will send information to the first author about the *arrival* and acceptance of the papers. A galley proof is also sent to the first author for *correction*. Hundred *offprints* are supplied free of charge.

Periodicals of the Hungarian Academy of Sciences are obtainable  
at the following addresses:

**AUSTRALIA**

C. B. D. LIBRARY AND SUBSCRIPTION SERVICE  
Box 4886, G. P. O., Sydney N.S.W. 2001  
COSMOS BOOKSHOP, 145 Ackland Street  
St. Kilda (Melbourne), Victoria 3182

**AUSTRIA**

GLOBUS, Hochstadtplatz 3, 1206 Wien XX

**BELGIUM**

OFFICE INTERNATIONAL DE LIBRAIRIE  
30 Avenue Marnix, 1050 Bruxelles  
LIBRAIRIE DU MONDE ENTIER  
162 rue du Midi, 1000 Bruxelles

**BULGARIA**

HEMUS, Bulvar Ruszki 6, Sofia

**CANADA**

PANNONIA BOOKS, P.O. Box 1017  
Postal Station "B", Toronto, Ontario M5T 2T8

**CHINA**

CNPICOR, Periodical Department, P.O. Box 50  
Peking

**CZECHOSLOVAKIA**

MAD'ARSKÁ KULTURA, Národní třída 22  
115 66 Praha  
PNS DOVOZ TISKU, Vinohradská 46, Praha 2  
PNS DOVOZ TLACE, Bratislava 2

**DENMARK**

EJNAR MUNKSGAARD, Norregade 6  
1165 Copenhagen K

**FEDERAL REPUBLIC OF GERMANY**

KUNST UND WISSEN ERICH BIEBER  
Postfach 46, 7000 Stuttgart 1

**FINLAND**

AKATEEMINEN KIRJAKAUPPA, P.O. Box 128 SF-00101  
Helsinki 10

**FRANCE**

DAWSON-FRANCE S. A., B. P. 40, 91121 Palaiseau  
EUROPERIODIQUES S. A., 31 Avenue de Versailles, 78170  
La Celle St. Cloud  
OFFICE INTERNATIONAL DE DOCUMENTATION ET  
LIBRAIRIE, 48 rue Gay-Lussac  
75240 Paris Cedex 05

**GERMAN DEMOCRATIC REPUBLIC**

HAUS DER UNGARISCHEN KULTUR  
Karl Liebknecht-Straße 9, DDR-102 Berlin  
DEUTSCHE POST ZEITUNGSVERTRIEBSAMT Straße der  
Pariser Kommüne 3-4, DDR-104 Berlin

**GREAT BRITAIN**

BLACKWELL'S PERIODICALS DIVISION  
Hythe Bridge Street, Oxford OX1 2ET  
BUMPUS, HALDANE AND MAXWELL LTD.  
Cowper Works, Olney, Bucks MK46 4BN  
COLLET'S HOLDINGS LTD., Denington Estate Wellingbo-  
rough, Northants NN8 2QT  
WM. DAWSON AND SONS LTD., Cannon House Folkstone,  
Kent CT19 5EE  
H. K. LEWIS AND CO., 136 Gower Street  
London WC1E 6BS

**GREECE**

KOSTARAKIS BROTHERS INTERNATIONAL  
BOOKSELLERS, 2 Hippokratous Street, Athens-143

**HOLLAND**

MEULENHOF-BRUNA B. V., Beulingstraat 2,  
Amsterdam  
MARTINUS NIJHOFF B.V.  
Lange Voorhout 9-11, Den Haag

**SWETS SUBSCRIPTION SERVICE**

347b Heereweg, Lisse

**INDIA**

ALLIED PUBLISHING PRIVATE LTD., 13/14  
Asaf Ali Road, New Delhi 110001  
150 B-6 Mount Road, Madras 600002  
INTERNATIONAL BOOK HOUSE PVT. LTD.  
Madame Cama Road, Bombay 400039  
THE STATE TRADING CORPORATION OF INDIA LTD.,  
Books Import Division, Chandralok 36 Janpath, New Delhi  
110001

**ITALY**

INTERSCIENTIA, Via Mazzè 28, 10149 Torino  
LIBRERIA COMMISSIONARIA SANSONI, Via Lamarmora 45,  
50121 Firenze  
SANTO VANASIA, Via M. Macchi 58  
20124 Milano  
D. E. A., Via Lima 28, 00198 Roma

**JAPAN**

KINOKUNIYA BOOK-STORE CO. LTD.  
17-7 Shinjuku 3 chome, Shinjuku-ku, Tokyo 160-91  
MARUZEN COMPANY LTD., Book Department, P.O. Box  
5050 Tokyo International, Tokyo 100-31  
NAUKA LTD. IMPORT DEPARTMENT  
2-30-19 Minami Ikebukuro, Toshima-ku, Tokyo 171

**KOREA**

CHULPANMUL, Phenjan

**NORWAY**

TANUM-TIDSKRIFT-SENTRALEN A.S., Karl Johansgatan  
41-43, 1000 Oslo

**POLAND**

WĘGIERSKI INSTYTUT KULTURY, Marszałkowska 80,  
00-517 Warszawa  
CKP-I W, ul. Towarowa 28, 00-958 Warszawa

**ROUMANIA**

D. E. P., Bucuresti  
ILEXIM, Calea Grivitei 64-66, Bucuresti

**SOVIET UNION**

SOJUZPECHAT — IMPORT, Moscow  
and the post offices in each town  
MEZHUNARODNAYA KNIGA, Moscow G-200

**SPAIN**

DIAZ DE SANTOS, Lagasca 95, Madrid 6

**SWEDEN**

GUMPERTS UNIVERSITETSBOKHANDL AB  
Box 346, 401 25 Goteborg 1

**SWITZERLAND**

KARGER LIBRI AG, Petersgraben 31, 4011 Basel

**USA**

EBSCO SUBSCRIPTION SERVICES  
P.O. Box 1943, Birmingham, Alabama 35201  
F. W. FAXON COMPANY, INC.  
15 Southwest Park, Westwood Mass. 02090  
READ-MORE PUBLICATIONS, INC.  
140 Cedar Street, New York, N. Y. 10006

**YUGOSLAVIA**

JUGOSLOVENSKA KNJIGA, Terazije 27, Beograd  
FORUM, Vojvode Mišića 1, 21000 Novi Sad

# **Acta Geodaetica, Geophysica et Montanistica Hungarica**

VOLUME 20, NUMBER 4, 1985

EDITOR-IN-CHIEF

**A TÁRCZY-HORNOCH**

EDITOR

**J VERŐ**

EDITORIAL BOARD

**A ÁDÁM, GY BARTA, B BÉLL, P BIRÓ,**

**L KAPOLYI, F KOVÁCS, F MARTOS, A MESKÓ, D RÁCZ,**

**J SOMOGYI, J ZÁMBÓ**



**Akadémiai Kiadó, Budapest**

AGGM 20 (4) 375-468 (1985) HU ISSN 0236-5758

# ACTA GEODAETICA, GEOPHYSICA et MONTANISTICA HUNGARICA

## A Quarterly Journal of the Hungarian Academy of Sciences

---

*Acta Geodaetica, Geophysica et Montanistica (AGGM)* publishes original reports on geodesy, geophysics and minings in English.

AGGM is published in yearly volumes of four numbers by

AKADÉMIAI KIADÓ

Publishing House of the Hungarian Academy of Sciences  
H-1054 Budapest, Alkotmány u. 21.

Manuscripts and editorial correspondence should be addressed to

*AGGM Editorial Office*  
H-9401 Sopron P.O. Box 5

*Subscription information*

Orders should be addressed to

KULTURA Foreign Trading Company  
H-1389 Budapest P.O. Box 149

### INSTRUCTIONS TO AUTHORS

*Manuscripts* should be sent to the editors (MTA Geodéziai és Geofizikai Kutató Intézet, AGGM Editorial Office, H-9401 Sopron, P.O.Box 5, HUNGARY). Only articles not submitted for publication elsewhere are accepted.

Manuscripts should be typewritten in duplicate, double-spaced, 25 lines with 50 letters each. The papers generally include the following components, which should be presented in the order listed.

1. Title, name of author(s), affiliation, dateline, abstract, keywords
2. Text, acknowledgements
3. References
4. Footnotes
5. Legends
6. Tables and illustrations

1. The *affiliation* should be as concise as possible and should include the complete mailing address of the authors. The *date of receipt* of the manuscript will be supplied by the editors. The abstract should not exceed 250 words and should clearly and simply summarize the most important methods and results. 5–10 significant expressions describing the content are used as *keywords*. Authors may recommend these keywords.

2. The *text* should be generally in English and as short and clear as possible. From Hungarian authors papers are also accepted in Hungarian.

The section heading should *not* be underlined or in capitals.

Please note that underlining denotes special types:

- single underlining: italics
- double underlining: bold-face roman

## CONTENTS

Effect of rock temperature on rock and gas outbursts — <i>Somosvári Zs</i> .....	375
Effect of the protective layer mining method on the reduction of rock and gas outburst danger — <i>Somosvári Zs</i> .....	397
Calculation of air losses and suitable ventilator distances for ventilating pipes — <i>Janositz J</i> . . . .	409
Study of joint application of anionic and nonionic surfactants in enhanced oil recovery — <i>Lakatos I,</i> <i>Milley Gy, Tóth J, Kristóf M, Capelle A, Wagner O, Lakatos-Szabó J, Felián B</i> .....	425
Integrating effect of hydromechanization of mining technological systems — <i>Patvaros J</i> .....	447
Materials law of isotropic rock continua — <i>Horváth R</i> .....	453
Properties of the Poynting-Thomson standard body during load decrease — <i>Horváth R</i> .....	463

PRINTED IN HUNGARY  
Akadémiai Kiadó és Nyomda, Budapest

## EFFECT OF ROCK TEMPERATURE ON ROCK AND GAS OUTBURSTS

Zs SOMOSVÁRI<sup>1</sup>

[Manuscript received February 1, 1983]

The effect of rock temperature on gas storage and outbursts is investigated in the paper. The thorough analysis of the temperature field of the earth's crust is followed by the investigation of gas content and pore gas pressure as functions of depth and rock temperature. The effect of temperature on the initial pore gas pressure is analyzed in detail. From the correlations between the main parameters of outbursts and temperature the conclusion has been drawn that the effect of rock temperature on outburst can be confined to its influence on the initial pore gas pressure during gas storage.

**Keywords:** adsorbed gas; free gas; gas outburst danger; geothermal gradient; pore gas pressure; rock temperature; specific methane output; terrestrial heat flow

### *Symbols*

$A$	gas pressure gradient
$b_0$	adsorption constant
$e$	void ratio
$gg$	geothermal gradient
$n$	porosity
$p_a$	atmospheric pressure
$p_{max}$	maximum pore gas pressure
$p$	pore gas pressure
$\Delta p$	change of pore gas pressure
$q'$	heat flux
$\bar{q}$	specific amount of methane
$q$	coefficient of brittleness
$Q$	adsorption potential
$R$	gas constant
$S$	gas saturation
$t$	temperature
$T$	absolute temperature
$T_a$	average annual temperature of air
$T_0$	adsorption constant
$V_{max}$	maximum amount of adsorbed gas
$V_a$	amount of absorbed gas
$V_f$	amount of free gas

<sup>1</sup> University for Heavy Industry, Faculty for Mining, M-3515 Miskolc, Hungary

$z$	co-ordinate of depth
$z_0$	depth of the beginning of gas phenomena
$z_n$	depth of the neutral rock zone
$\rho$	bulk density
$\lambda$	coefficient of thermal conductivity
$\lambda'$	equivalent coefficient of thermal conductivity
$\sigma_c$	uniaxial compressive strength
$\sigma_y$	yield point
$\phi$	angle of internal friction

## 1. Introduction

Since outbursts are explained as complex interactions between the two components of the gas-bearing rock (rock-gas system) and temperature is one of the parameters of state of the gas, the phenomenon (i.e. outburst) may also be influenced by the temperature. Temperature might also affect the formation of gas, the process of gas storage, the ratio of the free and adsorbed gas and the change of state of the free gas.

We will, therefore, analyze the effect of rock temperature on the parameters characterizing rock and gas outburst danger and gas danger as a function of depth.

## 2. Distribution of gas in the gas-bearing rock

The formation of coal-bearing deposits is combined with gas formation. Gaseous zones were formed in the coal seams according to Lidin (1963) by the following process: During coalification, carbondioxide and methane form with continuous passage after each other. These gases migrate towards the surface according to the sequence of their formation, carbondioxide at first and then methane. At the same time, gases of atmospheric origin *viz.* oxygen and nitrogen from the air—probably in form of solution in sickering water—reach deeper layers. The oxygen of the air is used up by biochemical and chemical reactions mainly producing carbondioxide. The main gas components are, therefore, methane, carbondioxide and nitrogen. According to the direction of motion of the gases, various gaseous zones are formed. Near to the surface nitrogen and carbondioxide occur predominantly. With increasing depth at first the carbondioxide content decreases and the methane content increases then by decreasing nitrogen content methane starts to dominate.

The formation of methane may be regarded as a gas producing reaction accompanying the biological and chemical coalification during geologic ages that expands over the whole coal mass. Gas formation takes place during the coalification as long as thermodynamic conditions produce suitable circumstances for it.

The methane formed in this way is partly adsorbed on the pore walls, partly it occurs as free gas inside of the pores and cracks of the coal. The greatest part of the

methane in the coal is adsorbed physically on the surface of the micropores, since their specific surface is extremely great: 100–400 m<sup>2</sup>/g. The volume of the micropores is independent of the elastic deformations of the rock and its effect on gas permeability is negligible. The specific surface of the macropores, 1–2 m<sup>2</sup>/g is by two orders of magnitude smaller than that of the micropores, therefore gas occurs in them mainly in form of free gas. Gas permeability is, however, determined by the macropores and cracks in the coal and latters are rather strongly affected by deformations. Deformations of the coal due to changes of load take place mainly at the expense of macropores and crack systems containing free gas.

Free gas in the macropores and crack systems of the coal can and does leave the place of origin and can and does fill the pores of the adjacent rocks.

The equilibrium of the adsorbed gas on the pore walls and the free gas in the pores is unambiguously determined by pore gas pressure  $p$  and temperature  $t$ . The cause of physical adsorption is the free surface energy of solids, in this case of rocks. The process of adsorption for a coal-methane system can be well interpreted by Langmuir's monomolecular adsorption theory, according to which adsorption proceeds as long as full monomolecular saturation is achieved on the surface. Physical adsorption is combined with energy release, the process of adsorption is exotherm, it transfers heat towards the surroundings. Measurements showed that the so-called differential adsorption heat related to unit amount of adsorbed gas decreases with the amount of adsorbed gas. This can be explained by two circumstances (Buzágh 1951, Erdey-Grúz and Schay 1964):

— There are places of different potential (activity) on the adsorbent due to its heterogeneity, and the gas molecules are adsorbed in the sequence of the potentials. Thus, with the advance of adsorption, the energy release decreases.

— A polymolecular adsorption layer is formed on the surface, therefore the adsorption of gas layers farther from the solid surface is accompanied with less energy release. This explanation is the basis of the polymolecular adsorption theory of Brunauer, Emmett and Teller.

Experiences show that the surface of the adsorbent (coal) can always provide sufficient place for the adsorbed amount of gas (methane) in form of monomolecular layers at temperatures and pressures common in nature. Therefore, the monomolecular theory meets the requirements of our investigations. The adsorbed volume of gas on the surface of the solid phase of unit mass becomes according to Langmuir's equation written for physical normal state (0°C temperature and 0.1 MPa pressure):

$$V_a = V_{\max} \frac{b_0 p}{b_0 p + e^{-\frac{Q}{RT}}} = \frac{V_{\max} p}{p + \frac{b_0}{F(T)}} = \frac{V_{\max} \frac{b_0 p}{F(T)}}{\frac{b_0}{F(T)} p + 1}; \quad \text{cm}^3/\text{g} \quad (1)$$

$$F(T) = e^{-\frac{Q}{RT}} = e^{-\frac{T_0}{T}}, \quad T_0 = \frac{Q}{R} \quad (2)$$

whereas

- $V_{\max}$  maximum amount of adsorbed gas at physical normal state (at 0°C temperature and 0.1 MPa pressure), cm<sup>3</sup>/g,  
 $p$  pore gas pressure, MPa,  
 $T$  absolute temperature, K,  
 $R$  gas constant, J/cm<sup>3</sup>K,  
 $Q$  adsorption potential (differential adsorption heat), J/cm<sup>3</sup>,  
 $b_0$  constant characterizing the solid-gas system, MPa<sup>-1</sup>.

In general,  $V_{\max} = 20\text{--}70$  cm<sup>3</sup>/g and  $F(T)/b_0 = 0.5\text{--}2.5$  MPa at  $T = 300$  K temperature. The gas constant of methane is  $R = 520$  J/kg,  $K = 3.27 \cdot 10^{-4}$  J/cm<sup>3</sup> K. The differential adsorption heat for a coal-methane system is  $Q = 0.5\text{--}1.5$  J/cm<sup>3</sup>, correspondingly,  $Q/R = T_0 = 1.5 \cdot 10^3\text{--}4.6 \cdot 10^3$  K.

Isotherms obeying Langmuir's law are illustrated in Fig. 1.

The amount of free gas related to unit mass of solid is in physical normal state

$$V_f = \frac{273ep}{T(1+e)\rho p_a} = \frac{273np}{T\rho p_a}, \quad \text{cm}^3/\text{g} \quad (3)$$

whereas

- $p_a$  atmospheric pressure (0.1 MPa),  
 $e$  void ratio,  
 $n$  porosity,  
 $\rho$  bulk (volumetric) density of the rock, g/cm<sup>3</sup>.

The total amount of gas can be written as

$$V_i = V_a + V_f, \quad \text{cm}^3/\text{g}. \quad (4)$$

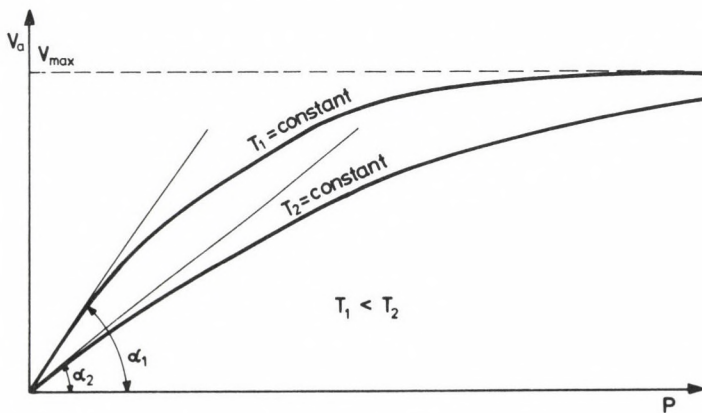


Fig 1. Adsorption isotherm

If pore gas pressure is  $p=0$ , the amounts of both free and adsorbed gas equal zero. For  $p \rightarrow \infty$  the amount of adsorbed gas  $V_a = V_{\max}$  is a finite quantity while  $V_f \rightarrow \infty$  holds for the free gas. For pore gas pressure values  $p=0.2-5$  MPa occurring in nature, we have  $V_a \gg V_f$ .

The amounts of adsorbed and free gas are in dynamic equilibrium, adsorption and desorption take place simultaneously, with equal rates of progress. Dynamic equilibrium for a given pore volume is determined by temperature and gas pressure.

### 3. Characteristics of the temperature field of the Earth's crust

From the depth of the Earth, a steady heat flow towards the surface takes place. The heat transfer proceeds by conduction obeying Fourier's law of heat conduction according to which the heat flow (the amount of heat transferred across a surface of unit area in a unit time) is proportional to the thermal gradient, i.e.

$$q' = \lambda \frac{\partial T}{\partial z} \quad (5)$$

whereas

$\lambda$  denotes the coefficient of thermal conductivity.

The reciprocal of thermal gradient  $dT/dz$ ,

$$gg = \frac{dz}{dT} \quad (6)$$

—as known—is called the geothermal gradient.

The temperature field of the intact Earth's crust can be approximately characterized by the average of the geothermal gradient as interpreted in Fig. 2.

$$gg = \tan^{-1} \alpha = \frac{z}{T - T_a}, \quad \frac{\text{m}}{^\circ\text{C}} \quad (7)$$

whereas

$T_a$  stands for the multiannual average of the annual mean temperature of air (in Hungary  $T_a = 10.6^\circ\text{C}$ ).

Substituting Eqs (6) and (7) into Eq. (5) we have

$$q' = \lambda' \frac{T - T_a}{z} \quad (8)$$

whereas

$\lambda'$  denotes the equivalent coefficient of the thermal conductivity.

It should be noted that the incorrect form

$$gg = \tan^{-1} \alpha' = \frac{z - z_n}{T - T_a} \quad (9)$$

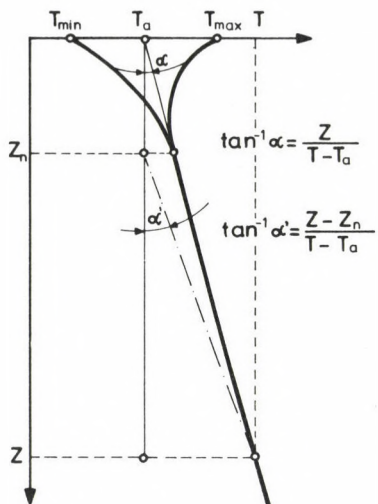


Fig. 2. Interpretation of the average geothermal gradient

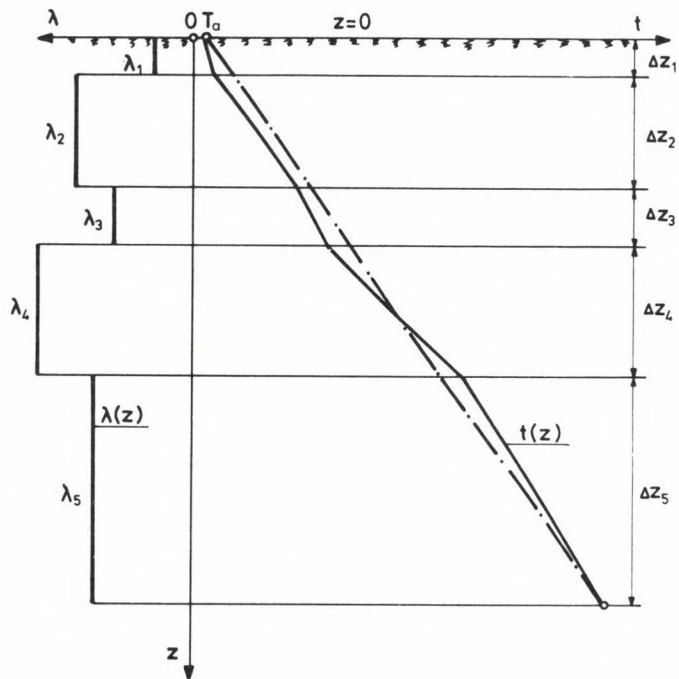


Fig. 3. Temperature vs. depth for a set of layers

of the geothermal gradient had been formerly generally used with  $z_n$  denoting the depth of the neutral rock zone where the annual variation of the surface temperature has no sensible effect. This inaccuracy in the interpretation may considerably distort the geothermal gradient for smaller depths (Boldizsár 1956, Boldizsár 1962).

For a multilayer heat conductor, as the Earth's crust, heat flow across a layer can be written by using the designations of Fig. 3 as:

$$q_i = q' = \lambda_i \frac{\Delta T_i}{\Delta z_i}. \quad (10)$$

The total temperature difference of the set of layers investigated

$$\Delta T = \sum_{i=1}^n \Delta T_i = \sum_{i=1}^n q_i \frac{\Delta z_i}{\lambda_i} = q' \sum_{i=1}^n \frac{\Delta z_i}{\lambda_i}. \quad (11)$$

Thus we have for the terrestrial heat flow

$$q' = \frac{\Delta T}{\sum_{i=1}^n \frac{\Delta z_i}{\lambda_i}} = \frac{\sum_{i=1}^n \Delta T_i}{\sum_{i=1}^n \frac{\Delta z_i}{\lambda_i}}. \quad (12)$$

The equivalent coefficient of thermal conductivity becomes

$$\lambda' = \frac{\sum_{i=1}^n \Delta z_i}{\sum_{i=1}^n \frac{\Delta z_i}{\lambda_i}} \quad (13)$$

while the average temperature gradient is

$$\frac{\Delta T}{\Delta z} = q' \frac{\sum_{i=1}^n \frac{\Delta z_i}{\lambda_i}}{\sum_{i=1}^n \Delta z_i} \quad (14)$$

and the average geothermal gradient will be

$$gg = \frac{\Delta z}{\Delta T} = \frac{\sum_{i=1}^n \Delta z_i}{q' \sum_{i=1}^n \frac{\Delta z_i}{\lambda_i}}. \quad (15)$$

The smaller the thermal conductivity (i.e. the greater the resistance) of a layer, the greater is the temperature fall caused by a heat flow crossing the layer. Thus the temperature gradient or geothermal gradient change as functions of depth and layering

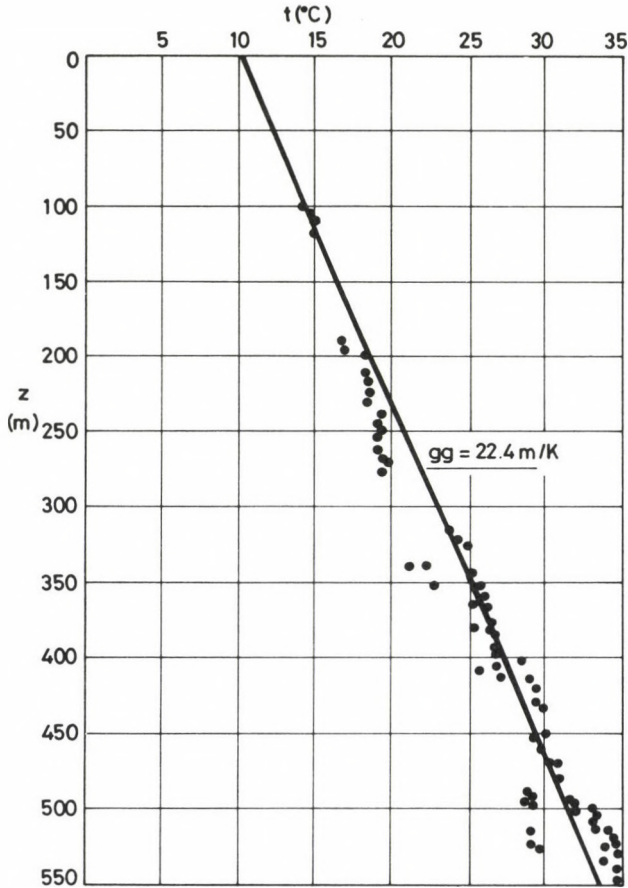


Fig. 4. Intact rock temperature as a function of depth in the Zobák and Hosszúhetény mines

in dependence of the thermal conductivity coefficients of the layers. The average geothermal gradient characterizes the temperature conditions with sufficient accuracy only if the thermal conductivity coefficients of the layers do not vary considerably. Otherwise the temperature conditions can only be assessed when knowing the heat flow  $q'$ , the coefficients of thermal conductivity  $\lambda_i$  and the layer thicknesses  $\Delta z_i$  (Boldizsár 1956, Boldizsár 1962, Boldizsár 1964).

Exact measurements of rock temperatures and of the thermal conductivity coefficient and calculations of terrestrial heat flow were carried out in Hungary by Boldizsár. The change with depth of the intact rock temperature measured in the twin shafts of Zobák and Hosszúhetény in Southern Hungary is illustrated in Fig. 4. The average temperature gradient is 44.7 K/km, the average geothermal gradient 22.36

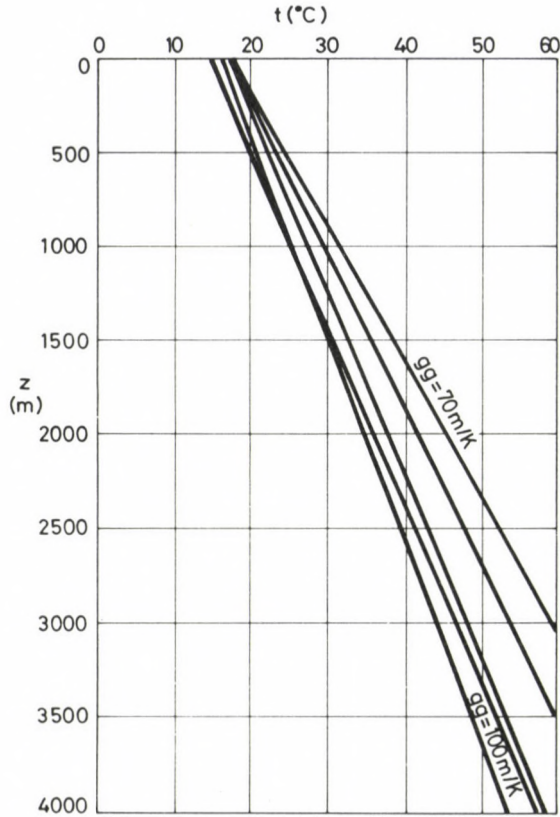


Fig. 5. Intact rock temperature in the deep mines of South Africa

m/K, the average heat flow  $2.75 \cdot 10^{-6}$  cal/cm<sup>2</sup>s = 0.1246 J/m<sup>2</sup>s and the average equivalent coefficient of heat conductivity  $\lambda' = 6.92 \cdot 10^{-3}$  cal/cm s°C = 2.8898 J/msK. For the Hungarian basin the following average values are valid:  $\lambda = 4.5 \cdot 10^{-3}$  cal/cm s°C = 1.885 J/msK,  $gg = 18.43$  m/K,  $q' = 2.44 \cdot 10^{-6}$  cal/cm<sup>2</sup>s = 0.1022 J/m<sup>2</sup>s (Boldizsár 1962).

In general, the geothermal gradient lies around 33 m/K. In the Hungarian basin the measured geothermal gradient values are considerably smaller, but much greater geothermal gradients can also be found elsewhere, e.g. in the deep mines of South Africa with working depths of 1500 to 3800 m the geothermal gradient lies between 70 and 100 m/K (Cook et al. 1967). The temperature of the intact rock as a function of depth for the South-African deep mining is illustrated in Fig. 5.

The great differences among the values of the geothermal gradient can be explained by the great variety of the terrestrial heat flow values  $q' = 0.58 \cdot 10^{-6}$  –

$-3.5 \cdot 10^{-6}$  cal/cm<sup>2</sup>s = 0.024–0.1382 J/m<sup>2</sup>s (Boldizsár 1962). This variety is accompanied by rather different coefficients of thermal conductivity ranging from  $4 \cdot 10^{-3}$  to  $12 \cdot 10^{-3}$  cal/cm s°C, i.e. from 1.68 to 5.03 J/msK.

#### 4. Gas content and gas pressure as functions of depth

In the quantitative analysis, the free gas can be neglected in comparison to the adsorbed one thus the total amount of gas can be taken approximately equal to the adsorbed one. Consequently, pore gas pressure can be written as

$$p = \frac{S}{1-S} \frac{e^{-\frac{T_0}{T}}}{b_0} \quad (16)$$

whereas  $S = V_a/V_{\max}$  denotes the gas saturation of the rock ( $S \leq 1$ ). Substituting

$$T = T_a + \frac{z}{gg} \quad (17)$$

into Eq. (16), we have for pore gas pressure as a function of depth

$$p = \frac{S}{1-S} \frac{e^{-\frac{T_0}{T_a + z/gg}}}{b_0}. \quad (18)$$

As seen from Eq. (18), the function pore gas pressure *vs.* depth depends on the saturation of the surface available for adsorption, i.e. on the quantity of  $S$ , on the adsorption parameters  $b_0$  and  $T_0$  of the solid-gas phase and on the geothermal gradient. To illustrate the effect of the geothermal gradient, we will plot the function

$$f(p) = p \frac{1-S}{S} = \frac{e^{-\frac{T_0}{T_a + z/gg}}}{b_0} \quad (19)$$

for various geothermal gradients.

Figures 6 to 8 show the gas pressure as a function of depth for various  $T_0$  and  $gg$  and for  $1/b_0 = 2 \cdot 10^4$  MPa. Parameter  $1/b_0$  is a multiplying factor, thus its effect is obvious. The variation of  $b_0$  within a real interval does not cause any change in the order of magnitude of gas pressure. The figures also show that the change of geothermal gradient brings about considerable changes in the gas pressure only in greater depths. However, changes of the gas pressure function due to those of parameter  $T_0$  can amount to one order of magnitude.

The effect of parameters  $T_0$  and  $b_0$  on gas pressure function is illustrated in Fig. 11, where the variation of the gas pressure function can be seen as the function of the parameter  $T_0$  at various values of  $1/b_0$  for the values  $z = 500$  m,  $T_a = 285$  K,  $gg = 30$  m/K.

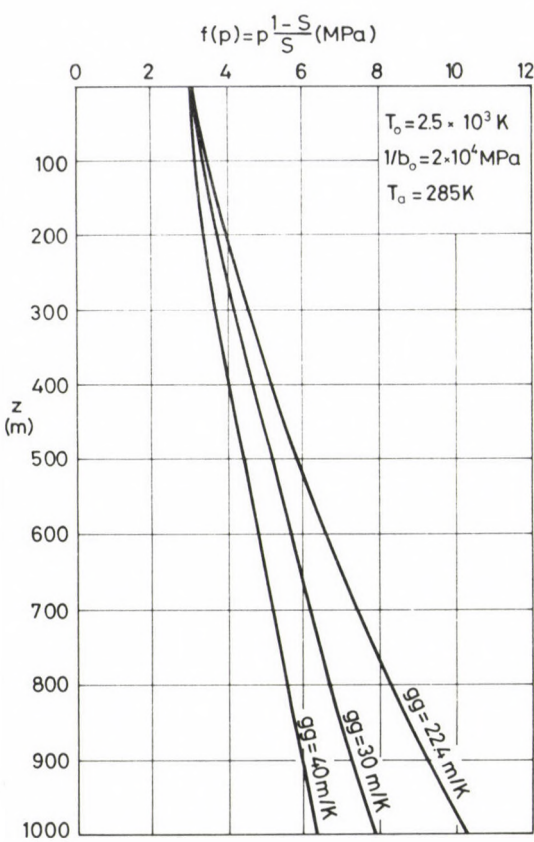


Fig. 6. Gas pressure function vs. working depth

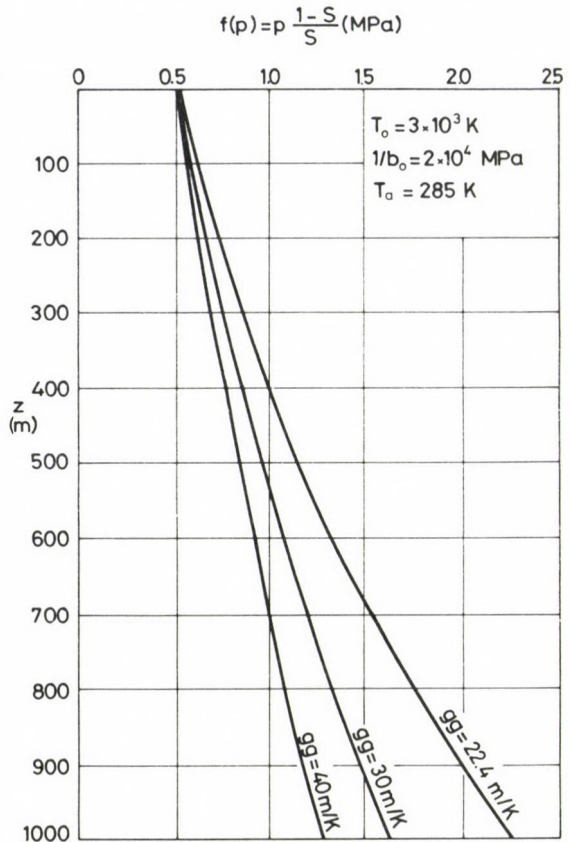


Fig. 7. Gas pressure function vs. working depth

Take into consideration that the smaller value of  $1/b_0$  belongs to a smaller  $T_0$ . It can be seen from the figure that the gas pressure function varies within a wide range in a given depth depending on the adsorption parameters  $T_0$  and  $b_0$ .

Data of *in situ* gas pressure published by various authors suggest that the pressure of free gas varies approximately linearly as a function of depth. Gas pressure vs. depth, in general, is written in the form

$$p = A(z - z_0) \tag{20}$$

whereas

- $z_0$  denotes the depth below the surface where gas phenomena begin ( $p = 0$ ),
- $A$  stands for gas pressure gradient ( $dp/dz = A$ ).

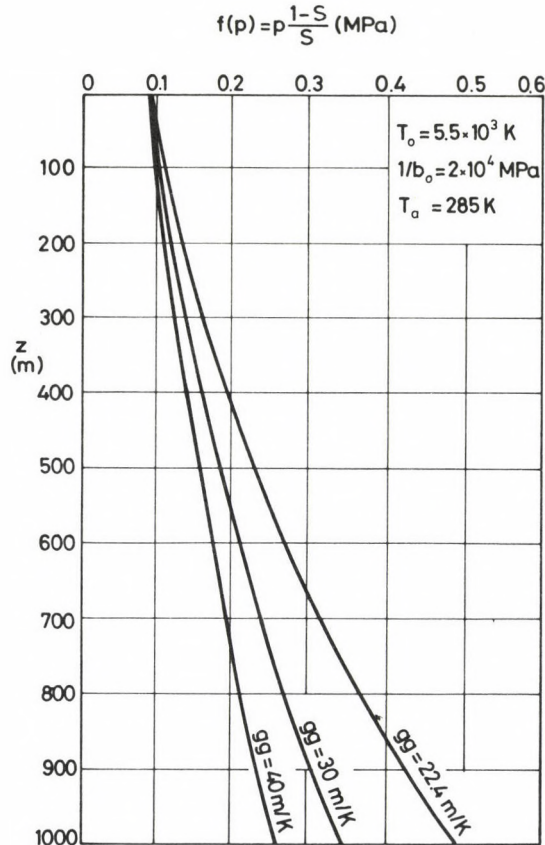


Fig 8. Gas pressure function vs. working depth

In the Donets basin in the USSR  $A = 0.01$  MPa/m,  $z_0 = 100$  m, in the Kemerovo region of the Kuznetsk basin  $A = 0.012$  MPa/m,  $z_0 = 180$  m and in the Kuzbass  $A = 0.009$  MPa/m,  $z_0 = 54$  m (Chernov and Puzirev 1979, Ivanov 1970, Ivanov et al. 1979). Measured gas pressure values are illustrated as functions of depth in Figs 9–10 (Ivanov 1970, Ivanov et al. 1979).

Using *in situ* measurement values of pore gas pressure, the saturation  $S$  and the gas content can be expressed as functions of depth

$$p = A(z - z_0) = \frac{S}{1-S} \frac{1}{b_0} e^{-\frac{T_0}{T_a + z/\theta\theta}}. \quad (21)$$

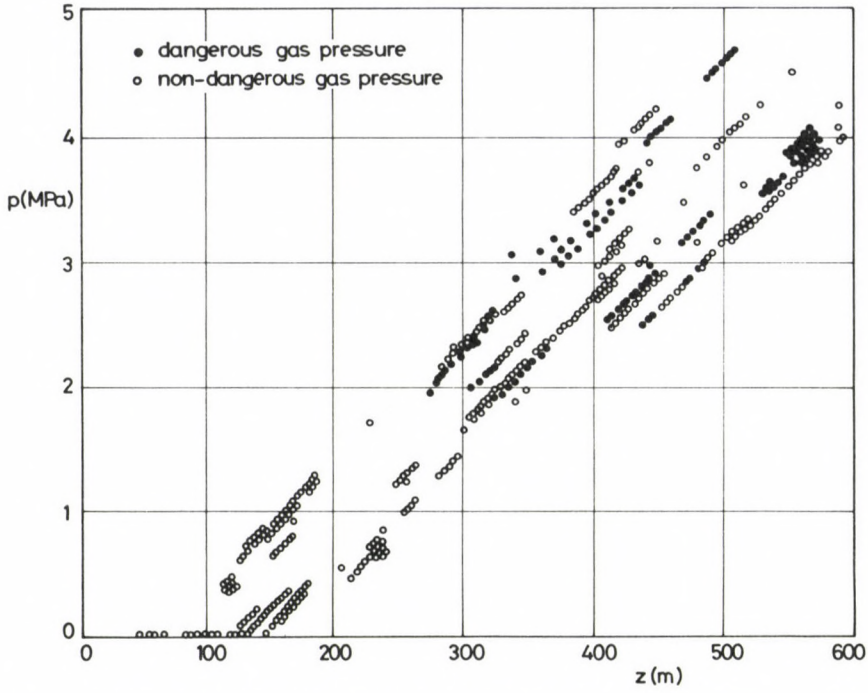


Fig. 9. Measured values of gas pressure in the Vorkuta region (USSR) plotted against depth

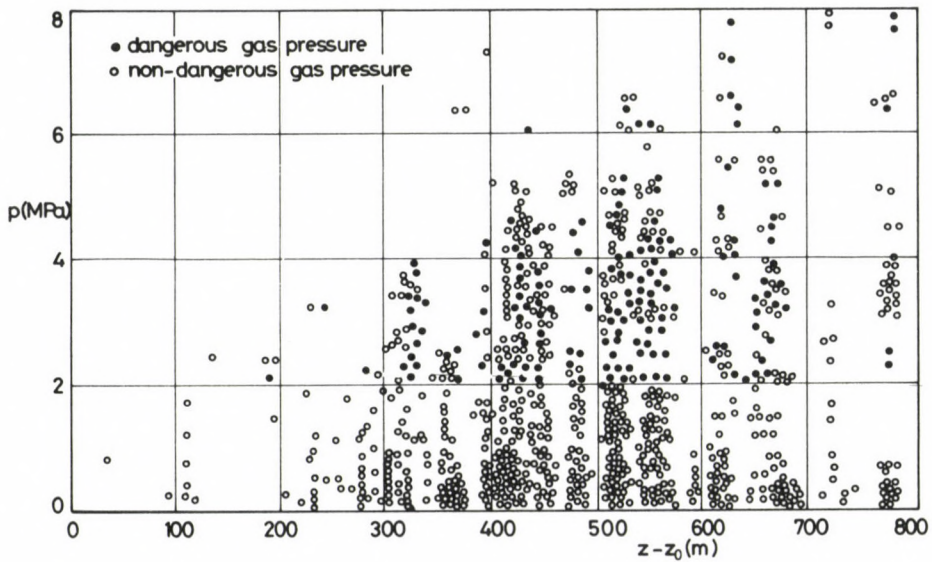


Fig. 10. Measured values of gas pressure in Donbass plotted against depth

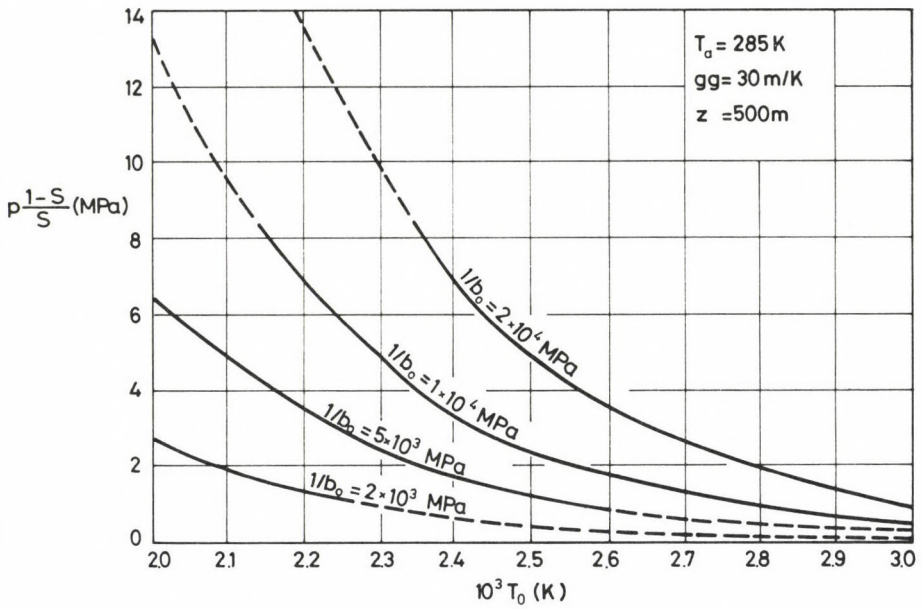


Fig. 11. Dependence of gas pressure function on the adsorption parameters

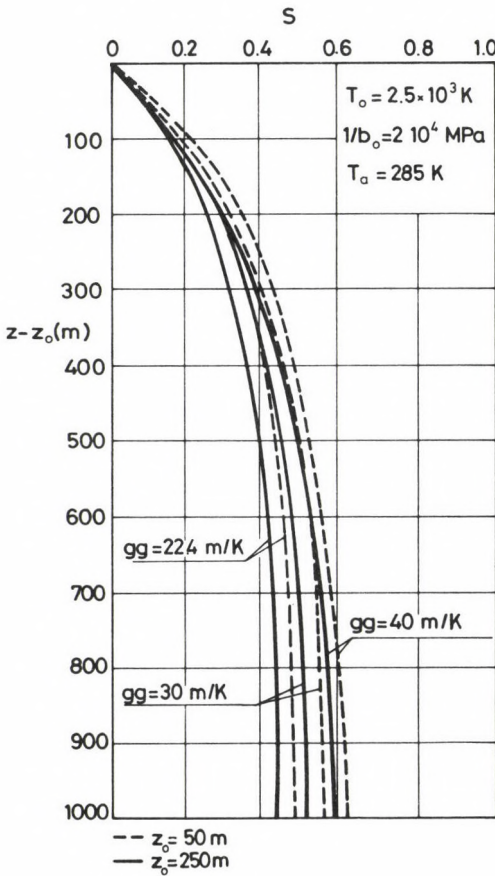


Fig. 12. Saturation as a function of depth

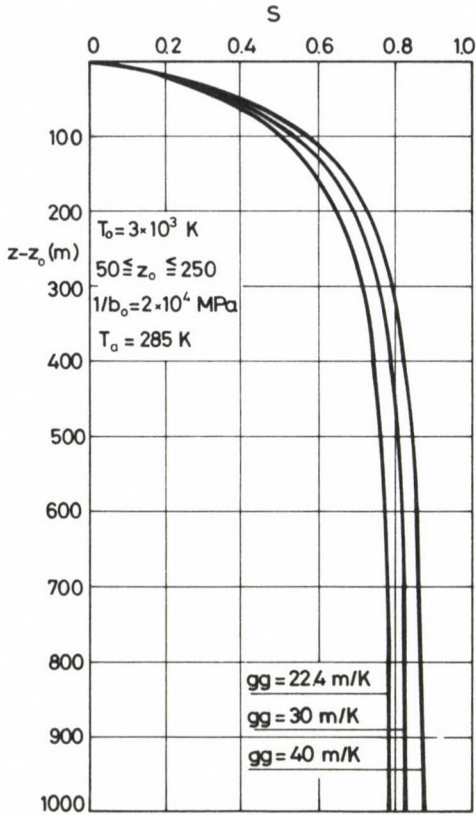


Fig. 13. Saturation as a function of depth

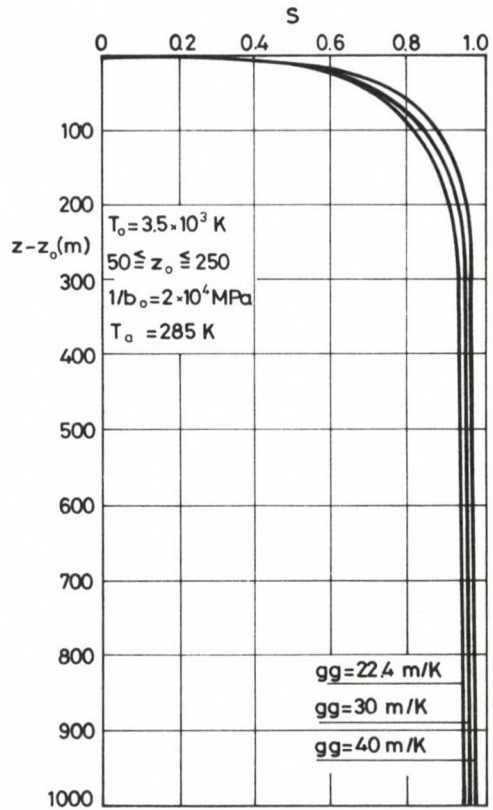


Fig. 14. Saturation as a function of depth

Rearranging, we have

$$S = \frac{1}{1 + \frac{1}{b_0 A (z - z_0) e^{\frac{T_0}{T_a + z/gg}}}} \quad (22)$$

Saturation is illustrated as a function of depth in Figs 11 to 14 with various values of parameters  $T_0$ ,  $gg$  and  $z_0$  for  $A = 0.01$  MPa/m,  $T_a = 285$  K and  $1/b_0 = 2 \cdot 10^4$  MPa. The figures indicate that  $z_0$  has a negligible effect on the change or measure of saturation below the depth  $z_0$ . If  $T_0$  is greater, the geothermal gradient has also hardly any effect on the saturation. With increasing depth the saturation takes up rather quickly an approximately constant value.

### 5. Specific gas output and gas content

The methane amount  $\bar{q}$  emitted while extracting 1 tonne of coal is composed of the following fraction after Lidin (1963):

- a) methane emitted by the extracted coal,  $q_1$
- b) methane emitted by the layer mined,  $q_2$
- c) methane emitted by the country rocks,  $q_3$
- d) methane emitted by the pillars left behind,  $q_4$
- e) methane emitted by the coal lost in the gob,  $q_5$
- f) methane emitted by the part of the layer left behind,  $q_6$
- g) methane emitted by the affected adjacent layer or layers,  $q_7$
- h) methane emitted by the country rocks of the adjacent layers,  $q_8$ .

Thus the specific methane output will be:

$$\bar{q} = q_1 + q_2 + q_3 + q_4 + q_5 + q_6 + q_7 + q_8, \quad \text{m}^3/\text{t}. \quad (23)$$

Less than half or a third of the specific methane output comes from the layer mined and even a smaller amount from the extracted coal. In fact, the greatest part of the methane is emitted by the surroundings. Therefore, the specific gas output is strongly affected by the production rate: specific gas output is high if production is low and it is low at high production rates because the total gas output is practically constant. High specific gas outputs experienced in the Mecsek Coal Mines are caused by low production rates. The specific gas output is also strongly influenced by the number and thickness of the adjacent layers affected by mining operations and the depression produced by ventilation. The total volume of gas emitted by the rocks in a long period is, after all, determined by the gas content, but specific gas output is not closely related to it. Therefore, conclusions about the gas content of the layer mined are difficult to make from the values of specific gas output and they are even less reliable concerning the prediction of gas outburst danger.

The detailed statistical analysis of the quantitative parameters of gas emission in the longwalls of the Mecsek Coal Mines was given by Kovács. He pointed out that the changes of gas output were not correlated to the daily production cycles. No difference was found between the gas emission of productive and non-productive shifts. Further, gas emission showed no significant difference between work-days and holidays either. These results suggest that the methane emitted by the extracted coal  $q_1$  is negligibly small with respect to the sum of the other components  $q_2 + q_3 + q_4 + q_5 + q_6 + q_7 + q_8$ .

The specific value of methane emission in the workings investigated in Mecsek was 6.7–14.9 m<sup>3</sup>/t (Kovács 1975). The specific gas output amounted, however, to 50 m<sup>3</sup>/t calculated for the Mecsek mines at a depth of 500 m (Szirtes 1971). The great difference suggests that the greatest part of the methane originates from gobs and other loosened parts of the rocks and not from the workings.

The ratio of the amounts of emitted gas and thrown-out rock due to outbursts approximates much better the gas content of the rock than the specific gas output of the mine. Gas is also emitted from the suddenly loosened rock masses, therefore, the emitted specific gas amount exceeds the gas content, but the gas developed during outbursts does not consist of as many components as that emitted by the whole of the mine. Therefore, the correlation between the specific gas output emitted during outbursts and the depth is characteristic of the change of gas content.

One of the parameters characterizing the intensity of outbursts is the amount of gas emitted during outbursts ( $\text{m}^3/\text{case}$ ). Experiences show that this parameter increases with increasing depth. Another parameter of outburst intensity is the amount of thrown-out rock in tonne (case or  $\text{m}^3$ ) case. Experiences tell that this parameter of outburst intensity also increases as a function of depth. This field, too, has been statistically investigated by Kovács in detail. Figure 15 illustrates both intensity parameters as functions of depth for the Pécs region in Southern Hungary (Kovács 1975) indicating that the ratio of the two intensity parameters is practically constant which suggests that gas content does not change significantly within the depth interval

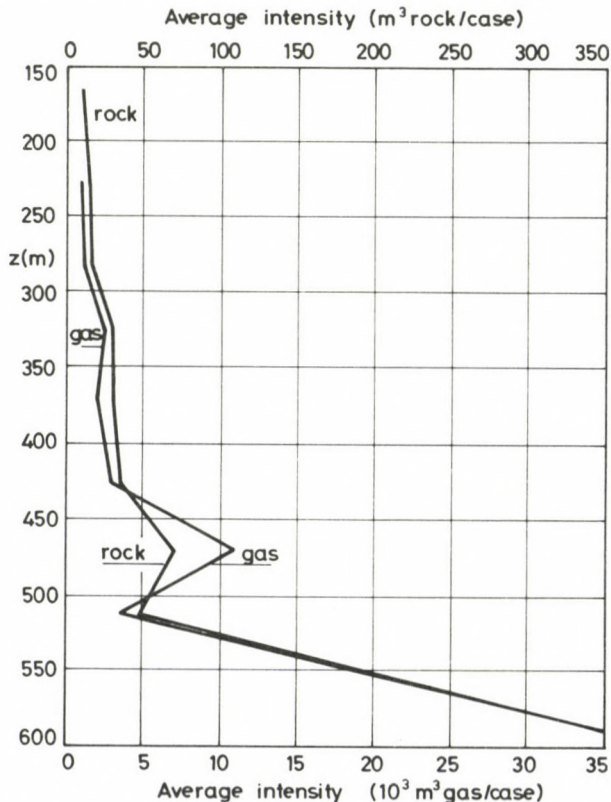


Fig. 15. Average intensity of outbursts in the Mecsek region as a function of working depth

investigated. Figure 16 shows the ratio of the two intensity parameters as a function of working depth. It can be seen that the average of the specific gas amount lies between 60 and 100 m<sup>3</sup> gas per m<sup>3</sup> rock for the outbursts investigated corresponding to an average methane emission of about 40–70 m<sup>3</sup>/t and slightly increasing with depth at a gradient of 0.07 m<sup>3</sup>/t in the interval 200–600 m. This rate of increase is far from being as high as that of the specific gas output of the mines having a gradient of about 0.14 m<sup>3</sup>/t in the Pécs region (Szirtes 1971).

Consequently, the specific gas output of the mine does not characterize the gas content either quantitatively or in dependence of depth. Therefore, an increase in the specific gas output of the mines with increasing depth does not indicate any increase of outburst danger, either.

Rock temperature may, however, have a strong influence on the dependence of the specific gas output of the mines on depth, since adsorption capability is lower and desorption capability is higher at higher temperature, thus the amount of gas emitted in unit time is greater with increasing temperature. This question will not be dealt with in more detail since it does not bear any significance on outburst danger.

In the followings the effect of rock temperature on outbursts will be analyzed.

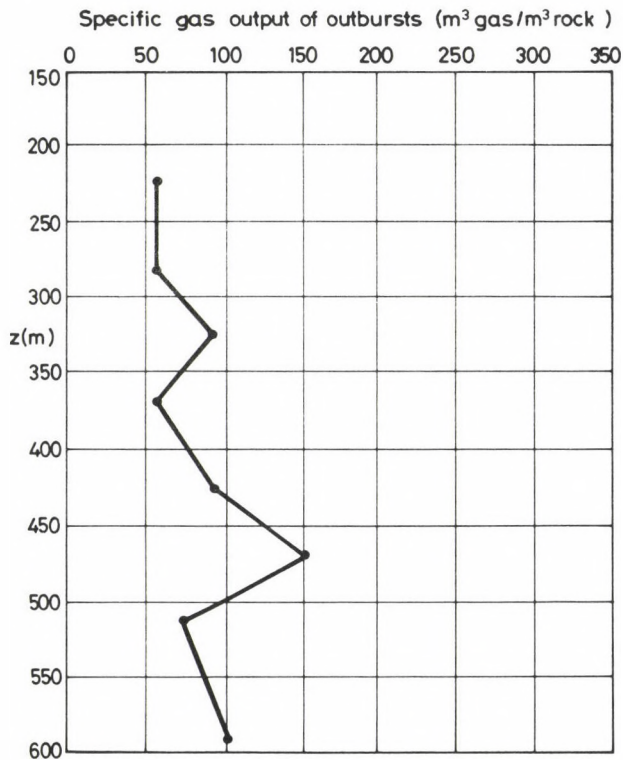


Fig. 16. Average specific methane output of outburst in the Mecsek region as a function of working depth

## 6. Effect of rock temperature on outbursts

Outbursts always occur at "fresh" rock faces, road heads, shaft soles and faces of workings. Rock surfaces and their surroundings are cooled by ventilation, but the cooling effect of ventilating air on the rock in front of "fresh" faces is negligible, thus approximately the intact rock temperature is valid in the domain of outbursts.

The basic condition of outbursts is expressed by the inequality (Somosvári 1981b, Somosvári 1982a, Somosvári 1982b)

$$\frac{p_{\max}}{\sigma_c} > \frac{1-q}{B-1} \quad (24)$$

$$q = \frac{\sigma_Y}{\sigma_c}, \quad B = \tan^2 \left( 45 + \frac{\Phi}{2} \right) \quad (25)$$

whereas

$p_{\max}$	maximum pore gas pressure in front of the rock face,
$\sigma_c$	uniaxial compressive strength of the gas-bearing rock,
$\sigma_Y$	yield point of the gas-bearing rock,
$q$	coefficient of brittleness of the gas-bearing rock,
$\Phi$	angle of internal friction of the gas-bearing rock.

These parameters are the main parameters of outburst danger. The change of rock temperature with increasing depth does not influence the parameters  $\sigma_c$ ,  $\sigma_Y$ ,  $q$  and  $\Phi$  but has a significant effect on the parameter  $p_{\max}$ . The maximum pore gas pressure is determined by the initial pore gas pressure  $p$  and the pore gas pressure increase  $\Delta p$  caused by rock volume decrease due to transferred stresses:

$$p_{\max} = p + \Delta p. \quad (26)$$

Rock temperature has an effect on the maximum pore gas pressure through the initial pore gas pressure and, in consequence, on the rise of outbursts.

The change of rock temperature as a function of depth together with the increasing gas saturation increases the initial pore gas pressure in a way that the effect of the rapid increase of gas saturation is stronger near the depth  $z_0$ , while in greater depths that of the increase of the rock temperature is more important.

The initial pore gas pressure is determined in a given depth—apart from the gas saturation and the rock temperature—by the adsorption parameters  $b_0$  and  $T_0$  of the rock. The great differences found all over the world in the pore gas pressure of the mines affected by outburst danger can be explained first of all by the differences of these parameters.

Mines affected by outburst danger in various places of the world can be divided into the following two groups according to the main parameters of outbursts:

a) The gas-bearing rock is strong, the pore gas pressure is high ( $p \cong 1-8$  MPa), outbursts occur in places of low rock strength and high gas pressure.

b) The gas-bearing rock is strongly penetrated by cracks and fissures, the strength and pore gas pressure is low ( $p \cong 0.2-1$  MPa), outburst also occur at low gas pressure. The conditions of Mecsek render this region into group *b*.

The great differences in the initial pore gas pressure of mine regions affected by outburst danger are not fully explained by the differences in the geothermal gradient. Either the gas saturation or the adsorption parameters of the rock  $b_0$  and  $T_0$  or both show great differences.

The macropores and crack systems of cracked and broken coal sorts allow a greater possibility for the gas to escape than a solid, compact coal does. Therefore a cracked coal is less saturated with gas, but here the rocks in the surroundings also have a considerable gas content. If the gas adsorption capability is greater than normal ( $b_0$  and  $T_0$  are too high), a great amount of gas can be stored even at a low pore gas pressure. Low gas pressures in areas belonging to the type *b* can be explained by the above arguments.

The rock temperature has only an effect on outbursts so far as it influences the gas pressure during gas storage.

## 7. Conclusions

Our investigations show that the rock temperature has an effect on gas storage on the one hand and it may influence the specific gas output of the mine through slow gas emission on the other. The effect of rock temperature on outbursts is so far limited that it determines the initial pore gas pressure.

The initial pore gas pressure depends on the gas adsorption capability (adsorption parameters) of the gas-bearing rock, on the gas saturation of the rock and on the rock temperature. In the depth interval  $0 \leq z \leq z_0$  the gas saturation is zero, therefore the pore gas pressure is also zero. In depths below  $z_0$  the gas saturation increases exponentially as a function of depth which in turn increases the gas pressure. In greater depths the gas saturation increases only very slightly, the rock temperature contributes here stronger to the increase of gas pressure. The linear or quasilinear change of gas pressure as a function of depth is, in consequence, a result of the exponential change of gas saturation and the linear change of rock temperature influencing the gas adsorption.

The pore gas pressure is basically determined—besides of the gas saturation—by the adsorption parameters of the rock-gas system.

The cracked and broken coal, the low gas pressure, the high specific gas output of the mines and the rapid increase of gas output with increasing depth in the Mecsek region can be explained by the following facts: From the cracked coal a great amount of gas can migrate into the surroundings during the long time of storage, this reduces the gas saturation in the coal seam, and produces at the same time a gas content in a greater

surrounding rock mass. If the adsorption capability of the coal is stronger, it can store great amounts of gas even at low gas saturation and low gas pressure. Gas emission may be very intensive in the mine even if gas content is low, because the dimensions of the gas-bearing rock are great. The specific gas output ( $\text{m}^3/\text{t}$ ) is high, because the production is delayed by the protection measures taken against outbursts, thus the amount of extracted coal becomes low, while the emitted amount of gas hardly depends on the amount of the coal extracted. The increase of the specific gas output with increasing depth can be partly explained by a temperature increase encouraging desorption. This is the reason of the fact that a small geothermal gradient in the Mecsek region increases the specific methane output.

## References

- Berecz E 1980: Physical chemistry. (In Hungarian) Tankönyvkiadó, Budapest
- Boldizsár T 1956: Effect of temperature field of the Earth's crust on the warming up of the air in deep mines. (In Hungarian) *Bányászati Lapok*, No. 9–10, 515–523.
- Boldizsár T 1962: Geothermal investigations in the coal, oil and water mining industry. In: *Mining Engineer's Handbook III*. (In Hungarian) Műszaki Könyvkiadó, Budapest, 847–856.
- Boldizsár T 1964: Geothermal map and terrestrial heat flow of Hungary. (In Hungarian) *MTA Műsz. Tud. Osztályának Közleményei*, 33, 307–327.
- Buzágh A 1951: Colloids. (In Hungarian) Akadémiai Kiadó, Budapest
- Chernov O Y, Puzirev V N 1979: Forecast of unexpected coal and gas outburst. (In Russian) Moscow
- Cook N G W, Denkhaus H G, Rapson W S 1967: Deep level mining research in South Africa. International Mining Conference, Moscow
- Erdey-Grúz T, Schay G 1964: Theoretical physical chemistry, Vol. II. (In Hungarian) Tankönyvkiadó, Budapest
- Ivanov B M 1970: Assessment of outburst danger of coal layers of the Donets basin from the Vorkutinski deposit. (In Russian) Nedra, Moscow
- Ivanov B M, Feyt G N, Yanovskaya M F 1979: Mechanical and physico-chemical properties of coals from layers affected by outburst danger. (In Russian) Izdatyelistvo "Nauka", Moscow
- Kovács F 1975: Determination of the expected measure and assessment of the economical effects of gas outburst danger. (In Hungarian) Doctor's thesis
- Kovács F 1983: Characteristics of gas release in longwall workings of mines with high gas output. *Acta Geod. Geoph. Mont. Hung.*, 18, 305–332.
- Lidin G D 1963: Verfahren zur Berechnung der Gasgefährdung von Abbauräumen auf Grund des Gasgehaltes der Flöze. III (Method to calculate gas danger of mine workings based on gas content of the strata. In German.). Nationaler Bergbaukongress, Salzburg
- Somosvári Zs 1980a: Investigation of the deterioration of the rock-gas system to clarify the cause of rock and gas outbursts. *Acta Geod. Geoph. Mont. Hung.*, 15, 257–269.
- Somosvári Zs 1980b: Investigation of the load assumption of rock-gas systems, aiming at the detection of the causes of rock and gas outbursts. *Acta Geod. Geoph. Mont. Hung.*, 15, 271–294.
- Somosvári Zs 1981a: Investigation of the rock-gas system in front of the face of workings in order to determine the cause of rock and gas outbursts. *Acta Geod. Geoph. Mont. Hung.*, 16, 131–149.
- Somosvári Zs 1981b: Basic functions of rock and gas outbursts in the face of workings. (In Russian) *Publ. Tech. Univ. Heavy Industry. Miskolc, Series A, Mining*. 36, 133–154.
- Somosvári Zs 1982a: Mechanism of rock and gas outbursts. *Acta Geod. Geoph. Mont. Hung.*, 17, 29–49.
- Somosvári Zs 1982b: Main parameters of the rock and gas outburst danger. *Acta Geod. Geoph. Mont. Hung.* 17, 51–66.
- Szirtes L 1971: Combat against coal and gas outbursts. (In Hungarian) Műszaki Könyvkiadó, Budapest



## EFFECT OF THE PROTECTIVE LAYER MINING METHOD ON THE REDUCTION OF ROCK AND GAS OUTBURST DANGER

Zs SOMOSVÁRI<sup>1</sup>

[Manuscript received February 1, 1983]

The reduction of the outburst danger achieved by the protective layer method is theoretically investigated. The general laws of the field of motion around workings are analyzed. The mechanism and the main parameters of outbursts are determined from the analysis of the gas-bearing rock by treating it as a rock-gas system and the effect of the protective layer method on the reduction of the outburst danger is assessed by analyzing the change of the main parameters.

**Keywords:** gas outburst danger; pore gas pressure; protective layer; rock outburst danger; rock parameters

### *Symbols*

$c$	cohesion
$E$	Young's modulus
$H$	depth of layer
$k$	gas permeability
$l_x$	semi-width of the worked-out area
$m$	Poisson's ratio
$n$	coefficient of the danger of outburst
$M$	worked-out thickness of layer
$p_{\max}$	maximum pore gas pressure
$q$	coefficient of brittleness
$s$	subsidence factor
$u$	horizontal displacement
$w$	vertical displacement
$w_H$	vertical displacement in the roof
$w_L$	vertical displacement in the floor
$z$	co-ordinate of depth
$\Delta\sigma$	deformational normal stress
$\Delta\tau$	deformational shear stress
$\sigma'_z$	primary vertical stress
$\sigma'_x$	primary horizontal stress
$\tau'$	primary shear stress
$\rho$	bulk density
$\varepsilon$	deformation
$\sigma_c$	uniaxial compressive strength
$\sigma_Y$	yield point
$\Phi$	angle of internal friction

<sup>1</sup> University for Heavy Industry, Faculty for Mining, H-3515 Miskolc, Hungary

## Introduction

Experiences proved that outbursts are less frequent in layers beneath or above previous mining operations. It has also been observed that the protective effect depends on the thickness of the layers between the protective and the protected layers, on the thickness of the protective layer, on the physical and mechanical properties of the intermediate layers, on the inclination of the layers, on the working depth and the time between working the protective and protected layers.

The protective effect is generally explained by the cracks in the protected and intermediate layers caused by mining activity in the protective layer beneath or above the dangerous one. One part of the gas content of the protected layer can escape and migrate towards the worked-out area, thus reducing the pore gas pressure in the protected layer. Szirtes (1971) states in his fundamental book that the theory of the protective layer mining method is not yet fully developed. He believes that the basic factor of the protective effect is the emergence of zones with reduced stress.

The results of our investigations concerning the physical causes and the mechanism of rock and gas outbursts enable a more detailed theoretical analysis of the effect of the protective layer mining method. The parameters, among them the time factor, will, however, not be included in our investigations.

At first, the general laws of the fields of motion and stress in the surroundings of workings have to be dealt with.

### General laws in the fields of motion and stress in the surroundings of workings

The equations

$$\begin{aligned} \int_{-\infty}^{\infty} \int_{-\infty}^{\infty} \Delta\sigma_z dx dy &= 0 \\ \int_{-\infty}^{\infty} \int_{-\infty}^{\infty} \Delta\tau_{z,x} dx dy &= 0 \\ \int_{-\infty}^{\infty} \int_{-\infty}^{\infty} \Delta\tau_{z,y} dy dx &= 0 \end{aligned} \quad (1)$$

are also valid in the surroundings of horizontal excavations, *viz.* workings opened in the earth's crust replaced by the material of an infinite semi-space. The designations are:

$\Delta\sigma_z$	vertical normal deformational stress,
$\Delta\tau_{z,x}$	vertical shear deformational stress in the plane perpendicular to $x$ ,
$\Delta\tau_{z,y}$	vertical shear deformational stress in the plane perpendicular to $y$ .

The changes of stress caused by excavations with respect to the original (primary) stresses are called deformational or induced stresses. Equations (1) express that the sum of the changes of stress caused by excavations is zero in the horizontal plane. With other words the increases of stress are compensated for by the decreases of stress because the opening of excavations causes only internal changes, the external load remains constant.

Before the opening of excavations, the primary elastic stresses

$$\sigma_z^* = z\rho g \quad (2)$$

$$\sigma_x^* = \frac{z\rho g}{m-1} \quad (3)$$

$$\tau_{xy}^* = \tau_{yx}^* = \tau_{xz}^* = \tau_{zx}^* = \tau_{yz}^* = \tau_{zy}^* = 0 \quad (4)$$

dominate in the homogeneous and isotropic semi-space under the effect of the dead weight, where:

- $\rho$  bulk density,
- $z$  co-ordinate of depth,
- $m$  Poisson's ratio.

Since in primary state the shear stresses equal zero both in the vertical and horizontal plane, the deformational shear stresses are the same as the stresses after the opening of excavations.

For the sake of theoretical investigations let us imagine an infinitely quickly advancing working with elastic initial deformations in its surroundings. In the following analysis we shall investigate more detailed the state of deformation in the plane of elasticity. This type of state emerges if one of the dimensions (in the  $y$ -direction) of the investigated excavation is infinitely great, thus the deformation in this direction is  $\varepsilon_y = 0$ .

Hooke's general law can be written for a planar state of deformation

$$\begin{aligned} \varepsilon_x &= \frac{1}{E} \frac{\Delta\sigma_x(m^2-1) - \Delta\sigma_z(m+1)}{m^2} \\ \varepsilon_y &= 0 \\ \varepsilon_z &= \frac{1}{E} \frac{\Delta\sigma_z(m^2-1) - \Delta\sigma_x(m+1)}{m^2} \end{aligned} \quad (5)$$

whereas

- $\varepsilon_z$  vertical deformation,
- $\varepsilon_x$  horizontal deformation,
- $\Delta\sigma_x$  horizontal normal deformational stress,
- $E$  Young's modulus,
- $\Delta\sigma_z$  vertical normal deformational stress.

From Eqs (5) we have

$$\Delta\sigma_z = \frac{Em^2[\varepsilon_x + (m-1)\varepsilon_z]}{(m+1)[(m-1)^2 - 1]}. \quad (6)$$

On substituting

$$\int_{-\infty}^{\infty} \int_{-\infty}^{\infty} [\varepsilon_x + (m-1)\varepsilon_z] dx dy = 0. \quad (7)$$

Further, with substitutions

$$\varepsilon_x = \frac{\partial u}{\partial x} \quad \text{and} \quad \varepsilon_z = \frac{\partial w}{\partial z} \quad (8)$$

whereas

$u$  horizontal displacement  
 $w$  vertical displacement

we have

$$\int_{-\infty}^{\infty} \int_{-\infty}^{\infty} \left[ \frac{\partial u}{\partial x} + (m-1) \frac{\partial w}{\partial z} \right] dx dy = 0. \quad (9)$$

Since there is no change in  $y$ -direction:

$$\int_{-\infty}^{\infty} \left[ \frac{\partial u}{\partial x} + (m-1) \frac{\partial w}{\partial z} \right] dx = 0. \quad (10)$$

Equation (10) can also be written in the form:

$$\int_{-\infty}^{\infty} \frac{\partial u(x, z)}{\partial x} dx + (m-1) \int_{-\infty}^{\infty} \frac{\partial w(x, z)}{\partial z} dx = 0. \quad (11)$$

The possible solutions are:

$$\int_{-\infty}^{\infty} \frac{\partial u(x, z)}{\partial x} dx = -(m-1) \int_{-\infty}^{\infty} \frac{\partial w(x, z)}{\partial z} dx \quad (12)$$

or

$$\int_{-\infty}^{\infty} \frac{\partial u(x, z)}{\partial x} dx = 0 \quad \text{and} \quad \int_{-\infty}^{\infty} \frac{\partial w(x, z)}{\partial z} dx = 0. \quad (13)$$

Surface measurements above underground workings prove that

$$\int_{-\infty}^{\infty} \frac{\partial u(x, z=0)}{\partial x} dx = 0, \quad (14)$$

i.e. the sum of extensions on the surface equals the sum of compressions, therefore the second solution is real and it is that should be dealt with.

We can write

$$\frac{\partial}{\partial x} \int_{-\infty}^{\infty} u(x, z) dx = 0 \quad (15)$$

the solutions of it may be

$$\int_{-\infty}^{\infty} u(x, z) dx = \begin{cases} \text{constant} \\ 0 \end{cases}, \quad (16)$$

i.e. the sum of the horizontal displacements is either constant or zero. Due to the symmetry in the horizontal displacements, the real solution is:

$$\int_{-\infty}^{\infty} u(x, z) dx = 0. \quad (17)$$

It follows for the vertical motions

$$\frac{\partial}{\partial z} \int_{-\infty}^{\infty} w(x, z) dx = 0 \quad (18)$$

the solutions of it can be

$$\int_{-\infty}^{\infty} w(x, z) dx = \begin{cases} \text{constant} \\ 0 \end{cases}, \quad (19)$$

i.e. the sum of the vertical displacements is either constant or zero.

Let us divide the semi-space into two domains: that above  $0 \leq z < H$  and that below  $H < z \leq \infty$  the working. Let the vertical displacement in the roof be  $w_H$  and that in the floor  $w_L$ .

Experiences tell that displacements in the roof are subsidences whose sum, i.e. the area below the subsidence curve does not equal zero. Therefore for this domain the following equation holds:

$$\int_{-\infty}^{\infty} w_H(x, z) dx = \text{constant} \quad (0 \leq z < H). \quad (20)$$

This equation says that the sum of subsidences, i.e. the area under the subsidence curve is the same on any level of the overlying layers. It can be proved that the area under the subsidence curve (Somosvári 1973) is

$$\int_{-\infty}^{\infty} w_H(x, z) dx = 2l_x Ms \tag{21}$$

whereas

- $s$  subsidence factor,
- $M$  worked-out thickness of layer,
- $2l_x$  width of worked-out area.

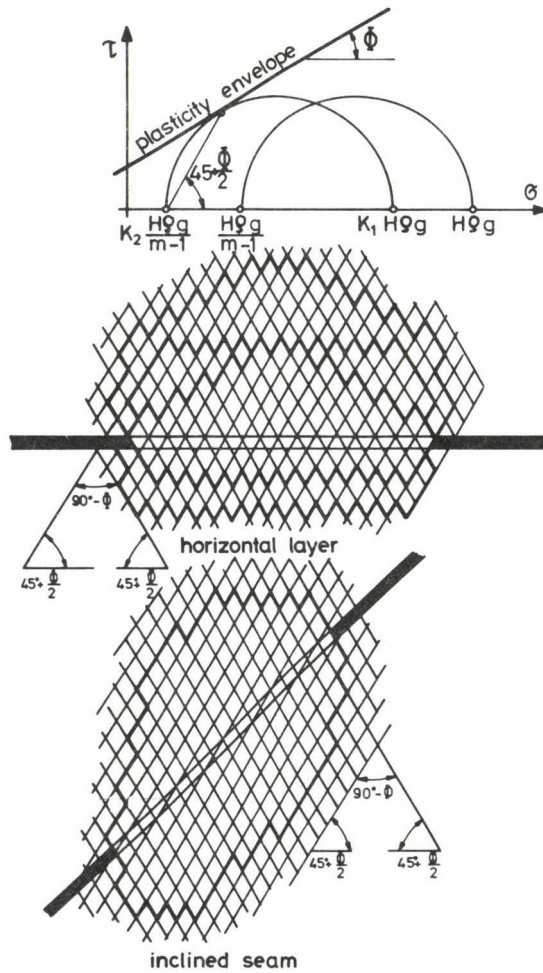


Fig. 1. Expansion of rocks surrounding a worked-out layer

Experiences show that the vertical displacements in the floor are subsidences and rises, therefore here the solution

$$\int_{-\infty}^{\infty} w_L(x, z) dx = 0 \quad (22)$$

holds, i.e. the sums of subsidences and rises are the same. Rises emerge beneath the worked-out area in consequence of the load decrease, while subsidences take place outside the worked-out area due to the transferred load. Consequently, beneath the worked-out area an increase of volume, i.e. an expansion sets in. Because of symmetry there also will be a volume increase, i.e. an expansion in the domain above the worked-out area.

Beneath and above the worked-out area a volume increase, i.e. a loosening or expansion takes place even if the rock is in elastic state. In most cases, however, the expansion is as intensive as to produce a plastic and cracked state in the surrounding rock. Using the protective layer mining method, the rocks beneath and above the worked-out layer suffer vertical expansion, i.e. the vertical and, consequently, the horizontal stresses decrease, until Mohr's circle characteristic for the state of stress does not reach the plasticity limit (Fig. 1). The rock gets now into a plastic and cracked state and slipping planes with an inclination angle of  $\alpha = 45 + \Phi/2$  are formed in the surrounding rock domain (Fig. 1). Along these planes more arching surfaces towards the roof can arise in dependence of the original cleatedness and system of cracks of the rock as well as in dependence of the strength and compressibility of the worked layer. The loosened rock masses are also limited by an arch beneath the protective layer (Fig. 1) which, however, can only be smaller than that in the roof because of the effect of dead weight. Since the expansion is principally vertical, the arch in the roof narrows with an increasing dip of the inclined seams, while that in the floor widens.

### Mechanism of rock and gas outbursts

The solid and gaseous phases of the gas-bearing rock form a load-bearing rock-gas system. The two phases of the system are in mutual physical (mechanical and thermal) interaction. At the beginning of outbursts mechanical interactions are decisive among these interactions.

The load on the rock is partly carried by the solid structure of the rock, partly by the free gas in the pores and cracks. The stresses in the structure are called effective stresses while the pressure in the free gas is the pore gas pressure. Any change in the pore gas pressure results in a change of the effective stresses and *vice versa*.

The pore gas pressure reduces the strength of the rock, because its expanding effect acts against the normal stress, hence the internal friction decreases. With increasing load on the solid structure the state approaches deterioration. In this

process it is of great importance whether the pore gas pressure increases or decreases, i.e. whether the strength increases or decreases with increasing load. If pore gas pressure increases with the increase of load on the solid structure, i.e. the strength reduces, the starting process of deterioration accelerates and proceeds in an explosion-like way. If pore gas pressure, however, decreases with the increase of load on the solid structure, i.e. the strength increases, deterioration starts only under high load on the one hand and the process of deterioration slows down on the other. Under natural circumstances a change of load combined with the reduction of rock volume brings about a situation in which the pore gas pressure increases, therefore this is the only case when deterioration proceeds in an explosion-like way. These circumstances can be found in the rock zones (rock cores) in front of the face of drifts and workings and beneath the shaft sole in the shaft sinking.

Rock and gas outbursts are nothing else than the deterioration processes of rich-in-gas rock zones in front of faces of drifts and workings and beneath shaft soles and this deterioration takes place in an explosion-like way under the reduction of rock volume.

The basic reason of outbursts is the strength reducing effect of pore gas pressure which induces a chain-reaction-like process, if the deterioration is combined with volume reduction which accelerates the process of deterioration and makes it explosion-like (Somosvári 1982a, Somosvári 1982b).

The great amount of gas released during outbursts comes from the gas adsorbed on the pore walls. Adsorption has namely a dynamic character: a continuous exchange of molecules takes place between the free gas and the adsorbed layer (adsorption and desorption). The equilibrium is achieved by an equal rate of these processes. Thus a quick, dynamic desorption can proceed in consequence of the rapid decrease of the pore gas pressure during outbursts.

The condition of deterioration can be written as

$$\frac{\sigma_C}{p_{\max}} < \frac{\tan^2\left(45 + \frac{\Phi}{2}\right) - 1}{1 - q} \quad (23)$$

for the places of the maxima of (effective) stresses in the solid structure of the rock zones in front of faces. In Eq. (23):

- $\sigma_C$  uniaxial compressive strength in the rock zone in front of faces,
- $\Phi$  angle of internal friction of the rock,
- $q$  rigidity coefficient of the rock ( $q = \sigma_Y / \sigma_C < 1$ )
- $p_{\max}$  maximum pore gas pressure in front of faces,
- $\sigma_Y$  yield point of the rock.

Our correlation is more precise if the condition of deterioration is expressed with cohesion instead of compressive strength because the compressive strength is a

function of the angle of internal friction and cohesion  $c$ :

$$\sigma_c = 2c \tan \left( 45 + \frac{\Phi}{2} \right). \quad (24)$$

On substituting we have for the condition of deterioration

$$\frac{c}{p_{\max}} < \frac{1}{1-q} \frac{\tan^2 \left( 45 + \frac{\Phi}{2} \right) - 1}{2 \tan \left( 45 + \frac{\Phi}{2} \right)}. \quad (25)$$

These inequalities contain the basic condition of deterioration. The outburst danger is high if cohesion is small, while the pore gas pressure, the internal friction and the coefficient of brittleness of the rock are great (Somosvári 1982a, Somosvári 1982b).

The parameters of these equations are the main parameters characterizing outburst danger. The parameters affecting outburst danger are Young's modulus  $E$ , Poisson's ratio, the void coefficient  $e$  and the gas permeability  $k$  of the rock, the cross-sectional dimension of the excavation  $R$ , the efficiency of the support applied  $CR$  and the initial pore gas pressure  $p_0$ . All these parameters influence the value of the maximum pore gas pressure. The maximum pore gas pressure in front of the face, i.e. the outburst danger is the greater, the greater the initial pore gas pressure, the Poisson's ratio and the drift cross-section is and the lower Young's modulus, the void coefficient (porosity), the gas permeability and the efficiency of the support is. These rock parameters are of course not independent of each other, e.g. cracked rocks with lower strength and lower cohesion have smaller Young's moduli and higher void coefficients and gas permeabilities.

### Effect of the protective layer mining method

The analysis of the effect of the protective layer mining method on rock and gas outburst has to deal first of all with the main and influencing parameters.

Using protective layer mining method, the load on the protected seam decreases and a volume increase sets in due to the transferred stresses irrespective of the fact whether the protecting mining operations are carried out beneath or above the protected seam. Volume increase results in turn in a reduction of the initial pore gas pressure. Previously closed crack surfaces will open due to the volume increase of the rock and, in consequence, the void coefficient and the gas permeability of the layer will also increase. Deformations give a cracked character to the protected layer which further increases the gas permeability and reduces the cohesion and strength related to zero pore gas pressure, Young's modulus, Poisson's ratio and the coefficient of

brittleness of the rock. If the intermediate layers are also cracked, the increase of gas permeability ensures an intensive escape of the gas and a further reduction of pore gas pressure.

The protective layer mining method brings about the following changes in the parameters of the protected layer:

pore gas pressure:	$p_0 - \Delta p$	$(\Delta p > 0)$
compressive strength:	$\sigma_{c0} - \Delta \sigma_c$	$(\Delta \sigma_c > 0)$
cohesion:	$c_0 - \Delta c$	$(\Delta c > 0)$
coefficient of brittleness:	$q_0 - \Delta q$	$(\Delta q > 0)$
void coefficient:	$e_0 - \Delta e$	$(\Delta e > 0)$
gas permeability:	$k_0 + \Delta k$	$(\Delta k > 0)$
Young's modulus:	$E_0 - \Delta E$	$(\Delta E > 0)$
Poisson's ratio:	$m_0 - \Delta m$	$(\Delta m > 0)$ .

The most changes in rock parameters act against bringing about of outbursts, but there are a few parameters whose changes increase the outburst danger. Such unfavourable changes are the reduction of the compressive strength related to zero pore gas pressure and those of the cohesion and of Young's modulus. These effects are, however, amply compensated for by the other changes.

For a quantitative assess of outburst danger let us introduce besides

$$B = \tan^2 \left( 45 + \frac{\Phi}{2} \right) \quad (26)$$

also the denotion

$$n = \frac{p_{\max}}{(1-q)c} \frac{B-1}{2\sqrt{B}}. \quad (27)$$

If  $n < 1$  there is no outburst danger, if  $n > 1$ , there exists an outburst danger.

The parameter characterizing outburst danger becomes for a layer protected by protective layer mining method:

$$n = \frac{p_{\max} - \Delta p}{(1-q + \Delta q)(c - \Delta c)} \frac{B-1}{2\sqrt{B}} \quad (28)$$

or

$$n = \frac{p_{\max} - \Delta p}{(1-q)c - [(1-q)\Delta c - \Delta q(c - \Delta c)]} \frac{B-1}{2\sqrt{B}}. \quad (29)$$

The outburst danger is less due to the protective layer mining method, if the change is characterized by:

$$\Delta p > (1-q)\Delta c - \Delta q(c - \Delta c). \quad (30)$$

Since coals affected by outburst danger are brittle, i.e.  $q \rightarrow 1$  and the cohesion does not decrease to zero, i.e.  $(c - \Delta c) > 0$ , our inequality (30) is always met if the protective layer mining method is applied, since:

$$(1 - q)\Delta c - \Delta q(c - \Delta c) < 0 \quad \text{and} \quad \Delta p > 0. \quad (31)$$

The inequality (31) shows that the greater the reduction of pore gas pressure  $\Delta p$  is, or the closer  $q$  stands to unity, i.e. the more brittle the coal, or the greater the reduction of brittleness  $\Delta q$ , or the greater the cohesion  $c$ , or the smaller the reduction of cohesion  $\Delta c$ , the greater the reduction of outburst danger will be due to the effect of protective layer mining method.

The action mechanism of the protective layer mining method can be explained as follows: Load reduction and, in consequence, volume increase take place in the affected part of the layer, which result in a decrease of pore gas pressure. Load reduction, volume increase and deformation open the closed cracks of the rock and may produce new cracks, therefore the gas permeability of the rock increases by orders of magnitude and the gas stored in the pores may escape through the crack systems of the intermediate layers, and the pore gas pressure can be further effectively reduced. Thus, a much lower maximum pore gas pressure can build up in front of the rock face, if later excavations are opened in the protected layer. Having more extended systems of cracks, the brittleness of the layer decreases. This kind of change of these parameters largely reduces the outburst danger. The angle of internal friction of the rock practically does not change, thus it has no effect on outburst danger. Cohesion decreases with the extension of cracks promoting the increase of outburst danger. This effect, however, is exceeded by that of reduction of brittleness and pore gas pressure, thus after all the degree of outburst danger concerning the protected layer always decreases.

### References

- Somosvári Zs 1973: Determination of the field of motion of roof rocks (for semihorizontal seams). (In Hungarian) Ph D Thesis, Miskolc
- Somosvári Zs 1982a: Mechanism of rock and gas outbursts. *Acta Geod. Geoph. Mont. Hung.*, 17, 29–49.
- Somosvári Zs 1982b: Main parameters of the rock and gas outburst danger. *Acta Geod. Geoph. Mont. Hung.*, 17, 51–66.
- Szirtes L 1971: Combatting coal and gas outburst. (In Hungarian) Műszaki Könyvkiadó, Budapest



## CALCULATION OF AIR LOSSES AND SUITABLE VENTILATOR DISTANCES FOR VENTILATING PIPES

J JANOSITZ<sup>1</sup>

[Manuscript received April 5, 1983]

This paper aims at evolving a calculation method which renders it simple and easy to determine the air loss of ventilating pipes and the suitable place of air pipe fans.

Setting out from the required flow rate of air at the end of the ventilating pipe the calculations provide the number of the air pipe fans to be set and their effective distance from each other. For the calculations we used the air transport function depending on the air pipe fan with given characteristic and the length  $L$  of the ventilating pipe with given gap-size. The corresponding values of this function cannot only be calculated but measured in a very simple way as well.

**Keywords:** air loss; air pipe fans; ventilation; ventilator distance

### *Symbols*

$2b$	gap width
$d$	hydraulic diameter
$D$	inner pipe diameter
$F$	cross-section
$h$	depression
$l, L$	length
$M$	operating point
$\Delta p$	pressure difference
$Q$	flow rate
$R$	resistance
$Re$	Reynolds-number
$U$	wetted perimeter
$v$	velocity
$\lambda$	friction factor
$\nu$	kinematic viscosity
$\rho$	density

### **Calculation of air loss between the air pipe members**

Both Hungarian and foreign studies generally calculate air loss of the air pipe fans as continuously changing values along the length, whereas air loss always related to a concrete place of the ventilating pipe (Fig. 1).

<sup>1</sup> Technical University for Heavy Industry, Miskolc, Hungary

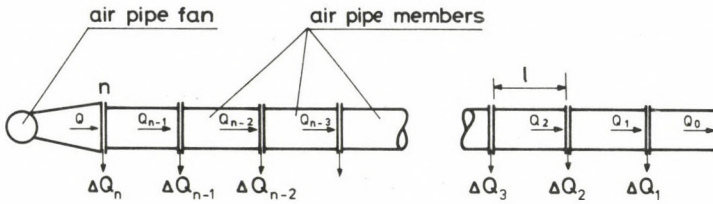


Fig. 1. Symbols representing air flow rates flowing through the air pipe members and flowing out at the joints

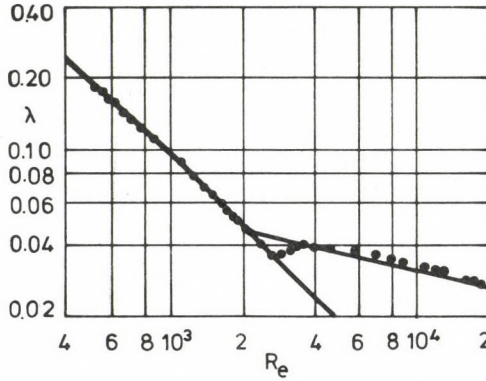


Fig. 2. Air friction factor of the flow in the gaps as a function of Reynolds-number

Let us consider how the quality of air escaping from the air pipe in these places changes as a function of leakage. Hahnemann and Ehrett (1942) found the relationship plotted in Fig. 2 both for sharp and rounded flanges between the resistance factor and the Reynolds-number.

The measurement results plotted in Fig. 2 below  $Re_{crit} < 3000$  are on the Poiseuille-line

$$\lambda = 96/Re \tag{1}$$

and above  $Re \geq 4000$  are on the Blasius-line

$$\lambda = \frac{0.3164}{\sqrt[4]{Re}} \tag{2}$$

In these relationships

$\lambda$  — air friction factor (without dimension)

$$Re = \frac{vd}{\nu} \tag{3}$$

$d$  — hydraulic diameter, m

$$d = \frac{4F}{U} = 4b \quad (4)$$

$2b$  — gap width, m

$F$  — gap cross section,  $m^2$

$U$  — gap perimeter wetted by the medium flowing in the gap, m

$v$  — mean velocity of the medium flowing in the gap, m/s

$\nu$  — kinematic viscosity of the medium flowing in the gap,  $m^2/s$ .

I.e. if the width of the joining flanges of the air pipes with diameter  $D$  is  $s$  and the mean value of the gap width on both sides of the sealing is  $2b$ , the flow rate of the outflowing air at the sealing is

$$Q = 4D\pi vb. \quad (5)$$

(Here the width of the joining flanges of the air pipes compared to  $D$  is negligible.)

The velocity of the outflowing air through the gaps obviously depends on the difference  $\Delta p$  of the pressure inside and outside the air pipes and the friction factor  $\lambda$  of the inner surface of the gaps, the size of the gap and the density of the air:

$$\Delta p = \lambda \frac{s}{4b} \cdot \rho \cdot \frac{v^2}{2}, \quad (6)$$

i.e.

$$v = \sqrt{\frac{8b \cdot \Delta p}{\lambda \cdot \rho \cdot s}}. \quad (7)$$

Making use of these results, depending on whether laminar or turbulent flow develops in the gaps, a different  $\lambda = \lambda(b)$  function can be substituted in the relationship of  $v$ .

Since

$$\lambda = \begin{cases} 96/Re & \text{if } Re \leq 3000 \\ \frac{0.3164}{\sqrt[4]{Re}} & \text{if } Re > 3000 \end{cases} \quad (8)$$

it follows that

$$v = \sqrt{\frac{8b \cdot \Delta p}{\lambda \cdot \rho \cdot s}} \quad (9)$$

and

$$Re = \frac{v \cdot 4b}{\nu}. \quad (10)$$

From the three relationships we have for  $Re \leq 3000$

$$\lambda = \frac{96}{\frac{4 \cdot b}{v} \cdot \sqrt{\frac{8b \cdot \Delta p}{\lambda \cdot \rho \cdot s}}}, \quad (11)$$

i.e.

$$\sqrt{\lambda} = \frac{12v}{b \sqrt{2b}} \cdot \frac{\sqrt{\rho \cdot s}}{\sqrt{\Delta p}} \quad (12)$$

from which

$$\lambda = \frac{144 \cdot v^2}{2b^3} \cdot \frac{\rho \cdot s}{\Delta p}. \quad (13)$$

Substituting this in  $v$

$$v = \frac{b^2}{3v} \cdot \frac{\Delta p}{\rho \cdot s}. \quad (14)$$

And if  $Re > 3000$ , one has similarly

$$\lambda = \frac{0.3164}{\sqrt[4]{\frac{4b}{v}} \sqrt{\frac{8b}{\lambda} \cdot \frac{\Delta p}{\rho \cdot s}}}. \quad (15)$$

From which

$$\lambda = \frac{0.3164^{\frac{8}{7}} \cdot (\rho \cdot s)^{\frac{1}{7}}}{\left(\frac{8b}{v}\right)^{\frac{2}{7}} \cdot (2b)^{\frac{1}{7}} \cdot (\Delta p)^{\frac{1}{7}}} \quad (16)$$

thus now  $v$  is

$$v = \sqrt[7]{\frac{8b \cdot \Delta p (\Delta p)^{\frac{1}{7}} (2b)^{\frac{1}{7}} \cdot \left(\frac{8b}{v}\right)^{\frac{2}{7}}}{0.3164^{\frac{8}{7}} \cdot (\rho \cdot s)^{\frac{1}{7}} \cdot (\rho \cdot s)}}. \quad (17)$$

With the possible reductions:

$$v = \frac{4 \cdot b^{\frac{5}{7}} \cdot \Delta p^{\frac{4}{7}}}{v^{\frac{1}{7}} \cdot (0.3164 \cdot \rho \cdot s)^{\frac{4}{7}}}. \quad (18)$$

Since under normal conditions

$$v = 15.37 \cdot 10^{-6} \quad \text{m}^2/\text{s} \quad (19)$$

and

$$\rho = 1.2 \quad \frac{\text{kg}}{\text{m}^3} \quad (20)$$

the flow rate of air in the gaps can be calculated by using

$$v = 33.885 \cdot b^{\frac{5}{7}} \cdot \left( \frac{\Delta p}{s} \right)^{\frac{4}{7}}. \quad (21)$$

Consequently, for planning duct-ventilation the following process is advisable:

Starting out from the necessary air quantity at the end of the ventilating pipe, the required pressure for the airflow in the air pipe and in the drift is calculated member by member and so is the air escape expected on the basis of pressure and gap size at the joining of the ventilating pipe.

### **Flow rate transportable by one air pipe fan as a function of the length of the ventilating pipe**

Let us take a ventilating pipe with a given diameter, tightness and length. Let us place an air pipe fan at one of the ends of the ventilating pipe and let us operate it in forcing method. Let  $Q$  be the flow rate through the air pipe fan and  $Q_0$  the flow rate at the end of the ventilating pipe. If the flow resistance of the leaks is independent whether the air is flowing out of or into the air pipes, then the flow rates in the ventilating pipe are the same for exhausting or forcing fan, they will differ only in the direction of the flow. This allows us to adapt the results obtained by examining the ventilation by forcing fan for the exhausting fan as well.

It can easily be proved that for a given ventilator and ventilating pipe the flow rates  $Q$  and  $Q_0$  depend on

- the flow resistance outside the ventilating pipe,
- the flow resistance inside the ventilating pipe and
- the air loss between the air pipe members.

With forcing ventilation the air flow outside the ventilating pipe starts when it leaves the ventilating pipe. In fore-winning faces the direction of the air leaving the air pipe turns back at the face and flows on in the opposite direction beside the ventilating pipe. The pressure loss of the air flow, between the points of leaving and reaching the ventilating pipe again, can be determined by the momentum equation written for the air flows (Prandtl 1965, p. 72.). In the calculations besides the friction pressure loss the loss due to the sudden increase in the cross-section must also be taken into account (Bende and Cifka 1974, p. 72.).

The value of the latter is

$$\Delta p_h = \frac{\rho}{2} (v_1 - v_2)^2 \quad \text{Pa}, \quad (22)$$

where  $v_1$  is the velocity of the air flowing out of the air pipe (m/s),  $v_2$  is the mean velocity of the air flowing backwards at the end of the air pipe in the drift (m/s) and  $\rho$  is the density of the air ( $\text{kg/m}^3$ ).

The local resistance is illustrated by the data of the Table found on page 968 of Mining Reference Book (1962). The local air resistance coefficient of a returning air flow concerned is  $\zeta \cong 3$  relying on the data of this Table. Thus the friction pressure loss is

$$\Delta p_s = 3 \cdot \frac{\rho}{2} \cdot v_2^2. \quad (23)$$

The total pressure loss at the end of the ventilating pipe is

$$\Delta p_t = \Delta p_h + \Delta p_s = \frac{\rho}{2} [(v_1 - v_2)^2 + 3v_2^2]. \quad (24)$$

From the continuity equation

$$F_1 v_1 = F_2 \cdot v_2, \quad (25)$$

where  $F_1$  is the free cross-section of the air pipe and  $F_2$  is that of the drift ( $\text{m}^2$ ).

For the pressure loss we have

$$p_t = \frac{\rho}{2} \cdot v_1^2 \left[ 1 - 2 \frac{F_1}{F_2} + 4 \left( \frac{F_1}{F_2} \right)^2 \right]. \quad (26)$$

Since  $F_1/F_2$  can be neglected in most cases

$$p_t \cong \frac{\rho}{2} v_1^2. \quad (27)$$

Let us now examine the pressure difference between the inner and outer sides of the air pipes at the joining points of the air pipe members.

Using the symbols in Fig. 1 the pressure difference at the joining place denoted by 1 will be

$$\Delta p_{1e} = \Delta p_t + \Delta p_{t1} + \Delta p_{v1}. \quad (28)$$

And at any other joining point

$$\Delta p_{ie} = \Delta p_{(i-1)e} + \Delta p_{li} + \Delta p_{vi}, \quad (29)$$

where

$$\begin{aligned} \Delta p_{li} &= R_{li} Q_{i-1}^2 \\ \Delta p_{vi} &= R_{vi} Q_{i-1}^2 \end{aligned} \quad i = 1, 2, \dots \quad (30)$$

In the relationships  $R$  is the air resistance ( $\text{kg/m}^7$ ) while subscript  $l$  refers to the air pipe,  $v$  to the drift and  $e$  denotes resultant quantities.

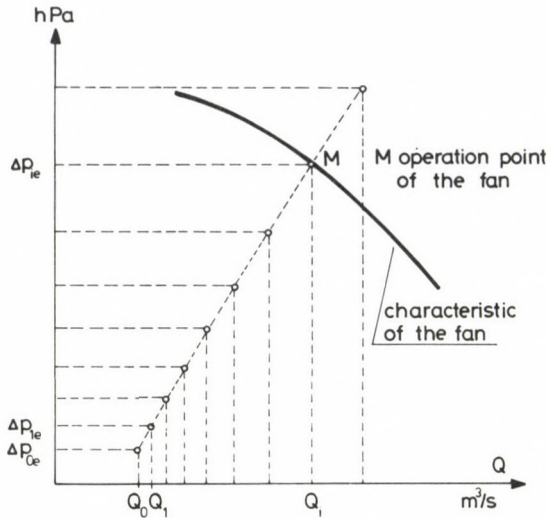


Fig. 3. Flow rate of air and depression necessary in the joints of the air pipe members for flow rate  $Q_0$  at the end of the ventilating pipe

Knowing the sizes of the gaps between the air pipe members air losses  $\Delta Q_i (i = 1, 2 \dots)$  can be calculated.

So

$$Q_i = Q_{i-1} + \Delta Q_i \tag{31}$$

Let us plot the corresponding values  $\Delta p_{ie}$  and  $Q_i (i = 0, 1, 2, \dots)$  on the plane  $Q-h$  (Fig. 3). In this figure the characteristic of the air pipe fan can also be plotted. The intersection of the curve laid across the set of points of the figure and the characteristic is an approximation of the operating point  $M$  of the fan. If on plane  $Q-h$  the coordinates of  $M$  are approximately  $Q_i$  and  $\Delta p_{ie}$ , this also means that with a given type of air pipe fan, an air quantity  $Q_0$  can be assured at the end of the ventilating pipe till  $i$  number air pipe units are installed. In case of fewer air pipe members the flow rate of air is greater than  $Q_0$  and it is smaller than  $Q_0$  if the ventilating pipe is longer.

These examinations show that the flow rate of air and depression of the air pipe fans are influenced by the air pipe resistance, air losses and the flow pressure loss outside the air pipes. The effect of the latter, however, if compared to that of the former is negligible in most cases.

In order to prove this claim let us examine resistances  $R_{l1}$  and  $R_{v1}$  of the unit-length air pipe and drift and let us compare these values.

Since

$$R_{l1} = 8 \cdot \frac{\lambda_l \cdot \rho}{d_l^5 \cdot \pi^2} \tag{32}$$

and

$$R_{v1} = \frac{\lambda_v \cdot \rho}{8} \cdot \frac{U}{F^3} = 8 \cdot \frac{\lambda_v \rho}{d_v^5 \cdot \pi^2} \quad (33)$$

where

$\lambda$  — air friction factor (dimensionless)

$d$  — hydraulic diameter, m

$$d = \frac{4F}{U} \quad (34)$$

$F$  — free cross-section of flow  $m^2$

It is also assumed for drifts that

$$F = \frac{d^2 \pi}{4} \quad (35)$$

$U$  — length of the contour lines of the free cross-section of flow, m.

The ratio of the air resistances of the two unit-lengths is

$$\frac{R_{v1}}{R_{l1}} = \frac{\lambda_v}{\lambda_l} \cdot \left( \frac{d_v}{d_l} \right)^5. \quad (36)$$

Usually it lies between

$$\frac{\lambda_v}{\lambda_l} = 3 - 10 \quad (37)$$

and

$$\frac{d_v}{d_l} = 4 - 8 \quad (38)$$

so it can be written that

$$\frac{R_{v1}}{R_{l1}} \leq \frac{10}{4^5} < \frac{1}{100}. \quad (39)$$

Thus compared to the air pipe resistance the drift resistance can generally be neglected. Consequently, compared to the pressure loss inside the air pipe the pressure loss of the drift of the same section is also negligible. Similarly, the pressure loss  $\Delta p_t$  at the end of the ventilating pipe is not considerable either compared to the depression of the air pipe fans even at great flow rates. Its value is only

$$\Delta p_t = \frac{\rho}{2} \frac{Q^2}{F_l^2} = \frac{1.2}{2} \cdot \frac{4 \cdot 5^2}{(0.4\pi)^2} \approx 38 \text{ Pa} \quad (40)$$

even for the smallest air pipe diameter ( $d_l = D = 0.4 \text{ m}$ ) and  $Q = 5 \text{ m/s}$  flow rate which is rarely transported in such air pipes.

Pressure loss like this already develops in a 0.8 m long air pipe if the flow rate is 5 m<sup>3</sup>/s, the pipe is perfectly tight, the air friction factor is very small ( $\lambda=0.015$ ) and the diameter is 0.4 m. Consequently, this value can also be neglected if the ventilating pipe is many times 10 m long. These negligible quantities render the examinations and calculations simple. Thus to calculate the expected air loss of the air pipe ventilation only the following data are necessary

- the gap parameter characterizing the expected air loss  $h$ ,
- the gap width  $s$ ,
- the air pipe diameter  $D$ ,
- the friction factor of the air pipe  $\lambda$  and
- the characteristic of the air pipe fan  $h=h(Q)$ .

From these data air flow rate  $Q$  of the air pipe fan can be calculated flowing into a ventilating pipe of  $n$  member each of length  $l$  and with an overall length  $L=ln$ , and air flow rate  $Q_0$  flowing out of the ventilating pipe. Owing to the great volume of the calculations it is advisable to use programmable microcomputer. The calculation can be done in an iterative way. Adopting the method of Fig. 3, for a selected  $Q_0$  flow rate  $Q$  flowing into the ventilating pipe and overpressure  $\Delta p$  can be calculated for  $n$  air pipe members. If point  $Q-\Delta p$  falls above the characteristic  $h=h(Q)$  on the  $Q-h$  plane, the starting value  $Q_0$  has to be decreased, otherwise it has to be increased. This means that the value of  $Q_0$  is altered till point  $Q-\Delta p$  belonging to  $Q_0$  falls within prescribed limits of the characteristic of the air pipe fan.

If both the characteristic of the air pipe fan and the parameters of the ventilating pipe are known, both  $Q_0$  flowing out at the end of the ventilating pipe and  $Q$  flowing through the air pipe fan at the beginning of the ventilating pipe will be a function of  $L$ , the length of the ventilating pipe.

The length of ventilating pipe with  $n$  members each of length  $l$  is  $L=nl$ . Thus  $L$  can take only discrete values and  $Q_0=Q_0(L)$  and  $Q=Q(L)$  also mean only relationships of discrete values. By illustrating these functions, sets of points will show on plane  $Q-L$ . If the value  $n$  is sufficiently great ( $n>10$ ), the points of these sets of points will be very close to each other. For convenience points next to each other are connected by straight lines; the function obtained this way will be used further on instead of the sets of points. Continuous functions of this type are shown in Fig. 4. To calculate the points of the function the equation of the characteristic in Fig. 5 was used and assumed that

- the diameter of the air pipe members is  $D=0.6$  m,
- the width of the flanges at the ends of the air pipe members is  $s=0.03$  m,
- the gap width between the sealing rings and the flange surfaces is  $2b=0.0004$  m and
- the mean friction factor of the inner surface of the ventilating pipe is  $\lambda=0.025$ .

Naturally, the gap width is very rarely constant. Its size can be different along the length of the ventilating pipe and at each joining along the flange surface. In spite of all this by

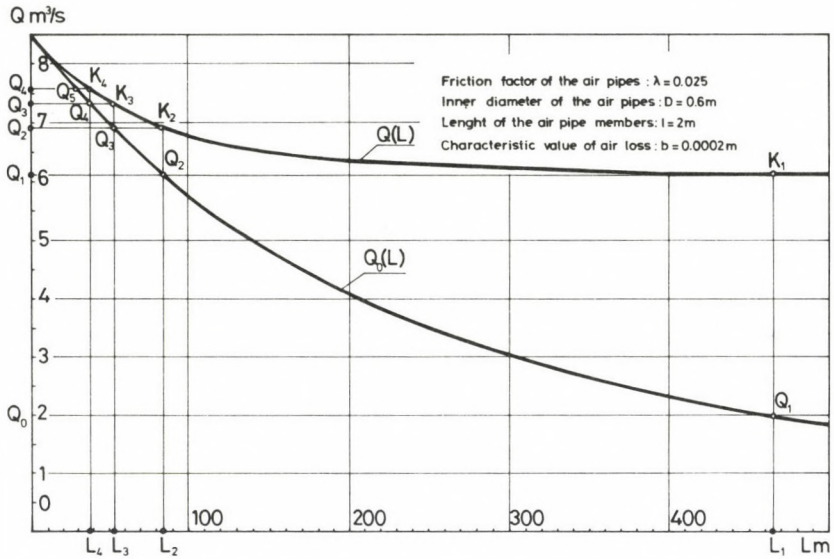


Fig. 4. Flow rate of SVM-6M Soviet air pipe fan and the flow rate reaching the end of ventilating pipe with given parameters as functions of distance

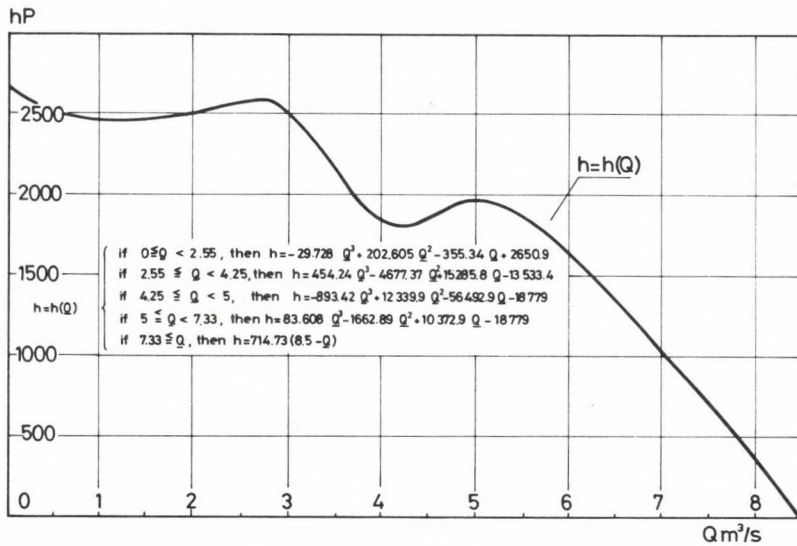


Fig. 5. Characteristic of SVM-6M Soviet air pipe fan

analysing and describing an idealized state, the flow phenomena in the ventilating pipe can be well characterized. Figure 4 was plotted with the listed parameters. By means of its curves the maximum ventilating pipe length  $L_1$  can be determined for a flow rate demand  $Q_0$  and, similarly, the number of the necessary air pipe fans if ventilation distances exceed  $L_1$  as well as the setting distance of the further air pipe fan compared to the previous one.

### Maximum air flow rate transportable by more air pipe fans along a given length

In this examination it is assumed that the characteristic of each air pipe fan to be installed and the previously listed parameters of each ventilating pipe member are the same.

Let us start the examination by determining the most favourable setting of two air pipe fans in the ventilating pipe. To do this different arrangements are represented in Fig. 6. If both fans are arranged in series at the beginning of the ventilating pipe, the over-pressure will be very high inside the air pipes at the beginning of the ventilating pipe. Where the pressure difference is great between the inner side of the air pipe and its outer environment, the air loss will also be greater. Subsequently out of the arrangements of Fig. 6, the smallest air flow rate  $Q_{01}$  at the end of the ventilating pipe can be expected for version 1. More air than this can be transported by arrangement 2, even more by 3 and the most by 4. With setting 4, however, there will be an exhausted part along the ventilating pipe already, where the air leaving the face will flow not out of the ventilating pipe but back into it. This circulation is not desirable in many cases, therefore solutions assuring over-pressure inside the air pipes will only be dealt with. Out of these solutions version 3 is the most favourable. The essence of this solution is that one fan assures the required depression and flow rate along one ventilating pipe. And the ventilating pipe length stretches as far as the next fan placed in the direction of the flow, if there are no more fans, as far as the end of the ventilating pipe.

Let us denote this sort of arrangement of the air pipe fans, their symbols and the distances between them as shown in Fig. 7. Let us determine these distances with  $Q_0 = 2 \text{ m}^3/\text{s}$ . The parameters of the ventilating pipe be the same as those in Fig. 4. Using function  $Q_0 = Q_0(L)$  of Fig. 4 the maximum ventilating pipe length belonging to flow rate  $Q_0 = 2 \text{ m}^3/\text{s}$  is  $L_1 = 464 \text{ m}$ . To this abscissa value point  $Q_1$  belongs on the curve  $Q_0 = Q_0(L)$  in Fig. 4 and point  $K_1$  on the curve  $Q = Q(L)$ . Figure 7 shows that flow rate  $Q_1$  flowing through air pipe fan 1 is equal to the flow rate leaving the  $L_2$ -long ventilating pipe. Thus  $L_2$  can be determined from Fig. 4 in the following way: an ordinate value equal to ordinate value  $Q_0 = Q(L_1)$  belonging to  $L_1$  has to be found on function  $Q_0 = Q_0(L)$  and its abscissa will give  $L_2$ . I.e. projecting point  $K_1$  horizontally on curve  $Q_0 = Q_0(L)$  point  $Q_2$  is obtained.

It can be seen that the arrangement of Fig. 4 ensures for flow rate  $Q_0$  to be transported with two air pipe fans for distance  $L_2 + L_1$  and the over-pressure inside the air pipes can be sustained along the whole length of the ventilating pipe.

As points with subscripts 2 were obtained from those with subscripts 1, points with subscripts 3 and 4 can also be constructed in the same way in Fig. 4. Naturally, this can be carried on and all lengths  $L_i$  interpreted in Fig. 6 can be determined in this way.

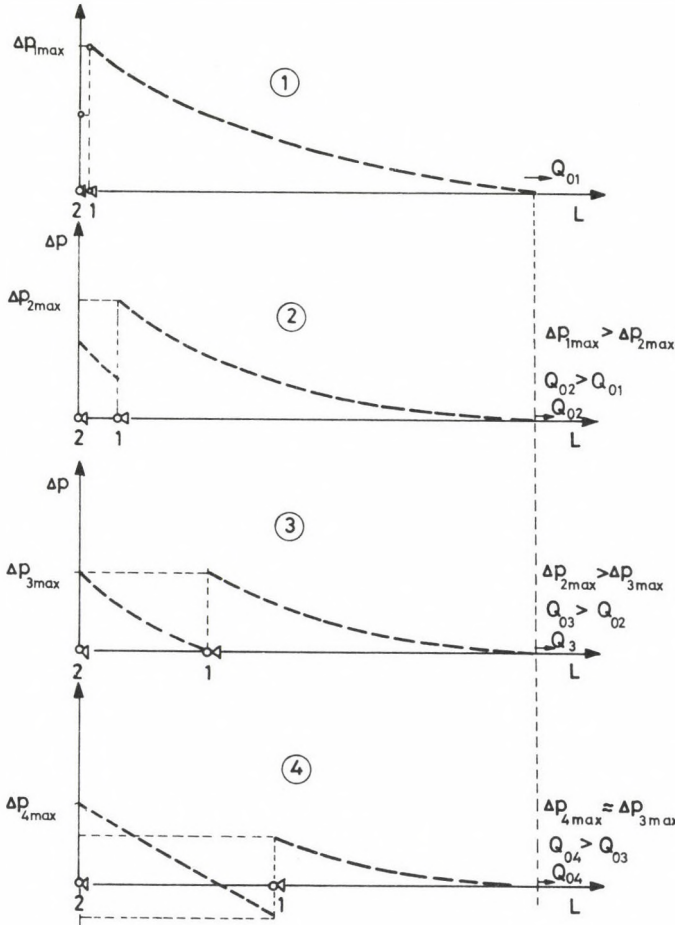


Fig. 6. Pressure difference between the ventilating pipe and the drift as a function of length for various arrangements of two air pipe fans.  $Q_{0i}$  denote flow rates at the end of ventilating pipes

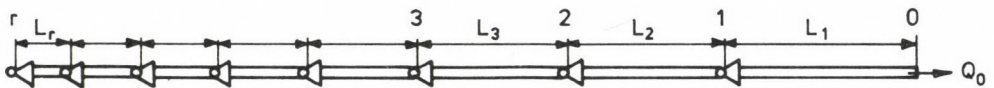


Fig. 7. Symbols denoting distances between the fans installed in the ventilating pipe

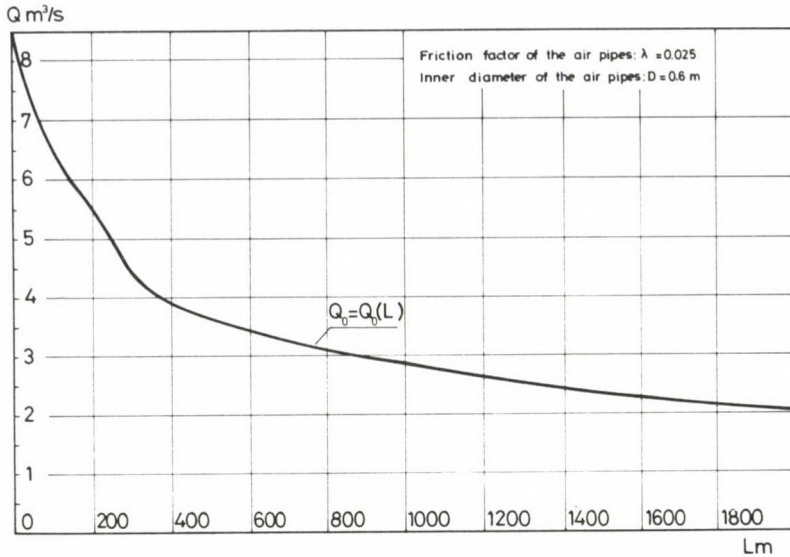


Fig. 8. Flow rate of SVM-6M Soviet air pipe fan transported to the end of ventilating pipe with given parameters as a function of distance without air losses

In Fig. 4  $L_2 = 84 \text{ m}$ ,  $L_3 = 52 \text{ m}$  and  $L_4 = 38 \text{ m}$ . Our data represent a state of good tightness. Obviously, even in this case by installing the second, third and fourth fans the potential to increase the air transportation distance is rapidly decreasing compared to the air transportation distance achieved by one fan.

In Fig. 8 results achieved by the Soviet air pipe fan SMV-6M are illustrated; flow rates obtainable at the end of the ventilating pipe without air loss are represented as a function of distance. This figure shows beyond question that one air pipe fan is sufficient for the distance  $L_1 + L_2 + L_3 + L_4 = 638 \text{ m}$  by improving the sealing and decreasing  $b$ . By this kind of decisions it is always advisable to take into account that in return for additional expenditure entailed by improving the sealing, with a longer ventilating pipe

- the expenses of purchase, installation and operation of one or more air pipe fans can be saved,
- better air supply can be achieved on the faces in most cases,
- the noise of the ventilating pipe environment will be smaller and
- the heat transferred to the transported air will also be smaller.

With air pipe fans the expenses of operation are not negligible besides those of purchase and installation. The power intake of the mentioned Soviet fan type alters between 12–14 kW depending on the transported flow rate of air. Calculating with an

average 13 kW and 1 Ft/kW electric energy cost, the energy cost of the operation is about 300 Ft per day.

From Fig. 8 it can also be assessed to what extent the air supply can be improved with a better sealing. If the difference in vertical sense between the two ends of the ventilating pipe can be neglected, the power consumption of the fan is entirely converted into heat-energy. And this heat is usually absorbed by the air.

The expected increase of enthalpy of the air for one air pipe fan is

$$\Delta h_{\max} = \frac{N}{\rho_t Q} \quad (41)$$

where

- $\Delta h_{\max}$  the increase of the enthalpy of the air in kJ/kg, assuming the energy converted into heat is fully absorbed by the air;
- $N = N(Q)$  the energy consumption of the air pipe fan in unit time in kW depending on the flow rate (for the fan SVM-6M one has  $N = \text{constant} = 12 \text{ kW}$ );
- $\rho_t$  average density of air flowing in and outside the ventilating pipe,  $\text{kg/m}^3$ ;
- $Q$  the flow rate of air flowing through the air pipe fan in  $\text{m}^3/\text{s}$ .

### Planning air pipe transportation from measurement data

In our investigations regular gaps were assumed between the air pipe members. These regular gaps allow to determine in the previously outlined way the air escape and the air transportation of the air pipe fan with a given characteristic depending on the length of the ventilating pipe. The accuracy of these calculations depends on how properly the values approaching the sizes of the actual gaps are chosen.

To find the right values and render the concrete planning more reliable it is advisable to carry out measurements. It is very simple in most cases. The ventilating pipe length of the partially ventilated faces is mostly not greater than a few meters in the beginning; it takes days and weeks for the ventilating pipe to become longer and reach a length of a few hundred meters.

Therefore, if the flow rate of air flowing through the air pipe fan and that reaching the end of the ventilating pipe and the length of the ventilating pipe are regularly measured from the beginning of ventilation, co-ordinates of several points of functions  $Q(L)$  and  $Q_0(L)$  are obtained by these measurements.

More points gained by further measurements to the above mentioned pair of curves can be obtained as long as one fan guarantees the necessary flow rate  $Q_0$  at the end of the ventilating pipe. The ventilating pipe length will now be  $L_1$  according to the previous symbols.

Plotting the so far measured values on  $Q-L$  plane, functions  $Q(L)$  and  $Q_0(L)$  can be drawn through the obtained points. Making use of these curves the number of air pipe fans necessary and the suitable arrangement can be determined for the maximum ventilating pipe length planned.

### References

- Bende I, Cifka I 1974: Mine ventilation, measurements and checking methods. Technical Publisher, Budapest
- Hahnemann H, Ehret L 1942: Der Strömungswiderstand im geraden, ebenen Spalt unter Berücksichtigung der Einlaufverluste. *Jahrbuch der deutschen Luftf.-forschung*, 186—207.
- Hartmann W 1942: Messung von Stopfbuchsverlusten. *VDI Forschung* 13, 165—188.
- Mining Reference Book 1962, Volume III. Mine ventilation. Technical Publisher, Budapest
- Prandtl L 1965: Strömungslehre. 7. Aufl. Friedr. Vieweg und Sohn. Braunschweig
- Schumacher W 1930: Untersuchungen über Strömung in engen Spalten. *Ingenieur-Archiv I.B.* 444—468.
- Tritnovsky K 1954: Untersuchungen an berührungsfreien Dichtungen. *Konstruktion*, 6, 389—392.
- Voss W 1956: Die Planung von Sonderbewetterungsanlagen. *Glückauf*, 92, 693—717.
- Winkler H 1958: Untersuchungen über das Verhalten berührungsfreier Dichtungen, insbesondere Durchblick-Stopfbüchsen für Turbomaschinen I. Teil. *Energietechnik*, 8, 388—394.
- Winkel R 1923: Die Wasserbewegung in Leitungen mit Ringsplatt-Durchflussquerschnitt (Labyrinthdichtungen). *Zeitschrift für angewandte Mathematik und Mechanik B.*, 3, 251—257.



## STUDY OF JOINT APPLICATION OF ANIONIC AND NONIONIC SURFACTANTS IN ENHANCED OIL RECOVERY

LAKATOS I<sup>1</sup>, MILLEY GY<sup>1</sup>, TÓTH J<sup>1</sup>, KRISTÓF M<sup>2</sup>, CAPELLE A<sup>3</sup>,  
WAGNER O<sup>1</sup>, LAKATOS-SZABÓ J<sup>1</sup>, FELIÁN B<sup>1</sup>

[Manuscript received February 3, 1984]

The paper deals with the joint application of nonionic and anionic surfactants in enhanced oil recovery. A detailed physico-chemical investigation of the liquid systems containing tensides, determination of a practical composition of displacement liquids, and optimization of the slug system by displacement tests were included into the studies. The tests were carried out under Algyő-2 formation conditions. The surfactants meet the rigorous requirements of a field application. As a result of laboratory experiments, the theoretical bases for a new, economic, and efficient oil recovery method could have been developed.

**Keywords:** anionic surfactants; displacement liquids; nonionic surfactants; oil recovery; sequential injection

### Introduction

The application of nonionic surfactants in enhanced oil recovery (EOR) has become an issue of central interest in recent years (Troguis et al. 1977, Hayes et al. 1979, Ramirez et al. 1980, Ziegler and Handy 1981, Capelle and Littmann 1982a, 1982 b). Laboratory investigations have shown that thermal stability and sorption properties of nonionic tensides, their effect on interfacial tension, wettability, and emulsification *etc.* are generally more favourable under reservoir conditions than those of other surfactants widely used at the present time. Accordingly, extensive research activity has been launched to determine the phase behaviour of micro- and macroemulsions, their rheological properties and flow behaviour in porous media, and finally the effect of surfactants on displacement efficiency.

This endeavour served as a professional background for the international agreement signed in 1979 by Chemische Fabrik Servo and MINERALIMPEX, with the main objective to study the nonionic and modified nonionic surfactants produced

<sup>1</sup> Chemical Research Laboratory for Mining of the Hungarian Academy of Sciences, H-3515 Miskolc-Egyetemváros, P.O.B. 2.

<sup>2</sup> Nagyalföld Oil and Gas Production Company, H-5001 Szolnok, P.O.B. 86

<sup>3</sup> AVEBE B. A., Foxhol, Holland

by the Dutch company as to their applicability for oil displacement in domestic hydrocarbon reservoirs, primarily in the Algyő-2 field.

The joint research included a detailed physico-chemical investigation of liquid systems containing surfactants, the determination of the convenient concentration of displacing phase, and optimization of the flooding system by displacement tests. As an ultimate goal the research envisaged the development of a new recovery technique and the preparation of an industrial pilot test. The paper shortly surveys the results of the two-year research program.

## Physico-chemical investigations

### *Characterization of surfactants*

Two surfactants of very similar structures but rather different in their physical and chemical properties were studied. One of them (which will be referred to as Product B) was a nonionic tenside, a 4-ethoxy-nonyl-phenol, with 100 % active content. The other (hereinafter referred to as Product A) represented a sulphonated derivative of the same tensides, and had an active content of 35 %.

Owing to their structure, the tensides showed different solubility. Whilst Product B was practically insoluble in water, the tenside A essentially dissolved only in the aqueous phase. When dispersed in water, the nonionic tenside formed water external emulsion for a short time, to be followed after several hours of standing by a gradual phase separation and settling out of the surfactant. The stability of the dispersed system

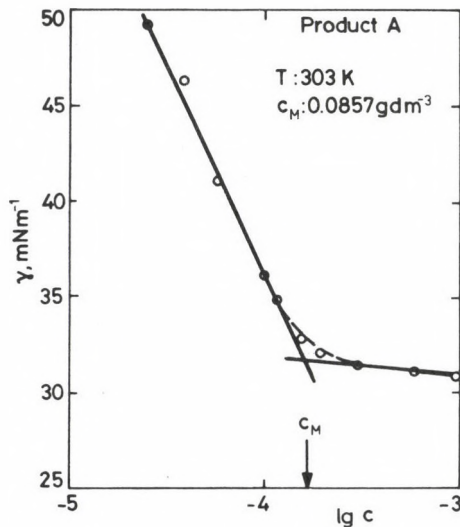


Fig. 1. Dependence of the interfacial tension on the concentration of Product B

was largely dependent on the electrolyte concentration of the aqueous phase and temperature, and prolonged opalescence has been indicative of the extremely small drop size of the dispersed tenside.

By calculating the thermodynamic functions for the micelle formation of ethoxylated nonyl-phenols it can be proved that the shorter the ethoxy chain length and the higher the temperature and the electrolyte (NaCl) concentration, the more stable will be the structure of micellar solutions (Bedó et al. 1984). Thus, the 4-ethoxy-nonyl-phenol and its sulphonated derivative can be regarded the most stable member of the homologous series. According to Fig. 1, the critical micelle concentration (c.m.c.) of the anionic tenside is less than  $0.1 \text{ g dm}^{-3}$  in an ion-free solutions, and the c.m.c. is even lower in presence of inorganic salts and at reservoir temperatures.

Due to the micelle formation ability of the anionic tenside, on the one hand, and the micelle and solutions structure, on the other, Product A solubilizes the water-insoluble nonionic Product B. The solubilization is a result of complex micelle formation. Thus, the aqueous solutions containing at least the same amount of Product A as Product B are completely transparent, and stable without separation of Product B.

#### *Thermal stability and compatibility of tensides*

The direct aim of the investigations was to determine the physical and chemical stability of tensides under Algyő-2 reservoir conditions in presence of formation liquids and rocks, since this parameter is one of the crucial criteria of field application. Further the studies were also concerned with the compatibility of surfactants with various materials, mainly with polymers used for mobility control.

The thermal treatments were carried out in a thermostated high-pressure cell. The tenside concentration was determined by gravimetric (phosphorus-tungsten-acid) and volumetric (two-phase titration) methods. Molecular spectroscopy was used to detect any possible structural changes. The interfacial and surface tensions of the initial and the thermal-treated solutions were determined under atmospheric conditions using the pendent drop technique and a Du Nouy tensiometer. The stability tests had in common that the final active content of the solutions was always  $10 \text{ g dm}^{-3}$ . In cases where both Product A and Product B were present in the solution, the tenside solution had the following composition:

Product A:	$7.50 \text{ g dm}^{-3}$
Product B:	$2.50 \text{ g dm}^{-3}$
<i>i</i> -Propyl-alcohol:	$1.50 \text{ g dm}^{-3}$ .

The results concerning the stability and compatibility of the surfactants can be summarized as follows:

- a) The nonionic and anionic tensides, separately or jointly, have excellent thermal stability; at 363 K and after thermal treatment of 48 hours no structural change can be detected by molecular spectroscopy.
- b) The stability of the tensides remains practically unchanged not only in an inert atmosphere but also in presence of oxygen and carbon-dioxide. Thus no stabilizers (oxygen scavengers) are required even under field conditions.
- c) The presence of oil and rocks has a negligible effect on stability of the surfactants.
- d) In presence of oil, a slight decolouration of the tenside solution is observed, but it is attributed to a partial solubilization of the oil, therefore this fact does not influence the tenside stability. Similarly the occasionally occurring opalescence comes from the insoluble Product B and a solubilization problem, respectively.

It was also proved by special stability tests that degradation did not occur even during a thermal treatment over 40 weeks, and the surfactants maintained their favourable properties intact. In this connection it is worth mentioning that properties

**Table I.** Effect of thermal treatment on interfacial tension

Experimental conditions ( $T=260\text{ K}$ ,  $p=20\text{ bar}$ )

Tenside	A	A + B	A	A + B	A + B	A + B	A + B	A + B	A + B
$c_{\text{FAA}}, \text{ g dm}^{-3}$	10	10	10	10	10	10	10	10	5
Water	NaCl	NaCl	Alg-2	Alg-2	Alg-2	Alg-2	Alg-2	Alg-2	Alg-2
Gas phase	N <sub>2</sub>	N <sub>2</sub>	N <sub>2</sub>	N <sub>2</sub>	N <sub>2</sub>	N <sub>2</sub>	O <sub>2</sub>	CO <sub>2</sub>	N <sub>2</sub>
Rock	—	—	—	—	Alg-2	Alg-2	Alg-2	Alg-2	Alg-2
Oil	—	—	—	—	—	Alg-2	Alg-2	Alg-2	Alg-2
Duration of treatment, h	Interfacial tension, $\text{mN m}^{-1}$								
0	6.4	10.5	5.3	10.5	6.3	7.0	7.1	5.1	4.9
1	6.3	9.5	5.4	10.4	5.5	7.3	7.7	6.6	5.1
3	5.9	9.9	6.0	10.4	6.4	7.3	7.9	8.4	5.1
6	6.0	10.0	5.2	10.0	6.5	7.6	7.8	5.85	5.0
12	6.2	9.7	5.5	10.5	6.8	7.6	8.1	6.28	4.8
24	6.2	10.3	5.5	10.6	5.9	7.8	7.0	6.74	5.0
36	6.1	9.9	—	—	—	8.2	7.3	7.05	4.8
48	—	—	—	—	—	9.4	7.9	7.15	4.8

influencing interfacial tension did not change either, as is demonstrated by data in Table I.

The compatibility study of tensides and polymers aimed to indicate whether any precipitation, rheological anomaly, *etc.* liable to prohibit their joint application occurs during the mixing of the two materials or solutions. Polymers having an average molecular mass of  $1-2 \cdot 10^6$ , and hydrolized 0–10–20–30% were used for the tests. Results of the experiments, which were also carried out under field conditions, proved that compatibility of Products A and B with both the homo- and copolymers does exist, and it satisfies even the most rigorous requirements. As a final result, it could be stated that the stability of 4-ethoxy-nonyl-phenol and its sulphonated form is excellent, and there are no stability and compatibility reasons that might preclude their application under field conditions.

#### *Effect of tensides on interfacial tension*

The interfacial tension of different water/oil systems was determined under formation conditions, by a special apparatus built on the pendent drop principle. Measurements were performed for two-phase systems both at equilibrium and non-equilibrium state. Our findings based on the experimental results are as follows:

a) In solutions made of formation water containing both nonionic and anionic tensides

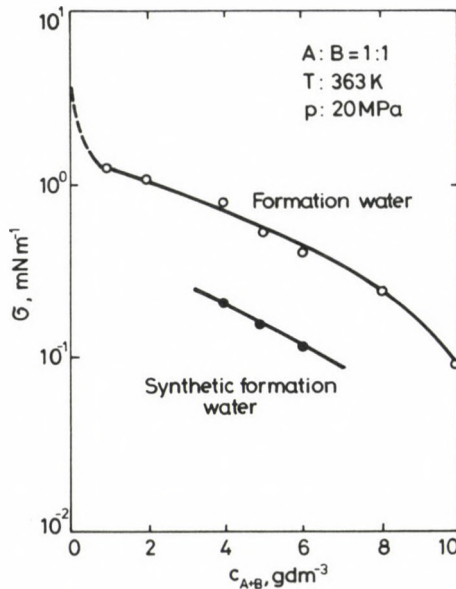


Fig. 2. Effect of tenside concentration on interfacial tension in natural and synthetic formation-water systems

the interfacial tension decreases by several orders of magnitude. The higher the tenside concentration, the greater the interfacial tension lowering (Fig. 2).

- b) Both the equilibrium and non-equilibrium interfacial tensions increase with temperature. At low temperature the phases at equilibrium have an interfacial tension that is an order of magnitude less than the non-equilibrium ones. Near formation temperature the two system exhibit approximately identical ( $0.1\text{--}0.15\text{ mN m}^{-1}$ ) interfacial tensions.
- c) The interfacial tension is largely influenced by the ratio of anionic to nonionic tensides present in the aqueous phase. Concerning the interfacial tension, it is advantageous if the amount of the nonionic components exceeds that of the anionic ones (Fig. 3).

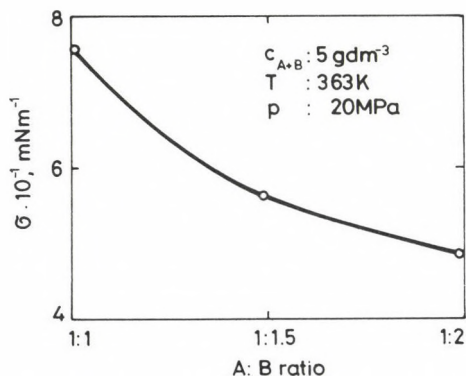


Fig. 3. Effect of the ratio of nonionic to anionic tenside on interfacial tension

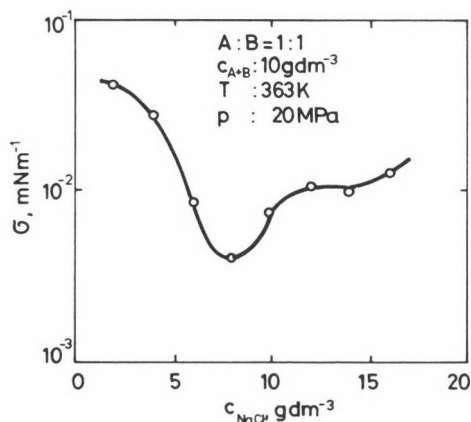


Fig. 4. Effect of sodium chloride on interfacial tension of an oil-water system containing both anionic and nonionic tensides

d) The interfacial tension is a function of salt concentration and the quality of salts present. In a system being in equilibrium, an increase in the salt concentration makes the interfacial tension *vs.* salt concentration curve take a minimum at  $3.4 \cdot 10^{-3} \text{ mN m}^{-1}$  (Fig. 4).

The final conclusion of decisive importance that may be drawn from the measurements is that under the reservoir conditions of the Algyó-2 field, the surfactants investigated ensure a minimum interfacial tension of  $10^{-2} \text{ mN m}^{-1}$ , one that largely satisfies the precondition of an efficient oil displacement beside the electrolyte concentration of the connate water.

### *Sorption phenomena of surfactants and polymers*

The detailed laboratory investigations also sought answer to the question concerning sorption losses occurring during the injection and the flow of the aqueous solution of the surfactants and the partially hydrolized polyacrylamide in the porous medium. To determine the retention of chemicals both unconsolidated and consolidated (artificial and natural) models were used, and the adsorbed amount was calculated for both the unit surface and unit weight of the adsorbent. The total and irreversible adsorption losses for surfactants and polymers were determined alike along with the effect of surfactants on polymer adsorption.

Nearly 95 % of the adsorbent was made up of the original rock. The remaining 5 % consisted of silicates, mainly quartz, with no significant sorption capacity. A vibration technique was employed to prepare the unconsolidated porous model. The flow rate of liquids in the adsorbent was identical with the average formation flow rate (0.5 m/day). After the saturation of the porous model, the volumetric sweep efficiency was determined using a  $0.5 \text{ g dm}^{-3}$  concentration solution labelled with potassium-iodide. The tenside adsorption was calculated after integration of the saturation curves. The saturation curves characteristic of Product A and A + B, respectively, for ratio A : B = 1 : 1 and serving as the calculation basis, are shown in Fig. 5. A similar way was followed to determine the polymer retention subsequent to the surfactant.

The most important results from the adsorption tests carried out under dynamic conditions are listed in Table II and some of the conclusions are as follows:

#### Surfactants

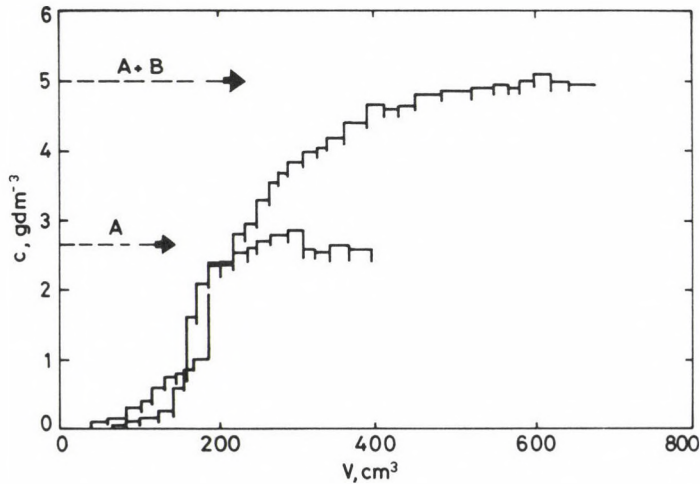
- a) The total adsorption of nonionic and anionic tensides are very similar and practically independent of water quality.
- b) The irreversibly adsorbed amount of anionic surfactant represents only 1/10 of the total adsorption loss. In presence of oil, irreversible adsorption slightly decreases, whereas it increases in a negligible extent with the concentration of the nonionic tenside.

**Table II.** Total and irreversible sorption loss of tensides and polymer at formation temperature and under dynamic condition

Without oil

Product A	Product B g dm <sup>-3</sup>	Polymer	Aqueous phase	Rock	<i>n</i> <sub>total</sub>			<i>n</i> <sub>irreversible</sub>	
					Product A	Product B	Polymer 10 <sup>-4</sup> g g <sup>-1</sup>	Product A	Product B
5	—	1	NaCl solution*	Alg-2	10.5	—	0.10	0.8	—
2.5	2.5	1	NaCl solution*	Alg-2	9.2	8.9	0.10	7.1	6.5
5	—	1	formation water	Alg-2	9.0	—	0.60	0.7	—
2.5	2.5	1	formation water	Alg-2	8.7	9.3	0.25	6.2	8.4
At residual water saturation									
5	—	1	formation water	Alg-2	8.4	—	0.20	2.4	—
2.5	2.5	1	formation water	Alg-2	11.3	24.4	0.79	2.0	20.6
At residual oil saturation									
5	—	1	formation water	Alg-2	9.3	—	0.15	1.4	—
2.5	2.5	1	formation water	Alg-2	10.3	11.0	0.20	1.6	7.2
—	5**	—	formation water	Alg-2	—	39.7	—	—	27.0
2.5	2.5	—	formation water	artificial	5.6	11.4	—	1.7	9.1
2.5	2.5	—	formation water	natural	6.6	9.9	—	2.5	8.5

\* 2 g dm<sup>-3</sup> NaCl solution  
 \*\* in i-Octane

**Fig. 5.** Saturation curves for Product A and A+B, on unconsolidated porous model prepared of reservoir rock

c) The nonionic tenside reveals very high irreversible retention. As much as 70–80% of the total loss can be regarded as an irreversible one, a fact that may be attributed to its dissolution into the oil phase. Accordingly, the irreversible retention largely depends on the presence of oil.

#### Polymer

- a) Polymer retention on the given model is of the order of  $10^{-4} \text{ g g}^{-1}$ . Preliminary adsorption of the surfactants reduces this value by about one order of magnitude.
- b) The amount of polymer specifically retained by the porous medium will be less if the solution of the two tensides' mixture is injected through the system, as against the case when only the solution of the anionic surfactant is used.

The above mentioned phenomena can be explained by micelle adsorption and the excellent oil-solubility of the nonionic tenside. In addition, much consideration was also paid to reduce the adsorption losses in order to enhance efficiency of the recovery technique. A preinjected chemical slug (NaCl, NaOH, and Na-silicate), and sodium-silicate applied simultaneously with the surfactant, respectively, served as a possible means for lowering the losses of surfactants and polymers. The data obtained are shown in Table III.

According to the experimental results all the preinjected chemical slugs are effective in lessening the total adsorbed amount, although the effect can be attributed to different reasons depending on the nature of the chemicals. However, it was clearly stated that of the chemicals, injection of NaCl solution proved to be most efficient and probably most economic. Applying sodium silicate and anionic tenside in the same solution, the general trend can be observed that up to a concentration of  $50 \text{ g dm}^{-3}$   $\text{SiO}_2$  the adsorbed amount is the less, the greater the solution's  $\text{SiO}_2$  concentration.

After all, the most important result is that in a solution containing silicate the adsorption loss of the surfactant can be reduced to about half of the initial value. This can contribute to a considerable extent to the improvement of profile and slug stability.

**Table III.** Effect of different chemicals (sacrificing agents) on sorption loss of Product A under dynamic condition

Product A $\text{g dm}^{-3}$	Chemical agent	$10^{-4} \text{ g g}^{-1}$	
		$n_{\text{total}}$	$n_{\text{irreversible}}$
5	—	9.33	1.43
5	$5 \text{ g dm}^{-3}$ NaOH (0.5 Vp)	7.25	4.17
5	$20 \text{ g dm}^{-3}$ NaCl (0.5 Vp)	6.23	1.00
5	$50 \text{ g dm}^{-3}$ $\text{SiO}_2$ (0.5 Vp)	8.56	1.15
5	$5 \text{ g dm}^{-3}$ $\text{SiO}_2^*$	6.68	1.05
5	$10 \text{ g dm}^{-3}$ $\text{SiO}_2^*$	7.26	0.99
5	$25 \text{ g dm}^{-3}$ $\text{SiO}_2^*$	4.96	0.80
5	$50 \text{ g dm}^{-3}$ $\text{SiO}_2^*$	3.98	0.66

\* In tenside solution

On the other hand, owing to the formation of silicate-tenside or silicate-micelle aggregates, a beneficial carrying effect develops in the system containing both materials. These two factors can be critical from the point of view of the efficiency and economy of the new displacing system.

#### *Emulsification in water-oil-tenside system*

In the natural water/oil system a high-viscosity W/O emulsion is usually formed. Depending on the relative amount of phases, the emulsions show plastic or pseudoplastic flow behaviour. In addition, the stable dispersions show thixotropic character, and the measure of thixotropy is a function of the concentration of the dispersed phase. Typically, an increase in the amount of dispersed phase causes the average diameter of dispersed (water) drops to become larger and hence the emulsion is getting gradually more and more polydisperse. It can be shown that, on the one hand, any increase in temperature results in a reduction in the emulsion's plasticity and kinetic stability and, on the other hand, plasticity, structural stability, and thixotropy of the emulsion are enhanced by the bi- and polyvalent cations present in the formation water—presumably as a result of physical and chemical processes taking place at the water/oil interface. It could also be clearly established that of the Algyő-2 oil components the asphaltenes not only stabilize the emulsion but have a decisive role in shaping of the rheological properties (Felián et al. 1983, Felián 1984).

Considering the generally known experiences *vis.* surfactants greatly influence—possibly even stabilize—natural emulsions, we deemed it necessary to carry out emulsion tests of adequate depth. The experiments performed under static conditions have led to the following principal statements (Felián and Lakatos 1982).

- a) The emulsions containing anionic and nonionic tensides, and having low viscosity are of a complex nature (of the O/W/O type). Depending on the amount of tenside, both W/O- and O/W-type emulsions may form. Since a phase inversion occurs at relatively low tenside concentrations, only an O/W emulsion can form at formation temperature at the relatively high ( $> 5 \text{ g dm}^{-3}$ ) tenside concentrations used in practical flooding. A W/O macroemulsion, and hence a phase inversion are liable to occur only when the nonionic tenside is used alone.
- b) It is advantageous that the plastic and apparent viscosities of the emulsions decrease considerably if the tenside concentration is increased.
- c) The lower limit to stable emulsions formation lies nearly at  $\text{WOR} = 0.5$ . Below this limit the emulsions formed from the natural water/oil system desintegrate and oil separates from the dispersion.
- d) With decreasing water/oil ratio the apparent viscosity of the emulsion greatly increases (Fig. 6).
- e) When the ratio of Product A to Product B is shifted in favor of the latter one, the emulsification of the system becomes less. At the same time, a change in the apparent

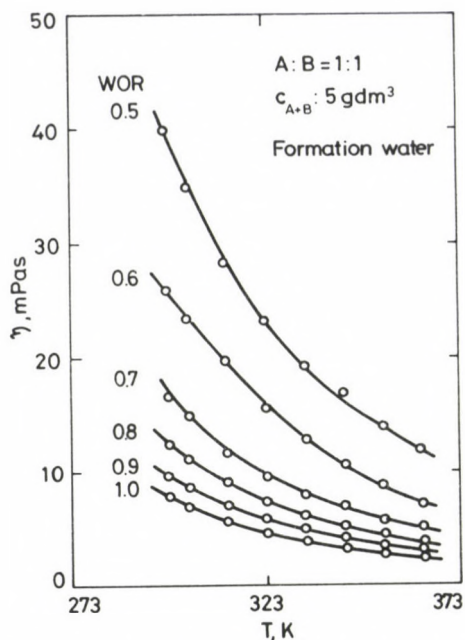


Fig. 6. Dependence of emulsion viscosity on temperature and water/oil ratio at shear rate of  $10^2 \text{ s}^{-1}$

viscosity of the emulsion takes place. For the cases investigated, the lowest viscosity can be reached with a composition A : B = 1 : 2 (Fig. 7).

- f) Emulsification and properties of the stable macroemulsion are influenced slightly, if at all, by the polyacrylamide in concentration range of  $0.1\text{--}1.0 \text{ g dm}^{-3}$ . The probable influence is that the polymer produces thickening of the aqueous phase, which can be neglected beside the apparent viscosity of the emulsion formed (Fig. 8).

The result from the laboratory experiments carried out under static conditions is not very reassuring if the mobility control design is considered. It seemed to be necessary that the macroemulsions regarded as stable one be subjected to dynamic studies as well. This was accomplished by injecting, at formation temperature, stable emulsions into artificially consolidated porous models of different pore volumes, and measuring the phase composition of the fluid produced. The results from the dynamic tests can be summarized as follows:

- a) In porous medium, the stable O/W emulsions demulsify under dynamic conditions and separate into three phases. Under normal conditions the volume of the emulsion phase does not amount to 20 % of the emulsion injected (Fig. 9).
- b) Demulsification depends only to a negligible extent on the pore volume of the model. In effluent the volume of the emulsion exceeds 50 % only if the porous model is less than 5 mm in length (or its pore volume is less than  $3 \text{ cm}^3$ , see Fig. 10).

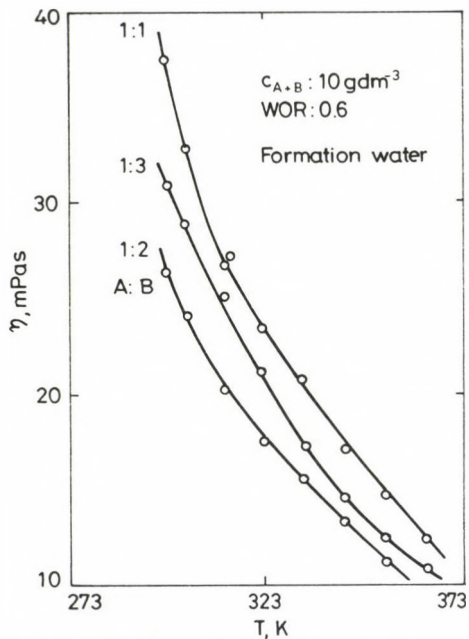


Fig. 7. Dependence of emulsion viscosity on temperature and the ratio of anionic to nonionic surfactant at constant tenside concentration

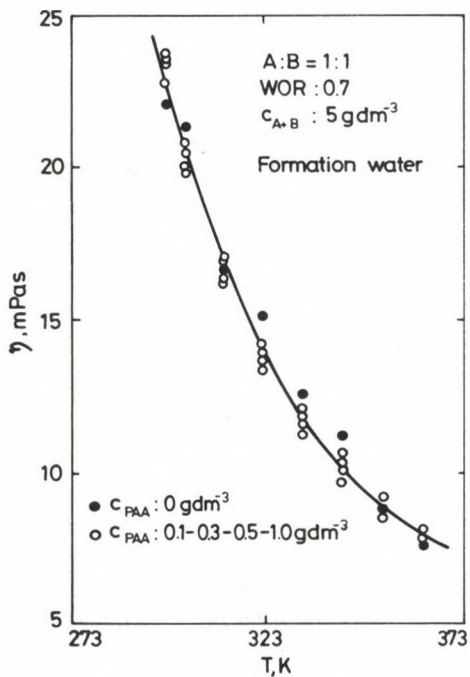


Fig. 8. Dependence of emulsion viscosity on temperature and polymer concentration

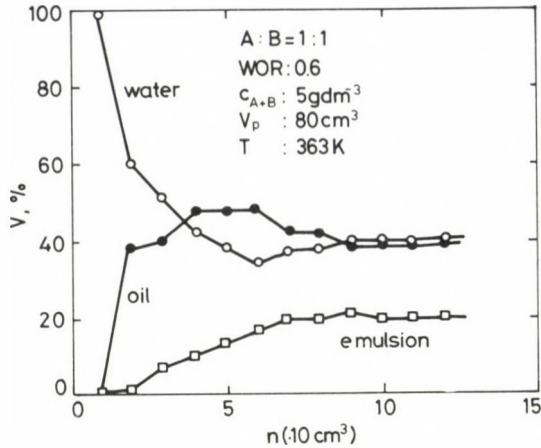


Fig. 9. Demulsification of emulsion injected through a porous medium, and the phase volume of emulsion as a function of injected volume (fraction number)

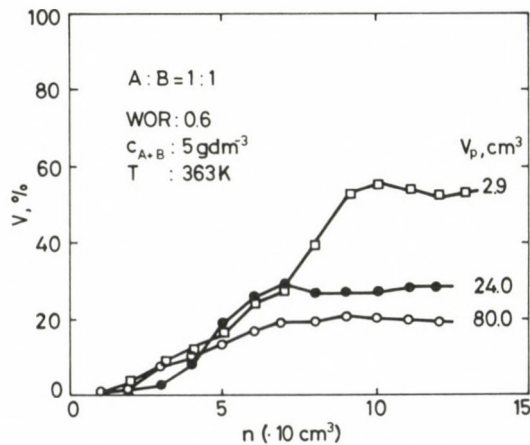


Fig. 10. Demulsification of emulsion in porous medium as a function of injected volume (fraction number) and pore volume of the core

c) Temperature probably plays a decisive role in demulsification. Although at 343 K the phase ratio is hardly different from that to be measured at 363 K, total volume of the oil and the aqueous phases separated at 323 K no longer exceeds 20 % (Fig. 11).

It can be assumed that the demulsification occurred under dynamic conditions is a result of an interaction between particles as well as between particles and wall and the shearing forces arising during the flow, although ageing of the microemulsion, adsorption of the tenside, a change in the c.m.c., *etc.* cannot be neglected either.

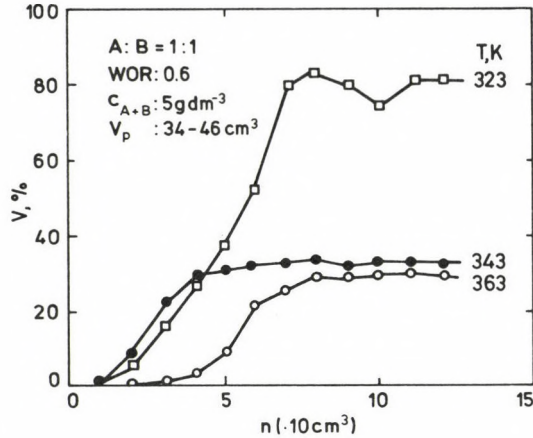


Fig. 11. Demulsification of emulsion in porous medium as a function of injected volume (fraction number) and temperature

It may be stated as a final conclusion that a spontaneous emulsification occurring under natural conditions—if it should occur at all—does not jeopardize the mobility control based on application of polymers, because the aqueous solution of both surfactants forms an emulsion with oil which demulsifies readily under dynamic conditions in a porous medium.

### Displacement tests

As regards the application of a given nonionic and anionic surfactants system, the decision cannot be made merely on the basis of the favourable physico-chemical test. It is also necessary to show, using displacement test of at least equal depth and volume, that a change in the interfacial properties during the flow of the tensides in a porous medium should lead directly to an increase in displacement efficiency. The basic object of the displacement test is to optimize the flooding system, predict the amount of surplus oil to be expected, and elucidate the displacement mechanism.

A reliable answer to this complicate problem can be given only by a great number of tests, usually involving complex measuring techniques. The displacement tests were carried out with a laboratory-designed and developed apparatus, using linear porous models. The medium-size (24 cm) and long (120 cm) models were prepared from consolidated porous cores. Natural rocks, in both consolidated and unconsolidated state were used for control measurements.

*Displacement tests in medium-length porous systems*

The experiments on medium-length, artificially consolidated cores had as the primary object to determine an optimum ratio of nonionic to anionic tensides and to estimate the tenside concentration to be used for the optimized ratio. In the displacement tests, the following experimental conditions were kept constant:

Rock sample:	synthetic sandstone without clay minerals
Core length:	24 cm
Permeability:	0.143 to 0.230 $\mu\text{m}^2$
Temperature:	363 K
Pressure:	20 MPa
Injection rate:	0.5 m/d

Alg-2 medium-grade oil and centrifuged Alg-2 formation water were used. The tenside solutions were also made of formation water under following conditions:

## Experiment series No. 1

Ratio A : B:	1 : 1	1.5 : 1	2 : 1	1 : 1.5
$c_{A+B}$ , g dm <sup>-3</sup> :	5	5	5	5

## Experiment series No. 2

Ratio A : B:	1 : 2	1 : 3	1 : 2	1 : 2	1 : 2
$c_{A+B}$ , g dm <sup>-3</sup> :	5	5	8	10	50

In addition some displacement tests were carried out with preinjection of Product B dispersion having 5 g dm<sup>-3</sup> concentration and immediately followed by 5 g dm<sup>-3</sup> Product A solution. The purpose of this test was to determine whether preadsorption of the primarily oil-soluble tenside and the postinjected anionic water-soluble surfactant would result in a greater displacement efficiency if the various ratios A : B developed in the porous medium, and these ratios might also take extreme values.

Since the displacement test on medium-size cores had an informative character, no polymer buffer was used. To ensure compatibility of results, 1 Vp surfactant solution was injected into the model in each case. In those tests where sequential injection was applied 0.5 Vp Product B dispersion, and 0.5 Vp Product A solution were injected.

The displacement tests consisted of the following steps:

- saturation with formation water;
- setting the initial oil saturation by the injection of Alg-2 oil;
- displacement with 1.0 Vp formation water;
- injection of surfactants (1.0 Vp)
- injection of labeled aqueous solution.

**Table IV.** Data of displacement tests using medium-length cores  
( $L = 24$  cm; water preflush = 1.0 Vp)

Serial number	$k_w$ $\mu\text{m}^2$	$\varphi$	$S_{oi}$ % Vp	Tenside			Output data		
				A : B	$c_{A+B}$ $\text{g dm}^{-3}$	Slug size Vp	Primer	Total	Surplus
							% O.O.I.P.		
1	0.146	0.290	70.4	1 : 1	5.0	1.0	48.3	52.2	3.9
2	0.151	0.282	69.4	1.5 : 1	5.0	1.0	47.6	54.3	6.7
3	0.143	0.298	70.2	2 : 1	5.0	1.0	49.0	57.2	8.2
4	0.155	0.301	69.7	2 : 1	5.0	1.0	48.3	56.0	7.7
5	0.160	0.293	70.9	1 : 1.5	5.0	1.0	48.0	56.6	8.6
6	0.173	0.303	71.0	1 : 2	5.0	1.0	49.8	72.2	22.4
7	0.170	0.300	69.0	1 : 3	5.0	1.0	48.7	76.2	27.5
8	0.169	0.307	72.0	1 : 2	8.0	1.0	50.0	81.8	31.8
9	0.165	0.298	70.8	1 : 2	10.0	1.0	49.0	83.4	34.4
10	0.169	0.303	69.8	1 : 2	50.0	1.0	48.9	63.1	17.2
11	0.230	0.312	71.5	B	5.0	0.5			
				A	5.0	0.5	50.2	86.6	36.4

The results of the displacement tests on medium-length, artificially consolidated sandstone models are listed in Table IV.

Modifying the ratio of nonionic to ionic tenside in favour of the latter, the results obtained confirm that:

- If  $5 \text{ g dm}^{-3}$  total tenside concentration is used, increasing the amount of Product A has hardly any influence on displacement efficiency.
- As a rule, no emulsion appears in the effluent.
- Modification of the ratio A : B (by even as much as A : B = 1 : 1.5) in favour of Product B results in a surplus yield of 8.6 % O.O.I.P, indicating the favourable effect of the nonionic tenside.

In the second step of the displacement tests, modifying the ratio A : B in favour of Product B to an extent of 1 : 2 and 1 : 3, and keeping the concentration at  $5 \text{ g dm}^{-3}$  resulted in the following:

- Small amount of emulsion was present in the effluent.
- The surplus oil increased to 22.4–36.4 % O.O.I.P. during the surfactant-aided displacement.
- An increase in the total concentration of surfactants does not result in a proportional increase in displacement efficiency, the surplus oil is even reducing, for a concentration of  $50 \text{ g dm}^{-3}$ , to 17.2 % O.O.I.P. Therefore, it is not economic to increase the concentration above  $8 \text{ g dm}^{-3}$ , since the surplus oil obtained in this case amounted to 31.8 % O.O.I.P.
- Increasing the ratio A : B in favour of Product B to a 1 : 3 level, a stable, viscous emulsion is present in the effluent, besides a production of surplus oil of 27.5 % O.O.I.P.

e) Using the mixture A : B = 1 : 3 at a total concentration of  $5 \text{ g dm}^{-3}$ , a stable emulsion phase (called "third phase") could be observed.

If the Product B dispersion and the solution of Product A were injected separately, experimental results showed that

- a) the amount of surplus oil increased, the yield of 36.4 % O.O.I.P. exceeding the surplus output obtained with the mixtures A : B = 1 : 2 and 1 : 3 at a total concentration of  $5 \text{ g dm}^{-3}$ , and
- b) of all the cases studied the system consisted of 0.5 Vp  $5 \text{ g dm}^{-3}$  Product B and 0.5 Vp  $5 \text{ g dm}^{-3}$  Product A, is most efficient; accordingly, further displacement tests were made in this direction.

#### *Displacement tests in a long-core porous system*

In the first series of long core displacement tests, reliability and reproducibility of the results obtained on 24 cm core samples were analyzed. Since it was evident from experimental observations that results could be reproduced and the injection sequence B – A was efficient, the further program of displacement tests were focussed on the optimization of the slug system and the investigations the polymer buffer.

The same slug sequence was employed as earlier. Tests were carried out on the long-core apparatus of the Laboratory. The flow test were supplemented by physico-chemical measurements and a quantitative chemical analysis. The latter included, of the two tensides, only the anionic one and the polymer.

Experimental conditions were as follows:

Rock sample:	synthetic sandstone without clay minerals and a model made of reservoir rock
Core length:	120 cm
Permeability:	0.086 to $0.210 \mu\text{m}^2$
Temperature:	363 K
Pressure:	20 MPa
Injection rate:	0.5 m/d
Liquid phases:	Alg-2 formation water, tensides (with Alg-2 formation water), and polymer solutions (with Alg-2 formation water)

The data obtained by the long-core tests are summarized in Table V, while the result got on a model made of natural rock material and using programmed polymer buffer is shown in Figs 12 and 13.

Finally, such a kind of long-core tests were carried out where the technical maximum of displacement efficiency has been handled jointly with economic considerations, *vis.* the attainable maximum surplus oil with the least amount of surfactant required was regarded as the best result.

**Table V.** Data of displacement tests using long-core porous system  
( $L = 120$  cm; water preflush = 1.0 Vp)

Serial number	$k_w$ $\mu\text{m}^2$	$\varphi$	$S_{oi}$ % Vp	Tenside				Polymer		Output data		
				B		A		g dm <sup>-3</sup>	Vp	Primer	Total	Surplus
				g dm <sup>-3</sup>	Vp	g dm <sup>-3</sup>	Vp					
1	0.173	0.303	70.3	5	0.5	5	0.5	—	—	49.0	80.6	31.6
2	0.197	0.313	68.5	3	0.5	5	0.5	1	1.0	50.2	87.7	37.5
3	0.210	0.297	72.0	5	0.3	5	0.5	1	1.0	49.8	94.4	44.6
4	0.192	0.285	70.3	5	0.5	5	0.5	1	1.0	51.3	89.3	38.0
5	0.187	0.303	68.8	5	0.2	5	0.3	1	0.3	50.3	74.0	23.7
6	0.186	0.308	70.1	5	0.3	3	0.5	1	0.3	49.1	81.1	32.0
7	0.195	0.312	68.3	3	0.5	3	0.5	1	0.3	50.5	77.7	27.2
8	0.179	0.296	69.5	5	0.5	3	0.3	1	0.3	49.5	85.4	35.9
9	0.176	0.310	71.1	3	0.5	5	0.5	1	0.3	49.7	80.1	30.4
10	0.195	0.321	70.2	5	0.3	5	0.3	1	0.3	49.8	81.6	31.8
11	0.190	0.323	68.8	3	0.3	3	0.3	1	0.3	49.2	74.8	25.6
12	0.182	0.307	69.4	8	0.2	5	0.2	1	0.3	50.3	86.5	36.2
13	0.172	0.310	68.3	8	0.2	5	0.2	1.5	0.1			
								0.5	0.1			
								0.3	0.1	49.0	86.7	37.7
14	0.175	0.305	69.0	9	0.05	5	0.1	1.2	0.1			
				4	0.1	2	0.1	0.5	0.1			
				2	0.05			0.3	0.1	49.3	84.7	35.4
15	0.183	0.297	70.2	9	0.05	5	0.1					
				4	0.1	2	0.1					
				2	0.05			1	0.3	49.8	86.6	36.8
16	0.170	0.288	69.0	10	0.05	5	0.1					
				5	0.1	2	0.1					
				2	0.05			1	0.3	49.1	85.1	36.0
17*	0.086	0.254	68.2	8	0.2	5	0.2	1	0.3	46.3	73.6	27.3
18**	0.210	0.346	67.0	8	0.2	5	0.2	1	0.3	57.1	85.5	28.4

Notes:

\*  $L = 24$  cm consolidated natural core (control measurement)

\*\*  $L = 120$  cm unconsolidated natural sandstone (control measurement)

The experiences from the first five long-core displacement tests can be summarized as follows:

- It was proved that the surfactant-aided displacement system injected in B–A sequence is an efficient one, the result obtained on the 24 cm core can be reproduced, and the long-core displacement test resulted in a surplus of 31.6 % O.O.I.P.
- Injection of the 0.5 Vp slug size is not required for the displacement process, i.e., the total mass of surfactants can be significantly reduced.
- Use of the polymer buffer has a favourable impact on the displacement process, and the buffer size to be injected—on a linear laboratory model—does not exceed 0.3 Vp.

Based on the results obtained from the subsequent displacement tests aimed to optimize the slug system it can be stated that

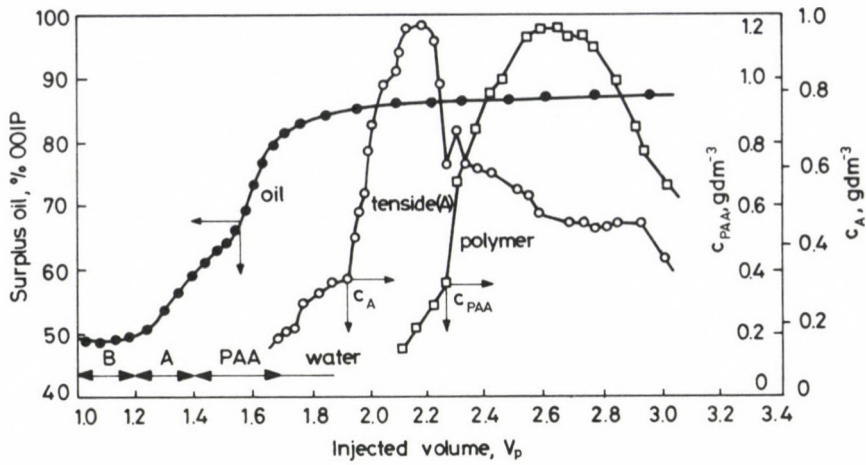


Fig. 12. Performance of the displacement test using artificially consolidated long-core model.

Slug system:

Product B:	0.2 Vp	8 g dm <sup>-3</sup>
Product A:	0.2 Vp	5 g dm <sup>-3</sup>
Polymer:	0.1 Vp	1.5 g dm <sup>-3</sup>
	0.1 Vp	0.5 g dm <sup>-3</sup>
	0.1 Vp	0.3 g dm <sup>-3</sup>

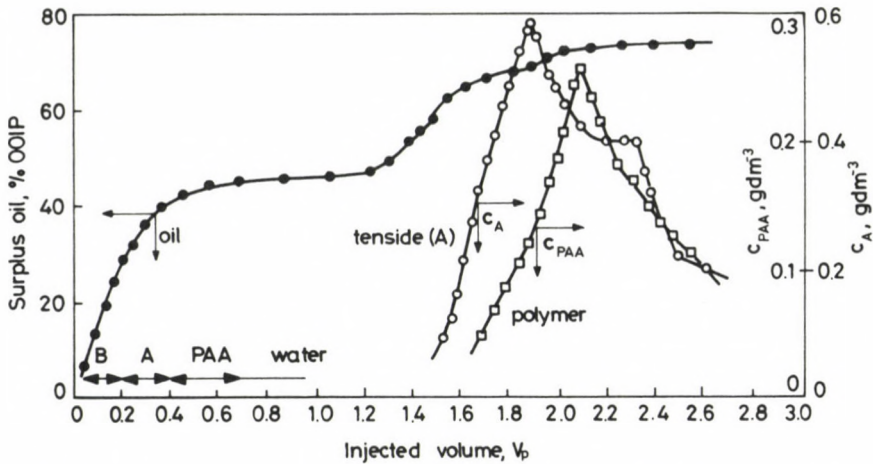


Fig. 13. Performance of the displacement test using medium-length unconsolidated natural sandstone model.

Slug system:

Product B:	0.2 Vp	8 g dm <sup>-3</sup>
Product A:	0.2 Vp	5 g dm <sup>-3</sup>
Polymer:	0.3 Vp	1 g dm <sup>-3</sup>

- a) since the primary aim of the test was to determine the attainable minimum amount of surfactant and polymer to be used, these tests have not been extended over parameter variations and such a wide range of concentrations as would make it possible to elucidate the displacement mechanism. In this respect it can be stated, however, that the displacement efficiency of the slug system is determined primarily by the amount of Product B. For Product B the optimum slug size and concentration are  $0.2 V_p$  and  $8 \text{ g dm}^{-3}$ ;
- b) the role of Product A is important because of the development of the favourable solution structure needed for an efficient displacement. Here the optimum slug size and concentration are  $0.2 V_p$  and  $5 \text{ g dm}^{-3}$ , respectively;
- c) if the injection sequence B—A, using optimum slug sizes and concentrations and a polymer buffer as an additional agent is applied, no liquid dispersions leading to pore structures blocking or barrier formation occurred.

The results of displacement tests are valid for the experimental conditions described. According to tests carried out in lower permeability systems at the Hungarian Hydrocarbon Research and Development Institute—owing to the nature of the system—mechanical entrapment of the dispersed Product B occurred with possible modification of the yield results when sequential slug injection was studied. In such cases, an answer to the problem consists in a partial or complete solubilization of Product B with Product A, still retaining, of course, the principle that in the slug injected first the concentration of nonionic tenside should exceed the amount of anionic tenside. The minimum applicable anionic tenside concentration is directly related to the c.m.c., which in the given case is less than  $0.1 \text{ g dm}^{-3}$ .

Finally, it can be stated that by use of the primarily oil-soluble, nonionic Product B and the primarily water-soluble Product A in the sequence B—A, and as a result of two years' systematic theoretical and laboratory research work, we have succeeded to develop a new and—as laboratory experiments verify—economic and efficient oil recovery method.

### Conclusions

The laboratory investigation of 4-ethoxy-nonyl-phenol (nonionic) and 4-ethoxy-nonyl-phenol-sulphonate (anionic) surfactants as probable candidates to be used in EOR has led to the following results:

- a) The nonionic, primarily oil-soluble tenside without additives forms a high viscosity emulsion in water/oil system. The anionic tenside solubilizes the nonionic tenside through formation of micelles, and results in a transparent displacing phase having stable micelle and solution structures. The structural stability of such a system is far the best among the ethoxylated nonyl-phenol derivatives.
- b) The thermal stability of the tensides is very favourable and there are no reasons associated with degradation and compatibility that would prohibit its use under field conditions.

- c) Under Algyő-2 field conditions the interfacial tension of the water/oil system is in the range of  $10^{-2} - 10^{-3}$  mN m<sup>-1</sup> satisfying the preconditions for an efficient oil displacement.
- d) The tensides show a favourable sorption loss of  $10^{-4}$  g g<sup>-1</sup> ( $10^{-6}$  g cm<sup>-2</sup>) under dynamic conditions, which can be further reduced by alkali silicates. The preadsorption of the tensides lowers considerably the polymer retention.
- e) The spontaneous emulsion formation taking place under natural conditions does not jeopardize mobility control, since the aqueous solution of tensides forms an instable emulsion with the oil under dynamic conditions in porous media.
- f) Using the nonionic and anionic tensides simultaneously (in the same solution), the displacement efficiency can be increased considerably.
- g) The sequential injection of the nonionic and anionic tensides is more efficient than injection in the same solution. The realized surplus yield exceeds 30 % O.O.I.P. by sequential injection.
- h) Although the displacement mechanism has not been clarified yet, it can be stated that the efficiency is primarily determined by the amount of the preinjected nonionic tenside.
- i) According to the displacement tests on linear porous models, sequential injection of the tensides followed by polymer buffer makes possible to realize a very favourable (10 kg/m<sup>3</sup>) specific tenside consumption.

As a result of the systematic survey carried out in the framework of an international cooperation, it has been succeeded to develop the theoretical bases for a new oil recovery method, which proved both economic and effective under laboratory conditions.

### References

- Bedő Zs, Berecz E, Lakatos I 1984: Structure of Micellar Solutions Containing Nonionic Surfactants, Part I. Micellization of Ethoxylated Nonyl-Phenols. (in Hungarian) *Magyar Kémiai Folyóirat*, 90, 198.
- Capelle A, Littmann W 1982a: Enhanced Oil Recovery with Modified Nonionic Surfactants. *Oil Gas-European Magazine*, 1, 53.
- Capelle A, Littmann W 1982b: Application of Modified Nonionic Surface Active Agents in Enhanced Oil Recovery. SPE Preprint 10601
- Felián B 1984: Emulsification of Water/Oil System and Colloid Chemical Properties of Macroemulsions. Ph. D. Thesis, JATE, Szeged
- Felián B, Lakatos I 1982: Properties of Stable Emulsions Containing Anionic and Nonionic Surfactants and Their Flow Behaviour in Porous Media. (In Russian) X. PETROLGEOCHEM, 294, Varna
- Felián B, Balázs J, Lakatos I 1983: Investigation of Crude Oil/Water Emulsions in Presence of Nonionic Surfactants. Part I. *Acta Phys. Chem. Univ. Szegediensis*, 29, 223.
- Hayes M E, Bourrel M, El-Emary M M, Schechter R S, Wade W H 1979: Interfacial Tension and Behaviour of Nonionic Surfactants. *Soc. Pet. Eng. J.*, 19, 349.
- Ramirez W F, Shuler P J, Friedman I 1980: Convection, Dispersion and Adsorption of Surfactants in Porous Media. *Soc. Pet. Eng. J.*, 20, 430.
- Trogus F J, Sophany T, Schechter R S, Wade W H 1977: Static and Dynamic Adsorption of Anionic and Nonionic Surfactants. *Soc. Pet. Eng. J.*, 17, 337.
- Ziegler V M, Handy L L 1981: Effect of Temperature on Surfactant Adsorption in Porous Media. *Soc. Pet. Eng. J.*, 21, 218.



## INTEGRATING EFFECT OF HYDROMECHANIZATION IN MINING TECHNOLOGICAL SYSTEMS

J PATVAROS<sup>1</sup>

[Manuscript received October 15, 1982]

To meet raw material demands, production in mechanical mining systems has to be concentrated on a few working places, and machinery with extremely high capacity is to be used. The continuity of mining operations has steadily improved due to this tendency, and the ratio of interruptions and pauses to working operations has decreased. It is obvious at the same time that the character of working operations still remains discrete even in the most modernly mechanized conventional mining systems.

Hydromechanization ensures a new type of linkage, i.e. integration within the mining systems. The grades of integration from simple to sophisticated can be given as follows (Arens 1975, Yufin 1974, Patvaros 1976, Zambó 1975):

- linking the mining operations (winning, loading, haulage, roof control, gob operations) locally and in time within a mining technological system;
- combining various working places (heading, face *etc.*) or various winning methods (longwall, short face) with hydromechanical tools of the same type within a mining technological system, e.g. underground mining;
- suitably combining various mining technological systems (open pit mining, underground mining, subwater mining, bore-hole mining);
- improving the quality of the extracted minerals and combining mining, mineral processing and utilization processes to ensure a versatile use;
- wider and more effective environment protection.

**Keywords:** excavation methods; hydromechanization; mining system

In mining systems with conventional mechanical technology mining operations (winning, loading, haulage) are carried out by various machines. Using hydro-mechanization, the continuity in space and time of these operations is ensured by water, as a universal operating medium. That means that water is the tool in the winning operations, it is the transport medium in the transport processes and it may even play the role of support in subwater mining systems. By flexibly changing any or both of the ejected water mass and velocity, the momentum of the jet can be easily and effectively adjusted to the strength properties of the rock or to the particle size distribution of the solid to be hydraulically transported.

Hydromechanization also ensures the combination of preparatory and working places into a unified system. In conventional underground mining methods (longwall

<sup>1</sup> Technical University for Heavy Industry, Department of Mining Engineering, Miskolc-Egyetemváros, Hungary

or pillar) winning, loading and haulage machines of various types are usually applied for drifting and working at the faces. The variety of equipment brings about a lot of problems in co-ordinating the machines and working places. Using hydraulic technology, identical or similar equipment and transport technology can be used in preparatory and working places and in certain cases even in the field of gob operations. The dimensions of winning, loading and haulage equipment using hydraulic technology are considerably smaller than those of conventional machinery of the same capacity. At the same time they may be easier adjusted to varying natural conditions. Because of smaller masses and dimensions of hydraulic equipment, shaft and drift cross-sections in deep mines can be reduced and open-pit machinery can be operated on softer ground. Adjustability of hydraulic technology to natural conditions is obvious in inclined seams where conventional winning and drifting cannot be used at all or only with great difficulty. It can be stated on the basis of the aforementioned that smaller masses and dimensions of hydraulic equipment and the technology using these machinery allow considerable savings in capital and operational costs even in mineral deposits with extremely irregular geometry.

Hydromechanization provides the widest variety of combinations of the four basic mining technological systems, *viz.* open pit mining, deep mining, subwater extraction and bore-hole mining. The main possibilities of combining technologies concerning technological units can be as follows:

- winning is carried out with conventional machinery in all technological systems but haulage proceeds hydraulically;
- winning, haulage and further treatment are made by means of hydromechanization.

For the combination of various mining technological systems locally and in time, following possibilities can be considered (Lobanov and Smoldirev 1974, Patvaros 1976, Patvaros 1979, Zambó et al. 1975):

- Locally and in time separated, using e.g. a main pipe for transporting various minerals extracted by various mining methods.
- At various places but simultaneously applying e.g. various mining technologies for extracting various minerals at different places of a major mineral deposit. This case can be illustrated by the open pit strip mining of sand deposits near the surface, subwater mining of deeper gravel deposits from barges, deep mining of coal from greater depth through shafts and drifts, and bore-hole mining of bauxite lenses on the basement rocks. Here, separate pipelines have to be constructed to transport various minerals, at least to a collecting line. In the collecting line the minerals can be transported periodically in batches to the mills.
- The most advanced version of combining mining technologies is the mutually supported system. A feasible example of this version can be a conventional open pit mine of deep mine whose steps or drifts are used to drill bore-holes for a bore-hole hydraulic mining system. In this case, too, the same hydraulic pipeline can be used for the various mining systems. Further advantage can be found in the flexibility of

the opening and development system of a given mining technology which can be used for other extraction technologies, too.

A common feature of the conventional mining systems using mechanical technology is the fact that the application of high-capacity machinery increases mineral losses and dilution. The technical-economical disadvantage due to these factors can usually be avoided by a separate processing plant only which improves the extracted mineral quality for further processing or utilization. The mine and the processing plant are generally separately located in conventional mining technologies which is the source of certain separation in their operation and of disunited surface transport, waste treatment and environment protection.

In hydraulic technological systems mining, mineral processing and eventual further treatment can be integrated into a single chain of processes with the aid of water as a universal medium. The subwater sand-gravel mining system using floating barges can be mentioned as an example which uses water to win the mineral, to transport the extracted material, to carry out mineral processing near the site of mining and to dispose of waste material to suitable places of the worked-out area. In this system water can be used in a closed circuit for various processes which enables the use of a minimum amount of water for technological purposes. Technological systems using closed water circuits involve minimum pollution to the environment (Patvaros 1976, Patvaros 1979, Zambó et al. 1975).

The hydraulic bore-hole bauxite mining method can be considered as a more advanced technological system and it may become a common mining method in the not too distant future. In this method bauxite washing is carried out near the site of mining and the separated waste is disposed of immediately in the worked-out area. A further step of integration can be achieved by hydraulically transporting the concentrated bauxite to the alumina factory and by injecting alkali solution in proper concentration into the pipeline. Thus chemical treatment of the raw ore may even begin during transportation. In the outlined method an effective combination of mining, mineral processing and metallurgical processes can be achieved by hydromechanization.

Using the hydraulic bore-hole mining method, excavations of irregular shape are produced in the mineral body (coal, bauxite *etc.*) whose stability depends on the strength of the adjacent rocks. The dimensions of the excavations can be characterized by the working radius which, on the other hand, determines the unsupported area.

The working radius and the dimensions of the unsupported area can only be increased as fast as no fracture process sets in the adjacent rocks which would lead to roof failure. Roof failure and other rock movements caused by hydraulic technology not only pollute the extracted useful mineral but may destroy the hydraulic mining equipment on the bottom.

The following solutions can solve the problems of supporting the underground excavations created by hydraulic bore-hole mining. One of the most effective solutions

may be to adjust the working radius to the properties of the actual adjacent rocks or to increase the advance speed to a maximum in order to prevent undesirable rock movements or at least to keep them at an acceptable rate. A different and technically more difficult solution would use increased water pressure in the mining excavations to balance rock pressure at least during the mining process.

Finally, the important integrating effect of hydromechanization should be emphasized concerning environment protection in connection with mining. Two examples may here be mentioned (Arens 1975, Patvaros 1976, Zambó et al. 1975):

- It is well known that the depth of mining of conventional excavation methods practiced at present (using walking dragline and clamshell excavators) is limited in 8–10 m when working mineral deposits of loose structure (sand, gravel). That very often brings about mineral losses as high as 60–80 percent. Building material mines of this kind expand horizontally rather rapidly and occupy increasing agricultural areas. Hydraulic mining methods, however, can reach a depth of 60 to 80 m in subsurface sand and gravel deposits enabling significantly higher mineral recovery and essentially lower mineral losses. With increasing depth working life of the mine also increases which is combined with a lower rate of occupying agricultural areas. It is considered a further advantage that filling up worked-out areas with hydraulic methods can technically and economically be carried out more efficiently than using conventional ones.
- The task of active water table reduction puts continuously increasing burden on the bauxite mining industry from both technical and economical points of view. The influence of active water table reduction on the static and dynamic groundwaters in an area with a radius of 20–30 km causes further problems. The hydraulic bore-hole mining method applied lately with promising results in one of the mineral lenses of the Bakony Bauxite Mines would solve all problems of environment protection in connection with active water table reduction. In the hydraulic bore-hole bauxite mining method water can be used as a general working medium for mining, mineral processing and even metallurgical purposes. This kind of the technological system ensures the use of water in a closed circuit, thus preventing pollution and long-lasting exploitation of water resources.

The aim of emphasizing the importance and possibilities in the various steps of integration of hydromechanization is to draw attention to the innovational reserves hidden in the utilization of water in almost all fields of mining. Countries with strong economies are only capable of manufacturing and modernizing machinery of conventionally mechanized mining technological systems. However, developing and producing methods and equipment making use of hydraulic technologies seem widely feasible in the various mining technological systems both inside Hungary and abroad.

### References

- Arens V Zh 1975: Geotechnological methods in mining of minerals. (In Russian) Nedra, Moscow
- Lobanov D P, Smoldirev A E 1974: Hydromechanization of geological-exploration and mining. (In Russian) Nedra, Moscow
- Patvaros J 1976: Feasibility of a mining system of new type for the extraction of bauxite deposits in Hungary. (In Hungarian) *Transactions of the Technical University of Heavy Industry. Ser. I. Mining.*, 22, 238–251.
- Patvaros J 1979: Feasibility of hydraulic bore-hole mining of bauxite lenses. (In Hungarian) *Transactions of the Technical University of Heavy Industry. Ser. I. Mining.*, 26, 97–114.
- Yufin A P 1974: Hydromechanization. (In Russian) Stroyizdat, Moscow
- Zambó J et al. 1975: Feasibility of geotechnical mining methods for the extraction of mineral deposits in Hungary. (In Hungarian) Research Report. Department of Mining Engineering, Technical University for Heavy Industry, Miskolc



## MATERIALS LAW OF ISOTROPIC ROCK CONTINUA

R HORVÁTH<sup>1</sup>

[Manuscript received May 11, 1983]

The fully general materials law of continua can be formulated from well-known thermodynamical laws. The so-called Poynting–Thomson's materials law being important in practical problems of rock mechanics is not deduced from the general law but determined through model analysis by compromising opposite requirements. The paper shows how the concrete materials model, the so-called Poynting–Thomson's standard body can be determined from the general materials law—within the validity of Onsager's theory.

**Keywords:** deformation tensor; materials equation; Onsager's theory; Poynting–Thomson body; rheology of rocks; rock continuum; stress tensor

### *Symbols*

$D$	deformation tensor
$E$	Young's modulus
$F$	stress tensor
$G$	shear modulus
$L$	momentum conduction tensor
$t$	time
$T$	stress deviator tensor
$\mathbf{u}$	displacement vector
$\mathbf{u} \circ \nabla$	deformation tensor
$U$	work
$\delta$	unit tensor of fourth order
$\varepsilon$	strain
$\eta$	creeping modulus
$\lambda$	conduction coefficient
$\mu$	conduction coefficient
$\theta$	relaxation coefficient
$\sigma$	stress
$\tau$	relaxation modulus
$\nabla$	Hamilton's differential operator

<sup>1</sup> Technical High School of Building Industry Ybl Miklós, Landler J. u. 2—4. H-4028 Debrecen

### Introduction

Materials law of continua (Fényes 1971, Asszonyi 1975, Asszonyi and Kapolyi 1976) can be determined from the law of the irreversible thermodynamics that states that the inhomogeneity of the characteristic intensive quantity of any interaction generates a conductive flow with an effect of equalizing inhomogeneities. The most general materials law has been determined by Asszonyi (1975) from Fényes's generalized form of Onsager's laws:

$$\text{with} \quad \mathbf{F} = \mathbf{L} \cdot \mathbf{u} \circ \nabla, \quad (1)$$

- $\mathbf{F}$  stress tensor
- $\mathbf{u}$  displacement vector,
- $\nabla$  Hamilton's differential operator,
- $\mathbf{u} \circ \nabla$  derivative displacement tensor (deformation tensor).

The matrix of momentum conduction tensor  $\mathbf{L}$  of fourth order is a positive definitive one and its 81 components are not independent of each other. Perfectly anisotropic media have a maximum of 21 independent coefficients. The number of independent coefficients for isotropic bodies is only 2. Though the rock in the infinite semi-space can by no means regarded as isotropic, it is still reasonable to investigate isotropic media because isotropy considerably simplifies the materials equation and, on the other hand, the physical equation of specially orthotropic materials being highly important in rock mechanics, can easily be determined from results obtained for isotropic materials (Asszonyi 1975). We will show the way how the equation of one of the rock mechanics' special materials models, the so-called Poynting–Thomson's standard body can be deduced from Eq. (1). Simultaneously, the physical meaning of rheological constants will also be interpreted in great detail.

### Materials equation of isotropic rock continua

The materials equation of isotropic continua can be obtained in the most easy way from Eq. (1) by considering symmetric tensors made of the derivative tensor  $\mathbf{u} \circ \nabla$ . There are only two such symmetric tensors and the stress tensor  $\mathbf{F}$  can be given as their linear combination (Asszonyi 1975):

$$\mathbf{F} = \lambda \frac{1}{2} [\nabla \circ \mathbf{u} + \mathbf{u} \circ \nabla] + \mu \nabla \mathbf{u}, \quad (2)$$

with  $\lambda$  and  $\mu$  denoting the two independent conduction coefficients.

Introducing the common tensor designation

$$\mathbf{D} = \frac{1}{2} [\nabla \circ \mathbf{u} + \mathbf{u} \circ \nabla] \quad (3)$$

it can be written

$$\mathbf{F} = \lambda \mathbf{D} + \mu \nabla \mathbf{u} \mathbf{l} \quad (4)$$

where  $\mathbf{D}$ , of course, does not denote the deformation tensor of common interpretation (Asszonyi 1975), but is a mere simplifying designation that in case of infinitesimal values, only can be regarded as a deformation in conventional sense. There is, of course, no problem in calling it deformation tensor, and we will use this term.

Let us now introduce the so-called stress deviator tensor

$$\mathbf{T} = \begin{vmatrix} \sigma_x - \sigma_0 & \tau_{yx} & \tau_{zx} \\ \tau_{xy} & \sigma_y - \sigma_0 & \tau_{zy} \\ \tau_{xz} & \tau_{yz} & \sigma_z - \sigma_0 \end{vmatrix}, \quad (5)$$

the stress sphere tensor

$$\mathbf{T}_0 = \begin{vmatrix} \sigma_0 & 0 & 0 \\ 0 & \sigma_0 & 0 \\ 0 & 0 & \sigma_0 \end{vmatrix}, \quad (6)$$

the deformation deviator tensor

$$\mathbf{E} = \begin{vmatrix} \varepsilon_x - \varepsilon_0 & \frac{1}{2} \gamma_{yx} & \frac{1}{2} \gamma_{zx} \\ \frac{1}{2} \gamma_{xy} & \varepsilon_y - \varepsilon_0 & \frac{1}{2} \gamma_{zy} \\ \frac{1}{2} \gamma_{xz} & \frac{1}{2} \gamma_{yz} & \varepsilon_z - \varepsilon_0 \end{vmatrix}, \quad (7)$$

and the deformation sphere tensor

$$\mathbf{E}_0 = \begin{vmatrix} \varepsilon_0 & 0 & 0 \\ 0 & \varepsilon_0 & 0 \\ 0 & 0 & \varepsilon_0 \end{vmatrix}, \quad (8)$$

with

$$\sigma_0 = \frac{1}{3} (\sigma_x + \sigma_y + \sigma_z) = \frac{1}{3} \text{inv}_1 \mathbf{F}, \quad (9)$$

$$\varepsilon_0 = \frac{1}{3} (\varepsilon_x + \varepsilon_y + \varepsilon_z) = \frac{1}{3} \text{inv}_1 \mathbf{D}. \quad (10)$$

Then, by distributing stress and deformation tensors

$$\mathbf{F} = \mathbf{T} + \mathbf{T}_0 \quad (11)$$

the materials equation can be written as (Asszonyi 1975)

$$\mathbf{D} = \mathbf{E} + \mathbf{E}_0, \quad (12)$$

$$\mathbf{T} = \lambda \mathbf{E}, \quad (13a)$$

$$\mathbf{T}_0 = (\lambda + 3\mu) \mathbf{E}_0. \quad (13b)$$

The conduction coefficients  $\lambda$  and  $\mu$  in Eqs (13) are scalar functions which depend on mechanical and thermodynamical data.

In Onsager's linear theory, the conduction coefficients "are considered as constants with regard to fluxes and forces in the linear law" (Gyarmati 1976) what means that in our case  $\lambda$  only depends on  $\dot{\mathbf{T}}, \dot{\mathbf{E}}, \ddot{\mathbf{E}}, \dots$  and on thermodynamical data. Assuming that the temperature is constant and the effects of the derivatives of higher than first order are negligible,  $\lambda$  depends only on  $\dot{\mathbf{T}}$  and  $\dot{\mathbf{E}}$ . Let us develop McLaurin's series of this function terminating it with the linear members:

$$\lambda = [\lambda]_{\substack{\dot{\mathbf{T}}=0 \\ \dot{\mathbf{E}}=0}} + \left[ \frac{\partial \lambda}{\partial \dot{\mathbf{T}}} \right]_{\substack{\dot{\mathbf{T}}=0 \\ \dot{\mathbf{E}}=0}} : \dot{\mathbf{T}} + \left[ \frac{\partial \lambda}{\partial \dot{\mathbf{E}}} \right]_{\substack{\dot{\mathbf{T}}=0 \\ \dot{\mathbf{E}}=0}} : \dot{\mathbf{E}}. \quad (14)$$

According to Eq. (13a),  $\lambda$  may depend through  $\mathbf{T}$  and  $\mathbf{E}$  on  $\dot{\mathbf{T}}$  and  $\dot{\mathbf{E}}$ , thus, applying the rule of differentiation of functions:

$$\left[ \frac{\partial \lambda}{\partial \dot{\mathbf{T}}} \right]_{0;0} = \left[ \frac{\partial \lambda}{\partial \mathbf{T}} : \frac{\partial \mathbf{T}}{\partial \dot{\mathbf{T}}} \right]_{0;0} = \mathbf{E}^{-1} : \left[ \frac{\partial \mathbf{T}}{\partial \dot{\mathbf{T}}} \right]_{0;0} \quad (15)$$

and

$$\left[ \frac{\partial \lambda}{\partial \dot{\mathbf{E}}} \right]_{0;0} = \left[ \frac{\partial \lambda}{\partial \mathbf{T}} : \frac{\partial \mathbf{T}}{\partial \dot{\mathbf{E}}} \right]_{0;0} = \mathbf{E}^{-1} : \left[ \frac{\partial \mathbf{T}}{\partial \dot{\mathbf{E}}} \right]_{0;0} \quad (16)$$

provided that  $\mathbf{E}$  as the measure of the inhomogeneity of the intensive quantity is independent of  $\dot{\mathbf{T}}$  and  $\dot{\mathbf{E}}$ .

Substituting Eqs (14), (15) and (16) into Eq. (13a), we have

$$\mathbf{T} = [\lambda]_{0;0} \mathbf{E} + \left[ \frac{\partial \mathbf{T}}{\partial \dot{\mathbf{E}}} \right]_{0;0} : \dot{\mathbf{E}} + \left[ \frac{\partial \mathbf{T}}{\partial \dot{\mathbf{T}}} \right]_{0;0} : \dot{\mathbf{T}}. \quad (17)$$

Assuming that the medium is isotropic, the tensors  $\left[ \frac{\partial \mathbf{T}}{\partial \dot{\mathbf{E}}} \right]_{0;0}$  and  $\left[ \frac{\partial \mathbf{T}}{\partial \dot{\mathbf{T}}} \right]_{0;0}$  of fourth order can be written as the products of a scalar figure and the unit tensor of fourth order:

$$\left[ \frac{\partial \mathbf{T}}{\partial \dot{\mathbf{E}}} \right]_{0;0} = 2\eta \delta, \quad (18)$$

$$\left[ \frac{\partial \mathbf{T}}{\partial \dot{\mathbf{T}}} \right]_{0;0} = -\tau \delta, \quad (19)$$

and by using the designations

$$[\lambda]_{0;0} = 2G, \quad (20)$$

$$\lambda + 3\mu = 3K \quad (21)$$

the equations of the well known Poynting–Thomson body are obtained:

$$\mathbf{T} = 2G\mathbf{E} + 2\eta\dot{\mathbf{E}} - \tau\dot{\mathbf{T}}, \quad (22a)$$

$$\mathbf{T}_0 = 3K\mathbf{E}_0. \quad (22b)$$

The materials constants can be interpreted more clearly when the equations are written for the uniaxial state of stress:

$$\sigma = [\lambda]_{\substack{\dot{\sigma}=0 \\ \dot{\varepsilon}=0}} \cdot \varepsilon + \left[ \frac{\partial \sigma}{\partial \dot{\varepsilon}} \right]_{\substack{\dot{\sigma}=0 \\ \dot{\varepsilon}=0}} \cdot \dot{\varepsilon} + \left[ \frac{\partial \sigma}{\partial \dot{\sigma}} \right]_{\substack{\dot{\sigma}=0 \\ \dot{\varepsilon}=0}} \cdot \dot{\sigma}, \quad (23)$$

and using the common designations, respectively

$$[\lambda]_{0;0} = E \quad (24)$$

$$\left[ \frac{\partial \sigma}{\partial \dot{\varepsilon}} \right]_{0;0} = \lambda \quad (25)$$

$$\left[ \frac{\partial \sigma}{\partial \dot{\sigma}} \right]_{0;0} = -\vartheta \quad (26)$$

we have

$$\sigma = E\varepsilon + \lambda\dot{\varepsilon} - \vartheta\dot{\sigma}, \quad (27)$$

with

$E$  — Young's modulus, MPa,

$\lambda$  — linear viscosity or creeping coefficient, MPah,

$\vartheta$  — relaxation constant, h.

One gets Eqs (27) and (22), too, if starts deducing from the definition of the elastic potential at isothermal processes, i.e. the free energy (Budó 1965, Posztnyikov 1969).

### Materials equations in the elastic zone

Equations (13) and—due to the limits considered—Eqs (22), too, are materials equations holding both in the elastic and plastic fields, but it has to be noted that the deviator- and sphere-tensors of stress, the deviator- and sphere-tensors of deformations as well as the coefficients mean here values of an elastic or plastic field. Let us once again write Eq. (22) with the variables denoting now the values of elastic state

$$\mathbf{T} = 2G\mathbf{E} + 2\eta\dot{\mathbf{E}} - \tau\dot{\mathbf{T}}, \quad (28a)$$

$$\mathbf{T}_0 = 3K\mathbf{E}_0. \quad (28b)$$

These equations characterize the behaviour of the elastic body in the form of differential equations.

If the differential equation (28a) is solved with respect to  $\mathbf{T}$ , an equivalent form, an integral equation of state is obtained. This form can easily be obtained by Laplace's transformation, too, which is especially suitable to describe simultaneously both the elastic and the plastic state:

$$\mathbf{T} = \frac{2\eta}{\tau}\mathbf{E} + \frac{2G\tau - 2\eta}{\tau^2} e^{-\frac{1}{\tau}t} \int_0^t e^{\frac{1}{\tau}t} \mathbf{E} dt. \quad (29)$$

The second member of the expression can be regarded as the convolution product of  $e^{\frac{1}{\tau}t}$  and  $\mathbf{E}$ . Using the rule of partial integration, another integral equation can be obtained where  $\dot{\mathbf{E}}$  is behind the integral sign:

$$\mathbf{T} = 2G\mathbf{E} + \frac{2\eta - 2G\tau}{\tau} e^{-\frac{1}{\tau}t} \int_0^t e^{\frac{1}{\tau}t} \dot{\mathbf{E}} dt. \quad (30)$$

One of the integral median theorems (Korn and Korn 1975) furnishes another equation of state especially suitable for the numerical solution of problems:

$$\mathbf{T} = \frac{2\eta}{\tau}\mathbf{E}(t) - \left(\frac{2\eta}{\tau} - 2G\right)\mathbf{E}(t_0), \quad (31)$$

whereas

$$0 < t_0 < t.$$

### Materials equation in the plastic zone

It is obvious from the aforementioned that materials equation valid for the plastic zone has also the shape of (13) and (22), respectively. Richter (1976) came to the same conclusions on the basis of different considerations. The materials equation suitable to characterize the rock behaviour in the plastic zone can be written as

$$\mathbf{T} = 2G_p\mathbf{E} + 2\eta_p\dot{\mathbf{E}} - \tau_p\dot{\mathbf{T}} \quad (32a)$$

with

$G_p$  — plastic shear modulus, MPa,

$\eta_p$  — plastic creeping modulus, MPah,

$\tau_p$  — plastic relaxation modulus, h,

and the equation of volumetric change will be

$$T_0 = 3K E_0, \quad (32b)$$

for compressible plastic materials and

$$E_0 = E_0^{\max} \quad (33)$$

for incompressible materials.

### Materials equation in the elastic and plastic zones

Eq. (28) characterizes the ideal case when deformations are elastic over the whole range, while Eq. (32) that when deformations can be regarded as plastic over the whole range.

If we assume that there is a limit in the range of deformations under which deformations are considered elastic and beyond which remaining deformations take place, i.e. the material does not regain its original state and shape after ceasing the loading, the question arises: Where is this limit? With other words the condition of plasticity as one of the basic questions in plastic theory, has to be defined. Asszonyi (1975) proved that the formation of the plastic state is connected with the level of energy brought into the system and not with the state of stress.

Theoretical and experimental investigations proved that the formation of the plastic state depends on the distortion work applied to the material. Until this work does not exceed a certain limit, deformations can be regarded as elastic, but the body is brought into plastic state as soon as distortion work exceeds it. Thus, the condition of plasticity can be written as (Asszonyi 1975)

$$U' = \int_0^E T : dE \geq U'_k. \quad (34)$$

If a further change of the volume of the body is not possible, i.e. the elastic work of volumetric change reached its maximum, a "fully developed plastic state" is formed (Asszonyi 1975)

$$\Phi_0 = \int_0^{E_0} T_0 : dE_0 = \Phi_0^{\max}. \quad (35)$$

Materials equation that equally holds for elastic and plastic state is obtained by transforming the equation of the plastic state into the elastic one. This can be done in the most easy way by the integral equation of state that gives the stress as a function of time. Let us denote the instant of the beginning of the plastic state, when distortion work reaches its limit, by  $t_0$ . The material keeps on staying in elastic state if

$$U' < U'_k$$

and

$$t < t_0,$$

and the materials equation can be written as

$$T = \frac{2\eta}{\tau} E(t) + \frac{2G\tau - 2\eta}{\tau^2} e^{-\frac{1}{\tau}t} \int_0^t e^{\frac{1}{\tau}t'} E(t') dt. \quad (36)$$

However, plastic state sets in if

$$U' \geq U'_k$$

and

$$t \geq t_0$$

while we have for the materials equation

$$T = T_0 + \frac{2\eta_p}{\tau_p} E(t - t_0) + \frac{2G_p\tau_p - 2\eta_p}{\tau_p^2} e^{-\frac{1}{\tau_p}(t - t_0)} \int_0^{t-t_0} \frac{1}{e^{\frac{1}{\tau_p}t'}} E(t') dt, \quad (37)$$

with

$$T_0 = \frac{2\eta}{\tau} E(t_0) + \frac{2G\tau - 2\eta}{\tau^2} e^{-\frac{1}{\tau}t_0} \int_0^{t_0} e^{\frac{1}{\tau}t'} E dt. \quad (38)$$

Equation (37) corresponds to Hohenemser–Prager's generalized body describing the model's behaviour in the form of an integral equation.

### Conclusions

Problems arising in mining industry require the use of rheological models, i.e. the understanding of rheology of rocks. It is, therefore, of great importance to clear the role of rheological models. It has been shown in the paper how one of the rock mechanics' special and important materials model, the equation of Poynting–Thomson's so-called standard body can be derived from the materials law originating from the basic equations of the irreversible thermodynamics. Simultaneously, the physical meaning of rock parameters has also been interpreted. The only approximation in our investigation was that the effect of the differential quotients of higher than first order was neglected. In the same sense the unknown function of momentum conduction coefficient  $\lambda$  was replaced by its tangent plane at  $\dot{\sigma} = 0$  and  $\dot{\varepsilon} = 0$ . The character of the approximation did not considerably restrict the range of validity of the original function, consequently the equations of state for both the elastic and the plastic zones could be determined. On the present level of our knowledge the effect of differential

quotients of higher order cannot be taken into account. Rock parameters can, of course, only be determined by *in-situ* measurements or in the lack of them by laboratory experiments if up-to-date laboratory facilities are available.

### References

- Asszonyi Cs 1975: On the rheological theory of rock continua. Doctor's Thesis (in Hungarian), Tatabánya
- Asszonyi Cs, Kapolyi L 1976: Determination of mechanical parameters of rocks. (In Hungarian) MTA VEAB Monográfiái, Veszprém
- Budó Á 1965: Mechanics. (In Hungarian) Tankönyvkiadó, Budapest
- Fényes I ed. 1971: Modern Concise Physical Encyclopaedia. (In Hungarian) Gondolat Könyvkiadó, Budapest
- Gyarmati I 1976: Non-equilibrium thermodynamics. (In Hungarian) Műszaki Könyvkiadó, Budapest
- Korn G A, Korn T M 1975: Mathematical handbook for engineers. (In Hungarian) Műszaki Könyvkiadó, Budapest
- Posztnyikov V S 1969: Internal separation in metals. (In Russian) Metallurgiya, Moscow
- Richter R 1976: Plastic state and deterioration of rocks. II. Materials equation of plastic rocks. (In Hungarian) *Bányászati és Kohászati Lapok*, *Bányászat*, 4, 282—286.



## PROPERTIES OF THE POYNTING-THOMSON STANDARD BODY DURING LOAD DECREASE

R HORVÁTH<sup>1</sup>

[Manuscript received May 11, 1984]

The parameters of the standard model frequently used in rockmechanical investigations can be determined by experiments only. Since in the analysis of experiments plastic properties of rocks have also to be taken into account, load decrease is an essential component of an experiment series on a certain specimen implying always elastic deformation. It is shown in the paper that creeping can also take place in elastic models during load decrease in dependence of the rate of load increase and decrease.

**Keywords:** creeping; elastic deformation; homogeneous materials; isotropic materials; load decrease; load increase; Poynting-Thomson body; rock continuum; stress tensor; uniaxial state of stress

### *Symbols*

$E$	Young's modulus
$t$	time
$\alpha$	ratio of rates of load decrease and increase
$\varepsilon$	strain
$\vartheta$	relaxation constant
$\lambda$	linear viscosity or creeping coefficient
$\sigma$	stress
$\sigma_a$	stress at the beginning of load decrease
$\dot{\sigma}_a$	rate of load decrease
$\dot{\sigma}_A$	rate of load increase

### **Introduction**

One of the basic equations of rock continua is the so-called materials equation. It shows the variation of the stress tensor during mechanical changes of state according to various materials structures. There is a general law describing this variation which holds for all mechanical processes of any materials system regarded as a continuum (Asszonyi 1975). In a part of rockmechanical investigations the material is considered homogeneous and isotropic and the materials equation of the rocks is represented by

<sup>1</sup> Technical High School of Building Industry Ybl Miklós, Landler J. u. 2—4. H-4027 Debrecen

Poynting-Thomson's materials model obtained by compromises (Asszonyi and Kapolyi 1976, Asszonyi and Richter 1974). Materials parameters in the model are essential for the understanding and "designing" of processes around mine excavations. The rock parameters are determined by laboratory experiments. For a careful design and a proper analysis of experiments a thorough knowledge of the properties of the model is required. The paper is not aimed at analysing the properties of this model in great detail, only the process of load decrease in laboratory experiments being a rather neglected problem, will be investigated here.

### Behaviour of the standard model at uniform load decrease

For the sake of simplicity the investigation will be carried out for a uniaxial state of stress. The materials equation of the model can be written (Asszonyi and Richter 1974):

$$\sigma = E\varepsilon + \lambda\dot{\varepsilon} - \vartheta\dot{\sigma}, \quad (1)$$

with

$\sigma$  — stress, MPa

$\varepsilon$  — strain

$E$  — Young's modulus

$\lambda$  — linear viscosity or creeping coefficient, MPah

$\vartheta$  — relaxation constant.

Let the load decrease be performed at a constant rate (Fig. 1)

$$\sigma = \sigma_a - \dot{\sigma}_a t, \quad (2)$$

whereas

$$\dot{\sigma}_a = \frac{\sigma_a}{t_1} > 0.$$

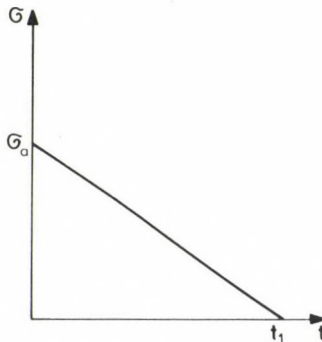


Fig. 1. Load decrease at a constant rate

Solving Eq. (1) we have

$$\varepsilon = -\frac{\dot{\sigma}_a}{E}t + \frac{\sigma_a + \dot{\sigma}_a\left(\frac{\lambda}{E} - \vartheta\right)}{E}(1 - e^{-\frac{E}{\lambda}t}) + \varepsilon_a e^{-\frac{E}{\lambda}t}, \quad (3)$$

whereas  $\sigma_a$  and  $\varepsilon_a$  denote stress and strain at the beginning of the load decrease.

In the analysis of Eq. (3) the question arises, whether function  $\varepsilon(t)$  decreases monotonously similarly to function  $\sigma(t)$  or has it a monotonously increasing section, too, within the interval  $0 \leq t \leq t_1$ ? To solve the problem the function has to be analysed by applying differential calculus. According to the theorem of monotonous increase, the differential quotient  $\frac{d\varepsilon}{dt}$  has to be investigated. The place of maximum or minimum can be found by putting  $\frac{d\varepsilon}{dt} = 0$ , i.e. applying the necessary condition of maxima and minima.

Having differentiated and solved the equation, we see that the function can have a maximum or a minimum at

$$t_0 = \frac{\lambda}{E} \ln \frac{\sigma_a - \dot{\sigma}_a\left(\vartheta - \frac{\lambda}{E}\right) - E\varepsilon_a}{\lambda} \frac{E}{\dot{\sigma}_a}. \quad (4)$$

The analysis of the sign of the first derivative shows that if a maximum or a minimum does exist in the interval  $(0; t_1)$ , the sign is positive in the interval  $(0; t_0)$ , i.e. the curve increases here strictly monotonously. In the interval  $(t_0; t_1)$ , however, the sign is negative, i.e. the curve decreases here strictly monotonously. The change of sign of the first derivative and the second derivative show that the function has a maximum here. Consequently, if the maximum falls into the interval  $(0; t_1)$ , then  $\varepsilon$  continues to increase at the beginning of load and starts to decrease only later.

The possible shapes of curve  $\varepsilon(t)$  are illustrated in Fig. 2. Let us now investigate at which of the various rates of load increase will lie the maximum within the interval  $(0; t_1)$ .

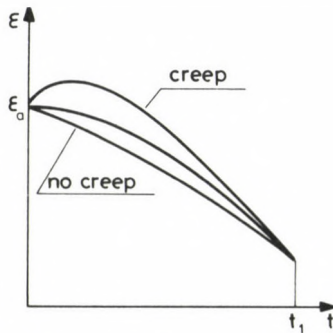


Fig. 2. Possible shapes of the curve  $\varepsilon(t)$

a) In case of a very fast load increase ( $\dot{\sigma}_A \rightarrow \infty$ ):

$$\varepsilon_a = \frac{\vartheta}{\lambda} \sigma_a$$

$$t_0 = \frac{\lambda}{E} \ln \left[ \left( 1 - \frac{\vartheta E}{\lambda} \right) \left( 1 + \frac{t_1 E}{\lambda} \right) \right] < t_1,$$

and

$$t_0 \geq 0$$

if

$$t_1 \geq \frac{\vartheta}{1 - \frac{\vartheta E}{\lambda}}. \quad (5)$$

b) In case of a very slow load increase ( $\dot{\sigma}_A \rightarrow 0$ ):

$$\varepsilon_a = \frac{\sigma_a}{E}$$

$$t_0 = \frac{\lambda}{E} \ln \left( 1 - \frac{\vartheta E}{\lambda} \right) < 0,$$

consequently, the maximum does not lie in the interval  $(0; t_1)$ .

c) In case of a load increase at a rate of  $\dot{\sigma}_A = \text{constant} > 0$ :

$$\varepsilon_a = \frac{1}{E} \left[ \sigma_a - \dot{\sigma}_A \left( \frac{\lambda}{E} - \vartheta \right) \left( 1 - e^{-\frac{E}{\lambda} \frac{\sigma_a}{\dot{\sigma}_A}} \right) \right]$$

$$t_0 = \frac{\lambda}{E} \ln \frac{\frac{\lambda}{E} - \vartheta + \frac{\dot{\sigma}_A}{\sigma_a} \left( \frac{\lambda}{E} - \vartheta \right) \left( 1 - e^{-\frac{E}{\lambda} \frac{\sigma_a}{\dot{\sigma}_A}} \right)}{\lambda} E.$$

Let us introduce the designation

$$\alpha = \frac{\dot{\sigma}_A}{\sigma_a} > 0.$$

We have

$$t_0 = \frac{\lambda}{E} \ln \frac{\left( \frac{\lambda}{E} - \vartheta \right) \left( 1 + \frac{1}{\alpha} - \frac{1}{\alpha} e^{-\frac{E}{\lambda} \alpha t_1} \right) E t_1}{\frac{\lambda}{E}}$$

and

$$t_0 \geq 0$$

if

$$t_1 \geq \frac{1}{\alpha} \frac{\lambda}{E} \ln \frac{1}{1 - \alpha \frac{\lambda}{9E}} \tag{6}$$

The inequality (6) is transformed into inequality (5) in the extreme case of infinitely fast load increase ( $\dot{\sigma}_A \rightarrow \infty, \alpha \rightarrow 0$ ).

The results show that with sufficiently long time of load decrease  $t_1$ , i.e. at a sufficiently slow or, in extreme case, at an infinitely slow load decrease, the creeping of the material dominates and the load increase considerably influences the results obtained during load decrease. The possible cases are illustrated in the co-ordinate systems  $\sigma - \varepsilon$  in Figs 3, 4 and 5. The curves of load decrease in case of very fast load increase are shown in Fig. 3 (case a), those in case of very slow load increase in Fig. 4 (case b) and those in case of constant load increase in Fig. 5 (case c).

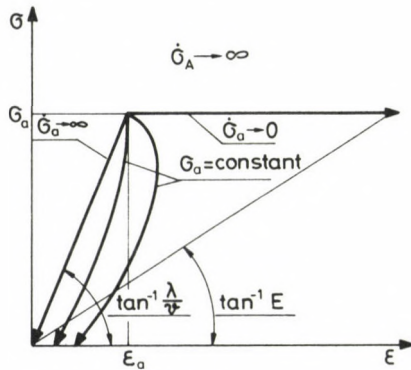


Fig. 3. Load decrease after a very fast load increase

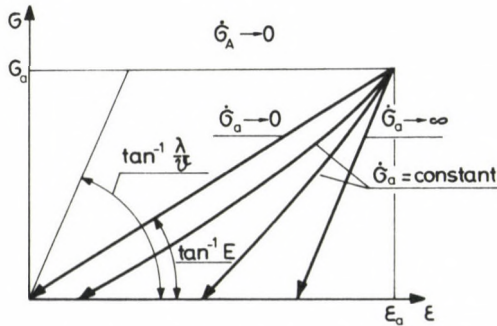


Fig. 4. Load decrease after a very slow load increase

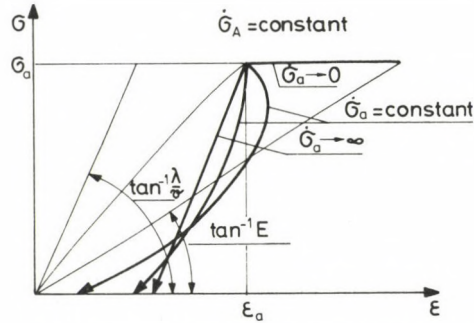


Fig. 5. Load decrease after a load increase at a constant rate

### Conclusions

The so-called standard body shows several interesting properties. Under certain conditions the body also shows creeping during load decrease and the load increase considerably affects the process of load decrease. The body shows the signs of a certain "memory". It has been shown that if the time of load decrease is sufficiently great, i.e. the rate of load decrease is sufficiently low, and the body is not in Hookean state, then—at the beginning of the load decrease—it continues its former deformation trend in spite of the load decrease.

These results can be used at the evaluation of uniaxial laboratory experiments for the determination of the rheological constants characterizing the elastic state.

### References

- Asszonyi Cs 1975: On the rheological theory of rock continua. Doctor's Thesis (in Hungarian), Tatabánya
- Asszonyi Cs, Kapolyi L 1976: Determination of mechanical parameters of rocks. (In Hungarian) MTA VEAB Monográfiái, Veszprém
- Asszonyi Cs, Richter R 1974: Introduction into the rheological theory of rock mechanics. (In Hungarian) NIM TK, Budapest
- Filcek H 1963: Stan naprezenia i odkształcenia wokółi wyrobiska chodnikowego jako funkcja czasu. Zeszyty Problemowe Górnictwa, Komitet górnictwa PAN 1
- Kleczeck Z 1969: Wpłyn czasu na sytozymalosc skal. Zeszyty Naukowe Akademii Gorniczo-Hutniczej, Gornictwo Z-15, Krakow, 67–73

- treble underlining: bold-face italics
- red underlining: Greek letters
- green underlining: script letters.

Rules for mathematical-physical notations:

- trigonometric, logarithmic, analytic symbols, symbols for units and functions are in roman type (not underlined)
- letter symbols in mathematical and physical formulas, scalars, and subscripts of algebraic and physical quantities are in italics (underlined)
- vectors, matrices, operators in probability theory are in bold-face roman type (double underlining)
- tensors, operators and some special functions are in script letters (green underlining). These cannot be bold.
- Greek letters (red underlining) cannot be bold or extra bold type (thus they cannot be used for vectors or tensors)
- void upper lines e.g. for vectors
- avoid possible confusion between o (letter) and 0 (zero), l (letter) and 1 (one),  $\nu$  (Greek nu) and  $v$ ,  $u$  (letters) etc.
- explain ambiguous or uncommon symbols by making marginal notes in pencil
- be careful about superscripts and subscripts
- formulae must be numbered consecutively with the number in parentheses to the right of the formula. References in text to the equations may then usually be made by the number in parenthesis. When the word equation is used with a number, it is to be abbreviated, Eq. or Eqs in the plural
- the International System of Units (SI) should be used.

Authors are liable for the cost of alteration in the *proofs*. It is, therefore, the responsibility of the author to check the text for errors of facts before submitting the paper for publication.

3. *References* are accepted only in the Harvard system. Citations in the text should be as:

- ... (Bomford 1971) ... or Bomford (1971)
- ... (Brosche and Sündermann 1976) ...
- ... (Gibbs et al. 1976b) ...

The list of references should contain names and initials of all authors (the abbreviation et al. is not accepted here); for *journal articles* year of publication, the title of the paper, title of the journal abbreviated, volume number, first and last page.

For *books* or *chapters in books*, the title is followed by the publisher and place of publication. All items must appear both in the text and references.

Examples:

- Bomford G 1971: *Geodesy*. Clarendon Press, Oxford
- Brosche P, Sündermann J 1976: Effects of oceanic tides on the rotation of the earth. Manuscript. Univ. of Bonn
- Buntebarth G 1976: Temperature calculations on the Hungarian seismic profile-section NP-2. In: *Goelectric and Geothermal Studies (East-Central Europe, Soviet Asia)*, KAPG Geophysical Monograph. Akadémiai Kiadó, Budapest, 561–566.
- Gibbs N E, Poole W G, Stockmeyer P K 1976a: An algorithm for reducing the bandwidth and profile of a sparse matrix. *SIAM J. Numer. Anal.*, 13, 236–250.
- Gibbs N E, Poole W G, Stockmeyer P K 1976b: A comparison of several bandwidth and profile reduction algorithms. *ACM Trans. on Math. Software*, 2, 322–330.
- Szarka L 1980: Potenciálterképezés analóg modellezéssel (Analogue modeling of potential mapping). *Magyar Geofizika*, 21, 193–200.

4. *Footnotes* should be typed on separate sheets.

5. *Legends* should be short and clear. The place of the tables and figures should be indicated in the text, on the margin.

6. *Tables* should be numbered serially with Roman numerals. Vertical lines are not used.

All the illustrations should contain the figure number and author's name in pencil on the reverse.

*Figures* will be redrawn. Therefore the most important point is clearness of the figures, even pencil-drawings are accepted (with a duplicate).

*Photographs* and *half-tone* illustrations should be sharp and well contrasted.

If a specific reduction or enlargement is required, please indicate this in blue pencil on the figure.

The editors will send information to the first author about the *arrival* and acceptance of the papers. A galley proof is also sent to the first author for *correction*. Hundred *offprints* are supplied free of charge.

Periodicals of the Hungarian Academy of Sciences are obtainable  
at the following addresses:

**AUSTRALIA**

C.B.D. LIBRARY AND SUBSCRIPTION SERVICE  
Box 4886, G.P.O., *Sydney N.S.W. 2001*  
COSMOS BOOKSHOP, 145 Ackland Street  
*St. Kilda (Melbourne), Victoria 3182*

**AUSTRIA**

GLOBUS, Höchstädtplatz 3, *1206 Wien XX*

**BELGIUM**

OFFICE INTERNATIONAL DE LIBRAIRIE  
30 Avenue Marnix, *1050 Bruxelles*  
LIBRAIRIE DU MONDE ENTIER  
162 rue du Midi, *1000 Bruxelles*

**BULGARIA**

HEMUS, Bulvar Ruszki 6, *Sofia*

**CANADA**

PANNONIA BOOKS, P.O. Box 1017  
Postal Station "B", *Toronto, Ontario M5T 2T8*

**CHINA**

CNPICOR, Periodical Department, P.O. Box 50  
*Peking*

**CZECHOSLOVAKIA**

MAD'ARSKÁ KULTURA, Národní třída 22  
*115 66 Praha*  
PNS DOVOZ TISKU, Vinohradská 46, *Praha 2*  
PNS DOVOZ TLAČE, *Bratislava 2*

**DENMARK**

EJNAR MUNKSGAARD, Norregade 6  
*1165 Copenhagen K*

**FEDERAL REPUBLIC OF GERMANY**

KUNST UND WISSEN ERICH BIEBER  
Postfach 46, *7000 Stuttgart 1*

**FINLAND**

AKATEEMINEN KIRJAKAUPPA, P.O. Box 128 SF-00101  
*Helsinki 10*

**FRANCE**

DAWSON-FRANCE S. A., B. P. 40, *91121 Palaiseau*  
EUROPÉRIODIQUES S. A., 31 Avenue de Versailles, *78170*  
*La Celle St. Cloud*  
OFFICE INTERNATIONAL DE DOCUMENTATION ET  
LIBRAIRIE, 48 rue Gay-Lussac  
*75240 Paris Cedex 05*

**GERMAN DEMOCRATIC REPUBLIC**

HAUS DER UNGARISCHEN KULTUR  
Karl Liebknecht-Straße 9, *DDR-102 Berlin*  
DEUTSCHE POST ZEITUNGSVERTRIEBSAMT Straße der  
Pariser Kommüne 3-4, *DDR-104 Berlin*

**GREAT BRITAIN**

BLACKWELL'S PERIODICALS DIVISION  
Hythe Bridge Street, *Oxford OX1 2ET*  
BUMPUS, HALDANE AND MAXWELL LTD.  
Cowper Works, *Olney, Bucks MK46 4BN*  
COLLET'S HOLDINGS LTD., Denington Estate *Wellingbo-*  
*rough, Northants NN8 2QT*  
WM. DAWSON AND SONS LTD., Cannon House *Folkstone,*  
*Kent CT19 5EE*  
H. K. LEWIS AND CO., 136 Gower Street  
*London WC1E 6BS*

**GREECE**

KOSTARAKIS BROTHERS INTERNATIONAL  
BOOKSELLERS, 2 Hippokratous Street, *Athens-143*

**HOLLAND**

MEULENHOF-BRUNA B. V., Beulingstraat 2,  
*Amsterdam*  
MARTINUS NIJHOFF B.V.  
Lange Voorhout 9-11, *Den Haag*

**SWETS SUBSCRIPTION SERVICE**

347b Heereweg, *Lisse*

**INDIA**

ALLIED PUBLISHING PRIVATE LTD., 13/14  
Asaf Ali Road, *New Delhi 110001*  
150 B-6 Mount Road, *Madras 600002*  
INTERNATIONAL BOOK HOUSE PVT. LTD.  
Madame Cama Road, *Bombay 400039*  
THE STATE TRADING CORPORATION OF INDIA LTD.,  
Books Import Division, Chandralok 36 Janpath, *New Delhi*  
*110001*

**ITALY**

INTERSCIENTIA, Via Mazzè 28, *10149 Torino*  
LIBRERIA COMMISSIONARIA SANSONI, Via Lamarmora 45,  
*50121 Firenze*  
SANTO VANASIA, Via M. Macchi 58  
*20124 Milano*  
D. E. A., Via Lima 28, *00198 Roma*

**JAPAN**

KINOKUNIYA BOOK-STORE CO. LTD.  
17-7 Shinjuku 3 chome, Shinjuku-ku, *Tokyo 160-91*  
MARUZEN COMPANY LTD., Book Department, P.O. Box  
5050 Tokyo International, *Tokyo 100-31*  
NAUKA LTD. IMPORT DEPARTMENT  
2-30-19 Minami Ikebukuro, *Toshima-ku, Tokyo 171*

**KOREA**

CHULPANMUL, *Phenjan*

**NORWAY**

TANUM-TIDSKRIFT-CENTRALEN A.S., Karl Johansgatan  
41-43, *1000 Oslo*

**POLAND**

WĘGIERSKI INSTYTUT KULTURY, Marszałkowska 80,  
*00-517 Warszawa*  
CKP-I W, ul. Towarowa 28, *00-958 Warszawa*

**ROUMANIA**

D. E. P., *Bucuresti*  
ILEXIM, Calea Grivitei 64-66, *Bucuresti*

**SOVIET UNION**

SOJUZPECHAT — IMPORT, *Moscow*  
and the post offices in each town  
MEZHDUNARODNAYA KNIGA, *Moscow G-200*

**SPAIN**

DIAZ DE SANTOS, Lagasca 95, *Madrid 6*

**SWEDEN**

GUMPERTS UNIVERSITETSBOOKHANDEL AB  
Box 346, *401 25 Göteborg 1*

**SWITZERLAND**

KARGER LIBRI AG, Petersgraben 31, *4011 Basel*

**USA**

EBSCO SUBSCRIPTION SERVICES  
P.O. Box 1943, *Birmingham, Alabama 35201*  
F. W. FAXON COMPANY, INC.  
15 Southwest Park, *Westwood Mass. 02090*  
READ-MORE PUBLICATIONS, INC.  
140 Cedar Street, *New York, N. Y. 10006*

**YUGOSLAVIA**

JUGOSLOVENSKA KNJIGA, Terazije 27, *Beograd*  
FORUM, Vojvode Mišića 1, *21000 Novi Sad*